Institutional Repository - Research Portal
Dépôt Institutionnel - Portail de la Recherche
researchportal.unamur.be
University of Namur

THESIS / THÈSE

**DOCTOR OF SCIENCES**

# Elaboration of quantum chemistry approaches for the simulation and the interpretation of vibrational Sum Frequency Generation signatures of functionalized surfaces

Tetsassi Feugmo, Conrard Giresse

*Award date:*
2018

*Awarding institution:*
University of Namur

Link to publication

**General rights**
Copyright and moral rights for the publications made accessible in the public portal are retained by the authors and/or other copyright owners and it is a condition of accessing publications that users recognise and abide by the legal requirements associated with these rights.

- Users may download and print one copy of any publication from the public portal for the purpose of private study or research.
- You may not further distribute the material or use it for any profit-making activity or commercial gain
- You may freely distribute the URL identifying the publication in the public portal ?

**Take down policy**
If you believe that this document breaches copyright please contact us providing details, and we will remove access to the work immediately and investigate your claim.

Download date: 05. May. 2023

Université de Namur
Faculté des Sciences
Département de Chimie
Laboratoire de Chimie Théorique

# Elaboration of quantum chemistry approaches for the simulation and the interpretation of vibrational Sum Frequency Generation signatures of functionalized surfaces

Thèse présentée par
Conrard Giresse Tetsassi Feugmo

*en vue de l'obtention du grade de Docteur en Sciences*

**Composition du jury**

Dr. Bertrand Busson (Université Paris Sud)
Dr. Yves Caudano (UNamur, Co-Promoteur)
Dr. Francesca Cecchet (UNamur)
Prof. Benoît Champagne (UNamur, Co-Promoteur)
Dr. Julien Guthmuller (Gdansk University of Technology)
Dr. Vincent Liégeois (UNamur, Président du jury)
Prof. Daniel Vercauteren (UNamur)

2018

UNIVERSITÉ DE NAMUR
Faculté des Sciences
Rue de Bruxelles, 61, B-5000 Namur, Belgium

**Elaboration of quantum chemistry approaches for the simulation and the interpretation of vibrational Sum Frequency Generation signatures of functionalized surfaces**

by Conrard Giresse Tetsassi Feugmo

## *Abstract*

In this thesis, I developed an approach to simulate and interpret the Sum-Frequency Generation (SFG) spectra of molecules adsorbed on different substrates. Vibrational SFG spectroscopy is a technique based on nonlinear optics to characterize surfaces. This approach encompasses two steps. First, the molecular properties (vibrational frequencies, IR and Raman quantities) are evaluated using methods implemented in standard quantum chemistry programs. Second, the macroscopic optical responses (the second-order nonlinear optical susceptibility tensors) of the adsorbate on its substrate are determined within the three-layer model of the interface. To carry out this latter step, a homemade Python program, named "`SFG-from-QM`", has been elaborated from scratch and the necessary equations have been implemented in it to account for the parameters of SFG measurements. This program can be installed on different operating systems (Mac OS X, Unix, Linux, Windows). The particularities of the approach consist in *i)* including a fragment of the substrate in the system during the quantum chemistry calculations. In particular, the ONIOM embedding scheme has been employed; *ii)* performing the calculations of molecular properties using first principles methods. Moreover, though most of these calculations are carried out at DFT levels, for the first time SFG spectra have been simulated using molecular properties evaluated at the CCSD level. These latter constitute reference data to substantiate DFT calculations. This approach has been illustrated in the case of organic monolayers (alkyl and alkylsilane chains) covalently bonded to inorganic surfaces [H−Si(111) and $SiO_2$] and for different polarization combinations (ppp, ssp, and sps), showing a good agreement with experiment and therefore demonstrating its ability to unravel the surface structure. Moreover, equations for SERS enhancement factor have been derived and applied in the case of thiophenol molecules adsorbed on gold surfaces, highlighting its dependency on the nature of the adsorption site.

**Élaboration d'une approche de chimie quantique pour la simulation et l'interprétation des signatures vibrationnelles de Génération de Fréquence Somme de surfaces fonctionnalisées**

par Conrard Giresse Tetsassi Feugmo

# *Résumé*

Au cours de cette thèse, j'ai développé une approche pour simuler et interpréter les spectres de génération de la fréquence somme (SFG) de molécules adsorbées sur différents substrats. La spectroscopie vibrationnelle SFG est une technique qui s'appuie sur l'optique nonlinéaire pour caractériser des surfaces. Cette approche comprend deux étapes. Tout d'abord, les propriétés moléculaires (fréquences de vibration, intensités IR et Raman) sont évaluées à l'aide de méthodes implementées dans les programmes standard de chimie quantique. Deuxièmement, les réponses optiques macroscopiques (le tenseur de susceptibilité optique nonlinéaire de second ordre) de l'adsorbat sur son substrat sont déterminées grâce au modèle à trois couches de l'interface. Pour réaliser cette dernière étape, un programme en Python fait maison et nommé "`SFG-from-QM`", a été élaboré complètement et les équations nécessaires y ont été implémentées pour prendre en compte les paramètres d'une mesure SFG. Ce programme peut être installé sur différents systèmes d'exploitation (Mac OS X, Unix, Linux, Windows). Les particularités de l'approche consistent à *i)* inclure un fragment du substrat dans le système lors des calculs de chimie quantique. En particulier, le schéma d'incorporation ONIOM a été utilisé; *ii)* effectuer les calculs des propriétés moléculaires en utilisant les méthodes des premiers principes. De plus, bien que la plupart de ces calculs soient effectués en recourant à la DFT, des spectres SFG ont été simulés pour la première fois en utilisant des propriétés moléculaires évaluées au niveau CCSD. Ces derniers constituent des données de référence pour corroborer les calculs DFT. Cette approche a été illustrée dans le cas de monocouches organiques (chaînes d'alkyle et d'alkylsilane) liées par covalence à des surfaces inorganiques [H−Si(111) et $SiO_2$] et pour différentes combinaisons de polarisation (ppp, ssp, et sps), montrant un bon accord avec l'expérience et démontrant ainsi sa capacité à révéler la structure de la surface. De plus, des expressions ont été dérivées pour le facteur d'exaltation relatif au phénomène SERS et elles ont été appliquées au cas de molécules de thiophénol adsorbées sur des surfaces d'or. En particulier, nous avons souligné que les signatures Raman et les exaltations dépendent de la nature du site d'absorption.

*"Comprendre la grandeur.*

*Nous devons apporter la joie de Jésus partout où nous irons ; il nous a accordé ce don. Nous avons été vraiment bénis, et les bénédictions continueront à jaillir de sa source éternelle d'amour. Il y aura des moments où nous ne comprendrons pas pourquoi les mauvaises choses se produisent, pourquoi le mal prévaut, pourquoi les ennuis nous envahissent, pourquoi même nous sommes ici sur terre. C'est alors que nous devrons prier, cherchant à comprendre la grandeur, cherchant à comprendre l'amour et cherchant à comprendre les autres. C'est avec cette attitude que nous pourrons vraiment apprécier le plan divin, que nous pourrons recevoir la grandeur que Dieu désire pour nous, parce qu'alors nous aimerons, et l'amour conquiert tout. La grandeur se trouve dans la croix. C'est le don le plus grand du ciel, c'est par elle que le Christ nous a donné la vie. ."*

Un père légionnaire du Christ

Huit ans au Laboratoire de Chimie Théorique de l'Université de Namur, c'est huit ans d'apprentissage de nouvelles notions, d'un nouveau mode de vie, huit ans de collaboration avec des personnes venant de tout horizon et huit ans de découverte de nouvelles régions, de nouveaux plats, de nouvelles bières. C'est huit ans à interrompre sans cesse Benoît Champagne, Vincent Liégeois, Yves Caudano, Francesca Cecchet, Pierre Beaujean, Orian Louant et Jean Quertinmont avec mes questions incessantes.

C'est une aventure assez anodine qui débuta en 2010 par un e-mail au Prof. Benoît Champagne. Depuis lors il y a eu plusieurs évènements, allant d'un master complémentaire en nanotechnologies, passant par l'épreuve du FRIA, la recherche continue de financements, puis un poste d'assistant aboutissant à la présentation d'une thèse de doctorat.

Pour tout cela, j'aimerais adresser un tout grand merci à mon promoteur le Prof. Benoît Champagne, de m'avoir donné l'opportunité d'acccomplir ce travail, pour son encadrement dans la recherche, dans l'enseignement et dans la rédaction.

Je remercie aussi mon autre promoteur le Dr. Yves Caudano, pour son encadrement et toutes les belles discussions scientifiques que nous avons eues au quotidien.

Un tout grand merci au Dr. Vincent Liégeois pour toute sa disponibilité, les discussions scientifiques, ses relectures et pour tout l'apprentissage notamment dans la programmation.

Je remercie Dr. Francesca Cecchet pour tous nos échanges notamment en ce qui concerne les conditions expérimentales, pour les manipulations effectuées.

Je remercie les membres du LCT, passé et présent, particulièrement Pierre Beaujean, Orian Louant et Jean Quertinmont pour leur disponibilité, leur soutien tant dans la recherche que dans la vie au quotidien

Je remercie aussi Fréderic Wautelet et Laurent Demelenne pour le support informatique, leur interventions quotidiennes.

Ces années n'ont pas juste été consacrées à la recherche, l'enseignement fut aussi une belle composante. J'aimerais donc remercier tous mes collègues assistants principalement le Dr. Diane Baillieul et le Dr. Isabelle Ravet pour leur encadrement et leurs conseils.

Une thèse n'est pas juste le laboratoire ou l'équipe de recherche, elle englobe tous les aspects de notre vie sentimentale, familiale et de société. Cette période n'a pas été faite que de joie ; il y a eu des moments difficiles et très difficiles même, notamment mon cancer. J'aimerais donc remercier mon épouse Marie-Paule Sangwa pour son soutien infini, ma famille, mes amis, principalement Jacques Kamdem, et toutes les personnes qui m'ont apporté leur soutien.

Pour terminer un ami m'a dit un jour : "Conrard on ne raconte pas une histoire qui est encore en cours". Donc affaire à suivre ....

*This is for you dear aunt, Marlyse TETSASSI. You left fingerprints of grace on my live. You shan't be forgotten.*

# Contents

# Abbreviations

| | |
|---|---|
| **ACP** | **A**tomic **C**ontribution **P**atterns |
| **AO** | **A**tomic **O**rbitals |
| **CC** | **C**oupled **C**luster |
| **CCSD** | **C**oupled **C**luster **S**ingles **D**oubles |
| **CG** | **C**oarse-**G**rained |
| **CI** | **C**onfiguration **I**nteraction |
| **CM** | **C**ontinuum **M**odel |
| **DFT** | **D**ensity **F**unctional **T**heory |
| **EELS** | **E**lectron **E**nergy **L**oss **S**pectroscopy |
| **EF** | **E**nhancement **F**actor |
| **GCM** | **G**roup **C**oupling **M**atrices |
| **GGA** | **G**eneralized **G**radient **A**pproximation |
| **HF** | **H**artree-**F**ock |
| **IR** | **I**nfra **R**ed |
| **LCAO** | **L**inear **C**ombination of **A**tomic **O**rbitals |
| **LDA** | **L**ocal **D**ensity **A**pproximation |
| **MBPT** | **M**any **B**ody **P**erturbation **T**heory |
| **MC SCF** | **M**ulti-**C**onfigurational **S**elf-**C**onsistent **F**ield |
| **MD** | **M**olecular **D**ynamics |
| **MM** | **M**olecular **M**echanics |
| **MO** | **M**olecular **O**bitals |
| **ONIOM** | **O**wn **N**-layered **I**ntegrated Molecular **O**rbital and Molecular **M**echanics |
| **QM** | **Q**uantum **M**echanics |
| **RAIRS** | **R**eflection **A**bsorption **I**nfrared **S**pectroscopy |
| **SCF** | **S**elf-**C**onsistent **F**ield |
| **SE** | **S**emi **E**mpirical |
| **SEIRAS** | **S**urface **E**nhanced **I**nfrared **A**bsorption **S**pectroscopy |
| **SERS** | **S**urface **E**nhanced **R**aman **S**pectroscopy |
| **SFG** | **S**um-**F**requency **G**eneration |

# Part I

# Introduction

# INTRODUCTION

## Motivations

Vibrations contain significant information on the structural, electronic and optical properties of molecules and supramolecular assemblies. Bringing them out to light and interpreting them allows us to understand the structure of these species as well as their organizations, their modifications following external disturbances (electrical stimuli, presence of ions, pH variation ...), their reactivity, as well as the dynamics of their processes of exchange and energy dissipation. In addition to traditional vibrational spectroscopies based on infrared light absorption or Raman inelastic scattering, many other vibrational techniques have been developed over the last three decades. Based on interactions between light and matter, they probe different facets of structures and molecular properties. These include nonlinear spectroscopies, those involving electronic resonance phenomena and techniques specific to chiral structures. The Sum-Frequency Generation (SFG) [1, 2] belongs to the first category while the resonant Raman technique [3] relates to the second. The Vibrational Raman optical activity (VROA) [4] is specific to chiral structures.

In recent years, many works were published in which the structural and electronic properties of chemi- and/or physi-sorbed molecules are calculated using the density functional theory (DFT) [5]. Much less has been achieved with respect to the evaluation of molecular vibrational, electrical and optical properties, such as polarizability or electronic absorption spectra. In addition, the formation of organic monolayers covalently-bonded to inorganic surfaces is a topic of intense research activity since many decades [6]. The main advantage of organic monolayers is to add functionality to the inorganic surface via suitable adaptation of their surface properties. Indeed, these functionalized materials keep the characteristics of the bulk material (electrical, magnetic, optical, mechanical and structural), while their surface properties (wetting, passivation, biochemical affinity, etc.) are tuned through a nanosized grafting [7, 8]. Furthermore, the monolayer-modified system is a suitable template for the controlled immobilization of biomolecules, for instance to build highly sensitive biosensing devices, including electrodes for molecular recognition [9]. The covalent attachment can be performed via coupling reactions between the chemically activated surfaces and molecules. Among these, silicon is one of the most widely used semiconductors in modern technology and organic monolayers covalently bonded to

silicon surfaces have gained much attention since their introduction [10], owing to their well-defined structure and the possibility to introduce diverse electrical and optical functionalities to the system [6, 11–13]. Nevertheless, the lack of control of those processes at the molecular level might result in the formation of multilayers where the molecules have lost active conformation or orientation [14–16]

My project concerns (simply resonant) SFG spectroscopy. Since its first observe by in 1987 by Zhu, Suhr, and Shen [17], SFG has been developed to become a powerful spectroscopic technique, currently employed in a broad range of multidisciplinary research fields, including surface science, materials chemistry, biophysics, and electrochemistry. Indeed, its intrinsic surface specificity and extreme sensitivity makes SFG a technique of choice to probe systems at their molecular scale. The SFG activity appears in the vicinity of the vibrational resonances, i.e. when the frequency of the infrared excitation wave (IR) corresponds to a vibrational transition ($\omega = 2\pi\nu = \Delta E/\hbar$). In the harmonic approximation, the amplitude of the transition is related to a vibrational first hyperpolarizability

$$\beta_{ijk} \propto \sum_{p=1}^{3N-6} \frac{\left(\frac{\partial \alpha_{ij}}{\partial Q_p}\right)_e \left(\frac{\partial \mu_k}{\partial Q_p}\right)_e}{\omega_p - \omega_{IR} - i\Gamma_p}, \tag{1}$$

whose elements in the numerator also determine the activities in IR and Raman spectroscopy. This expression informs us that a vibration mode will be active in SFG if the mode is simultaneously active in IR and Raman. More generally, this condition can only be fulfilled if the molecule is not centrosymmetric and its organization on the macroscopic scale is also non-centrosymmetric. These conditions of symmetry make SFG a selective and interface-specific vibrational spectroscopy (the SFG response of an isotropic medium is zero). Then, SFG has been used to analyze interfacial structures, providing qualitative and quantitative insights into surface coverage [18–20], composition and environment [21], as well as molecular order and orientation [20, 22–24].

## Contributions

Revealing (supra) molecular structures from experimental spectra is a challenge and often the extracted information remains very cursory in comparison to the complexity and richness of the signal. Reaching a deep level of interpretation is therefore a challenge to which theoretical simulations and more particularly those derived from quantum mechanics can contribute. In this last decade, research in the Theoretical Chemistry Laboratory (UNamur) was carried out in this framework and focused on the development of methods for simulation and interpretation of vibrational spectra, Raman, hyper-Raman, Raman resonant, VROA [25] and also SFG [26] in collaboration with the Laser and Spectroscopy Laboratory (UNamur). Thus, recent work has

shown how the experimental/theoretical amalgam provides access to structural information on the organization of self-assembled organic layers [22, 27].

My doctoral thesis aims at developing quantum chemistry approaches to simulate and interpret vibrational SFG signatures of functionalized surfaces with the particularity of i) including the substrate in the system during the calculations; ii) performing the simulations with first-principles calculations. My work will lead to the development of powerful tools for simulating and interpreting SFG spectra and the implementation of a new computational program to improve the level of analysis. My program can therefore be used in the areas of functionalized surface design. From a simulation point of view, the approach that I develop i) includes the characterization of molecular responses at the quantum level, ii) takes into account the optical properties of the medium by a three-layer model [The interface and the two media (bulk) it separates] determining the Fresnel factors and iii) evaluates the macroscopic response (the second-order susceptibility), by a sum on the different molecular components.

My thesis is divided in two parts. The first part consists of five chapters and is dedicated to the theoretical background. Indeed, in the first chapter, we derive explicit expressions for the response functions (electric susceptibilities) that describe the linear and nonlinear interactions between a system and an external electric field. In the second chapter, I review the basic concepts of electromagnetic wave propagation in linear and nonlinear materials (Fresnel formula). Then, I derive the expressions of the molecular first (polarizability) and second-order (hyperpolarizability) response functions through use of the density matrix formulation of quantum mechanics. These molecular response functions are used to give the expressions of the macroscopic response (the nonlinear optical susceptibility). Chapter 3 is dedicated to the vibrational spectroscopies. It starts by a quick review on molecular vibrations and the harmonic approximation. Then, I describe the basic theoretical aspects of IR, Raman, and SFG spectroscopies. The fourth chapter focus on the quantum chemistry background. The general framework of the Schrödinger equation and the Hamiltonian operator are presented, as well as the Hartree-Fock, the Coupled Cluster, and the Density Functional Theory approximation methods. Finally, in the fifth chapter I describe my approach and the homemade program developed for the simulation and the interpretation of SFG signatures.

In the second part, Chapters 6 to 9, results are presented under the form of the corresponding publications. Given that the SFG intensity is directly related to the IR and Raman activities, I start by some simulations of IR and Raman signatures of aromatic thiols adsorbed on small gold clusters (Chapter 6). Then, Chapters 7 and 8 report SFG simulations on alkyl chains covalently bonded to hydrogen-terminated Si(111) substrates and alkylsilanes adsorbed onto amorphous silica surfaces. Considering that all the previous calculations were done at the DFT level, Chapter 9 presents the first SFG spectra based on molecular properties calculated at the coupled cluster single and double (CCSD) level of approximation, which are simulated for interfacial model alkyl chains.

# References

[1] Shen, Y. R. *Nature* **1989**, *337*, 519–525.

[2] Shen, Y. R. *Fundamentals of Sum-Frequency Spectroscopy*; Cambridge Molecular Science; Cambridge University Press, 2016.

[3] Long, D. A. *The Raman Effect*; A Unified Treatment of the Theory of Raman Scattering by Molecules; Wiley, 2002.

[4] Barron, L. D. *Molecular Light Scattering and Optical Activity*, 2nd ed.; Cambridge University Press, 2004.

[5] (a) Peverati, R.; Baldridge, K. K. *J. Chem. Theory Comput.* **2008**, *4*, 2030–2048; (b) Morari, C.; Rungger, I.; Rocha, A. R.; Sanvito, S.; Melinte, S.; Rignanese, G.-M. *ACS Nano* **2009**, *3*, 4137–4143; (c) Goel, S.; Velizhanin, K. A.; Piryatinski, A.; Tretiak, S.; Ivanov, S. A. *J. Phys. Chem. Lett.* **2010**, *1*, 927–931; (d) Harb, M.; Rabilloud, F.; Simon, D. *J. Phys. B-At. Mol. Opt.* **2011**, *44*; (e) Chen, K. J.; Charaf-Eddin, A.; Selvam, B.; Boucher, F.; Laurent, A. D.; Jacquemin, D. *J. Phys. Chem. C* **2015**, *119*, 3684–3696; (f) Prajongtat, P.; Suramitr, S.; Nokbin, S.; Nakajima, K.; Mitsuke, K.; Hannongbua, S. *J. Mol. Graph. Model.* **2017**, *76*, 551–561.

[6] Ulman, A. *Chem. Rev.* **1996**, *96*, 1533–1554.

[7] Yamashita, R.; Takeuchi, Y.; Kikuchi, H.; Shirai, K.; Yamauchi, T.; Tsubokawa, N. *Polym. J.* **2006**, *38*, 844–851.

[8] Li, H.; Yan, Y.; Liu, B.; Chen, W.; Chen, S. *Powder Technol.* **2007**, *178*, 203–207.

[9] Wagner, P.; Nock, S.; Spudich, J. A.; Volkmuth, W. D.; Chu, S.; Cicero, R. L.; Wade, C. P.; Linford, M. R.; Chidsey, C. E. D. *J. Struct. Biol.* **1997**, *119*, 189–201.

[10] Linford, M. R.; Fenter, P.; Eisenberger, P. M. *J. Am. Chem. Soc.* **1995**, *117*, 3145–3155.

[11] Faucheux, A.; Gouget-Laemmel, A. C.; Henry de Villeneuve, C.; Boukherroub, R.; Ozanam, F.; Allongue, P.; Chazalviel, J.-N. *Langmuir* **2006**, *22*, 153–162.

[12] Touahir, L.; Allongue, P.; Aureau, D.; Boukherroub, R.; Chazalviel, J. N.; Galopin, E.; Gouget-Laemmel, A. C.; de Villeneuve, C. H.; Moraillon, A.; Niedziółka-Jönsson, J.; Ozanam, F.; Andresa, J. S.; Sam, S.; Solomon, I.; Szunerits, S. *Bioelectrochemistry* **2010**, *80*, 17–25.

[13] Seitz, O.; Fernandes, P. G.; Mahmud, G. A.; Wen, H.-C.; Stiegler, H. J.; Chapman, R. A.; Vogel, E. M.; Chabal, Y. J. *Langmuir* **2011**, *27*, 7337–7340.

[14] Ye, S.; Saito, T.; Nihonyanagi, S.; Uosaki, K.; Miranda, P. B.; Kim, D.; Shen, Y.-R. *Surface Science* **2001**, *476*, 121–128.

[15] Ishibashi, T.-a.; Ara, M.; Tada, H.; Onishi, H. *Chem. Phys. Lett.* **2003**, *367*, 376–381.

[16] Asanuma, H.; Noguchi, H.; Uosaki, K.; Yu, H.-Z. *J. Phys. Chem. B* **2006**, *110*, 4892–4899.

[17] Zhu, X. D.; Suhr, H.; Shen, Y. R. *Phys. Rev. B* **1987**, *35*, 3047–3050.

[18] Wang, H.-f.; Gan, W.; Lu, R.; Rao, Y.; Wu, B.-h. *Int. Rev. Phys. Chem.* **2005**, *24*, 191–256.

[19] (a) Jacob, J. D. C.; Rittikulsittichai, S.; Lee, T. R.; Baldelli, S. *J. Phys. Chem. C* **2013**, *117*, 9355–9365; (b) Zhang, C.; Myers, J. N.; Chen, Z. *Langmuir* **2014**, *30*, 12541–12550, PMID: 25263030.

[20] Roeters, S. J.; Van Dijk, C. N.; Torres-Knoop, A.; Backus, E. H. G.; Campen, R. K.; Bonn, M.; Woutersen, S. *J. Phys. Chem. A* **2013**, *117*, 6311–6322.

[21] (a) Tang, C. Y.; Allen, H. C. *J. Phys. Chem. A* **2009**, *113*, 7383–7393; (b) Park, Y. B.; Lee, C. M.; Kafle, K.; Park, S.; Cosgrove, D. J.; Kim, S. H. *Biomacromolecules* **2014**, *15*, 2718–2724; (c) Ennist, J. H.; Gobrogge, E. A.; Schlick, K. H.; Walker, R. A.; Cloninger, M. J. *ACS Appl. Mater. Interfaces* **2014**, *6*, 18087–18097; (d) Meltzer, C.; Paul, J.; Dietrich, H.; Jäger, C. M.; Clark, T.; Zahn, D.; Braunschweig, B.; Peukert, W. *J. Am. Chem. Soc.* **2014**, *136*, 10718–10727; (e) Sorenson, S. A.; Patrow, J. G.; Dawlaty, J. M. *J. Am. Chem. Soc.* **2017**, *139*, 2369–2378.

[22] Cecchet, F.; Lis, D.; Guthmuller, J.; Champagne, B.; Fonder, G.; Mekhalif, Z.; Caudano, Y.; Mani, A. A.; Thiry, P. A.; Peremans, A. *J. Phys. Chem. C* **2010**, *114*, 4106–4113.

[23] (a) Mani, A. A.; Schultz, Z. D.; Champagne, B.; Humbert, C.; Dreesen, L.; Gewirth, A. A.; White, J. O.; Thiry, P. A.; Peremans, A.; Caudano, Y. *App. Sur. Sci.* **2004**, *237*, 445–450; (b) Mani, A. A.; Schultz, Z. D.; Caudano, Y.; Champagne, B.; Humbert, C.; Dreesen, L.; Gewirth, A. A.; White, J. O.; Thiry, P. A.; Peremans, A. *J. Phys. Chem. B* **2004**, *108*, 16135–16138; (c) Lis, D.; Peremans, A.; Sartenaer, Y.; Caudano, Y.; Mani, A. A.; Dreesen, L.; Thiry, P. A.; Guthmuller, J.; Champagne, B.; Cecchet, F. *J. Phys. Chem. C* **2009**, *113*, 9857–9864; (d) Lis, D.; Cecchet, F. *ChemPhysChem* **2016**, *17*, 2645–2649.

[24] (a) Verreault, D.; Hua, W.; Allen, H. C. *J. Phys. Chem. Lett.* **2012**, *3*, 3012–3028; (b) Rich, C. C.; Mattson, M. A.; Krummel, A. T. *J. Phys. Chem. C* **2016**, *120*, 6601–6611; (c) Takeshita, N.; Okuno, M.; Ishibashi, T.-a. *Phys. Chem. Chem. Phys.* **2017**, *19*, 2060–2066; (d) Jang, J. H.; Lydiatt, F.; Lindsay, R.; Baldelli, S. *J. Phys. Chem. A* **2013**, *117*, 6288–6302; (e) Lu, X.; Myers, J. N.; Chen, Z. *Langmuir* **2014**, *30*, 9418–9422; (f) Wang, Z.; Han, X.; He, N.; Chen, Z.; Brooks, C. L. *J. Phys. Chem. B* **2014**, *118*, 12176–12185, PMID: 25265065; (g) Liu, S.; Fourkas, J. T. *J. Phys. Chem. B* **2014**, *118*, 8406–8419.

[25] (a) Quinet, O.; Champagne, B. *J. Chem. Phys.* **2001**, *115*, 6293–6299; (b) Quinet, O.; Champagne, B. *J. Chem. Phys.* **2002**, *117*, 2481–2488; (c) Quinet, O.; Champagne, B.; Rodriguez, V. *J. Chem. Phys.* **2006**, *124*, 244312; (d) Liǵeois, V.; Ruud, K.; Champagne, B.

*J. Chem. Phys.* **2007**, *127*, 204105; (e) Guthmuller, J.; Champagne, B.; Moucheron, C.; De Mesmaeker, A. K. *J Phys. Chem. B* **2010**, *114*, 511–520.

[26] Guthmuller, J.; Cecchet, F.; Lis, D.; Caudano, Y.; Mani, A. A.; Thiry, P. A.; Peremans, A.; Champagne, B. *ChemPhysChem* **2009**, *10*, 2132–2142.

[27] Cecchet, F.; Lis, D.; Guthmuller, J.; Champagne, B.; Caudano, Y.; Silien, C.; Mani, A. A.; Thiry, P. A.; Peremans, A. *ChemPhysChem* **2010**, *11*, 607–615.

# Part II

# Theoretical Background

# Chapter 1

# Radiation-Matter Interactions: Nonlinear Optics

The field of Nonlinear optics (NLO) is concerned with understanding the radiation-matter interactions. When the material response, i.e. the electric polarization $\vec{P}$, is a nonlinear function of the applied electromagnetic field $\vec{E}$ of the light.

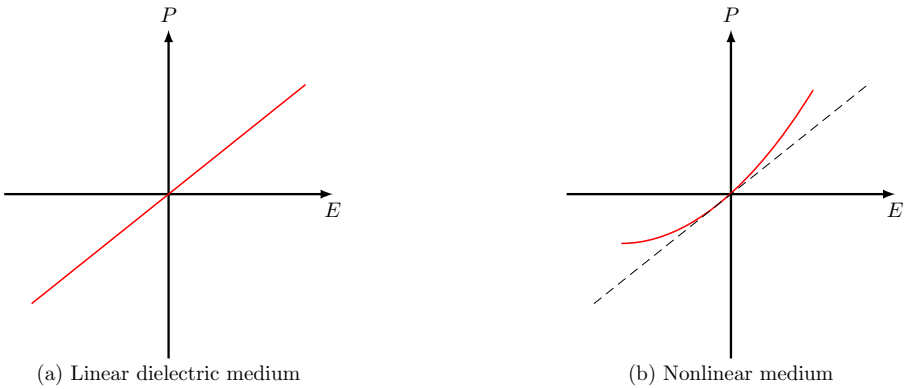


(a) Linear dielectric medium (b) Nonlinear medium

FIGURE 1.1: The relation between the polarization vector and electric field

Indeed, if the incident field is weak and the medium isotropic, the induced dipoles are proportional to the electric field (Fig. 1.1a) and aligned along this field. The material behaves as a linear dielectrics. The dipole moment per unit volume or the polarization $\vec{P}$ of medium is then:

$$\begin{aligned} \vec{P} &\equiv \vec{P}^{(0)} + \vec{P}^{(1)} \\ &\equiv \vec{P}^{(0)} + \chi^{(1)} \cdot \vec{E} \end{aligned} \tag{1.1}$$

where $\vec{E}$ is the applied field, $\vec{P}^{(0)}$ is the static polarization, and $\chi^{(1)}$ the first-order susceptibility (linear).

On the contrary, if the incident field is strong, the dipoles do not vary linearly with the applied field (Fig. 1.1b). $\vec{P}$ is no more parallel to $\vec{E}$ and can point in any direction, depending on the direction of the electric field and on the material anisotropy. To account for this, the susceptibility (which relates $\vec{P}$ and $\vec{E}$) must be a tensor. The polarization of the medium $\vec{P}$ is then:

$$\begin{aligned}\vec{P} &\equiv \vec{P}^{(0)} + \vec{P}^{(1)} + \vec{P}^{(2)} + \dots \\ &\equiv \vec{P}^{(0)} + \chi^{(1)} \cdot \vec{E} + \chi^{(2)} : \vec{E}\vec{E} + \dots \end{aligned} \tag{1.2}$$

where $\chi^{(2)}$ is the second-order susceptibility characterizing the nonlinear response of the medium.

In order to understand wave propagation in nonlinear media and the resulting phenomena, one must solve two coupled problems: (i) the radiation of an electromagnetic field by the oscillation of the charges and the nonlinear response of materials to the fields; (ii) how the various multipole moments are affected by light depending on the variation of the electric field from point to point in the material. These require an understanding of both the nonlinear Maxwell equations as well as the mechanisms of the nonlinear response of the material at the quantum level.

In this chapter, we shall derive explicit expressions for the response functions that describe the interactions of a system and an external electric field, based on the lecture notes of Kuzyk [1] and the book of Barnerjee [2]. Then, we review some of the properties of optical waves propagating through a medium. To this end, we enunciate Maxwell's equations and derive the wave equations in the case of Sum Frequency Generation (SFG). In addition Fresnel formulas are generalized for the three layer model.

## 1.1 Response functions

When the applied electric field strength is much smaller than the electric fields that hold an atom or molecule together the nonlinear properties of a material are described by expanding the polarization in power series of the electric field. For a pure electric case it reads:

$$\begin{aligned} P(\vec{E}) &= \vec{P}^{(0)}(\vec{E}) + \vec{P}^{(1)}(\vec{E}) + \vec{P}^{(2)}(\vec{E}) + \dots \\ \vec{P} &= \sum_{n=0}^{\infty} \vec{P}^{(n)}(\vec{r}, t). \end{aligned} \tag{1.3}$$

In the time domain formulation, $i$-component of the first-order polarization reads

$$P_i^{(1)}(\vec{r}, t) = \varepsilon_0 \int_{space} \mathrm{d}\vec{\mathrm{R}} \int_{-\infty}^{+\infty} \mathrm{d}\tau \; T_{ij}^{(1)}(\vec{r}, t; \vec{\mathrm{R}}, \tau) E_j(\vec{\mathrm{R}}, \tau), \tag{1.4}$$

where $T_{ij}(\vec{r}, t; \vec{\mathrm{R}}, \tau)$ is the response function, which carries all of the informations that relate the applied electric field to the polarization:

- $T_{ij}(\vec{r}, t; \vec{\mathrm{R}}, \tau)$ is a tensor: it accounts for the anisotropy of the material.
- The polarization at one point $\vec{r}$ of the material is determined by the fields at other points $\vec{\mathrm{R}}$ of the material, thus $T_{ij}(\vec{r}, t; \vec{\mathrm{R}}, \tau)$ is non local and the integration is carried out over the whole space.
- The polarization at a given time $t$ depends on the electric field at previous times $\tau$, thus it is also "non local" in time and retardation effects are accounted for by performing the integration over time.

Let's consider only the temporal dependence at a particular point in space. In addition, assuming that the response function is local: i.e. the polarization at a point $\vec{r}$ depends only on the value of the field at this point $\vec{r}$ and the materials is homogeneous,

$$P_i^{(1)}(\vec{r}, t) = \varepsilon_0 \int_{-\infty}^{+\infty} T_{ij}^{(1)}(t, \tau) E_j(\vec{r}, \tau)\, \mathrm{d}\tau. \tag{1.5}$$

This equation is characteristic of a linear system whose response to an impulse $\delta(t-\tau)$ is equal to $T_{ij}^{(1)}(t, \tau)$. If the system is time-invariant, $T_{ij}^{(1)}(t, \tau) = T_{ij}^{(1)}(t - \tau)$, then Eq. (1.5) reads

$$P_i^{(1)}(\vec{r}, t) = \varepsilon_0 \int_{-\infty}^{+\infty} T_{ij}^{(1)}(t - \tau) E_j(\vec{r}, \tau)\, \mathrm{d}\tau. \tag{1.6}$$

If we assume that $T^{(1)}$ obeys the causality condition $T_{ij}^{(1)}(t-\tau) = 0$ for $\tau > t$ (i.e. the polarization is only possible after the application of the field) and defining $\tau' = t - \tau$, Eq. (1.6) reads

$$P_i^{(1)}(\vec{r}, t) = \varepsilon_0 \int_{0}^{+\infty} T_{ij}^{(1)}(\tau') E_j(\vec{r}, t - \tau')\, \mathrm{d}\tau' \tag{1.7}$$

This is the polarization of a material at time $t$ due to the fields acting locally over all times in the past.

### 1.1.1 Frequency domain of response functions: electric susceptibilities

Often it is more convenient and appropriate to consider the polarization in the frequency domain [1]. The Fourier transforms of the electric field are defined by:

$$E_j(t) = \int_{-\infty}^{+\infty} \mathrm{d}\omega E_j(\omega) e^{-i\omega t}, \tag{1.8}$$

and

$$E_j(\omega) = \frac{1}{2\pi} \int_{-\infty}^{+\infty} \mathrm{d}t E_j(t) e^{i\omega t}. \tag{1.9}$$

By introducing Eq. (1.8) into Eq. (1.7), one obtains

$$P_i^{(1)}(t) = \varepsilon_0 \int_0^{+\infty} T_{ij}^{(1)}(\tau') \int_{-\infty}^{+\infty} E_j(\omega) e^{-i\omega(t-\tau')} \mathrm{d}\omega \mathrm{d}\tau',$$

$$= \varepsilon_0 \int_{-\infty}^{+\infty} \left( \int_0^{+\infty} T_{ij}^{(1)}(\tau') e^{i\omega\tau'} d\tau' \right) E_j(\omega) e^{-i\omega t} \mathrm{d}\omega, \tag{1.10}$$

$$= \varepsilon_0 \int_{-\infty}^{+\infty} \chi_{ij}^{(1)}(-\omega;\omega) E_j(\omega) e^{-i\omega t} \mathrm{d}\omega. \tag{1.11}$$

Here we introduce the first-order electric susceptibility[1]

$$\chi_{ij}^{(1)}(-\omega;\omega) = \int_0^{+\infty} T_{ij}^{(1)}(\tau') e^{i\omega\tau'} \mathrm{d}\tau'. \tag{1.12}$$

Then, one transforms the polarization into frequency space according to,

$$P_i^{(1)}(\omega) = \frac{1}{2\pi} \int_{-\infty}^{+\infty} P_i^{(1)}(t) e^{i\omega t} \mathrm{d}t, \tag{1.13}$$

substituting Eq. (1.11) into Eq. (1.13) gives

$$P_i^{(1)}(\omega) = \frac{1}{2\pi} \varepsilon_0 \int_{-\infty}^{+\infty} \int_{-\infty}^{+\infty} \chi_{ij}^{(1)}(-\omega_p;\omega_p) E_j(\omega_p) e^{-i\omega_p t} e^{i\omega t} \mathrm{d}\omega_p \mathrm{d}t. \tag{1.14}$$

Considering that

$$\delta(\omega_p - \omega) = \frac{1}{2\pi} \int_{-\infty}^{+\infty} e^{-i(\omega_p - \omega)t} \mathrm{d}t, \tag{1.15}$$

[1]Throughout our text we introduce the notation $\chi^{(n)}(-\omega_{out};\omega_{in})$. The negative sign on the outgoing frequencies represents energy leaving the material, whereas the positive frequencies to the right of the semicolon represent energy entering the system. This notation explicitly denotes energy conservation where, $\sum \omega_{in} = \sum \omega_{out}$.

we obtain

$$P_i^{(1)}(\omega) = \int_{-\infty}^{+\infty} \varepsilon_0 \chi_{ij}^{(1)}(-\omega_p, \omega_p) E_j(\omega_p) \delta(\omega_p - \omega) \mathrm{d}\omega_p,$$

$$= \varepsilon_0 \chi_{ij}^{(1)}(-\omega, \omega) E_j(\omega). \tag{1.16}$$

In the frequency domain, the linear polarization describes a simple relationship between the electric field and the first-order electric susceptibility. The susceptibility is defined as the Fourier transform of the response function.

### 1.1.2 Nonlinear response

The nonlinear response can be found with the same procedures. For the second order case, we begin with the relationship between the contribution to the second-order polarization $\boldsymbol{P_i^{(2)}}(t)$ and the response function $T_{ijk}^{(2)}$,

$$P_i^{(2)}(t) = \varepsilon_0 \int_{-\infty}^{+\infty} \int_{-\infty}^{+\infty} T_{ijk}^{(2)}(\tau_p, \tau_q) E_j(t - \tau_p) E_k(t - \tau_q) \mathrm{d}\tau_p \mathrm{d}\tau_q$$

$$= \varepsilon_0 \int_{-\infty}^{+\infty} \int_{-\infty}^{+\infty} T_{ijk}^{(2)}(\tau_p, \tau_q) \left( \int_0^{+\infty} E_j(\omega_p) e^{-i\omega_p(t-\tau_p)} d\omega_p \right) \left( \int_0^{+\infty} E_k(\omega_q) e^{-i\omega_q(t-\tau_q)} \mathrm{d}\omega_q \right) \mathrm{d}\tau_p \mathrm{d}\tau_q$$

$$= \varepsilon_0 \int_{-\infty}^{+\infty} d\omega_p \int_{-\infty}^{+\infty} \mathrm{d}\omega_q \int_0^{+\infty} \mathrm{d}\tau_p \int_0^{+\infty} \mathrm{d}\tau_q \, T_{ijk}^{(2)}(\tau_p, \tau_q) e^{i\omega_p \tau_p} e^{i\omega_q \tau_q} E_j(\omega_p) E_k(\omega_q) e^{-i\omega_p t} e^{-i\omega_q t}. \tag{1.17}$$

Then, we simplify the expression by introducing the second-order susceptibility,

$$\chi_{ijk}^{(2)}(-\omega; \omega_p, \omega_q) = \int_0^{+\infty} \mathrm{d}\tau_p \int_0^{+\infty} \mathrm{d}\tau_q \, T_{ijk}^{(2)}(\tau_p, \tau_q) e^{i\omega_p \tau_p} e^{i\omega_q \tau_q} \tag{1.18}$$

The second-order polarization, then, is related to the second-order susceptibility by

$$P_i^{(2)}(t) = \varepsilon_0 \int_{-\infty}^{+\infty} \mathrm{d}\omega_p \int_{-\infty}^{+\infty} \mathrm{d}\omega_q \, \chi_{ijk}^{(2)}(-\omega; \omega_p, \omega_q) E_j(\omega_p) E_k(\omega_q) e^{-i\omega_p t} e^{-i\omega_q t}. \tag{1.19}$$

Again, applying the inverse Fourier transform of $P_i^{(2)}(t)$, one obtains

$$P_i^{(2)}(\omega) = \frac{1}{2\pi}\varepsilon_0 \int_{-\infty}^{+\infty} d\omega_p \int_{-\infty}^{+\infty} \mathrm{d}\omega_q \int_{-\infty}^{+\infty} \mathrm{d}t\ \chi_{ijk}^{(2)}(-\omega;\omega_p,\omega_q)E_j(\omega_p)E_k(\omega_q)e^{-i(\omega_p+\omega_q-\omega)t},$$

$$= \varepsilon_0 \int_{-\infty}^{+\infty} \mathrm{d}\omega_p \int_{-\infty}^{+\infty} \mathrm{d}\omega_q\ \chi_{ijk}^{(2)}(-\omega;\omega_p,\omega_q)E_j(\omega_p)E_k(\omega_q)\delta(\omega_p+\omega_q-\omega),$$

$$= \varepsilon_0 \int_{-\infty}^{+\infty} \chi_{ijk}^{(2)}(-\omega;\omega_p,\omega_q)E_j(\omega_p)E_k(\omega_q)\mathrm{d}\omega_q, \qquad \text{with} \quad \omega = \omega_p + \omega_q. \tag{1.20}$$

Then, if the radiations ($E_k(\omega_q)$) are mono-chromatics like for laser, Eq. (1.20) reads

$$P_i^{(2)}(\omega) = \varepsilon_0 \chi_{ijk}^{(2)}(-\omega;\omega_p,\omega_q)E_j(\omega_p)E_k(\omega_q) \tag{1.21}$$

In general, the polarization of a material depends on the response functions that characterize it, and can be expressed as

$$P_i = P_i^{(0)} + \varepsilon_0 \sum_{j=X,Y,Z} \chi_{ij}^{(1)} E_j + \varepsilon_0 \sum_{j=X,Y,Z} \sum_{k=X,Y,Z} \chi_{ijk}^{(2)} E_j E_k + \ldots, \tag{1.22}$$

where $P_i$ is the $i$-component of the polarization. The first two terms refer to linear optics, whereas the $\chi^{(n)}$ ($n \geq 2$) are the nonlinear terms.

## 1.2 Wave propagation

### 1.2.1 Maxwell's equations

The fundamental theory of electromagnetic fields is based on Maxwell's equations. In the differential form, they are expressed as[2]

$$\vec{\nabla} \cdot \vec{\boldsymbol{E}} = \frac{\boldsymbol{\rho}}{\varepsilon_0} \qquad \text{Gauss's law} \tag{1.23}$$

$$\vec{\nabla} \cdot \vec{\boldsymbol{B}} = 0 \qquad \text{Gauss's for magnetism} \tag{1.24}$$

$$\vec{\nabla} \times \vec{\boldsymbol{E}} + \frac{\partial \vec{\boldsymbol{B}}}{\partial t} = 0 \qquad \text{Maxwell-Faraday equation} \tag{1.25}$$

$$\vec{\nabla} \times \vec{\boldsymbol{B}} - \mu_0\varepsilon_0 \frac{\partial \vec{\boldsymbol{E}}}{\partial t} = \mu_0 \vec{\boldsymbol{J}} \qquad \text{Maxwell-Ampère equation,} \tag{1.26}$$

[2]Throughout the text, we use the bold for quantities with complex components that vary in time

where $\vec{\boldsymbol{E}}$ [$\mathrm{V}\cdot\mathrm{m}^{-1}$] and $\vec{\boldsymbol{B}}$ [$\mathrm{J}\cdot\mathrm{A}^{-1}\cdot\mathrm{m}^{-2}$] are the electric field strength and the magnetic flux density, respectively. $\vec{\boldsymbol{J}}$ [$\mathrm{A}\cdot\mathrm{m}^{-2}$] is the current density and $\boldsymbol{\rho}$ [$\mathrm{C}\cdot\mathrm{m}^{-3}$] denotes the volume electric charge density. $\vec{\boldsymbol{J}}$ and $\boldsymbol{\rho}$ are the sources generating the electromagnetic fields. $\varepsilon_0$ [$8.85\times10^{-12}\,\mathrm{C}\cdot\mathrm{V}^{-1}\cdot\mathrm{m}^{-1}$] is the electric permittivity and $\mu_0$ [$4\pi\times10^{-7}\,\mathrm{J}\cdot\mathrm{A}^{-2}\cdot\mathrm{m}^{-1}$] the magnetic permeability of vacuum.

Moreover, the electric and magnetic flux densities are related to the the electric and magnetic field by the so called the constitutive relations,

$$\vec{\boldsymbol{D}} = \varepsilon\vec{\boldsymbol{E}} = \varepsilon_0\vec{\boldsymbol{E}} + \vec{\boldsymbol{P}} \tag{1.27}$$

$$\vec{\boldsymbol{B}} = \mu\vec{\boldsymbol{H}} = \mu_0\vec{\boldsymbol{H}} + \vec{\boldsymbol{M}} \tag{1.28}$$

where $\vec{\boldsymbol{H}}$ [$\mathrm{A}\cdot\mathrm{m}^{-1}$] is the magnetic field strength, and $\vec{\boldsymbol{D}}$ [$\mathrm{C}\cdot\mathrm{m}^{-2}$] the electric flux density. $\varepsilon$ and $\mu$ are the electric permittivity and magnetic permeability of the medium, respectively. $\vec{\boldsymbol{P}}$ and $\vec{\boldsymbol{M}}$ are the polarization and the magnetization of the medium, respectively. The charge and current densities read

$$\boldsymbol{\rho} = \boldsymbol{\rho_f} - \vec{\nabla}\cdot\vec{\boldsymbol{P}} \tag{1.29}$$

$$\vec{\boldsymbol{J}} = \vec{\boldsymbol{J}}_{\boldsymbol{f}} + \frac{\partial\vec{\boldsymbol{P}}}{\partial t} + \vec{\nabla}\times\vec{\boldsymbol{M}} + \cdots \tag{1.30}$$

Here, one identifies the charge density due to the polarization of the material as $\vec{\nabla}\cdot\vec{\boldsymbol{P}}$, and the current due to the polarization and magnetization of the material as $\dfrac{\partial\vec{\boldsymbol{P}}}{\partial t}$ and $\vec{\nabla}\times\vec{\boldsymbol{M}}$, respectively. $\boldsymbol{\rho_f}$ is the free charges density and $\vec{\boldsymbol{J}}_{\boldsymbol{f}}$ the free charges current.

### 1.2.2 Propagation of plane waves at the interface of two homogeneous media

Here, we are interested by the reflection and the refraction of plane waves at the interface of two homogeneous media. Indeed, when a wave passes through an interface its properties can be modified: i.e the direction of propagation, the speed of propagation, as well as the amplitude and the phase of the field. In the following, we will discuss the first two properties, relying on the approaches presented in the books of Barnerjee [2] and Boyd [3] as well as that presented in the thesis of Caudano [4]. To that end, we consider a plane wave incident from a transparent medium (Fig. 1.2) with permittivity $\varepsilon_I$ and propagating in a lossy[3] medium characterized by the complex permittivity $\varepsilon_T(\omega) = \varepsilon_T^{'}(\omega) + i\varepsilon_T^{''}(\omega)$. $\theta_i$, $\theta_r$, and $\theta_t$ are the incidence, the reflection, and the refraction angles, respectively.

[3] A medium in which an amount of the energy of a propagating electromagnetic wave is absorbed per unit distance traveled by the wave

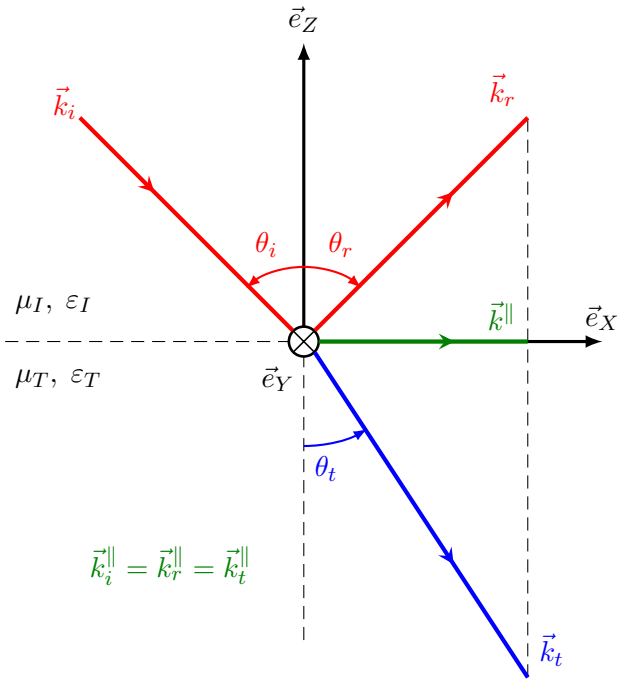


FIGURE 1.2: Illustration of Snell-Descartes Law

The electric field vectors are represented by plane waves of the form

$$\vec{\boldsymbol{E}}_{\boldsymbol{i}}(\vec{\boldsymbol{r}},\boldsymbol{t}) = \vec{E}_i^{(0)} \mathrm{e}^{i\left(\vec{k}_i\cdot\vec{r}-\omega_i t\right)}, \tag{1.31}$$

$$\vec{\boldsymbol{E}}_{\boldsymbol{r}}(\vec{\boldsymbol{r}},\boldsymbol{t}) = \vec{E}_r^{(0)} \mathrm{e}^{i\left(\vec{k}_r\cdot\vec{r}-\omega_r t\right)}, \tag{1.32}$$

$$\vec{\boldsymbol{E}}_{\boldsymbol{t}}(\vec{\boldsymbol{r}},\boldsymbol{t}) = \vec{E}_t^{(0)} \mathrm{e}^{i\left(\vec{k}_t\cdot\vec{r}-\omega_t t\right)}, \tag{1.33}$$

where the superscript (0) indicates that the quantity is taken at $Z = 0$, and the propagation vectors read:

$$\vec{k}_i = k_i(\sin\theta_i\,\vec{e}_X - \cos\theta_i\,\vec{e}_Z) \quad = k_{i_X}\,\vec{e}_X - k_{i_Z}\,\vec{e}_Z, \tag{1.34a}$$

$$\vec{k}_r = k_r(\sin\theta_r\,\vec{e}_X + \cos\theta_r\,\vec{e}_Z) \quad = k_{r_X}\,\vec{e}_X + k_{r_Z}\,\vec{e}_Z, \tag{1.34b}$$

$$\vec{k}_t = k_t(\sin\theta_t\,\vec{e}_X - \cos\theta_t\,\vec{e}_Z) \quad = k_{t_X}\,\vec{e}_X - k_{t_Z}\,\vec{e}_Z, \tag{1.34c}$$

with the dispersion relations:

$$k_i = \omega\sqrt{\mu_I\varepsilon_I} = \frac{\omega}{v_I} = k_0 n_I = \frac{\omega}{c} n_I, \tag{1.35a}$$

$$k_r = k_i, \tag{1.35b}$$

$$k_t = \omega\sqrt{\mu_T\varepsilon_T} = \frac{\omega}{v_T} = k_0\tilde{n}_T = \frac{\omega}{c}\tilde{n}_T, \tag{1.35c}$$

where $\tilde{n}_T = \sqrt{\varepsilon_T^{(r)}\mu_T^{(r)}}$ is the complex refractive index of medium "T", $\varepsilon_T^{(r)}$ and $\mu_T^{(r)}$ are the relative permittivity and permeability, respectively, and $k_0 = \omega\sqrt{\mu_0\varepsilon_0}$.

From the Maxwell equations, four (boundary) conditions need to be maintained at the interface:

$$D_T^{\perp} - D_I^{\perp} = \sigma_{\text{surf}}, \tag{1.36}$$
$$B_T^{\perp} - B_I^{\perp} = 0, \tag{1.37}$$
$$\vec{E}_T^{\parallel} - \vec{E}_I^{\parallel} = 0, \tag{1.38}$$
$$\vec{H}_T^{\parallel} - \vec{H}_I^{\parallel} = \vec{J}_{\text{surf}}, \tag{1.39}$$

where $\sigma_{\text{surf}}$ $[\text{C} \cdot \text{m}^{-2}]$, and $\vec{J}_{\text{surf}}$ $[\text{A} \cdot \text{m}^{-2}]$ are the surface electric charge density and the surface current density, respectively.

The phase matching condition at the interface ($Z = 0$) reads:

$$\begin{cases} \mathrm{e}^{i\left(\vec{k}_i \cdot \vec{r} - \omega_i t\right)}|_{Z=0} = \mathrm{e}^{i\left(\vec{k}_r \cdot \vec{r} - \omega_r t\right)}|_{Z=0} = \mathrm{e}^{i\left(\vec{k}_t \cdot \vec{r} - \omega_t t\right)}|_{Z=0}, \\ \omega_i = \omega_r = \omega_t = \omega, \\ k_{i_X} = k_{r_X} = k_{t_X} = k_X. \end{cases} \tag{1.40}$$

According to Eq. (1.34)

$$k_{i_Z} = \sqrt{k_i^2 - k_X^2} \quad \text{and} \quad k_{t_Z} = \sqrt{k_t^2 - k_X^2}. \tag{1.41}$$

When the medium "T" is also transparent ($\varepsilon_T$ is real $\Leftrightarrow$ $\tilde{n}_T(\omega) = n_T$) and non-magnetic ($\mu_T = \mu_0$) the third line of Eq. (1.40) becomes:

$$k_i \sin\theta_i = k_r \sin\theta_r = k_0 n_I \sin\theta_i = k_t \sin\theta_t = k_0 n_T \sin\theta_t \tag{1.42}$$
$$n_I \sin\theta_i = n_T \sin\theta_t \tag{1.43}$$

which are the Snell-Descartes law.

### 1.2.3 Fresnel formulas in uniform optical medium (isotopic)

The efficiency with which the incoming radiation produces a field at the interface is described by the linear Fresnel factors; the same factors that describe reflection and refraction of light beams at an interface. These factors describe the amplitude of the electric field, $E$, at various locations relative to an incident field. In this section we review the two last properties mentioned in Section 1.2.2, which are the variation of the amplitude of the fields at the interface as well as that of the phase of each field. The wave vector and normal directions are commonly referenced to the incidence plane (X-Z)(Fig. 1.3). When the electric field oscillates in that plane the light is termed $p$-polarized, whereas when it is perpendicular to that plane it is $s$-polarized. So, the electric field of $s$-polarized light is along the Y axis at the surface. In contrast, the field of $p$-polarized light at the surface has a component that is along the X axis and a component that

is along the Z axis; the balance between X and Z depends on the angle between the propagation direction and the surface normal[4].

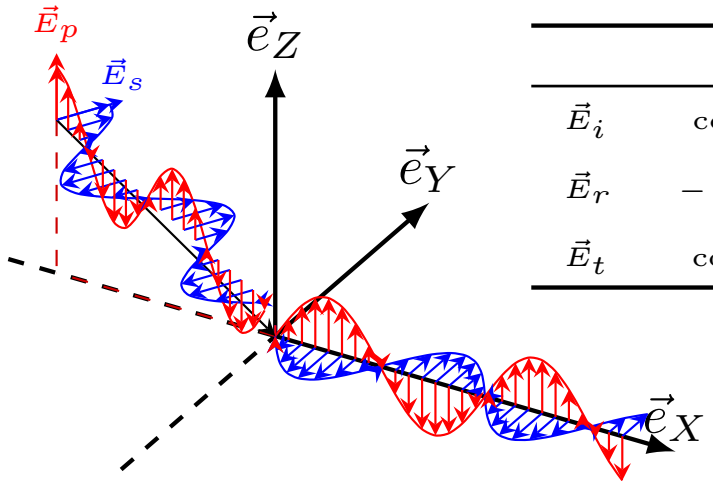


| | $p$ wave | $s$ wave |
|---|---|---|
| $\vec{E}_i$ | $\cos\theta_i\ \vec{e}_X + \sin\theta_i\ \vec{e}_Z$ | $\vec{e}_Y$ |
| $\vec{E}_r$ | $-\cos\theta_i\ \vec{e}_X + \sin\theta_i \vec{e}_Z$ | $\vec{e}_Y$ |
| $\vec{E}_t$ | $\cos\theta_t\ \vec{e}_X + \sin\theta_t\ \vec{e}_Z$ | $\vec{e}_Y$ |

FIGURE 1.3: The plane of incidence is defined by the surface normal and the propagation direction. Polarization is defined with respect to this plane: $p$-polarized in the plane and $s$-polarized perpendicular to the plane.

For a plane wave, the magnetic field vector is related to the electric field and the propagation vectors by:

$$\begin{aligned}\omega\vec{\boldsymbol{B}} = \vec{k}\times\vec{\boldsymbol{E}} \Longrightarrow \vec{\boldsymbol{H}} &= \frac{1}{\omega\mu}\vec{k}\times\vec{\boldsymbol{E}}, \qquad k = \omega\sqrt{\mu\varepsilon} \\ &= \frac{\omega\sqrt{\mu\varepsilon}}{\omega\mu}\vec{e_k}\times\vec{\boldsymbol{E}} \quad = \frac{1}{\eta}\vec{e_k}\times\vec{\boldsymbol{E}}, \end{aligned} \tag{1.44}$$

$$\begin{aligned}\vec{\boldsymbol{E}} &= -\frac{1}{\omega\varepsilon}\vec{k}\times\vec{\boldsymbol{H}}, \\ &= -\frac{\omega\sqrt{\mu\varepsilon}}{\omega\varepsilon}\vec{e_k}\times\vec{\boldsymbol{H}} \quad = -\eta\vec{e_k}\times\vec{\boldsymbol{H}}, \end{aligned} \tag{1.45}$$

where $\vec{e_k}$ is the direction of the wave vector and $\eta = \sqrt{\dfrac{\mu}{\varepsilon}}$ is known as the intrinsic impedance of the medium

Let's suppose that the media are non-magnetic ($\mu = \mu_0$) and that there is no current at the interface $\vec{J}_{\text{surf}} = 0$, the bounding conditions for the parallel components (Eqs. (1.38) and (1.39))

[4]To obtain the relationships between the norms of the electric fields for $X = 0$, $t = 0$, and $Z = 0$ ($|E_i^{(0)}|$, $|E_r^{(0)}|$, $|E_t^{(0)}|$), one needs to insert Eq. (1.43) into the boundary conditions. But first, we need to differentiate between two separate polarization states: $p$ (vertical) and $s$ (horizontal) linearly polarized light.

read:

$$\vec{E}_T^{\,\parallel} = \vec{E}_I^{\,\parallel}, \tag{1.46}$$
$$\vec{H}_T^{\,\parallel} = \vec{H}_I^{\,\parallel}, \tag{1.47}$$

which leads to the following relationships:

$$H_i^{(0)\parallel} + H_r^{(0)\parallel} = H_t^{(0)\parallel}, \tag{1.48}$$
$$E_i^{(0)\parallel} + E_r^{(0)\parallel} = E_t^{(0)\parallel}. \tag{1.49}$$

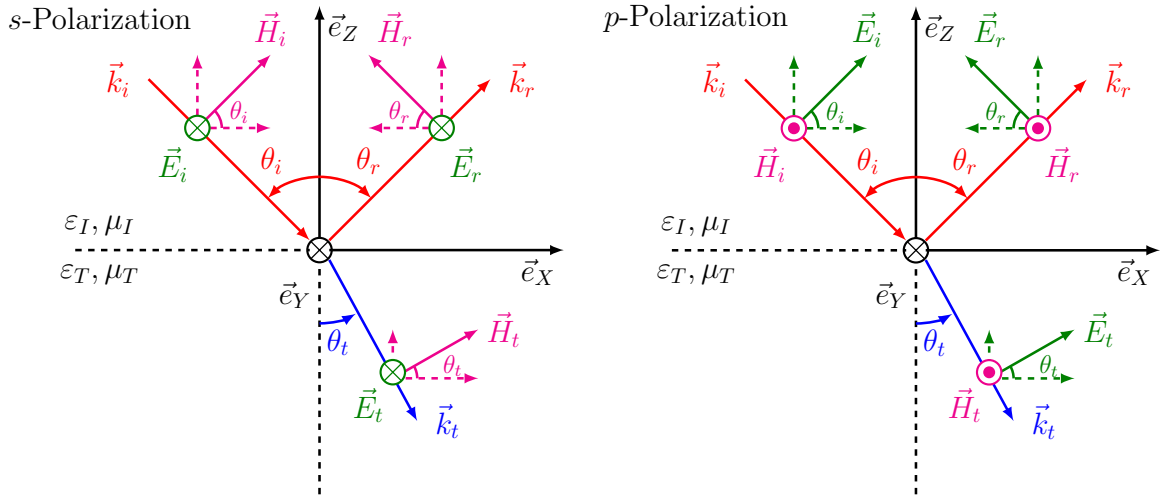


FIGURE 1.4: Definition of the *s*-polarization (left) and *p*-polarization (right) of the electromagnetic field at the interface.

## ***p*-Polarization**

The field vectors read (see Fig. 1.4):

$$\vec{\boldsymbol{E}}_{\boldsymbol{i}}^{\boldsymbol{p}} = E_i^{(0)} \left(\cos\theta_i\, \vec{e}_X + \sin\theta_i\, \vec{e}_Z\right) \mathrm{e}^{i\left(k_{i_X} X - k_{i_Z} Z - \omega t\right)} \tag{1.50a}$$
$$\vec{\boldsymbol{E}}_{\boldsymbol{r}}^{\boldsymbol{p}} = E_r^{(0)} \left(-\cos\theta_i\, \vec{e}_X + \sin\theta_i \vec{e}_Z\right) \mathrm{e}^{i\left(k_{r_X} X + k_{r_Z} Z - \omega t\right)} \tag{1.50b}$$
$$\vec{\boldsymbol{E}}_{\boldsymbol{t}}^{\boldsymbol{p}} = E_t^{(0)} \left(\cos\theta_t\, \vec{e}_X + \sin\theta_t\, \vec{e}_Z\right) \mathrm{e}^{i\left(k_{t_X} X - k_{t_Z} Z - \omega t\right)} \tag{1.50c}$$

$$\vec{\boldsymbol{H}}_{\boldsymbol{i}}^{\boldsymbol{p}} = -H_i^{(0)}\, \vec{e}_Y\, \mathrm{e}^{i\left(k_{i_X} X - k_{i_Z} Z - \omega t\right)} \tag{1.51a}$$
$$\vec{\boldsymbol{H}}_{\boldsymbol{r}}^{\boldsymbol{p}} = -H_r^{(0)}\, \vec{e}_Y\, \mathrm{e}^{i\left(k_{r_X} X + k_{r_Z} Z - \omega t\right)} \tag{1.51b}$$
$$\vec{\boldsymbol{H}}_{\boldsymbol{t}}^{\boldsymbol{p}} = -H_t^{(0)}\, \vec{e}_Y\, \mathrm{e}^{i\left(k_{t_X} X - k_{t_Z} Z - \omega t\right)} \tag{1.51c}$$

The complex amplitudes of the incident, reflected, and transmitted fields can be represented as

$$\vec{\boldsymbol{E}}_{\boldsymbol{i}}^{\boldsymbol{p}} = -\frac{1}{\omega\varepsilon_I}\vec{k}_i \times \vec{\boldsymbol{H}}_{\boldsymbol{i}}^{\boldsymbol{p}} = \frac{H_i^{(0)}}{\omega\varepsilon_I}\left(-k_{i_Z}\vec{e}_X - k_{i_X}\vec{e}_Z\right), \tag{1.52}$$

$$\vec{\boldsymbol{E}}_{\boldsymbol{r}}^{\boldsymbol{p}} = -\frac{1}{\omega\varepsilon_I}\vec{k}_r \times \vec{\boldsymbol{H}}_{\boldsymbol{r}}^{\boldsymbol{p}} = \frac{H_r^{(0)}}{\omega\varepsilon_I}\left(k_{r_Z}\vec{e}_X - k_{r_X}\vec{e}_Z\right), \tag{1.53}$$

$$\vec{\boldsymbol{E}}_{\boldsymbol{t}}^{\boldsymbol{p}} = -\frac{1}{\omega\varepsilon_T}\vec{k}_t \times \vec{\boldsymbol{H}}_{\boldsymbol{t}}^{\boldsymbol{p}} = \frac{H_t^{(0)}}{\omega\varepsilon_T}\left(-k_{t_Z}\vec{e}_X - k_{t_X}\vec{e}_Z\right). \tag{1.54}$$

From the Boundary conditions (Eq. (1.47)):

$$\frac{H_i^{(0)}}{\varepsilon_I}k_{i_Z} - \frac{H_r^{(0)}}{\varepsilon_I}k_{r_Z} = \frac{H_t^{(0)}}{\varepsilon_T}k_{t_Z}. \tag{1.55}$$

When combining with Eq. (1.48), it then follows that:

$$H_r^{(0)} = \frac{\varepsilon_T k_{i_Z} - \varepsilon_I k_{t_Z}}{\varepsilon_T k_{r_Z} + \varepsilon_I k_{t_Z}} H_i^{(0)} = \frac{\varepsilon_T k_{I_Z} - \varepsilon_I k_{T_Z}}{\varepsilon_T k_{I_Z} + \varepsilon_I k_{T_Z}} H_i^{(0)}, \tag{1.56}$$

$$H_t^{(0)} = \frac{\varepsilon_T}{\varepsilon_I}\frac{\varepsilon_I\left(k_{i_Z} + k_{r_Z}\right)}{\varepsilon_T k_{r_Z} + \varepsilon_I k_{t_Z}} H_i^{(0)} = \frac{2\varepsilon_T k_{I_Z}}{\varepsilon_T k_{I_Z} + \varepsilon_I k_{T_Z}} H_i^{(0)}, \tag{1.57}$$

where $k_{i_Z} = k_{r_Z} = k_{I_Z}$ , and the subscripts "$I$" and "$T$" stand for the media. It is straightforward from Eq. (1.44) that

$$E_i^{(0)} = \eta_I H_i^{(0)}, \qquad E_r^{(0)} = \eta_I H_r^{(0)}, \qquad E_t^{(0)} = \eta_T H_t^{(0)}. \tag{1.58}$$

Then the coefficients of reflection and transmission read:

$$r_p = \frac{E_r^{(0)}}{E_i^{(0)}} = \frac{\varepsilon_T k_{I_Z} - \varepsilon_I k_{T_Z}}{\varepsilon_T k_{I_Z} + \varepsilon_I k_{T_Z}}, \tag{1.59}$$

$$t_p = \frac{E_t^{(0)}}{E_i^{(0)}} = \frac{2\varepsilon_T k_{I_Z}}{\varepsilon_T k_{I_Z} + \varepsilon_I k_{T_Z}}\sqrt{\frac{\varepsilon_I}{\varepsilon_T}} \tag{1.60}$$

### ***s*-Polarization**

The electric and magnetic field vectors reads (see Fig. 1.4):

$$\vec{\boldsymbol{E}}_{\boldsymbol{i}}^{\boldsymbol{s}} = E_i^{(0)}\,\vec{e}_Y\,\mathrm{e}^{i\left(k_{i_X}X - k_{i_Z}Z - \omega t\right)} \tag{1.61a}$$

$$\vec{\boldsymbol{E}}_{\boldsymbol{r}}^{\boldsymbol{s}} = E_r^{(0)}\,\vec{e}_Y\,\mathrm{e}^{i\left(k_{r_X}X + k_{r_Z}Z - \omega t\right)} \tag{1.61b}$$

$$\vec{\boldsymbol{E}}_{\boldsymbol{t}}^{\boldsymbol{s}} = E_t^{(0)}\,\vec{e}_Y\,\mathrm{e}^{i\left(k_{t_X}X - k_Z Z - \omega t\right)} \tag{1.61c}$$

$$\vec{\boldsymbol{H}}_{\boldsymbol{i}}^{\boldsymbol{s}} = H_i^{(0)} \left(\cos\theta_i \, \vec{e}_X + \sin\theta_i \, \vec{e}_Z\right) \mathrm{e}^{i\left(k_{i_X} X - k_{i_Z} Z - \omega t\right)} \tag{1.62a}$$

$$\vec{\boldsymbol{H}}_{\boldsymbol{r}}^{\boldsymbol{s}} = H_r^{(0)} \left(-\cos\theta_i \, \vec{e}_X + \sin\theta_i \vec{e}_Z\right) \mathrm{e}^{i\left(k_{r_X} X + k_{r_Z} Z - \omega t\right)} \tag{1.62b}$$

$$\vec{\boldsymbol{H}}_{\boldsymbol{t}}^{\boldsymbol{s}} = H_t^{(0)} \left(\cos\theta_t \, \vec{e}_X + \sin\theta_t \, \vec{e}_Z\right) \mathrm{e}^{i\left(k_{t_X} X - k_{t_Z} Z - \omega t\right)} \tag{1.62c}$$

Similarly to the $p$-polarization, the complex amplitudes of the incident, reflected, and transmitted fields can be represented as

$$\vec{\boldsymbol{H}}_{\boldsymbol{i}}^{\boldsymbol{s}} = \frac{1}{\omega\mu_0} \vec{k}_i \times \vec{\boldsymbol{E}}_{\boldsymbol{i}}^{\boldsymbol{s}} = \frac{E_i^{(0)}}{\omega\mu_0} \left(k_{i_Z} \vec{e}_X + k_{i_X} \vec{e}_Z\right), \tag{1.63}$$

$$\vec{\boldsymbol{H}}_{\boldsymbol{r}}^{\boldsymbol{s}} = \frac{1}{\omega\mu_0} \vec{k}_r \times \vec{\boldsymbol{E}}_{\boldsymbol{r}}^{\boldsymbol{s}} = \frac{E_r^{(0)}}{\omega\mu_0} \left(-k_{r_Z} \vec{e}_X + k_{r_X} \vec{e}_Z\right), \tag{1.64}$$

$$\vec{\boldsymbol{H}}_{\boldsymbol{t}}^{\boldsymbol{s}} = \frac{1}{\omega\mu_0} \vec{k}_t \times \vec{\boldsymbol{E}}_{\boldsymbol{t}}^{\boldsymbol{s}} = \frac{E_t^{(0)}}{\omega\mu_0} \left(k_{t_Z} \vec{e}_X + k_{t_X} \vec{e}_Z\right). \tag{1.65}$$

From the Boundary conditions (Eq. (1.46)):

$$\begin{aligned} E_i^{(0)} k_{i_Z} - E_r^{(0)} k_{r_Z} &= E_t^{(0)} k_{t_Z}, \\ \left(E_i^{(0)} - E_r^{(0)}\right) k_{I_Z} &= E_t^{(0)} k_{T_Z}. \end{aligned} \tag{1.66}$$

One can therefore derive the coefficients of reflection and transmission as:

$$r_s = \frac{E_r^{(0)}}{E_i^{(0)}} = \frac{k_{I_Z} - k_{T_Z}}{k_{I_Z} + k_{T_Z}}, \tag{1.67}$$

$$t_s = \frac{E_t^{(0)}}{E_i^{(0)}} = \frac{2k_{I_Z}}{k_{I_Z} + k_{T_Z}}. \tag{1.68}$$

Using the expression of the wave vectors ]Eq. (1.34)], the Fresnel formulas as a function of the incident ($\theta_i$) and transmission ($\theta_t$) angles are given in Table 1.1.

TABLE 1.1: Fresnel formulas as a function of the incident ($\theta_i$) and transmission ($\theta_t$)angles

| | $p$ wave | $s$ wave |
|---|---|---|
| Reflected | $r_p = \dfrac{n_T \cos\theta_i - n_I \cos\theta_t}{n_T \cos\theta_i + n_I \cos\theta_t}$ | $r_s = \dfrac{n_I \cos\theta_i - n_T \cos\theta_t}{n_I \cos\theta_i + n_T \cos\theta_t}$ |
| Transmitted | $t_p = \dfrac{2n_I \cos\theta_i}{n_T \cos\theta_i + n_I \cos\theta_t}$ | $t_s = \dfrac{2n_I \cos\theta_i}{n_I \cos\theta_i + n_T \cos\theta_t}$ |

When taking into account the Snell-Descartes law [Eq. (1.43)], $\theta_t$ can be related to $\theta_i$:

$$\sin\theta_t = \frac{n_I}{n_T}\sin\theta_i,$$
$$\cos\theta_t = \sqrt{1-\sin^2\theta_t} \quad = \sqrt{1-\frac{n_I^2}{n_T^2}\sin^2\theta_i}.$$

The Fresnel formulas as a function of the incident angle $\theta_i$ can be rewritten as given in Table 1.2, whereas Fig. 1.5 displays a sketch for $n_I = 1$ and $n_T = 1.5$.

TABLE 1.2: Fresnel formulas in function of the incident angle $\theta_i$

| | $p$ wave | $s$ wave |
|---|---|---|
| Reflected | $r_p = \dfrac{n_T\cos\theta_i - n_I\sqrt{1-\frac{n_I^2}{n_T^2}\sin^2\theta_i}}{n_T\cos\theta_i + n_I\sqrt{1-\frac{n_I^2}{n_T^2}\sin^2\theta_i}}$ | $r_s = \dfrac{n_I\cos\theta_i - n_T\sqrt{1-\frac{n_I^2}{n_T^2}\sin^2\theta_i}}{n_I\cos\theta_i + n_T\sqrt{1-\frac{n_I^2}{n_T^2}\sin^2\theta_i}}$ |
| Transmitted | $t_p = \dfrac{2n_I\cos\theta_i}{n_T\cos\theta_i + n_I\sqrt{1-\frac{n_I^2}{n_T^2}\sin^2\theta_i}}$ | $t_s = \dfrac{2n_I\cos\theta_i}{n_I\cos\theta_i + n_T\sqrt{1-\frac{n_I^2}{n_T^2}\sin^2\theta_i}}$ |

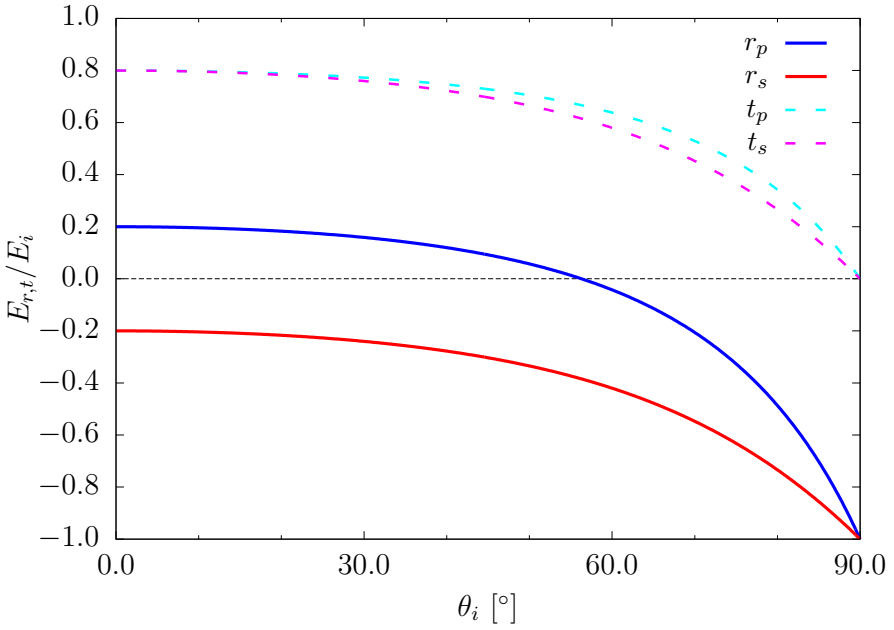


FIGURE 1.5: Reflection and transmission coefficients, for the $s$ and $p$ polarized wave. Curves are plotted using the expressions in Table 1.2, for $n_I = 1$ and $n_T = 1.5$

## Total electric field at the surface

Let's define the total field at the surface as

$$\vec{E}_{\text{tot}}^{(0)} = \vec{E}_i^{(0)} + \vec{E}_r^{(0)} \tag{1.69}$$

where $\vec{E}_i^{(0)}$ and $\vec{E}_r^{(0)}$ are given in Eqs. (1.50) and (1.61) for the $s$ and $p$ polarizations

$$\vec{E}_i^{(0)} = E_i^{(0)} \left[\cos\phi \left(\cos\theta_i \vec{e}_X + \sin\theta_i \, \vec{e}_Z\right) + \sin\phi \, e^{i\varphi} \vec{e}_Y\right], \tag{1.70}$$

$$\vec{E}_r^{(0)} = E_i^{(0)} \left[r_p \cos\phi \left(-\cos\theta_i \vec{e}_X + \sin\theta_i \vec{e}_Z\right) + r_s \sin\phi \, e^{i\varphi} \vec{e}_Y\right], \tag{1.71}$$

where $\varphi$ is the phase angle between the incident $s$ and $p$ polarized fields, and $\cos\phi$ and $\sin\phi$ define their relative amplitude. The total electric field can be written as :

$$\vec{E}_i^{(0)} + \vec{E}_r^{(0)} = \begin{pmatrix} (\cos\theta_i - r_p \cos\theta_i)\cos\phi \\ (1+r_s)\sin\phi \, e^{i\varphi} \\ (\sin\theta_i + r_p \sin\theta_i)\cos\phi \end{pmatrix} E_i^{(0)} = \begin{pmatrix} \cos\theta_i \, (1-r_p)\cos\phi \\ (1+r_s)\sin\phi \, e^{i\varphi} \\ \sin\theta_i \, (1+r_p)\cos\phi \end{pmatrix} E_i^{(0)}$$

$$\vec{E}_{\text{tot}}^{(0)} = \begin{pmatrix} 1-r_p & 0 & 0 \\ 0 & 1+r_s & 0 \\ 0 & 0 & 1+r_p \end{pmatrix} \vec{E}_i^{(0)} = F \vec{E}_i^{(0)}. \tag{1.72}$$

The tensor $F$ is denoted as the "**Fresnel factor**". The $X$ and $Z$ contributions comes from the $p$-polarization and the $Y$components from the $s$-polarization.

By using the Fresnel formulas, we obtain:

$$\vec{E}_{\text{tot}}^{(0)} = \begin{pmatrix} 1 - \dfrac{\varepsilon_T k_{I_Z} - \varepsilon_I k_{T_Z}}{\varepsilon_T k_{I_Z} + \varepsilon_I k_{T_Z}} & 0 & 0 \\ 0 & 1 + \dfrac{k_{I_Z} - k_{T_Z}}{k_{I_Z} + k_{T_Z}} & 0 \\ 0 & 0 & 1 + \dfrac{\varepsilon_T k_{I_Z} - \varepsilon_I k_{T_Z}}{\varepsilon_T k_{I_Z} + \varepsilon_I k_{T_Z}} \end{pmatrix} E_i^{(0)},$$

$$= \begin{pmatrix} \dfrac{2\varepsilon_I k_{T_Z}}{\varepsilon_T k_{I_Z} + \varepsilon_I k_{T_Z}} & 0 & 0 \\ 0 & \dfrac{2k_{I_Z}}{k_{I_Z} + k_{T_Z}} & 0 \\ 0 & 0 & \dfrac{2\varepsilon_T k_{I_Z}}{\varepsilon_T k_{I_Z} + \varepsilon_I k_{T_Z}} \end{pmatrix} E_i^{(0)}, \tag{1.73}$$

then, using Eqs. (1.34), (1.35) and (1.41) the diagonal elements of the F matrix can be rewritten as

$$\begin{cases} \mathrm{F_{XX}} &= \dfrac{2\varepsilon_I k_{T_Z}}{\varepsilon_T k_{I_Z} + \varepsilon_I k_{T_Z}} &= \dfrac{2\varepsilon_I^{(r)}\sqrt{\varepsilon_T^{(r)} - \varepsilon_I^{(r)}\sin^2\theta}}{\varepsilon_T^{(r)}\sqrt{\varepsilon_I^{(r)}}\cos\theta + \varepsilon_I^{(r)}\sqrt{\varepsilon_T^{(r)} - \varepsilon_I^{(r)}\sin^2\theta}} \\ \mathrm{F_{YY}} &= \dfrac{2k_{I_Z}}{k_{I_Z} + k_{T_Z}} &= \dfrac{2\sqrt{\varepsilon_I^{(r)}}\cos\theta}{\sqrt{\varepsilon_I^{(r)}}\cos\theta + \sqrt{\varepsilon_T^{(r)} - \varepsilon_I^{(r)}\sin^2\theta}} \\ \mathrm{F_{ZZ}} &= \dfrac{2\varepsilon_T k_{I_Z}}{\varepsilon_T k_{I_Z} + \varepsilon_I k_{T_Z}} &= \dfrac{2\varepsilon_T^{(r)}\sqrt{\varepsilon_I^{(r)}}\cos\theta}{\varepsilon_T^{(r)}\sqrt{\varepsilon_I^{(r)}}\cos\theta + \varepsilon_I^{(r)}\sqrt{\varepsilon_T^{(r)} - \varepsilon_I^{(r)}\sin^2\theta}} \end{cases} \tag{1.74}$$

### 1.2.4 Poynting vector and the Intensity

The Poynting vector $\vec{S}(t)$ gives the instantenous rate of electromagnetic energy flowing in the direction of propagation:

$$\vec{S}(t) = \vec{E}(t) \times \vec{H}(t). \tag{1.75}$$

The intensity $I$ is the mean rate of energy flowing, which is the average of the magnitude of $\vec{S}(\vec{r}, t)$ over a complete period of the wave. For a plane wave,

$$\begin{aligned} \left\langle \vec{S} \right\rangle_t = \frac{1}{2}\mathrm{Re}\left(\vec{\boldsymbol{E}} \times \vec{\boldsymbol{H}}^*\right) &= \frac{1}{2}\left(\vec{E}^{(0)} \times \vec{H}^{(0)}\right) \\ &= \frac{1}{2\mu}\left(\vec{E}^{(0)} \times \vec{B}^{(0)}\right) \\ &= \frac{1}{2\omega\mu}\left[\vec{E}^{(0)} \times (\vec{k} \times \vec{E}^{(0)})\right], \quad \vec{k} = k_0 n \vec{e}_k \\ &= \frac{k_0 n}{2\omega\mu}|\vec{E}^{(0)}|^2 \vec{e}_k, \qquad k_0 = \omega\sqrt{\mu_0\varepsilon_0} \\ &= \frac{n\sqrt{\mu_0\varepsilon_0}}{2\mu}|\vec{E}^{(0)}|^2 \vec{e}_k. \end{aligned} \tag{1.76}$$

For a non-magnetic medium ($\mu = \mu_0$):

$$\begin{aligned} \left\langle \vec{S} \right\rangle_t &= \frac{1}{2}\frac{n\sqrt{\mu_0\varepsilon_0}}{\mu_0}|\vec{E}^{(0)}|^2 \vec{e}_k \\ &= \frac{1}{2} n \sqrt{\frac{\epsilon_0}{\mu_0}}|\vec{E}^{(0)}|^2 \vec{e}_k \\ &= \frac{1}{2} n c \epsilon_0 |\vec{E}^{(0)}|^2 \vec{e}_k, \qquad c = \frac{1}{\sqrt{\mu_0\varepsilon_0}}. \end{aligned} \tag{1.77}$$

Then, the intensity can be written as

$$I = \left|\left\langle \vec{\boldsymbol{S}} \right\rangle_t\right| = \frac{1}{2} n c \epsilon_0 |\vec{E}^{(0)}|^2. \tag{1.78}$$

From this, we can define the reflectance **R** and the transmittance **T** as the ratio between the intensity of the different vectors:

$$\mathrm{R} = \frac{(1/2) n_I \epsilon_0 c |\vec{E}_r^{(0)}|^2}{(1/2) n_I \epsilon_0 c |\vec{E}_i^{(0)}|^2} = \left(\frac{E_r^{(0)}}{E_i^{(0)}}\right)^2, \tag{1.79}$$

$$\mathrm{T} = \frac{(1/2) n_T \epsilon_0 c |\vec{E}_t^{(0)}|^2}{(1/2) n_I \epsilon_0 c |\vec{E}_i^{(0)}|^2} \frac{\cos\theta_t}{\cos\theta_i} = \frac{n_T \cos\theta_t}{n_I \cos\theta_i} \left(\frac{E_t^{(0)}}{E_i^{(0)}}\right)^2. \tag{1.80}$$

The corresponding expressions for both polarizations are given in Table 1.3, whereas Fig. 1.6 displays a sketch for $n_I = 1$ and $n_T = 1.5$.

Table 1.3: Reflectance and Transmittance

| | $p$ wave | $s$ wave |
|---|---|---|
| R | $\left(\frac{n_T \cos\theta_i - n_I \cos\theta_t}{n_T \cos\theta_i + n_I \cos\theta_t}\right)^2$ | $\left(\frac{n_I \cos\theta_i - n_T \cos\theta_t}{n_I \cos\theta_i + n_T \cos\theta_t}\right)^2$ |
| | $= \left(\frac{n_T \cos\theta_i - n_I \sqrt{1 - \frac{n_I^2}{n_T^2}\sin^2\theta_i}}{n_T \cos\theta_i + n_I \sqrt{1 - \frac{n_I^2}{n_T^2}\sin^2\theta_i}}\right)^2$ | $= \left(\frac{n_I \cos\theta_i - n_T \sqrt{1 - \frac{n_I^2}{n_T^2}\sin^2\theta_i}}{n_I \cos\theta_i + n_T \sqrt{1 - \frac{n_I^2}{n_T^2}\sin^2\theta_i}}\right)^2$ |
| T | $\frac{4 n_I n_T \cos\theta_i \cos\theta_t}{(n_T \cos\theta_i + n_I \cos\theta_t)^2}$ | $\frac{4 n_I n_T \cos\theta_i \cos\theta_t}{(n_I \cos\theta_i + n_T \cos\theta_t)^2}$ |
| | $= \frac{4 n_I n_T \cos\theta_i \sqrt{1 - \frac{n_I^2}{n_T^2}\sin^2\theta_i}}{\left(n_T \cos\theta_i + n_I \sqrt{1 - \frac{n_I^2}{n_T^2}\sin^2\theta_i}\right)^2}$ | $= \frac{4 n_I n_T \cos\theta_i \sqrt{1 - \frac{n_I^2}{n_T^2}\sin^2\theta_i}}{\left(n_I \cos\theta_i + n_T \sqrt{1 - \frac{n_I^2}{n_T^2}\sin^2\theta_i}\right)^2}$ |
| R + T | 1 | 1 |

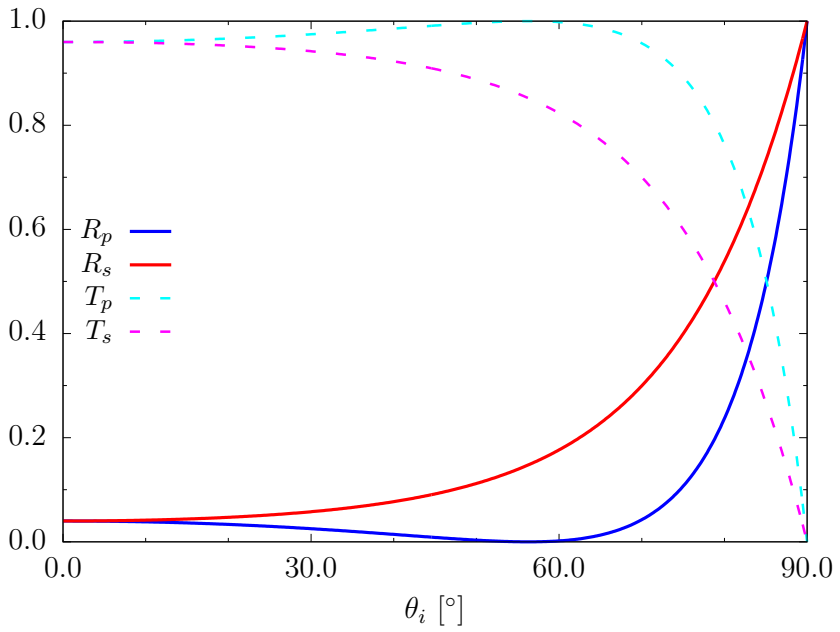


FIGURE 1.6: Reflectance R and transmittance T (Table 1.3) when the wave is propagating from a less to more refractive medium. $n_I = 1$, $n_T = 1.5$

## 1.3 Wave equations at boundaries of optical nonlinear media

### 1.3.1 Wave equations in nonlinear media

Here, we are interested in the solution of Maxwell's equations (Eqs. (1.23) to (1.26)) in regions of space that contain no free charges and no free currents, so that

$$\boldsymbol{\rho_f} = 0 \qquad \text{and} \qquad \vec{\boldsymbol{J}}_{\boldsymbol{f}} = \vec{0}. \tag{1.81}$$

We also assume that

$$\vec{\nabla} \times \vec{\boldsymbol{M}} = \vec{0}. \tag{1.82}$$

By considering Eq. (1.25)

$$\vec{\nabla} \times \vec{\boldsymbol{E}} = -\frac{\partial \vec{\boldsymbol{B}}}{\partial t}, \qquad \text{Maxwell-Faraday}$$
$$\vec{\nabla} \times \vec{\nabla} \times \vec{\boldsymbol{E}}(\vec{r}, t) = -\frac{\partial}{\partial t}\left[\vec{\nabla} \times \vec{\boldsymbol{B}}(\vec{r}, t)\right]. \tag{1.83}$$

Then, inserting Eqs. (1.26), (1.28) and (1.30) in to Eq. (1.83) one obtains

$$\vec{\nabla} \times \vec{\nabla} \times \vec{\boldsymbol{E}}(\vec{r},t) = -\frac{\partial}{\partial t}\left\{\mu_0 \frac{\partial}{\partial t}\left[\varepsilon_0 \vec{\boldsymbol{E}}(\vec{r},t) + \vec{\boldsymbol{P}}(\vec{r},t)\right]\right\} \tag{1.84}$$

$$-\nabla^2 \vec{\boldsymbol{E}}(\vec{r},t) = -\mu_0 \frac{\partial^2 \vec{\boldsymbol{D}}(\vec{r},t)}{\partial t^2}, \tag{1.85}$$

where

$$\vec{\nabla} \times \vec{\nabla} \times \vec{\boldsymbol{E}}(\vec{r},t) = \nabla\left[\nabla \cdot \vec{\boldsymbol{E}}(\vec{r},t)\right] - \nabla^2 \vec{\boldsymbol{E}}(\vec{r},t) = -\nabla^2 \vec{\boldsymbol{E}}(\vec{r},t). \tag{1.86}$$

The polarization $\vec{\boldsymbol{P}}$ and displacement vector $\vec{\boldsymbol{D}}$ can be split in to linear and nonlinear parts as

$$\vec{\boldsymbol{P}} = \vec{\boldsymbol{P}}^{(1)} + \vec{\boldsymbol{P}}^{(NL)} \tag{1.87}$$

$$\vec{\boldsymbol{D}} = \vec{\boldsymbol{D}}^{(1)} + \vec{\boldsymbol{D}}^{(NL)} \tag{1.88}$$

where the linear part of $\vec{\boldsymbol{D}}^{(1)}$ is given by

$$\begin{aligned} \vec{\boldsymbol{D}}^{(1)} &= \varepsilon_0 \vec{\boldsymbol{E}} + \vec{\boldsymbol{P}}^{(1)} \\ &= \varepsilon_0 \varepsilon^{(r)} \vec{\boldsymbol{E}}, \quad \text{where} \quad \varepsilon^{(r)} \quad \text{is a scalar quantity.} \end{aligned} \tag{1.89}$$

Using Eqs. (1.87) to (1.89), Eq. (1.85) can be written as

$$-\nabla^2 \vec{\boldsymbol{E}}(\vec{r},t) + \mu_0 \frac{\partial^2 \vec{\boldsymbol{D}}^{(1)}(\vec{r},t)}{\partial t^2} = -\mu_0 \frac{\partial^2 \vec{\boldsymbol{P}}^{(NL)}(\vec{r},t)}{\partial t^2} \tag{1.90}$$

$$-\nabla^2 \vec{\boldsymbol{E}}(\vec{r},t) + \mu_0 \varepsilon_0 \varepsilon^{(r)} \frac{\partial^2 \vec{\boldsymbol{E}}(\vec{r},t)}{\partial t^2} = -\mu_0 \frac{\partial^2 \vec{\boldsymbol{P}}^{(NL)}(\vec{r},t)}{\partial t^2} \tag{1.91}$$

Eq. (1.91) is non-homogenous differential equation. The general solution consists of the solution of the homogeneous equation plus one particular solution of the inhomogeneous equation. For the case of a dispersive medium[5], we must consider each frequency component of the field separately. We then represent the total electric field and the total polarization as the sum of their various frequency components:

$$\vec{\boldsymbol{E}}(\vec{r},t) = \sum_q \vec{\boldsymbol{E}}(k_q,\omega_q) = \sum_q \vec{E}_q e^{i(\vec{k}_q \cdot \vec{r} - \omega_q t)}, \tag{1.92}$$

$$\vec{\boldsymbol{P}}^{\boldsymbol{NL}}(\vec{r},t) = \sum_{n\geq 2} \vec{\boldsymbol{P}}^{(\boldsymbol{n})} = \sum_m \vec{\boldsymbol{P}}^{\boldsymbol{NL}}(k_m,\omega_m) = \sum_m \vec{P}_m^{NL} e^{i(\vec{k}_m \cdot \vec{r} - \omega_m t).} \tag{1.93}$$

Inserting Eqs. (1.92) and (1.93) in to Eq. (1.91), one finds that a new plane wave $\vec{E}(k,\omega)$ of the electric field verifies the equation if its frequency $\omega$ is in the range of the frequency of the non linear polarization. We write

[5] a dispersive medium is a medium in which waves of different frequencies travel at different velocities (this occurs because the index of refraction of the medium is frequency-dependent.)

$$\left[-\nabla^2 - \omega^2\mu_0\varepsilon_0\varepsilon^{(r)}(\omega)\right]\vec{\boldsymbol{E}}(k,\omega) = \mu_0\omega^2\vec{\boldsymbol{P}}^{\boldsymbol{NL}}_{\boldsymbol{m}}(k_m,\omega_m=\omega). \tag{1.94}$$

In Eq. (1.94), it clearly appears that the frequencies of the electric field $\vec{\boldsymbol{E}}(k,\omega)$ and of the polarization $\vec{\boldsymbol{P}}^{\boldsymbol{NL}}(k_m,\omega_m=\omega)$ are identical, whereas their associated wave vectors are different. Equality of these wave vectors corresponds to the phase matching condition.

Now, we consider that the frequency $\omega$ of the outgoing wave is the linear combination of $n$ original frequencies. Then, to characterize the amplitudes of the electric field at the frequency $\omega$ and at the $n$ initial frequencies, there exists a set of $n+1$ coupled differential equations arising from Eq. (1.94). Let us consider the lowest-order (second-order) nonlinearity with three waves (Fig. 1.7) at frequencies $\omega_1$, $\omega_2$, and $\omega_3 = \omega_1+\omega_2$. We obtain a system of three complex nonlinear coupled wave vector equations,

$$\begin{aligned}
\left[-\nabla^2 - \omega_1^2\mu_0\varepsilon_0\varepsilon^{(r)}(\omega_1)\right]\vec{\boldsymbol{E}}(k_1,\omega_1) &= \mu_0\omega_1^2\vec{\boldsymbol{P}}^{\boldsymbol{(2)}}(\omega_1)\\
&= \mu_0\omega_1^2\,\varepsilon_0\chi^{(2)}(\omega_1=-\omega_2+\omega_3):\vec{\boldsymbol{E}}^{*}(k_2,\omega_2)\vec{\boldsymbol{E}}(k_3,\omega_3), \qquad (1.95a)\\
\left[-\nabla^2 - \omega_2^2\mu_0\varepsilon_0\varepsilon^{(r)}(\omega_2)\right]\vec{\boldsymbol{E}}(\boldsymbol{k_2},\boldsymbol{\omega_2}) &= \mu_0\omega_2^2\vec{\boldsymbol{P}}^{\boldsymbol{(2)}}(\omega_2)\\
&= \mu_0\omega_2^2\,\varepsilon_0\chi^{(2)}(\omega_2=\omega_3-\omega_1):\vec{\boldsymbol{E}}(k_3,\omega_3)\vec{\boldsymbol{E}}^{*}(k_1,\omega_1), \qquad (1.95b)\\
\left[-\nabla^2 - \omega_3^2\mu_0\varepsilon_0\varepsilon^{(r)}(\omega_3)\right]\vec{\boldsymbol{E}}(\boldsymbol{k_3},\boldsymbol{\omega_3}) &= \mu_0\omega_3^2\vec{\boldsymbol{P}}^{\boldsymbol{(2)}}(\omega_3)\\
&= \mu_0\omega_3^2\,\varepsilon_0\chi^{(2)}(\omega_3=\omega_1+\omega_2):\vec{\boldsymbol{E}}(k_1,\omega_1)\vec{\boldsymbol{E}}(k_2,\omega_2). \qquad (1.95c)
\end{aligned}$$

In these equations, $\varepsilon^{(r)}(\omega)$ and $\chi^{(2)}$ are complex quantities. The solutions of Eq. (1.95c) must satisfy boundary conditions. Moreover, we neglect the coupling with Eqs. (1.95a) and (1.95b). This imposes the equality of the parallel components (Fig. 1.2) of the wave vectors of the fields oscillating at the same frequency. The X-Y plane is parallel to the surface (The $\vec{e}_Z$ axis is normal to the interface). The incident wave vectors ($\vec{k}_{1i}$ and $\vec{k}_{2i}$) are oriented so that their $Y$-component are opposite ($k_{1i,Y} = -k_{2i,Y}$) as shown in Fig. 1.7.

$$(\vec{k}_{1i}+\vec{k}_{2i})\cdot\vec{r}^{\parallel} = \vec{k}_{3r}\cdot\vec{r}^{\parallel} = \vec{k}_{3t}\cdot\vec{r}^{\parallel} = \vec{k}_{3s}\cdot\vec{r}^{\parallel}. \tag{1.96}$$

It follows that

$$\begin{aligned}
k_{3r,X} = k_{3s,X} &= k_{1t,X} + k_{2t,X} = k_{1i,X} + k_{2i,X},\\
k_{3r,Y} = k_{3s,Y} &= k_{1t,Y} + k_{2t,Y} = k_{1i,Y} + k_{2i,Y} = 0.
\end{aligned} \tag{1.97}$$

Cancellation of the second line in Eq. (1.97) comes from the particular choice of the axis. It results that all the field oscillating at the frequency $\omega_3$ propagates in the same plane ($Y = 0$, see Fig. 1.7). The reflection and refraction laws of the nonlinear wave comes from the conservation

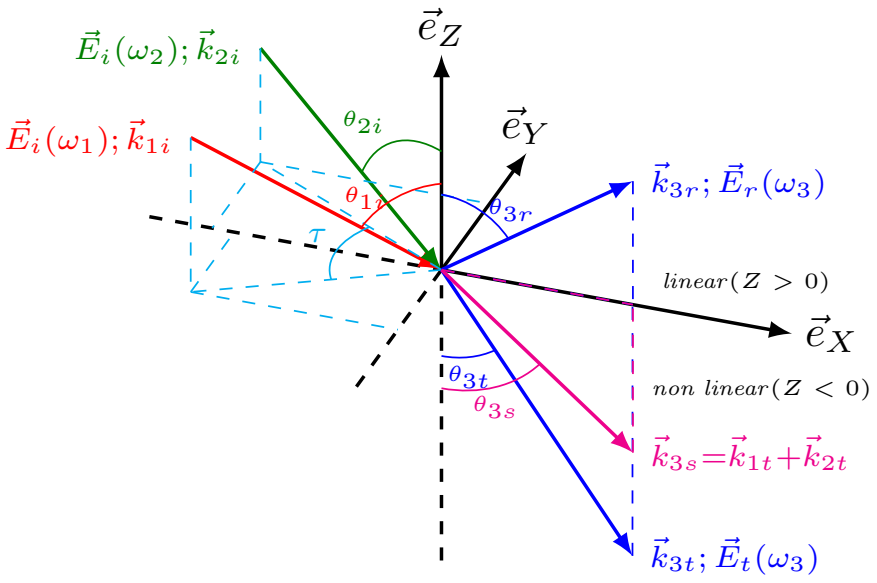


FIGURE 1.7: Geometrical relationships between the wave vectors of two planes waves, incident on the plane boundary of a nonlinear medium, and the reflected and transmitted waves at the sum frequency

of $\vec{k}^{\parallel}$.

$$\vec{k}^{\parallel}_{1i} + \vec{k}^{\parallel}_{2i} = \vec{k}^{\parallel}_{3s} = \vec{k}^{\parallel}_{3r} = \vec{k}^{\parallel}_{3t}, \tag{1.98}$$

$$\begin{aligned}
\left\|\vec{k}_{3s}\right\|^2 &= \left|\vec{k}_{1i}\right|^2 \sin^2\theta_{1i} + \left|\vec{k}_{2i}\right|^2 \sin^2\theta_{2i} + 2\cos\tau \left|\vec{k}_{1i}\right| \left|\vec{k}_{2i}\right| \sin\theta_{1i}\sin\theta_{2i}, \\
&= \left|\vec{k}_{3s}\right|^2 \sin^2\theta_{3s}, \\
&= \left|\vec{k}_{3r}\right|^2 \sin^2\theta_{3r}, \\
&= \left|\vec{k}_{3t}\right|^2 \sin^2\theta_{3t},
\end{aligned} \tag{1.99}$$

$$k^2 = \varepsilon^{(r)}\omega^2/c^2. \tag{1.100}$$

The reflected and refracted angles depend explicitly on the frequencies

$$\begin{aligned}
\varepsilon_T^{(r)}\omega_3^2\sin^2\theta_{3t} &= \varepsilon_I^{(r)}\omega_3^2\sin^2\theta_{3r}, \\
&= \varepsilon_I^{(r)}\omega_1^2\sin^2\theta_{1i} + \varepsilon_I^{(r)}\omega_2^2\sin^2\theta_{2i} + 2\cos\tau\left[\left(\varepsilon_I^{(r)}\right)^2\omega_1\omega_2\sin\theta_{1i}\sin\theta_{2i}\right].
\end{aligned} \tag{1.101}$$

Eq. (1.101) is extremely important since it states that the process at $\omega_3$ is directional, which facilitates the collections of photons in the experiment.

When both incident waves are in the same incident plane ($\tau = 0$ or $\pi$), Eq. (1.101) simplifies as

$$\begin{aligned}\omega_3\sqrt{\varepsilon_I^{(r)}}\sin\theta_{3r} &= \omega_3\sqrt{\varepsilon_T^{(r)}}\sin\theta_{3t},\\ &= \omega_1\sqrt{\varepsilon_I^{(r)}}\sin\theta_{1i} \pm \omega_2\sqrt{\varepsilon_I^{(r)}}\sin\theta_{2i}.\end{aligned} \tag{1.102}$$

Directions of nonlinear wave depend on the directions and the frequencies of the incident waves (Fig. 1.8). The plus sign of Eq. (1.102) applies if the input beams are copropagating and the minus sign if they are counterpropagating. Moreover, the reflected and transmitted waves generated at the nonlinear frequency verify the Snell-Descartes law Eq. (1.43)

$$\begin{aligned}\omega_3\sqrt{\varepsilon_I^{(r)}}\sin\theta_{3r} &= \omega_3\sqrt{\varepsilon_T^{(r)}}\sin\theta_{3t},\\ \frac{\sin\theta_{3r}}{\sin\theta_{3t}} &= \frac{\sqrt{\varepsilon_T^{(r)}}}{\sqrt{\varepsilon_I^{(r)}}}.\end{aligned} \tag{1.103}$$

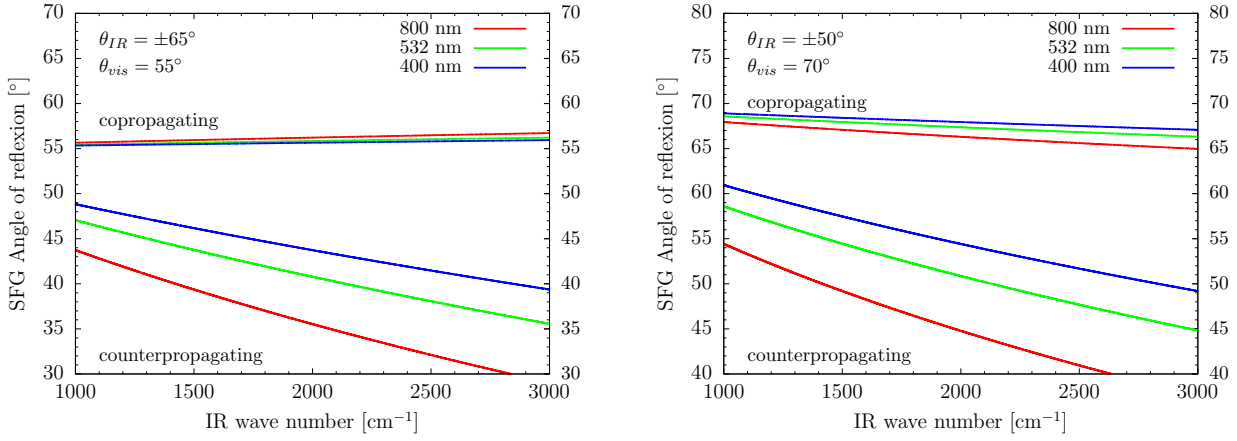


FIGURE 1.8: Dependence of the reflected angle of the nonlinear wave as a function of the wavenumber of the incident waves. $\lambda_1 = 800$ nm, 532 nm, and 400 nm; $\omega_2 \propto \bar{\nu}_{IR} : 1000 - 3000$ cm$^{-1}$. Reproduced from Caudano [4]

### 1.3.2 Sum-Frequency Generation (SFG) at interfaces

Often, Eq. (1.95) cannot be solved exactly and must be solved using approximations. For example, in the case of SFG of thin film, one can assume that the decrease in the intensity of the pump beams is negligible, as well as the nonlinear polarization at the incident frequencies. Thus, one should consider only one wave equation (Eq. (1.95c)), the amplitudes of the initial frequencies being treated as parameters.

The electric field at the frequency ($\omega_3$) should obey Maxwell's nonlinear optical equation:

$$\vec{\nabla} \times \vec{\boldsymbol{E}} = -\frac{\partial \vec{\boldsymbol{B}}}{\partial t} = i\omega_3 \vec{\boldsymbol{B}}, \tag{1.104a}$$

$$\vec{\nabla} \times \vec{\boldsymbol{H}} = -\frac{\partial \varepsilon_0 \varepsilon^{(r)} \vec{\boldsymbol{E}}}{\partial t} + \frac{\partial \vec{\boldsymbol{P}}^{(2)}(\vec{r},t)}{\partial t} = i\omega_3 \varepsilon_0 \varepsilon^{(r)} \vec{\boldsymbol{E}} - i\omega_3 \vec{\boldsymbol{P}}^{(2)}(\vec{r},t). \tag{1.104b}$$

Eqs. (1.104a) and (1.104b) are non-homogenous differential equations. The general solution consists of the solution of the homogeneous equation plus one particular solution of the inhomogeneous equation. Far from the interface, the solution of these equations are homogeneous waves:

$$\vec{\boldsymbol{E}}_{tot}^{+\infty} = \vec{E}_{3r} \mathrm{e}^{i(\vec{k}_{3r}\cdot\vec{r}-\omega_3 t)}, \tag{1.105a}$$

$$\vec{\boldsymbol{E}}_{tot}^{-\infty} = \vec{E}_{3t} \mathrm{e}^{i(\vec{k}_{3t}\cdot\vec{r}-\omega_3 t)}. \tag{1.105b}$$

Consider the interface between two semi-infinite media Fig. 1.9. $\varepsilon_I$ $\varepsilon_l$, and $\varepsilon_T$ are the electric permittivity of the incident medium, the thin film, and the substrate, respectively. According to Fig. 1.9 the interface is perpendicular to the $Z$-axis and the thickness of the thin film $d$ tends to 0.

For a thin film, the nonlinear source is an effective polarization, which can be modeled by using a $\delta$ Dirac's function at the depth $Z = 0$ from the interface

$$\vec{\boldsymbol{P}}^{(\mathbf{2})} \approx \vec{P}_{surf}^{(2)} \mathrm{e}^{i\vec{k}^{\parallel}\cdot\vec{r}} \delta(Z), \tag{1.106}$$

where the complex amplitude of the polarization depends on the depth $Z$ $\left(\vec{P}_{surf}^{(2)} = P_{surf}^{(2)}(Z)\vec{\hat{p}}\right)$ and $\vec{k}_{\parallel}$ is the parallel component of the polarization wave vector at the interface. $\vec{\hat{p}}$ is the direction of the nonlinear polarization

$$\vec{\hat{p}} = \hat{p}_X \vec{e}_X + \hat{p}_Y \vec{e}_Y + \hat{p}_Z \vec{e}_Z. \tag{1.107}$$

The solution for the transmitted and reflected nonlinear radiations from the interface can be determined by solving Maxwell's equations with a nonlinear source of polarization occupying a finite volume and then taking the limit as the thickness goes to zero.

To deduce the intensity of the reflected and transmitted waves in the first and second linear environments, we must first determine the contribution value of the oscillating electric field to the sum-frequency in the thin film, and then make use of boundary conditions.

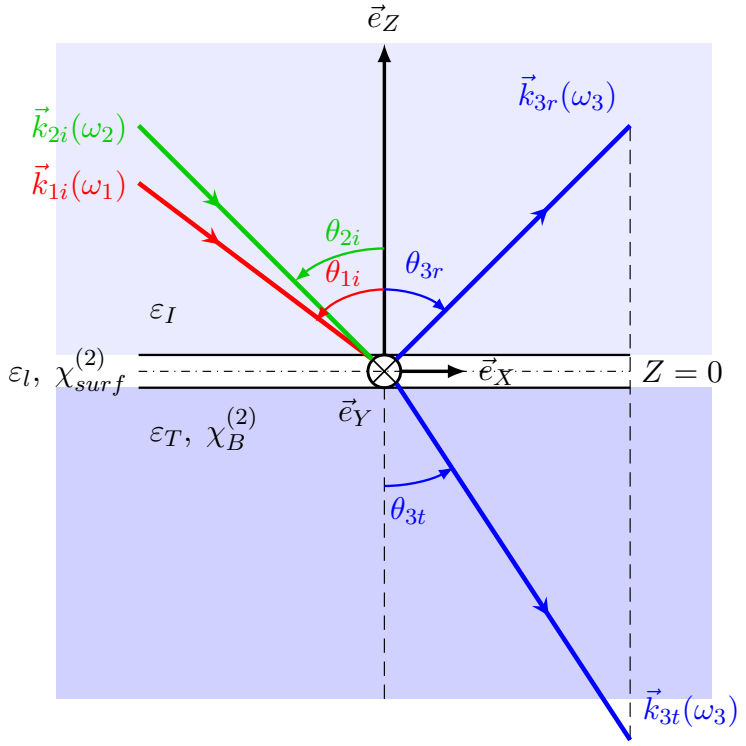


FIGURE 1.9: Schematic representation of SFG at the interface between a linear medium and nonlinear medium. This figure shows the $XZ$-plane, and $Z = 0$ defines the interface

The boundary conditions for the perpendicular components of the flux density (Eq. (1.36)) read (no charge at the surface $\equiv \sigma_{\text{surf}} = 0$),

$$D_l^{\perp} = D_I^{\perp} \Longrightarrow \varepsilon_l E_l^{\perp} = \varepsilon_I E_I^{\perp}, \tag{1.108}$$

$$E_l^{\perp} = \frac{\varepsilon_I}{\varepsilon_l} E_I^{\perp}. \tag{1.109}$$

The components of the reflected electric field at the surface of the film is given by:

$$\vec{E}_l^{NL} = F\vec{E}_{li}. \tag{1.110}$$

The Fresnel Factors $F$ can be derived from Eq. (1.73) as :

$$F = \begin{pmatrix} \dfrac{2\varepsilon_I k_{T_Z}}{\varepsilon_T k_{I_Z} + \varepsilon_I k_{T_Z}} & 0 & 0 \\ 0 & \dfrac{2k_{I_Z}}{k_{I_Z} + k_{T_Z}} & 0 \\ 0 & 0 & \dfrac{\varepsilon_I}{\varepsilon_l} \dfrac{2\varepsilon_T k_{I_Z}}{\varepsilon_T k_{I_Z} + \varepsilon_I k_{T_Z}} \end{pmatrix}, \tag{1.111}$$

where the diagonal terms can be denoted as

$$\begin{cases} \mathrm{F_{XX}} &= \dfrac{2\varepsilon_I k_{T_Z}}{\varepsilon_T k_{I_Z} + \varepsilon_I k_{T_Z}} &= \dfrac{2\varepsilon_I^{(r)}\sqrt{\varepsilon_T^{(r)} - \varepsilon_I^{(r)}\sin^2\theta}}{\varepsilon_T^{(r)}\sqrt{\varepsilon_I^{(r)}}\cos\theta + \varepsilon_I^{(r)}\sqrt{\varepsilon_T^{(r)} - \varepsilon_I^{(r)}\sin^2\theta}}, \\ \mathrm{F_{YY}} &= \dfrac{2k_{I_Z}}{k_{I_Z} + k_{T_Z}} &= \dfrac{2\sqrt{\varepsilon_I^{(r)}}\cos\theta}{\sqrt{\varepsilon_I^{(r)}}\cos\theta + \sqrt{\varepsilon_T^{(r)} - \varepsilon_I^{(r)}\sin^2\theta}}, \\ \mathrm{F_{ZZ}} &= \dfrac{\varepsilon_I}{\varepsilon_l}\dfrac{2\varepsilon_T k_{I_Z}}{\varepsilon_T k_{I_Z} + \varepsilon_I k_{T_Z}} &= \dfrac{\varepsilon_I^{(r)}}{\varepsilon_l^{(r)}}\dfrac{2\varepsilon_T^{(r)}\sqrt{\varepsilon_I^{(r)}}\cos\theta}{\varepsilon_T^{(r)}\sqrt{\varepsilon_I^{(r)}}\cos\theta + \varepsilon_I^{(r)}\sqrt{\varepsilon_T^{(r)} - \varepsilon_I^{(r)}\sin^2\theta}}. \end{cases} \tag{1.112}$$

The complete problem for the slab of finite thickness was solved by Bloembergen and Pershan [5]. An alternative approach deriving boundary conditions to match electric and magnetic fields across the polarized sheet was also proposed by Heinz [6, 7], which has also been used by Caudano [4], and recently by Shen [8].

Heinz derived the following expression for the radiated field at the sum-frequency, at the interface in terms of the pump fields in the bulk media:

$$\vec{\hat{e}}^{\perp} \cdot \vec{E}_{3r} = i\frac{1}{2}\frac{\omega_3}{c}\frac{1}{\sqrt{\varepsilon^{(r)}}\cos\theta_{3r}}\left[F_3(\omega_3)\vec{\hat{e}}^{\perp} \cdot \chi_s^{(2)} : F_1(\omega_1)\vec{\hat{e}}_{1i}F_2(\omega_2)\vec{\hat{e}}_{2i}\right] E_{1i}^{(0)}E_{2i}^{(0)} \tag{1.113}$$

where, $\vec{\hat{e}}^{\perp}$ is the polarization vector associated with $\vec{E}_{3r}$. $\vec{\hat{e}}^{\perp}$ is perpendicular to the wave vector $\vec{k}_{3r}$. $\vec{\hat{e}}_{1i}$ and $\vec{\hat{e}}_{2i}$ are the polarization vectors of the pump fields $\vec{E}_{1i}^{(0)}$ and $\vec{E}_{2i}^{(0)}$. $\chi_s^{(2)}$ is the effective nonlinear susceptibility of the thin film. $F_I$ is a second rank tensor describing propagation into the interface (Fresnel factor).

Considering that the nonlinear polarization vanishes in the media $I$, and the conservation of the parallel component of the wave vector at the interface ($\vec{k}_{3r}^{\parallel} = \vec{k}_{3t}^{\parallel} = \vec{k}^{\parallel}$), the solutions of Maxwell's equations can be derived in the form

$$\vec{\boldsymbol{E}}(r) = f(Z)\vec{\boldsymbol{E}}_{tot}^{-\infty}(\vec{r}) + f(Z)\vec{\boldsymbol{E}}_{tot}^{+\infty}(\vec{r}) + \vec{e}_{Int}e^{i\vec{k}^{\parallel}\cdot\vec{r}}\delta(Z), \tag{1.114a}$$

$$\vec{\boldsymbol{B}}(r) = f(Z)\vec{\boldsymbol{B}}_{tot}^{-\infty}(\vec{r}) + f(Z)\vec{\boldsymbol{B}}_{tot}^{+\infty}(\vec{r}), \tag{1.114b}$$

where the function $f$ corresponds to a step function

$$f(Z) = \begin{cases} 0 & Z < 0, \\ 1 & Z > 0. \end{cases} \tag{1.115}$$

The $\vec{e}_{Int}$ term describes the auto-spanned field at the interface. $\vec{e}_{Int}$ can be related to the nonlinear polarization by:

$$\varepsilon_0 \varepsilon_l^{(r)} \vec{e}_{Int} = -P_Z^{(2)} \vec{e}_Z = -P^{(2)}(Z=0) \hat{p}_Z \vec{e}_Z. \tag{1.116}$$

Then, the solutions of Eq. (1.104) can be derived (after applying the boundary conditions: $(Z = Z_0 = 0)$ in the form:

$$E_{3r,Y} \mathrm{e}^{iZ_0 \cdot k_{3r,Z}} - E_{3t,Y} \mathrm{e}^{iZ_0 \cdot k_{3t,Z}} = 0, \tag{1.117a}$$

$$-E_{3r,X} \mathrm{e}^{iZ_0 \cdot k_{3r,Z}} + E_{3t,X} \mathrm{e}^{iZ_0 \cdot k_{3t,Z}} + ik^{\parallel} P^{(2)} \hat{p}_Z \frac{1}{\varepsilon_0 \varepsilon_l^{(r)}} = 0, \tag{1.117b}$$

$$H_{3r,Y} \mathrm{e}^{iZ_0 \cdot k_{3r,Z}} - H_{3t,Y} \mathrm{e}^{iZ_0 \cdot k_{3t,Z}} = -i\omega_3 P^{(2)} \hat{p}_X, \tag{1.117c}$$

$$-H_{3r,X} \mathrm{e}^{iZ_0 \cdot k_{3r,Z}} + H_{3t,X} \mathrm{e}^{iZ_0 \cdot k_{3t,Z}} = -i\omega_3 P^{(2)} \hat{p}_Z. \tag{1.117d}$$

Taking into consideration the definition of the amplitude of the fields in each polarization (Fig. 1.10), and the relationships between the electric and magnetic fields of plane waves ($\mu_0 \omega H = kE$), two cases can be defined:

**$s$-polarization**

$$\vec{\hat{p}} = \hat{p}_Y \vec{e}_Y, \tag{1.118}$$

$$\begin{cases} E_{3r} \mathrm{e}^{iZ_0 \cdot k_{3r,Z}} & = E_{3t} \mathrm{e}^{iZ_0 \cdot k_{3t,Z}}, \\ k_{3r} \cos\theta_{3r} E_{3r} \mathrm{e}^{iZ_0 \cdot k_{3r,Z}} + k_{3t} \cos\theta_{3t} E_{3t} \mathrm{e}^{iZ_0 \cdot k_{3t,Z}} & = +i\mu_0 \omega_3^2 P^{(2)} \hat{p}_Y. \end{cases} \tag{1.119}$$

**$p$-polarization**

$$\vec{\hat{p}} = \hat{p}_X \vec{e}_X + \hat{p}_Z \vec{e}_Z \tag{1.120}$$

$$\begin{cases} -\cos\theta_{3r} E_{3r} \mathrm{e}^{iZ_0 \cdot k_{3r,Z}} - \cos\theta_{3t} E_{3t} \mathrm{e}^{iZ_0 \cdot k_{3t,Z}} & = -ik^{\parallel} P^{(2)} \hat{p}_Z \frac{1}{\varepsilon_0 \varepsilon_l^{(r)}}, \\ +k_{3r} E_{3r} \mathrm{e}^{iZ_0 \cdot k_{3r,Z}} - k_{3t} E_{3t} \mathrm{e}^{iZ_0 \cdot k_{3t,Z}} & = -i\mu_0 \omega_3^2 P^{(2)} \hat{p}_X. \end{cases} \tag{1.121}$$

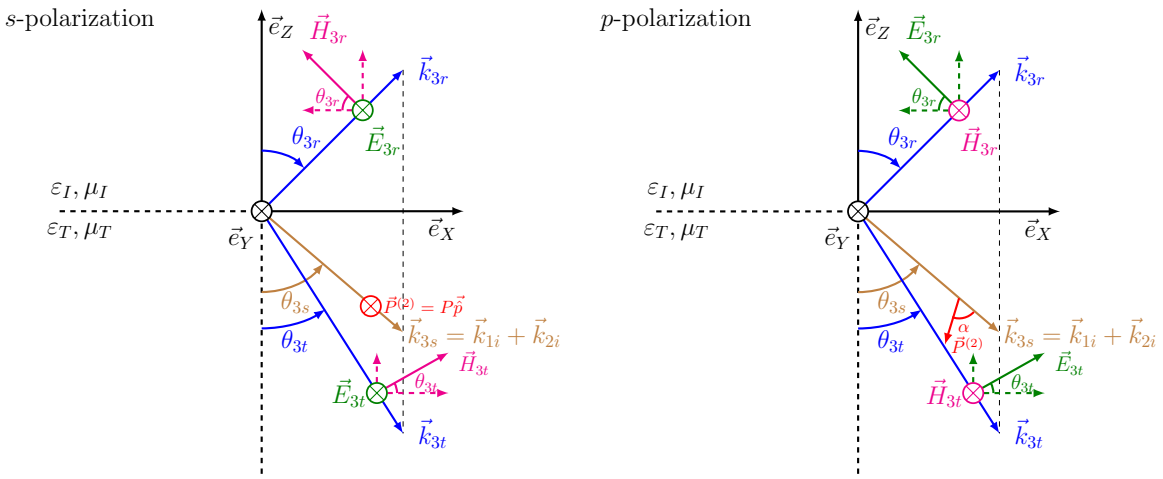


FIGURE 1.10: The angles for the nonlinear polarization and the transmitted and reflected waves generated by this polarization, for the case that the electric vectors are normal ($s$-polarized) and parallel ($p$-polarized) to the plane of reflection.

Solving Eqs. (1.119) and (1.121) lead to,

$$E_{3r}^{s} = i\frac{\omega_3^2}{c^2}\frac{1}{k_{3r}\cos\theta_{3r} + k_{3t}\cos\theta_{3t}}\hat{p}_Y\frac{P^{(2)}(Z_0)}{\varepsilon_0}\mathrm{e}^{iZ_0\cdot k_{3r,z}}, \tag{1.122a}$$

$$E_{3t}^{s} = i\frac{\omega_3^2}{c^2}\frac{1}{k_{3r}\cos\theta_{3r} + k_{3t}\cos\theta_{3t}}\hat{p}_Y\frac{P^{(2)}(Z_0)}{\varepsilon_0}\mathrm{e}^{iZ_0\cdot k_{3t,z}}, \tag{1.122b}$$

and

$$E_{3r}^{p} = i\frac{1}{k_{3t}\cos\theta_{3r} + k_{3r}\cos\theta_{3t}}\left[\frac{1}{\varepsilon_l}k_{3t}k^{\parallel}\hat{p}_Z - \frac{\omega_3^2}{c^2}\cos\theta_{3t}\hat{p}_X\right]\frac{P^{(2)}(Z_0)}{\varepsilon_0}\mathrm{e}^{iZ_0\cdot k_{3r,z}}, \tag{1.123a}$$

$$E_{3t}^{p} = i\frac{1}{k_{3t}\cos\theta_{3r} + k_{3r}\cos\theta_{3t}}\left[\frac{1}{\varepsilon_l}k_{3r}k^{\parallel}\hat{p}_Z + \frac{\omega_3^2}{c^2}\cos\theta_{3r}\hat{p}_X\right]\frac{P^{(2)}(Z_0)}{\varepsilon_0}\mathrm{e}^{iZ_0\cdot k_{3t,z}}. \tag{1.123b}$$

Then, using the expression of the parallel component of the wave vector ($k^{\parallel} = k_{3r}\sin\theta_{3r} = k_{3t}\sin\theta_{3t}$), as well as the appropriate transformations, the fields reflected by the interface at sum-frequency, in terms of Fresnel factors read:

$$E_{3r}^{s} = i\frac{\omega_3}{c}\frac{1}{2\sqrt{\varepsilon_I^{(r)}}\cos\theta_{3r}}\left[\frac{2k_{3r,Z}}{k_{3r,Z} + k_{3t,Z}}\right]\hat{p}_Y\frac{P^{(2)}(Z_0)}{\varepsilon_0}\mathrm{e}^{iZ_0\cdot k_{3r,Z}}, \tag{1.124a}$$

$$\begin{aligned} E_{3r}^{p} = {} & i\frac{\omega_3}{c}\frac{1}{2\sqrt{\varepsilon_I^{(r)}}\cos\theta_{3r}}\left[\frac{2\varepsilon_I k_{3t,Z}}{\varepsilon_T k_{3r,Z} + \varepsilon_I k_{3t,Z}}\right]\hat{p}_X(-\cos\theta_{3r})\frac{P^{(2)}(Z_0)}{\varepsilon_0}\mathrm{e}^{iZ_0\cdot k_{3r,Z}} \\ & + i\frac{\omega_3}{c}\frac{1}{2\sqrt{\varepsilon_I^{(r)}}\cos\theta_{3r}}\left[\frac{2\varepsilon_T k_{3r,Z}}{\varepsilon_T k_{3r,Z} + \varepsilon_I k_{3t,Z}}\frac{\varepsilon_I}{\varepsilon_l}\right]\hat{p}_Z\sin\theta_{3r}\frac{P^{(2)}(Z_0)}{\varepsilon_0}\mathrm{e}^{iZ_0\cdot k_{3r,Z}}, \end{aligned} \tag{1.124b}$$

while

$$E_{3t}^{s} = i\frac{\omega_3}{c}\frac{1}{2\sqrt{\varepsilon_T^{(r)}}\cos\theta_{3t}}\left[\frac{2k_{3t,Z}}{k_{3r,Z}+k_{3t,Z}}\right]\hat{p}_Y\frac{P^{(2)}(Z_0)}{\varepsilon_0}\mathrm{e}^{iZ_0\cdot k_{3t,Z}}, \tag{1.125a}$$

$$\begin{aligned} E_{3t}^{p} = {} & i\frac{\omega_3}{c}\frac{1}{2\sqrt{\varepsilon_T^{(r)}}\cos\theta_{3t}}\left[\frac{2\varepsilon_T k_{3r,Z}}{\varepsilon_I k_{3r,Z}+\varepsilon_T k_{3t,Z}}\right]\hat{p}_X\cos\theta_{3t}\frac{P^{(2)}(Z_0)}{\varepsilon_0}\mathrm{e}^{iZ_0\cdot k_{3t,Z}} \\ & + i\frac{\omega_3}{c}\frac{1}{2\sqrt{\varepsilon_T^{(r)}}\cos\theta_{3t}}\left[\frac{2\varepsilon_I k_{3t,Z}}{\varepsilon_I k_{3r,Z}+\varepsilon_T k_{3t,Z}}\frac{\varepsilon_T}{\varepsilon_l}\right]\hat{p}_Z\sin\theta_{3t}\frac{P^{(2)}(Z_0)}{\varepsilon_0}\mathrm{e}^{iZ_0\cdot k_{3t,Z}}, \end{aligned} \tag{1.125b}$$

characterize the field generated at the sum frequency by the interface and transmitted in the substrate.

**In the Chapter 3 we will rely on Eqs. (1.113) and (1.125) to derive the equations for intensities reflected at the sum-frequency for different sets of polarizations.**

# References

[1] Kuzyk, M. G. *Lecture Notes in Nonlinear Optics*; http://nlosource.com/LectureNotesBook.pdf, 2010.

[2] Barnerjee, P. P. *Nonlinear Optics:Theory, Numerical Modeling, and Applications*, 1st ed.; Optical Science and Engineering; CRC Press, 2003.

[3] Boyd, R. W. *Nonlinear Optics*; Third Edition; Elsevier, 2008.

[4] Caudano, Y. Contribution à l'étude d'interfaces par spectroscopies vibrationnelles linéaires et non linéaires. Ph.D. thesis, Facultés Universitaires Notre-Dame de la Paix, Namur, Belgium, 2000.

[5] Bloembergen, N.; Pershan, P. S. *Phys. Rev.* **1962**, *128*, 606–622.

[6] Heinz, T. F. Nonlinear Optics of Surfaces and Adsorbates. Ph.D. thesis, University of California, Berkeley, 1982.

[7] Heinz, T. F. In *Nonlinear Surface Electromagnetic Phenomena*; Ponath, H.-E., Stegeman, G., Eds.; Elsevier: Amsterdam, 1991; Chapter 5, pp 353–416.

[8] Shen, Y. R. *Fundamentals of Sum-Frequency Spectroscopy*; Cambridge University Press: Cambridge, 2016.

# Chapter 2

# Quantum Theory of Nonlinear Susceptibilities

In Chapter 1, we reviewed the basic concepts of electromagnetic wave propagation in linear and nonlinear materials. However, optical propagation in many materials is nonlinear, in the sense that the polarization depends nonlinearly on the optical field in the medium. Then, molecular nonlinear optics is the description of the change of the molecular optical properties by the presence of an intense light field. In general, the response of the charges depends on the frequency of the electric field, and the hyperpolarizabilities are therefore frequency-dependent. Knowing that the electric field separates charges in a material, the charge distribution can be described as a series of moments. Indeed, electric field induces a dipole moment, a field gradient (the quadrupole), etc. This interaction is formulated using the concept of the nonlinear response of the material at the quantum level.

In this chapter, we use time-dependent perturbation theory and assume that the solutions to the eigenvalue problem of the unperturbed system are known. This approach relies on that developed by Boyd [1] as well as Kuzyk [2]. In practice we are of course not able to obtain exact solutions even to the unperturbed system, but our analysis will nevertheless highlight the dependence of the hyperpolarizabilities on other molecular parameters such as excitation energies and transition moments. Then, we derive the expressions for the molecular first and second-order response functions that describe the system.

## 2.1 Calculating the Nonlinear Optical Susceptibilities

### 2.1.1 Schrödinger equation

For a quantum-mechanical system in a particular quantum-mechanical state that we designate $s$, we can describe all the physical properties of the system in terms of its wavefunction $\psi_s(\vec{r}, t)$.

This wavefunction obeys the time-dependent Schrödinger equation:

$$i\hbar\frac{\partial\psi_s(\vec{r},t)}{\partial t} = \hat{H}\psi_s(\vec{r},t), \tag{2.1}$$

where $\hat{H}$ is the Hamiltonian operator of the system. In order to determine how the wavefunction evolves in time, it is often helpful to make explicit use of the fact that the eigenstates of the unperturbed Hamiltonian $\hat{H}_0$ form a complete set of basis functions. We can hence represent the wavefunction of state $s$ as

$$\psi_s(\vec{r},t) = \sum_n C_n^s(t)u_n(\vec{r}). \tag{2.2}$$

The functions $u_n(\vec{r})$ are the eigensolutions to the time-independent Schrödinger equation

$$\hat{H}_0 u_n(\vec{r}) = E_n u_n(\vec{r}), \tag{2.3}$$

and are therefore orthonormal

$$\int u_m^*(\vec{r})u_n(\vec{r})\,\mathrm{d}\tau \equiv \langle m|n\rangle = \delta_{mn}. \tag{2.4}$$

The expansion coefficient $C_n^s(t)$ gives the probability amplitude that the system is found in state $|n\rangle$ by measurement performed at time $t$. The time evolution of $\psi_s(\vec{r},t)$ can be specified in terms of the time evolution of each of the expansion coefficient $C_n^s(t)$.

To determine how these coefficients evolve in time, we introduce Eq. (2.2) into Schrödinger's equation (Eq. (2.1)):

$$\begin{aligned} i\hbar\sum_n \frac{dC_n^s(t)}{dt}u_n(\vec{r}) &= \sum_n C_n^s(t)\hat{H}u_n(\vec{r}), \\ i\hbar\sum_n \frac{dC_n^s(t)}{dt}|n\rangle &= \sum_n C_n^s(t)\hat{H}|n\rangle. \end{aligned} \tag{2.5}$$

Then, let's multiply Eq. (2.5) by $\langle m|$

$$i\hbar\sum_n \frac{dC_n^s(t)}{dt}\langle m|n\rangle = \sum_n C_n^s(t)\langle m|\hat{H}|n\rangle, \tag{2.6}$$

and after accounting for the orthogonality relation Eq. (2.4) and defining $H_{mn} = \langle m|\hat{H}|n\rangle$, one obtains

$$i\hbar\frac{d}{dt}C_m^s(t) = \sum_n C_n^s(t)H_{mn}. \tag{2.7}$$

### 2.1.2 Density operator and quantum Liouville equation

The expectation value of any observable quantity can be calculated in terms of the wavefunction of the system. A basic postulate of quantum mechanics states that any observable quantity $O$ is associated with a Hermitian operator $\hat{O}$. The expectation value of $\hat{O}$ is then obtained according to the prescription

$$\langle \hat{O} \rangle = \langle \psi_s | \hat{O} | \psi_s \rangle. \tag{2.8}$$

Here, the angular brackets denote a quantum-mechanical average and

$$\langle \psi_s(t)| = \sum_m C_m^{s^*}(t) \langle m| \quad \text{since} \quad |\psi_s(t)\rangle = \sum_n C_n^s(t)|n\rangle. \tag{2.9}$$

The expectation value $\langle \hat{O} \rangle$ can then be expressed in terms of the probability amplitudes $C_n^s(t)$ by introducing Eq. (2.9) into Eq. (2.8) to obtain

$$\langle \hat{O} \rangle = \sum_m \sum_n C_m^{s^*} C_n^s O_{mn}, \tag{2.10}$$

where we have introduced the matrix elements $O_{mn}$ of the operator $\hat{O}$, defined through

$$O_{mn} = \langle m | \hat{O} | n \rangle. \tag{2.11}$$

Under the circumstances where the precise state of the system is unknown, the density matrix formalism can be used to describe the system in a statistical sense. Let us denote by $p_s$ the probability that the system is in the state $s$. The quantity $p_s$ is to be understood as a classical rather than a quantum-mechanical probability. Hence $p_s$ simply reflects our lack of knowledge of the actual quantum-mechanical state of the system.

$$\sum_n |C_n^s|^2 = 1 \quad \text{quantum-mechanical probability}, \tag{2.12}$$

$$\sum_s p_s = 1 \quad \text{classical probability}. \tag{2.13}$$

The ensemble average is

$$\overline{\langle O \rangle} = \sum_s p_s \langle \psi_s | \hat{O} | \psi_s \rangle, \tag{2.14}$$

where the over-bar denotes an ensemble average, that is, an average over all of the possible states of the system. Again, Eq. (2.8) can be employed to rewrite this quantity as:

$$\begin{aligned}\overline{\langle O\rangle} &= \sum_s p_s \sum_{mn} C_m^{s^*} C_n^s O_{mn}, \\ &= \sum_{mn} \rho_{nm} O_{mn}. \end{aligned} \tag{2.15}$$

In terms of $p_s$, we define the elements of the density matrix of the system by

$$\rho_{nm} = \sum_s p_s C_m^{s^*} C_n^s = \overline{C_m^{s^*} C_n^s}. \tag{2.16}$$

The density matrices combine both quantum and classical probabilities. The diagonal elements $\rho_{nn}$ give the "**population**" of the system in energy eigenstate $|n\rangle$, whereas the off-diagonal elements $\rho_{nm}$ gives the "**coherence**" between levels $|n\rangle$ and $|m\rangle$, in the sense that $\rho_{mn}$ will be nonzero only if the system is in a coherent superposition of energy eigenstate $|n\rangle$ and $|m\rangle$.

$$\rho_{nn} = \sum_s p_s |C_n^s|^2, \tag{2.17}$$

$$\rho_{nm} = \sum_s p_s C_m^{s^*} C_n^s. \tag{2.18}$$

The double summation in the Eq. (2.15) can be simplified as follows[1]:

$$\begin{aligned}\overline{\langle O\rangle} &= \sum_{mn} \rho_{nm} O_{mn} = \sum_n \left( \sum_m \rho_{nm} O_{mn} \right), \\ &= \sum_n \big(\rho O\big)_{nn} = \mathrm{tr}\big(\rho O\big). \end{aligned} \tag{2.19}$$

Note that the corresponding density operator is expressed in the terms of the *bra* and *ket* wave functions

$$\hat{\rho} = \sum_{mn} \rho_{nm} |n\rangle\langle m| = \sum_s p_s |\psi_s\rangle\langle\psi_s|, \tag{2.20}$$

and that its matrix elements are obtained by projection on the eigenstates such as to recover Eq. (2.16)

$$\rho_{nm} = \langle n|\hat{\rho}|m\rangle = \sum_s p_s \langle n|\psi_s\rangle\langle\psi_s|m\rangle = \sum_s p_s C_n^s C_m^{s^*}. \tag{2.21}$$

Knowing that the expectation value of any observable quantity can be determined straightforwardly in terms of the density matrix, in order to determine how any expectation value evolves in time, it is thus only necessary to determine how the density matrix itself evolves in time. By

[1]Density matrices can be used to calculate the expectation value of any observable $\hat{O}$

direct time differentiation of Eq. (2.20), we find that

$$\begin{aligned}\frac{\partial\hat{\rho}}{\partial t} &= \frac{\partial}{\partial t}\sum_s p_s|\psi_s\rangle\langle\psi_s|,\\ &= \sum_s \frac{\partial p_s}{\partial t}|\psi_s\rangle\langle\psi_s| + \sum_s p_s\left(\frac{\partial|\psi_s\rangle}{\partial t}\langle\psi_s| + |\psi_s\rangle\frac{\partial\langle\psi_s|}{\partial t}\right).\end{aligned} \tag{2.22}$$

Let us assume that the classic probability is time-independent.

$$\frac{\partial\hat{\rho}}{\partial t} = \sum_s p_s\left(\frac{\partial|\psi_s\rangle}{\partial t}\langle\psi_s| + |\psi_s\rangle\frac{\partial\langle\psi_s|}{\partial t}\right), \tag{2.23}$$

we can then evaluate the second term straightforwardly by using Schrödinger's equation

$$\begin{aligned}\frac{\partial\hat{\rho}}{\partial t} &= -\frac{i}{\hbar}\sum_s p_s(\hat{H}|\psi_s\rangle\langle\psi_s| - |\psi_s\rangle\langle\psi_s|\hat{H}),\\ &= -\frac{i}{\hbar}\Big[\hat{H}\Big(\sum_s p_s|\psi_s\rangle\langle\psi_s|\Big) - \Big(\sum_s p_s|\psi_s\rangle\langle\psi_s|\Big)\hat{H}\Big].\end{aligned} \tag{2.24}$$

The evolution of the density matrix is therefore given by its commutator with the Hamiltonian:

$$\frac{\partial\hat{\rho}}{\partial t} = -\frac{i}{\hbar}\Big(\hat{H}\hat{\rho} - \hat{\rho}\hat{H}\Big) = -\frac{i}{\hbar}\Big[\hat{H},\hat{\rho}\Big], \tag{2.25}$$

which is known as the **Liouville's quantum equation**.

If now we consider that the classical probability is time-dependent, one gets

$$\frac{\partial\hat{\rho}}{\partial t} = -\frac{i}{\hbar}\Big[\hat{H},\hat{\rho}\Big] + \sum_s \frac{\partial p_s}{\partial t}|\psi_s\rangle\langle\psi_s|. \tag{2.26}$$

The second term represents the interactions of the system that can not be conveniently included in the Hamiltonian. There is more than one way to model such interactions. One can include such effects in the formalism by adding phenomenological damping terms to the equation of motion Eq. (2.25). We shall often model such processes by taking the density matrix equation to have the form

$$\frac{\partial\hat{\rho}_{nm}}{\partial t} = -\frac{i}{\hbar}\Big[\hat{H},\hat{\rho}\Big]_{nm} - \underbrace{\gamma_{nm}\big(\rho_{nm} - \rho_{nm}^{(eq)}\big)}_{\substack{\text{exponential decay with}\\ \text{respect to the equilibrium}}}. \tag{2.27}$$

We are thereby asserting that at thermal equilibrium the excited states of the system may contain population (i.e., $\rho_{nm}^{(eq)} \neq 0$), but that thermal excitation, which is expected to be an incoherent process, cannot produce any coherent superpositions of atomic states ($\rho_{nm}^{(eq)} = 0$ for $n \neq m$).

Since $\gamma_{nm}$ is the decay rate, we assume that

$$\begin{cases} \rho_{nm}^{(eq)} = 0 & \text{for } n \neq m, \\ \gamma_{nm} = \gamma_{mn} & \text{physical assumption.} \end{cases} \tag{2.28}$$

### 2.1.3 Perturbed solution of the density matrix equation

The evolution of the density matrix can be determined using perturbation theory. The Hamiltonian can be split into two parts as

$$\hat{H} = \hat{H}_0 + \lambda \hat{V}(t) \tag{2.29}$$

where $\hat{H}_0$ is the Hamiltonian for the free system and $\hat{V}(t)$ represents the dipolar energy of interaction of the system with the externally applied electric radiation field [$\hat{V}(t) = -\lambda\vec{\hat{\mu}} \cdot \vec{E}(t)$], with $\vec{\hat{\mu}} = -e\vec{\hat{r}}$). This interaction is assumed to be weak in the sense that in the ground state the expectation value and matrix elements of $\hat{V}$ are much smaller than the expectation value of $\hat{H}_0$. The density matrix equation of motion with the phenomenological inclusion of damping is given by Eq. (2.27)

$$\frac{\partial \hat{\rho}_{nm}}{\partial t} = -\frac{i}{\hbar}\Big[\hat{H}, \hat{\rho}\Big]_{nm} - \gamma_{nm}\big(\rho_{nm} - \rho_{nm}^{(eq)}\big). \tag{2.30}$$

Then, using Eq. (2.29) the commutator splits into two terms

$$\Big[\hat{H}, \hat{\rho}\Big]_{nm} = \Big[\hat{H}_0, \hat{\rho}\Big]_{nm} + \lambda\Big[\hat{V}, \hat{\rho}\Big]_{nm}. \tag{2.31}$$

The commutator can thus be expanded as

$$\begin{aligned} \Big[\hat{H}_0, \hat{\rho}\Big]_{nm} &= \sum_l (H_{0,nl}\rho_{lm} - \rho_{nl}H_{0,lm}), \\ &= \sum_l (E_n\delta_{nl}\rho_{lm} - \rho_{nl}\delta_{lm}E_m), \\ &= E_n\rho_{nm} - E_m\rho_{nm} = (E_n - E_m)\rho_{nm}, \end{aligned} \tag{2.32}$$

$$\Big[\hat{V}, \hat{\rho}\Big]_{nm} = \sum_l (V_{nl}\rho_{lm} - \rho_{nl}V_{lm}). \tag{2.33}$$

Through use of Eqs. (2.32) and (2.33), the density matrix equation of motion [Eq. (2.27)] thus becomes

$$\begin{aligned}\frac{\partial \rho_{nm}}{\partial t} &= -i\rho_{nm}\omega_{nm} - \frac{i}{\hbar}\sum_l (V_{nl}\rho_{lm} - \rho_{nl}V_{lm}) - \gamma_{nm}\big(\rho_{nm} - \rho_{nm}^{(eq)}\big), \\ &= -i\rho_{nm}\omega_{nm} - \frac{i}{\hbar}\Big[\hat{V}, \hat{\rho}\Big]_{nm} - \gamma_{nm}\big(\rho_{nm} - \rho_{nm}^{(eq)}\big), \end{aligned} \tag{2.34}$$

where $\omega_{nm} = \frac{E_n - E_m}{\hbar}$.

We now seek a solution to Eq. (2.34) in the form of a power series in $\lambda$:

$$\rho_{nm} = \rho_{nm}^{(0)} + \lambda\rho_{nm}^{(1)} + \lambda^2\rho_{nm}^{(2)} + \cdots . \tag{2.35}$$

We thereby obtain the set of equations

$$\frac{\partial \rho_{nm}^{(0)}}{\partial t} = -i\omega_{nm}\rho_{nm}^{(0)} - \gamma_{nm}\big(\rho_{nm}^{(0)} - \rho_{nm}^{(eq)}\big), \tag{2.36a}$$

$$\frac{\partial \rho_{nm}^{(1)}}{\partial t} = -(i\omega_{nm} + \gamma_{nm})\rho_{nm}^{(1)} - i\hbar^{-1}\Big[\hat{V}, \hat{\rho}^{(0)}\Big]_{nm}, \tag{2.36b}$$

$$\frac{\partial \rho_{nm}^{(2)}}{\partial t} = -(i\omega_{nm} + \gamma_{nm})\rho_{nm}^{(2)} - i\hbar^{-1}\Big[\hat{V}, \hat{\rho}^{(1)}\Big]_{nm}, \tag{2.36c}$$

$$\vdots$$

$$\frac{\partial \rho_{nm}^{(k)}}{\partial t} = -(i\omega_{nm} + \gamma_{nm})\rho_{nm}^{(k)} - i\hbar^{-1}\Big[\hat{V}, \hat{\rho}^{(k-1)}\Big]_{nm}. \tag{2.36d}$$

Eq. (2.36a) describes the time evolution of the system in the absence of any external field. We take the steady-state[2] solution to this equation to be

$$\rho_{nm}^{(0)}(t) = \rho_{nm}^{(eq)}, \tag{2.37}$$

where for the reasons given in Eq. (2.28)

$$\rho_{nm}^{(eq)} = 0 \quad \text{for} \quad n \neq m. \tag{2.38}$$

Then, the successive higher-order contributions can be found by the integration of the recurrence relation [Eq. (2.36d)]

$$\rho_{nm}^{(k)} = e^{-(i\omega_{nm}+\gamma_{nm})t}\int_{-\infty}^{t} \frac{-i}{\hbar}\Big[\hat{V}(t'), \hat{\rho}^{(k-1)}(t')\Big]_{nm} e^{(i\omega_{nm}+\gamma_{nm})t'}\, \mathrm{d}t'. \tag{2.39}$$

[2]In systems theory, a system or a process is in a steady state if the variables (called state variables) which define the behavior of the system or the process are unchanging in time.

## 2.2 Molecular response functions

For a molecule, it is appropriate to characterize the response to an electric field by its dipole moment, given by

$$\mu_\alpha = \mu_\alpha^0 + \sum_\beta \alpha_{\alpha\beta} E_\beta + \frac{1}{2}\sum_{\beta\gamma} \beta_{\alpha\beta\gamma} E_\beta E_\gamma + \frac{1}{6}\sum_{\beta\gamma\zeta} \gamma_{\alpha\beta\gamma\zeta} E_\beta E_\gamma E_\zeta + \cdots \tag{2.40}$$

where $\mu_\alpha$ is the $\alpha$-component of the dipole moment of the molecule; where $\mu_\alpha^0$ is the $\alpha$-component of the static permanent dipole moment; $\alpha_{\alpha\beta}$ is the $\alpha\beta$-component of the polarizability, $\beta_{\alpha\beta\gamma}$ is the $\alpha\beta\gamma$-component of the first hyperpolarizability, and $\gamma_{\alpha\beta\gamma\zeta}$ is the $\alpha\beta\gamma\zeta$-component of the second hyperpolarizability.

### 2.2.1 First-order response: Polarizability

The first-order response is obtained from the first-order recurrence relation [Eq. (2.39)]

$$\rho_{nm}^{(1)} = e^{-(i\omega_{nm}+\gamma_{nm})t} \int_{-\infty}^{t} \frac{-i}{\hbar} \left[\hat{V}(t'), \hat{\rho}^{(0)}\right]_{nm} e^{(i\omega_{nm}+\gamma_{nm})t'} \, \mathrm{d}t'. \tag{2.41}$$

As before the interaction Hamiltonian is given by

$$\hat{V}(t') = -\vec{\hat{\mu}} \cdot \vec{E}(t'). \tag{2.42}$$

We represent the applied field as

$$\vec{E}(t') = \sum_q \vec{E}_q e^{-i\omega_q t'}. \tag{2.43}$$

The commutator can be expressed as

$$\begin{aligned} \left[\hat{V}(t'), \hat{\rho}^{(0)}\right]_{nm} &= \sum_l \left( V_{nl}(t')\rho_{lm}^{(0)} - \rho_{nl}^{(0)} V_{lm}(t') \right), \\ &= -\sum_l \left( \vec{\mu}_{nl}\rho_{lm}^{(0)} - \rho_{nl}^{(0)}\vec{\mu}_{lm} \right) \cdot \vec{E}(t'), \\ &= -\left(\rho_{mm}^{(0)} - \rho_{nn}^{(0)}\right) \vec{\mu}_{nm} \cdot \vec{E}(t'). \end{aligned} \tag{2.44}$$

Then, Eq. (2.41) can be rewritten as

$$\rho_{nm}^{(1)} = \frac{i}{\hbar} e^{-(i\omega_{nm}+\gamma_{nm})t}\left(\rho_{mm}^{(0)} - \rho_{nn}^{(0)}\right)\vec{\mu}_{nm} \cdot \sum_q \vec{E}_q^{\,(0)} \int_{-\infty}^{t} e^{[i(\omega_{nm}-\omega_q)+\gamma_{nm})]t'}\, \mathrm{d}t',$$

$$= \frac{1}{\hbar}\left(\rho_{mm}^{(0)} - \rho_{nn}^{(0)}\right) \sum_q \frac{\vec{\mu}_{nm} \cdot \vec{E}_q}{(\omega_{nm} - \omega_q) - i\gamma_{nm}} e^{-i\omega_q t} \tag{2.45}$$

the first-order response can be found from the first-order density matrix

$$\langle \vec{\boldsymbol{\mu}}(t)\rangle^{(1)} = \mathrm{tr}\left[\hat{\rho}^{(1)}\hat{\vec{\mu}}\right] = \sum_{n,m} \rho_{nm}^{(1)} \vec{\mu}_{mn},$$

$$\langle \vec{\boldsymbol{\mu}}(t)\rangle^{(1)} = \frac{1}{\hbar}\sum_{nm}\left(\rho_{mm}^{(0)} - \rho_{nn}^{(0)}\right) \sum_q \frac{\vec{\mu}_{nm} \cdot \vec{E}_q}{(\omega_{nm} - \omega_q) - i\gamma_{nm}} \vec{\mu}_{mn} e^{-i\omega_q t}. \tag{2.46}$$

We are interested in the various frequency components of $\langle \vec{\boldsymbol{\mu}}\rangle^{(1)}$, whose complex amplitudes $\langle \vec{\mu}(\omega_q)\rangle$ are defined through

$$\langle \vec{\boldsymbol{\mu}}\rangle^{(1)} = \sum_q \langle \vec{\mu}(\omega_q)\rangle^{(1)} e^{-i\omega_q t}, \tag{2.47}$$

$$\langle \vec{\mu}(\omega_q)\rangle^{(1)} = \sum_{\alpha,\beta} \alpha^{\alpha\beta}(-\omega_q;\omega_q) E_q^{\beta} \vec{e}_\alpha, \tag{2.48}$$

so that,

$$\alpha^{\alpha\beta}(-\omega_q;\omega_q) = \frac{1}{\hbar}\sum_{nm}\left(\rho_{mm}^{(0)} - \rho_{nn}^{(0)}\right)\frac{\mu_{mn}^{\alpha}\mu_{nm}^{\beta}}{(\omega_{nm} - \omega_q) - i\gamma_{nm}}. \tag{2.49}$$

The polarizability can be expressed in terms of the population of each level

$$\alpha^{\alpha\beta}(-\omega_q;\omega_q) = \frac{1}{\hbar}\sum_{nm}\left(\rho_{mm}^{(0)}\frac{\mu_{mn}^{\alpha}\mu_{nm}^{\beta}}{(\omega_{nm} - \omega_q) - i\gamma_{nm}} - \rho_{nn}^{(0)}\frac{\mu_{mn}^{\alpha}\mu_{nm}^{\beta}}{(\omega_{nm} - \omega_q) - i\gamma_{mn}}\right). \tag{2.50}$$

The dummy indices $n$ and $m$ of the second term are switched: $n \leftrightarrow m$

$$\alpha^{\alpha\beta}(-\omega_q;-\omega_q) = \frac{1}{\hbar}\sum_{nm}\left(\rho_{mm}^{(0)}\frac{\mu_{mn}^{\alpha}\mu_{nm}^{\beta}}{(\omega_{nm} - \omega_q) - i\gamma_{nm}} - \rho_{mm}^{(0)}\frac{\mu_{nm}^{\alpha}\mu_{mn}^{\beta}}{(\omega_{mn} - \omega_q) - i\gamma_{nm}}\right),$$

$$= \frac{1}{\hbar}\sum_{nm}\rho_{mm}^{(0)}\left(\frac{\mu_{mn}^{\alpha}\mu_{nm}^{\beta}}{(\omega_{nm} - \omega_q) - i\gamma_{nm}} + \frac{\mu_{nm}^{\alpha}\mu_{mn}^{\beta}}{(\omega_{nm} + \omega_q) + i\gamma_{nm}}\right). \tag{2.51}$$

where $\omega_{nm} = -\omega_{mn}$ and $\gamma_{nm} = \gamma_{mn}$

At low temperature only the ground state is occupied: $\rho^{(0)}_{mm} = |g\rangle\langle g|$

$$\begin{aligned}\alpha^{\alpha\beta}(-\omega_q;\omega_q) &= \frac{1}{\hbar}\sum_{nm}\delta_{gm}\left(\frac{\mu^{\alpha}_{mn}\mu^{\beta}_{nm}}{(\omega_{nm}-\omega_q)-i\gamma_{nm}}+\frac{\mu^{\alpha}_{nm}\mu^{\beta}_{mn}}{(\omega_{nm}+\omega_q)+i\gamma_{nm}}\right),\\ &= \frac{1}{\hbar}\sum_{n}\left(\frac{\mu^{\alpha}_{gn}\mu^{\beta}_{ng}}{(\omega_{ng}-\omega_q)-i\gamma_{ng}}+\frac{\mu^{\alpha}_{ng}\mu^{\beta}_{gn}}{(\omega_{ng}+\omega_q)+i\gamma_{ng}}\right).\end{aligned} \tag{2.52}$$

### 2.2.2 Second-order response: First hyperpolarizability

In the present section, we calculate the second-order nonlinear optical susceptibility through the use of the density matrix formulation of quantum mechanics. From the perturbation expansion [Eq. (2.39)], the general result for the second-order correction to $\hat{\rho}$ is given by

$$\rho^{(2)}_{nm} = e^{-(i\omega_{nm}+\gamma_{nm})t}\int_{-\infty}^{t}\frac{-i}{\hbar}\left[\hat{V}(t'),\hat{\rho}^{(1)}\right]_{nm}e^{(i\omega_{nm}+\gamma_{nm})t'}\,\mathrm{d}t', \tag{2.53}$$

In addition, using a development similar to Eq. (2.44) and inserting Eq. (2.45) in the commutator of Eq. (2.53) one obtains

$$\begin{aligned}\left[\hat{V}(t'),\hat{\rho}^{(1)}\right]_{nm} =& -\hbar^{-1}\sum_{l}\left(\rho^{(0)}_{mm}-\rho^{(0)}_{ll}\right)\sum_{q,r}\frac{[\vec{\mu}_{lm}\cdot\vec{E}_q][\vec{\mu}_{nl}\cdot\vec{E}_r]}{(\omega_{lm}-\omega_q)-i\gamma_{lm}}e^{-i(\omega_q+\omega_r)t'}\\ &+\hbar^{-1}\sum_{l}\left(\rho^{(0)}_{ll}-\rho^{(0)}_{nn}\right)\sum_{q,r}\frac{[\vec{\mu}_{nl}\cdot\vec{E}_q][\vec{\mu}_{lm}\cdot\vec{E}_r]}{(\omega_{nl}-\omega_q)-i\gamma_{nl}}e^{-i(\omega_q+\omega_r)t'},\end{aligned} \tag{2.54}$$

so that, after inserting into Eq. (2.53), one obtains

$$\begin{aligned}\rho^{(2)}_{nm} =& e^{-(i\omega_{nm}+\gamma_{nm})t}\left[\int_{-\infty}^{t}\frac{i}{\hbar^2}\sum_{l}\left(\rho^{(0)}_{mm}-\rho^{(0)}_{ll}\right)\sum_{q,r}\frac{[\vec{\mu}_{lm}\cdot\vec{E}_q][\vec{\mu}_{nl}\cdot\vec{E}_r]}{(\omega_{lm}-\omega_q)-i\gamma_{lm}}e^{-i(\omega_q+\omega_r)t'}e^{(i\omega_{nm}+\gamma_{nm})t'}\,\mathrm{d}t'\right.\\ &\left.-\int_{-\infty}^{t}\frac{i}{\hbar^2}\sum_{l}\left(\rho^{(0)}_{ll}-\rho^{(0)}_{nn}\right)\sum_{q,r}\frac{[\vec{\mu}_{nl}\cdot\vec{E}_q][\vec{\mu}_{lm}\cdot\vec{E}_r]}{(\omega_{nl}-\omega_q)-i\gamma_{nl}}e^{-i(\omega_q+\omega_r)t'}e^{(i\omega_{nm}+\gamma_{nm})t'}\,\mathrm{d}t'\right],\end{aligned} \tag{2.55}$$

$$\begin{aligned}\rho^{(2)}_{nm} =& e^{-(i\omega_{nm}+\gamma_{nm})t}\left[\frac{i}{\hbar^2}\sum_{l}\left(\rho^{(0)}_{mm}-\rho^{(0)}_{ll}\right)\sum_{q,r}\frac{[\vec{\mu}_{lm}\cdot\vec{E}_q][\vec{\mu}_{nl}\cdot\vec{E}_r]}{(\omega_{lm}-\omega_q)-i\gamma_{lm}}\right.\\ &\left(\frac{1}{-i\omega_q-i\omega_r+i\omega_{nm}+\gamma_{nm}}\right)e^{-i(\omega_q+\omega_r)t}e^{(i\omega_{nm}+\gamma_{nm})t}\\ &-\frac{i}{\hbar^2}\sum_{l}\left(\rho^{(0)}_{ll}-\rho^{(0)}_{nn}\right)\sum_{q,r}\frac{[\vec{\mu}_{nl}\cdot\vec{E}_q][\vec{\mu}_{lm}\cdot\vec{E}_r]}{(\omega_{nl}-\omega_q)-i\gamma_{nl}}\\ &\left.\left(\frac{1}{-i\omega_q-i\omega_r+i\omega_{nm}+\gamma_{nm}}\right)e^{-i(\omega_q+\omega_r)t}e^{(i\omega_{nm}+\gamma_{nm})t}\right],\end{aligned}$$

$$\rho^{(2)}_{nm} = \left[ \frac{i}{\hbar^2} \sum_l \left(\rho^{(0)}_{mm} - \rho^{(0)}_{ll}\right) \sum_{q,r} \frac{[\vec{\mu}_{lm}\cdot\vec{E}_q][\vec{\mu}_{nl}\cdot\vec{E}_r]}{(\omega_{lm}-\omega_q)-i\gamma_{lm}} \left( \frac{1}{-i\omega_q - i\omega_r + i\omega_{nm} + \gamma_{nm}} \right) e^{-i(\omega_q+\omega_r)t} \right.$$
$$\left. - \frac{i}{\hbar^2} \sum_l \left(\rho^{(0)}_{ll} - \rho^{(0)}_{nn}\right) \sum_{q,r} \frac{[\vec{\mu}_{nl}\cdot\vec{E}_q][\vec{\mu}_{lm}\cdot\vec{E}_r]}{(\omega_{nl}-\omega_q)-i\gamma_{nl}} \left( \frac{1}{-i\omega_q - i\omega_r + i\omega_{nm} + \gamma_{nm}} \right) e^{-i(\omega_q+\omega_r)t} \right],$$

$$= \sum_l \sum_{q,r} e^{-i(\omega_q+\omega_r)t} \left[ \frac{\left(\rho^{(0)}_{mm} - \rho^{(0)}_{ll}\right)}{\hbar^2} \frac{[\vec{\mu}_{lm}\cdot\vec{E}_q][\vec{\mu}_{nl}\cdot\vec{E}_r]}{[(\omega_{lm}-\omega_q)-i\gamma_{lm}][(\omega_{nm}-\omega_q-\omega_r)-i\gamma_{nm}]} \right.$$
$$\left. - \frac{\left(\rho^{(0)}_{ll} - \rho^{(0)}_{nn}\right)}{\hbar^2} \frac{[\vec{\mu}_{nl}\cdot\vec{E}_q][\vec{\mu}_{lm}\cdot\vec{E}_r]}{[(\omega_{nl}-\omega_q)-i\gamma_{nl}][(\omega_{nm}-\omega_q-\omega_r)-i\gamma_{nm}]} \right], \tag{2.56}$$

$$= \sum_{q,r} \sum_l K_{nml} e^{-i(\omega_q+\omega_r)t}. \tag{2.57}$$

The expectation value of the atomic dipole moment is then found from the second-order density matrix:

$$\langle \vec{\boldsymbol{\mu}}(t)\rangle^{(2)} = \mathrm{tr}\left[\hat{\rho}^{(2)}\hat{\vec{\mu}}\right] = \sum_{n,m} \rho^{(2)}_{nm}\vec{\mu}_{mn},$$
$$= \sum_{q,r} \sum_{l,m,n} e^{-i(\omega_q+\omega_r)t} K_{nml}\vec{\mu}_{mn},$$
$$= \frac{1}{\hbar^2} \sum_{q,r} \sum_{l,m,n} e^{-i(\omega_q+\omega_r)t} \left[ \left(\rho^{(0)}_{mm} - \rho^{(0)}_{ll}\right) \frac{\left(\vec{\mu}_{lm}\cdot\vec{E}_q\right)\left(\vec{\mu}_{nl}\cdot\vec{E}_r\right)}{\left(\omega_{lm}-\omega_q-i\gamma_{lm}\right)\left(\omega_{nm}-\omega_q-\omega_r-i\gamma_{nm}\right)} \vec{\mu}_{mn} \right.$$
$$\left. - \left(\rho^{(0)}_{ll} - \rho^{(0)}_{nn}\right) \frac{\left(\vec{\mu}_{nl}\cdot\vec{E}_q\right)\left(\vec{\mu}_{lm}\cdot\vec{E}_r\right)}{\left(\omega_{nl}-\omega_q-i\gamma_{nl}\right)\left(\omega_{nm}-\omega_q-\omega_r-i\gamma_{nm}\right)} \vec{\mu}_{mn} \right]. \tag{2.58}$$

Again, we are interested in the various frequency components [Eq. (2.47)]. In particular, in the complex amplitude of the component of the dipole moment oscillating at frequency $\omega_q + \omega_r$:

$$\langle \vec{\mu}(\omega_q,\omega_r)\rangle^{(2)} = \frac{1}{\hbar^2} \sum_{l,m,n} \vec{\mu}_{mn} \left[ \left(\rho^{(0)}_{mm} - \rho^{(0)}_{ll}\right) \frac{\left(\vec{\mu}_{lm}\cdot\vec{E}_q\right)\left(\vec{\mu}_{nl}\cdot\vec{E}_r\right)}{\left(\omega_{lm}-\omega_q-i\gamma_{lm}\right)\left(\omega_{nm}-\omega_q-\omega_r-i\gamma_{nm}\right)} \right.$$
$$\left. - \left(\rho^{(0)}_{ll} - \rho^{(0)}_{nn}\right) \frac{\left(\vec{\mu}_{nl}\cdot\vec{E}_q\right)\left(\vec{\mu}_{lm}\cdot\vec{E}_r\right)}{\left(\omega_{nl}-\omega_q-i\gamma_{nl}\right)\left(\omega_{nm}-\omega_q-\omega_r-i\gamma_{nm}\right)} \right]. \tag{2.59}$$

We now define first hyperpolarizability through the equation

$$\langle \vec{\mu}(\omega_q,\omega_r)\rangle^{(2)} = \sum_{\alpha,\beta,\gamma} \beta^{\alpha\beta\gamma}(-\omega_q-\omega_r;\omega_q,\omega_r) E^{\beta}_r E^{\gamma}_q \vec{e}_\alpha$$

$$\langle\vec{\mu}(\omega_q,\omega_r)\rangle^{(2)} = \frac{1}{\hbar^2}\sum_{\alpha,\beta,\gamma} E_r^{\beta} E_q^{\gamma} \sum_{l,m,n} \Bigg[ \left(\rho_{mm}^{(0)} - \rho_{ll}^{(0)}\right) \frac{\mu_{mn}^{\alpha}\mu_{lm}^{\gamma}\mu_{nl}^{\beta}}{\left(\omega_{lm} - \omega_q - i\gamma_{lm}\right)\left(\omega_{nm} - \omega_q - \omega_r - i\gamma_{nm}\right)} - \left(\rho_{ll}^{(0)} - \rho_{nn}^{(0)}\right) \frac{\mu_{mn}^{\alpha}\mu_{nl}^{\gamma}\mu_{lm}^{\beta}}{\left(\omega_{nl} - \omega_q - i\gamma_{nl}\right)\left(\omega_{nm} - \omega_q - \omega_r - i\gamma_{nm}\right)} \Bigg] \vec{e}_{\alpha}. \tag{2.60}$$

The first hyperpolarizability reads

$$\beta^{\alpha\beta\gamma}\left(-\omega_q - \omega_r; \omega_q, \omega_r\right) = \frac{1}{\hbar^2}\sum_{l,m,n} \Bigg[ \left(\rho_{mm}^{(0)} - \rho_{ll}^{(0)}\right) \frac{\mu_{mn}^{\alpha}\mu_{lm}^{\gamma}\mu_{nl}^{\beta}}{\left(\omega_{lm} - \omega_q - i\gamma_{lm}\right)\left(\omega_{nm} - \omega_q - \omega_r - i\gamma_{nm}\right)} \tag{2.61a}$$

$$- \left(\rho_{ll}^{(0)} - \rho_{nn}^{(0)}\right) \frac{\mu_{mn}^{\alpha}\mu_{nl}^{\gamma}\mu_{lm}^{\beta}}{\left(\omega_{nl} - \omega_q - i\gamma_{nl}\right)\left(\omega_{nm} - \omega_q - \omega_r - i\gamma_{nm}\right)} \Bigg]. \tag{2.61b}$$

We have labeled the two terms that appear in this expression (2.61a) and (2.61b) so that we can keep track of how these terms contribute to our final expression. Eq. (2.61) does not possess intrinsic permutation symmetry, which we require the susceptibility to possess.

$$\beta^{\alpha\beta\gamma}\left(-\omega_q - \omega_r; \omega_q, \omega_r\right) \neq \beta^{\alpha\gamma\beta}\left(-\omega_q - \omega_r; \omega_r, \omega_q\right). \tag{2.62}$$

We therefore define the first hyperpolarizability to be one-half the sum of the right-hand side of Eq. (2.61) with an analogous expression obtained by simultaneously interchanging $\omega_q$ with $\omega_r$

$$\beta^{\alpha\beta\gamma}\left(-\omega_q - \omega_r; \omega_q, \omega_r\right) = \frac{1}{2}\left[\beta^{\alpha\beta\gamma}\left(-\omega_q - \omega_r; \omega_q, \omega_r\right) + \beta^{\alpha\gamma\beta}\left(-\omega_q - \omega_r; \omega_r, \omega_q\right)\right]. \tag{2.63}$$

We thereby obtain the result

$$\beta^{\alpha\beta\gamma}\left(-\omega_q - \omega_r; \omega_q, \omega_r\right) = \frac{1}{2\hbar^2}\sum_{l,m,n} \Bigg\{ \left(\rho_{mm}^{(0)} - \rho_{ll}^{(0)}\right) \Bigg[ \frac{\mu_{mn}^{\alpha}\mu_{lm}^{\gamma}\mu_{nl}^{\beta}}{\left(\omega_{lm} - \omega_q - i\gamma_{lm}\right)\left(\omega_{nm} - \omega_q - \omega_r - i\gamma_{nm}\right)} \tag{2.64a}$$

$$+ \frac{\mu_{mn}^{\alpha}\mu_{lm}^{\beta}\mu_{nl}^{\gamma}}{\left(\omega_{lm} - \omega_r - i\gamma_{lm}\right)\left(\omega_{nm} - \omega_q - \omega_r - i\gamma_{nm}\right)} \Bigg] \tag{2.64b}$$

$$- \left(\rho_{ll}^{(0)} - \rho_{nn}^{(0)}\right) \Bigg[ \frac{\mu_{mn}^{\alpha}\mu_{nl}^{\gamma}\mu_{lm}^{\beta}}{\left(\omega_{nl} - \omega_q - i\gamma_{nl}\right)\left(\omega_{nm} - \omega_q - \omega_r - i\gamma_{nm}\right)} \tag{2.64c}$$

$$+ \frac{\mu_{mn}^{\alpha}\mu_{nl}^{\beta}\mu_{lm}^{\gamma}}{\left(\omega_{nl} - \omega_r - i\gamma_{nl}\right)\left(\omega_{nm} - \omega_q - \omega_r - i\gamma_{nm}\right)} \Bigg] \Bigg\}. \tag{2.64d}$$

This expression displays intrinsic permutation symmetry. We thereby recast first hyperpolarizability into the form (Appendix A)

$$\beta^{\alpha\beta\gamma}(-\omega_q-\omega_r;\omega_q,\omega_r)=\frac{1}{2\hbar^2}\sum_{l,m,n}\rho_{ll}^{(0)}\Bigg[\frac{\mu_{ln}^{\alpha}\mu_{nm}^{\beta}\mu_{ml}^{\gamma}}{\left(\omega_{ml}-\omega_q-i\gamma_{ml}\right)\left(\omega_{nl}-\omega_q-\omega_r-i\gamma_{nl}\right)} \tag{2.65a}$$

$$+\frac{\mu_{ln}^{\alpha}\mu_{nm}^{\gamma}\mu_{ml}^{\beta}}{\left(\omega_{ml}-\omega_r-i\gamma_{ml}\right)\left(\omega_{nl}-\omega_q-\omega_r-i\gamma_{nl}\right)} \tag{2.65b}$$

$$+\frac{\mu_{ln}^{\beta}\mu_{nm}^{\alpha}\mu_{ml}^{\gamma}}{\left(\omega_{ml}-\omega_q-i\gamma_{ml}\right)\left(\omega_{nm}+\omega_q+\omega_r+i\gamma_{nm}\right)} \tag{2.65c}$$

$$+\frac{\mu_{ln}^{\gamma}\mu_{nm}^{\alpha}\mu_{ml}^{\beta}}{\left(\omega_{ml}-\omega_r-i\gamma_{ml}\right)\left(\omega_{nm}+\omega_q+\omega_r+i\gamma_{nm}\right)} \tag{2.65d}$$

$$+\frac{\mu_{ln}^{\gamma}\mu_{nm}^{\alpha}\mu_{ml}^{\beta}}{\left(\omega_{nl}+\omega_q+i\gamma_{nl}\right)\left(\omega_{mn}-\omega_q-\omega_r-i\gamma_{mn}\right)} \tag{2.65e}$$

$$+\frac{\mu_{ln}^{\beta}\mu_{nm}^{\alpha}\mu_{ml}^{\gamma}}{\left(\omega_{nl}+\omega_r+i\gamma_{nl}\right)\left(\omega_{mn}-\omega_q-\omega_r-i\gamma_{mn}\right)} \tag{2.65f}$$

$$+\frac{\mu_{ln}^{\gamma}\mu_{nm}^{\beta}\mu_{ml}^{\alpha}}{\left(\omega_{nl}+\omega_q+i\gamma_{nl}\right)\left(\omega_{ml}+\omega_q+\omega_r+i\gamma_{ml}\right)} \tag{2.65g}$$

$$+\frac{\mu_{ln}^{\beta}\mu_{nm}^{\gamma}\mu_{ml}^{\alpha}}{\left(\omega_{nl}+\omega_r+i\gamma_{nl}\right)\left(\omega_{ml}+\omega_q+\omega_r+i\gamma_{ml}\right)}\Bigg]. \tag{2.65h}$$

### 2.2.3 From microscopic to macroscopic responses

Each component of the generated surface polarization reads (cf Eq. (1.21))

$$P_I^{(2)}(\omega_q,\omega_r)=\varepsilon_0\sum_{J,K}\sum_{q,r}\chi_{IJK}^{(2)}(-\omega_q-\omega_r;\omega_q,\omega_r)F_J E_J^{(0)}(\omega_r)F_K E_K^{(0)}(\omega_q) \tag{2.66}$$

where the $F$ are the Fresnel factors.

The relationship between the molecular first hyperpolarizability $\beta$ and bulk (macroscopic) susceptibility $\chi^{(2)}$ is calculated under the assumption that the molecular nonlinear optical properties are not severely perturbed by neighboring molecules. The bulk susceptibility is, then, the statistical average of the molecular first hyperpolarizability [3],

$$\chi_{IJK}^{(2)}=\frac{N}{\varepsilon_0}\sum_{\alpha,\beta,\gamma}\langle T_{I\alpha,J\beta,K\gamma}(\phi,\theta,\xi)\beta_{\alpha\beta\gamma}(-\omega_q-\omega_r;\omega_q,\omega_r)\rangle \tag{2.67}$$

where $N$ is the number density of the nonlinear optical molecules, T is the transformation matrix between the laboratory and molecular coordinate systems (related by the Euler angles

$\phi$, $\theta$, and $\xi$), and the angle brackets denote the statistical average. $\chi^{(2)}_{IJK}$ **is one of the key quantities that we need for calculating the SFG intensities. More details are given in Section 3.4.**

# References

[1] Boyd, R. W. *Nonlinear Optics*; Third Edition; Elsevier, 2008.

[2] Kuzyk, M. G. *Lecture Notes in Nonlinear Optics*; http://nlosource.com/LectureNotesBook.pdf, 2010.

[3] Kielich, S. *IEEE J. Quantum Electron.* **1969**, *5*, 562–568.

# Chapter 3

# Vibrational Spectroscopies of Molecules on Surfaces

In Chapters 1 and 2, some of the basics concepts on radiation-matter interactions are discussed. In particular, we have discussed the propagation of a light beam in the context of linear and nonlinear optics, as well as the response of materials (polarizability and hyperpolarizabilities). These interactions could also be studied in terms of Spectroscopy. Indeed, Spectroscopy is the study of the spectrum of a physical phenomenon, that means the decomposition in energy scale, or any other quantity related to energy (frequency, wavelength, etc.). Depending on the nature of the interaction different types of spectroscopy can be distinguished. Among others, vibrational spectroscopy is a powerful mean of identification, characterization, structure elucidation of surface species generated upon molecular adsorption and the species generated by surface reactions. In addition there are a number of techniques that have been specifically developed to study the vibrations of molecules at interfaces (RAIRS, SERS, EELS, SFG, etc.).

This chapter will start by a quick review on molecular vibrations and the harmonic approximation, dealing with Schrödinger equation of the nuclei, normal modes, and harmonic oscillator. Then, a description of the basic theoretical aspects of some vibrational spectroscopies are discussed. They are arranged in this order: IR, Raman, then SFG. Indeed, in the harmonic approximation to be SFG active a normal mode should be both IR and Raman active.

# 3.1 Molecular Vibrations

## 3.1.1 The Schrödinger equation for the nuclei

Within the Born-Oppenheimer approximation, the Hamiltonian for the nuclei ($A$) contains two terms: the kinetic energy of the nuclei and a potential $V$:

$$\hat{H}^{\text{Nucl}} = -\sum_{A}^{N} \sum_{\alpha=x,y,z} \frac{\hbar^2}{2M_A} \frac{\partial^2}{\partial R_{A\alpha}^2} + V(\vec{R}_1, \vec{R}_2, \ldots, \vec{R}_N). \tag{3.1}$$

The potential $V$ describes the potential energy surface (PES), and is made of two terms:

- The electronic energy, solution of the electronic Hamiltonian for a given geometry: $\epsilon^{\text{elec}}(\vec{r}_1, \vec{r}_2, \ldots, \vec{r}_N)$,
- The repulsion between all pairs of nuclei: $\frac{1}{2}\sum_A \sum_{B\neq A} \frac{e^2}{4\pi\varepsilon_0} \frac{Z_A Z_B}{|\vec{R}_{AB}|}$

In order to solve the Schrödinger equation of the nuclei, we need to know the potential $V$. The potential can always be decomposed as a Taylor series:

$$\begin{aligned} V = \underbrace{V_0}_{\text{set to 0}} + \sum_{A\alpha}^{3N} \underbrace{\left(\frac{\partial V}{\partial R_{A\alpha}}\right)_e}_{=0} R_{A\alpha} + \frac{1}{2}\sum_{A\alpha}^{3N}\sum_{B\beta}^{3N} \left(\frac{\partial^2 V}{\partial R_{A\alpha}\partial R_{B\beta}}\right)_e R_{A\alpha}R_{B\beta} \\ + \frac{1}{6}\sum_{A\alpha}^{3N}\sum_{B\beta}^{3N}\sum_{C\gamma}^{3N} \left(\frac{\partial^3 V}{\partial r_{A\alpha}\partial R_{B\beta}\partial R_{C\gamma}}\right)_e R_{A\alpha}R_{B\beta}R_{C\gamma} + \ldots, \end{aligned} \tag{3.2}$$

where the subscript "$e$" stand for the equilibrium geometry. Within that geometry, the second term of Eq. (3.2) is equal to 0, and the Hamiltonian for the nuclei is therefore given by

$$\hat{H}^{\text{Nucl}} = -\sum_{A\alpha}^{3N} \frac{\hbar^2}{2M_A} \frac{\partial^2}{\partial R_{A\alpha}^2} + \frac{1}{2}\sum_{A\alpha}^{3N}\sum_{B\beta}^{3N} \left(\frac{\partial^2 V}{\partial R_{A\alpha}\partial R_{B\beta}}\right)_e R_{A\alpha}R_{B\beta} + \ldots \tag{3.3}$$

We define a new set of coordinates, the mass-weighted Cartesian coordinates:

$$R_{A\alpha}^{\text{m}} = \sqrt{M_A} R_{A\alpha}, \tag{3.4}$$

so that the Hamiltonian reads:

$$\hat{H}^{\mathrm{Nucl}} = -\frac{\hbar^2}{2}\sum_{A\alpha}^{3N}\frac{\partial^2}{\partial(R^{\mathrm{m}}_{A\alpha})^2} + \frac{1}{2}\sum_{A\alpha}^{3N}\sum_{B\beta}^{3N}\left(\frac{\partial^2 V}{\partial R^{\mathrm{m}}_{A\alpha}\partial R^{\mathrm{m}}_{B\beta}}\right)_e R^{\mathrm{m}}_{A\alpha}R^{\mathrm{m}}_{B\beta}, + \ldots \tag{3.5}$$

Let's introduce the normal mode coordinates as unitary transformation of the mass-weighted Cartesian coordinates:

$$Q_k = \sum_{A\alpha}^{3N} R^{\mathrm{m}}_{A\alpha}U_{A\alpha,k}, \tag{3.6}$$

$$R^{\mathrm{m}}_{A\alpha} = \sum_k Q_k U_{A\alpha,k}. \tag{3.7}$$

Using this definition, the Hamiltonian can be rewritten as:

$$\begin{aligned}\hat{H}^{\mathrm{Nucl}} &= -\frac{\hbar^2}{2}\sum_k\sum_l\sum_{A\alpha}^{3N}\frac{\partial}{\partial Q_k}\frac{\partial}{\partial Q_l}U_{A\alpha,k}U_{A\alpha,l} \\ &+ \frac{1}{2}\sum_k\sum_l\sum_{A\alpha}^{3N}\sum_{B\beta}^{3N}U_{A\alpha,k}U_{B\beta,l}\left(\frac{\partial^2 V}{\partial R^{\mathrm{m}}_{A\alpha}\partial R^{\mathrm{m}}_{B\beta}}\right)_e Q_kQ_l + \ldots \\ &= -\frac{\hbar^2}{2}\sum_k\frac{\partial^2}{\partial Q_k^2} + \frac{1}{2}\sum_k\omega_k^2Q_k^2 + \ldots\end{aligned} \tag{3.8}$$

In the previous equation, the unitary transformation $\boldsymbol{U}$ was chosen such that:

$$\sum_{A\alpha}^{3N}\sum_{B\beta}^{3N}U_{A\alpha,k}U_{B\beta,l}\underbrace{\left(\frac{\partial^2 V}{\partial R^{\mathrm{m}}_{A\alpha}\partial R^{\mathrm{m}}_{B\beta}}\right)_e}_{H^{\mathrm{m}}_{A\alpha,B\beta}} = \omega_k^2\delta_{kl}, \tag{3.9}$$

$$\boldsymbol{U}^\dagger\boldsymbol{H}^{\mathrm{m}}\boldsymbol{U} = \boldsymbol{\omega}^2. \tag{3.10}$$

This is an eigenvalue problem.

- The eigenvalues give the frequencies of the normal modes: $\omega_k^2 = 4\pi^2\nu_k^2 = 4\pi^2c^2\bar{\nu}_k^2$
- The eigenvectors are the normal mode coordinate expressions in terms of the mass-weighted Cartesian ones: $U_{A\alpha,k} = \langle R^{\mathrm{m}}_{A\alpha}|Q_k\rangle = Q_{A\alpha,k}$
- $Q^{\mathrm{c}}_{A\alpha,k} = (1/\sqrt{M_A})Q_{A\alpha,k}$ are the components of the $k^{\mathrm{th}}$ mode in terms of Cartesian coordinates.

## 3.1.2 The harmonic approximation

### 3.1.2.1 Mechanical harmonicity

The Hamiltonian expression (Eq. (3.3)) in the normal coordinate basis reads:

$$\hat{H} = -\frac{\hbar^2}{2}\sum_k \frac{\partial^2}{\partial Q_k^2} + \frac{1}{2}\sum_k \omega_k^2 Q_k^2 + \frac{1}{6}\sum_k\sum_l\sum_m F_{klm}Q_kQ_lQ_m + \dots \tag{3.11}$$

In the harmonic approximation, we neglect all the terms that are beyond the quadratic terms (green terms), and the Hamiltonian becomes:

$$\hat{H} = \sum_k \left[-\frac{\hbar^2}{2}\frac{\partial^2}{\partial Q_k^2} + \frac{1}{2}\omega_k^2 Q_k^2\right]. \tag{3.12}$$

The Hamiltonian is separable, so that the wave functions $|v^i\rangle$, eigenfunctions of the Schrödinger equation are products of the harmonic oscillator wave functions $|v_k^i(Q_k)\rangle$, while their energy are sums of harmonic oscillator energies:

$$|v^i\rangle = \prod_k |v_k^i(Q_k)\rangle, \tag{3.13}$$

$$E_{v^i} = \sum_k E_{v_k^i}^k. \tag{3.14}$$

The harmonic oscillator wave function and energy are given by:

$$|v_k^i(Q_k)\rangle = \sqrt{\frac{1}{2^{\nu_k^i}\nu_k^i!}}\left(\frac{\omega_k}{\pi\hbar}\right)^{1/4} e^{-\frac{\omega_k Q_k^2}{2\hbar}} H_{\nu_k^i}\left(\sqrt{\omega_k/\hbar}Q_k\right), \tag{3.15}$$

$$E_{v_k^i}^k = \hbar\omega_k(\nu_k^i + \frac{1}{2}), \tag{3.16}$$

where $H_\nu(x)$ are the Hermite polynomials (Table 3.1), $\nu_k^i = 0, 1, 2, \dots$ is the quantum number associated to the $k$ normal mode for the $i$ state.

The Hermite polynomials satisfy the equation:

$$H_\nu''(x) - 2xH_\nu'(x) + 2\nu H_\nu(x) = 0, \tag{3.17}$$

and the recursion relation

$$H_{\nu+1}(x) = 2xH_\nu(x) - 2\nu H_{\nu-1}(x). \tag{3.18}$$

TABLE 3.1: Hermite polynomials

| $\nu$ | $H_\nu(x)$ |
|---|---|
| 0 | $1$ |
| 1 | $2x$ |
| 2 | $4x^2 - 2$ |
| 3 | $8x^3 - 12x$ |
| 4 | $16x^4 - 48x^2 + 12$ |
| 5 | $32x^5 - 160x^3 + 120x$ |
| 6 | $64x^6 - 480x^4 + 720x^2 - 120$ |

#### 3.1.2.2 Harmonic oscillator properties

**Normalization**

Let's start with the overlap between two one-dimensional vibrational wave functions:

$$\langle v_k^i(Q_k)|v_k^f(Q_k)\rangle = \sqrt{\frac{1}{2^{\nu_k^i+\nu_k^f}\nu_k^i!\nu_k^f!}}\sqrt{\frac{\omega_k}{\pi\hbar}}\int_{-\infty}^{\infty} e^{-\frac{\omega_k Q_k^2}{\hbar}} H_{\nu_k^i}\left(\sqrt{\omega_k/\hbar}Q_k\right) H_{\nu_k^f}\left(\sqrt{\omega_k/\hbar}Q_k\right)\,\mathrm{d}Q_k \tag{3.19}$$

Let's define a new variable $x = \sqrt{\omega_k/\hbar}Q_k$ and $\mathrm{d}x = \sqrt{\omega_k/\hbar}\,\mathrm{d}Q_k$

$$\langle v_k^i(Q_k)|v_k^f(Q_k)\rangle = \sqrt{\frac{1}{2^{\nu_k^i+\nu_k^f}\nu_k^i!\nu_k^f!}}\sqrt{\frac{1}{\pi}}\int_{-\infty}^{\infty} e^{-x^2} H_{\nu_k^i}(x)\, H_{\nu_k^f}(x)\,\mathrm{d}x \tag{3.20}$$

where the integral over $x$ works out as

$$\int_{-\infty}^{\infty} e^{-x^2} H_{\nu_k^i}(x)\, H_{\nu_k^f}(x)\,\mathrm{d}x = \begin{cases} 0 & \text{if } \nu_k^i \neq \nu_k^f \\ \sqrt{\pi}2^{\nu_k^i}\nu_k^i! & \text{if } \nu_k^i = \nu_k^f \end{cases}, \tag{3.21}$$

so that the overlap value confirms the orthogonalization:

$$\langle v_k^i(Q_k)|v_k^f(Q_k)\rangle = \sqrt{\frac{1}{2^{\nu_k^i+\nu_k^f}\nu_k^i!\nu_k^f!}}\sqrt{\frac{1}{\pi}}\left[\sqrt{\pi}2^{\nu_k^i}\nu_k^i!\delta_{\nu_k^i\nu_k^f}\right] = \delta_{\nu_k^i\nu_k^f} \tag{3.22}$$

**Expectation value with $Q_k$**

$$\langle v_k^i(Q_k)|Q_k|v_k^f(Q_k)\rangle \tag{3.23}$$

$$= \sqrt{\frac{1}{2^{\nu_k^i+\nu_k^f}\nu_k^i!\nu_k^f!}}\sqrt{\frac{\hbar}{\pi\omega_k}}\int_{-\infty}^{\infty} e^{-x^2} H_{\nu_k^i}(x)\, H_{\nu_k^f}(x)\, x\,\mathrm{d}x \tag{3.24}$$

By using the recursive relation, derived from Eq. (3.18),

$$xH_\nu(x) = \nu H_{\nu-1}(x) + \frac{1}{2}H_{\nu+1}(x), \tag{3.25}$$

the previous integral can be rewritten:

$$\begin{aligned}
&\langle v_k^i(Q_k)|Q_k|v_k^f(Q_k)\rangle \\
&= \left[\int_{-\infty}^{\infty} e^{-x^2} H_{\nu_k^i}(x)\, \nu_k^f H_{\nu_k^f-1}(x)\, \mathrm{d}x + \frac{1}{2}\int_{-\infty}^{\infty} e^{-x^2} H_{\nu_k^i}(x)\, H_{\nu_k^f+1}(x)\, \mathrm{d}x\right]
\end{aligned} \tag{3.26}$$

$$= \sqrt{\frac{1}{2^{\nu_k^i+\nu_k^f}\nu_k^i!\nu_k^f!}}\sqrt{\frac{\hbar}{\pi\omega_k}}\left[\nu_k^f\sqrt{\pi}2^{\nu_k^i}\nu_k^i!\delta_{\nu_k^i,\nu_k^f-1} + \frac{1}{2}\sqrt{\pi}2^{\nu_k^i}\nu_k^i!\delta_{\nu_k^i,\nu_k^f+1}\right] \tag{3.27}$$

In practice, the expectation value of $Q_k$ obeys to the following rules

$$\langle v_k^i(Q_k)|Q_k|v_k^f(Q_k)\rangle = \begin{cases} 0 & \text{if } \nu_k^i = \nu_k^f \\ \sqrt{\frac{\hbar}{2\omega_k}}\sqrt{\nu_k^i+1} & \text{if } \nu_k^i = \nu_k^f - 1 \\ \sqrt{\frac{\hbar}{2\omega_k}}\sqrt{\nu_k^i} & \text{if } \nu_k^i = \nu_k^f + 1 \\ 0 & \text{for other cases} \end{cases} \tag{3.28}$$

Using similar development, the general rules that obeys the expectation of $Q_k^2$ can be derived as

$$\langle v_k^i(Q_k)|Q_k^2|v_k^f(Q_k)\rangle = \begin{cases} \frac{\hbar}{\omega_k}\left(\nu_k^i + \frac{1}{2}\right) & \text{if } \nu_k^i = \nu_k^f \\ \frac{\hbar}{2\omega_k}\sqrt{(\nu_k^i+2)(\nu_k^i+1)} & \text{if } \nu_k^i = \nu_k^f - 2 \\ \frac{\hbar}{2\omega_k}\sqrt{(\nu_k^i)(\nu_k^i-1)} & \text{if } \nu_k^i = \nu_k^f + 2 \\ 0 & \text{for other cases} \end{cases} \tag{3.29}$$

#### 3.1.2.3 Double harmonic approximation

For any vibrational spectroscopies, the intensity associated to the fundamental transition is given by the following integral:

$$P_\zeta = \langle v_0|P(Q)|v_{1\zeta}\rangle \tag{3.30}$$

The expectation value of the electrical property $P$ can be expanded as a Taylor series in $Q$'s:

$$P(Q) = P^0 + \sum_k \left(\frac{\partial P}{\partial Q_k}\right)_e Q_k + \frac{1}{2}\sum_k\sum_l \left(\frac{\partial^2 P}{\partial Q_k \partial Q_l}\right)_e Q_k Q_l + \ldots \tag{3.31}$$

In the double harmonic approximation, in addition to the Hamiltonian truncated at the quadratic term [i.e. the vibrational wavefunctions are limited to the harmonic contribution Eq. (3.15)] we only consider the first two terms (in green) of the property $P$ [Eq. (3.30)] so that the intensity associated to a fundamental transition from the ground state to a normal mode $\zeta$ therefore reads:

$$
\begin{aligned}
P_\zeta =& P^0 \langle 0|0_1 \dots 0_\zeta \dots 1_\zeta \dots 0_{3N-6}\rangle + \sum_k \left(\frac{\partial P}{\partial Q_k}\right)_e \langle 0|Q_k|0_1 \dots 0_\zeta \dots 1_\zeta \dots 0_{3N-6}\rangle \\
=& P^0 \langle 0_1|0_1\rangle\langle 0_2|0_2\rangle \dots \langle 0_\zeta|1_\zeta\rangle \dots \langle 0_{3N-6}|0_{3N-6}\rangle \\
&+ \left(\frac{\partial P}{\partial Q_1}\right)_e \langle 0_1|Q_1|0_1\rangle\langle 0_2|0_2\rangle \dots \langle 0_\zeta|1_\zeta\rangle \dots \langle 0_{3N-6}|0_{3N-6}\rangle \\
&+ \left(\frac{\partial P}{\partial Q_2}\right)_e \langle 0_1|0_1\rangle\langle 0_2|Q_2|0_2\rangle \dots \langle 0_\zeta|1_\zeta\rangle \dots \langle 0_{3N-6}|0_{3N-6}\rangle \\
&+ \dots \\
&+ \left(\frac{\partial P}{\partial Q_\zeta}\right)_e \langle 0_1|0_1\rangle\langle 0_2|0_2\rangle \dots \langle 0_\zeta|Q_\zeta|1_\zeta\rangle \dots \langle 0_{3N-6}|0_{3N-6}\rangle \\
&+ \left(\frac{\partial P}{\partial Q_{3N-6}}\right)_e \langle 0_1|0_1\rangle\langle 0_2|0_2\rangle \dots \langle 0_\zeta|1_\zeta\rangle \dots \langle 0_{3N-6}|Q_{3N-6}|0_{3N-6}\rangle + \dots \\
=& \left(\frac{\partial P}{\partial Q_\zeta}\right)_e \underbrace{\langle 0_1|0_1\rangle}_{=1} \underbrace{\langle 0_2|0_2\rangle}_{=1} \dots \underbrace{\langle 0_\zeta|Q_\zeta|1_\zeta\rangle}_{=\sqrt{\frac{\hbar}{2\omega_\zeta}}} \dots \underbrace{\langle 0_{3N-6}|0_{3N-6}\rangle}_{=1} \\
=& \sqrt{\frac{\hbar}{2\omega_\zeta}} \left(\frac{\partial P}{\partial Q_\zeta}\right)_e .
\end{aligned}
\tag{3.32}
$$

In the double harmonic approximation:

- The intensity associated to a normal mode $\zeta$ is related to the derivative of a property with respect to this normal mode coordinates.
- Only transitions when just one vibrational quantum number changes by unity are allowed ($\hbar\omega_\zeta$).

### 3.1.3 Beyond the harmonic model: Anharmonic corrections

The truncation of the Taylor expansion of the molecular potential energy after the quadratic term is an approximation, and in real molecules the neglected terms might be important, particularly for large displacements from equilibrium. The typical form of the potential energy surface is shown in Fig. 3.1a, and because at high excitation it is less confining than a parabola, the energy levels converge instead of staying uniformly separated. Thus, normal vibrational frequencies computed with molecular orbital methods are well known to be overestimated due to the harmonic approximation (and the incomplete consideration of electron correlation), in comparison with experimental fundamental frequencies. Therefore, it is common practice to scale these

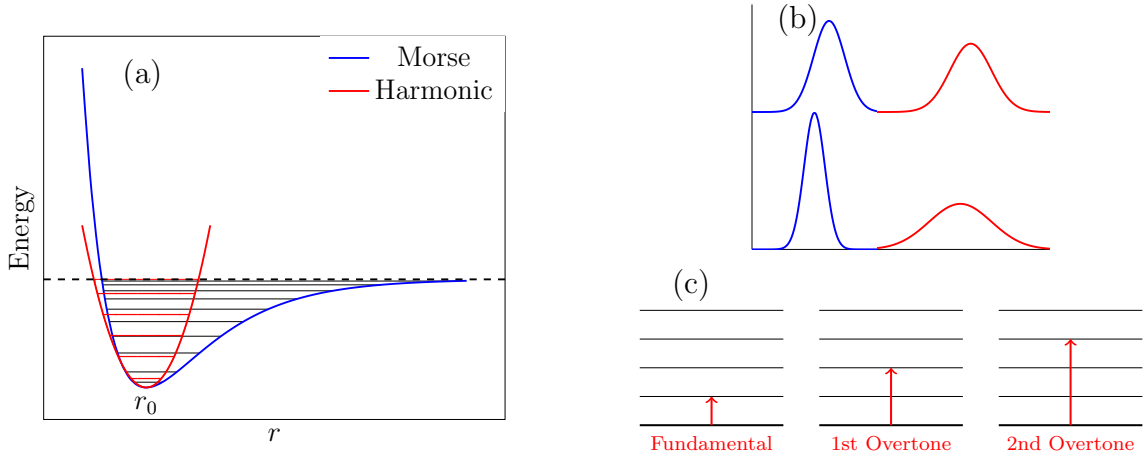


FIGURE 3.1: (a) Potential energy curves of a diatomic molecule: Morse potential (blue line, $V(r) = D_e\left([1 - e^{-a(r-r_0)}]^2 - 1\right)$), harmonic parabolic potential (red line $V(x) = 1/2\ kx^2$). (b) Example of intensity and frequency shifts due to Fermi resonance. The bottom top bands represent two fundamental vibrations without Fermi resonance, and the top bands show the change in bands as a result of these resonance coupling. (c) Energy levels for fundamental and overtone infrared bands.

frequencies by an empirical factor[1] leading to an improved and often sufficient agreement with experiment for a wide range of systems. These scaling factors vary depending on the level of calculation and of the basis set used to evaluate the Hessian [1–7].

### 3.1.4 Overtone, combination bands, and Fermi resonance

In vibrational spectroscopy, an overtone band is the spectral band that occurs in a vibrational spectrum of a molecule when the molecule makes a transition (Fig. 3.1c) from the ground state ($v = 0$) to the second excited state ($v = 2$). Combination bands arise when two modes absorbing at fundamental wavenumbers $\bar{\nu}_1$ and $\bar{\nu}_2$ absorb energy simultaneously. The resulting band will appear at $(\bar{\nu}_1 + \bar{\nu}_2)$ wavenumber, but it is also possible to have a difference band where the wavenumbers are substracted.

Fermi resonance (Fig. 3.1b) results in the shifting of the energies and intensities of absorption bands that have nearly the same energy and symmetry in both IR and Raman spectroscopies. The two bands are usually a fundamental vibration and either an overtone or combination band. The wavefunctions for the two resonant vibrations mix according to the anharmonic oscillator approximation, and the result is a shift in frequency and a change in intensity in the spectrum. As a result, two strong bands are observed in the spectrum, instead of the expected strong and weak bands. It is not possible to determine the contribution from each vibration because of the resulting mixed wave function.

[1]However, it would have been more appropriate to explicitly account for the anharmonicity with the use of Morse-like potentials (higher-order terms of the potential energy surface) but this would have substantially increased the computational needs for moderate improvement.

## 3.2 Infrared absorption spectroscopy

Infrared spectroscopy is a technique based on the vibrations of the atoms of a molecule. An infrared spectrum is commonly obtained by passing infrared radiation through a sample and determining what fraction of the incident radiation is absorbed at a particular energy. The energy at which any peak in an absorption spectrum appears corresponds to the frequency of a vibrational transition of the system.

### 3.2.1 IR intensity

In the most basic terms, the infrared spectrum is formed as a consequence of the absorption of electromagnetic radiation at frequencies that correlate with the transition energy between two vibrational levels of a molecule (Fig. 3.2). The transition rate of infrared absorption from an initial state $|i\rangle$ to a continuum of final states $|f\rangle$ is given by

$$W_{i\to f} = \frac{\pi\left(\vec{\mu}^{fi}\cdot\vec{E}\right)^2}{2\hbar}\rho_f, \tag{3.33}$$

where $\vec{\mu}^{fi}$ is the transition dipole moment, $\vec{E}$ the total electric field, and $\rho_f = \dfrac{\mathrm{d}n}{\mathrm{d}\varepsilon}$ the density of final state (the number of levels per unit energy), and the scalar product

$$\begin{aligned}\left(\vec{\mu}^{fi}\cdot\vec{E}\right)^2 &= \left(\mu_X^{fi}E_X+\mu_Y^{fi}E_Y+\mu_Z^{fi}E_Z\right)^2\\ &=\mu_X^{fi}\mu_X^{fi}E_X^2+\mu_Y^{fi}\mu_Y^{fi}E_Y^2+\mu_Z^{fi}\mu_Z^{fi}E_Z^2\\ &\quad+2\mu_X^{fi}\mu_Y^{fi}E_XE_Y+2\mu_X^{fi}\mu_Z^{fi}E_XE_Z+2\mu_Y^{fi}\mu_Z^{fi}E_YE_Z.\end{aligned} \tag{3.34}$$

In this equation both $\vec{\mu}^{fi}$ and $\vec{E}$ are defined in the laboratory system coordinates $(X,Y,Z)$. However, $\vec{\mu}$ is a molecular quantity i.e. calculated in the molecular system coordinates $(x,y,z)$. One therefore needs to transform it into the laboratory system coordinates:

$$\mu_I^{fi} = \sum_{\alpha}^{x,y,z}\mu_\alpha^{fi}T_{I\alpha}, \tag{3.35}$$

where the $T_{I\alpha}$ are the elements of the rotation matrix.

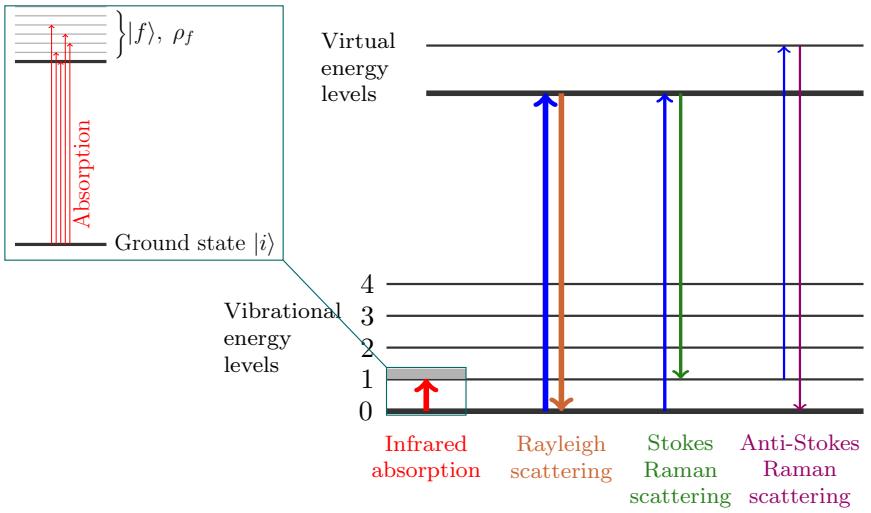


FIGURE 3.2: IR and Raman energy levels

Applying this transformation and considering that the molecules are randomly oriented (isotropic average of the tensor components) one obtains:

$$\begin{aligned}\left\langle \mu_I^{fi}\mu_J^{fi}\right\rangle &= \left\langle \left(\sum_{\alpha}^{x,y,z}\mu_\alpha^{fi}T_{I\alpha}\right)\left(\sum_{\beta}^{x,y,z}\mu_\beta^{fi}T_{J\beta}\right)\right\rangle \\ &= \sum_{\alpha,\beta}^{x,y,z}\mu_\alpha^{fi}\mu_\beta^{fi}\left\langle T_{I\alpha}T_{J\beta}\right\rangle, \\ &= \sum_{\alpha,\beta}^{x,y,z}\mu_\alpha^{fi}\mu_\beta^{fi}\frac{\delta_{\alpha\beta}}{3}, \end{aligned} \tag{3.36}$$

where $\langle\rangle$ defines the orientational average. Eq. (3.34) therefore reads ($\vec{\mu}=\vec{\mu}^{fi}$)

$$\begin{aligned}\left\langle\left(\vec{\mu}\cdot\vec{E}\right)^2\right\rangle &= \frac{1}{3}\left(\mu_x^2+\mu_y^2+\mu_z^2\right)E_X^2+\frac{1}{3}\left(\mu_x^2+\mu_y^2+\mu_z^2\right)E_Y^2+\frac{1}{3}\left(\mu_x^2+\mu_y^2+\mu_z^2\right)E_Z^2, \\ &= \frac{1}{3}\left(\mu_x^2+\mu_y^2+\mu_z^2\right)\left(E_X^2+E_Y^2+E_Z^2\right), \\ &= \frac{1}{3}\left(\mu_x^2+\mu_y^2+\mu_z^2\right)E^2, \end{aligned} \tag{3.37}$$

and Eq. (3.33) becomes,

$$\begin{aligned}W_{fi} =& \frac{\pi}{6\hbar}\,\rho_f\left[\left(\mu_x^{fi}\right)^2+\left(\mu_y^{fi}\right)^2+\left(\mu_z^{fi}\right)^2\right]E^2, \\ =& \frac{1}{6\varepsilon_0\hbar^2}\,\rho_{rad}\left[\left(\mu_x^{fi}\right)^2+\left(\mu_y^{fi}\right)^2+\left(\mu_z^{fi}\right)^2\right], \end{aligned} \tag{3.38}$$

where $\rho_{rad} = \bar{U}h\rho_f$ is the radiant energy density or energy density of radiations states and $\bar{U} = \dfrac{\varepsilon_0 E^2}{2}$ is the energy density of the electromagnetic field [8]. Each photon has an energy $h\nu$. The rate of change of energy density is

$$U = \frac{d\bar{U}}{dt} = -h\nu W_{fi}\, n(\nu)\mathrm{d}\nu, \tag{3.39}$$

where $n(\nu)\mathrm{d}\nu$ is the number density of molecules able to absorb light of frequency in the range $\nu$ to $\nu + \mathrm{d}\nu$.

Now considering that the absorption occurs within a slab of thickness $\mathrm{d}l$ (Beer-Lambert Law Fig. 3.3),

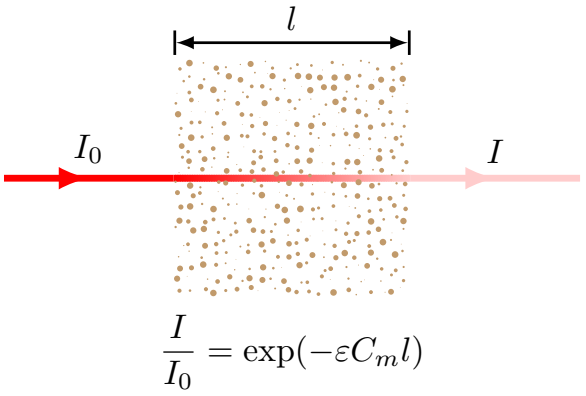


FIGURE 3.3: Beer-Lambert Law (Reproduced from www.texample.net/tikz). The dots represent the absorbing species. $I_0$ is the initial light intensity, $I$ is the light intensity after it passes through the sample, $C_m$ is the concentration of the sample, $l$ is the path length, and $\varepsilon$ is the absorption coefficient.

$$\begin{aligned}
\frac{\mathrm{d}\bar{U}}{\mathrm{d}t} = \frac{\mathrm{d}I(\nu)}{\mathrm{d}l}\mathrm{d}\nu &= -h\nu W_{fi}\, n(\nu)\mathrm{d}\nu, \qquad (3.40)\\
\mathrm{d}I(\nu) &= -h\nu W_{fi}\, n(\nu)\mathrm{d}l,\\
&= -h\nu n(\nu)\,\frac{1}{6\varepsilon_0\hbar^2}\,\rho_{rad}\left[\left(\mu_x^{fi}\right)^2 + \left(\mu_y^{fi}\right)^2 + \left(\mu_z^{fi}\right)^2\right]\mathrm{d}l,\\
&= -Ih\nu\,\frac{n(\nu)}{c}\,\frac{1}{6\varepsilon_0\hbar^2}\left[\left(\mu_x^{fi}\right)^2 + \left(\mu_y^{fi}\right)^2 + \left(\mu_z^{fi}\right)^2\right]\mathrm{d}l,\\
\mathrm{d}I(\nu) &= -\varepsilon(\nu)C_m I\mathrm{d}l \quad \Rightarrow \quad I = I_0 e^{-\varepsilon(\nu)C_m l}, \qquad (3.41)
\end{aligned}$$

where $\rho_{rad} = \dfrac{I}{c}$, with $I$ the light intensity, $\varepsilon(\nu)$ is the absorption coefficient, and $C_m$ the molar concentration of the sample. The absorption coefficient therefore reads

$$\varepsilon(\nu) = \frac{h}{6\varepsilon_0\hbar^2}\,\frac{n(\nu)\nu}{C_m c}\left[\left(\mu_x^{fi}\right)^2 + \left(\mu_y^{fi}\right)^2 + \left(\mu_z^{fi}\right)^2\right]. \tag{3.42}$$

Let's introduce the integrated absorption as

$$\int \varepsilon(\nu)\mathrm{d}\nu = \frac{h}{6\varepsilon_0\hbar^2}\left[\left(\mu_x^{fi}\right)^2+\left(\mu_y^{fi}\right)^2+\left(\mu_z^{fi}\right)^2\right]\frac{1}{cC_m}\int n(\nu)\nu\mathrm{d}\nu. \tag{3.43}$$

However, this integrated absorption coefficient can also be defined as the sum of the absorption coefficients over a band, and it corresponds to the area under the plot of molar absorption coefficient as a function of wavenumber

$$\begin{aligned} A = \int_{\text{band}} \varepsilon(\bar{\nu})\mathrm{d}\bar{\nu} =& \frac{h}{6\varepsilon_0\hbar^2}\left[\left(\mu_x^{fi}\right)^2+\left(\mu_y^{fi}\right)^2+\left(\mu_z^{fi}\right)^2\right]\frac{1}{C_m c}\int_{\text{band}} n(\bar{\nu})\bar{\nu}\mathrm{d}\bar{\nu}, \\ =& \frac{h}{6\varepsilon_0\hbar^2}\left[\left(\mu_x^{fi}\right)^2+\left(\mu_y^{fi}\right)^2+\left(\mu_z^{fi}\right)^2\right]\frac{1}{cC_m}N\bar{\nu}_{fi}, \\ =& N_A\left(\frac{2\pi\hbar\bar{\nu}_{fi}}{c}\right)\frac{1}{6\varepsilon_0\hbar^2}\left[\left(\mu_x^{fi}\right)^2+\left(\mu_y^{fi}\right)^2+\left(\mu_z^{fi}\right)^2\right], \\ =& \frac{\pi\nu_{fi}N_A}{3\varepsilon_0\hbar c^2}\left[\left(\mu_x^{fi}\right)^2+\left(\mu_y^{fi}\right)^2+\left(\mu_z^{fi}\right)^2\right], \end{aligned} \tag{3.44}$$

where $N = N_A C_m$ is the volume density of molecules and $\bar{\nu} = \bar{\nu}_{fi}$ is considered constant over the interval. In Eq. (3.44), each component of the dipole moment can be expressed using the Taylor expansion and the harmonic approximation (Section 3.1.2.3)

$$\mu_\alpha = (\mu_\alpha)_e + \sum_k^{3N-6}\left(\frac{\partial\mu_\alpha}{\partial Q_k}\right)_e Q_k \tag{3.45}$$

Therefore, for normal mode $p$ the transition dipole moment between $|v_i\rangle = |0\rangle$ and $|v_f\rangle = |1\rangle$ reads

$$\mu_\alpha^{fi} = (\mu_\alpha)_e \underbrace{\langle v_f|v_i\rangle}_{0} + \sum_k^{3N-6}\left(\frac{\partial\mu_\alpha}{\partial Q_k}\right)_e \langle v_f|Q_k|v_i\rangle \tag{3.46}$$

where the first term is equal to zero [Eq. (3.22)] and the second is non-zero only if $|v_f\rangle$ and $|v_i\rangle$ differ by one quantum number in only one mode of vibration [Eq. (3.28)]:

$$\left(\mu_\alpha^{fi}\right)_p = \left(\frac{\hbar}{4\pi\nu_p}\right)^{\frac{1}{2}}\left(\frac{\partial\mu_\alpha}{\partial Q_p}\right)_e \tag{3.47}$$

One therefore obtains

$$\begin{aligned} A = I_p^{IR} =& \frac{\pi\nu_p N_A}{3\varepsilon_0\hbar c^2}\left(\frac{\hbar}{4\pi\nu_p}\right)\sum_\alpha^{x,y,z}\left(\frac{\partial\mu_\alpha}{\partial Q_p}\right)_e^2, \\ I_p^{IR} =& \frac{N_A}{12\varepsilon_0 c^2}\left[\left(\frac{\partial\mu_x}{\partial Q_p}\right)_e^2+\left(\frac{\partial\mu_y}{\partial Q_p}\right)_e^2+\left(\frac{\partial\mu_z}{\partial Q_p}\right)_e^2\right] \equiv \left[\mathrm{m}\cdot\mathrm{mol}^{-1}\right] \end{aligned} \tag{3.48}$$

### 3.2.2 Selection rules for IR spectroscopy

The general rule for the vibrational transition $v_i \rightarrow v_f$ to be IR active is that at least one of the three products $\langle v_f|\mu_\alpha|v_i\rangle$ (with $\alpha = x, y, z$) is non-zero. This evaluation can be simplified using the vanishing integral theorem and group theory: this theorem states that the product $\langle v_f|\mu_\alpha|v_i\rangle$ vanishes if the product of the symmetry representation of $|v_f\rangle$, $\mu_\alpha$, and $|v_i\rangle$ does not contain the totally symmetric irreducible representation $\Gamma_1$ of the group:

$$\langle v_f|\mu_\alpha|v_i\rangle \neq 0 \Rightarrow \Gamma(v_f) \otimes \Gamma(\mu_\alpha) \otimes \Gamma(v_i) \supset \Gamma_1 \tag{3.49}$$

This general rule makes no statement as to the intensity with which a permitted transition will appear in the IR spectrum. Thus its expresses a necessary condition but not a sufficient one for IR activity.

For example, the $CH_3$ group (associated to the $C_{3v}$ symmetry) possesses three stretching modes which are all IR active i) one symmetric mode ($A_1$) ($\mu_\alpha = \mu_z$, see Table 3.2) and a pair of doubly-degenerate asymmetric modes ($E$) ($\mu_\alpha = \mu_x,\ \mu_y$). The vibrational ground state $|v_i\rangle$ corresponds to the totally symmetric representation ($\Gamma(v_i) = \Gamma_1 = A_1$, and $\Gamma(v_f) = A_1, E$) so that

$$\Gamma(v_f) \otimes \Gamma(\mu_\alpha) \otimes \Gamma(v_i) = \left\{ \begin{matrix} E \\ A_1 \end{matrix} \right\} \otimes \left\{ \begin{matrix} E \\ A_1 \end{matrix} \right\} \otimes A_1 \supset A_1 \tag{3.50}$$

TABLE 3.2: Characters table for space group $C_{3v}$

| Symmetry species | Symmetry operations | | | | |
|---|---|---|---|---|---|
| | E | $2\,C_3$ | $3\sigma_v$ | IR | Raman |
| $A_1$ | 1 | 1 | 1 | $z$ | $x^2+y^2,\ z^2$ |
| $A_2$ | 1 | 1 | $-1$ | $R_z$ | |
| E | 2 | $-1$ | 0 | $(x, y)$ $(R_x, R_z)$ | $(x^2-y^2, xy)$ $(xz, yz)$ |

## 3.3 Raman scattering spectroscopy

When light interacts with matter, it can scatter inelastically. During that process (Fig. 3.2), the material absorbs energy and the emitted photon has a lower energy than the absorbed photon (this outcome is labeled Stokes Raman scattering) or the material loses energy and the emitted photon has a higher energy than the absorbed photon (this outcome is labeled anti-Stokes Raman scattering). The Raman effect, was experimentally discovered in 1928 by Raman and Krishnan [9] in India. The energy difference between the absorbed and emitted photon corresponds to the energy difference between two resonant states of the material.

### 3.3.1 Raman Intensity

#### The Transition Polarizability Tensor $\alpha^{fi}$

In the Appendix A under the Born-Oppenheimer and Placzek's approximations, the expression of the $\alpha_{\alpha\beta}$ component of the transition polarizability is derived in the form:

$$\begin{aligned}(\alpha_{\alpha\beta})^{fi} &= \frac{1}{\hbar}\sum_{e_r \neq e_g} \frac{2\omega_{e_r e_g}}{\left(\omega_{e_r e_g}^2 - \omega_0^2\right)} \langle v_f | \langle e_g | \mu_\alpha | e_r \rangle \langle e_r | \mu_\beta | e_g \rangle | v_i \rangle , \\ &= \left\langle v_f \left| (\alpha_{\alpha\beta}(Q))^{electronic} \right| v_i \right\rangle \end{aligned} \tag{3.51}$$

where $|e_g\rangle$ and $|e_r\rangle$ are the ground electronic and virtual excited states, respectively. $|v_i\rangle$ and $|v_f\rangle$ are the ground vibrational and first excited states, respectively.

Near equilibrium geometry, the polarizability is expanded along the vibrational normal coordinates:

$$\alpha_{\alpha\beta}^{elec}(Q) = (\alpha_{\alpha\beta})_e + \sum_k \left(\frac{\partial \alpha_{\alpha\beta}}{\partial Q_k}\right)_e Q_k + \frac{1}{2}\sum_{k,l}\left(\frac{\partial^2 \alpha_{\alpha\beta}}{\partial Q_k \partial Q_l}\right)_e Q_k Q_l + \cdots \tag{3.52}$$

Within the double harmonic approximation (Section 3.1.2.3), the expansion is truncated after the first-order term and for a given transition, one obtains:

$$\left\langle v_f \left| \alpha_{\alpha\beta}^{elec}(Q) \right| v_i \right\rangle = (\alpha_{\alpha\beta})_e \underbrace{\langle v_f | v_i \rangle}_{0} + \sum_k \left(\frac{\partial \alpha_{\alpha\beta}}{\partial Q_k}\right)_e \langle v_f | Q_k | v_i \rangle . \tag{3.53}$$

Again, the first term is equal to zero [Eq. (3.22)] and the second is non-zero only if $|v_f\rangle$ and $|v_i\rangle$ differ by one quantum number in only one mode of vibration [Eq. (3.28)]. Now assuming that $|v_i\rangle$ is the ground vibrational state i.e. $|v_i\rangle = |0\rangle$ while the final state is $|v_f\rangle = |1_p\rangle$ , i.e. the oscillator $p$ is in the first excited states and all the others in their ground state:

$$\langle 1_p | \alpha_{\alpha\beta}^{elec}(Q) | 0 \rangle = \sqrt{\frac{\hbar}{2\omega_p}} \left(\frac{\partial \alpha_{\alpha\beta}}{\partial Q_p}\right)_e . \tag{3.54}$$

Then, the $\alpha_{\alpha\beta}$ of the transition polarizability associated to the $p$ normal mode reads:

$$(\alpha_{\alpha\beta})_p^{fi} = \sqrt{\frac{\hbar}{2\omega_p}} \left(\frac{\partial \alpha_{\alpha\beta}}{\partial Q_p}\right)_e , \tag{3.55}$$

$$= \sqrt{\frac{h}{8\pi^2 c \bar{\nu}_p}} \left(\frac{\partial \alpha_{\alpha\beta}}{\partial Q_p}\right)_e . \tag{3.56}$$

### Intensity of the scattered radiation

Let us consider a monochromatic light characterized by its frequency $\omega_0$, its state of polarization $\hat{p}^i$ [linear ($\perp^i$ or $\|^i$), circular, unpolarized ($n^i$)], its propagation vector $\vec{n}_0^i$ and its flux density (irradiance) $\mathscr{I} = \frac{1}{2}c\varepsilon_0 \left(E_i^{(0)}\right)^2 \equiv [\mathrm{Js^{-1}m^{-2}}]$ (where $E_i^{(0)}$ is the amplitude of the electric field strength of the incident radiation). As a result of the interaction of the incident radiation with a material system some scattered radiations are produced. These scattered radiations consist in a number of different frequency components propagating in various directions in space (Fig. 3.4). A component of the scattered radiation is similarly characterized by $\omega_s$, $\hat{p}^s$ (state of polarization of the scattered radiation), $\vec{n}_0^s$, and its intensity $I$. In the following, $I(\theta; \hat{p}^s, \hat{p}^i)$ is the intensity of the radiation of polarization state $\hat{p}^s$ scattered along a general direction $Oa$ defined by $\theta$.

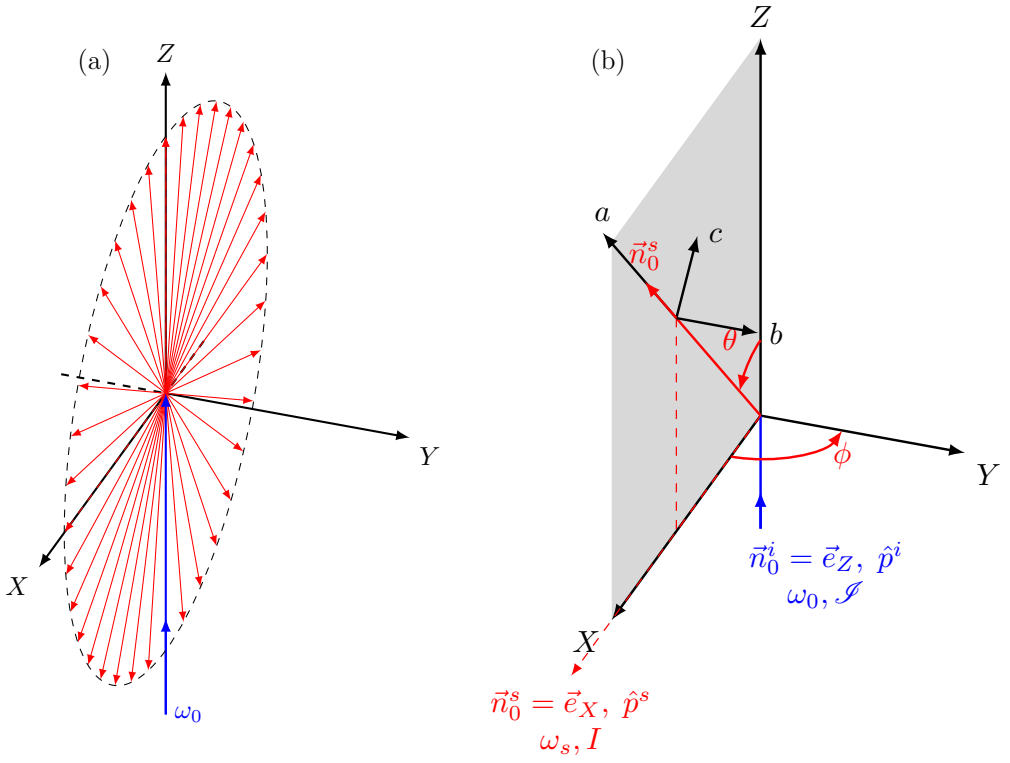


FIGURE 3.4: (a) Scattering in every direction. (b) Illumination geometry. The scattering sample is located at the origin O and the direction of illumination is such that $\vec{n}_0^i = \vec{e}_Z$ and $\vec{n}_0^s = \vec{e}_a$. The scattered plane is the xz plane (grey area), and the general direction of observation is $Oa$, which makes an angle $\theta$ with the $Z$-axis. Important special case of the observation direction is $\theta = \pi/2$ ($\vec{n}_0^s = \vec{e}_X$)

By considering an assembly of N randomly oriented molecules (**isotropic average of tensor components**) irradiated with a monochromatic light, the properties of the radiation scattered along $\vec{n}_0^s$ may be expressed alternatively in terms of its Stokes parameters $S^s(\theta)$ [10]:

$$S^s(\theta) \propto \frac{1}{r^2}\left\{F\left(a^2,\beta^2,\delta^2,\theta,P,\eta,\zeta\right)\right\}\left(E_i^{(0)}\right)^2 \tag{3.57}$$

where $r$ is the distance along the observation direction at which the observation is made, $E_i^{(0)}$ refers to the incident radiation. The function $F\left(a^2,\beta^2,\delta^2,\theta,P,\eta,\zeta\right)$ involves the combinations of the transition tensor invariants $a^2,\beta^2$ and $\delta^2$ (which define the isotropic averages of the transition tensor components), the angle $\theta$ and the polarization characteristics $P$, $\eta$ and $\zeta$ of the incident radiation (see Table 3.3), provided the molecules are non-chiral. The functions $F\left(a^2,\beta^2,\delta^2,\theta,P,\eta,\zeta\right)$ can be found in ref [10].

TABLE 3.3: Polarization characteristics for unpolarized and linear polarized light (The parameters $P$, $\eta$, and $\zeta$ are defined by the polarization ellipse [11]

| $\hat{p}^i$ | $P$ | $\eta$ | $\zeta$ |
|---|---|---|---|
| $n^i$ | 0 | - | - |
| $\perp^i$ | 1 | 0 | 0 |
| $\parallel^i$ | 1 | 0 | $\pi/2$ |

For an incident light of pulsation $\omega_0$ ($\vec{n}_0^i = \vec{e}_Z$), the intensity of the scattered radiation ($\vec{n}_0^s = \vec{e}_Z$, $\theta = \pi/2$) at a distance $X$ from the origin O along the direction defined by $\vec{e}_X$ is determined by the Stokes parameters

$$S_0^s(\pi/2) = N_{v_i}\left(\frac{\omega_s^2}{4\pi\varepsilon_0 c^2 X}\right)^2 \frac{\hbar}{2\omega_{p0}}\left\{\left(\frac{45a_p^2+13\beta_p^2}{90}\right)S_0^i - \left(\frac{45a_p^2+\beta_p^2}{90}\right)S_1^i\right\}, \tag{3.58}$$

$$S_1^s(\pi/2) = N_{v_i}\left(\frac{\omega_s^2}{4\pi\varepsilon_0 c^2 X}\right)^2 \frac{\hbar}{2\omega_{p0}}\left\{\left(\frac{45a_p^2+\beta_p^2}{90}\right)S_0^i - \left(\frac{45a_p^2+\beta_p^2}{90}\right)S_1^i\right\}, \tag{3.59}$$

$$S_2^s(\pi/2) = 0, \tag{3.60}$$

$$S_3^s(\pi/2) = 0, \tag{3.61}$$

where $a_p^2$ and $\beta_p^2$ are the isotropic symmetric and anti-symmetric invariants of the transition polarizability tensor, respectively (in the Einstein notation)

$$a_p^2 = \frac{1}{9}\left(\frac{\partial\alpha_{\alpha\alpha}}{\partial Q_p}\right)_e\left(\frac{\partial\alpha_{\beta\beta}}{\partial Q_p}\right)_e, \tag{3.62}$$

$$\beta_p^2 = \left[3\left(\frac{\partial\alpha_{\alpha\beta}}{\partial Q_p}\right)_e\left(\frac{\partial\alpha_{\alpha\beta}}{\partial Q_p}\right)_e - \left(\frac{\partial\alpha_{\alpha\alpha}}{\partial Q_p}\right)_e\left(\frac{\partial\alpha_{\beta\beta}}{\partial Q_p}\right)_e\right]. \tag{3.63}$$

$N_{v_i}$ is the number of molecules in the initial vibrational state $v_i$. $\omega_s$ is the pulsation of the scattered radiation. The Stokes parameters of the incident light are given by

$$S_0^i = \left(E_i^{(0)}\right)^2, \tag{3.64a}$$

$$S_1^i = P\left(E_i^{(0)}\right)^2 \cos(2\eta)\cos(2\zeta), \tag{3.64b}$$

$$S_2^i = P\left(E_i^{(0)}\right)^2 \cos(2\eta)\sin(2\zeta), \tag{3.64c}$$

$$S_3^i = P\left(E_i^{(0)}\right)^2 \sin(2\eta), \tag{3.64d}$$

$$P = \left[\left(S_1^i\right)^2 + \left(S_2^i\right)^2 + \left(S_3^i\right)^2\right]^{\frac{1}{2}} / S_0^i, \tag{3.64e}$$

$S_0$ is the total intensity measured, $S_3$ is the intensity of the circular polarized beam, $S_1$ and $S_2$ define the intensity of the linear polarized beam.

The Stokes parameters for scattered radiation linearly polarized with $E_{s,Y}^{(0)} \neq 0$ ($\hat{p}^s = \perp^s$) and $E_{s,Z}^{(0)} \neq 0$ ($\hat{p}^s = \|^s$) are given by

$$S_0^s\left(\pi/2; \perp^s, \hat{p}^i\right) = \frac{1}{2}\left\{S_0^s(\pi/2) + S_1^s(\pi/2)\right\}, \tag{3.65}$$

$$S_1^s\left(\pi/2; \|^s, \hat{p}^i\right) = \frac{1}{2}\left\{S_0^s(\pi/2) - S_1^s(\pi/2)\right\}. \tag{3.66}$$

The relationship between the intensity of the radiation I $[\mathrm{J}\cdot\mathrm{s}^{-1}\cdot\mathrm{sr}^{-1}\cdot\mathrm{molecule}^{-1}]$ from a single molecule and the irradiance $\mathscr{I}[\mathrm{J}\cdot\mathrm{s}^{-1}\cdot\mathrm{m}^{-2}]$ of the incident radiation has the general form

$$I = \frac{\mathrm{d}\sigma(\theta)}{\mathrm{d}\Omega}\mathscr{I}, \tag{3.67}$$

$$\mathscr{I} = \frac{1}{2}c\varepsilon_0 S_0 = \frac{1}{2}c\varepsilon_0\left(E_i^{(0)}\right)^2, \tag{3.68}$$

where $\dfrac{\mathrm{d}\sigma(\theta)}{\mathrm{d}\Omega}$ $[\mathrm{m}^2\cdot\mathrm{sr}^{-1}\cdot\mathrm{molecule}^{-1}]$ is the differential scattering cross-section per unit of solid angle $\Omega$ of the Raman intensity detected at an angle $\theta$ of the detector. To convert the Stokes parameters of the scattered radiation to intensities we multiply by the factor $\dfrac{1}{2}c\varepsilon_0 X^2$, and use $\left(E_i^{(0)}\right)^2 = 2\mathscr{I}/c\varepsilon_0$

$$I\left(\pi/2; \perp^s, \hat{p}^i\right) = N_{v_i}\left(\frac{\omega_s^2}{4\pi\varepsilon_0 c^2}\right)^2 \frac{\hbar}{2\omega_{p0}}\left\{\left(\frac{45a_p^2 + 7\beta_p^2}{90}\right) - \left(\frac{45a_p^2 + \beta_p^2}{90}\right) P\cos(2\eta)\cos(2\zeta)\right\}\mathscr{I}, \tag{3.69a}$$

$$I\left(\pi/2; \|^s, \hat{p}^i\right) = N_{v_i}\left(\frac{\omega_s^2}{4\pi\varepsilon_0 c^2}\right)^2 \frac{\hbar}{2\omega_{p0}}\left\{\frac{6\beta_p^2}{90}\right\}\mathscr{I}. \tag{3.69b}$$

For natural radiation (unpolarized $\equiv\ \hat{p}^i = n^i$) incident light the Raman intensity reads,

$$I\left(\pi/2;\perp^s,n^i\right) = N_{v_i}\left(\frac{\omega_s^2}{4\pi\varepsilon_0 c^2}\right)^2 \frac{\hbar}{2\omega_{p0}}\left\{\left(\frac{45a_p^2+7\beta_p^2}{90}\right)\right\}\mathscr{I}, \tag{3.70a}$$

$$I\left(\pi/2;\|^s,n^i\right) = N_{v_i}\left(\frac{\omega_s^2}{4\pi\varepsilon_0 c^2}\right)^2 \frac{\hbar}{2\omega_{p0}}\left\{\frac{6\beta_p^2}{90}\right\}\mathscr{I}, \tag{3.70b}$$

$$N_{v_i} = \frac{N}{1-e^{\left(-\frac{\hbar\omega_p}{KT}\right)}}, \tag{3.70c}$$

and the differential cross-section for the scattered radiation(stokes Raman) linearly polarized with $E_{s,Y}^{(0)} \neq 0$ ($\hat{p}^s = \perp^s$) can therefore be expressed as,

$$\frac{{}^n\mathrm{d}\sigma(\pi/2)_p}{\mathrm{d}\Omega} = \frac{\omega_p^4}{16\pi\varepsilon_0^2 c^4}\frac{\hbar}{2\omega_{p0}}\left[\frac{45a_p^2+7\beta_p^2}{90}\right]\frac{1}{1-e^{\left(-\frac{\hbar\omega_p}{KT}\right)}} \equiv [\mathrm{m}^2\cdot\mathrm{sr}^{-1}\cdot\mathrm{molecule}^{-1}]. \tag{3.71}$$

### 3.3.2 Selection rules for Raman scattering

It follows from Eq. (3.51) that for a general vibrational transition from $v_i$ to $v_f$ to be Raman active, at least one of the products $\langle v_f|\alpha_{\alpha\beta}|v_i\rangle$ must be non-zero. Again, using the vanishing integral theorem and group theory (see Section 3.2.2) one finds

$$\langle v_f|\left(\alpha_{\alpha\beta}\right)|v_i\rangle \neq 0 \Rightarrow \Gamma(v_f)\otimes\Gamma\left(\alpha_{\alpha\beta}\right)\otimes\Gamma(v_i) \supset \Gamma_1 \tag{3.72}$$

This general rule makes no statement as to the intensity with which a permitted transition will appear in the Raman spectrum. In some cases the intensity may be so low as to be unobservable experimentally. It is even possible that the intensity may be fortuitously zero. Thus the general rule expresses a necessary condition but not a sufficient one for Raman activity.

### 3.3.3 Surface-enhanced Raman scattering (SERS)

In 1974, Fleischmann et al. [12] reported an unexpectedly strong Raman signal from a monolayer of pyridine adsorbed on an electrochemically roughened silver electrode. They explained the signal strength as the result of the large number of molecules on the increased surface area of the rough electrode. In 1977, Jeanmaire and Duyne [13] and Albrecht and Creighton [14] confirmed independently that result, a Raman enhancement of about a $10^5 - 10^6$ factor compared with the signal from the pyridine molecules in the absence of metal, and they concluded that such a strong signal can not be explained by an increase in surface area alone.

Thereafter, it has been established that SERS is primarily a phenomenon associated with the enhancement of the electromagnetic field in the vicinity of small metal particles that are optically excited near an intense dipolar resonance such as a polarized surface-plasmon [15, 16]. An

increased Raman signal appears due to magnification of both the incident (the field enhancement scales as $E^4$, where $E$ is the local optical field) and Raman-scattered fields, an effect known as "*Electromagnetic enhancement*" (Fig. 3.5).

Moreover, it has also been suggested that the electromagnetic mechanism is not the only one that contributes to the enhancement. The electronic interaction between the molecules and the metal surface can also modify the scattering process itself and produce a larger cross section than what occurs by scattering light from the molecule alone, an effect known as "*Electronic enhancement or chemical SERS*" [17–19].

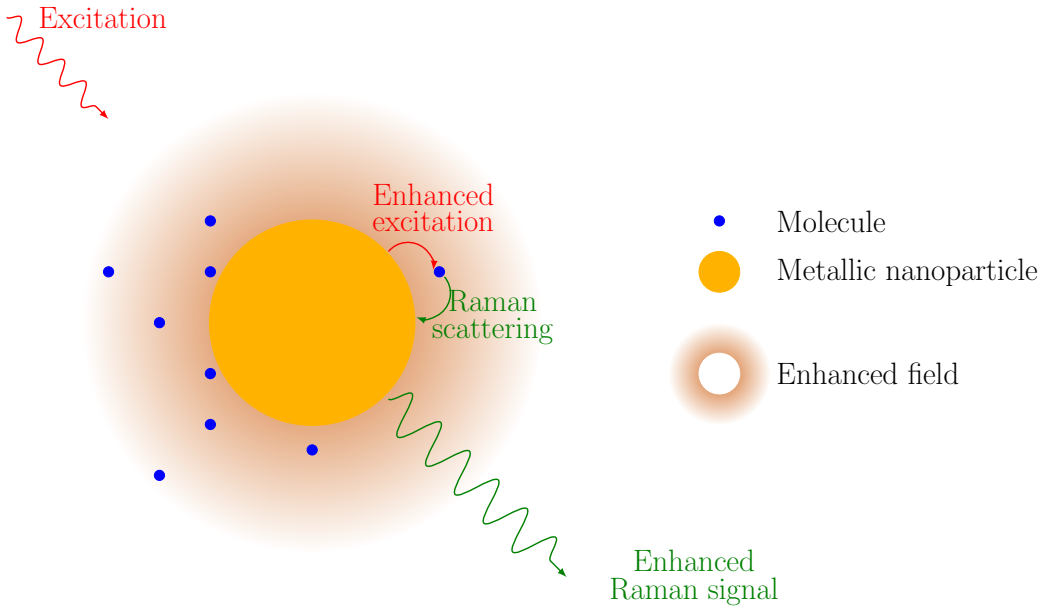


FIGURE 3.5: Schematic illustration of the electromagnetic SERS enhancement using the two process mechanism.

The enhancement factors can be evaluated with Eq. (3.73). Experimentally they are as high as $10^{14-15}$, which is sufficient to allow even single molecule detection using Raman. Further reading on the topic can be found in refs [20–22].

$$\begin{aligned} EF =& \frac{\mathrm{I_{SERS}}}{\mathrm{I_{Raman}}}, \\ =& \frac{\sigma_{\mathrm{SERS}}}{\mathrm{d}\Omega} \Big/ \frac{\sigma_{\mathrm{Raman}}}{\mathrm{d}\Omega}. \end{aligned} \tag{3.73}$$

where $\mathrm{I_{SERS}}$ and $\sigma_{\mathrm{SERS}}$ are the SERS intensity and cross-section, respectively, whereas $\mathrm{I_{Raman}}$ and $\sigma_{\mathrm{Raman}}$ are the Raman intensity and cross-section, respectively.

## 3.4 Vibrational Sum-frequency Generation spectroscopy

### 3.4.1 General description

Infrared-visible Sum-frequency Generation (SFG) is a second-order nonlinear optical process in which a tunable infrared $\omega_{IR}$ laser beam is mixed with a visible $\omega_{vis}$ laser beam to generate an output beam at the sum frequency $\omega_{SFG} = \omega_{IR} + \omega_{vis}$ (see Fig. 3.6). The generated SFG signal is reflected from the substrate according to the phase-matching condition given in Eq. (1.101):

$$\begin{aligned}\varepsilon_I^{(r)}\omega_{SFG}^2\sin^2\theta_{SFG} = \varepsilon_I^{(r)}\omega_{IR}^2\sin^2\theta_{IR} + \varepsilon_I^{(r)}\omega_{vis}^2\sin^2\theta_{vis} \\ + 2\cos\tau\left[\left(\varepsilon_I^{(r)}\right)^2\omega_{IR}\omega_{vis}\sin\theta_{IR}\sin\theta_{vis}\right].\end{aligned} \tag{3.74}$$

In most applications, $\tau = 0$ so that after using $\sqrt{\varepsilon_I^{(r)}(\omega)} = n_I(\omega)$ Eq. (3.74) simplifies to

$$n_I(\omega_{SFG})\omega_{SFG}\sin\theta_{SFG} = n_I(\omega_{IR})\omega_{IR}\sin\theta_{IR} + n_I(\omega_{vis})\omega_{vis}\sin\theta_{vis}, \tag{3.75}$$

showing that the two wave are copropagating (Fig. 1.8).

### 3.4.2 Electric fields and orientation factors

For most of interfacial studies, the goal is to determine the orientation of the molecules at interfaces. This information can be found by studying the behaviors of the components of the surface susceptibility with respect to the polarization of the incoming electric fields. These components of the surface susceptibility are related to the first hyperpolarizability of the molecules constituting the interfacial region. Since the output intensity is affected by the molecular orientation, within the independent molecule approximation, the surface susceptibility is the orientation average of the molecular first hyperpolarizabilities. It is the orientation averaging constrained by the symmetry of the surface that results in the vanishing of several elements of the surface susceptibility tensor. Similarly, molecular symmetry often simplifies the molecular first hyperpolarizability tensor. Vibrational resonances (SFG) further limit the number of significant tensor elements. The nonzero nonresonant tensor elements may be combined with the nonresonant background from the substrate or from the solvent.

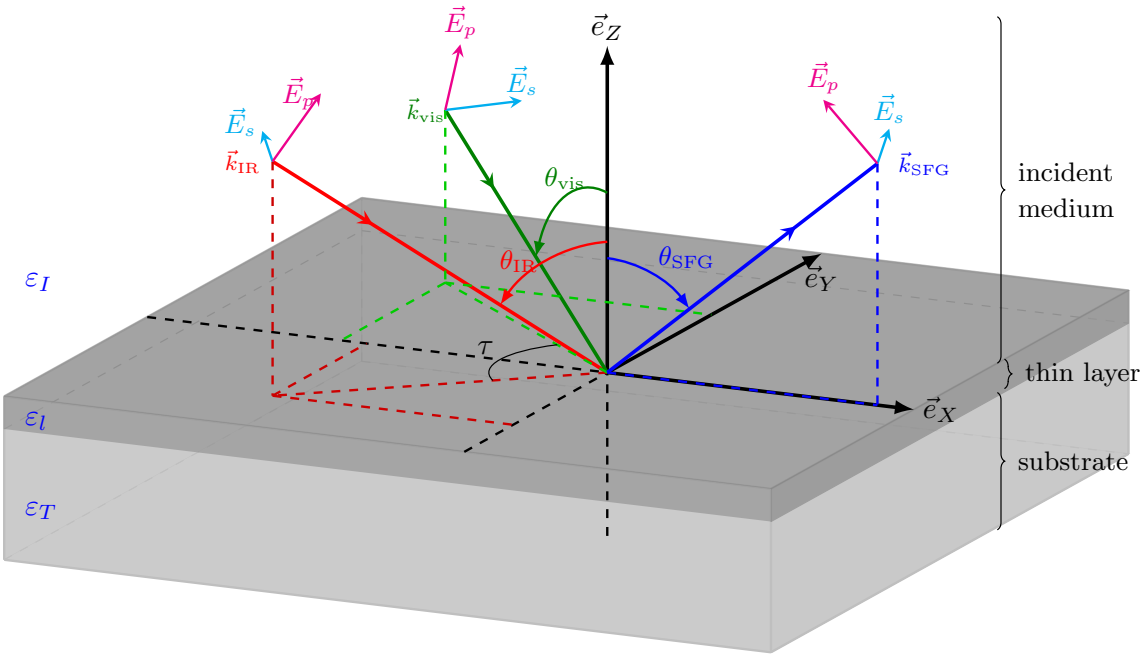


FIGURE 3.6: Geometry of a SFG experiment in the reflection configuration and representation of the three-layer model. $p$ (parallel) denotes a beam polarization in the plane of incidence, while $s$ (senkrecht) corresponds to a polarization perpendicular to the plane of incidence. For the angles see Table 3.4

The orientation average consists of determining the projection of the product of the molecular infrared and Raman transition moments onto the surface infrared and visible oscillating electric fields, then averaging over all allowed molecular orientations. The infrared (Raman) transition moment is described within the molecular coordinate system, so that projection onto the surface coordinates system consists of projecting the molecular $(x, y, x)$ axes onto the surface (X, Y, Z) axes [23] and averaging over all molecular orientations (Fig. 3.7). This is the origin of the $3 \times 3 \times 3$ orientation tensor.

Surface symmetry simplifies this tensor. For any surface with an $X - Z$ and $Y - Z$ reflection plane, the surface susceptibility must be invariant to interchange of $+Y$ and $-Y$ ($+X$ and $-X$, respectively): $\chi^{(2)}_{IJ+Y} = \chi_{IJ-Y} = -\chi^{(2)}_{IJY(I,J\neq Y)}$. All tensor elements with one or three $Y$ subscripts are zero. This reduces the number of independent nonzero surface tensor elements to seven: $\chi^{(2)}_{XXZ}, \chi^{(2)}_{XZX}, \chi^{(2)}_{ZXX}, \chi^{(2)}_{YYZ}, \chi^{(2)}_{YZY}, \chi^{(2)}_{ZYY}$, and $\chi^{(2)}_{ZZZ}$. For vibrationally resonant, visible nonresonant SFG, the first two subscripts refer to the Raman transition moment and the last to the infrared transition element. In addition, if the surface is isotropic, then $X$ and $Y$ are equivalent, so there are four independent components: $\chi^{(2)}_{ZZZ}, \chi^{(2)}_{XXZ} = \chi^{(2)}_{YYZ}, \chi^{(2)}_{XZX} = \chi^{(2)}_{YZY}, \chi^{(2)}_{ZXX} = \chi^{(2)}_{ZYY}$.

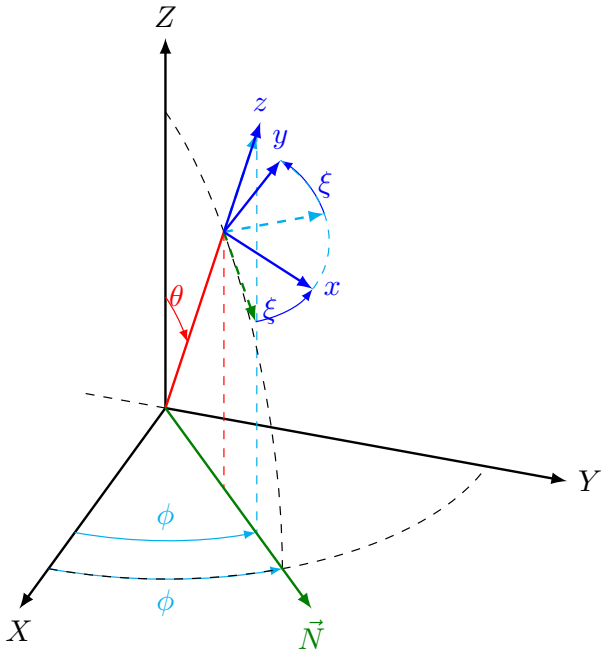


FIGURE 3.7: Illustration of the relationships between the laboratory (X, Y, Z) and the molecular $(x, y, z)$ coordinates systems. For the definition of the angles see Table 3.4

TABLE 3.4: Angles defined with respect to the laboratory coordinates system

| Angle | Measures |
|---|---|
| $\theta$ | Tilt angle between the laboratory $Z$ and the molecular $z$ axis |
| $\xi$ | Angle between the line of nodes $\vec{N}$ and the $x$ axis. |
| $\phi$ | Angle between the $X$ axis and the line of nodes $\vec{N}$ (free rotation in isotropic surface) |
| $\theta_j$ | Angle between the laboratory $Z$ and beams propagation direction $\vec{k}_j$ |
| $\tau$ | Angle between visible and infrared propagation planes |

These macroscopic surface susceptibility elements, $\chi^{(2)}_{IJK}$, result from the first hyperpolarizability elements $\beta_{\alpha\beta\gamma}$ and are related via the average of the projection of the $\alpha\beta\gamma$ onto the $IJK$, $\langle IJK|\alpha\beta\gamma\rangle$:

$$\begin{aligned}\chi^{(2)}_{IJK} &\simeq N_s \sum_{\alpha,\beta,\gamma} \langle IJK|\alpha\beta\gamma\rangle \beta_{\alpha\beta\gamma}, \\ &\simeq N_s \sum_{\alpha,\beta,\gamma} \langle T_{I\alpha,J\beta,K\gamma}(\phi,\theta,\xi)\beta_{\alpha\beta\gamma}\rangle, \end{aligned} \tag{3.76}$$

where $N_s$ is the surface density of molecules. A general formulation for $\langle IJK|\alpha\beta\gamma\rangle$ has been given in Appendix B and the final expressions are given below:

$$\begin{aligned}\frac{2}{N_s} \times \langle \chi^{(2)}_{ZZZ} \rangle_\phi(\theta,\xi) = &\cos^3(\theta)[\beta_{zzz}] \\ &+ \sin(\theta)\sin(\xi)[\beta_{zzy} + \beta_{zyz} + \beta_{yzz}] \\ &- \sin(\theta)\cos(\xi)[\beta_{xzz} + \beta_{zxz} + \beta_{zzx}] \\ &+ \sin^2(\theta)\cos(\theta)\sin^2(\xi)[\beta_{yyz}\beta_{yzy} + \beta_{zyy}] \\ &+ \sin^2(\theta)\cos(\theta)\cos^2(\xi)[\beta_{xxz} + \beta_{xzx} + \beta_{zxx}] \\ &- \sin^2(\theta)\cos(\theta)\sin(\xi)\cos(\xi)[\beta_{zyx} + \beta_{yzx} + \beta_{zxy} + \beta_{xzy} + \beta_{yxz} + \beta_{xyz}] \\ &+ \sin^3(\theta)\sin(\xi)[\beta_{xxy} + \beta_{xyx} + \beta_{yxx} - \beta_{yzz} - \beta_{zyz} - \beta_{zzy}] \\ &+ \sin^3(\theta)\cos(\xi)[\beta_{xzz} + \beta_{zxz} + \beta_{zzx} - \beta_{xyy} - \beta_{yxy} - \beta_{yyx}] \\ &+ \sin^3(\theta)\sin^3(\xi)[\beta_{yyy} - \beta_{xxy} - \beta_{xyx} - \beta_{yxx}] \\ &+ \sin^3(\theta)\cos^3(\xi)[-\beta_{xxx} + \beta_{xyy} + \beta_{yxy} + \beta_{yyx}] \end{aligned} \tag{3.77}$$

$$\begin{aligned}2\frac{1}{N_s} \times \langle \chi^{(2)}_{ZXX} \rangle_\phi(\theta,\xi) = &\sin^2(\theta)\cos(\theta)[\beta_{zzz}] + \cos(\theta)[\beta_{zxx} + \beta_{zyy}] \\ &- \sin^2(\theta)\cos(\theta)\sin^2(\xi)[\beta_{yyz} + \beta_{yzy} + \beta_{zyy}] \\ &- \sin^2(\theta)\cos(\theta)\cos^2(\xi)[\beta_{xxz} + \beta_{xzx} + \beta_{zxx}] \\ &+ \sin^2(\theta)\cos(\theta)\sin(\xi)\cos(\xi)[\beta_{zyx} + \beta_{yzx} + \beta_{zxy} + \beta_{xzy} + \beta_{yxz} + \beta_{xyz}] \\ &+ \sin(\theta)\sin(\xi)[\beta_{yyy} + \beta_{yxx} - \beta_{zyz} - \beta_{zzy}] \\ &+ \sin(\theta)\cos(\xi)[-\beta_{xxx} - \beta_{xyy} + \beta_{zxz} + \beta_{zzx}] \\ &+ \sin^3(\theta)\sin(\xi)[-\beta_{xxy} - \beta_{xyx} - \beta_{yxx} + \beta_{yzz} + \beta_{zyz} + \beta_{zzy}] \\ &+ \sin^3(\theta)\cos(\xi)[\beta_{xyy} + \beta_{yxy} + \beta_{yyx} - \beta_{xzz} - \beta_{zxz} - \beta_{zzx}] \\ &+ \sin^3(\theta)\sin^3(\xi)[-\beta_{yyy} + \beta_{xxy} + \beta_{xyx} + \beta_{yxx}] \\ &+ \sin^3(\theta)\cos^3(\xi)[\beta_{xxx} - \beta_{xyy} - \beta_{yxy} - \beta_{yyx}] \end{aligned} \tag{3.78}$$

$$\begin{aligned}2\frac{1}{N_s} \times \langle \chi^{(2)}_{XZX} \rangle_\phi(\theta,\xi) = &\sin^2(\theta)\cos(\theta)[\beta_{zzz}] + \cos(\theta)[\beta_{xzx} + \beta_{yzy}] \\ &- \sin^2(\theta)\cos(\theta)\sin^2(\xi)[\beta_{yyz} + \beta_{yzy} + \beta_{zyy}] \\ &- \sin^2(\theta)\cos(\theta)\cos^2(\xi)[\beta_{xxz} + \beta_{xzx} + \beta_{zxx}] \\ &+ \sin^2(\theta)\cos(\theta)\sin(\xi)\cos(\xi)[\beta_{zyx} + \beta_{yzx} + \beta_{zxy} + \beta_{xzy} + \beta_{yxz} + \beta_{xyz}] \\ &+ \sin(\theta)\sin(\xi)[\beta_{yyy} + \beta_{xyx} - \beta_{yzz} - \beta_{zzy}] \\ &+ \sin(\theta)\cos(\xi)[-\beta_{xxx} - \beta_{yxy} + \beta_{xzz} + \beta_{zzx}] \\ &+ \sin^3(\theta)\sin(\xi)[-\beta_{xxy} - \beta_{xyx} - \beta_{yxx} + \beta_{yzz} + \beta_{zyz} + \beta_{zzy}] \\ &+ \sin^3(\theta)\cos(\xi)[\beta_{xyy} + \beta_{yxy} + \beta_{yyx} - \beta_{xzz} - \beta_{zxz} - \beta_{zzx}] \\ &+ \sin^3(\theta)\sin^3(\xi)[-\beta_{yyy} + \beta_{xxy} + \beta_{xyx} + \beta_{yxx}] \\ &+ \sin^3(\theta)\cos^3(\xi)[\beta_{xxx} - \beta_{xyy} - \beta_{yxy} - \beta_{yyx}] \end{aligned} \tag{3.79}$$

$$
\begin{aligned}
2\frac{1}{N_s} \times \langle \chi^{(2)}_{XXZ} \rangle_\phi(\theta,\xi) = & \sin^2(\theta)\cos(\theta)[\beta_{zzz}] + \cos(\theta)[\beta_{xxz} + \beta_{yyz}] \\
& - \sin^2(\theta)\cos(\theta)\sin^2(\xi)[\beta_{yyz} + \beta_{yzy} + \beta_{zyy}] \\
& - \sin^2(\theta)\cos(\theta)\cos^2(\xi)[\beta_{xxz} + \beta_{xzx} + \beta_{zxx}] \\
& + \sin^2(\theta)\cos(\theta)\sin(\xi)\cos(\xi)[\beta_{zyx} + \beta_{yzx} + \beta_{zxy} + \beta_{xzy} + \beta_{yxz} + \beta_{xyz}] \\
& + \sin(\theta)\sin(\xi)[\beta_{yyy} + \beta_{xxy} - \beta_{yzz} - \beta_{zyz}] \\
& + \sin(\theta)\cos(\xi)[-\beta_{xxx} - \beta_{yyx} + \beta_{xzz} + \beta_{zxz}] \\
& + \sin^3(\theta)\sin(\xi)[-\beta_{xxy} - \beta_{xyx} - \beta_{yxx} + \beta_{yzz} + \beta_{zyz} + \beta_{zzy}] \\
& + \sin^3(\theta)\cos(\xi)[\beta_{xyy} + \beta_{yxy} + \beta_{yyx} - \beta_{xzz} - \beta_{zxz} - \beta_{zzx}] \\
& + \sin^3(\theta)\sin^3(\xi)[-\beta_{yyy} + \beta_{xxy} + \beta_{xyx} + \beta_{yxx}] \\
& + \sin^3(\theta)\cos^3(\xi)[\beta_{xxx} - \beta_{xyy} - \beta_{yxy} - \beta_{yyx}]
\end{aligned} \tag{3.80}
$$

### 3.4.3 Harmonic approximation in SFG

In this section, we treat the molecular vibrational contribution to the simply IR resonant IR-visible Sum-Frequency Generation (SFG) process (Fig. 3.8). The vibrational first hyperpolarizability is given by (see also Appendix A)

$$
\begin{aligned}
\beta^{\alpha\beta\gamma}(-\omega_{SFG};\omega_{IR},\omega_{vis}) = & \frac{1}{2\hbar}\sum_{v_i,v_f}\frac{\langle v_f|\mu^\gamma_{gg}|v_i\rangle}{\left(\omega_{v_f v_i} - \omega_{IR} - i\gamma_{v_f v_i}\right)} \\
& \left\langle v_i\middle|\frac{1}{\hbar}\sum_e \frac{\mu^\alpha_{ge}\mu^\beta_{eg}}{\left(\omega_{eg} - \omega_{SFG} - i\gamma_{eg}\right)} + \frac{\mu^\beta_{ge}\mu^\alpha_{eg}}{\left(\omega_{eg} + \omega_{SFG} + i\gamma_{eg}\right)}\middle|v_f\right\rangle,
\end{aligned} \tag{3.81}
$$

where we recognize the $\alpha\beta$ component of the transition polarizability $\alpha_{v_i v_f}$ Eq. (3.51)

$$
\left(\alpha^{\alpha\beta}\right)_{v_i v_f} = \left\langle v_i\middle|\frac{1}{\hbar}\sum_e \frac{\mu^\alpha_{ge}\mu^\beta_{eg}}{\left(\omega_{eg} - \omega_{SFG} - i\gamma_{eg}\right)} + \frac{\mu^\beta_{ge}\mu^\alpha_{eg}}{\left(\omega_{eg} + \omega_{SFG} + i\gamma_{eg}\right)}\middle|v_f\right\rangle. \tag{3.82}
$$

To simplify the calculations we assumed that $\frac{1}{\omega_{SFG}} \simeq \frac{1}{\omega_{Vis}}$, then Eq. (3.82) become

$$
\left(\alpha^{\alpha\beta}(\omega_{Vis})\right)_{v_i v_f} = \left\langle v_i\middle|\frac{1}{\hbar}\sum_e \frac{\mu^\alpha_{ge}\mu^\beta_{eg}}{\left(\omega_{eg} - \omega_{Vis} - i\gamma_{eg}\right)} + \frac{\mu^\beta_{ge}\mu^\alpha_{eg}}{\left(\omega_{eg} + \omega_{Vis} + i\gamma_{eg}\right)}\middle|v_f\right\rangle. \tag{3.83}
$$

The first hyperpolarizability can be written in term of the polarizability and the dipole moment as

$$\beta^{\alpha\beta\gamma}(-\omega_{SFG};\omega_{IR},\omega_{vis}) = \frac{1}{2\hbar}\frac{1}{2\hbar}\sum_{v_i,v_f}\frac{\langle v_f|\mu^{\gamma}_{gg}|v_i\rangle}{(\omega_{v_fv_i}-\omega_{IR}-i\gamma_{v_fv_i})}\left(\langle v_i|\alpha^{\alpha\beta}(\omega_{Vis})|v_f\rangle\right). \tag{3.84}$$

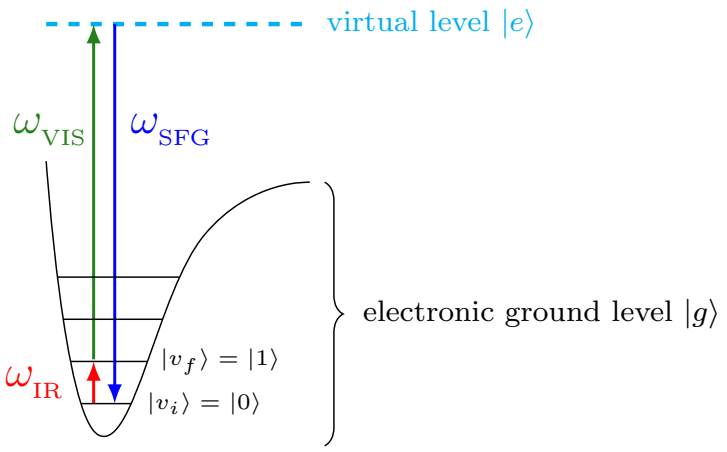


FIGURE 3.8: Energy levels in SFG process

Following the same procedure as for the IR and Raman intensities, near equilibrium geometry, the dipole moment and the polarizability are expanded along the vibrational normal coordinates:

$$\mu^{\gamma}(Q) = (\mu^{\gamma})_e + \sum_k \left(\frac{\partial\mu^{\gamma}}{\partial Q_k}\right)_e Q_k + \frac{1}{2}\sum_{k,l}\left(\frac{\partial^2\mu^{\gamma}}{\partial Q_k\partial Q_l}\right)_e Q_kQ_l + \cdots \tag{3.85}$$

$$\alpha^{\alpha\beta}(Q) = (\alpha^{\alpha\beta})_e + \sum_k \left(\frac{\partial\alpha^{\alpha\beta}}{\partial Q_k}\right)_e Q_k + \frac{1}{2}\sum_{k,l}\left(\frac{\partial^2\alpha^{\alpha\beta}}{\partial Q_k\partial Q_l}\right)_e Q_kQ_l + \cdots \tag{3.86}$$

Within the double harmonic approximation (Section 3.1.2.3), the expansion is truncated after the first order and one obtains

$$\langle v_f|\mu^{\gamma}(Q)|v_i\rangle = \underbrace{(\mu^{\gamma})_e\langle v_f|v_i\rangle}_{0} + \sum_k \left(\frac{\partial\mu^{\gamma}}{\partial Q_k}\right)_e \langle v_f|Q_k|v_i\rangle, \tag{3.87}$$

$$\langle v_i|\alpha^{\alpha\beta}(Q)|v_f\rangle = \underbrace{(\alpha^{\alpha\beta})_0\langle v_i|v_f\rangle}_{0} + \sum_k \left(\frac{\partial\alpha^{\alpha\beta}}{\partial Q_k}\right)_e \langle v_i|Q_k|v_f\rangle \tag{3.88}$$

The first term is equal to zero. The second is non-zero only if $v_i$ and $v_f$ vibrational states differ by one quantum number in only one mode of vibration (Eq. (3.28)).

Now, assuming that $v_i$ is the ground vibrational state, i.e. $v_i = 0$, while the final state is $v_f = 1_p$, i.e. the $p^{\text{th}}$ oscillator is in its first excited state and all the others in their ground states:

$$\langle 1_p|\mu^\gamma(Q)|0\rangle = \sqrt{\frac{\hbar}{2\omega_p}}\left(\frac{\partial\mu^\gamma}{\partial Q_p}\right)_e, \tag{3.89}$$

$$\langle 0|\alpha^{\alpha\beta}(Q)|1_p\rangle = \sqrt{\frac{\hbar}{2\omega_p}}\left(\frac{\partial\alpha^{\alpha\beta}}{\partial Q_p}\right)_e, \tag{3.90}$$

$$\begin{aligned}\beta^{\alpha\beta\gamma}(-\omega_{SFG};\omega_{IR},\omega_{vis}) =& \frac{1}{2\hbar}\sum_p \frac{\langle 1_p|\mu^\gamma|0\rangle}{(\omega_p-\omega_{IR}-i\gamma_p)}\langle 0|\alpha^{\alpha\beta}|1_p\rangle, \\ =& \sum_p \frac{1}{4\omega_p}\frac{\left(\frac{\partial\mu^\gamma}{\partial Q_p}\right)_e\left(\frac{\partial\alpha^{\alpha\beta}}{\partial Q_p}\right)_e}{(\omega_p-\omega_{IR}-i\gamma_p)} \equiv [\mathrm{C^3m^3J^{-2}}].\end{aligned} \tag{3.91}$$

### 3.4.4 SFG intensities

The observed intensity is related to the surface susceptibility and it is polarization dependent. Three polarizations are required to describe the experiment: the polarizations of the SF beam, of the visible input beam, and that of the infrared input. Thus, there are eight potential polarization combinations. If the surface has an $Z-X$ and $Z-Y$ mirror planes, then those combinations with an odd number of $s$-polarized beams have zero intensity. Like for the surface susceptibility, the SF and visible terms represent a Raman process, so $I_{sps}$ and $I_{pss}$ differ only by a Fresnel factor, thus there are four unique configurations: *ssp*, *sps*, *pss* and *ppp*.

Heinz [24] showed that under the electric dipole approximation, the SFG signal $I_{SFG}$ generated by the nonlinear polarization is proportional to the surface susceptibility tensor $\chi^{(2)}$ as well as to the amplitude of the electric field of the IR ($E_{IR}$ ) and visible ($E_{vis}$) beams:

$$I_{SFG}(-\omega_{SFG};\omega_{vis},\omega_{IR}) \propto \left|(F_{SFG}\cdot\vec{\hat{e}}^{\perp})\cdot\vec{\vec{\chi}}^{(2)}:\, F_{vis}\vec{\boldsymbol{E}}(\omega_{vis})F_{IR}\vec{\boldsymbol{E}}(\omega_{IR})\right|^2 \tag{3.92}$$

where the $F$'s are the Fresnel factors and $\vec{\hat{e}}^{\perp}$ is a vector perpendicular to the SFG wave vector. Then, by evaluating the tensor product and using the expression of the field reflected by the interface at sum-frequency (for each polarization, Eq. (1.124)) the output intensity has been derived for each set of polarizations as (see Appendix B for the complete development):

$$\underbrace{\frac{I_{ssp}}{I_{IR}I_{vis}}}_{\mathrm{J^{-1}sm^2}} = \underbrace{\frac{\omega_{SFG}^2}{2c^3\varepsilon_0 n_1(\omega_{SFG})n_1(\omega_{IR})n_1(\omega_{vis})\cos^2\theta_{SFG}}}_{\mathrm{m^{-2}C^{-1}Vs}} \underbrace{\left|\sin\theta_{IR}\chi^{(2)}_{YYZ}F_Y^{SFG}F_Y^{vis}F_Z^{IR}\right|^2}_{|\chi^{(2),\,eff}_{YYZ}|^2 \equiv \mathrm{m^4V^{-2}}}}, \tag{3.93}$$

$$\frac{I_{pss}}{I_{IR}I_{vis}} = \frac{\omega_{SFG}^2}{2c^3\varepsilon_0 n_1(\omega_{SFG})n_1(\omega_{IR})n_1(\omega_{vis})\cos^2\theta_{SFG}}\left|\sin\theta_{SFG}\chi^{(2)}_{ZYY}F_Z^{SFG}F_Y^{vis}F_Y^{IR}\right|^2, \tag{3.94}$$

$$\frac{I_{sps}}{I_{IR}I_{vis}} = \frac{\omega_{SFG}^2}{2c^3\varepsilon_0 n_1(\omega_{SFG})n_1(\omega_{IR})n_1(\omega_{vis})\cos^2\theta_{SFG}}\left|\sin\theta_{vis}\chi^{(2)}_{YZY}F_Y^{SFG}F_Z^{vis}F_Y^{IR}\right|^2, \tag{3.95}$$

$$\begin{aligned}\frac{I_{ppp}}{I_{IR}I_{vis}} =& \frac{\omega_{SFG}^2}{2c^3\varepsilon_0 n_1(\omega_{SFG})n_1(\omega_{IR})n_1(\omega_{vis})\cos^2\theta_{SFG}}\times \\ &\Big|-\cos\theta_{SFG}\cos\theta_{vis}\sin\theta_{IR}\;\chi^{(2)}_{XXZ}\;F_X^{SFG}F_X^{vis}F_Z^{IR} \\ &-\cos\theta_{SFG}\sin\theta_{vis}\cos\theta_{IR}\;\chi^{(2)}_{XZX}\;F_X^{SFG}F_Z^{vis}F_X^{IR} \\ &+\sin\theta_{SFG}\cos\theta_{vis}\cos\theta_{IR}\;\chi^{(2)}_{ZXX}\;F_Z^{SFG}F_X^{vis}F_X^{IR} \\ &+\sin\theta_{SFG}\sin\theta_{vis}\sin\theta_{IR}\;\chi^{(2)}_{ZZZ}\;F_Z^{SFG}F_Z^{vis}F_Z^{IR}\Big|^2.\end{aligned} \tag{3.96}$$

### 3.4.5 Nonlinear optical susceptibility

The interface second-order susceptibility contains a resonant (vibrational) and a non-resonant (electronic) term:

$$\chi^{(2)} = \chi^{(2),NR} + \chi^{(2),R}. \tag{3.97}$$

Considering that the non-resonant terms arise only from the substrate it should be similar for all the vibrational normal modes and therefore can be taken as a constant multiplied by a phase term

$$\chi^{(2),NR}_{IJK} = Ce^{i\varphi_{SFG}}, \tag{3.98}$$

while the resonant terms reads

$$\chi^{(2),R}_{IJK} = \frac{N_s}{\varepsilon_0}\sum_{\alpha,\beta,\gamma}\langle\Phi_{I\phi}\Phi_{J\theta}\Phi_{K\xi}\rangle\beta^{\alpha\beta\gamma} \tag{3.99}$$

$$= \frac{N_s}{\varepsilon_0} \sum_{\alpha,\beta,\gamma} \langle T_{I\alpha,J\beta,K\gamma}(\phi,\theta,\xi)\rangle \beta^{\alpha\beta\gamma}(-(\omega_q+\omega_r);\omega_q,\omega_r),$$

where $\beta^{\alpha\beta\gamma}$ is given by Eq. (3.91). One can defines

$$A^{\alpha\beta\gamma} = \underbrace{\left(\frac{\partial \mu^{\gamma}}{\partial Q_p}\right)_e \left(\frac{\partial \alpha^{\alpha\beta}}{\partial Q_p}\right)_e}_{\mathrm{C^3mJ^{-1}Kg^{-1}}}, \tag{3.100}$$

so that

$$\underbrace{\chi^{(2),R}_{IJK}}_{\mathrm{m^2V^{-1}}} = \underbrace{\frac{N_s}{\varepsilon_0}}_{\mathrm{VC^{-1}m^{-1}}} \underbrace{\sum_p \frac{1}{4\omega_p} \frac{1}{(\omega_p - \omega_{IR} - i\gamma_p)} \sum_{\alpha,\beta,\gamma} \langle T_{I\alpha,J\beta,K\gamma}(\phi,\theta,\xi)\rangle A^{\alpha\beta\gamma}(\omega_{vis})}_{\mathrm{C^3m^3J^{-2}}}. \tag{3.101}$$

The interface second-order susceptibility therefore reads

$$\chi^{(2)}_{IJK} = \left[ \overbrace{\left|\chi^{(2),\mathrm{NR}}_{IJK}\right| e^{i\varphi_{\mathrm{SFG}}}}^{\text{non-resonant}} + \overbrace{\underbrace{\frac{N_s}{\varepsilon_0}}_{\mathrm{VC^{-1}m^{-1}}} \sum_p \frac{A_{IJK}}{4\omega_p} \frac{1}{(\omega_p - \omega_{IR} - i\gamma_p)}}^{\text{resonant}} \right]. \tag{3.102}$$

$$\chi^{(2),\mathrm{R}}_{IJK} \equiv [\mathrm{m^2V^{-1}}]$$

Considering that

$$e^{i\varphi_{SFG}} = (\cos\varphi_{SFG} + i\sin\varphi_{SFG}), \tag{3.103}$$

$$\begin{aligned} \chi^{(2)}_{IJK} = &+ \underbrace{\left|\chi^{(2),\mathrm{NR}}_{IJK}\right| \cos\varphi_{SFG} + \frac{N_s}{\varepsilon_0} \sum_p \frac{A_{IJK}}{4\omega_p} \frac{(\omega_p - \omega_{IR})}{(\omega_p - \omega_{IR})^2 + \gamma_p^2}}_{\chi^{(2)real}_{IJK}} \\ &+ i \underbrace{\left[ \left|\chi^{(2),\mathrm{NR}}_{IJK}\right| \sin\varphi_{SFG} + \frac{N_s}{\varepsilon_0} \sum_p \frac{A_{IJK}}{4\omega_p} \frac{\gamma_p}{(\omega_p - \omega_{IR})^2 + \gamma_p^2} \right]}_{\chi^{(2)imag}_{IJK}}. \end{aligned} \tag{3.104}$$

In the applications, we focus on substrates without any electronic transition close to the visible (incident) and/or SFG wavelengths, so that the non-resonant contribution to the second-order nonlinear susceptibility will be assumed negligible [25, 26].

# References


[1] Bauschlicher, C. W. J.; Partridge, H. *J. Chem. Phys.* **1995**, *103*, 1788–1791.

[2] Scott, A. P.; Radom, L. *J. Phys. Chem.* **1996**, *100*, 16502–16513.

[3] Andersson, M. P.; Uvdal, P. *J. Phys. Chem. A* **2005**, *109*, 2937–2941.

[4] Merrick, J. P.; Moran, D.; Radom, L. *J. Phys. Chem.* **2007**, *111*, 11683–11700.

[5] Alecu, I. M.; Zheng, J.; Zhao, Y.; Truhlar, D. G. *J. Chem. Theory Comput.* **2010**, *6*, 2872–2887.

[6] Kesharwani, M. K.; Brauer, B.; Martin, J. M. L. *J. Phys. Chem. A* **2015**, *119*, 1701–1714.

[7] NIST, CCCBDB. https://cccbdb.nist.gov/vsfx.asp, 2015.

[8] Atkins, P. W.; Friedman, R. S. *Molecular Quantum Mechanics*; Oxford University Press, 2011.

[9] Raman, C. V.; Krishnan, K. S. *Nature* **1928**, *121*, 501–502.

[10] Long, D. A. *The Raman Effect*; A Unified Treatment of the Theory of Raman Scattering by Molecules; Wiley, 2002.

[11] Barron, L. D. *Molecular light scattering and optical activity*; Cambridge University Press, 2004.

[12] Fleischmann, M.; Hendra, P.; McQuillan, A. *Chem. Phys. Lett.* **1974**, *26*, 163 – 166.

[13] Jeanmaire, D. L.; Duyne, R. P. V. *J. Electroanal. Chem. Interfacial. Electrochem.* **1977**, *84*, 1 – 20.

[14] Albrecht, M. G.; Creighton, J. A. *J. Am. Chem. Soc.* **1977**, *99*, 5215–5217.

[15] Kerker, M. *Selected Papers on Surface-Enhanced Raman Scattering*; SPIE, Bellingham, WA, 1990.

[16] Douketis, C.; Haslett, T. L.; Wang, Z.; Moskovits, M.; Iannotta, S. *J. Chem. Phys.* **2000**, *113*, 11315–11323.

[17] Billmann, J.; Otto, A. *Sol. State. Commun.* **1982**, *44*, 105 – 107.

[18] McMahon, J. J.; Dougherty, T. P.; Riley, D. J.; Babcock, G. T.; Carter, R. L. *Surf. Sci.* **1985**, *158*, 381 – 392.

[19] Otto, A. *J. Raman. Spect* **2005**, *36*, 497–509.

[20] Aroca, R. *Surface-Enhanced Vibrational Spectroscopy*; John Wiley & Sons: Chichester, UK, 2006.

[21] Madey, T. E.; Yates Jr, J. T. In *Vibrational Spectroscopy of Molecules on Surfaces*; Yates, J. T., Madey, T. E., Eds.; Springer Science & Business Media, 2013.

[22] Boujday, S.; de la Chapelle, M. L.; Srajer, J.; Knoll, W. *Sensors (Switzerland)* **2015**, *15*, 21239–21264.

[23] Moad, A. J.; Simpson, G. J. *J. Phys. Chem. B* **2004**, *108*, 3548–3562.

[24] Heinz, T. F. In *Nonlinear Surface Electromagnetic Phenomena*; Ponath, H.-E., Stegeman, G., Eds.; Elsevier: Amsterdam, 1991; Chapter 5, pp 353–416.

[25] Busson, B.; Tadjeddine, A. *J Chem. Phys. C* **2009**, *113*, 21895–21902.

[26] Yamaguchi, S.; Shiratori, K.; Morita, A.; Tahara, T. *J Chem. Phys.* **2011**, *134*, 184705.

# Chapter 4

# Quantum Chemistry Background

The description of a stationary system at the quantum level as well as of its molecular properties are in principle determined by the wave function, denoted $|\psi\rangle$. This wave function must satisfy the non-relativistic time-independent Schrödinger equation.

$$\hat{H}|\psi\rangle = E|\psi\rangle, \tag{4.1}$$

where $\hat{H}$ is the Hamiltonian of the system and $E$ the total energy.

However, this equation can be solved only for a system made by two particles such as hydrogenoïds. For systems with more than two particles, the existence of several interactions between them makes the problem too complicated, and we must resort to approximate solutions. General approximations concern the expression of the Hamiltonian itself, and the form of the wave function. In order to solve this equation, we then have mathematical methods (variational or perturbation methods) known as quantum chemical methods to obtain accurate approximate functions. This general framework is presented in this chapter, which begins with the study of the Schrödinger equation and the Hamiltonian operator. Then we briefly present the approximation methods [1, 2].

## 4.1 Schrödinger equation and the Born-Oppenheimer approximation

The Hamiltonian (in atomic units) of a system made by $N$ electrons and $M$ nuclei reads [2]:

$$\hat{H} = \underbrace{-\sum_{i=1}^{N}\frac{1}{2}\nabla_i^2}_{\hat{T}_e} \underbrace{-\sum_{A=1}^{N}\frac{1}{2M_A}\nabla_A^2}_{\hat{T}_N} \underbrace{-\sum_{i=1}^{N}\sum_{A=1}^{M}\frac{Z_A}{r_{iA}}}_{\hat{V}_{eN}} + \underbrace{\sum_{i=1}^{N}\sum_{j>i}^{N}\frac{1}{r_{ij}}}_{\hat{V}_{ee}} + \underbrace{\sum_{A=1}^{M}\sum_{B>A}^{M}\frac{Z_A Z_B}{R_{AB}}}_{\hat{V}_{NN}}. \tag{4.2}$$

In the above equation, $\hat{T}_e$, $\hat{T}_N$, $\hat{V}_{eN}$, $\hat{V}_{ee}$, and $\hat{V}_{NN}$ are the operators for the kinetic energy of the electrons, the operator for the kinetic energy of the nuclei, the Coulomb attraction between electrons and nuclei, the Coulomb repulsion between electrons, and between nuclei, respectively. $\nabla_i^2$ and $\nabla_A^2$ are the Laplacian operator acting on the coordinates of the $i$th electron and the $A$th nucleus. $M_A$ is the ratio of the mass of nucleus A to the mass of an electron, and $Z_A$ is the atomic number of nucleus A. In order to solve Eq. (4.1) we should therefore know the correct expression of each term of the Hamiltonian.

The first approximation is that of Born-Oppenheimer, which allows splitting up the motions of the electrons from those of the nuclei. The approximation is put into practice by "clamping" the nuclei of a molecule of interest. That means fixing their position coordinates to correspond to some chosen arrangement or structure. Electrons are therefore considered as moving in a fixed field created by the nuclei, and are thus subject to a *constant* nuclear potential. Within this approximation, the terms $\hat{T}_N$ can be neglected, whereas $\hat{V}_{NN}$ is constant (Eq. (4.2)). The electronic hamiltonian reads

$$\begin{aligned}\hat{H}_{\text{elec}} &= \hat{T}_e + \hat{V}_{eN} + \hat{V}_{ee},\\ &= -\sum_{i=1}^{N}\frac{1}{2}\nabla_i^2 - \sum_{i=1}^{N}\sum_{A=1}^{M}\frac{Z_A}{r_{iA}} + \sum_{i=1}^{N}\sum_{j>i}^{N}\frac{1}{r_{ij}},\end{aligned} \tag{4.3}$$

and the electronic Schrödinger equation

$$\hat{H}_{\text{elec}}|\psi_{\text{elec}}(R_A, r_i)\rangle = E_{\text{elec}}|\psi_{\text{elec}}(R_A, r_i)\rangle, \tag{4.4}$$

is solved to give the electronic energy $E_{\text{elec}} = E_{\text{elec}}(R_A)$ for this clamped structure (electronic energy parametrically on the nuclear coordinates).

Then, the total wave function and the total energy read:

$$\psi_{\text{total}}(R_A, r_i) = \psi_{\text{elec}}(R_A, r_i)\psi_{\text{nucl}}(R_A), \tag{4.5}$$

$$E_{\text{total}} = E_{\text{elec}} + \sum_{A=1}^{M} \sum_{B>A}^{M} \frac{Z_A Z_B}{R_{AB}}. \tag{4.6}$$

Despite the separation of the movements, the electronic repulsion term $\hat{V}_{ee}$ appearing in the electronic hamiltonian (Eq. (4.3)) makes Eq. (4.4) difficult to solve. To overcome this major difficulty several methods have been developed.

## 4.2 Hartree-Fock method

One of the first attempts to overcome the problem of repulsion between electrons was that of Hartree [3] and Fock [4] who first assumed that the electrons do not interact with each others (i.e., that $\hat{V}_{ee} = 0$), and expressed the global wave function as a product (Hartree product $\equiv$ HP) of monoelectronic wave functions.

$$\psi_{HP}(x_1, x_2, \dots x_i, x_j, \dots x_N) = \Phi_1(x_1)\Phi_2(x_2)\dots\Phi_i(x_i)\Phi_j(x_j)\dots\Phi_N(x_N), \tag{4.7}$$

where $\Phi(x) = \phi(r)\alpha$ is a spin-orbital (just the product of a spatial orbital and either the $\alpha$ or $\beta$ spin function). However, these Hartree product wave functions ($\psi_{HP}$) do not satisfy Pauli exclusion principle (a consequence of the antisymmetry principle). In order to fulfill thE latter, wavefunctions constructed on the basis of a Slater determinant [5] have been adopted:

$$\psi(x_1, x_2, \dots x_N) = \frac{1}{\sqrt{N!}} \begin{vmatrix} \Phi_1(x_1) & \Phi_2(x_1) & \dots & \Phi_N(x_1) \\ \Phi_1(x_2) & \Phi_2(x_2) & \dots & \Phi_N(x_2) \\ \vdots & \vdots & \ddots & \vdots \\ \Phi_1(x_N) & \Phi_2(x_N) & \dots & \Phi_N(x_N) \end{vmatrix}, \tag{4.8}$$

One can write the electronic Hamiltonian (Eq. (4.4)) much more simply, as

$$\begin{aligned} \hat{H}_{\text{elec}} &= \sum_{i=1}^{N} \left( -\frac{1}{2}\nabla_i^2 - \sum_{A=1}^{M} \frac{Z_A}{r_{iA}} \right) + \sum_{i<j}^{N} \frac{1}{r_{ij}}, \\ &= \sum_{i}^{N} h_i(r_i) + \sum_{i<j}^{N} v_{ij}^{HF}(r_i, r_j), \end{aligned} \tag{4.9}$$

one thereby introduce $h_i$ and $v_{ij}^{HF}$, the one-electron and two-electron operator, respectively.

Then, the best spin-orbitals are obtained by minimizing the energy using the variational method (Rayleigh ratio).

$$E_{\text{elec}} = \frac{\langle\psi|\hat{H}_{\text{elec}}|\psi\rangle}{\langle\psi|\psi\rangle}. \tag{4.10}$$

For a system with $N$ occupied spin-orbitals , it is straightforward to show that the electronic energy is given by:

$$E_{\text{elec}} = \sum_{i}^{N} h_{ii} + \frac{1}{2}\sum_{ij}^{N} \left[J_{ij} - K_{ij}\right], \tag{4.11}$$

where $h_{ii}$, $J_{ij}$, and $K_{ij}$ are the energy contributions associated with the core Hamiltonian, the Coulomb operator, and the exchange operator, respectively.

$$h_{ii} = \langle i|h|i\rangle = \int dx_1 \Phi_i^*(x_1) h(r_1) \Phi_i(x_1), \tag{4.12}$$

$$J_{ij} = \langle ij|ij\rangle = \int dx_1 dx_2 \Phi_i^*(x_1)\Phi_j^*(x_2)\frac{1}{r_{12}}\Phi_i(x_1)\Phi_j(x_2), \tag{4.13}$$

$$K_{ij} = \langle ij|ji\rangle = \int dx_1 dx_2 \Phi_i^*(x_1)\Phi_j^*(x_2)\frac{1}{r_{12}}\Phi_j(x_1)\Phi_i(x_2). \tag{4.14}$$

The Hartree-Fock equation reads:

$$\underbrace{\left\{h(r_1) - \sum_{j=1}^{N}\left[J_j(r_1) - K_j(r_1)\right]\right\}}_{f(r_1)}\Phi_i(x_1) = \sum_{j=1}^{N}\varepsilon_{ij}\Phi_i(x_1). \tag{4.15}$$

We thus obtain $N$ mono-electronic equations for the spin-orbital $\Phi_1, \Phi_2, \ldots \Phi_n$. The term in square bracket is the Fock operator denoted $f$. Diagonalization of the energy term $\varepsilon_{ij}$ leads to an eigenvalues problem known as the canonical Hartree-Fock equation:

$$f\phi_i = \varepsilon_i\phi_i \qquad (i = 1, 2, 3, \ldots \infty). \tag{4.16}$$

The Fock operator whose eigenfunctions are $\phi_i$ is defined on the basis of the functions $\phi_i$ themselves. We must therefore use an iterative method to solve it. It is called the self-consistent field (SCF) method.

Moreover in 1951 Roothaan [6] and Hall [7] proposed a method based on the linear combination of atomic orbitals (LCAO) formalism of Mulliken:

$$\phi_i = \sum_{k} C_{ki}|\chi_k\rangle \tag{4.17}$$

where the $\chi_k$ are the atomic orbitals and the $C_{ki}$ are the coefficients that are the unknowns of the problem. Introducing Eq. (4.17) in to Eq. (4.16) one obtains

$$f \sum_k C_{ki}|\chi_k\rangle = \varepsilon_i \sum_k C_{ki}|\chi_k\rangle, \tag{4.18}$$

then, the multiplication of Eq. (4.18) by $\langle\chi_l|$ gives

$$\begin{aligned} \sum_k C_{ki}\langle\chi_l|f|\chi_k\rangle &= \varepsilon_i \sum_k C_{ki}\langle\chi_l|\chi_k\rangle, \\ \sum_k C_{ki}\left(f_{lk} - \varepsilon_i S_{lk}\right) &= 0. \end{aligned} \tag{4.19}$$

Eq. (4.19) can be written under the matrix form as:

$$FC = SC\varepsilon. \tag{4.20}$$

In Eq. (4.19), $k$ and $l$ refer to the atomic orbitals, while $f_{lk}$ and $S_{lk} = \langle\chi_l|\chi_k\rangle$ represent the elements of the Fock matrix, and the overlap matrix, respectively.

However, a systematic error on the SCF energy is due to the orbital approximation, which does not take into account the fact that the movements of the electrons are correlated. Indeed, the Hartree-Fock wave function does not correctly describe the interactions between electrons and therefore overestimates the probability of finding two electrons close to each other. These short-range correlation effects are Coulomb holes [8]. The energy of Roothaan is equal to the Hartree-Fock energy when the atomic basis set is infinite. In the Hartree-Fock theory the lowest energy obtainable is $E^{HF}$, the Hartree-Fock limit. According to Löwdin [9], the correlation energy of a system corresponds to the difference between the exact non-relativistic energy and the Hartree-Fock energy:

$$E^{corr} = E - E^{HF}. \tag{4.21}$$

In order to recover this correlation energy, and therefore improve the quality of the wave function *variational methods* (with Slater Determinants) such as Valence Bond method (VB), Configuration Interaction method (CI), and Multiconfigurational Self-Consistent Field method (MC SCF) and *non-variational methods* (with Slater Determinants) such as Coupled Cluster method (CC), Many Body Perturbation Theory (MBPT), and Equation-of-motion method (EOM-CC) are commonly used. Among these methods, we used of the Coupled Cluster techniques during this thesis, so that it is briefly described in the following section.

## 4.3 The Coupled Cluster method (CC)

### 4.3.1 The exponential ansatz

The essential idea in CC theory is to write the exact wave function for the ground state as an exponential ansatz :

$$\begin{aligned} |\psi_{CC}\rangle &= e^{\hat{T}}|\Phi_0\rangle, \\ &= \left(1 + \hat{T} + \frac{\hat{T}^2}{2!} + \frac{\hat{T}^3}{3!} + \cdots\right)|\Phi_0\rangle, \end{aligned} \tag{4.22}$$

where $e^{\hat{T}}$ is a wave operator, $\hat{T}$ is the cluster operator, and $|\Phi_0\rangle$ the reference Slater determinant (it can be the Hartree-Fock determinant). Moreover an intermediate normalization of the function $|\psi_{CC}\rangle$ is assumed:

$$\langle\psi_{CC}|\Phi_0\rangle = 1 \tag{4.23}$$

The cluster operator $\hat{T}$ is defined by a sum of excitation operators:

$$\hat{T} = \hat{T}_1 + \hat{T}_2 + \hat{T}_3 + \cdots, \tag{4.24}$$

$$\hat{T}_1|\Phi_0\rangle = \sum_{i}^{occ}\sum_{a}^{unocc} t_i^a \Phi_i^a, \tag{4.25}$$

$$\hat{T}_2|\Phi_0\rangle = \sum_{i<j}^{occ}\sum_{a<b}^{unocc} t_{ij}^{ab} \Phi_{ij}^{ab}, \tag{4.26}$$

$$\hat{T}_3|\Phi_0\rangle = \sum_{i<j<k}^{occ}\sum_{a<b<c}^{unocc} t_{ijk}^{abc} \Phi_{ijk}^{abc}, \tag{4.27}$$

where, $\hat{T}_1$ contains excitations involving one electron only, $\hat{T}_2$ contains excitations involving two electrons only, and so on. The subscripts $i, j, \ldots$ refer to the spin-orbitals occupied in $\Phi_0$, and $a, b, \ldots$ refer to unoccupied ones, and $t_{i,j,\ldots}^{a,b,\ldots}$ represent amplitudes, i.e. the numbers whose determination is the goal of the CC method. Moreover, the truncation of the operator $\hat{T}$ defines the coupled cluster method:

$$\begin{aligned} CCS: &\quad \hat{T}_1, \\ CCSD: &\quad \hat{T}_1 + \hat{T}_2, \\ CCSDT: &\quad \hat{T}_1 + \hat{T}_2 + \hat{T}_3, \\ CCSDTQ: &\quad \hat{T}_1 + \hat{T}_2 + \hat{T}_3 + \hat{T}_4. \\ &\quad \vdots \end{aligned}$$

As example

$$\begin{aligned} |\psi_{CCSD}\rangle &= e^{\hat{T}_1+\hat{T}_2}|\Phi_0\rangle, \\ &= \left[1+\hat{T}_1+\left(\hat{T}_2+\frac{1}{2}\hat{T}_1^2\right)+\left(\hat{T}_1\hat{T}_2+\frac{1}{6}\hat{T}_1^3+\cdots\right)+\cdots\right]|\Phi_0\rangle, \end{aligned} \tag{4.28}$$

### 4.3.2 The Coupled Cluster energy and amplitudes

The exact wave function $|\psi_{CC}\rangle$ should satisfy the non-relativistic time-independent Schrödinger equation:

$$\begin{aligned} \hat{H}|\psi_{CC}\rangle &= E|\psi_{CC}\rangle, \\ \langle\psi_{CC}|\hat{H}|\psi_{CC}\rangle &= E\langle\psi_{CC}|\psi_{CC}\rangle \end{aligned} \tag{4.29}$$

The most natural way to calculate the coupled cluster states would seem to be by using the *variational method*, i.e. minimizing the expectation value of the Hamiltonian with respect to the amplitudes

$$E_{\min} = \min_t \frac{\langle\psi_{CC}|\hat{H}|\psi_{CC}\rangle}{\langle\psi_{CC}|\psi_{CC}\rangle} \tag{4.30}$$

However, the coupled cluster wave function includes all excited determinants up to $N$-fold excitations which contribute to these expectation values, giving too complex equations to be efficiently solved. A more convenient approach for obtaining the coupled cluster energy and amplitudes is the *projection method*. In practice, it is often more convenient to first multiply the Schrödinger equation from the left by the operator $e^{-\hat{T}}$

$$\begin{aligned} \hat{H}e^{\hat{T}}|\Phi_0\rangle &= Ee^{\hat{T}}|\Phi_0\rangle, \\ e^{-\hat{T}}\hat{H}e^{\hat{T}}|\Phi_0\rangle &= Ee^{-\hat{T}}e^{\hat{T}}|\Phi_0\rangle, \\ e^{-\hat{T}}\hat{H}e^{\hat{T}}|\Phi_0\rangle &= E|\Phi_0\rangle. \end{aligned} \tag{4.31}$$

then, to project on the reference and excited state determinants:

$$\langle\Phi_0|e^{-\hat{T}}\hat{H}e^{\hat{T}}|\Phi_0\rangle = E, \tag{4.32}$$

$$\langle\Phi_{ij\ldots}^{ab\ldots}|e^{-\hat{T}}\hat{H}e^{\hat{T}}|\Phi_0\rangle = 0. \tag{4.33}$$

Eqs. (4.32) and (4.33) give the coupled cluster energy and amplitude, respectively, and they are known as the *linked coupled cluster equations*.

## 4.4 Density Functional Theory (DFT)

The principle of the Density Functional Theory (DFT) consists on the reduction of number of degrees of freedom of the system by expressing the total energy of the system in terms of the electron density $\rho(\vec{r})$.

$$\rho(\vec{r}) = N \sum_{\sigma_1=-\frac{1}{2},\frac{1}{2}} \int \mathrm{d}x_2 \mathrm{d}x_3 \ldots \mathrm{d}x_N |\psi(\vec{r},\sigma_1,\vec{r}_2,\sigma_2,\ldots,\vec{r}_N,\sigma_N)|^2. \tag{4.34}$$

According to this definition, $\rho$ represents the density of the electron cloud carrying N electrons:

$$\int \rho(\vec{r})\mathrm{d}\tau = N \tag{4.35}$$

Let us go through the main steps and aspects of DFT by following first the seminal presentation due to Parr and Yang [10]. In 1964, Hohenberg and Kohn proved two theorems [11]. The first theorem may be stated as follows **" The external potential $V(\vec{r})$ is determined within a trivial additive constant by the electron density $\rho(\vec{r})$"**. Since $\rho(\vec{r})$ determines the number of electron, it follows that the ground-state electronic density $\rho_0$ and the ground-state wave function $\psi_0$ can be used alternatively as full description of the ground state of the system.

The electronic Hamiltonian has the form:

$$\hat{H} = \hat{T} + \hat{U} + \hat{V}, \tag{4.36}$$

where $\hat{T}$, $\hat{U}$, $\hat{V}$ represent the kinetic energy, the electron repulsion and the electron-nuclei attraction operators, respectively. Then the energy can be written under the following form:

$$\begin{aligned} E_v[\rho] &= T[\rho] + U[\rho] + V[\rho], \\ &= \int \rho(\vec{r})v(\vec{r})\mathrm{d}\tau + F^{HK}[\rho], \end{aligned} \tag{4.37}$$

where

$$\begin{aligned} \int \rho(\vec{r})v(\vec{r})\mathrm{d}\tau &= \langle\psi|\hat{V}|\psi\rangle = V[\rho], \\ F^{HK}[\rho] &= T[\rho] + U[\rho], \end{aligned} \tag{4.38}$$

and

$$U[\rho] = J[\rho] + \text{nonclassical term}. \tag{4.39}$$

$J[\rho]$ is the classical electron-electron Coulomb repulsion and the nonclassical term defines the *"exchange-correlation energy"*, which is very difficult to catch.

In the second theorem they establish an analogue of the variational principle : **" For a given number of electrons and external potential $v$ there exists a functional of the trial density, $\rho'(\vec{r}) \geqslant 0$, denoted $E_v^{HK}[\rho']$, for which the following variational principle is satisfied: "**

$$E_v^{HK}[\rho'] \geqslant E_v[\rho] = E_0 \qquad \left(\int \rho'(\vec{r})\mathrm{d}\tau = N\right), \tag{4.40}$$

where $E_0$ stands for the true ground state energy and $E_v^{HK}[\rho']$ is the energy functional

$$\begin{aligned} E_0 &= \min \langle\psi|\hat{H}|\psi\rangle, \\ &= \min \langle\psi|\hat{T}+\hat{U}+\hat{V}|\psi\rangle, \\ &= \min \left\{\int \rho'(\vec{r})v(\vec{r})\mathrm{d}\tau + \langle\psi|\hat{T}+\hat{U}|\psi\rangle\right\}, \\ &= \min \left\{\int \rho'(\vec{r})v(\vec{r})\mathrm{d}\tau + F^{HK}[\rho']\right\}, \\ &= \min E_v^{HK}[\rho']. \end{aligned} \tag{4.41}$$

The ground state energy of a many electron system can be obtained by minimizing the energy functional

$$\delta\left\{E_v[\rho] - \mu\left[\int \rho(\vec{r})\mathrm{d}\tau - N\right]\right\} = 0 \tag{4.42}$$

which gives the Euler-Langrange equation

$$\mu = \frac{\delta E_v[\rho]}{\delta\rho(\vec{r})} = v(\vec{r}) + \frac{\delta F^{HK}[\rho]}{\delta\rho(\vec{r})}, \tag{4.43}$$

where $\mu$ is the chemical potential.

### 4.4.1 The Kohn-Sham Approach

Pure (or "orbital-free") DFT attempts to compute the energy of interacting electrons, as a functional of the density, in practice it is not very accurate. This is due to the lack of accurate approximations for the kinetic energy functional. In order to overcome this problem Kohn and Sham [12] proposed an alternative approach which consist of working instead with a system of non-interacting electrons, so that they reintroduce one-electron wavefunctions (orbitals) into the formalism to treat the kinetic and the electron-electron interaction energy terms. In general, the wavefunction of the non-interacting electrons is different from that of the interacting ones and so is the density. Then, comparison between the exact ground-state kinetic energy and that of Kohn-Sham is given in the table below.

| Exact | Kohn-Sham |
|---|---|
| $T = \sum_i^{\infty} n_i \langle \psi_i \vert \frac{-1}{2} \nabla^2 \vert \psi_i \rangle$ | $T_s[\rho] = \sum_i^{N} n_i \langle \Phi_i \vert \frac{-1}{2} \nabla^2 \vert \Phi_i \rangle$ |
| $\rho(\vec{r}) = \sum_i^{\infty} n_i \sum_\sigma \vert \psi_i(\vec{r}, \sigma) \vert^2$ | $\rho(\vec{r}) = \sum_i^{N_{occ}} \sum_\sigma \vert \Phi_i(\vec{r}, \sigma) \vert^2$ |
| $\infty$ number of natural spin-orbitals with $0 \leq n_i \leq 1$ | $n_i = 1$ for $N$ spin-orbitals, and 0 for the rest |

The Hamiltonian of the corresponding non-interacting reference system reads

$$\hat{H}_s = \sum_i^N \left( \frac{-1}{2} \nabla^2 \right) + \sum_i^N v_s(\vec{r}), \tag{4.44}$$

in which there are no electron-electron repulsion terms, and for which the ground-state electron density is exactly $\rho$. For this system there will be an exact one-determinant ground-state wave function,

$$\Psi_s = \frac{1}{\sqrt{N!}} \left[ \Phi_1(x_1), \Phi_2(x_2), \ldots, \Phi_N(x_N) \right]. \tag{4.45}$$

The spin-orbitals are obtained by solving a one-electron equation:

$$\hat{h}_s \Phi_n(\vec{r}) = \left[ \frac{-1}{2} \nabla^2 + v_s(\vec{r}) \right] \Phi_n(\vec{r}) = \varepsilon_n \Phi_n(\vec{r}), \tag{4.46}$$

and the total energy functional is given by

$$E[\rho] = \int \rho(\vec{r}) v(\vec{r}) \mathrm{d}\tau + F[\rho] \quad \text{whith} \quad F[\rho] = T_s[\rho] + J[\rho] + E_{xc}[\rho]. \tag{4.47}$$

Here $E_{xc}$ is called the exchange-correlation energy. Since the exact kinetic energy has been replaced by $T_s$

$$E_{xc}[\rho] = T[\rho] - T_s[\rho] + V_{ee}[\rho] - J[\rho]. \tag{4.48}$$

This non-classical term now contains a contribution from the remaining part to the kinetic energy. The Euler equation [Eq. (4.43)] now becomes

$$\mu = v_{eff}(\vec{r}) + \frac{\delta T_s[\rho]}{\delta \rho(\vec{r})}, \tag{4.49}$$

with

$$v_{eff}(\vec{r}) = v(\vec{r}) + \int \frac{\rho(\vec{r'})}{|\vec{r} - \vec{r'}|} \mathrm{d}\tau' + v_{xc}(\vec{r}) \quad \text{and} \quad v_{xc}(\vec{r}) = \frac{\delta E_{xc}[\rho]}{\delta \rho(\vec{r})}. \tag{4.50}$$

where, the first term is electron-nuclei interaction, the second term is the electron-electron electrostatic interaction while the third is the non-classical exchange-correlation potential.

In the KS approach, evaluating the density does not proceed via the Euler equation, but by solving the N one-electron equations:

$$\left[ \frac{-1}{2} \nabla^2 + v_{eff}(\vec{r}) \right] \Phi_n(\vec{r}) = \varepsilon_n \Phi_n(\vec{r}). \tag{4.51}$$

In Eq. (4.50), the first two terms are well defined, whereas the third $v_{xc}(\vec{r})$ ($E_{xc}[\rho]$) is the one to determine. So, if we knew the exact $E_{xc}[\rho]$ we could solve Eq. (4.51) for the exact ground state energy and density. However the exact functional is unknown and we therefore make use of approximations.

## 4.4.2 Exchange-correlation functional approximations

### 4.4.2.1 Local Density Approximation (LDA) and Local Spin Density Aproximation (LSDA)

The general idea of LDA is to take the known result for a homogenous system and apply it locally to a non-homogeneous one. So, the local exchange correlation energy per electron is approximated as a simple function of the local charge density :

$$E_{xc}^{LDA}[\rho] = \int \rho(\vec{r}) \varepsilon_{xc}(\rho(\vec{r})) \mathrm{d}\tau, \tag{4.52}$$

The corresponding exchange-correlation potential reads

$$v_{xc}^{LDA}(\vec{r}) = \frac{\delta E_{xc}[\rho]}{\delta \rho(\vec{r})} = \varepsilon_{xc}(\rho(\vec{r})) + \rho(\vec{r}) \frac{\delta \varepsilon_{xc}(\rho(\vec{r}))}{\delta \rho(\vec{r})}, \tag{4.53}$$

and the KS orbital equations read

$$\left[ \frac{-1}{2} \nabla^2 + v(\vec{r}) + \int \frac{\rho(\vec{r'})}{|\vec{r} - \vec{r'}|} \mathrm{d}\tau' + v_{xc}^{LDA}(\vec{r}) \right] \Phi_n(\vec{r}) = \varepsilon_n \Phi_n(\vec{r}). \tag{4.54}$$

The self-consistent solution of (Eq. (4.54)) defines de the Kohn-Sham local density approximation (KS-LDA), which in the literature is usually simply called the LDA method. Within the LDA, $\varepsilon_{xc}(\rho)$ is a function of only the local value of the density. It can be separated into exchange and

correlation contributions:

$$\varepsilon_{xc}(\rho) = \varepsilon_x(\rho) + \varepsilon_c(\rho). \tag{4.55}$$

Dirac [13] derived that exchange energy reads $\varepsilon_x(\rho) = -\frac{3}{4}\left(\frac{3}{\pi}\rho\right)^{1/3}$. For $\varepsilon_c$, numerical values have been determined and interpolated to get analytical form by Vosko, Wilk, and Nusair(VWN) [14].

In the Local Spin Density Aproximation (LSDA), the electrons of opposite spin are placed in different Kohn-Sham orbitals.

#### 4.4.2.2 Generalized Gradient Approximation (GGA)

In the generalized gradient approximation a functional form is adopted, which ensures that the exchange hole is negative definite [15]. This leads to an energy functional that depends on both the density and its gradient but retains the analytic properties of the exchange correlation hole inherent to the LDA:

$$E_{xc}^{GGA}[\rho] = \int \rho(\vec{r})\varepsilon_{xc}(\rho, \nabla\rho)\mathrm{d}\tau. \tag{4.56}$$

For instance the exchange formula due to Becke [16] reads,

$$E_x^{Becke}[\rho] = E_x^{LSDA}[\rho] - \sum_\sigma \int F^B(S_\sigma)\rho^{4/3}(\vec{r})\mathrm{d}\tau, \tag{4.57}$$

where

$$F^B(S_\sigma) = \frac{\beta S_\sigma^2}{1 + 6\beta S_\sigma \sinh^{-1}(S_\sigma)}, \tag{4.58}$$

and

$$S_\sigma(\vec{r}) = \frac{|\Delta\rho(\vec{r})|}{\rho^{4/3}(\vec{r})}, \tag{4.59}$$

is the reduced density gradient. In Eq. (4.58), the coefficient $\beta$ (0.0042) is an empirical factor.

Number of GGA functionals have been developed. The most popular ones are PBE (proposed in 1996 by Perdew, Burke and Ernzerhof [17]) and BLYP (the combination of the exchange functional by Becke and the correlation functional of Lee, Yang, and Parr [18], both in 1988). GGA fuctionals give reliable results for chemical bonds, but mostly fail for describing van der Waals or dispersion interactions.

#### 4.4.2.3 Hybrids GGA functionals

There is an exact connection between the non-interacting density functional system and the fully interacting many-body system via the integration of the work done in gradually turning on the electron-electron interactions. This adiabatic connection approach [19] allows the exact functional to be formally written as:

$$E_{xc}[\rho] = \frac{1}{2}\int \mathrm{d}\tau \mathrm{d}\tau' \int_{\lambda=0}^{1} d\lambda \frac{\lambda e^2}{|\vec{r}-\vec{r'}|}\left[\left\langle \rho(\vec{r})\rho(\vec{r'})\right\rangle_{\rho,\lambda} - \rho(\vec{r})\delta(\vec{r}-\vec{r'})\right], \tag{4.60}$$

where the expectation value $\langle \cdots \rangle_{\rho,\lambda}$ is the density-density correlation functional that is computed at density $\rho(\vec{r'})$ for a system described by the effective potential

$$v_{eff} = v + \frac{1}{2}\sum_{i\neq j}\frac{\lambda e^2}{|\vec{r_i}-\vec{r_j}|}. \tag{4.61}$$

The adiabatic integration approach suggests a different approximation for the exchange-correlation functional. At $\lambda = 0$ the non-interacting system corresponds exactly to the Hartree-Fock solution, while the LDA and GGA functionals are constructed to be excellent approximations for the fully interacting homogeneous electron gas, that is, a system with $\lambda = 1$

$$E_{xc} = aE^{HF} + bE_{xc}^{GGA} = aE_x^{\lambda=0} + \cdots + bE_c^{\lambda=1}, \tag{4.62}$$

As example, the B3LYP functional [20] uses a different mixing scheme involving three mixing parameters:

$$E_{xc}^{B3LYP} = aE_x^{\lambda=0} + (1-a)E_x^{LSDA} + bE_x^{B88} + cE_c^{LYP} + (1-c)E_c^{LSDA}, \tag{4.63}$$

with $a = 0.20, b = 0.72, c = 0.81$. Then, $a$ also defines the Hartree-Fock exchange rate, which in this case is equal to 20%. The B3LYP functional has been shown to yield accurate results for many molecular properties [21].

#### 4.4.2.4 Meta-GGA and hybrids meta-GGA functionals

These functionals depend, in addition to the density and its first-order derivative, also on the Kohn-Sham kinetic-energy density $\eta(\vec{r})$ . The form of the functional is typically.

$$E_{xc}^{mGGA}[\rho] = \int \rho(\vec{r})\varepsilon_{xc}(\rho, \nabla\rho, \eta)\mathrm{d}\tau, \tag{4.64}$$

where $\tau$ the kinetic energy density of the occupied Kohn-Sham orbitals reads

$$\eta_\sigma(\vec{r}) = \frac{1}{2}\sum_{i}^{occ} |\nabla\Phi_{i\sigma}(\vec{r})|^2. \tag{4.65}$$

The additional degree of freedom is then used to satisfy additional constraints on $E_{xc}$, such as a self-interaction correlation functional. A number of functionals within the mGGA and hybrids mGGA family have been developed [22–24].

#### 4.4.2.5 Long-range corrected functionals

Usual approximations for the exchange-correlation functional $E_{xc}[\rho]$ (LDA, GGA,...) fail in describing long-range effects such those appearing when applying an external electrical field or those related to charge transfer excitations. Savin suggested formulating the LC scheme [25], which is now called the "range-separation hybrid (RSH) exchange functional," by combining the long-range corrected exchange functionals with short-range correlation functionals. Within these LC schemes, the two-electron operator is divided into short- and long-range parts by using the error function $\mathrm{erf}(r)$:

$$\frac{1}{r_{12}} = \frac{\mathrm{erf}(\omega r_{12})}{r_{12}} + \frac{1-\mathrm{erf}(\omega r_{12})}{r_{12}}, \tag{4.66}$$

where the parameter $\omega$ defines the range of these operators. The first term is long ranged (LR), while the second term is short ranged (SR). The $\omega$ parameter, depends on the corrected exchange functional. Various LDA range-separated functionals (RSHX- LDA) have been developed [26–28] (LC-BLYP, LC-$\omega$PBE ...), with the functional in the form:

$$E_{xc}^{RSHXLDA} = E_x^{LR-HF} + E_x^{SR-LSDA} + E_c^{LSDA}. \tag{4.67}$$

The optimal $\omega$ values for RSHXLDA were found to be 0.5 bohr$^{-1}$ for molecular systems, and 0.4 bohr$^{-1}$ for solid-state systems [29].

In 2004, Yanai et al. [30] developed a new hybrid exchange–correlation functional using the Coulomb-attenuating method (CAM-B3LYP). The CAM-B3LYP functional comprises of 19% Hartree-Fock (HF) and 81% Becke 1988 (B88) exchange at short-range while 65% HF and 35% B88 at long-range. The intermediate region is smoothly described through the standard error function with parameter $\omega = 0.33$ bohr$^{-1}$.

Long-range correction is also applied to a semiempirical functional. In 2008, Chai and Head-Gordon [31] proposed the following expression for the LC hybrid functionals:

$$E_{xc}^{LC-DFT} = E_x^{LR-HF} + c_x E_x^{SR-HF} + E_x^{SR-DFT} + E_c^{DFT}, \tag{4.68}$$

where $c_x$ is a fractional number to be determined. The first long-range corrected semiempirical functional is the $\omega$B97X functional, where B97 indicates the B97 functional. For $c_x = 0$ , it is simply called the $\omega$B97 functional.

#### 4.4.2.6 Empirical atom-atom dispersion corrections

Further improvements to the XC-functional in view of describing London dispersion forces are done by incorporating empirical atom-atom dispersion corrections following the general strategy of the DFT-D scheme [32]. So, the total energy reads

$$E^{DFT} = E^{KS-DFT} + E^{disp}, \tag{4.69}$$

where $E^{KS-DFT}$ is the usual self-consistent Kohn-Sham energy as obtained from the chosen density functional and $E^{disp}$ is an empirical dispersion correction given by

$$E^{disp} = -S_6 \sum_{i=1}^{N_{at}-1} \sum_{j=i+1}^{N_{at}} \frac{C_6^{ij}}{R_{ij}^6} f_{damp}(R_{ij}), \tag{4.70}$$

where $N_{at}$ is the number of atoms in the system, $C_6^{ij}$ denotes the dispersion coefficient for the atom pair $ij$, $R_{ij}$ is an interatomic distance, and $f_{damp}(R_{ij})$ is a damping factor:

$$f_{damp}(R_{ij}) = \frac{1}{1 + e^{-d(R_{ij}/R_r - 1)}}. \tag{4.71}$$

Chai and Head-Gordon [33] re-optimized the $\omega$B97X functional to include empirical atom–atom dispersion corrections and the resulting functional is $\omega$B97X-D ($\omega = 0.2$ Bohr$^{-1}, c_x = 0.22$, $a = 6$). They used an unscaled dispersion correction given by

$$E^{disp} = -\sum_{i=1}^{N_{at}-1} \sum_{j=i+1}^{N_{at}} \frac{C_6^{ij}}{R_{ij}^6} f_{damp}(R_{ij}), \tag{4.72}$$

and introduced a damping function in the form

$$f_{damp}(R_{ij}) = \frac{1}{1 + a(R_{ij}/R_r)^{-12}}, \tag{4.73}$$

where $a$ is the nonlinear parameter that controls the strength of dispersion corrections.

$$E_{xc}^{\omega\text{B97X-D}} = E_x^{LR-HF} + 0.22E_x^{SR-HF} + E_x^{SR-B97} + E_c^{B97} + E_c^{disp}. \tag{4.74}$$

## 4.5 Summary of quantum chemistry methods

In the previous section, we briefly presented the Hartree-Fock (HF), the Coupled Cluster (CC), and the Density Functional Theory (DFT) methods. Table 4.1 therefore summarizes some key characteristics of these methods. **CCSD is considered as the reference method**. The scaling of the computational methods - as determined for the "original" implementation without linear scaling algorithms - is given as power of N, which describes the size of the system (number of electrons, number of atomic orbitals). The CPU time is illustrated for IR and Raman activities calculations on Butane molecule (with the aug-cc-pVDZ basis set, *vide supra* Section 4.7.5), and using the Gaussian09 package [37].

TABLE 4.1: Summary of quantum chemistry methods

| Theory | Wave function | Electron correlation | Variational | Size-consistent | Scaling | Max size | CPU time† |
|---|---|---|---|---|---|---|---|
| HF | Yes | No | Yes | Yes | $N^2$-$N^3$ | $10^3$ atoms | $1\times10^3$ sec |
| CCSD | Yes | Yes | No | Yes | $N^6$ | $10^1$atoms | $6\times10^5$ sec |
| DFT | No/Yes | Yes | Yes | Yes | $N^2$-$N^3$ | $10^3$ atoms | $2\times10^3$ sec |

†Calculations were performed using 2 processors and 4 GB of memory on Westmere CPUs (2.66 GHz)

## 4.6 The ONIOM Method

The Own N-layered Integrated Molecular Orbital and Molecular Mechanics (ONIOM) method is a hybrid computational approach developed by Morokuma and co-workers [34, 35] that enables different methods (e.g., QM, SE, MM, coarse-grained (CG), and continuum model (CM) methods) to be applied to different parts of a molecule/system and combined to produce reliable results at reduced computational time. The method has been developed for the purpose of accurate ab initio modeling of chemical systems containing a large number of atoms. Within the method, the system is partitioned into two or more parts or layers, where the interesting or difficult part of the system (the inner layer) is treated at a "high" level of theory and the rest of the system (the outer layer) is described by a computationally less demanding method.

In a two-layered ONIOM (ONIOM2) approach (Fig. 4.1), a model system is cut out from the real system, and the ONIOM2 energy reads

$$E_{\mathrm{ONIOM2}} = E^{\mathrm{low}}_{\mathrm{real}} - E^{\mathrm{low}}_{\mathrm{model}} + E^{\mathrm{high}}_{\mathrm{model}} \tag{4.75}$$

In addition the gradient ($G$) and the Hessian ($H$) are respectively given by

$$G_{\text{ONIOM2}} = G^{\text{low}}_{\text{real}} - G^{\text{low}}_{\text{model}} \times J + G^{\text{high}}_{\text{model}} \times J \tag{4.76}$$

$$H_{\text{ONIOM2}} = H^{\text{low}}_{\text{real}} - J^T \times H^{\text{low}}_{\text{model}} \times J + J^T \times H^{\text{high}}_{\text{model}} \times J \tag{4.77}$$

where $J$ (its transposed $J^T$) is the Jacobian matrix that projects the forces of the model system (link) atoms onto the coordinate space of the full system. $J$ is a function of the atomic coordinates of the model system and of the link atoms.

Moreover, the ONIOM method has been used for the simulation of different properties [36] and systems including energy, gradient, Hessian, geometry optimization, excited states, explicit solvation, transition states. **We used the two-layered ONIOM schemes as implemented in the Gaussian09 package [37] for the SFG spectra of alkylsilanes functionalizing amorphous silica (Chapter 8).**

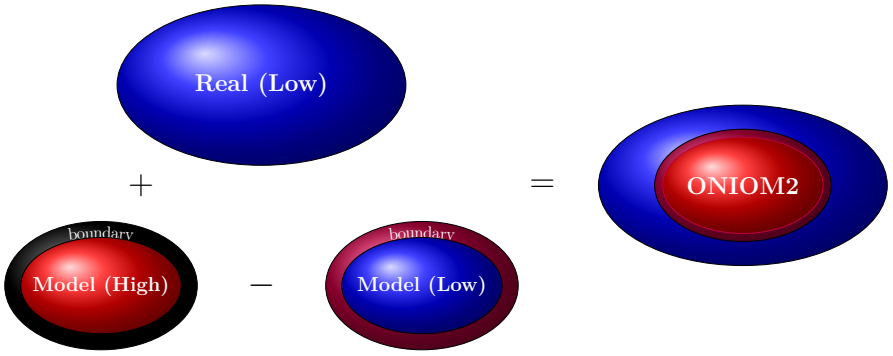


FIGURE 4.1: Schematic representation of two-layered ONIOM

## 4.7 Basis sets

As already introduced and discussed in Sections 4.2 and 4.4.1, calculations are performed within the LCAO scheme, so that the atomic orbitals (basis set) have first to be selected to describe the chemical or physical properties of the system. Larger basis sets give better approximations to the molecular orbitals (MO) and better description of the wavefunction, but they require higher computational costs. Basis sets should therefore be carefully designed to give the best description at the lowest computational cost. A basis set refers to a set of atom-centered functions used to describe the atomic orbitals, known as basis functions. These basis functions could be represented by Eqs. (4.78) and (4.79),

$$\text{Slater-type Orbital} \ : \ \chi^{STO}_{abc}(x,y,z) = N x^a y^b z^c e^{-\zeta r}, \tag{4.78}$$

$$\text{Gaussian-type Orbital} \ : \ \chi^{GTO}_{abc}(x,y,z) = N x^a y^b z^c \sum_{i=1}^{K} c_i e^{-\zeta_i r^2}, \tag{4.79}$$

in which, N is a normalization factor, $a + b + c$ is the angular momentum, $\zeta_i$ and $\zeta$ are the exponents of $\chi$ (it controls the width of the orbital), $K$ is the degree of contraction of $\chi$, and $c_i$ are the contraction coefficients of $\chi$. The Slater orbitals (from the hydrogenic wave functions) are more accurate, but they take much longer to compute the corresponding two-electron integrals. Hehre, Stewart, and Pople [38] proposed to use linear combinations of Gaussian functions to mimic the Slater functions.

### 4.7.1 Minimal basis sets

The simplest possible atomic orbital representation is called a minimal basis set. Minimal basis sets contain the minimum number of basis functions to accommodate all the electrons in the atom [$1^{st}$ row : a single function ($1s$), $2^{nd}$ row : 5 functions ($1s, 2s, 2p_x, 2p_y, 2p_z$), ... ]. The most common minimal basis set is "STO-nG" basis sets (the combination of n Gaussian functions mimicking the Slater functions). The STO-3G basis set is a minimal basis set. **This latter was used in Chapter 8 for calculations on the bulk-like part of the $SiO_2$ substrate.**

### 4.7.2 Split-Valence basis sets

Minimal basis sets are not well suited to model the bonding effects because the exponents do not vary. So, the orbitals have a fixed size and therefore cannot expand or contract as a function of the chemical environment. To improve these latter, split-valence basis sets model each valence orbital by two or more basis functions that have different exponents. They allow for size variations that occur in bonding. For electrons near the nucleus the potential is spherical and one function is suitable but since the energy is sensitive to the position of the electron, it is preferable to take a large contraction of Gaussians. On the other hand, in the valence region the electron density is delocalized over several atoms, far from the spherical symmetry. For a better description each orbital is "split" into several contractions and this leads to the so-called multiple zeta basis sets.

### 4.7.3 Additional basis functions

#### 4.7.3.1 Polarization functions

Polarization functions have higher angular momentum. They allow for anisotropic variations that occur in bonding. They consist in adding p, d ... functions to the H atoms and d, f, g ... functions to heavy (non-hydrogen) atoms.

#### 4.7.3.2 Diffuse functions

Diffuse basis functions are additional functions with small exponents, and are therefore spatially delocalized. They allow for accurate modelling of systems with weakly bound electrons, such as anions, neutral molecules with unshared pairs, and excited states.

### 4.7.4 Pople's basis sets

The notation for the split-valence basis sets arising from Ditchfield, Hehre, and Pople [39] is typically X-YZG. As examples, 3-21G and 6-31G are double split valence basis sets, and 6-311G is a triple split valence basis set. **The 3-21G and 6-31G basis sets were used in the Chapter 8 for calculations on the bulk-like part of the $SiO_2$ substrate**.

The presence of the polarization functions is indicated in the Pople notation by appending an asterisk. As example 6-31G* or 6-31G(d) includes d functions on the heavy atoms, while 6-31G** or 6-31G(d,p) includes d functions on heavy atoms and p functions on hydrogen atoms. **The 6-311G* basis set was used in Chapters 6 to 8 for the calculations on the thiophenol, the decyl chain, and the alkylsilane**.

The presence of the diffuse functions is symbolized by the addition of a plus sign (+), like in 6-31+G. A second + implies that diffuse functions are added to the hydrogen atoms.

### 4.7.5 Dunning's Correlation-Consistent basis sets

Another type of most widely-used basis sets are those developed by Dunning [40], designed for converging post-Hartree–Fock calculations systematically to the complete basis set limit using empirical extrapolation techniques. The notation is typically cc-pVNZ where N = D, T, Q, 5, 6 ... (D=double, T=triple, etc.). The "cc-p", stands for "correlation-consistent polarized". They include successively additional shells of polarization (correlation) functions (d, f, g, etc.). Examples of these are cc-pVDZ (Double-zeta) and cc-pVTZ (Triple-zeta). A prefix "aug" means that one set of diffuse functions is added for every angular momentum present in the basis, so that aug-cc-pVDZ (for C atom has diffuse s,p,d) and aug-cc-pVTZ are the augmented versions of the preceding basis sets. **The aug-cc-pVDZ basis set was used in Chapter 9 to perform calculations on butane molecule.**

### 4.7.6 Effective Core Potentials (ECPs)

For larger atoms Effective Core Potentials (ECPs) are often used [41]. These replace the core electrons with an effective potential and have two main advantages:

- They reduce the number of electrons (cheaper)
- They can be parameterized to take into account relativistic effects [42]

The valence electrons are still modelled using GTOs. **Example of these is the cc-pVDZ-PP basis set employed to perform the calculations on the gold substrates in Chapter 6.** The "PP" stands for "pseudopotential" [or, synonymously, effective core potentials (ECPs)].

# References

[1] Piela,; Lucjan, *Ideas of Quantum Chemistry*; Elsevier, 2006.

[2] Szabo, A.; Ostlund, N. S. *Modern Quantum Chemistry: Introduction to Advanced Electronic Structure Theory*; Dover Publications Inc., 1996.

[3] Hartree, D. R. *Proc. Camb. Phil. Soc.* **1927**, *24*, 89–110.

[4] Fock, V. *Z. Phys.* **1930**, *61*, 126–148.

[5] Slater, J. C. *Phys. Rev.* **1928**, *32*, 339–348.

[6] Roothaan, C. C. J. *Rev. Mod. Phys.* **1951**, *23*, 69–89.

[7] Hall, G. G. *Proc. Roy. Soc.* **1951**, *205*, 541–552.

[8] Coulson, C. A.; Neilson, A. H. *Proc. Phys. Soc.* **1961**, *78*, 831.

[9] Löwdin, P. O. *Avan. Chem. Phys.* **1959**, *2*, 207.

[10] Parr, R. G.; Yang, W. *Density-Functional Theory of Atoms and Molecules*; Oxford University Press, 1989.

[11] Hohenberg, P.; Kohn, W. *Phys. Rev.* **1964**, *136*, B864–B871.

[12] Kohn, W.; Sham, L. J. *Phys. Rev.* **1965**, *140*, A1133–A1138.

[13] Dirac, P. A. M. *Math. Proc. Cambridge Philos. Soc.* **1930**, *26*, 361–375.

[14] Vosko, S. H.; Wilk, L.; Nusair, M. *Can. J. Phys.* **1980**, *58*, 1200–1211.

[15] Perdew, J. P.; Yue, W. *Phys. Rev. B* **1986**, *33*, 8800–8802.

[16] Becke, A. D. *Phys. Rev. A* **1988**, *38*, 3098–3100.

[17] Perdew, J. P.; Burke, K.; Ernzerhof, M. *Phys. Rev. Lett.* **1996**, *77*, 3865–3868.

[18] Lee, C.; Yang, W.; Parr, R. G. *Phys. Rev. B* **1988**, *37*, 785–789.

[19] Gunnarsson, O.; Lundqvist, B. I. *Phys. Rev. B* **1976**, *13*, 4274–4298.

[20] Koch, W.; Holthausen, M. C. *A Chemist's Guide to Density Functional Theory*; Wiley-VCH Verlag GmbH, 2001; pp 65–91.

[21] Koch, W.; Holthausen, M. C. *A Chemist's Guide to Density Functional Theory*; John Wiley & Sons: Weinheim, FRG, 2015.

[22] Tschinke, V.; Ziegler, T. *Can. J. Chem.* **1989**, *67*, 460–472.

[23] Neumann, R.; Handy, N. C. *Chem. Phys. Lett.* **1997**, *266*, 16–22.

[24] Perdew, J. P.; Kurth, S.; Zupan, A.; Blaha, P. *Phys. Rev. Lett.* **1999**, *82*, 2544–2547.

[25] Savin, A. In *Recent Developments and Applications of Modern Density Functional Theory*; Seminario, J., Ed.; Theoretical and Computational Chemistry; Elsevier, 1996; Vol. 4; pp 327 – 357.

[26] Iikura, H.; Tsuneda, T.; Yanai, T.; Hirao, K. *J. Chem. Phys.* **2001**, *115*, 3540–3544.

[27] Vydrov, O. A.; Scuseria, G. E. *J. Chem. Phys.* **2006**, *125*, 234109.

[28] Song, J.-W.; Hirosawa, T.; Tsuneda, T.; Hirao, K. *J. Chem. Phys.* **2007**, *126*, 154105.

[29] Gerber, I. C.; Ángyán, J. G.; Marsman, M.; Kresse, G. *J. Chem. Phys.* **2007**, *127*, 054101.

[30] Yanai, T.; Tew, D. P.; Handy, N. C. *Chem. Phys. Lett.* **2004**, *393*, 51–57.

[31] Chai, J.-D.; Head-Gordon, M. *J. Chem. Phys.* **2008**, *128*, 084106.

[32] Grimme, S. *J. Comput. Chem.* **2006**, *27*, 1787–1799.

[33] Chai, J.-D.; Head-Gordon, M. *Phys. Chem. Chem. Phys.* **2008**, *10*, 6615.

[34] Svensson, M.; Humbel, S.; Froese, R. D. J.; Matsubara, T.; Sieber, S.; Morokuma, K. *J. Phys. Chem.* **1996**, *100*, 19357–19363.

[35] Dapprich, S.; Komáromi, I.; Byun, K. S.; Morokuma, K.; Frisch, M. J. *J. Mol. Struct. Theochem.* **1999**, *461-462*, 1–21.

[36] Chung, L. W.; Sameera, W. M. C.; Ramozzi, R.; Page, A. J.; Hatanaka, M.; Petrova, G. P.; Harris, T. V.; Li, X.; Ke, Z.; Liu, F.; Li, H.-B.; Ding, L.; Morokuma, K. *Chem. Rev.* **2015**, *115*, 5678–5796.

[37] Frisch, M. J. et al. Gaussian 09 Revision D.01. Gaussian Inc. Wallingford CT 2009.

[38] Hehre, W. J.; Stewart, R. F.; Pople, J. A. *J. Chem. Phys.* **1969**, *51*, 2657–2664.

[39] Ditchfield, R.; Hehre, W. J.; Pople, J. A. *J. Chem. Phys.* **1971**, *54*, 724–728.

[40] Dunning, J., Thom H. *J. Chem. Phys.* **1989**, *90*, 1007–1023.

[41] (a) Figgen, D.; Rauhut, G.; Dolg, M.; Stoll, H. *Chem. Phys.* **2005**, *311*, 227 – 244, Relativistic Effects in Heavy-Element Chemistry and Physics. In Memoriam Bernd A. Hess (1954–2004); (b) Peterson, K. A.; Puzzarini, C. *Theo. Chem. Acc.* **2005**, *114*, 283–296.

[42] (a) Douglas, M.; Kroll, N. M. *Ann. Phys.* **1974**, *82*, 89 – 155; (b) Hess, B. A. *Phys. Rev. A* **1985**, *32*, 756–763; (c) Reiher, M. *Theo. Chem. Acc.* **2006**, *116*, 241–252; (d) Jorge, F. E.; Canal Neto, A.; Camiletti, G. G.; Machado, S. F. *J. Chem. Phys.* **2009**, *130*, 064108.

# Chapter 5

# Methods of Simulation and Interpretation Tools

## 5.1 Methods of simulation of the SFG signatures

### 5.1.1 Road map

The theoretical formalism has been carried out in close collaboration with the experimentalists. These efforts led to the elaboration of powerful tools for simulating and interpreting SFG spectra that can therefore be used in the areas of functionalized surface design. Our approach presents the following particularities i) the substrate is included in the system during the calculations; ii) all the simulations are based on first-principles calculations. This approach encompasses several steps (Fig. 5.1):

1. The molecular properties (vibrational frequencies, IR and Raman quantities) are calculated using first principle approaches implemented in standard quantum chemistry programs.
2. Using the homemade Python code, molecular properties are extracted from QM programs output files, then macroscopic optical responses are evaluated. This step includes different sub-calculations:
   - Evaluation of the SFG angle $\theta_{SFG}(\theta_{IR}, \theta_{vis}, n_1)$ (Eq. (3.75)).
   - Evaluation of the Fresnel factors $F_{IJK}[\theta_i, \varepsilon_1, \varepsilon_2(\omega_i), \varepsilon_l]$ (Eq. (1.112), $i \equiv$ SFG, vis, and IR).
   - Evaluation of the molecular vibrational first hyperpolarizability elements $\beta_{\alpha\beta\gamma}$( Eq. (3.91)).
   - Evaluation of the surface susceptibility elements, $\chi^{(2)}_{IJK}$ (Eq. (3.104)), via the average orientation tensor.

3. The SFG intensities are evaluated for different configuration setups: *ssp*, *pss*, *sps*, and *ppp* (Eqs. (3.93) to (3.96)).

4. The SFG spectrum of each configuration (*ppp*, *ssp*, *sps*, and *pss*) is generated for the defined IR wavenumber region.

The originality of our approach is the ease with which the orientation of the molecules at the surface can be determined, as well as the identification of the vibrational normal modes corresponding to each peak of the spectra so that the analysis and the interpretation of the experimental spectra are clearly improved, and the prediction of new systems of interest become possible.

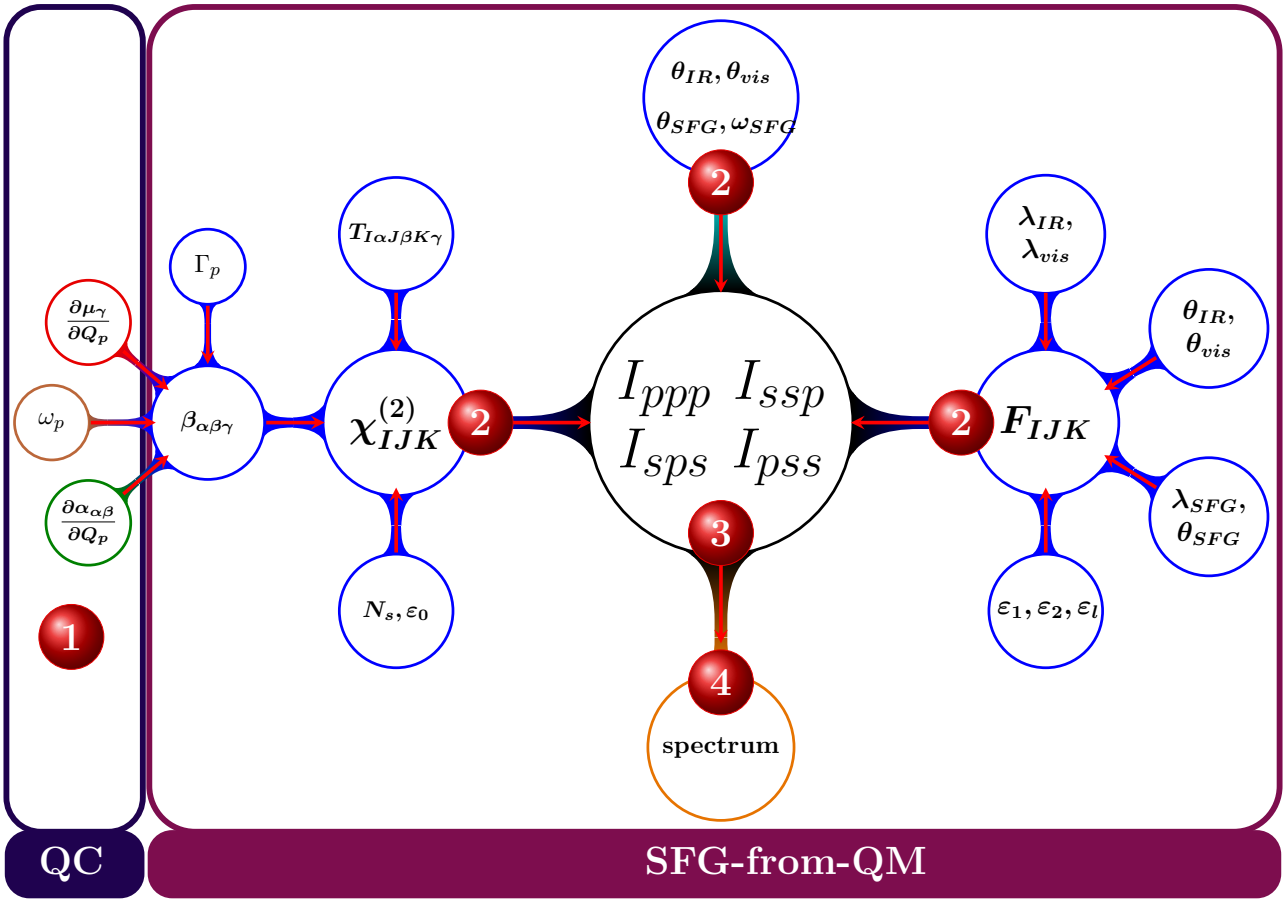


FIGURE 5.1: Road map of the computational procedure. **Step 1**: Evaluation of molecular vibrational properties with quantum chemistry programs (QC). **Step 2**: Evaluation of the molecular ($\beta_{\alpha\beta\gamma}$) and the macroscopic NLO responses with the homemade Program. The $F_{IJK}$ and $\chi^{(2),R}_{IJK}$ are the Fresnel factors and the nonlinear susceptibility components, respectively. $T_{I\alpha J\beta K\gamma}$ is the transformation matrix between the molecular and laboratory coordinates systems. $\varepsilon_1, \varepsilon_2$, and $\varepsilon_l$ are the dielectric constants of the incident medium, the substrate, and the interface, respectively. **Step 3**: Calculation of the intensities for the different configuration setups. **Step 4**: Simulation of the spectrum.

### 5.1.2 Description of the program

To automate our approach a homemade Python program named "`SFG-from-QM`" has been implemented to simulate and interpret the SFG spectra of molecules adsorbed on different substrates. This program is a part of larger project[1] on vibrational spectroscopies (IR, Raman, VROA ...) developed in our lab. Indeed, it takes advantage of different sub-programs available in the project to read or evaluate derivatives of molecular properties with respect to normal modes, from output files of quantum chemistry programs. Moreover, it can be installed on different operating systems (Mac OS X, Unix, Linux, Windows) so that the script called "`SFG-from-QM.py`" can take the input and output data files as command-line arguments. The usage is hence as follows:

```
SFG-from-QM.py [options]
```

where the options are

```
-i INPUTFILE, --inputfile=INPUTFILE
                #Input QM file. Default:None
--IR_angle=IR_ANGLE
                #Angle of incidence of the IR beam in degrees.
                #Default:65.0
--vis_angle=VIS_ANGLE
                #Angle of incidence of the visible beam in degrees.
                #Default:55.0
--substrate=SUBSTRATE
                #Type of substrate:{Au, Si, Pt, Ag, SiO2, TiO2}
--n_substrate=N_SUBSTRATE
                #Refractive index of the substrate at
                #SFG:Vis:IR frequencies  eg 3+0.5j:4+0.4j:3+0j
--plane1=PLANE1 #Three atoms defining the interface plane. eg 1,2,3
--atom=ATOM     #One  atom of the adsorbed molecule  to  define
                # the direction of laboratory Z-axis. eg 1
--Tilt_angle=TILT_ANGLE
                #Euler tilt angle (theta) in degrees. eg 60.0
--Rot_angle=ROT_ANGLE
                #Euler rotation angle (xi) in degrees. eg 60.0
--chi_NR=CHI_NR #Amplitude of the non-resonant susceptibility
                # in m^2/V, default: None, eg 0.12
```

[1]The Vibrational Spectroscopies project was initiated in the LCT of UNamur by Vincent Liégeois

```
--phase_angle=PHASE_ANGLE
                #Dephasing angle between the non-resonant and the
                #resonnant terms of the susceptibility in degrees.
                #Default:None, eg 180
-x XSCALE, --xscale=XSCALE
                #Abscisse scale:xmin:xmax:unit.
                #Default: 200.0:1800.0:cm-1
-s STEP, --step=STEP
                #Step in cm-1 for the abscisse. Default:1.0
--n_film=N_FILM #Refractive index of the thin film. Default:1.0
--n_1=N_1       #Refractive index of the incident medium.
                #Default:1.0
--symm=SYMM     #Symmetry for susceptibility tensor. Default:C1
                #Available:{ C1, C3V, C2V}
-f SCALINGFACTOR, --xscalingfactor=SCALINGFACTOR
                #Scaling factor on the frequencies. Default:1.0
-o OUTPUTFILE, --outputfile=OUTPUTFILE
                #Generic name for the outputfiles.
                #Default: inputfilename_
-t TITLE, --title=TITLE
                #Title name for the pdf file
--Damping=DAMPING
                #Damping factor in cm-1. Default:4.0
--nb_extrema=NB_EXTREMA
                #Number of extrema on the spectrum.
                #Ask 0 for no extrema and none for all of them.
                #Default:None
-w PULSATION, --pulsation=PULSATION
                #Pulsation of the incident laser light to use
```

As example, using the command-line

```
SFG-from-QM.py -i gaussian.fchk  --substrate Pt -x 2800.0:3050.0:cm-1 -f 0.96 \
--n_film=1.4  --Damping=4.0   --Tilt_angle=37  --Rot_angle=54 \
--nb_extrema=5 --IR_angle=65.0 --vis_angle=55.0
```

generates five files reported in Table 5.1.

TABLE 5.1: List of files generated by `SFG-from-QM`

| files | description |
|---|---|
| sfg_ppp.pdf | spectrum for ppp polarization combination (see Fig. 5.2) |
| sfg_pss.pdf | spectrum for pss polarization combination |
| sfg_sps.pdf | spectrum for sps polarization combination |
| sfg_ssp.pdf | spectrum for ssp polarization combination |
| sfg.dat | output data file that contains all the calculated physical quantities as well as the data to plot each spectrum |

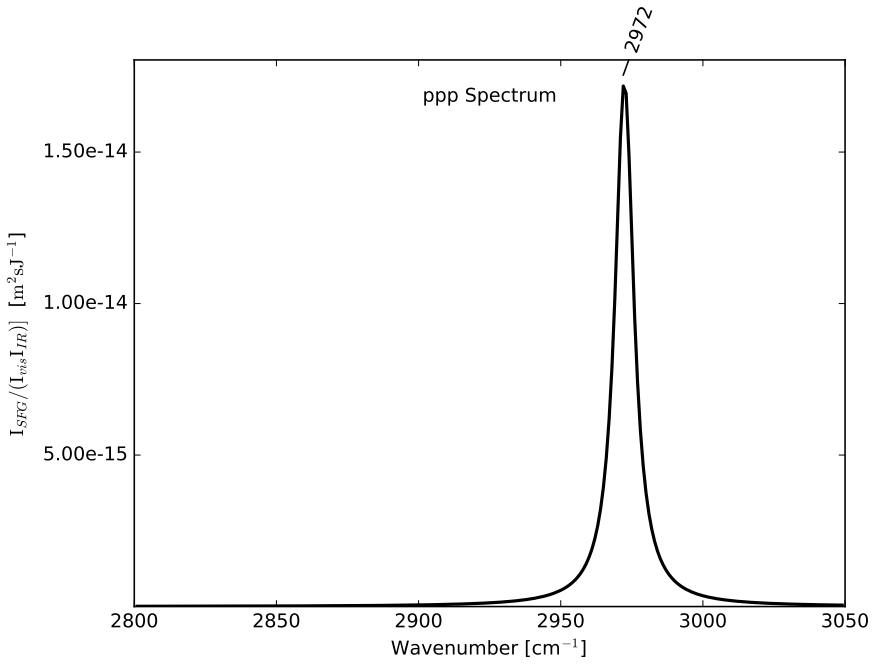


FIGURE 5.2: Examples of sfg_ppp.pdf file generated by `SFG-from-QM`

### 5.1.3 DrawVib and DrawSpectrum

In addition to `SFG-from-QM.py`, our approach is now a part of **DrawVib** [1] and **DrawSpectrum** [2] programs available on the Apple App Store for the Mac OS operating systems. **DrawVib** has similar interface to **DrawSpectrum**, and allows visualizing simultaneously the spectrum and the system or normal modes in 3-D. Fig. 5.3 displays a screen capture of **DrawVib** in which we can see a spectrum similar to that of Fig. 5.2 as well as different parameters. Indeed with **DrawVib** and **DrawSpectrum** it is easy to vary some parameters and directly observe the impact on the spectrum.

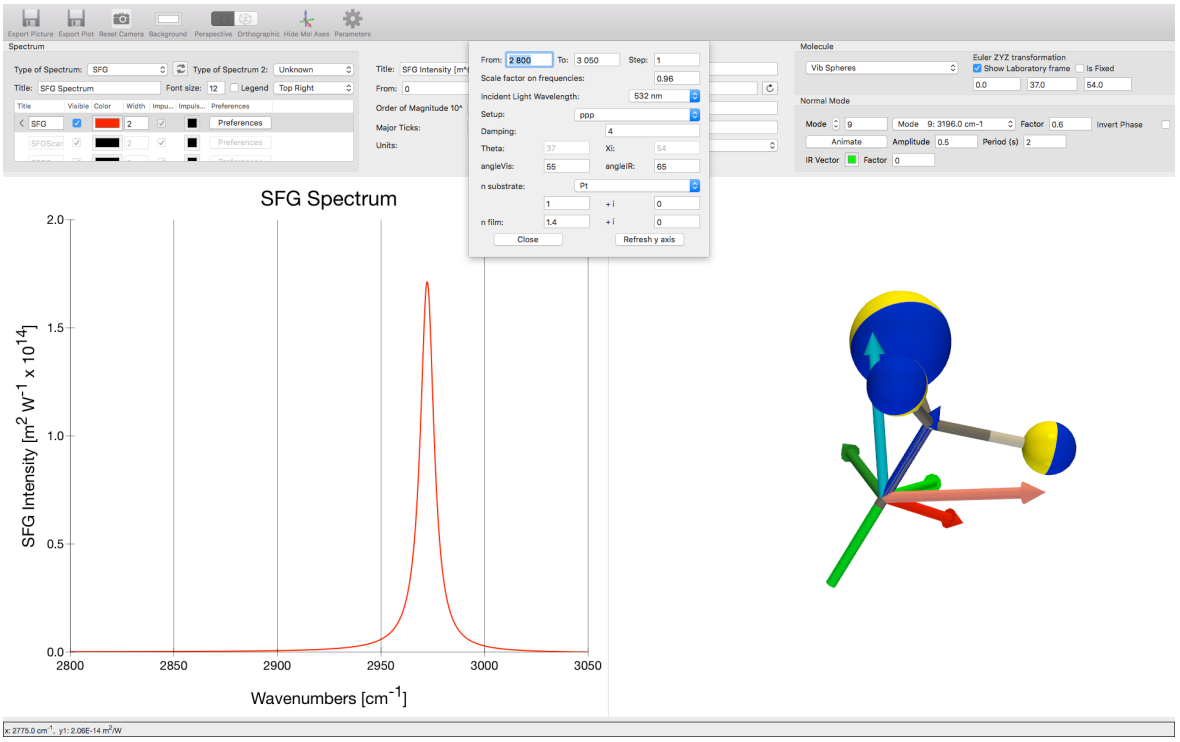


FIGURE 5.3: Screen capture of **DrawVib**

### 5.1.4 Alternative methods for SFG simulations

Several other groups are also tackling the simulation of SFG spectra. Each group has its specificities, which depend on the nature of the interface (gas/solid, gas/liquid, liquid/solid, liquid/liquid, and solid/solid), on the computational method (QM, MM, QM/MM, MD, *ab initio* MD, ...), and on the levels of approximation to describe or not anharmonicity effects or contributions beyond the electric dipole approximation. Generally, based on the available computational resources, choices have to be made: for instance, to favor the level of calculation (*ab initio* calculations) in spite of reduced system sizes or to sacrifice the level of approximation to account for the dynamics of the system.

Among the groups active in the field, we would like to highlight the following ones: 1) Morita and co-workers (Tohoku University, Japan) are known to use MD simulations approaches. In some of their works, they described the Fermi resonance effects on the SFG signature of C−H vibrations [3]. They also addressed the electric quadrupole contribution to the nonresonant background of SFG [4]. 2) In Université Paris-Sud 11 (France), Busson and co-workers have addressed the effects of electric field gradients and quadrupole contributions on the SFG spectra [5]. 3) At the University of Victoria (Canada), Hore and co-workers have developed an approach relying on MD simulations to provide SFG spectra of biomolecular structures [6]. Indeed, for even larger molecules, such as peptides and proteins resonances spaced so closely together that the SFG spectrum appears as if it contains only a few bands. Highly overlapping vibrational modes cannot be resolved in an experiment. 4) Bonn, Nagata and co-workers (Max Planck Institute

for Polymer Research, Germany) [7] have employed approaches accounting for Fermi resonances and combination bands such as the Vibrational Self-Consistent Field (VSCF) method [8]. They also reviewed the current state-of-the-art of three levels MD simulations (*ab initio*, Force Field and Coarse-Grained). They discussed the advantages, the potential, and the limitations of each method for studying aqueous interfaces, by assessing computations of the SFG spectra and surface tension [9]. 5) Geiger (Northwestern University, United States), Bastista and co-workers (Yale University, United States) also used the VSCF method, together with ONIOM approach [10]. In addition, they have assessed the performance of the DFT for computing the SFG spectra. They reported that hybrid functionals such as B3LYP, $\omega$B97X-D, PBE0, and B97-1 in combination with a modest basis sets, such as 6-311G(d,p), provides good agreement with experimental data and much better performance than pure functionals such as PBE and BP86 [11]. 6) Richmond and co-worker (University of Oregon, United States) have relied on classical MD and QM (DFT) calculations to investigate the structure of atmospherically relevant organic molecules at the air/water interface using SFG [12].

All these groups combine both experimental and theoretical approaches and most of the calculations rely on *ab initio*, Force Field and Coarse-Grained MD, or periodic boundary conditions methods (plane-wave basis sets). Only few calculations are based on first principles methods (particularly DFT), and in those cases only a single molecule is included in the calculations.

## 5.2 Interpretation tools

### 5.2.1 Normal mode overlaps

The normal coordinates constitute a basis in which the corresponding Hessian matrix is diagonal (see Section 3.1):

$$\boldsymbol{Q}^T \boldsymbol{H}^m \boldsymbol{Q} = \boldsymbol{H}^q, \tag{5.1}$$

where $H^q_{pp} = \omega_p^2 = 4\pi^2\nu_p^2$, with $\nu_p$ being the $p$-th vibrational frequency. The columns of the matrix $\boldsymbol{Q}$, $\boldsymbol{Q}_p$, are the normal coordinates in terms of mass-weighted Cartesian displacements. The components of the $p$-th normal mode in terms of Cartesian coordinates $\boldsymbol{Q}^c_p$ then read:

$$Q^c_{i\alpha,p} = (1/\sqrt{m_i})Q_{i\alpha,p}. \tag{5.2}$$

These normal modes are normalized such as:

$$1 = \sum_{i\alpha} Q^2_{i\alpha,p} = \sum_{i\alpha} (Q^c_{i\alpha,p})^2 m_i \tag{5.3}$$

The normal coordinates constitute a complete basis set. One can therefore express the normal coordinates of a given molecule as a function of the normal coordinates of a reference molecule providing that they have the same number of atoms (normal modes coordinates):

$$\begin{aligned} |\boldsymbol{Q}_p^B\rangle &= \sum_l^A |\boldsymbol{Q}_l^A\rangle\langle\boldsymbol{Q}_l^A|\boldsymbol{Q}_p^B\rangle, \\ &= \sum_l^A U_{lp}^{AB}|\boldsymbol{Q}_l^A\rangle, \end{aligned} \tag{5.4}$$

where $U_{lp}^{AB}$ is the transformation matrix from one set to the other and is unitary. From the orthogonality of the two sets of normal coordinates ($\boldsymbol{Q}_l^A$, $\boldsymbol{Q}_p^B$), one can define the overlap [13] between modes $l$ and $p$, of molecules A and B, respectively:

$$\begin{aligned} \langle\boldsymbol{Q}_p^B|\boldsymbol{Q}_p^B\rangle &= 1, \\ &= \sum_l^A \langle\boldsymbol{Q}_p^B|\boldsymbol{Q}_l^A\rangle\langle\boldsymbol{Q}_l^A|\boldsymbol{Q}_p^B\rangle, \\ &= \sum_l^A \left(U_{pl}^{BA}\right)^\dagger U_{lp}^{AB}, \\ &= \sum_l^A O_{l,p}^{AB}. \end{aligned} \tag{5.5}$$

The overlap is therefore defined as:

$$\begin{aligned} O_{l,p}^{AB} &= \langle\boldsymbol{Q}_l^A|\boldsymbol{Q}_p^B\rangle^2 = (U_{lp}^{AB})^2, \\ &= \left(\sum_{i\alpha} Q_{i\alpha,l}^A Q_{i\alpha,p}^B\right)^2. \end{aligned} \tag{5.6}$$

Each set of normal coordinates is given in its own mass-weighted Cartesian displacements. It is therefore necessary to first align the molecules.

By extension, one can define the transformation matrix between the normal modes of a common fragment F of two molecules having different numbers of atoms:

$$\begin{aligned} |\boldsymbol{Q}_p^{B,F}\rangle &= \sum_{l,m}^A |\boldsymbol{Q}_l^{A,F}\rangle\langle\boldsymbol{Q}_l^{A,F}|\boldsymbol{Q}_m^{A,F}\rangle^{-1}\langle\boldsymbol{Q}_m^{A,F}|\boldsymbol{Q}_p^{B,F}\rangle, \\ &= \sum_{l,m}^A (S_{lm}^{A,F})^{-1} T_{mp}^{AB,F}|\boldsymbol{Q}_l^{A,F}\rangle, \\ &\approx \sum_l^A T_{lp}^{AB,F}|\boldsymbol{Q}_l^{A,F}\rangle, \end{aligned} \tag{5.7}$$

where the transformation matrix and the overlap between modes $l$ and $p$, of molecules A and B (with different number of atoms), respectively, by specifying a fragment F read:

$$\begin{aligned} T_{lp}^{AB,F} &= \langle \boldsymbol{Q}_l^{A,F} | \boldsymbol{Q}_p^{B,F} \rangle, \\ &= \sum_{i\alpha}^{F} Q_{i\alpha,l}^{A} Q_{i\alpha,p}^{B}, \end{aligned} \tag{5.8}$$

$$\begin{aligned} O_{l,p}^{AB,F} &= \langle \boldsymbol{Q}_l^{A,F} | \boldsymbol{Q}_p^{B,F} \rangle^2 = (T_{lp}^{AB,F})^2, \\ &= \left( \sum_{i\alpha}^{F} Q_{i\alpha,l}^{A} Q_{i\alpha,p}^{B} \right)^2. \end{aligned} \tag{5.9}$$

A normal node in a fragment corresponds to a truncation of the displacements of atoms to keep only those which involve the atoms of the fragment. In this case, the two sets of normal coordinates are not orthonormal:

$$\langle \boldsymbol{Q}_l^{A,F} | \boldsymbol{Q}_l^{A,F} \rangle = S_{ll}^{A,F} = \sum_{i\alpha}^{F} Q_{i\alpha,l}^{A} Q_{i\alpha,l}^{A} < 1, \tag{5.10}$$

$$\langle \boldsymbol{Q}_p^{B,F} | \boldsymbol{Q}_p^{B,F} \rangle = S_{pp}^{B,F} = \sum_{i\alpha}^{F} Q_{i\alpha,p}^{B} Q_{i\alpha,p}^{B} < 1. \tag{5.11}$$

This means that:

$$\sum_{l}^{A} O_{l,p}^{AB,F} < 1 \text{ and } \sum_{p}^{B} O_{l,p}^{AB,F} < 1. \tag{5.12}$$

If two modes have the same shape within a given fragment, they will have a large value of overlap but it can only be equal to 1 if the fragment F consists of the whole molecules. In order to better analyze the similarity between the shape of two normal modes, we define a new quantity called similarity:

$$\begin{aligned} S_{l,p}^{AB,F} &= \frac{O_{l,p}^{AB,F}}{\langle \boldsymbol{Q}_l^{A,F} | \boldsymbol{Q}_l^{A,F} \rangle \langle \boldsymbol{Q}_p^{B,F} | \boldsymbol{Q}_p^{B,F} \rangle}, \\ &= \frac{\langle \boldsymbol{Q}_l^{A,F} | \boldsymbol{Q}_p^{B,F} \rangle \langle \boldsymbol{Q}_l^{A,F} | \boldsymbol{Q}_p^{B,F} \rangle}{\langle \boldsymbol{Q}_l^{A,F} | \boldsymbol{Q}_l^{A,F} \rangle \langle \boldsymbol{Q}_p^{B,F} | \boldsymbol{Q}_p^{B,F} \rangle}. \end{aligned} \tag{5.13}$$

As example Fig. 5.4, displays the normal modes overlaps between the acetonitrile ($CH_3-CN$) and cholоromethane ($CH_3-Cl$) in the 2300-3200 $cm^{-1}$ region. Mode 12 of $CH_3-CN$ matches mode 8 of $CH_3-Cl$, while mode 11 of $CH_3-CN$ matches mode 9 of $CH_3-Cl$.

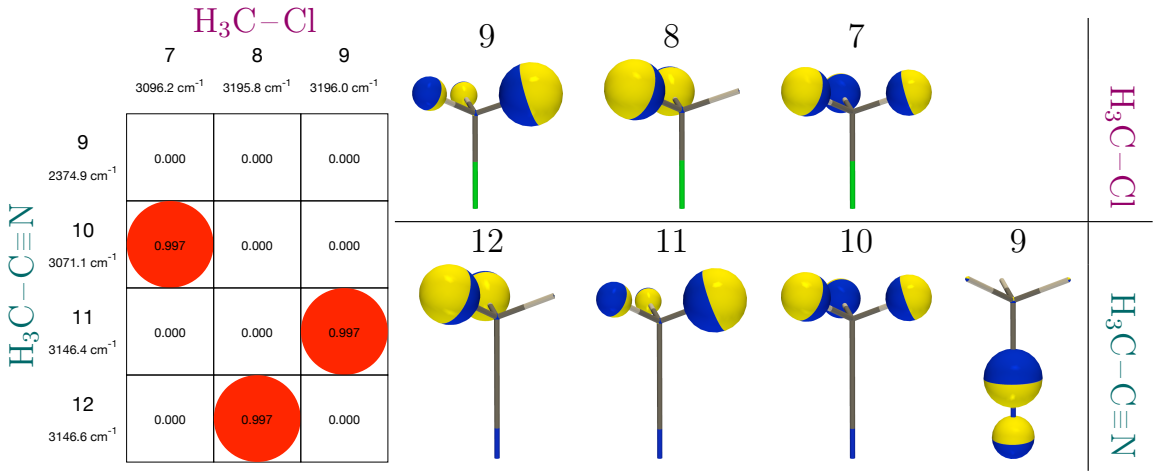


FIGURE 5.4: Overlaps between normal modes of acetonitrile ($CH_3-CN$) and cholоromethane ($CH_3-Cl$) in the 2300-3200 $cm^{-1}$ region. The match has been done on the $-CH_3$ fragment of each molecule. The red circle represent the similarities $S_{l,p}^{AB,F}$, and the values are given inside. The normal modes are sketched by sphere with hemispheres of different colors.

### 5.2.2 Group Coupling Matrices (GCM) and Atomic Contribution Pattern (ACP)

The infrared and Raman intensities [Eqs. (3.48) and (3.71)] can also be expressed in term of the Cartesian derivatives of the dipole moment and the polarizability tensor:

$$I_p = K_p \sum_{i,j}^{N} \sum_{\alpha\beta}^{3} Q_{i\alpha,p}^{c} V_{i\alpha,j\beta} Q_{j\beta,p}^{c} = \sum_{i,j}^{N} I_{ij,p}, \tag{5.14}$$

where $V_{i\alpha,j\beta}$ is defined as

$$V_{i\alpha,j\beta}^{\mathrm{IR}} = \sum_{\xi} \left(\frac{\partial \mu_\xi}{\partial R_{i\alpha}}\right)_e \left(\frac{\partial \mu_\xi}{\partial R_{j\beta}}\right)_e, \tag{5.15}$$

$$V_{i\alpha,j\beta}^{\mathrm{Raman}} = [90V(a^2)_{i\alpha,j\beta} + 14V(\beta^2)_{i\alpha,j\beta}] \quad \text{with,} \tag{5.16}$$

$$V(a^2)_{i\alpha,j\beta} = \sum_{\xi\eta} \frac{1}{9} \left(\frac{\partial \alpha_{\xi\xi}}{\partial R_{i\alpha}}\right)_e \left(\frac{\partial \alpha_{\eta\eta}}{\partial R_{j\beta}}\right)_e, \tag{5.17}$$

$$V(\beta^2)_{i\alpha,j\beta} = \sum_{\xi\eta} \frac{1}{2} \left[3 \left(\frac{\partial \alpha_{\xi\eta}}{\partial R_{i\alpha}}\right)_e \left(\frac{\partial \alpha_{\xi\eta}}{\partial R_{j\beta}}\right)_e - \left(\frac{\partial \alpha_{\xi\xi}}{\partial R_{i\alpha}}\right)_e \left(\frac{\partial \alpha_{\eta\eta}}{\partial R_{j\beta}}\right)_e\right]. \tag{5.18}$$

The IR or Raman intensity can therefore be decomposed into mono-nuclear ($I_{ii,p}$, diagonal) and di-nuclear ($I_{ij,p}$, off-diagonal) contributions: this is known as the Group Coupling Matrix (GCM) scheme of Hug [14]

To visualize atomic contributions of individual atoms, one therefore needs to split the di-nuclear contributions denoted as Atomic Pattern Contribution (ACP):

$$I_{i,p} = \sum_j I_{ij,p} r^1_{ij,p} + I_{ji,p} r^2_{ji,p}. \tag{5.19}$$

where $r^1_{ij,p}$ and $r^2_{ji,p}$ are weighting coefficients for the di-nuclear terms.

Fig. 5.5 displays an example of the IR intensity GCM and ACP for the modes 10 and 12 (Fig. 5.4) of $CH_3CN$ molecule. Since only the symmetric part contributes to the total intensity of the vibrational modes, GCM are best represented by upper triangular matrices, with off-diagonal elements equal to the sum of the two off-diagonal halves of the full matrix.

These advanced tools are now implemented into the `pyvib2` [15, 16] and DrawMol programs [17].

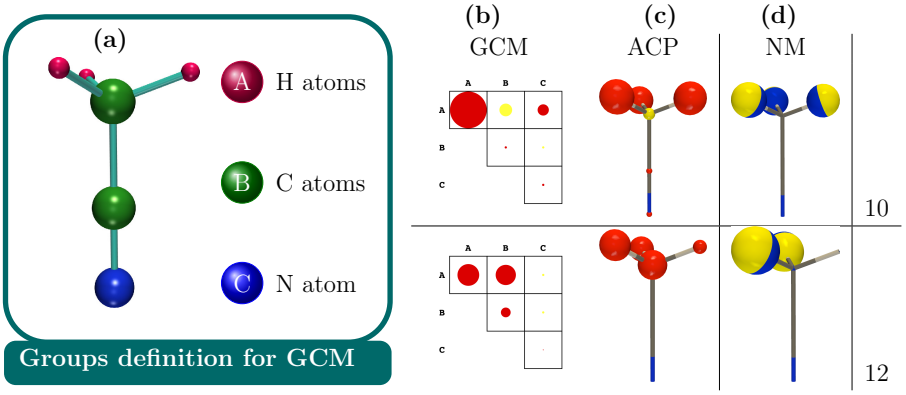


FIGURE 5.5: (a) Groups definition for the GCM analysis. (b) Illustration of IR GCM within modes 10 and 12 of $CH_3CN$, using groups defined in (a). The areas of the circles are directly proportional to the coupling contributions Eq. (5.14). (c) Illustration of IR ACP within modes 10 and 12 of $CH_3CN$. Sphere surfaces are proportional to the atomic contributions to the IR intensity. For both GCM and ACP the color reflects the sign: red for positive and yellow for negative.

### 5.2.3 Enhancement factor for SERS

The intensity coupling matrix (from which the intensities are the diagonal elements) associated to any vibrational spectroscopy reads:

$$I^A_{ll'} = \sum_{i\alpha} \sum_{j\beta} Q^{Ac}_{i\alpha,l} V^A_{i\alpha,j\beta} Q^{Ac}_{j\beta,l'}, \tag{5.20}$$

$$I^B_{pp'} = \sum_{i\alpha}\sum_{j\beta} Q^{Bc}_{i\alpha,p} V^B_{i\alpha,j\beta} Q^{Bc}_{j\beta,p'}. \tag{5.21}$$

Now, we want to express the intensity of molecule B ($I^B_{pp}$) with respect to the intensity coupling matrix of A ($I^A_{ll'}$). From Eqs. (5.7) and (5.8), we can express the intensity (and more generally the intensity coupling matrix) of molecule B in terms of the normal modes of molecule A, both molecules having a common fragment F:

$$\begin{aligned} I^{B,F}_p &= \sum_{i\alpha}^{F}\sum_{j\beta}^{F} Q^{Bc}_{i\alpha,p} V^B_{i\alpha,j\beta} Q^{Bc}_{j\beta,p}, && (5.22)\\ &= \sum_{l,l'}\sum_{i\alpha}^{F}\sum_{j\beta}^{F} T^{AB,F}_{lp} Q^{Ac}_{i\alpha,l} V^B_{i\alpha,j\beta} Q^{Ac}_{j\beta,l'} T^{AB,F}_{l'p}, \\ &= \sum_{l,l'} T^{AB,F}_{lp} T^{AB,F}_{l'p} \sum_{i\alpha}^{F}\sum_{j\beta}^{F} Q^{Ac}_{i\alpha,l} V^B_{i\alpha,j\beta} Q^{Ac}_{j\beta,l'}, && (5.23)\\ &= \sum_{l,l'} I^{A,B,F}_{ll',p} = \sum_{l} I^{A,B,F}_{l,p}. && (5.24) \end{aligned}$$

$I^{A,B}_{ll',p}$, gives the intensity for the $p$ normal mode of molecule B in terms of coupling between the normal modes of molecule A, while $I^{A,B}_{l,p}$ gives the intensity for the $p$ normal mode of molecule B in terms of the normal modes of molecule A, where the coupling terms have been separated into two equal parts.

We would like to define an enhancement factor as the ratio between the intensity of molecule B over the intensity of molecule A:

$$\begin{aligned} \mathrm{En}^{A,B}_{l,p} &= \frac{I^B_p}{I^A_l}, \\ &= \frac{\sum_{i\alpha}\sum_{j\beta} Q^{Bc}_{i\alpha,p} V^B_{i\alpha,j\beta} Q^{Bc}_{j\beta,p}}{\sum_{i\alpha}\sum_{j\beta} Q^{Ac}_{i\alpha,l} V^A_{i\alpha,j\beta} Q^{Ac}_{j\beta,l}}. \end{aligned} \tag{5.25}$$

The problem is that the enhancement should reflect the changes in the Cartesian derivatives of the properties between the two molecules ($V^A_{i\alpha,j\beta} \neq V^B_{i\alpha,j\beta}$) and should not depend on the changes of normal modes between the two molecules. The previous definition is therefore only valid if $\langle Q^A_l | Q^B_p \rangle^2 \approx 1$. A more general definition would be:

$$\begin{aligned} \mathrm{En}^{A,B,F}_{\mathrm{band}} &= \frac{\sum_p^{\mathrm{band}} I^{B,F}_p}{\sum_l^{\mathrm{band}} I^{A,F}_l}, \\ &= \frac{\sum_p^{\mathrm{band}} \sum_{i\alpha}^{F}\sum_{j\beta}^{F} Q^{Bc}_{i\alpha,p} V^B_{i\alpha,j\beta} Q^{Bc}_{j\beta,p}}{\sum_l^{\mathrm{band}} \sum_{i\alpha}^{F}\sum_{j\beta}^{F} Q^{Ac}_{i\alpha,l} V^A_{i\alpha,j\beta} Q^{Ac}_{j\beta,l}}. \end{aligned} \tag{5.26}$$

Indeed, the transformation matrix $\boldsymbol{T}^{AB,F}$ is, in general, not a unitary matrix. However, it is most of the time constituted by blocks (defining a band) that are quasi unitary. We can therefore

show that the sum of the intensities of the modes of molecule B for one band is related to the sum of the intensities of the modes of the same band in molecule A:

$$\sum_{p}^{\text{band}} I_p^{B,F} = \sum_{p}^{\text{band}} \sum_{i\alpha}^{F} \sum_{j\beta}^{F} Q_{i\alpha,p}^{Bc} V_{i\alpha,j\beta}^{B} Q_{j\beta,p}^{Bc}, \tag{5.27}$$

$$= \sum_{p}^{\text{band}} \sum_{l,l'} T_{lp}^{AB,F} T_{l'p}^{AB,F} \sum_{i\alpha}^{F} \sum_{j\beta}^{F} Q_{i\alpha,l}^{Ac} V_{i\alpha,j\beta}^{B} Q_{j\beta,l'}^{Ac},$$

$$= \sum_{l,l'} \left[ \sum_{p}^{\text{band}} T_{lp}^{AB,F} T_{l'p}^{AB,F} \right] \sum_{i\alpha}^{F} \sum_{j\beta}^{F} Q_{i\alpha,l}^{Ac} V_{i\alpha,j\beta}^{B} Q_{j\beta,l'}^{Ac}, \tag{5.28}$$

$$= \sum_{l}^{\text{band}} \sum_{i\alpha}^{F} \sum_{j\beta}^{F} Q_{i\alpha,l}^{Ac} V_{i\alpha,j\beta}^{B} Q_{j\beta,l}^{Ac}. \tag{5.29}$$

Inserting this relationship into the definition of the enhancement factor (Eq. (5.26)) gives:

$$\begin{aligned} \text{En}_{\text{band}}^{A,B,F} &= \frac{\sum_{p}^{\text{band}} \sum_{i\alpha}^{F} \sum_{j\beta}^{F} Q_{i\alpha,p}^{Bc} V_{i\alpha,j\beta}^{B} Q_{j\beta,p}^{Bc}}{\sum_{l}^{\text{band}} \sum_{i\alpha}^{F} \sum_{j\beta}^{F} Q_{i\alpha,l}^{Ac} V_{i\alpha,j\beta}^{A} Q_{j\beta,l}^{Ac}}, \\ &= \frac{\sum_{l}^{\text{band}} \sum_{i\alpha}^{F} \sum_{j\beta}^{F} Q_{i\alpha,l}^{Ac} V_{i\alpha,j\beta}^{B} Q_{j\beta,l}^{Ac}}{\sum_{l}^{\text{band}} \sum_{i\alpha}^{F} \sum_{j\beta}^{F} Q_{i\alpha,l}^{Ac} V_{i\alpha,j\beta}^{A} Q_{j\beta,l}^{Ac}}. \end{aligned} \tag{5.30}$$

As we can see from Eq. (5.30), the enhancement factor does not depend anymore the difference of normal modes between molecules A and B. The equality between Eq. (5.28) and Eq. (5.29) is only fulfilled if:

$$\sum_{p}^{\text{band}} T_{lp}^{AB,F} T_{l'p}^{AB,F} = \delta_{ll'} \delta_{l\text{band}}. \tag{5.31}$$

**This enhancements factor was used in Chapter 6 (Section 6.3.4) to calculate the Raman relative enhancements of Thiophenol adsorbed on gold surfaces.**

# References


[1] Liégeois, V. DrawVib. http://www.unamur.be/sciences/chimie/drawvib.

[2] Liégeois, V. DrawSpectrum. http://www.unamur.be/sciences/chimie/drawspectrum.

[3] (a) Wang, L.; Ishiyama, T.; Morita, A. *J. Phys. Chem. A* **2017**, *121*, 6687–6700; (b) Wang, L.; Ishiyama, T.; Morita, A. *J. Phys. Chem. A* **2017**, *121*, 6701–6712; (c) Ishiyama, T.; Sokolov, V. V.; Morita, A. *J. Chem. Phys.* **2011**, *134*, 024509; (d) Ishiyama, T.; Sokolov, V. V.; Morita, A. *J. Chem. Phys.* **2011**, *134*, 024510.

[4] (a) Morita, A. *Theory of Sum Frequency Generation Spectroscopy*; Springer, 2018; (b) Yamaguchi, S.; Shiratori, K.; Morita, A.; Tahara, T. *J. Chem. Phys.* **2011**, *134*, 184705.

[5] (a) Busson, B.; Dalstein, L. *J. Chem. Phys.* **2018**, *149*, 154701; (b) Busson, B.; Dalstein, L. *J. Chem. Phys.* **2018**, *149*, 034701.

[6] (a) Hall, S. A.; Jena, K. C.; Covert, P. A.; Roy, S.; Trudeau, T. G.; Hore, D. K. *J. Phys. Chem. B* **2014**, *118*, 5617–5636; (b) Roy, S.; Hung, K.-K.; Stege, U.; Hore, D. K. *Appl. Spectrosc. Rev.* **2014**, *49*, 233–248.

[7] Ohto, T.; Backus, E. H. G.; Mizukami, W.; Hunger, J.; Bonn, M.; Nagata, Y. *J. Phys. Chem. C* **2016**, *120*, 17435–17443.

[8] Roy, T. K.; Gerber, R. B. *Phys. Chem. Chem. Phys.* **2013**, *15*, 9468–9492.

[9] Nagata, Y.; Ohto, T.; Backus, E. H. G.; Bonn, M. *J. Phys. Chem. B* **2016**, *120*, 3785–3796.

[10] Ho, J.; Psciuk, B. T.; Chase, H. M.; Rudshteyn, B.; Upshur, M. A.; Fu, L.; Thomson, R. J.; Wang, H.-f.; Geiger, F. M.; Batista, V. S. *J. Phys. Chem. C* **2016**, *120*, 12578–12589.

[11] Chase, H. M.; Rudshteyn, B.; Psciuk, B. T.; Upshur, M. A.; Strick, B. F.; Thomson, R. J.; Batista, V. S.; Geiger, F. M. *J. Phys. Chem. B* **2016**, *120*, 1919–1927.

[12] (a) Gordon, B. P.; Moore, F. G.; Scatena, L. F.; Valley, N. A.; Wren, S. N.; Richmond, G. L. *J. Phys. Chem. A* **2018**, *122*, 3837–3849; (b) Valley, N. A.; Richmond, G. L. *J. Phys. Chem. C* **2016**, *120*, 14122–14129; (c) Wren, S. N.; Gordon, B. P.; Valley, N. A.; McWilliams, L. E.; Richmond, G. L. *J. Phys. Chem. A* **2015**, *119*, 6391–6403.

[13] Hug, W.; Fedorovsky, M. *Theo. Chem. Acc.* **2006**, *119*, 113–131.

[14] Hug, W. *Chem. Phys.* **2001**, *264*, 53–69.

[15] Fedorovsky, M. PyVib2, a program for analyzing vibrational motion and vibrational spectra. http://pyvib2.sourceforge.net, 2007.

[16] Liégeois, V.; Champagne, B. *Theo. Chem. Acc.* **2012**, *131*, 1–15.

[17] Liégeois, V. DrawMol. http://www.unamur.be/sciences/chimie/drawmol.

# Part III

# Results and Discussions

Tetsassi Feugmo, C. G.; Liégeois, V. *ChemPhysChem* **2013**, 14, 1633–1645

**Personal contribution:** I designed the investigation by selecting the systems, I ran all calculations, and simulated the IR and Raman spectra with custom programs. Then, I proposed analyses, discussed these with my co-author, and I wrote the first draft of the paper.

# Chapter 6

# Analyzing the Vibrational Signatures of Thiophenol Adsorbed on Small Gold Clusters from DFT Calculations.

In this chapter, using Density Functional Theory (DFT), we calculate the Infrared (IR) and Raman signatures of the thiophenol (TP) molecule adsorbed on gold clusters mimicking the different types of adsorption sites and we analyze these signatures using advanced tools implemented into the `pyvib2` program. First, we follow the evolution of the vibrational normal modes from the isolated TP molecule to those of TP adsorbed on different clusters in order to highlight the influence of the site of adsorption on the vibrational motions. The use of the overlap matrix between the modes enables to highlight mode permutations, mode mixings, and mode splittings, which depend not only on the adsorption but also on the type of cluster and of its symmetry. Second, the IR and Raman signatures have been analyzed using the group coupling matrices (GCM) and the atomic contribution patterns (ACP) based on Hug decomposition scheme. Key results encompass *i)* the better sensitivity of Raman than IR with respect to the nature of the coordination site, *ii)* an IR criterion distinguishing *on-top* coordination (onefold-coordinated) with respect to *bridge* (twofold-coordinated) and *hcp-hollow* site coordinations (threefold-coordinated), and *iii)* the best agreement to the experimental Raman spectrum obtained for a bridge two-fold coordination owing to signatures from 500 to 1200 $cm^{-1}$ region.

## 6.1 Motivations

Surfaces and interfaces play a prominent role for numbers of applications in life and materials science due to their structures and composition, which differ from those of bulk materials. Under these conditions, surfaces characterization and determination of their properties are essential to understand the fundamental physico-chemical phenomena that can occur at the interfaces.

From this knowledge, the interface can then be tuned in order to exhibit specific properties for applications in molecular electronics, catalysis, sensing devices, etc [1].

The vibrational responses of an interface are distinctive signatures of its chemical composition, as well as of its structure and organization. Indeed, the vibrations are fingerprints of the chemical bonds, and are very sensitive to the environment. Hence, the normal modes of vibration are specific to the nature of the chemical terminations of the surface and of the adsorbates present on the surface [2], which allows to identify the adsorption binding sites or to determine the orientation of the vibrational active groups [3–5]. Therefore, various vibrational spectroscopic techniques such as Surface Enhanced Infrared Absorption Spectroscopy (SEIRAS), Surface Enhanced Raman Spectroscopy (SERS), and Sum Frequency Generation (SFG) Spectroscopy have been developed for probing molecules adsorbed on metal nanostructures or substrates with nanoscale roughness [6–8]. Among these molecules, thiols on gold surfaces are extensively studied. Indeed, substantial amount of work has been carried out on the electromagnetic and chemical contributions to the SERS spectra [9], on molecular orientations at interfaces [10], and on the chemical interactions between thiol and gold surface [11]. However, the exact nature of the chemisorption site for thiols on Au surfaces is still unclear since details of individual molecules chemisorbed on a surface are quite complicated to obtain experimentally. On the other hand, selective enhancements of the Raman cross sections, as well as its dependence on the binding site have not yet been clarified.

This chapter report on Density Functional Theory (DFT) simulations of the IR and Raman spectra of the thiophenol (TP) molecule, a prototypical aromatic thiol, bound to small gold clusters, built from 7 to 15 atoms and mimicking different chemisorption sites. A key point of the present work is therefore to point out the IR and Raman spectral fingerprints specific to the nature of the binding site. In fact, on an unreconstructed face-centered-cubic Au(111) surface, several sites are available for bonding: *i)* the "*hollow*" (fcc and hcp) sites, threefold-coordinated, implying three Au atoms linked to the S atom; *ii)* the "*bridge*" site (twofold-coordinated), lying on top of a Au-Au bond, where a pair of Au atoms share the S atom; and *iii)* the "*top*"site (onefold-coordinated) where the S atom is linked to a single Au atom. Interpretations of SERS data [12] indicate a preference for the occupation of either the top or bridge sites, while the bridge occupation is substantiated by high-resolution electron energy loss spectroscopy [13]. On the other hand, several theoretical calculations support the *bridge* site occupation [14–16] but others point out a preference for the *hollow* site [17]. This work describes the spectroscopic signatures associated to the three different kinds of binding site using first principles calculations. In particular, we employ new tools to interpret these spectra and to unravel the impact of the adsorption on the vibrational normal modes as well as on the IR and Raman intensities. These include similarity analysis, group coupling matrices (GCM), and atomic contribution patterns (ACP). These results and their discussions on the IR and then Raman spectra will be presented after a brief introduction on the theoretical and computational aspects.

## 6.2 Theoretical and computational aspects

All calculations were performed with DFT using the B3LYP exchange-correlation [18] functional as implemented in the Gaussian09 program [19]. The 6-311G* basis set was adopted for the C, H, and S atoms, while the cc-pVDZ basis set was chosen for the Au atoms. For the latter, the 60 core electrons are treated by a small-core relativistic pseudopotentials [20], while the remaining 19 valence electrons are explicitly treated using a double-zeta polarized basis set [21]. The ground-state geometry of the isolated TP molecule and of the TP-$Au_n$ complexes were optimized (without considering any external dielectrics) under the condition that the residual forces are smaller than $10^{-5}$ au. The vibrational normal modes and wavenumbers were calculated under the harmonic approximation using the same level of theory. To correct for the anharmonicity effects, the wavenumbers were scaled by a factor of 0.96 [22].

The IR intensity of the $p^{\text{th}}$ normal mode was calculated as the integrated absorption [23], which, in the double harmonic approximation reads:

$$A_p = \int_{\text{band}} \varepsilon_p(\bar{\nu})\,\mathrm{d}\bar{\nu} = \frac{N_A}{12\varepsilon_0 c^2}\sum_{\alpha}^{3}\left(\frac{\partial\mu_\alpha}{\partial Q_p}\right)_0\left(\frac{\partial\mu_\alpha}{\partial Q_p}\right)_0 \qquad [\mathrm{m\,mol^{-1}}], \tag{6.1}$$

in which $\varepsilon_0$, $c$, and $N_A$ are the vacuum permittivity, the speed of the light in vacuo, the Avogadro number. $\left(\frac{\partial\mu_\alpha}{\partial Q_p}\right)_0$ is the derivatives of the $\alpha$-component of the dipole moment with respect to the $Q_p$ normal coordinate evaluated at equilibrium geometry.

The Raman intensity of the $p^{\text{th}}$ normal mode was estimated as the differential Raman scattering cross-sections $\frac{^n\mathrm{d}\sigma(\theta)_p}{\mathrm{d}\Omega}$ [24], which, in the double harmonic approximation reads:

$$\frac{^n\mathrm{d}\sigma(\pi)_p}{\mathrm{d}\Omega} = \frac{\pi^2(\bar{\nu}_0-\bar{\nu}_p)^3\bar{\nu}_0}{\varepsilon_0^2}\left[\frac{h}{8\pi^2 c\bar{\nu}_p}\frac{90a_p^2+14\beta_p^2}{90}\right]\frac{1}{1-e^{\left(-\frac{hc\bar{\nu}_p}{kT}\right)}} \qquad [\mathrm{m^2\,sr^{-1}}], \tag{6.2}$$

in which $\bar{\nu}_0$, $\bar{\nu}_p$, $h$ and $k$ are the exciting wavenumber, the vibrational wavenumber of the $p^{\text{th}}$ normal mode, the Planck and Boltzmann constants; $a_p^2$ and $\beta_p^2$ are the Raman invariants, which are evaluated from the first-order derivatives of the polarizability tensor components with respect to the $Q_p$ normal coordinate at equilibrium geometry. Eq. (6.2) assumes a particular experimental setup: observation of the total scattered beam perpendicular to an incoming laser beam ($\theta = \pi$) having natural polarization. For both Eqs. (6.1) and (6.2), the first-order derivatives are evaluated using the Gaussian09 package. IR and Raman spectra were simulated (with a homemade program) from these molecular properties. Each peak is described by a Lorentzian function with a FWHM of 10 $\mathrm{cm^{-1}}$. An incident light wavelength of 633 nm is adopted (in agreement with the experimental spectra we referred to in this work) in all the Raman scattering tensor calculations.

To analyze the vibrational normal modes, the `pyvib2` program [25] was used. Our analysis aims at pointing out the changes of normal modes when the molecule is adsorbed on the different

sites. The comparison of the normal modes of vibration is based on the overlaps between the modes of pairs of molecules or of molecular fragments. First of all, the normal modes are defined as the eigenvectors of the mass-weighted Hessian matrix $\boldsymbol{H}^m$, which contains the second order derivative of the total electronic energy $E$ with respect to the Cartesian atomic displacements $R_{i\alpha}$ evaluated at equilibrium geometry:

$$H^{(m)}_{i\alpha,j\beta} = \frac{1}{\sqrt{m_i m_j}} \left( \frac{\partial^2 E}{\partial R_{i\alpha} \partial R_{j\beta}} \right)_0 . \tag{6.3}$$

In the above expression, $i$ and $j$ refer to nuclei while $\alpha$ and $\beta$ are the $x, y, z$ Cartesian directions. $m_i$ is the atomic mass of nucleus $i$. The eigenvalue problem is therefore the following:

$$\boldsymbol{H}^q = \boldsymbol{Q}^T \boldsymbol{H}^m \boldsymbol{Q}, \tag{6.4}$$

in which $\boldsymbol{H}^q$ is a diagonal matrix containing the squares of the angular frequencies, $H^q_{pp} = 4\pi^2 c^2 \bar{\nu}_p^2$ (i.e. the eigenvalues of $\boldsymbol{H}^m$) with $\bar{\nu}_p$ the vibrational wavenumber of mode $p$. The $p^{\text{th}}$ column of the unitary matrix $\boldsymbol{Q}$, denoted $\boldsymbol{Q}_p$, is the $p^{\text{th}}$ normal modes in terms of the mass-weighted Cartesian displacements. The individual elements of this matrix are denoted $Q_{i\alpha,p}$ with $|\boldsymbol{Q}_p|^2 = \sum_{i\alpha}^{3N} (Q_{i\alpha,p})^2 = 1$. The components of the $p^{\text{th}}$ normal mode in terms of Cartesian displacements is expressed as $Q^c_{i\alpha,p} = (1/\sqrt{m_i}) Q_{i\alpha,p}$.

Given the normal modes $\boldsymbol{Q}_p$ are eigenvectors, they constitute a complete orthonormal basis set. One can therefore express the normal coordinates of one molecule as a function of those of another molecule, providing that they have the same numbers of atoms [26]:

$$|Q^B_l\rangle = \sum_p^A |Q^A_p\rangle \langle Q^A_p | Q^B_l \rangle = \sum_p^A U^{AB}_{p,l} |Q^A_p\rangle, \tag{6.5}$$

in which $U^{AB}_{p,l}$ is the transformation matrix from one set to the other and is unitary. From the orthogonality of the two sets of normal coordinates $(Q^A_p, Q^B_l)$, the overlap between the modes $p$ and $l$ of the molecules A and B is defined as the square of the scalar product between two normal modes [26]:

$$O^{A,B}_{p,l} = \langle Q^A_p | Q^B_l \rangle^2 = (U^{AB}_{p,l})^2, \tag{6.6}$$

in which $\sum_p^A O^{A,B}_{p,l} = \sum_l^B O^{A,B}_{p,l} = 1$. If $Q^A_p$ and $Q^B_l$ are identical, the overlap is equal to 1, whereas it goes to zero if they are completely different, i.e. orthogonal. By extension, for molecules A and B having different numbers of atoms, but common fragment F:

$$|Q^{B,F}_l\rangle \approx \sum_p^A T^{AB,F}_{p,l} |Q^{A,F}_p\rangle, \tag{6.7}$$

in which [Eq. (6.8)]

$$T_{p,l}^{AB,F} = \langle Q_p^A | Q_l^B \rangle = \sum_{i\alpha}^{F} Q_{i\alpha,p}^A Q_{i\alpha,l}^B \tag{6.8}$$

is the transformation matrix. The overlap between the modes $p$ and $l$ can be defined as:

$$\begin{aligned} O_{p,l}^{AB,F} &= \langle Q_p^{A,F} | Q_l^{B,F} \rangle^2 = (T_{p,l}^{AB,F})^2 \\ &= \left( \sum_{i\alpha}^{F} Q_{i\alpha,p}^A Q_{i\alpha,l}^B \right)^2 . \end{aligned} \tag{6.9}$$

For their analysis, the IR and Raman intensities are decomposed into mononuclear and heteronuclear contributions following the scheme introduced by Hug [27][ Eq. (6.10)]:

$$I_p = K_p \sum_{i,j}^{N} \sum_{\alpha,\beta}^{3} Q_{i\alpha,p}^c V_{i\alpha,j\beta} Q_{j\beta,p}^c = \sum_{i,j}^{N} I_{ij,p} \ , \tag{6.10}$$

In which $V_{i\alpha,j\beta}$ is defined as [Eqs. (6.11) and (6.12)]:

$$V_{i\alpha,j\beta}^{\mathrm{IR}} = \sum_{\xi} \left( \frac{\partial \mu_\xi}{\partial R_{i\alpha}} \right)_0 \left( \frac{\partial \mu_\xi}{\partial R_{j\beta}} \right)_0 , \tag{6.11}$$

$$V_{i\alpha,j\beta}^{\mathrm{Raman}} = [90V(a^2)_{i\alpha,j\beta} + 14V(\beta^2)_{i\alpha,j\beta}], \tag{6.12}$$

with [ Eqs. (6.13) and (6.14)]

$$V(a^2)_{i\alpha,j\beta} = \sum_{\xi,\eta} \frac{1}{9} \left( \frac{\partial \alpha_{\xi\xi}}{\partial R_{i\alpha}} \right)_0 \left( \frac{\partial \alpha_{\eta\eta}}{\partial R_{j\beta}} \right)_0 , \tag{6.13}$$

$$V(\beta^2)_{i\alpha,j\beta} = \sum_{\xi,\eta} \frac{1}{2} \left[ 3 \left( \frac{\partial \alpha_{\xi\eta}}{\partial R_{i\alpha}} \right)_0 \left( \frac{\partial \alpha_{\xi\eta}}{\partial R_{j\beta}} \right)_0 - \left( \frac{\partial \alpha_{\xi\xi}}{\partial R_{i\alpha}} \right)_0 \left( \frac{\partial \alpha_{\eta\eta}}{\partial R_{j\beta}} \right)_0 \right] ; \tag{6.14}$$

$\left( \frac{\partial \mu_\xi}{\partial R_{i\alpha}} \right)_0$ and $\left( \frac{\partial \alpha_{\xi\eta}}{\partial R_{i\alpha}} \right)_0$ are the derivatives of the $\xi$-component of the dipole moment and of the $\xi\eta$-component of the polarizability tensor with respect to the Cartesian atomic displacement $R_{i\alpha}$ evaluated at equilibrium geometry, respectively. Then, using straightforward summation, Eq. (6.10) can be generalized to groups of atoms. The diagonal terms ($I_{ii,p}$) are mononuclear or intra-group while the off-diagonal terms ($I_{ij,p}$) are di-nuclear or inter-group, respectively. Since only the symmetric part contributes to the total intensity of the vibrational modes, they are best represented by upper triangular matrices, with off-diagonal elements equal to the sum of the two off-diagonal halves of the full matrix. In the GCM scheme of Hug [27], the matrix elements are visualized as circles, with an area proportional to the ($I_{ij,p}$) values, whereas their color is related to their sign. In our analysis *i)* the factor of proportionality is chosen such as an inscribed circle contains a defined percentage of the sum of the intensities over all the normal

modes and *ii)* this percentage is tunable but fixed for each spectroscopy. The ACP represent the atomic contributions of each atom to the IR or Raman intensities of a given normal mode $p$. They are obtained by taking the self-contribution of the atom ($I_{ii,p}$) and then splitting the di-nuclear terms ($I_{ij,p}$) between the corresponding atoms. Spheres are then drawn on each atom with their surface area proportional to the value of the contribution ($I_{ii,p}$). Their color reflects the sign: red for positive and yellow for negative.

Complementary to the overlap between the normal mode of molecules A and B, we defined an enhancement factor (EF) as the ratio between the intensity of molecule B over the intensity of molecule A. Considering that the enhancement should reflect the changes in the Cartesian derivatives of the properties between the two molecules ($V^A_{i\alpha,j\beta} \neq V^B_{i\alpha,j\beta}$) and should not depend on the changes of normal modes between the two molecules, the EF is calculated as the ratio of the sum of the intensities under a given band for both molecules A and B:

$$\begin{aligned} \mathrm{EF}^{A,B,F}_{\mathrm{band}} &= \frac{\sum_{l}^{\mathrm{band}} \sum_{i\alpha}^{F} \sum_{j\beta}^{F} Q^{B,c}_{i\alpha,l} V^{B}_{i\alpha,j\beta} Q^{B,c}_{j\beta,l}}{\sum_{p}^{\mathrm{band}} \sum_{i\alpha}^{F} \sum_{j\beta}^{F} Q^{A,c}_{i\alpha,p} V^{A}_{i\alpha,j\beta} Q^{A,c}_{j\beta,p}} \\ &= \frac{\sum_{p}^{\mathrm{band}} \sum_{i\alpha}^{F} \sum_{j\beta}^{F} Q^{A,c}_{i\alpha,p} V^{B}_{i\alpha,j\beta} Q^{A,c}_{j\beta,p}}{\sum_{p}^{\mathrm{band}} \sum_{i\alpha}^{F} \sum_{j\beta}^{F} Q^{A,c}_{i\alpha,p} V^{A}_{i\alpha,j\beta} Q^{A,c}_{j\beta,p}} \end{aligned} \tag{6.15}$$

in which $F$ is the common fragment, and where a band is defined as a block of coupled modes in the transformation between modes of molecules A and B ($T^{AB,F}_{p,l}$). Indeed the two equations are identical if the transformation is unitary.

## 6.3 Results and discussion

### 6.3.1 Optimized structures and binding energy

Fig. 6.1 presents the optimized structures of the complexes and Table 6.1 reports characteristic bond distances. It is first important to note that from our calculation, the isolated TP molecule has a planar structure, which is consistent with previous results [28]. Furthermore, the C-S and S-H bond lengths, and the C-S-H angle amount to 1.789 Å, 1.350 Å, and 96.7 °, respectively. These values are in good agreement with the microwave spectroscopy values [5, 28] of 1.770 Å, 1.330 Å, and 96 °, respectively. For the complexes, the Au-S bond distance increases with the coordination number of the S atom, typically by 0.1 Å for each increase of the coordination number by one unit.

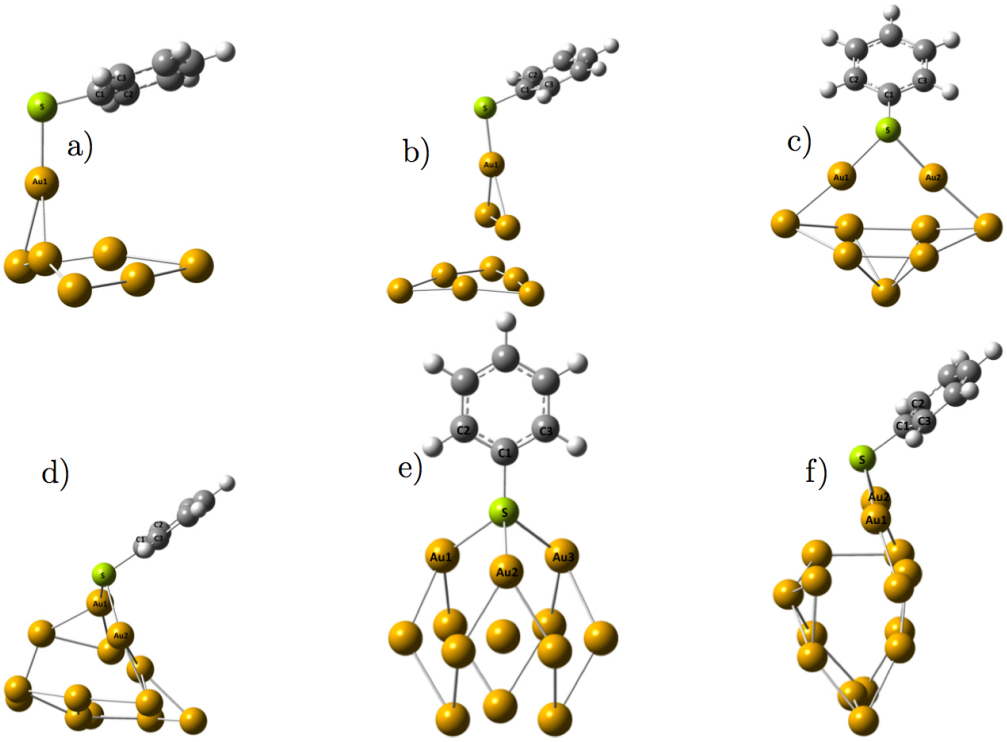


FIGURE 6.1: Optimized structures of TP-$Au_n$ complexes. a) Ph-S-$Au_7$ (onefold-coordinated≡*on-top*); b) Ph-S-$Au_9$ (onefold-coordinated≡*on-top*); c) Ph-S-$Au_9$ (twofold-coordinated≡*bridge*); d) Ph-S-$Au_{13}$ (twofold-coordinated≡*bridge*); e) Ph-S-$Au_{13}$ (threefold-coordinated≡*hcp-hollow*); f) Ph-S-$Au_{15}$ (twofold-coordinated≡*bridge*). The names onefold-, twofold- and threefold-coordinated are directly related to the number of Au atom linked to the S atom.

The adsorption energy was evaluated considering the adsorption reaction of the TP accompanied by the liberation of $\frac{1}{2}$ $H_2$ molecule [29]

$$E_B = \left[\left(\frac{1}{2}E_{H_2} + E_{PhS-Au_n}\right) - (E_{PhS-H} + E_{Au_n})\right] \tag{6.16}$$

in which the $E_x$ are the electronic energies for the optimized structures, except for the bare clusters for which the same geometries as in the complexes were used. These values are reported in Table 6.1. It is also common to find in the literature an alternative expression for $E_B$, which corresponds to the adsorption of the $C_6H_5S$ radical [15, 29]. In such a case, the $E_B$ values are simply shifted by the energy of the homolytic dissociation of the thiophenol S-H bond, $E_{PhS-H} - (E_{PhS\bullet} + \frac{1}{2}E_{H_2})$, which amounts to -38.9 kcal/mol at the current level of calculation. In general, the ordering of the binding energy amplitude is onefold-coordinated < threefold-coordinated ∼ twofold-coordinated, while the Au-S bond length trend is onefold-coordinated < twofold-coordinated < threefold-coordinated (see Table 6.1). Then, for a given coordination number, the amplitude of the binding energy decreases with the cluster size.

For example, for the twofold-coordinated, $E_B$ amounts to -42.0, -33.4, and -31.1 kcal/mol for clusters containing 9 (C3), 13 (C4), and 15 (C6) Au atoms, respectively. The position of the phenyl ring with respect to the cluster also appears to be correlated with the $E_B$ amplitude: *i)*

in the onefold-coordinated complexes (C1, C2), the phenyl ring is almost parallel to the cluster; *ii)* in the threefold-coordinated complex (C5), it is perpendicular to the plane containing the 3 Au atoms directly bonded to the S atom, whereas *iii)* in the twofold-coordinated complexes (C3, C4, C6), it is tilted. Therefore, the binding energy does not depend solely on the S-Au bond distance and on the coordination of the S atom, but also on the cluster-adsorbate geometry and on the size of the cluster.

TABLE 6.1: Selected optimized bond distances (Å) for TP and its complexes with Au clusters calculated at the B3LYP/6-311G*(C, S, H)/cc-pVDZ (Au) level of calculation. Binding energies ($E_B$) (kcal/mol) are also given.

| | TP | C1 | C2 | C3 | C4 | C5 | C6 |
|---|---|---|---|---|---|---|---|
| | | onefold | onefold | twofold | twofold | threefold | twofold |
| d($C_1$-S) | 1.798 | 1.795 | 1.789 | 1.808 | 1.804 | 1.802 | 1.806 |
| d($Au_1$-S) | | 2.321 | 2.328 | 2.393 | 2.456 | 2.522 | 2.412 |
| d($Au_2$-S) | | - | - | 2.393 | 2.429 | 2.517 | 2.411 |
| d($Au_3$-S) | | - | - | - | - | 2.544 | - |
| $E_B$ (Eq. (6.16)) | | -21.2 | -19.5 | -42.0 | -33.4 | -32.5 | -31.1 |

### 6.3.2 Vibrational normal modes

As shown in previous works (simulation and experiment) [5, 9, 16, 30], the adsorption of TP leads to variations of the vibrational wavenumbers ranging typically from 1 to 30 $cm^{-1}$, in either direction (Fig. 6.2). In general the wavenumber under 600 $cm^{-1}$ ($c$, $e$) are blue shifted, while the others are red shifted. In addition to these shifts that result from the perturbation by the Au environment of the TP electronic structure and force constants, the adsorption process is at the origin of new modes, like modes $a_1$ and $a_2$ (Table 6.2), characterized by the motion of the S atom in the Au atom environment, or like the modes intrinsic to the Au clusters spanning the very low wavenumber region (from 4 to 160 $cm^{-1}$).

To highlight the changes in the vibrational normal modes upon adsorption, Fig. 6.3 displays the overlaps between the vibrational normal modes of the isolated TP molecule and of its complexes. In the Supporting Informations, Table D.1 provides a complete list of matching modes between the isolated TP and its complexes. Table 6.2 lists the mode assignments and the wavenumbers for the isolated TP and its complexes, while Fig. 6.4 sketches the atomic displacements of key normal modes. Note that in Table 6.2, we concentrate on three different types of clusters, C1, C3, and C5 but that the whole set of wavenumbers for the 6 adsorption sites are given in the Supporting Informations (Table D.2).

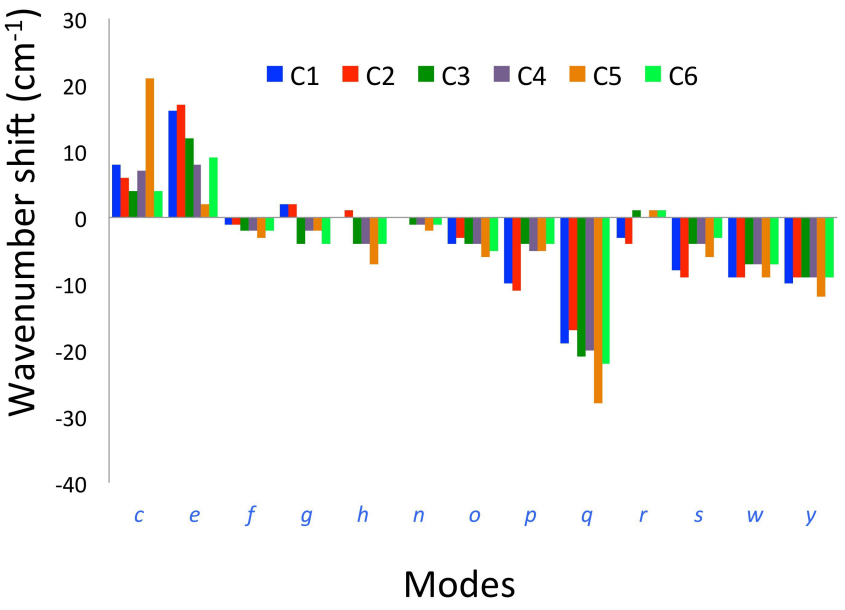


FIGURE 6.2: Wavenumber shift of the principal Raman-active modes (located between 400 $cm^{-1}$ and 1600 $cm^{-1}$) of the six complexes. Modes are labeled in Table 6.2.

Deviations of the overlap matrix from the diagonal form mean that upon adsorption, modes are split, permuted, or mixed. As shown in Fig. 6.3, these effects occur for several types of modes, showing also an impact of the coordination number on these mixing patterns. For instance, mode 2 of TP splits into two (C2, C3, and C6) or three (C1, C4) modes. Looking at the atomic displacements, the pairs of modes resulting from the TP mode 2 (label *b*) splitting, i.e. modes 21 and 23 for C1 while modes 26 and 28 for C3, differ by the amplitudes of the motion of the S atom and of the C atom attached to it (Fig. 6.4). One can therefore conclude that modes 23 (C1) and 28 (C3) are signatures of the adsorption but that they borrow some character from the ring out-of-plane distortion at 176 $cm^{-1}$. Interestingly, this splitting is not observed for the *hollow* (threefold-coordinated) site.

The adsorption can also permute the wavenumbers ordering of modes, like modes 4 and 5 of TP (labels *c* and *d*), occurring at almost the same frequency, which become modes 43 and 42 in the C5 cluster with a wavenumber difference of 20 $cm^{-1}$. The same permutation appears for C3 whereas for C1, the characters of modes 4 and 5 of TP are mixed in modes 24 and 25.

Modes 8 and 9 of TP (labels *g* and *h*) are slightly mixed to build modes 28 and 29 (or 34 and 35) of the *on-top* C1 (C2) cluster. This mixing is stronger for the *bridge* (twofold-coordinated) sites while it is absent for the *hollow* (threefold-coordinated) site. These couplings nicely illustrate the impact of the lift of planar symmetry that occurs upon adsorption. Indeed, in the planar TP molecule, mode 8 corresponds to an out-of plane deformation whereas mode 9 is a typical in-plane ring breathing mode (Fig. 6.4). When the molecule is adsorbed, the system is no more planar and therefore this pair of modes belongs now to the same symmetry representation, which allows their mixing (modes 28 and 29 in C1 as well as modes 34 and 35 in C3).

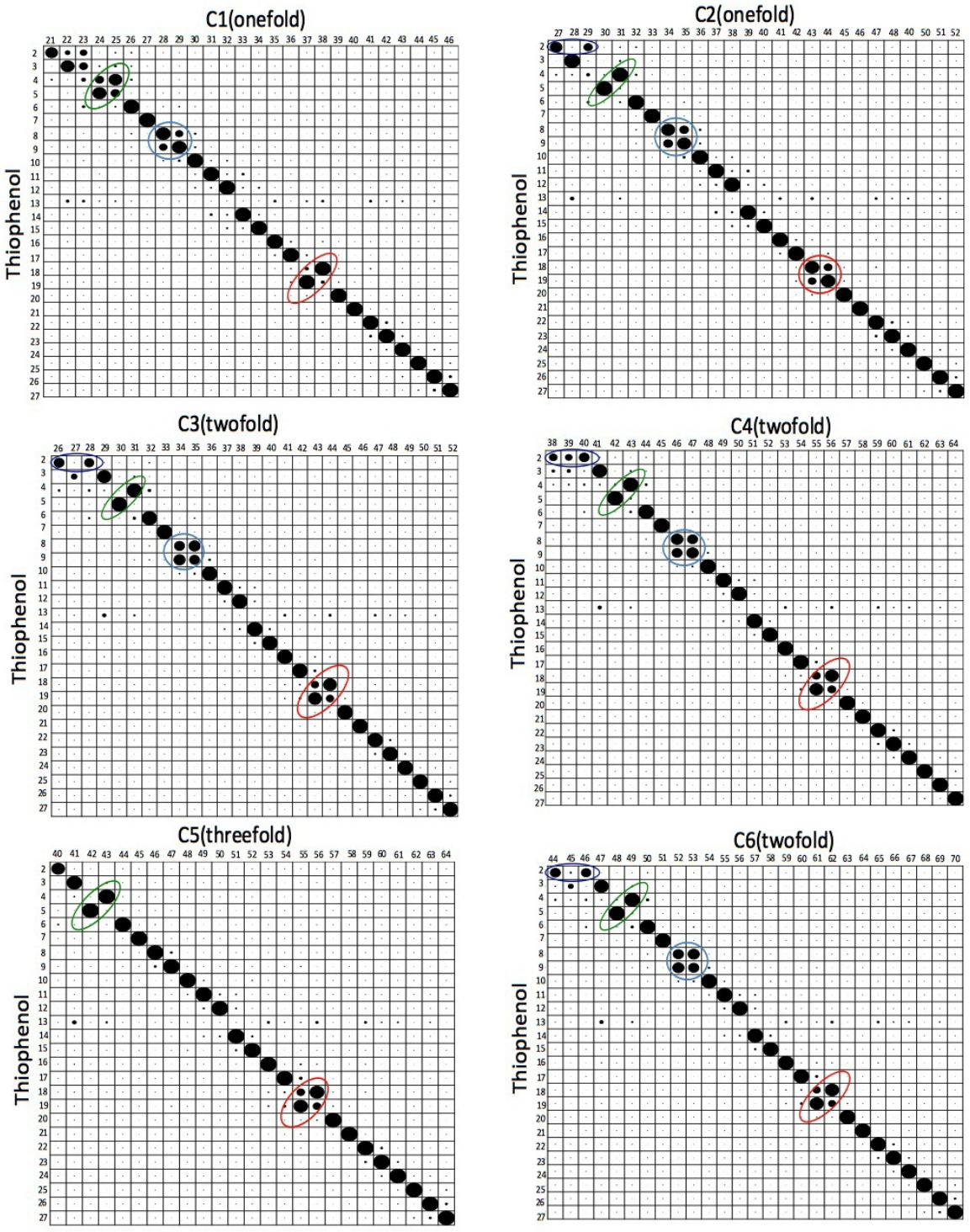


FIGURE 6.3: Vibrational normal modes overlaps $O_{p,l}^{A,B,F}$ between the isolated TP and its complexes. The fragment is constituted of all the atoms except the Au atoms and the terminal H atom (bonded to the S atom) of the TP molecule. Dark blue, green, blue, and red circles highlight different splitting, permutation or mixing of modes. The surface of the each circle is proportional to the overlap.

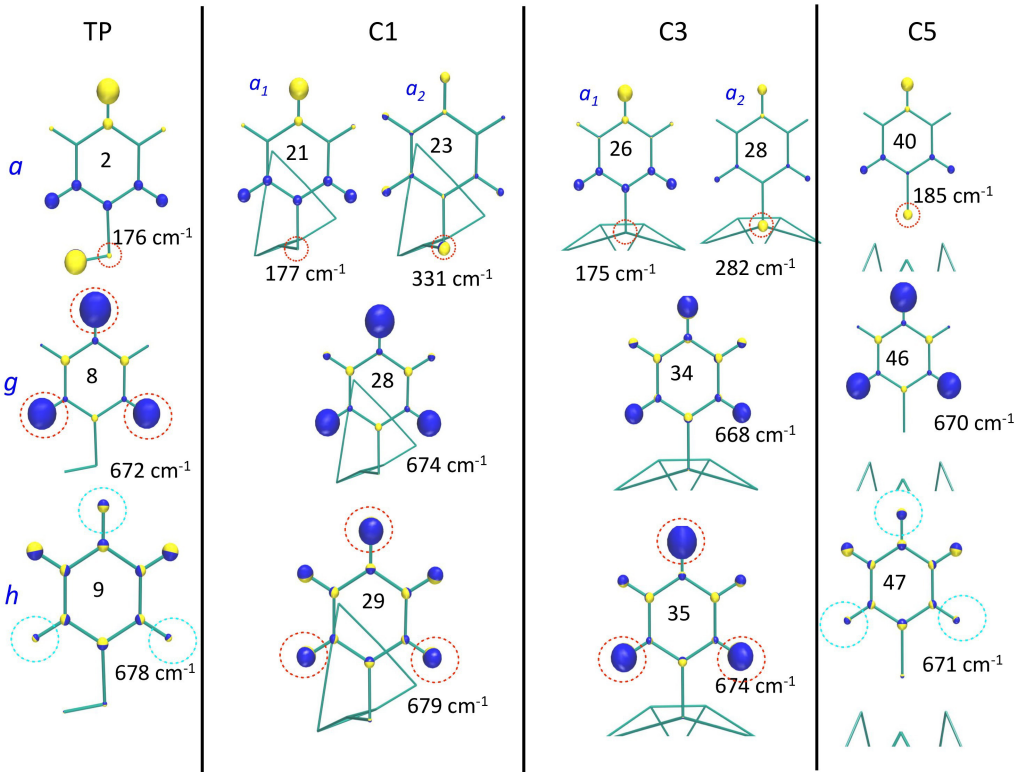


FIGURE 6.4: Sketch of selected vibrational normal modes of the isolated TP and its complexes. The direction of the atomic displacements is perpendicular to the junction plane between the two hemispheres of distinct color while their amplitudes are proportional to the sphere radius. The wavenumber, wavenumber ordering, and the normal mode label are given for each mode.

In-plane displacements of modes 18 and 19 (labels $p$ and $g$) of TP also mix in the presence of the metallic cluster. The overlap patterns show that their characters almost interchange: mode 18 (1064 $cm^{-1}$) is more similar to the high wavenumber modes (modes 38 and 44 for C1 and C3, respectively) whereas mode 19 (1070 $cm^{-1}$) has the largest overlaps with the low wavenumber modes (modes 37 and 43 for C1 and C3). This mixing is also influenced by the symmetry of the clusters and by the anchoring type in C3 and C5, contrary to the asymmetric structures of TP and C1 ( Fig. 6.4).

### 6.3.3 IR spectra

Fig. 6.6 depicts the simulated IR spectra of the isolated and adsorbed TP, whereas the whole list of IR intensities is given in Table D.3. First, a huge band at around 3000 $cm^{-1}$ dominates all the calculated spectra. This band corresponds to the C-H stretching modes (Table 6.2, modes $\alpha$, $\beta$, $\varepsilon$, $\sigma$, and $\eta$). Moreover, well defined peaks are observed *i)* for the [$\nu$(CC)] at around 1550 $cm^{-1}$ (peak $y$), *ii)* for the [$\delta$(CH) + $\nu$(CC)] close to 1450 $cm^{-1}$ (peak $w$), *iii)* for the [$\nu$(CS) + $\delta$(CH) + $\nu$(CC)] and [$\nu$(CC) + $\delta$(CH)] modes at around 1050 $cm^{-1}$ (particularly the peaks $q$

TABLE 6.2: B3LYP versus experimental wavenumbers ($cm^{-1}$) for the isolated TP and its complexes with Au clusters. Calculated wavenumbers were scaled by a factor of 0.96.

| label[a] | assignments[b] | TP | C1[c] | C3 | C5 | Exp1[d] | Exp2 | Exp3 |
|---|---|---|---|---|---|---|---|---|
| | | | onefold | twofold | threefold | | | |
| $a_1$ | r-o-d + $\gamma$(CS) | 176 | 177(+1) | 175(−1) | | 185 | | 189 |
| $a_2$ | | | 331(+154) | 282(+106) | 238(+62) | | | |
| $b$ | $\delta$(CS)+$\nu$(AuS) | 267 | 259(−8) | 343(+76) | 321(+54) | 278 | | 275 |
| $c$ | $\nu$(CS)+$\nu$(AuS) | 393 | 401(+8) | 397(+4) | 414(+21) | 412 | | 420 |
| $d(16b)$ | $\gamma$(CH) | 394 | 397(+3) | 395(+1) | 394(0) | | | |
| $e(16a)$ | $\omega$(CH) + $\gamma$(SH) | 457 | 472(+16) | 468(+12) | 459(+2) | 462 | | 470[e] |
| $f(6a)$ | r-i-d | 608 | 607(−1) | 606(−2) | 605(−3) | 615 | | |
| $g(4)$ | $\omega$(CH) + r-o-d | 672 | 674(+2) | 668(−4) | 670(−2) | 689 | | |
| $h(6b)$ | $\delta$(CCC) + r-i-d | 678 | 679(+1) | 674(−4) | 671(−7) | 697 | | 692 |
| $i(11)$ | $\omega$(CH) | 710 | 723(+14) | 721(+11) | 719(+9) | 737 | | |
| $j(10b)$ | $\omega$(CH) | 799 | 811(+13) | 807(+8) | 807(+8) | 836 | | |
| $k(10a)$ | $\gamma$(CH) +$\delta$(SH) | 853 | 877(+24) | 877(+24) | 879(+25) | 904 | | |
| $\Omega_1$ | $\delta$(SH) | 901 | - | - | - | 914 | | |
| $l(17b)$ | $\gamma$(CH) + r-o-d | 913 | 924(+12) | 926(+13) | 926(+13) | 958 | | |
| $m(5)$ | $\gamma$(CH) | 942 | 945(+3) | 950(+8) | 952(+10) | 991 | | |
| $n(12)$ | r-i-d + $\nu$(CC) | 976 | 976(0) | 975(−1) | 974(−2) | 1000 | 1000 | 999 |
| $o(18a)$ | $\nu$(CC) + $\delta$(CH) | 1006 | 1003(−3) | 1002(−4) | 1000(−6) | 1024 | 1026 | 1022 |
| $p(18b)$ | $\nu$(CC) + $\delta$(CH) | 1064 | 1054(−10) | 1059(−4) | 1058(−5) | 1070 | 1068 | 1078 |
| $q$ | $\nu$(CS) + $\delta$(CH)+$\nu$(CC) | 1070 | 1051(−19) | 1049(−21) | 1042(−28) | 1092 | | |
| $r(14)$ | $\delta$(CH) | 1140 | 1137(−3) | 1140(0) | 1140(01) | 1118[e] | | 1181 |
| $s(9a)$ | $\delta$(CH) | 1165 | 1157(−8) | 1161(−4) | 1159(−6) | 1157 | | |
| $t(9b)$ | $\nu$(CC) | 1267 | 1255(−12) | 1261(−6) | 1262(−5) | 1272 | | |
| $u(3)$ | $\delta$(CH) + $\nu$(CC) | 1307 | 1296(−11) | 1300(−8) | 1298(−9) | 1328 | | |
| $v(19a)$ | $\delta$(CH) + $\nu$(CC) | 1424 | 1415(−9) | 1418(−6) | 1418(−6) | 1441 | | |
| $w(19b)$ | $\delta$(CH) + $\nu$(CC) | 1459 | 1450(−9) | 1453(−7) | 1450(−9) | 1481 | 1472 | 1473 |
| $x(8b)$ | $\nu$(CC) | 1559 | 1550(−8) | 1556(−3) | 1555(−3) | 1576 | | |
| $y(8a)$ | $\nu$(CC) | 1570 | 1560(−10) | 1562(−9) | 1559(−12) | 1581 | 1574 | 1584 |
| $\Omega_2$ | $\nu$(SH) | 2486 | - | - | - | 2566 | | |
| $\alpha(13)$ | $\nu$(CH) | 3035 | 3032(−3) | 3040(+5) | 3041(+7) | 3037 | | |
| $\beta(7b)$ | $\nu$(CH) | 3039 | 3041(+2) | 3047(+8) | 3048(+9) | 3048 | | |
| $\varepsilon(3)$ | $\nu$(CH) | 3049 | 3055(+6) | 3058(+9) | 3057(+9) | 3056 | | |
| $\eta(20b)$ | $\nu$(CH) | 3054 | 3063(+9) | 3063(+9) | 3063(+8) | 3086 | | |
| $\sigma(2)$ | $\nu$(CH) | 3066 | 3067(+1) | 3069(+3) | 3069(+3) | 3150 | 3060 | |

[a] The assignments in parentheses refer to Wilson notation [31] of the benzene molecule.

[b] $\delta$ = in-plane bending, $\gamma$ = out-of-plane bending, $\nu$ = stretching, $\omega$ = wagging, r-i-d = ring in-plane deformation, r-o-d = ring out-of-plane deformation.

[c] The values in parentheses are the wavenumber differences with respect to the isolated TP molecule.

[d] Exp1= from neat TP (Ref [30]), Exp2= from IR spectra of TP on Au(111) gold surface (Ref. [5]), and Exp3= from SERS of TP onto a roughened SiGe surface coated with 30 nm of Au (Ref. [30]).

[e] Values from Ref [32]

and $p$), and *iv)* for the [$\nu$(CC) + $\delta$(CH)] and [r-i-d + $\nu$(CC)] at around 1000 cm$^{-1}$ (peaks $o$ and $n$). Furthermore, the presence of the Au substrate hardly alters the IR intensities. From the ACP and GCM (Fig. 6.7), we see that among the systems, the contributions to the IR intensities have generally similar patterns but with different amplitudes. However, there are also modes for which the variations are stronger. For instance, mode $q$ has an intensity of 27.1 km.mol$^{-1}$ in the isolated TP molecule but smaller intensities of 1.7, 0.6, and 4.7 km.mol$^{-1}$ for the C1, C3, and C5 systems, respectively. The ACP sketches, which show a smaller or even a negative contribution of the C atom directly bonded to the S atom account for this intensity reduction. Moreover, considering the GCM, this reduction is shown to originate from the smaller positive contribution of the C-S group and the larger negative contributions from the coupling between the C-S group and the C-H groups in *ortho*. On the opposite, the intensity of mode $n$ increases with the adsorption and with the coordination number (from 0.8 km.mol$^{-1}$ in TP to 4.3, 7.3, and 14.0 km.mol$^{-1}$ for C1, C3, and C5, respectively). From the ACP and GCM, one observes that the contribution from the C-H groups in ortho (of the S atom) and the coupling between these C-H groups and the C-S group are indeed more positive when the coordination number of the S atom increases. The simulated spectral profiles are in close agreement with the experimental IR spectrum of neat TP and Surface Enhanced Infrared Absorption Spectroscopy (SEIRAS) spectrum of TP on Au (111) surface displayed in Fig. 6.6a and Fig. 6.6b. In particular, the bands $y$, $w$, $p+q$, $o$, and $n$ are in accordance with those of the experimental SEIRAS spectrum, with the relative increase of mode $n$ intensity upon adsorption also reproduced by our simulation. However, for both the neat and adsorbed TP, one observes that the broad band around 3000 cm$^{-1}$ (C-H stretching region) has a huge intensity in our simulation compared to experiment. Note that in the experimental SEIRAS spectrum, peak $v$ has not been pointed out, though it might be present in the spectral noise. On the basis of both the experimental and theoretical spectra and their consistency, the signatures of the TP coordination are *i)* the disappearance of the peaks $\Omega_1$ and $\Omega_2$ as well as of peak $t$ and *ii)* the relative intensity of the $o$ peak that increases with respect to the sum of the intensities of peaks $p$ and $q$. Our simulations also point out that the intensity of the peak $s$ relative to that of peak $u$ is much larger in the case of *on-top* mono-coordination while they are similar for the twofold and threefold coordinations. Unfortunately, the experimental spectrum has not been recorded in the corresponding wavenumber region.

### 6.3.4 Raman spectra

Unlike the intensities observed in the IR spectra, the presence of the Au substrate enhances globally the Raman cross-sections and also leads to specific variations in the relative intensities. From Eq. (6.15), one can calculate the EF of each band due to adsorption. To compare with experiment, we normalize all the EFs by that of mode $n$ . Assuming that the electromagnetic enhancement is the same for all modes [33–35], this relative enhancement will reflect only the chemical enhancement. Fig. 6.8 displays the comparison between the calculated and experimental relative enhancements [9, 16]. Remarkably, the calculations show consistent agreement with

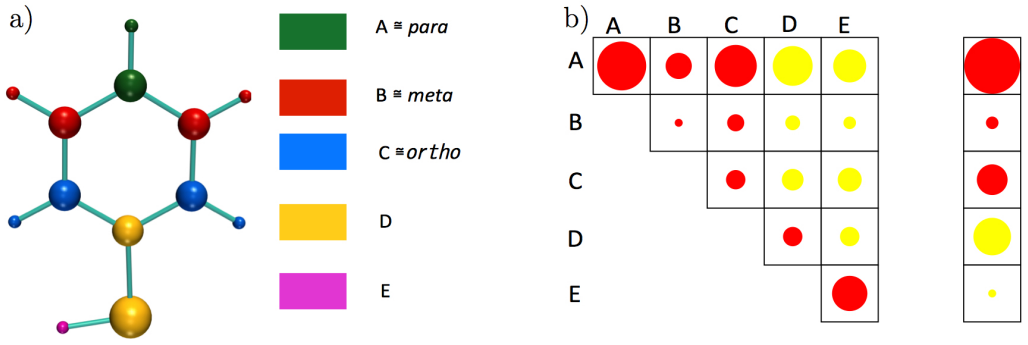


FIGURE 6.5: a) Groups definition for the GCM analysis. In the complexes, the group E is defined by the Au atoms. b) Illustration of GCM with groups defined by a). The areas of the circles are directly proportional to the coupling contributions Eq. (6.10) ($\sum_{i\in\text{group1}}\sum_{j\in\text{group2}} I_{ij,p}$, where the groups 1 and 2 can be the same or different). Red and yellow color spheres represent positive and negative contributions, respectively. Each box in the additional column (only for the Raman intensity) corresponds to the sum of the atomic contributions (ACP) over the atoms within a group.

experiment. Moreover, one also observes when comparing this latter to Fig. 6.2 that the most enhanced modes are those with a large wavenumber shift ($c$, $q$, $y$), and that the C5 complex leads to the best reproduction of the experimental relative enhancements.

The simulated Raman spectra of the isolated and adsorbed TP are depicted in Fig. 6.9c to Fig. 6.9i, whereas the whole list of Raman intensities is given in Table D.4. In general, the spectral profiles of the onefold-coordinated complexes differ largely from those of the twofold- and threefold-coordinated complexes. Indeed, the peaks $c$ [$\nu$(CS)+$\nu$(AuS)], $q$ [$\nu$(CS) + $\delta$(CH)+$\nu$(CC)], and $y$ [$\nu$(CC)], and sometimes $a_2$ [r-o-d + $\gamma$(CS)] dominate the spectra of the twofold-coordinated and threefold-coordinated species, while the peaks $c$ [$\nu$(CS)+$\nu$(AuS)], $b$ [$\delta$(CS)+$\nu$(AuS)], and $a_2$ [r-o-d + $\gamma$(CS)] located in the 200-400 cm$^{-1}$ region (Fig. 6.9d to Fig. 6.9e ) dominate the spectrum in the case of the onefold coordination. As shown in Table 6.2 , those modes involve the displacement of the S atom, with the exception of mode $y$ [$\nu$(CC)]. The $c$, $q$, and $y$ peaks are located in three spectral regions, on which our analysis successively focuses.

The first region located between 200 and 400 cm$^{-1}$ is characterized by the peaks $a_2$, $b$, and $c$ (Fig. 6.9). As shown in Figs. 6.10 and 6.11, the Raman intensities of these modes globally decrease when the coordination number of the binding site increases. From the ACP and the GCM, we see that a large part of the intensity of those modes come from the S atom contribution. For the C1, C3, and C5 complexes, mode $c$ has a higher intensity than modes $a_2$ and $b$. This can be related by the positive contributions of the groups B and C for mode $c$, compared to their small values for the two other modes. Moreover, when comparing the intensities of the C1 and C2 complexes on the one hand, and those of the C3, C4 and C6 complexes on the other hand, one observes that the intensities of the peaks $a_2$, $b$, and $c$ vary with the size and geometry of the cluster (i.e. the orientation of the phenyl ring with respect to the gold cluster). Indeed, in C2 (onefold-coordinated) and C6 (twofold-coordinated) complexes were the phenyl ring points out from the cluster surface (Fig. 6.1), the peak $a_2$ dominates the spectrum; and this can be

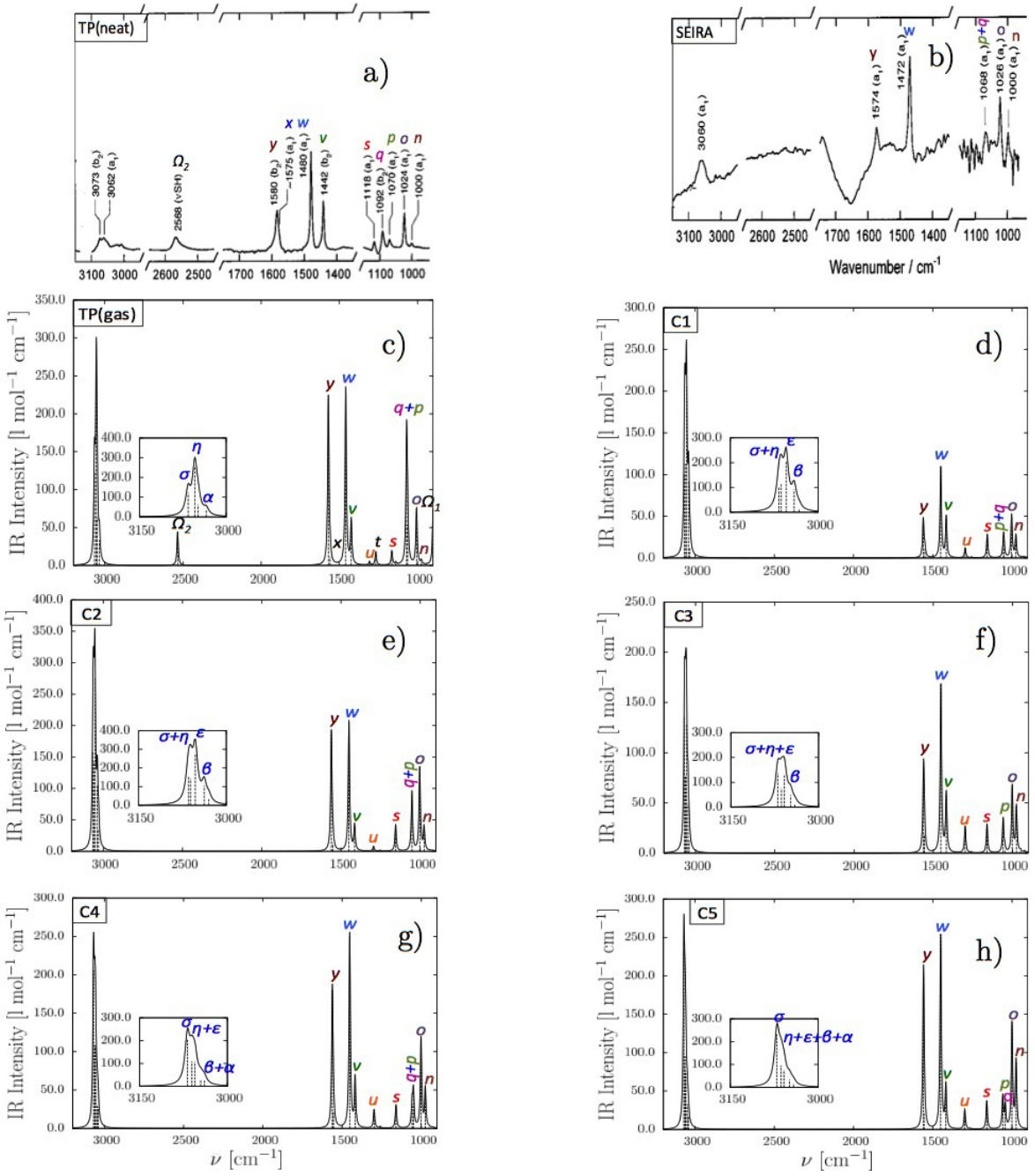


FIGURE 6.6: Comparison between the experimental and simulated IR spectra. a) Experimental IR spectrum of neat TP [5]; b) Experimental IR spectrum of TP adsorbed on an Au (111) surface [5]; c) Simulated spectrum of isolated TP; (d-h) Simulated spectra of TP adsorbed on Au surface.

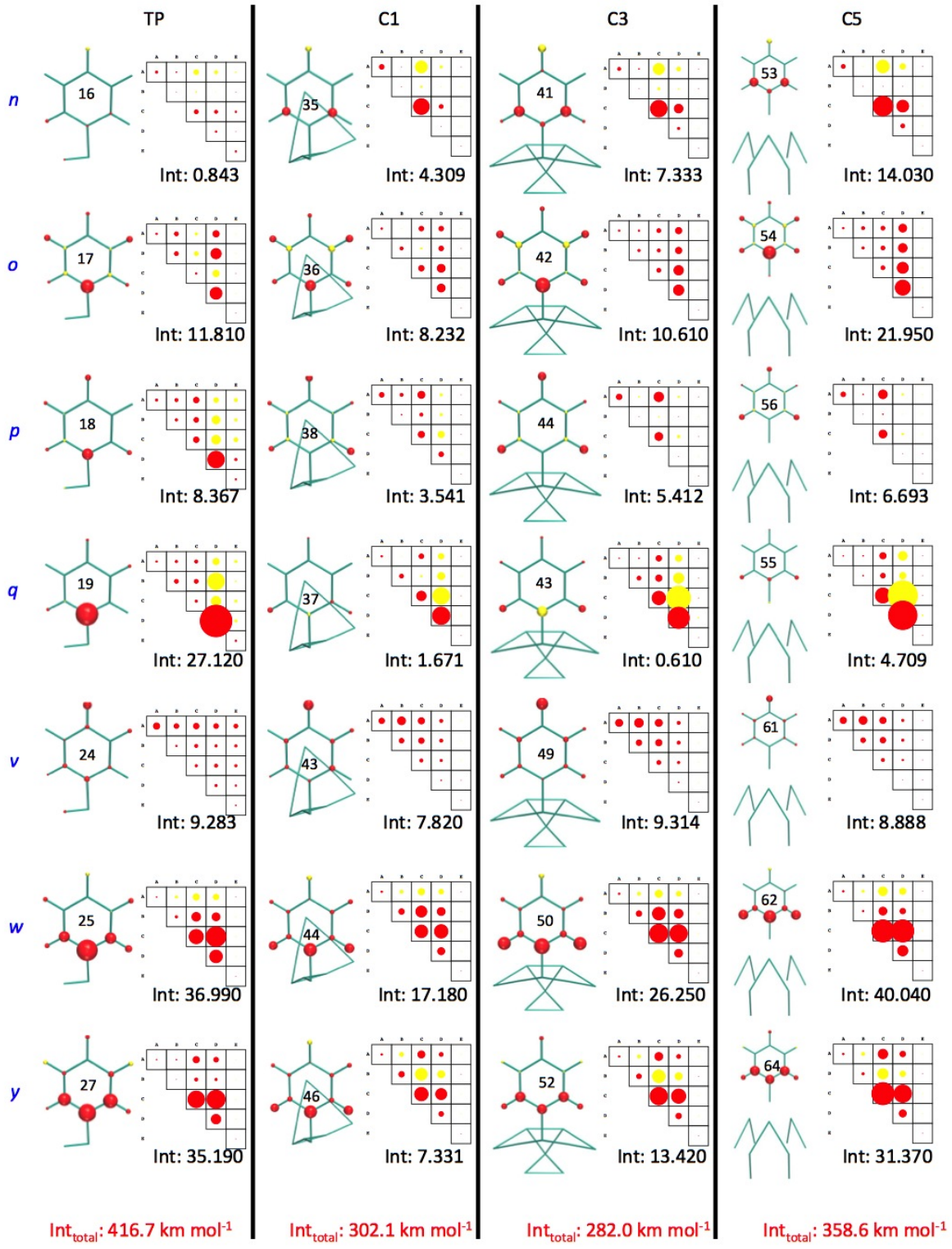


FIGURE 6.7: Sketch of the IR Atomic Contribution Patterns (left), and Group Coupling Matrices (right) for the main peaks. The ACP sphere surfaces are proportional to the atomic contribution to the IR intensities. Red and yellow color spheres represent positive and negative contributions, respectively. The GCM representation is detailed in Fig. 6.5. The numbers in red color below each column specify the total intensities, which are the sums of all the normal mode intensities. The inscribed circle is defined to contain 4% of the total intensity. IR intensities are given in km.mol$^{-1}$.

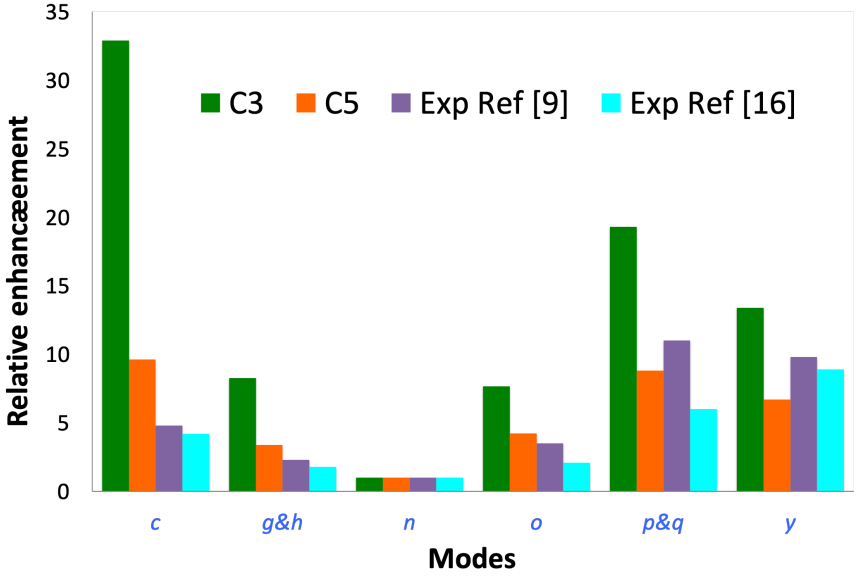


FIGURE 6.8: Calculated Raman relative enhancements for the C3 and C5 complexes together with the experimental ones taken from Refs [9] and [16].

explained by the contributions of the S atom (Fig. 6.11), which are larger compared to those of the other complexes (Fig. 6.10).

In the second region around 1000 $cm^{-1}$, the peaks $n$ [r-i-d + $\nu$(CC)], $o$ [$\nu$(CC) + $\delta$(CH)], and $q$ [$\nu$(CS) + $\delta$(CH)+$\nu$(CC)] are dominant and their relative intensities are similar for the twofold- and threefold-coordinated complexes, whereas in the case of *on-top* coordination, peak $o$ has much a smaller intensity than the other two modes. These 3 vibrational modes involve in-plane motions of the atoms. As shown in the ACP and GCM, most of the intensity of those peaks originate from the groups C and D, which are close to the surface. Among these modes, mode $q$ is the most intense by about a factor of 2. This can be explained by the positive coupling between the groups C and D, which is negative in modes $n$ and $o$.

Finally, the last region located between 1400 $cm^{-1}$ and 1600 $cm^{-1}$ is characterized by the peaks $y$ [$\nu$(CC)] and $w$ [ $\delta$(CH) + $\nu$(CC)]. In all the spectra, mode $y$ has the highest intensity, which is comparable to that of mode $q$. The GCM pattern explains the difference between modes $y$ and $w$: in the former, groups A, B, C, and D display positive intra-group and inter-group contributions, while in the mode $w$, the intensity also originates from the same groups, but some coupling terms are negative.

The experimental Raman spectrum of neat TP and Surface Enhanced Raman Spectroscopy (SERS) spectrum of TP adsorbed on a roughened SiGe surface coated with 30 nm of Au [16] are also displayed in Fig. 6.9a and Fig. 6.9b. The calculated spectral profiles are in close agreement with experiment, even better than for the IR spectra. In the case of neat TP, the simulated spectrum on the isolated molecule displays all the important peaks. The major deviations include the underestimation of the relative scattering intensity of mode $n$ but the overestimation

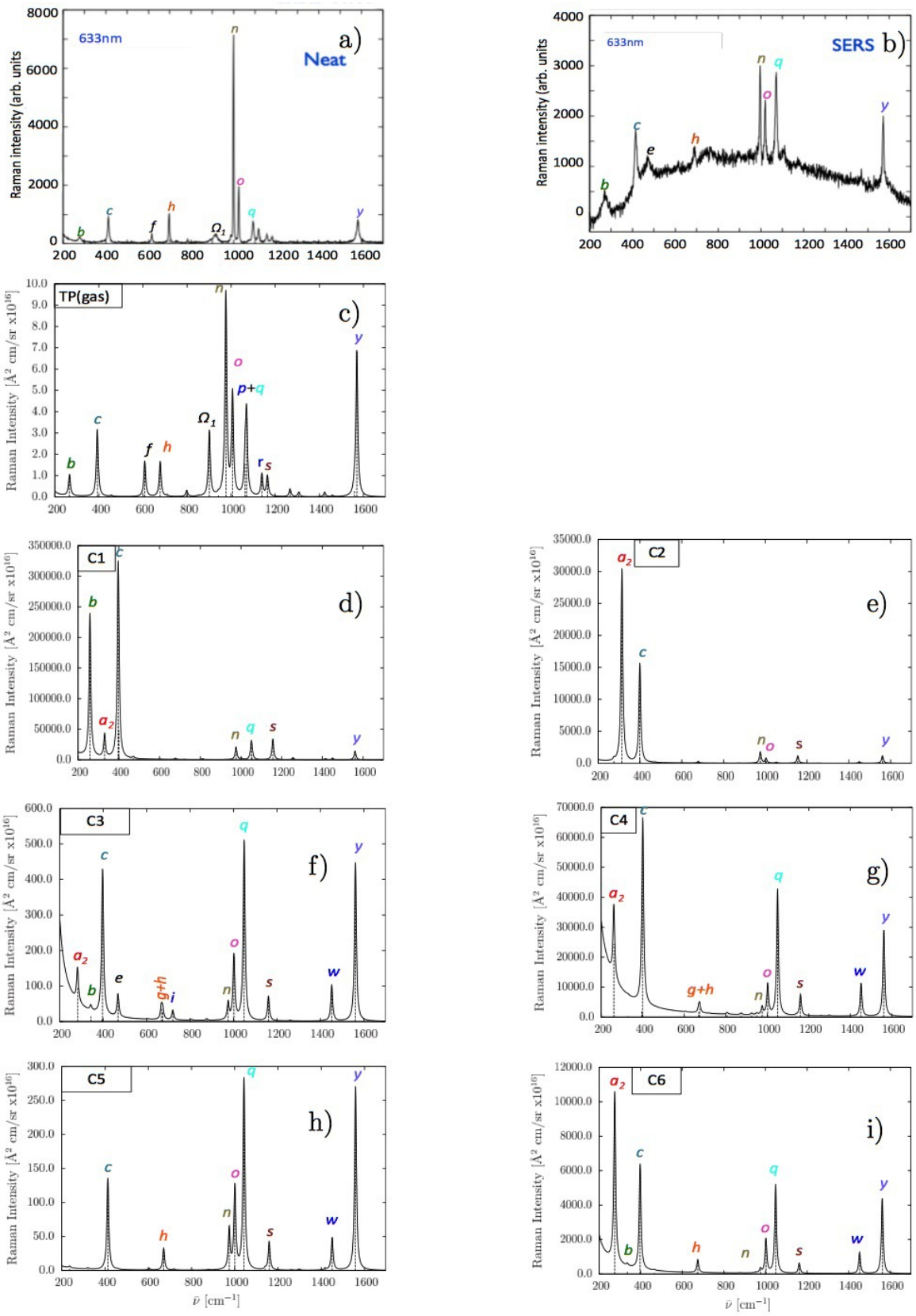


FIGURE 6.9: Comparison between the experimental and simulated Raman spectra. a) Experimental Raman spectrum of neat TP [16] (Copyright (2011) by The American Physical Society); b) Experimental SERS spectrum of TP adsorbed on a roughened SiGe surface coated with 30 nm of Au [16] (Copyright (2011) by The American Physical Society); c) Simulated Raman spectrum of isolated TP; (d-i) Simulated Raman spectra of TP adsorbed on Au clusters.

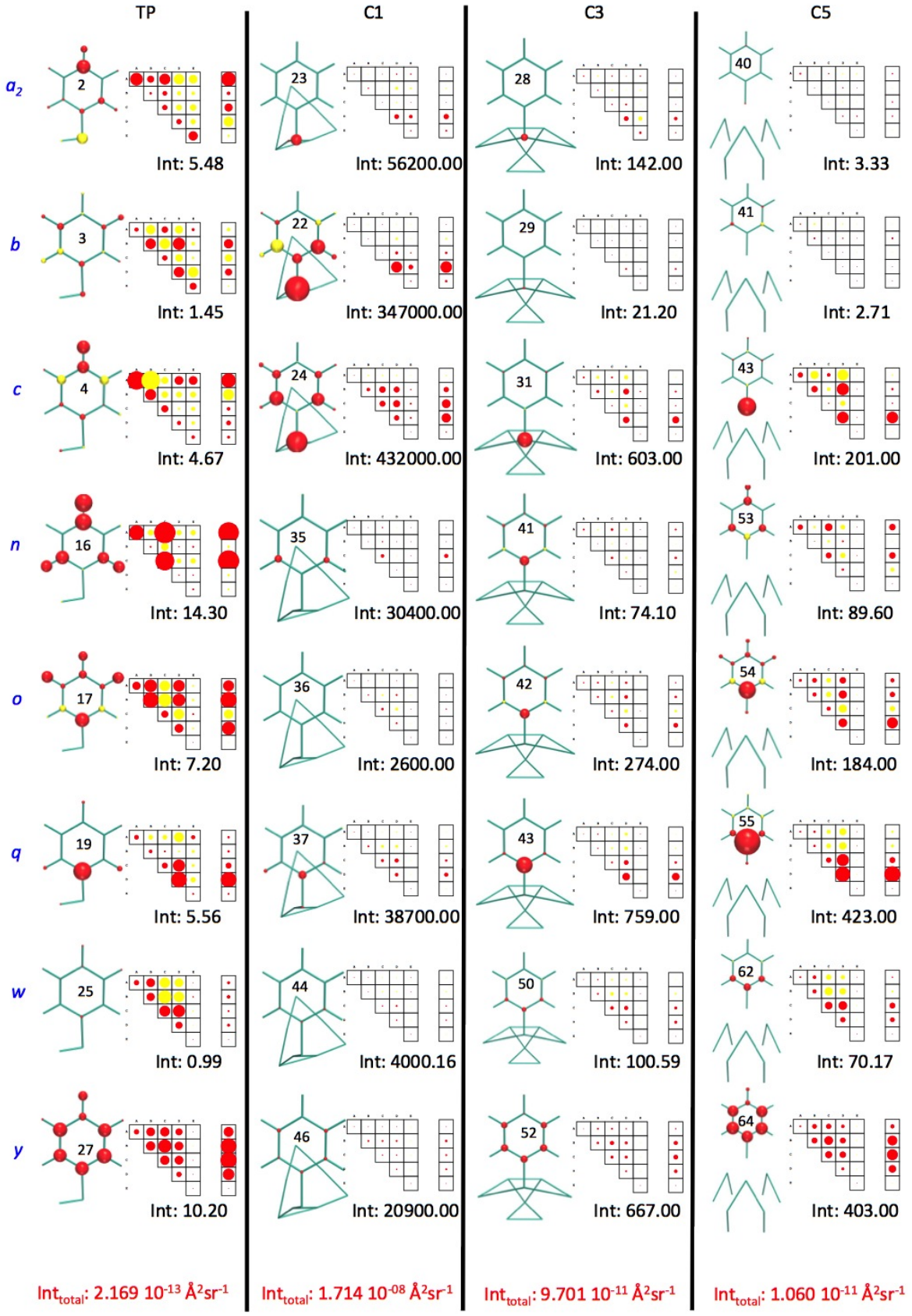


FIGURE 6.10: Sketch of the Raman Atomic Contribution Patterns (left), and Group Coupling Matrices (right) for the main peaks discussed in the text. The ACP sphere surfaces are proportional to the atomic contributions to the Raman cross sections. Red and yellow color spheres represent positive and negative contributions, respectively. The GCM representation is detailed in Fig. 6.5. The numbers in red color below each column specify the total intensities, which are the sums of all the normal mode Raman intensities. The inscribed circle is defined to contain 3% of the total intensity. Raman intensities are given in $10^{-15}$Å$^2$sr$^{-1}$.

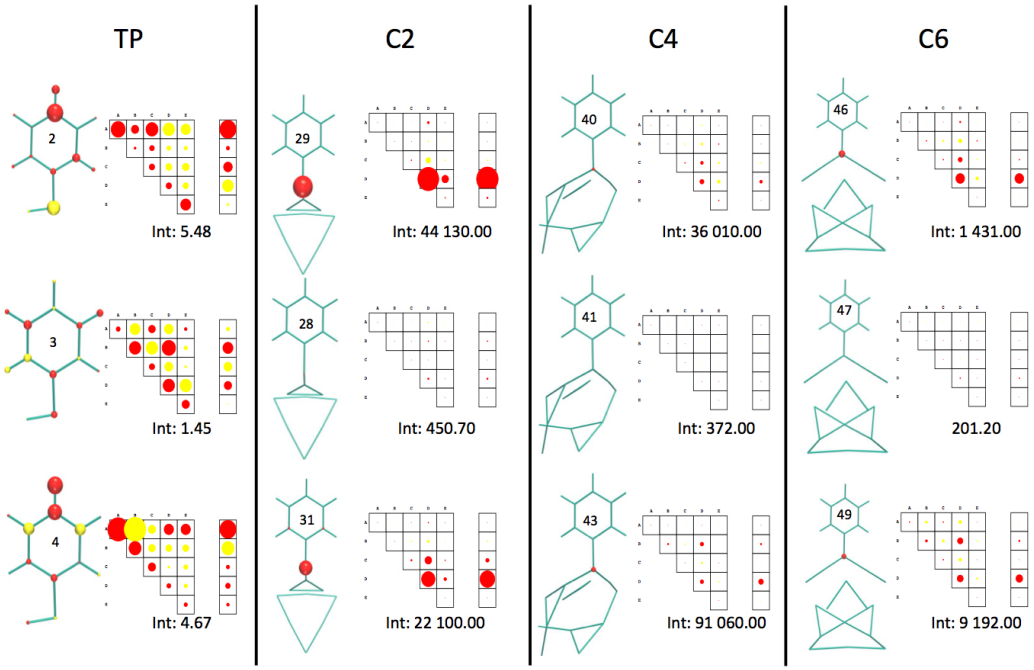


FIGURE 6.11: Sketch of the Raman Atomic Contribution Patterns (left), and Group Coupling Matrices (right) for the modes $a_2$, $b$ , and $c$ in the C2 ,C4, and C6 complexes. See caption of Fig. 6.10 for more details.

for mode $y$. We make the hypothesis that this comes from the neglect of the solvent effects. More importantly, for the clusters, the best agreement with experiment is obtained for the complexes with a twofold-coordinated binding site of the S atom, and especially for the C3 complex (Fig. 6.9f). Upon adsorption, the experimental SERS spectrum keeps the $c$ and $y$ peaks but with a relative increase of intensity. Then, the dominant peak $n$ is replaced by a triplet of peaks of similar intensities ($n$, $o$, $q$). The simulated spectra for the mono-coordinated species do not reproduce this later feature. In the case of the threefold-coordinated site, the $e$ peak is missing, like in the C4 and C6 spectra. On the other hand, in C3, the bands $c$ [$\nu$(CS)+$\nu$(AuS)], $e$ [$\gamma$(CH) + $\gamma$(SH)], $h$ [$\delta$(CCC) + r-i-d], $o$ [$\nu$(CC)s + $\delta$(CH)], $q$ [$\nu$(CS) + $\delta$(CH)+$\nu$(CC)], and $y$ [$\nu$(CC)] are in accordance with those of the experimental SERS spectrum. Nevertheless, some well defined peaks of the simulated C3 spectrum like $i$ [$\omega$(CH)], $s$ [$\delta$(CH)] and $w$ [$\delta$(CH) + $\nu$(CC)] (Fig. 6.9f) have not been highlighted by the authors of the experimental SERS spectrum, though analysis of Fig. 6.9b shows the possible presence of peaks of low intensity in the background. In addition, it is worth noting that the peak $b$ in the experimental SERS spectrum (Fig. 6.9b) attributed in the literature to the [$\delta$(CS)+$\nu$(AuS), Table 6.2, TP] might be the $a_2$ [r-o-d + $\gamma$(CS), Table 6.2,TP], while this latter could appear further away, as shown in Fig. 6.9f ($a_2$ and $b$).

## 6.4 Conclusions

By employing DFT, we have calculated the IR and Raman signatures of the TP molecule adsorbed on gold clusters mimicking the different types of adsorption sites and we have brought

out the effects of the adsorption and of the coordination site using the normal mode overlaps, the group coupling matrices (GCM), and atomic contribution patterns (ACP) based on the decomposition scheme introduced by Hug [27] and implemented into the `pyvib2` program [25]. First, we have followed the evolution of the vibrational normal modes from the isolated TP molecule to those of TP adsorbed on the different clusters; by relying on the overlap matrix between the modes to highlight mode permutations, mode mixings, and mode splittings, which depend not only on the adsorption but also on the type of cluster and on its symmetry. For the Raman spectra, one observes a larger impact of the adsorption site on the relative intensities than in the case of IR, in particular for the signatures of the vibrational modes located between 200 $cm^{-1}$ and 400 $cm^{-1}$ $\big(a_2$ [r-o-d + $\gamma$(CS)], $b$ [$\delta$(CS)+$\nu$(AuS)], and $c$ [$\nu$(CS)+$\nu$(AuS)]$\big)$, which greatly depend on the contribution of the S atom.

Second, using the GCM and the ACP, we have shown how the contributions of an atom or of a group of atoms to the Raman intensities vary with the adsorption site. Thus, for the low frequencies vibrational modes, the intensity increases with the contribution of the S atom, which vary with its coordination site. This enables to explain selective enhancements of the vibrational modes, and therefore changes in the spectral profiles. Moreover, this contribution varies both with the coordination and with the orientation of the phenyl with respect to the cluster. Indeed, we see for example that the peak $a_2$ always dominates the spectrum when the phenyl ring points out from the cluster surface (Fig. 6.1b to Fig. 6.1f). On the basis of these features, the best agreement with the experimental spectrum of Ref. [16] was found for the C3 complex corresponding to a twofold-coordinated site, while when considering only the strongest peaks ($c$, $h$, $n$, $o$, $q$, $y$), the C5 complex (threefold-coordinated) shows also a consistent agreement with experimental relative enhancements.

Although there is a general good agreement between the experimental and simulated spectra, there remain some deviations (particularly located at around 3000 $cm^{-1}$ in IR spectra, and around 1000 $cm^{-1}$ in Raman spectra), which can partly be related to the effects of the TP orientation on the surface and the geometry of the experimental setup (the angle of incidence and the polarizations of the beams). Indeed, experimentally, the SEIRAS and the SERS intensities depend on the latter, while our simulations account for an average of components of the $\partial\mu/\partial Q$ vector and of the $\partial\alpha/\partial Q$ tensor. Furthermore the optimized structures were calculated in gas phase for a single isolated molecule. Future work will address those effects as well as the impact of the anharmonicity and of the exchange-correlation functional.

# References

[1] (a) Dubois, L. H.; Nuzzo, R. G. *Ann. Rev. Phys. Chem.* **1992**, *43*, 437–463; (b) Hoyer, P. *Langmuir* **1996**, *12*, 1411–1413; (c) Ulman, A. *Chem. Rev* **1996**, *96*, 1533–1554, PMID: 11848802; (d) Moriguchi, I.; Maeda, H.; Teraoka, Y.; Kagawa, S. *Chem. of Mater.* **1997**, *9*, 1050–1057; (e) Wagner, P.; Nock, S.; Spudich, J. A.; Volkmuth, W. D.; Chu, S.; Cicero, R. L.; Wade, C. P.; Linford, M. R.; Chidsey, C. E. *J. of Struc. Biol.* **1997**, *119*, 189 – 201; (f) Mahajan, S.; Baumberg, J. J.; Russell, A. E.; Bartlett, P. N. *Phys. Chem. Chem. Phys.* **2007**, *9*, 6016–6020.

[2] (a) Seitz, O.; Dai, M.; Aguirre-Tostado, F. S.; Wallace, R. M.; Chabal, Y. J. *J. Am. Chem. Soc.* **2009**, *131*, 18159–18167; (b) Michalak, D. J.; Amy, S. R.; Aureau, D.; Dai, M.; Estève, A.; Chabal, Y. J. *Nat. Mat.* **2010**, *9*, 1–6; (c) Lis, D.; Guthmuller, J.; Champagne, B.; Humbert, C.; Busson, B.; Tadjeddine, A.; Peremans, A.; Cecchet, F. *Chem. Phys. Lett.* **2010**, *489*, 12 – 15; (d) Seitz, O.; Fernandes, P. G.; Mahmud, G. A.; Wen, H.-C.; Stiegler, H. J.; Chapman, R. A.; Vogel, E. M.; Chabal, Y. J. *Langmuir* **2011**, *27*, 7337–7340; (e) Humbert, C.; Pluchery, O.; Lacaze, E.; Tadjeddine, A.; Busson, B. *Phys. Chem. Chem. Phys.* **2012**, *14*, 280–289.

[3] Tetsassi Feugmo, C. G.; Champagne, B.; Caudano, Y.; Cecchet, F.; Chabal, Y. J.; Liégeois, V. *J. Phys.: Condens. Matter* **2012**, *24*, 124111.

[4] (a) Carron, K. T.; Hurley, L. G. *J. Phys. Chem.* **1991**, *95*, 9979–9984; (b) Szafranski, C. A.; Tanner, W.; Laibinis, P. E.; Garrell, R. L. *Langmuir* **1998**, *14*, 3580–3589.

[5] Wan, L.-J.; Terashima, M.; Noda, H.; Osawa, M. *J. Phys. Chem. B* **2000**, *104*, 3563–3569.

[6] (a) Anderson, M. S. *App. Phys. Lett.* **2003**, *83*, 2964–2966; (b) Hillenbrand, R.; Taubner, T.; Keilmann, F. *Nature* **2007**, *418*, 159–162; (c) Willets, K. A.; Duyne, R. P. V. *Annu.l Rev. Phys. Chem.* **2007**, *58*, 267–297, PMID: 17067281; (d) Stiles, P. L.; Dieringer, J. A.; Shah, N. C.; Duyne, R. P. V. *Annu.l Rev. Phys. Chem.* **2008**, *1*, 601–626, PMID: 20636091; (e) Pluchery, O.; Humbert, C.; Valamanesh, M.; Lacaze, E.; Busson, B. *Phys. Chem. Chem. Phys.* **2009**, *11*, 7729–7737.

[7] (a) Arenas, J. F.; López Tocón, I.; Otero, J. C.; Marcos, J. I. *J. Phys. Chem.* **1996**, *100*, 9254–9261; (b) Lombardi, J. R.; Birke, R. L. *J. Phys. Chem. C* **2008**, *112*, 5605–5617; (c) Jensen, L.; Aikens, C. M.; Schatz, G. C. *Chem. Soc. Rev.* **2008**, *37*, 1061–1073; (d) Morton, S. M.; Jensen, L. *J. Am. Chem. Soc.* **2009**, *131*, 4090–4098, PMID: 19254020.

[8] Lang, X.; Yin, P.; You, T.; Jiang, L.; Guo, L. *ChemPhysChem* **2011**, *12*, 2468–2475.

[9] (a) Saikin, S. K.; Olivares-Amaya, R.; Rappoport, D.; Stopa, M.; Aspuru-Guzik, A. *Phys. Chem. Chem. Phys.* **2009**, *11*, 9401–9411; (b) Saikin, S. K.; Chu, Y.; Rappoport, D.; Crozier, K. B.; Aspuru-Guzik, A. *J. Phys. Chem. Lett.* **2010**, *1*, 2740–2746.

[10] (a) Guthmuller, J.; Cecchet, F.; Lis, D.; Caudano, Y.; Mani, A. A.; Thiry, P. A.; Peremans, A.; Champagne, B. *ChemPhysChem* **2009**, *10*, 2132–2142; (b) Cecchet, F.; Lis, D.; Guthmuller, J.; Champagne, B.; Fonder, G.; Mekhalif, Z.; Caudano, Y.; Mani, A. A.; Thiry, P. A.; Peremans, A. *J. Phys. Chem. C* **2010**, *114*, 4106–4113.

[11] (a) Larsson, J. A.; Nolan, M.; Greer, J. C. *J. Phys. Chem. B* **2002**, *106*, 5931–5937; (b) Bilić, A.; Reimers, J. R.; Hush, N. S. *J. Chem. Phys.* **2005**, *122*, 094708; (c) Jayanthi, N.; Cruz, J.; Pandiyan, T. *Chem. Phys. Lett.* **2008**, *455*, 64 – 71; (d) Ferrighi, L.; Pan, Y.-x.; Grönbeck, H.; Hammer, B. *J. Phys. Chem. C* **2012**, *116*, 7374–7379.

[12] Joo, S. W.; Han, S. W.; Kim, K. *J. Colloid Interface Sci.* **2001**, *240*, 391 – 399.

[13] Hayashi, T.; Morikawa, Y.; Nozoye, H. *J. Chem. Phys.* **2001**, *114*, 7615–7621.

[14] (a) Vargas, M. C.; Giannozzi, P.; Selloni, A.; Scoles, G. . *Phys. Chem. B* **2001**, *105*, 9509–9513; (b) Gottschalck, J.; Hammer, B. *J. Chem. Phys.* **2002**, *116*, 784–790.

[15] Nara, J.; Higai, S.; Morikawa, Y.; Ohno, T. *J. Chem. Phys.* **2004**, *120*, 6705.

[16] Zayak, A.; Hu, Y.; Choo, H.; Bokor, J.; Cabrini, S.; Schuck, P.; Neaton, J. *Phys. Rev. Lett.* **2011**, *106*, 083003.

[17] (a) Sellers, H.; Ulman, A.; Shnidman, Y.; Eilers, J. E. *J. Am. Chem. Soc.* **1993**, *115*, 9389–9401; (b) Sellers, H. *Surf. Sci.* **1993**, *294*, 99 – 107; (c) Beardmore, K.; Kress, J.; Bishop, A.; Grønbech-Jensen, N. *Synth. Met.* **1997**, *84*, 317 – 318; (d) Gronbeck, H.; Curioni, A.; Andreoni, W. *J. Am. Chem. Soc.* **2000**, *122*, 3839–3842.

[18] Becke, A. D. *J. Chem. Phys.* **1993**, *98*, 5648–5652.

[19] Frisch, M. J. et al. Gaussian-09 Revision D.01. Gaussian Inc. Wallingford CT 2009.

[20] Figgen, D.; Rauhut, G.; Dolg, M.; Stoll, H. *Chem. Phys.* **2005**, *311*, 227 – 244, Relativistic Effects in Heavy-Element Chemistry and Physics. In Memoriam Bernd A. Hess (1954–2004).

[21] Peterson, K. A.; Puzzarini, C. *Theo. Chem. Acc.* **2005**, *114*, 283–296.

[22] Scott, P. A.; Radom, L. *J. Phys. Chem.* **1996**, *100*, 16502–16513.

[23] Wilson, E. B.; Decius, J. C.; Cross, P. C. *Molecular Vibrations: The Theory of Infrared and Raman Vibrational spectra*; Dover publications, 1980.

[24] Long, D. A. *The Raman Effect*; A Unified Treatment of the Theory of Raman Scattering by Molecules; Wiley, 2002.

[25] Fedorovsky, M. PyVib2, a program for analyzing vibrational motion and vibrational spectra. http://pyvib2.sourceforge.net, 2007.

[26] Hug, W.; Fedorovsky, M. *Theo. Chem. Acc.* **2006**, *119*, 113–131.

[27] Hug, W. *Chem. Phys.* **2001**, *264*, 53–69.

[28] Larsen, N. W.; Schulz, L. *J. Molec. Struct.* **2009**, *920*, 30 – 39.

[29] Letardi, S.; Cleri, F. *J. Chem. Phys.* **2004**, *120*, 10062.

[30] Li, S.; Wu, D.; Xu, X.; Gu, R. *J. Raman. Spectrosc.* **2007**, *38*, 1436–1443.

[31] Wilson, E. B. *Phys. Rev.* **1934**, *45*, 706–714.

[32] Joo, T. H.; Kim, M. S.; Kim, K. *J. Raman. Spectrosc.* **1987**, *18*, 57–60.

[33] Biggs, K. B.; Camden, J. P.; Anker, J. N.; Duyne, R. P. V. *J. Phys. Chem. A* **2009**, *113*, 4581–4586.

[34] Aggarwal, R. L.; Farrar, L. W.; Diebold, E. D.; Polla, D. L. *J. Raman Spectrosc.* **2009**, 1331–1333.

[35] Moore, J. E.; Morton, S. M.; Jensen, L. *J. Phys. Chem. Lett.* **2012**, *3*, 2470–2475.

Tetsassi Feugmo, C. G.; Liégeois, V.; Champagne, B. *J. Phys. Chem. C* **2015**, 119, 3180–3191

**Personal contribution:** I implemented the SFG equations in a new custom Python program. I selected the systems for illustration, and ran all calculations. Finally, I proposed analyses, discussed these with my co-authors, and I wrote the first draft of the paper.

# Chapter 7

# Theoretical Investigation of Vibrational Sum-Frequency Generation Signatures of Functionalized H-Si(111)

In this chapter, developments towards a general approach for simulating and interpreting the sum-frequency generation signatures of functionalized surfaces are reported. This approach encompasses two steps, (1) the molecular properties (vibrational frequencies, IR and Raman quantities) are evaluated using first principles approaches implemented in standard quantum chemistry programs and (2) the macroscopic optical responses (the second-order nonlinear optical susceptibility tensor) of the adsorbate on its substrate are determined within the three-layer model of the interface. A homemade code has been written to carry out this second step, including (1) the evaluation of the Fresnel factor and (2) the molecular orientation in the laboratory frame. These approach and program allow generating the SFG spectra for different combinations of molecular orientations and experimental set-ups, as well as identifying the vibrational modes in order to facilitate their analysis. Then, the approach is illustrated in the case of a decyl chain covalently bonded to hydrogen-terminated Si(111) $\left[\equiv \mathrm{Si}{-}(\mathrm{CH_2})_9\mathrm{CH_3}\right]$. The simulated *ppp* spectrum agrees closely with experiment, whereas the agreement gets worse upon freezing parts of the chain, demonstrating that the SFG signature originates from a large part of the decyl chain. Calculations have also been performed for the other sets of polarizations (*sps*, *ssp*, and *pss*), highlighting that the spectral profile is shown to vary considerably from *ppp* to *ssp*, *sps*, and *pss*, which has been attributed to the combined effect of the Fresnel factors and the structure of the $\chi^{(2),R}$ tensor. The impact of the orientation of the alkyl chain (tilt and rotation angles) on the *ppp* SFG intensity has then been monitored by reducing the system to an isolated decane molecule and the changes in the SFG spectral pattern related to the orientation of the IR dipole moment.

## 7.1 Motivations

The formation of organic monolayers covalently-bonded to inorganic surfaces is a topic of intense research activity since two decades [1]. The main advantage of organic monolayers is to add functionality to the inorganic surface via suitable adaptation of their surface properties. Indeed, these functionalized materials keep the characteristics of the bulk material (electrical, magnetic, optical, mechanical and structural), while their surface properties (wetting, passivation, biochemical affinity, etc. ..) are tuned through a nanosized grafting [2, 3]. Furthermore, the monolayer-modified system is suitable as template for the controlled immobilization of biomolecules, for instance to build highly sensitive biosensing devices, including electrodes for molecular recognition [4]. The covalent attachment can be performed via coupling reactions between the chemically activated surfaces and molecules. Among these, silicon is one of the most widely used semiconductors in modern technology and organic monolayers covalently bonded to silicon surfaces have gained much attention since their introduction [5], owing to their well-defined structure and the possibility to introduce diverse electrical and optical functionalities to the system [1, 6–8]. Nevertheless, the lack of control of those processes at the molecular level might result in the formation of multilayers where the molecules have lost active conformation or orientation [9–11].

During the past decade, infrared-visible Sum Frequency Generation (SFG) spectroscopy has been adopted to monitor the interface formation, to determine its structure and therefore to help improving the efficiency of the immobilization of biomolecules [12–14]. Indeed, SFG presents the advantage of being sensitive only to the regions of the material where the inversion symmetry is broken [15, 16]. Moreover, theoretical approaches promote an increased understanding of molecular interactions at interface via the elucidation of its structure, through spectral assignment of the vibrational signatures [17–32].Therefore the complexity of the spectra calls for the development of simulation and interpretation tools [22, 23, 26, 29, 31, 33–49].

Infrared-visible SFG is a second-order nonlinear optical process in which a tunable infrared $\omega_{IR}$ laser beam is mixed with a visible $\omega_{vis}$ laser beam to generate an output beam at the sum frequency $\omega_{SFG} = \omega_{IR} + \omega_{vis}$ (see Fig. 7.1). The generated SFG signal $\omega_{SFG}$ is reflected from the substrate, according to the phase-matching condition,

$$\omega_{SFG} \sin \Psi_{SFG} = \omega_{vis} \sin \Psi_{vis} + \omega_{IR} \sin \Psi_{IR} \quad . \tag{7.1}$$

Under the electric dipole approximation, the SFG signal $I_{SFG}(\omega_{IR})$ generated by the nonlinear polarization is proportional to the effective surface susceptibility tensor $\chi^{(2),\,eff}$ as well as to the amplitude of the electric field of the IR and visible beams:

$$I(-\omega_{SFG}; \omega_{vis}, \omega_{IR}) \propto \left| \chi^{(2),\,eff} : E_{vis} E_{IR} \right|^2 , \tag{7.2}$$

where $E_{vis}$ and $E_{IR}$ are the corresponding electric field vectors. This interface second-order susceptibility containing a resonant (vibrational) and a non-resonant (electronic) term, reads :

$$\chi^{(2),eff}_{IJK} \propto F_I^{SFG} F_J^{vis} F_K^{IR} \left[ \overbrace{\left|\chi^{(2),NR}_{IJK}\right| e^{i\Phi_{SFG}}}^{non-resonant} + \underbrace{\overbrace{\underbrace{\frac{N_s}{\varepsilon_0}}_{\mathrm{VC^{-1}m^{-1}}} \sum_{\alpha,\beta,\gamma} \langle T_{I\alpha J\beta K\gamma}(\phi,\theta,\xi)\rangle \beta_{\alpha\beta\gamma}(-\omega_{SFG};\omega_{vis},\omega_{IR})}^{resonant}}_{\chi^{(2),R}_{IJK} \equiv [\mathrm{m^2V^{-1}}]} \right], \tag{7.3}$$

with

$$\beta_{\alpha\beta\gamma}(-\omega_{SFG};\omega_{vis},\omega_{IR}) = \sum_p \underbrace{\frac{1}{4\omega_p} \frac{\left(\frac{\partial\alpha_{\alpha\beta}(\omega_{vis})}{\partial Q_p}\right)_e \left(\frac{\partial\mu_\gamma}{\partial Q_p}\right)_e}{\left(\omega_p - \omega_{IR} - i\Gamma_p\right)}}_{\mathrm{C^3m^3J^{-2}}} = \sum_p \frac{1}{4\omega_p} \frac{A_{\alpha\beta\gamma}}{\left(\omega_p - \omega_{IR} - i\Gamma_p\right)}. \tag{7.4}$$

$\Phi_{SFG}$ is the phase angle between the resonant and non-resonant terms, $N_S$ is the surface density, the $F_I$ terms are the Fresnel factors, $T$ is the transformation matrix between the laboratory and molecular coordinate systems (connected by the Euler angles $\phi, \theta$, and $\xi$), and $\beta_{\alpha\beta\gamma}$ is the $\alpha\beta\gamma$ element of the molecular vibrational first hyperpolarizability tensor. In Eq. (7.4), $\Gamma_p$ is the damping coefficient, $\omega_p$ is the vibrational frequency of the $p^{th}$ vibrational mode, and $\omega_{IR}$ is the incident IR frequency. $\left(\frac{\partial\mu_\gamma}{\partial Q_p}\right)_e$ and $\left(\frac{\partial\alpha_{\alpha\beta}(\omega_{vis})}{\partial Q_p}\right)_e$ are the derivatives of the $\gamma$ and the $\alpha\beta$ components of the dipole moment and dynamic (at pulsation $\omega_{vis}$) polarizability with respect to the normal coordinate $Q_p$, evaluated at the equilibrium. As shown in Eq. (7.4), the signal is enhanced when $\omega_{IR}$ is resonant with $\omega_p$, and, to be SFG detectable, a vibrational mode must be both Raman- and IR-active. The $\chi^{(2),R}_{IJK}$ [Eq. (7.3)] elements are calculated using the Euler transformations, where $\alpha, \beta, \gamma$ define the molecular coordinates system $(x, y, z)$ and $I, J, K$ the laboratory coordinates $(X, Y, Z)$. For an achiral and isotropic surface (X-Z mirror plane, Fig. 7.1) only seven (but four independent) non-zero $\chi^{(2)}_{IJK}$ elements remain: $\chi^{(2)}_{ZZZ}$; $\chi^{(2)}_{ZXX} = \chi^{(2)}_{ZYY}$; $\chi^{(2)}_{XZX} = \chi^{(2)}_{YZY}$; $\chi^{(2)}_{XXZ} = \chi^{(2)}_{YYZ}$, and the intensity of the generated SFG signal is given by linear combinations of these effective second-order susceptibility ($\chi^{(2),eff}$) tensor elements. These linear combinations can be probed with four sets of polarization of the incident and generated beams denoted *ssp*, *sps*, *pss* and *ppp*. Considering for example the *ssp* polarization set, both *s*-polarized SFG and visible light have the electric field polarized along the $Y$ direction (first, $I$, and second, $J$, indices), while the IR *p*-polarized light has the electric field in the $XZ$ plane (third index, $K$). Thus, the *ssp* combination is assessed by using the $\chi^{(2)}_{YYZ}$ element, and it therefore probes vibrational modes with a IR dipole moment $\left(\frac{\partial\mu_\gamma}{\partial Q_p}\right)_e$ perpendicular to the interface. Using the same arguments, the *sps* configuration ($\chi^{(2)}_{YZY}$) detects vibrational modes with a dipole moment parallel to the surface, while in *ppp* configuration ($\chi^{(2)}_{ZZZ}$, $\chi^{(2)}_{XXZ}$, $\chi^{(2)}_{XZX}$, and $\chi^{(2)}_{ZXX}$) vibrational modes with both perpendicular and parallel dipole components are probed. The corresponding SFG intensities for each polarization set are given by:

$$\underbrace{\frac{I_{ssp}}{I_{IR}I_{vis}}}_{\mathrm{J^{-1}sm^2}} = \underbrace{\frac{\omega_{SFG}^2}{2c^3\varepsilon_0 n_1(\omega_{SFG})n_1(\omega_{IR})n_1(\omega_{vis})\cos^2\psi_{SFG}}}_{\mathrm{m^{-2}C^{-1}Vs}} \underbrace{\left|\sin\psi_{IR}\chi^{(2)}_{YYZ}F_Y^{SFG}F_Y^{vis}F_Z^{IR}\right|^2}_{|\chi^{(2),\,eff}_{YYZ}|^2 \equiv \mathrm{m^4V^{-2}}} \tag{7.5}$$

$$\frac{I_{pss}}{I_{IR}I_{vis}} = \frac{\omega_{SFG}^2}{2c^3\varepsilon_0 n_1(\omega_{SFG})n_1(\omega_{IR})n_1(\omega_{vis})\cos^2\psi_{SFG}}\left|\sin\psi_{SFG}\chi^{(2)}_{ZYY}F_Z^{SFG}F_Y^{vis}F_Y^{IR}\right|^2 \tag{7.6}$$

$$\frac{I_{sps}}{I_{IR}I_{vis}} = \frac{\omega_{SFG}^2}{2c^3\varepsilon_0 n_1(\omega_{SFG})n_1(\omega_{IR})n_1(\omega_{vis})\cos^2\psi_{SFG}}\left|\sin\psi_{vis}\chi^{(2)}_{YZY}F_Y^{SFG}F_Z^{vis}F_Y^{IR}\right|^2 \tag{7.7}$$

$$\begin{aligned}\frac{I_{ppp}}{I_{IR}I_{vis}} =& \frac{\omega_{SFG}^2}{2c^3\varepsilon_0 n_1(\omega_{SFG})n_1(\omega_{IR})n_1(\omega_{vis})\cos^2\psi_{SFG}}\times \\ &\Big|-\cos\psi_{SFG}\cos\psi_{vis}\sin\psi_{IR}\;\chi^{(2)}_{XXZ}\;F_X^{SFG}F_X^{vis}F_Z^{IR} \\ &-\cos\psi_{SFG}\sin\psi_{vis}\cos\psi_{IR}\;\chi^{(2)}_{XZX}\;F_X^{SFG}F_Z^{vis}F_X^{IR} \\ &+\sin\psi_{SFG}\cos\psi_{vis}\cos\psi_{IR}\;\chi^{(2)}_{ZXX}\;F_Z^{SFG}F_X^{vis}F_X^{IR} \\ &+\sin\psi_{SFG}\sin\psi_{vis}\sin\psi_{IR}\;\chi^{(2)}_{ZZZ}\;F_Z^{SFG}F_Z^{vis}F_Z^{IR}\Big|^2\end{aligned} \tag{7.8}$$

Moreover, to improve the spectral analysis and therefore to better assign the peaks, the intensities at the frequency of each mode can be calculated.

$$I_{SFG}(\omega_q) \propto \left|\sum \chi^{(2)}_{IJK}(\omega_q)F_I^{SFG}F_J^{vis}F_K^{IR}\right|^2 \tag{7.9}$$

In this equation, the resonant contribution of mode $q$ to the susceptibility is given by :

$$\chi^{(2),R}_{IJK}(\omega_q) = \frac{N_s}{\varepsilon_0}\sum_{\alpha,\beta,\gamma}\left\langle T_{I\alpha J\beta K\gamma}(\phi,\theta,\xi)\sum_p \frac{1}{4\omega_p}\frac{\left(\frac{\partial\alpha_{\alpha\beta}(\omega_{vis})}{\partial Q_p}\right)_e\left(\frac{\partial\mu_\gamma}{\partial Q_p}\right)_e}{\left(\omega_p-\omega_q-i\Gamma_p\right)}\right\rangle \tag{7.10}$$

In this article we report on recent developments of a program for the simulation and the interpretation of the SFG signatures and on its application to probe the structure of organic layers

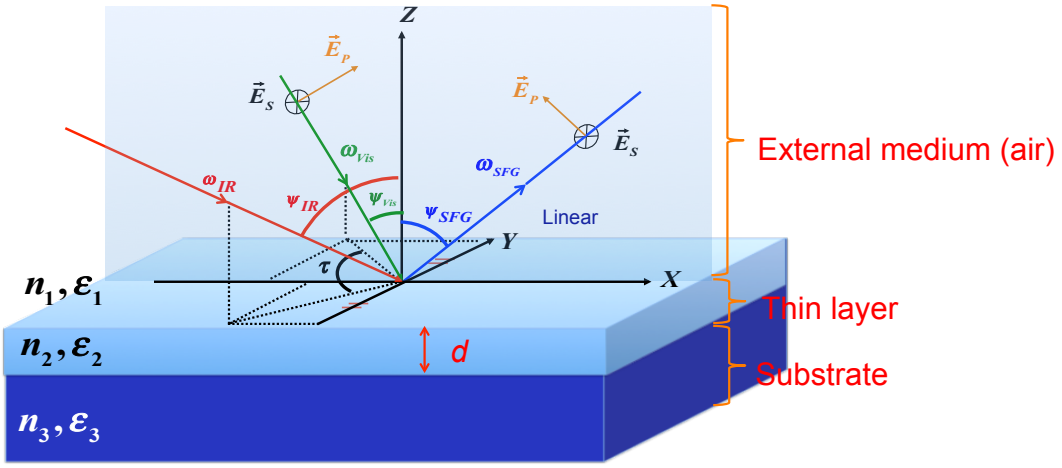


FIGURE 7.1: Geometry of a SFG experiment in the reflection configuration and representation of the three-layer model. $p$ (parallel) denotes a beam polarization in the plane of incidence (XZ), while $s$ (senkrecht) corresponds to a polarization perpendicular to the plane of incidence (Y).

at silicon interfaces. The general method that has been developed combines Density Functional Theory (DFT) calculations to evaluate the molecular properties with a three-layer approach to determine the macroscopic response of the interface. The latter step, which accounts explicitly for the nature of the surface, has been implemented in a homemade code.

## 7.2 Models of the functionalized H-Si(111) surface

Experimentally [50], n-alkyl monolayers convalently bonded to H-Si(111) surface are prepared by heat induced addition of 1-alkenes on ≡Si-H samples via Si-C linkages (≡ $Si-C_nH_{2n+1}$). Thus, to highlight the impact of the silicon surface, two types of structure were employed (Fig. 7.2). First, the surface is explicitly taken into account (Fig. 7.2a). To model the H-Si(111) surface, a cluster was build with four silicon layers where hydrogen atoms saturate the dangling bonds. The surface orientation is defined by its normal corresponding to the laboratory $Z$-axis, chosen to be perpendicular to the plane passing through the six H atoms of the surface. The molecular $z$-axis is fitted using the least squares approach, as the best vector through the C atoms of the alkyl chain, and pointing away from the anchoring site. The $y$-axis is in the carbon backbone plane, pointing away from the surface, while the $x$-axis defines the normal of the backbone plane. The orientation of molecule (and the molecular frame) at the surface is completely defined by two angles: the tilt angle ($\theta$) and the rotation angle ($\xi$). Thus, $\theta$ is defined as the angle between the alkyl chain long axis ($z$) and the normal to the surface ($Z$) :

$$\theta = \arccos(\vec{e}_Z \cdot \vec{e}_z) \tag{7.11}$$

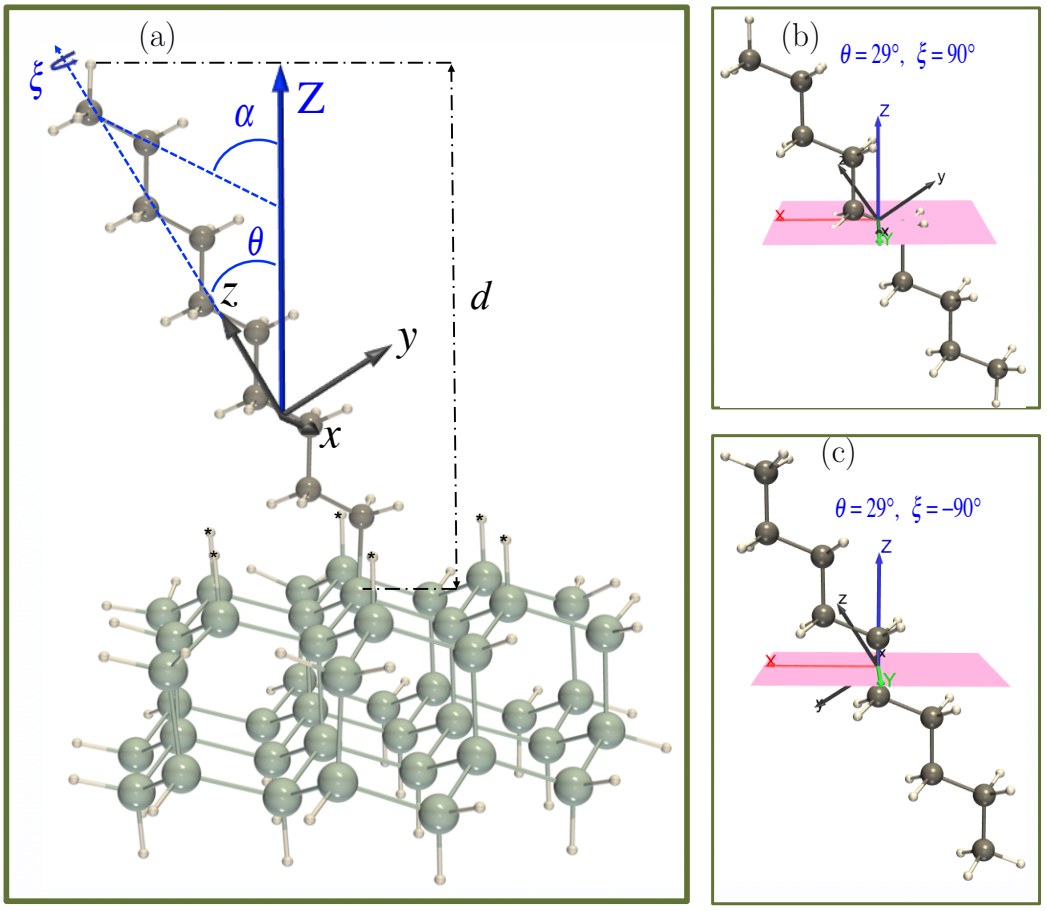


FIGURE 7.2: Geometry of the interface and definition of the Euler angles ($\theta$, $\xi$) connecting the laboratory coordinate system (X, Y, Z) to the molecular coordinate system $(x, y, z)$. (a) Optimized structure of the $\equiv$ Si$-(CH_2)_9CH_3$ system: $\theta$ and $\alpha$ are the alkyl chain and methyl tilt angles, respectively. $\xi$ is the Euler rotation angle. $d$ is the monolayer thickness. Hydrogen atoms marked by * are the real atoms of the surface, while the other H atoms are used to saturate the dangling bonds. (b) and (c) *all-trans* decane optimized structure adopting two orientations. See the text for more details.

while $\xi$ gives the orientation of the molecule around the $z$-axis and is calculated as:

$$\xi = \arctan\left(\frac{\vec{e}_Z \cdot \vec{e}_y}{-\vec{e}_Z \cdot \vec{e}_x}\right), \tag{7.12}$$

and therefore $\xi = 0.0$ (or $\pi$) when $\vec{e}_y$ and $\vec{e}_Z$ are perpendicular. One should note that when $\theta = 0.0$, $\xi$ does not have meaning anymore. The monolayer was modeled with one decyl chain covalently bonded to the Si cluster $\left[\equiv \text{Si}-(CH_2)_9CH_3\right]$. Second, an isolated decane molecule was considered (Fig. 7.2b and (Fig. 7.2c). In both approaches the molecule can adopt the same orientation, which in the former is fixed by the optimized geometry, while in the latter it can be further modulated to our convenience by setting $\theta$ and $\xi$ in order to probe their impact on the SFG signatures.

## 7.3 Methods of calculation and overview of the program

The calculations on the isolated molecule and on the molecule adsorbed on H-Si(111) surface were carried out with the Gaussian09 package [51], using the $\omega$B97X-D exchange-correlation functional [52], which includes empirical atom-atom dispersion corrections. It also includes long-range (with a range-separating parameter, $\mu = 0.20$) and short-range exact exchange. The 6-311G(d) basis set was found to be a good compromise between accuracy and computational needs [22]. In a first step, full geometry optimizations of the two model systems were performed under the constraint that the residual forces are smaller than $10^{-5}$ au.

Then, harmonic vibrational frequencies and normal modes were calculated analytically at the same level of approximation, by setting large atomic masses (1000 amu) for those H atoms saturating the Si dangling bonds, i.e. those that do not belong to the top area, to mimic larger and thicker silicon layers. To account for missing anharmonic effects as well as for the limitations of the XC functional, the harmonic vibrational frequencies were scaled by a factor of 0.95 [53]. To trace back the part of the chain from where the SFG signal originates, the models were refined by freezing some portions of the alkyl chain. The motions of these molecular moieties are frozen by setting large atomic masses (1000 amu) to the hydrogen and/or carbon atoms (Fig. 7.3) in the vibrational frequency calculations: (i) *Free chain*: the whole alkyl chain is set free (Fig. 7.3c); (ii) *Free ethyl*: all the atoms of the alkyl chain are frozen except those of the terminal ethyl group (Figs. 7.3b and 7.3d); (iii) *Free methyl*: all the atoms of the alkyl chain are frozen except those of the terminal methyl group (Fig. 7.3e); (iv) *Frozen methyl*: one terminal methyl group is frozen (Fig. 7.3a).

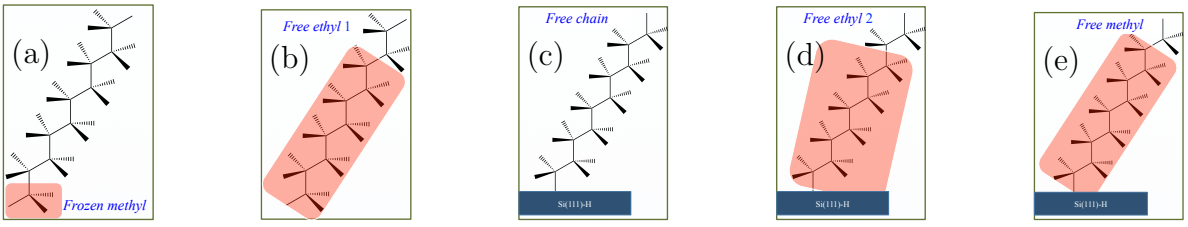


FIGURE 7.3: Schematic representation of the models. (a) *Frozen methyl* ; (b) *Free ethyl 1* ; (c) *Free chain*; (d) *Free ethyl 2*; and (e) *Free methyl*. The motions of the H and C atoms in the colored box are hampered by setting large atomic masses (1000 amu).

Then, the SFG spectra were simulated with a homemade program according to the maproad displayed in Fig. 7.4. It makes use of the Raman tensors $[\partial\alpha_{\alpha\beta}(\omega_{vis})/\partial Q_p]_e$ and IR vectors $(\partial\mu_\gamma/\partial Q_p)_e$ of each vibrational normal mode and of the Fresnel factors of the Si/monolayer/air interface to determine the components of the $\chi^{(2),\,eff}$ tensor and finally the SFG intensity for each polarizations combination, by taking into account the experimental geometry (Fig. 7.1). The non-resonant term of $\chi^{(2),\,eff}$ [Eq. (7.3)] is assumed to be zero for the present application, while the surface density $N_s$, the damping coefficient $\Gamma_p$, and the dielectric constant of the thin film $\varepsilon_2$ were set here to $10^{10}$ molecules/m$^2$, 4.0 cm$^{-1}$, and 1.0, respectively. The simulations were

carried out with the IR and visible incident beams at 50° and 70° with respect to the sample surface normal [50]. The visible wavelength was kept constant at 532 nm, while the IR frequency was swept in the C-H stretching region (2800 - 3100 $cm^{-1}$), as well as the Si-H stretching region (2000 − 2200 $cm^{-1}$).

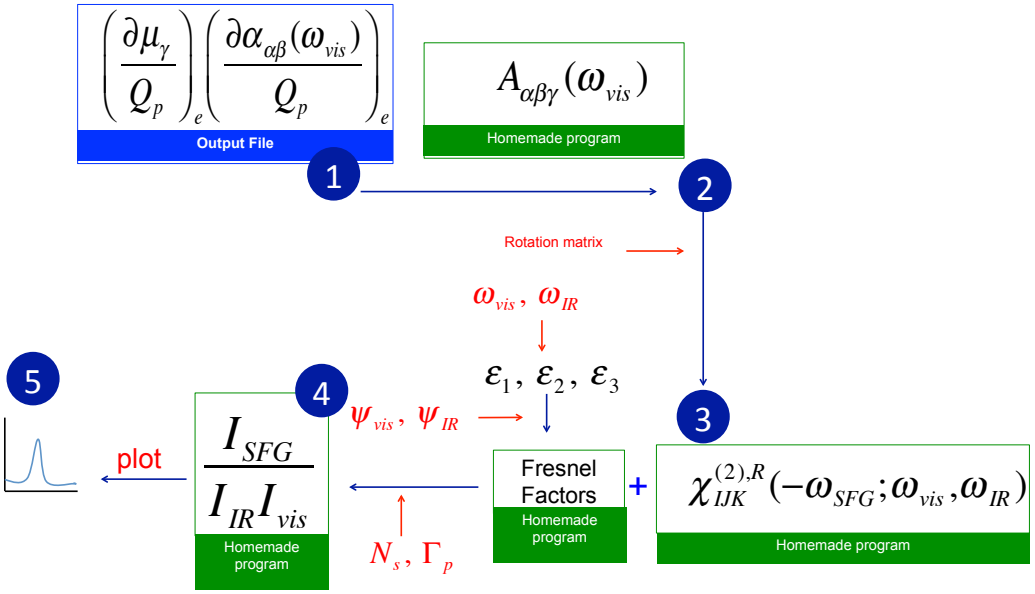


FIGURE 7.4: Road Map of the computational procedure.

## 7.4 Geometrical structures

Selected geometrical parameters of the functionalized surface are given in Table 7.1 while the fully optimized geometry is sketched in **??**. The tilt angle of the decyl chain $\theta$ (with respect to the surface normal) amounts to 43° , while the $CH_3$ tilt angle $\alpha$ to 67°. In the literature, the average tilt angle of decyl chain in decyl monolayers on silicon has been reported to be 35° ± 5 [5, 17, 54] (corresponding to a $CH_3$ tilt angle of ∼ 70°). Moreover, the thickness $d$ calculated as the distance between the projection on the laboratory $Z$-axis of one of the terminal H atoms of the alkyl chain and the plane passing through the Si atoms of the first layer amounts to 12.6 Å, which agrees with the experimental value

## 7.5 Vibrational frequencies

Harmonic vibrational frequencies were calculated for the five models sketched in Fig. 7.2. The vibrational frequencies of key modes located in the Si-H and C-H stretching regions are compared to experiment [17] in Table 7.2 whereas their atomic displacements are sketched in Fig. 7.5. The agreement with experiment is good, showing in the case of the Si-H stretching vibrations, that

TABLE 7.1: Selected optimized geometrical parameters determined at the ωB97X-D/6-311G(d) level of approximation and comparison with experiment.

| parameter | ωB97X-D | Experiment |
|---|---|---|
| Si-H (Å) | 1.492 | 1.480[a] |
| Si-Si (Å) | 2.366 | 2.330[a] |
| Si-C (Å) | 1.897 | 1.850[a] |
| $d$ (Å) | 12.639 | 12.8±1 |
| $\theta(^\circ)$ | 43 | $35 \pm 5$ |
| $\xi(^\circ)$ | 90 | - |
| $\alpha(^\circ)$ | 67 | 70 |

[a] Formal bond length values [55].

TABLE 7.2: Selected vibrational frequencies ($cm^{-1}$) of the alkyl chain and the Si(111) surface determined at the ωB97X-D/6-311G(d) level.

| modes[a] | label | Frozen methyl | Free chain | Free ethyl 2 | Free methyl | Exp1[b] | Exp2 |
|---|---|---|---|---|---|---|---|
| | | (a) | (c) | (d) | (e) | | |
| $\nu_{sym}$(Si−H) | $g_1^+$ | - | 2080 | 2080 | 2080 | | 2070[c] |
| $\nu_{sym}$(Si−H) | $g_2^+$ | - | 2090 | 2087 | 2090 | | 2083[c] |
| $\nu_{sym}(CH_2)$ | $d_1^+$ | 2878 | 2881 | | | | |
| $\nu_{sym}(CH_2)$ | $d_2^+$ | 2884 | 2886 | 2883 | | 2850 | 2850[d] |
| $\nu_{sym}(CH_3)$ | $r^+$ | 2888 | 2888 | 2888 | 2888 | 2876 | 2878[d] |
| $\nu_{as}(CH_2)$ | $d_1^-$ | 2889 | 2891 | | | | |
| $\nu_{as}(CH_2)$ | $d_2^-$ | 2890 | 2893 | | | | |
| $\nu_{as}(CH_2)$ | $d_3^-$ | 2895 | 2894 | | | | |
| $\nu_{as}(CH_2)$ | $d_4^-$ | 2911 | 2913 | | | | |
| $\nu_{as}(CH_2)$ | $d_5^-$ | 2920 | 2925 | 2914 | | 2905 | 2920[d] |
| $\nu_{as}(CH_2)$ | $d_6^-$ | 2934 | 2933 | | | 2932 | 2940[d] |
| $\nu_{as}(CH_3)$ | $r^-$ | 2960 | 2962 | 2962 | 2961 | 2960 | 2962[d] |

[a] $\nu$ symbols indicate the nature of the stretching mode; [b] Experimental values for $n$-decane in liquid phase [56]; [c] Experimental values obtained from ATR-FTIR of undecanoic acid-terminated silicon surface [6]; [d] Experimental values for decyl chain covalently bonded to H-Si(111) [50].

small Si clusters are reliable for describing the surface. So, one observes that upon adsorption the symmetric Si-H stretching mode splits into two modes, labeled herein $g_1^+$ and $g_2^+$, distant by 10 $cm^{-1}$. The vibrational frequencies of the C-H stretching modes of the alkyl chain vary by a maximum of 5 $cm^{-1}$ upon adsorption [Table 7.2, from (a) to (c)].

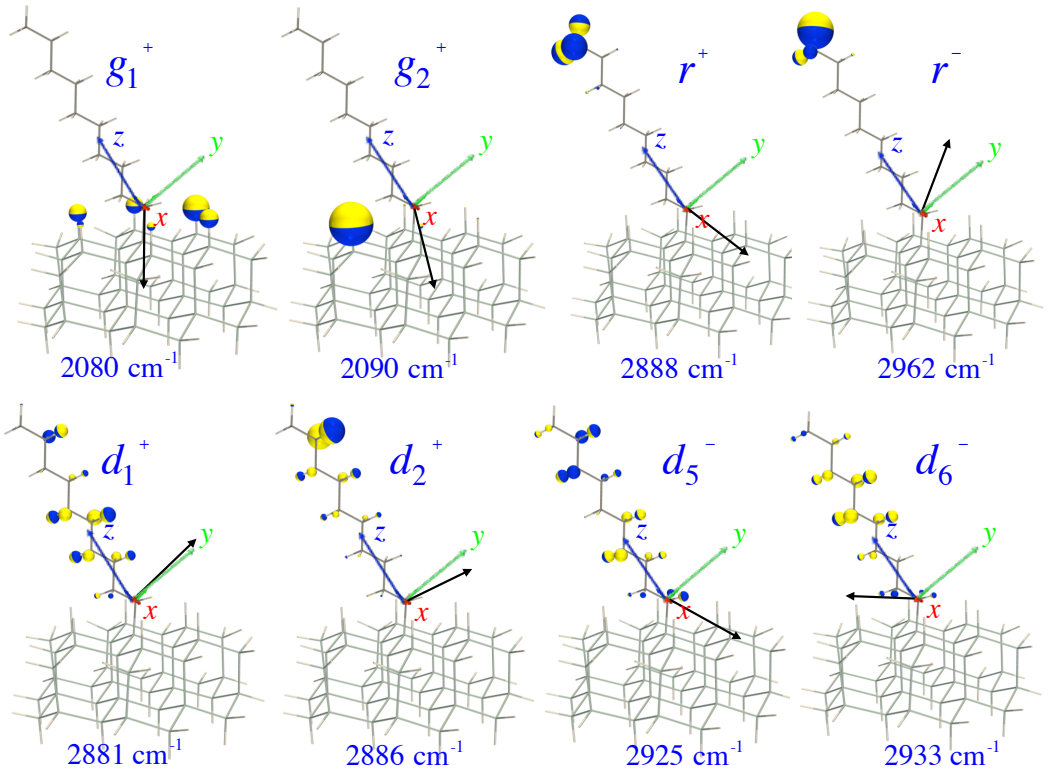


FIGURE 7.5: Sketch of selected vibrational normal modes of the $\equiv$ Si$-(CH_2)_9CH_3$ system [model (c)]. Modes are visualized with Pyvib2 [57].The direction of the atomic displacements is perpendicular to the junction plane between the two hemispheres of distinct color, whereas their amplitudes are proportional to the sphere radius. The IR vectors are shown in the molecular frame axes (red, green, and blue arrows) as black arrows. The normal modes labels and frequencies are given for each mode.

## 7.6 SFG signatures

### 7.6.1 By taking explicitly into account the surface

Figure 7.6 depicts the simulated *ppp* SFG spectra for the different models of the decyl monolayer on hydrogen-terminated Si(111) surface (Fig. 7.3) in comparison to experiment. The red lines under the peaks correspond to the SFG intensities calculated at the frequency of each mode [Eq. (7.9)]. Globally, the calculated spectral profiles in the C-H stretching region are in good agreement with experiment (Fig. 7.6a). The spectra are composed of three major peaks, 2888 $cm^{-1}$ ($r^+$), 2915 – 2920 $cm^{-1}$ ($d_5{}^-$) or 2933 – 2935 $cm^{-1}$ ($d_6{}^-$), and 2960–2961 $cm^{-1}$ ($r^-$). The peaks due to the $CH_3$ group ($r^+$ and $r^-$) are very strong compared to those of the $CH_2$ group. This aspect originates from the *all-trans* conformation of the alkyl chain. In that conformation, only the terminal $CH_3$ group is non centrosymmetric, and therefore contributes to the SFG spectrum whereas the $CH_2$ groups exhibit approximately inversion symmetry (except the one directly bonded to the $CH_3$ group) and are therefore weakly SFG active. This observation is corroborated by analyzing their IR and Raman intensities (Table 7.3). Indeed, for several $CH_2$ vibrations, when they are IR active, they are almost Raman inactive and vice versa (except $d_2{}^+$

located on the $CH_2$ directly bonded to the $CH_3$, Fig. 7.5) whereas the $CH_3$ vibrations display both intense IR and Raman activities. However, for the *Free chain* (Fig. 7.6b), many $CH_2$ vibrations contribute weakly as shown by the number of red lines under the $r^+$ peak.

Detailed analysis reveals that freezing some portions of the alkyl chain affects the spectral profile. First, going from *Free chain* (Fig. 7.6b) to *Free ethyl 2* (Fig. 7.6c), mode $d_6^-$ disappears and is replaced by $d_5^-$. The latter is located on the remaining free $CH_2$ group, and therefore is shifted because some portions of the chain are frozen. Indeed, most of the $CH_2$ stretching mode are hampered and therefore no longer contribute to $r^+$ peak, leading to the decline of its intensity. Second, from *Free ethyl 2* (Fig. 7.6c) to *Free methyl* (Fig. 7.6d), the peak $d_5^-$ vanishes. Indeed, in the latter all the $CH_2$ groups are frozen (Fig. 7.3e). Then, by comparing the simulated spectra to experiment (Fig. 7.6a), it appears that the *Free chain* model better correlates with it, owing to the peak around 2940 $cm^{-1}$ assigned to the $d_6^-$ $CH_2$ asymmetric stretching[1]. Experimentally, the peak located in that region is assigned to the Fermi resonance between $r^+$ and the C-H bending overtone. The underestimation of the intensity of the 2940 $cm^{-1}$ peak is therefore attributed to the anharmonicity effects, missing in the simulations but needed to account for Fermi resonance effects. However Fig. 7.6a also reveals the presence of a weak peak around 2910 $cm^{-1}$ that could be assigned from the simulations to $CH_2$ asymmetric stretching. This very weak intensity can be attributed to little disorder in the monolayer where gauche defects break centrosymmetry [58].

TABLE 7.3: $\omega$B97X-D/6-311G(d) IR, Raman, and SFG vibrational signatures for the $\equiv Si-(CH_2)_9CH_3$ system (calculated with the *Free chain*).

| label | IR[a] | Raman[a] | $\chi^{(2),Rb}_{ZZZ}$ | $\chi^{(2),Rb}_{XXZ}$ | $\chi^{(2),Rb}_{XZX}$ | $\chi^{(2),Rb}_{ZXX}$ | $\chi^{(2),Rb}_{YYZ}$ | $\chi^{(2),Rb}_{YZY}$ | $\chi^{(2),Rb}_{ZYY}$ |
|---|---|---|---|---|---|---|---|---|---|
| $g_1^+$ | 275.00 | 630.00 | 2947 | 577 | 20 | 338 | 577 | 20 | 338 |
| $g_2^+$ | 150.00 | 432.00 | 2309 | 409 | 8 | 233 | 409 | 8 | 233 |
| $d_1^+$ | 45.10 | 3.95 | 107 | 76 | 41 | 33 | 76 | 41 | 33 |
| $d_2^+$ | 123.00 | 57.10 | 160 | 131 | 31 | 46 | 131 | 31 | 46 |
| $r^+$ | 44.00 | 184.00 | 188 | 134 | 18 | 43 | 134 | 18 | 43 |
| $d_1^-$ | 0.02 | 206.00 | 156 | 109 | 15 | 32 | 109 | 15 | 32 |
| $d_2^-$ | 17.80 | 11.40 | 109 | 86 | 15 | 27 | 86 | 15 | 27 |
| $d_3^-$ | 36.00 | 13.90 | 93 | 78 | 9 | 25 | 78 | 9 | 25 |
| $d_4^-$ | 1.17 | 44.40 | 20 | 25 | 2 | 7 | 25 | 2 | 7 |
| $d_5^-$ | 0.90 | 11.10 | 22 | 25 | 13 | 5 | 25 | 13 | 5 |
| $d_6^-$ | 98.50 | 7.61 | 50 | 26 | 10 | 19 | 26 | 10 | 19 |
| $r^-$ | 51.30 | 149.00 | 324 | 19 | 14 | 86 | 19 | 14 | 86 |

[a] IR Intensities (km/mol) and Raman Intensities ($Å^4$/amu); [b] Moduli of $\chi^{(2),R}_{IJK}(\omega_q)$ tensor elements $\equiv \times 10^{-7}[m^2V^{-1}]$

[1]However, the experimental spectrum shows a weak peak around 2915 $cm^{-1}$ . This peak does not exist on the *Free chain* simulation, but it is well reproduced on the *Free methyl* simulation ($d_5^-$). From this point of view, this latter better correlates the experiment.

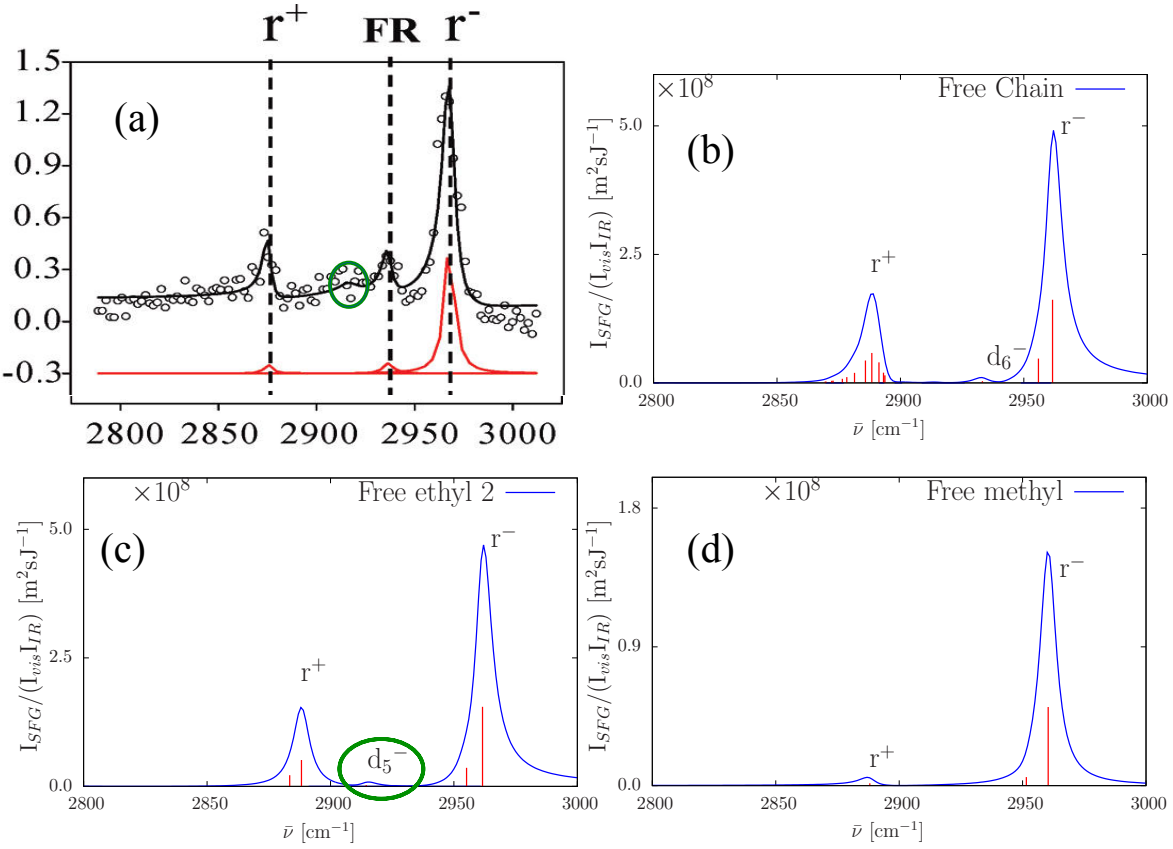


FIGURE 7.6: Comparison between the experimental and simulated SFG (*ppp*) spectra. (a) Experimental [50] *ppp* SFG spectra of $\equiv$ Si$-(CH_2)_9CH_3$; **"adapted with permission from H. Asanuma, H. Noguchi, Y. Huang, K. Uosaki, and H.Z. Yu, J. Phys. Chem. C 2009 113, 21139-21146. Copyright 2014 ACS."**; the solid lines (in black) show the best fits to the experimental data (open circles) based on Eqs 1 and 2 in Ref [50]; the deconvoluted peaks are shown in red at the bottom. (b) – (d) simulated SFG spectra (*ppp*) of $\equiv$ Si$-(CH_2)_9CH_3$. SFG intensities were calculated according to Eq. (7.8) assuming a damping factor of 4 cm$^{-1}$. Red lines under the peaks correspond to the SFG intensities calculated at the frequency of each mode [Eq. (7.9)] (see main text for details).

Calculations were then performed for the other sets of polarizations (*sps*, *ssp*, and *pss*: Fig. 7.7). In the left column (*Free chain*), from bottom (*ppp*) to top, the spectral profile varies considerably for the *ssp*, and *sps* sets of polarizations, while it remains almost similar for *pss* set of polarizations. This is accompanied by a decrease in the SFG intensity by about a magnitude of $10^4$ (potentially explaining why, in the literature, measurements are reported only for the *ppp* set of polarizations). For the *ssp*, and *sps* sets, the peak associated to the stretching of the $CH_2$ bonded to $CH_3$ becomes stronger than those of the $CH_3$ group, and the spectra are dominated by $d_2^+$ (*Free chain* and *Free ethyl 2*). These behaviors are related, on the one hand, to the variation of the Fresnel factors, and on the other hand, to that of the $\chi^{(2)}$ components contributing to the SFG intensities [Eqs. (7.5) to (7.8)]. By analyzing Table 7.4, listing the calculated square moduli of the Fresnel factors, one observes that the *ssp*, *sps*, and *pss* configurations are associated with similar amplitudes of $F_i^{SFG}F_j^{vis}F_k^{IR}$, which are about 1000 times smaller than with the *ppp* configuration. This comes mostly from the $\chi_{zzz}$ set. Note that, for this Si surface,

TABLE 7.4: Square Moduli of the Fresnel Factors computed for the three layers model. $\lambda_{vis}$= 532.0 nm ($\psi_{vis}$ = 70°)[a]; $\omega_{IR}$ = 2000-3000 cm$^{-1}$ ($\psi_{IR}$ = 50°)[a]; $\lambda_{SFG}$ = 480.8 − 458.8 nm ($\psi_{SFG}$ = 66 − 68°)[a].

| | $\lvert F_i^{SFG} F_j^{vis} F_k^{IR}\rvert^2$ | polarization sets |
|---|---|---|
| $F_Z^{SFG} F_Z^{vis} F_Z^{IR}$ | $2.0 \times 10^{0}$ | *ppp* |
| $F_X^{SFG} F_X^{vis} F_Z^{IR}$ | $6.8 \times 10^{-3}$ | *ppp* |
| $F_X^{SFG} F_Z^{vis} F_X^{IR}$ | $1.5 \times 10^{-2}$ | *ppp* |
| $F_Z^{SFG} F_X^{vis} F_X^{IR}$ | $1.7 \times 10^{-2}$ | *ppp* |
| $F_Y^{SFG} F_Y^{vis} F_Z^{IR}$ | $7.4 \times 10^{-4}$ | *ssp* |
| $F_Y^{SFG} F_Z^{vis} F_Y^{IR}$ | $3.5 \times 10^{-3}$ | *sps* |
| $F_Z^{SFG} F_Y^{vis} F_Y^{IR}$ | $3.6 \times 10^{-3}$ | *pss* |

[a] Refractive index $n$ and extinction coefficient $k$ of Si have been interpolated from the values of Ref [59] for $\lambda_{vis}$, $\lambda_{SFG}$, and each value of $\omega_{IR}$. $n_{\mathrm{SAM}} = 1.0$

the *ssp* case presents a smaller Fresnel coefficient than the *sps* one whereas for metallic surfaces the *sps* polarizations set possesses usually smaller Fresnel factors owing to the damped IR electric field oriented parallel to the surface. Hence, the larger intensities of the *ppp* polarizations configuration result from the fact that both the IR and UV electric fields possess components normal to the surface. Moreover, the change of spectral profile as well as the change in intensity as a function of the polarizations is also related to the relative amplitude of the $\chi^{(2),R}$ tensor elements (Table 7.3). One observes that modes clearly appearing on the spectra (Fig. 7.7) are those with large values of the IR and/or Raman intensities ($d_2^+$,$r^+$, and $r^-$), as well as the tensor components. Indeed, as shown is Eqs. (7.5) to (7.8), for each set of polarizations, the intensity is directly proportional to the corresponding $\chi^{(2)}$ tensor components. Globally, the $\chi_{ZZZ}$ and $\chi_{XXZ}$ (or $\chi_{YYZ}$) terms (the IR electric field is normal to the surface) dominate over the $\chi_{XZX}$ (or $\chi_{YZY}$) and $\chi_{ZXX}$ (or $\chi_{ZYY}$) terms (the IR electric field is parallel to the surface). When considering the modes individually, one observes that the $\chi_{ZZZ}$ (*ppp*) and $\chi_{ZYY}$ (*pss*) components of the $r^-$ mode are larger than that of $d_2^+$ and $r^+$, and the former therefore dominates the corresponding spectra (Fig. 7.7). For the other components ($\chi_{YYZ}$ and $\chi_{YZY}$), the observation is opposite. Indeed, $r^+$ intensities are weak compared to those of $d_2^+$ and $r^+$, and the latter therefore dominate the *ssp* ($\chi_{YYZ}$) and *sps* ($\chi_{YZY}$) spectra.

The SFG spectrum was then simulated for the Si-H stretching region (2000 − 2200 cm$^{-1}$) and the *ppp*, *sps*, *ssp*, and *pss* sets of polarizations (Fig. 7.8). The *ppp* spectrum (bottom) is composed of two peaks. The one at low frequency originates from several Si-H stretching modes (see the red lines under the peak) and therefore exhibit the strongest intensity, while that at high frequency comes from only one mode ($g_2^+$, 2090 cm$^{-1}$). Thus, the former is dominated by the $g_1^+$ mode (2080 cm$^{-1}$), which involves Si-H symmetric stretching of a larger number of H atoms (Fig. 7.5). Going from *ppp* to *ssp*, *sps* and *pss* leads to a decrease in intensities, whereas the spectral profiles are quasi identical. Indeed, all the H atoms stretch in the same direction and are therefore affected in the same way when changing the orientation of the electric fields. Moreover, the intensities of the Si-H stretching modes are even larger than those of the C-H

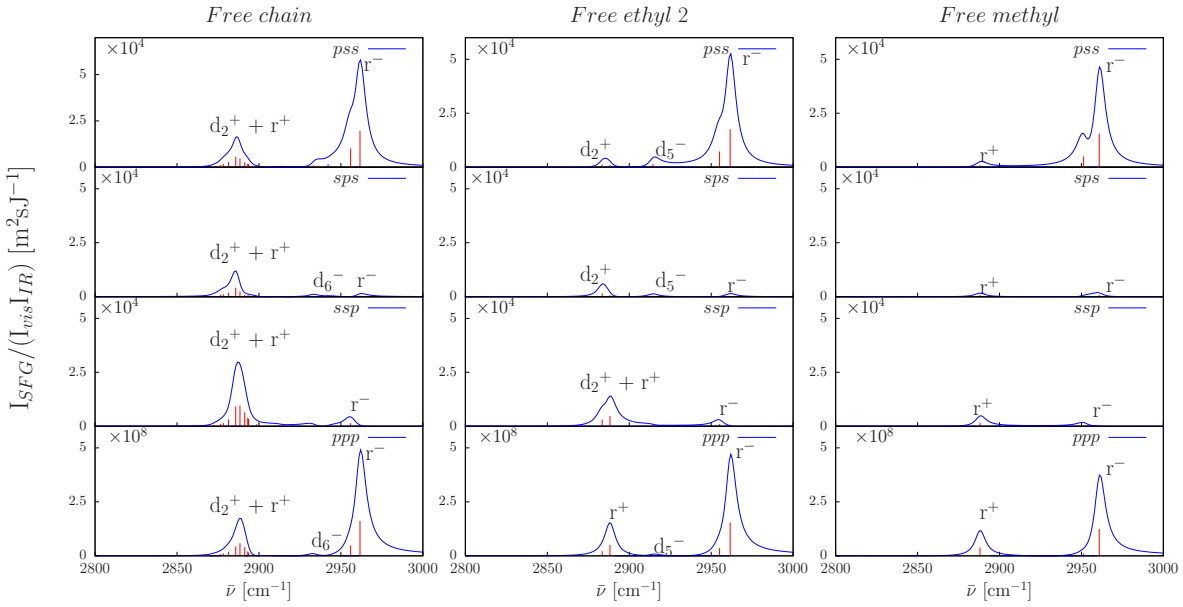


FIGURE 7.7: Simulated SFG spectra for the four sets of polarizations (*ppp*, *ssp*, *sps*, and *pss*) and the three models, in the C-H stretching region.

stretching modes (2800 - 3100 $cm^{-1}$). This larger intensity is explained by the derivatives of the dipole moment with respect to the normal coordinates, which are almost perpendicular to the surface (Fig. 7.5) and have a larger amplitude because of the larger polarity of the Si-H bond. Besides leading to large IR and Raman intensities they lead to dominant $\chi^{(2)}_{ZZZ}$ tensor components for the $g_1^+$ and $g_2^+$ modes.

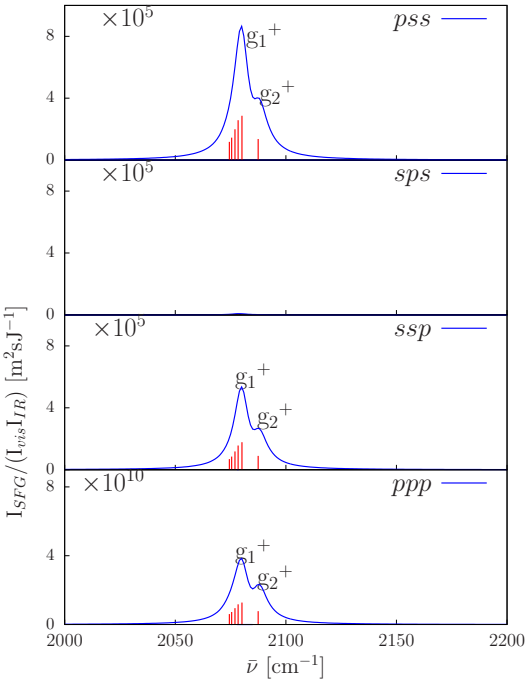


FIGURE 7.8: Simulated SFG spectra for the four sets of polarizations (*ppp*, *ssp*, *sps*, and *pss*) in the Si-H stretching region. Spectra were simulated with the *Free chain* model.

### 7.6.2 Without the surface: dependence on the rotation angle $\xi$

The impact of the orientation of the alkyl chain on the *ppp* SFG intensity was then studied by simulating spectra with specific values of $\xi$ ($\theta$ was kept constant at 43°), for the isolated decane molecule models (Figure 7.10). The spectral profile strongly depends on the sign of $\xi$ and in particular the relative intensities of the $r^+$ and $r^-$ peaks vary considerably. From negative to positive values of $\xi$, the intensity of the peak $r^+$ decreases while that of the peak $r^-$ increases. By analyzing Table 7.5, one observes that due to symmetry reasons, the $x$ component of their IR vectors as well as the $xy$ and $xz$ components of the Raman tensors are almost equal to zero. This observation is consistent with the fact that the IR vectors are in the $yz$ plane. Then, one observes on Fig. 7.11 that for the $r^+$ mode, going from negative (Fig. 7.11b) to positive (Fig. 7.11a) values of $\xi$, the IR vector switches from normal to tilted with respect to the surface, explaining the decrease of its intensity. on the contrary, for the $r^-$ mode ( Fig. 7.11d to Fig. 7.11c), the IR vector switches from parallel to almost normal with respect to the surface, leading to an increase of the intensity.

A global picture of these trends was highlighted by means of a scan on the rotation angle $\xi$ (from -180° to 180°) for two given tilt angles $\theta$ (43° and 35°), corresponding to the values obtained from $\omega$B97X-D calculations and experiment, respectively (Table 7.1). The results are depicted in Fig. 7.9. First, for $\theta = 43°$ (Fig. 7.9b, *Frozen methyl*), one observes two red spots corresponding to the large values of *ppp* intensity: around 2888 $cm^{-1}$ (-140°< $\xi$ <-40°) related to $r^+$ and around 2960 $cm^{-1}$ (40°< $\xi$ <160°) associated to $r^-$, in agreement with the above observation (Figure 7.10). Moving to *Free ethyl 1* (Figs. 7.9c and 7.9d) the spot around -140°< $\xi$ <-40° becomes less intense, while a small white spot appears around 40°< $\xi$ <160°, which is also consistent with the above observation (Figure 7.10). Second, from bottom ($\theta = 43°$, Figs. 7.9b and 7.9d) to top ($\theta = 35°$, Figs. 7.9a and 7.9c), the spots located around 2888 $cm^{-1}$ becomes less intense. Thus, the $r^+$ peak is expected to be less intense and sharp.

TABLE 7.5: $\omega$B97X-D/6-311G(d) components of the IR Vectors (a.u.) and Raman tensors (a.u.) of $r^+$ and $r^-$ decane vibrational normal modes in the molecular coordinates system (Fig. 7.11)

| | $\partial\mu_x/Q_p$ | $\partial\mu_y/Q_p$ | $\partial\mu_z/Q_p$ | $\partial\alpha_{xx}/Q_p$ | $\partial\alpha_{yy}/Q_p$ | $\partial\alpha_{zz}/Q_p$ | $\partial\alpha_{xy}/Q_p$ | $\partial\alpha_{xz}/Q_p$ | $\partial\alpha_{yz}/Q_p$ |
|---|---|---|---|---|---|---|---|---|---|
| $r^+$ | 0.000 | -0.122 | 0.172 | -7.940 | -6.734 | -7.367 | 0.001 | 0.001 | -0.590 |
| $r^-$ | 0.001 | -0.178 | -0.138 | -3.185 | 0.076 | 8.452 | 0.010 | -0.006 | 5.120 |

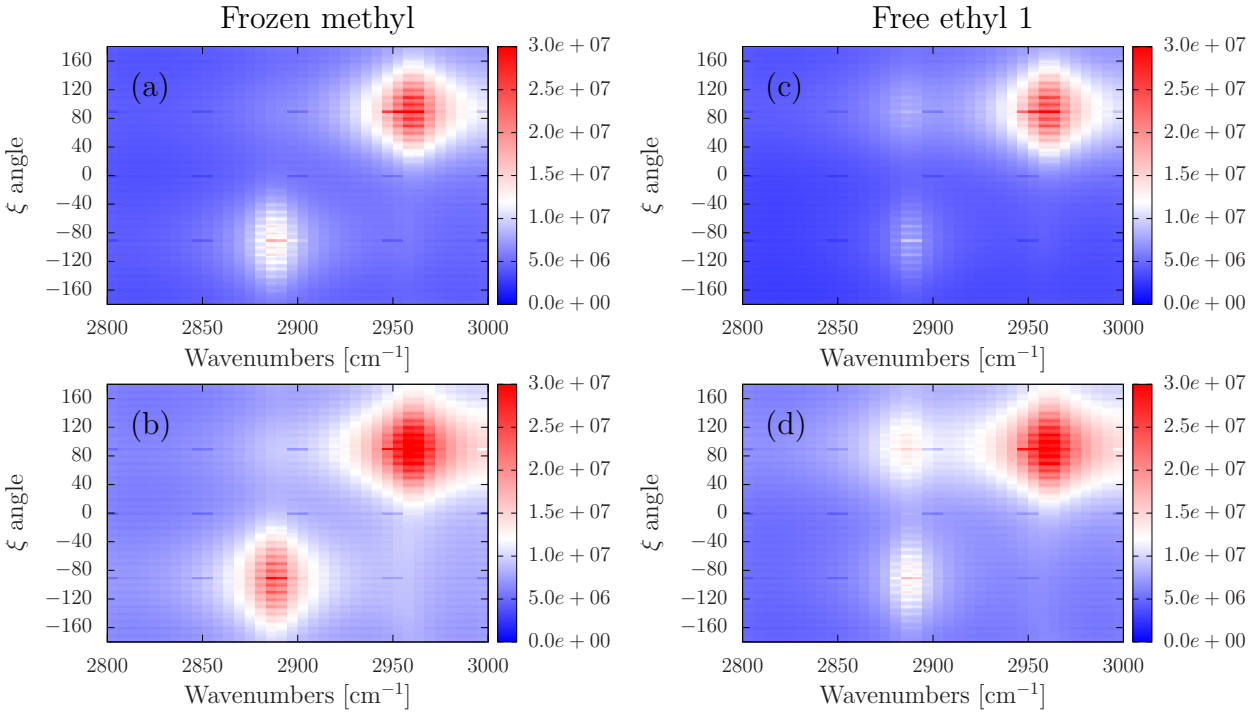


FIGURE 7.9: Map of *ppp* intensity as a function of the rotation angle $\xi$ for two values of the tilt angle: $\theta = 35°$ (top) and $\theta = 43°$ (bottom).

## 7.7 Conclusions

This work has reported on developments towards simulating and interpreting the sum-frequency generation signatures of functionalized surfaces. The elaborated approach encompasses two steps. First, the molecular properties (vibrational frequencies, IR and Raman quantities) are evaluated using first principles approaches implemented in standard quantum chemistry programs. Second, the macroscopic optical responses (the second-order nonlinear optical susceptibility tensor) of the adsorbate on its substrate are determined within the three-layer model of the interface. This latter step relies on a newly-developed homemade program, which calculates the Fresnel factor and accounts for the molecular orientation in the lab frame. This program allows generating the SFG spectra for different combinations of molecular orientations and experimental set-ups, as well as identifying the vibrational modes in order to facilitate their analysis.

The approach has been illustrated in the case of a decyl chain covalently bonded to hydrogen-terminated Si(111) $\left[\equiv \mathrm{Si}{-}(\mathrm{CH_2})_9\mathrm{CH_3}\right]$. The system is modeled with or without explicitly taking into account the nature of the surface while different moieties of the chain can be frozen to trace back the part of the chain from where the SFG signal originates. The molecular property calculations are performed at the DFT level with the $\omega$B97X-D XC-functional. When considering the whole system, the simulated *ppp* spectrum agrees closely with experiment, whereas the agreement gets worse upon freezing parts of the chain. Calculations have also been performed

for the other sets of polarizations (*sps*, *ssp*, and *pss*), highlighting that the spectral profile varies considerably from *ppp* to *ssp*, *sps*, and *pss*. First, the SFG intensity decreases by about 4 orders of magnitude. Second, the peaks associated to the vibrational modes located on the $CH_2$ group bonded to the $CH_3$ become stronger than those of the $CH_3$ group, owing to the $\chi^{(2),R}$ tensor elements.

When reducing the system to an isolated decane molecule, the impact of the orientation of the alkyl chain (tilt and rotation angles) on the *ppp* SFG intensity can be monitored, highlighting the IR wavelength region where the SFG intensities are strong. For instance, upon going from negative to positive values of the $\xi$ rotation angle, the intensity of the $CH_3$ symmetric stretching decreases while that of the asymmetric one increases, which has been related to the orientation of the IR dipole moment.

In the future, similar approach will be applied to investigate structural and SFG signatures of monolayer on metallic (such as gold) or insulating (such as silica) surfaces. In addition, the model will be improved by addressing the non resonant part of the susceptibility, as well as the anharmonicity effects.

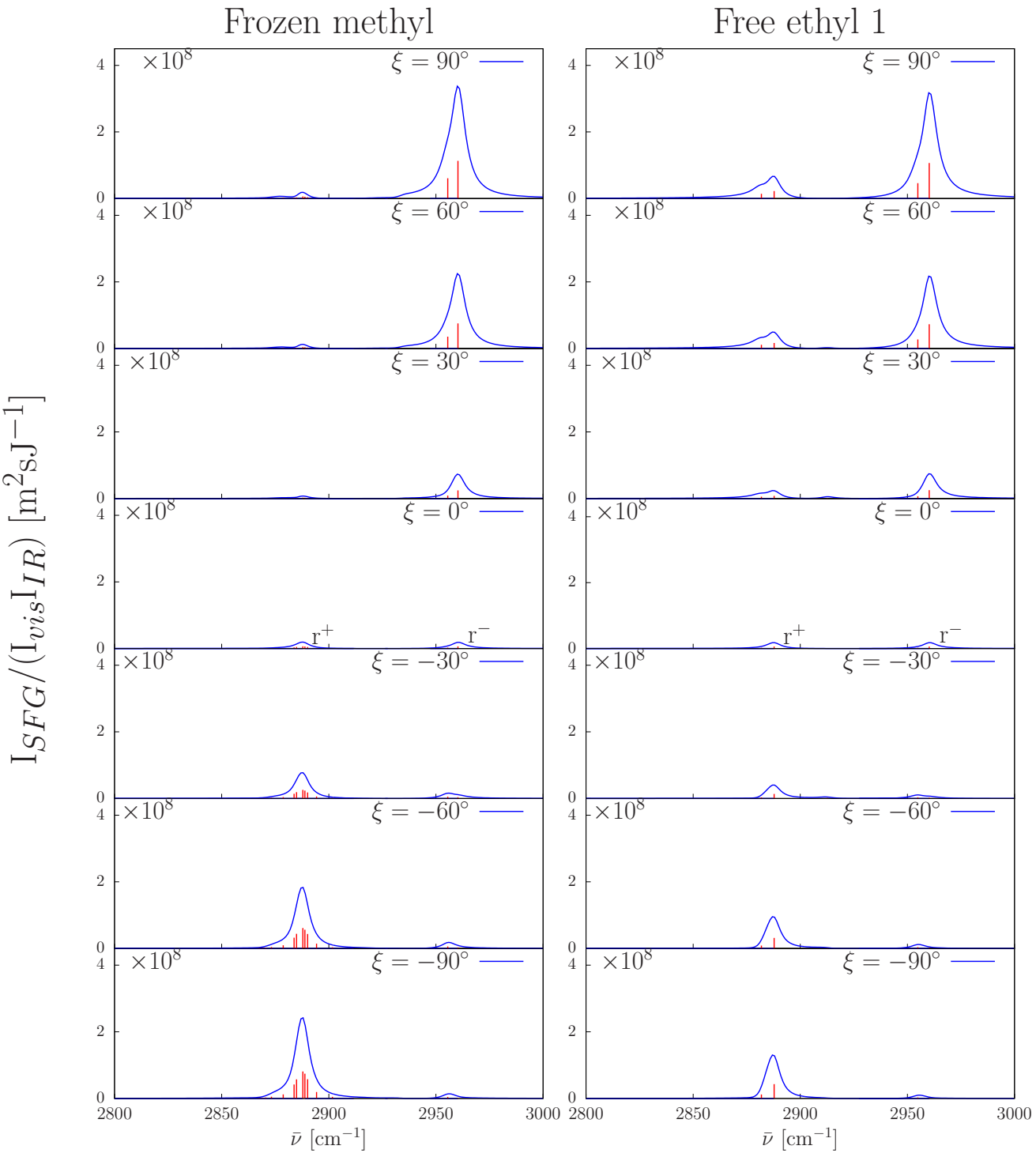


FIGURE 7.10: Simulated SFG spectra for the isolated decane molecule [models (a) and (b)], in *ppp* polarizations configuration. $\theta$ is set to 43°, while the spectra are simulated for different values of $\xi$.

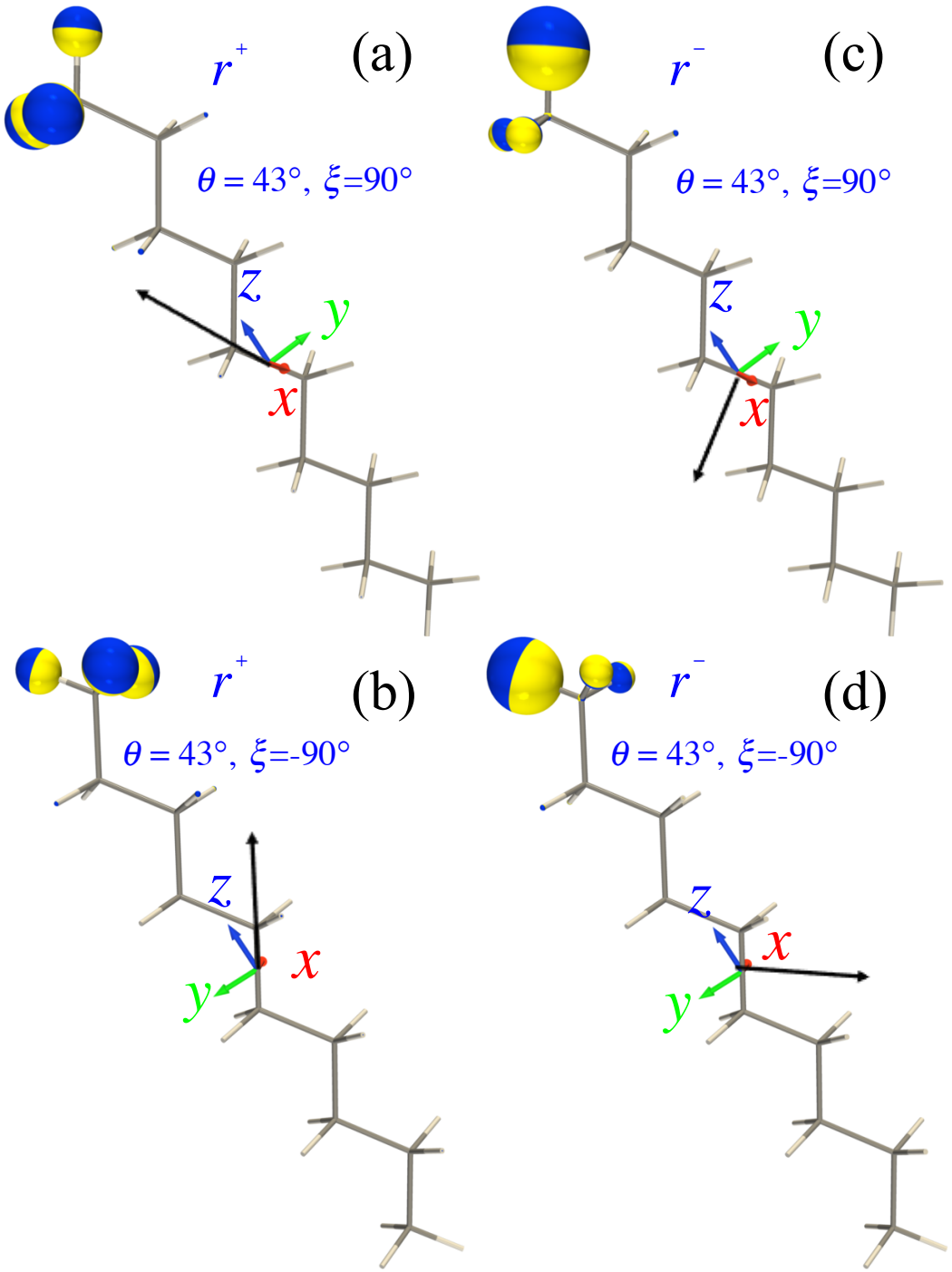


FIGURE 7.11: Sketch of $r^-$ (2960 $cm^{-1}$) and $r^+$ (2888 $cm^{-1}$) vibrational normal modes of the isolated decane molecule [model (a)] for two given orientations. The direction of the atomic displacements is perpendicular to the junction plane between the two hemispheres of distinct color, whereas their amplitudes are proportional to the sphere radius. The IR vectors $[(\partial\mu(x,y,z)/Q_p)_e]$ are shown in the molecular frame axes (red, green, and blue arrows) as black arrows.

# References

[1] Ulman, A. *Chem. Rev.* **1996**, *96*, 1533–1554.

[2] Yamashita, R.; Takeuchi, Y.; Kikuchi, H.; Shirai, K.; Yamauchi, T.; Tsubokawa, N. *Polym. J.* **2006**, *38*, 844–851.

[3] Li, H.; Yan, Y.; Liu, B.; Chen, W.; Chen, S. *Powder Technol.* **2007**, *178*, 203–207.

[4] Wagner, P.; Nock, S.; Spudich, J. A.; Volkmuth, W. D.; Chu, S.; Cicero, R. L.; Wade, C. P.; Linford, M. R.; Chidsey, C. E. D. *J. Struct. Biol.* **1997**, *119*, 189–201.

[5] Linford, M. R.; Fenter, P.; Eisenberger, P. M. *J. Am. Chem. Soc.* **1995**, *117*, 3145–3155.

[6] Faucheux, A.; Gouget-Laemmel, A. C.; Henry de Villeneuve, C.; Boukherroub, R.; Ozanam, F.; Allongue, P.; Chazalviel, J.-N. *Langmuir* **2006**, *22*, 153–162.

[7] Touahir, L.; Allongue, P.; Aureau, D.; Boukherroub, R.; Chazalviel, J. N.; Galopin, E.; Gouget-Laemmel, A. C.; de Villeneuve, C. H.; Moraillon, A.; Niedziółka-Jönsson, J.; Ozanam, F.; Andresa, J. S.; Sam, S.; Solomon, I.; Szunerits, S. *Bioelectrochemistry* **2010**, *80*, 17–25.

[8] Seitz, O.; Fernandes, P. G.; Mahmud, G. A.; Wen, H.-C.; Stiegler, H. J.; Chapman, R. A.; Vogel, E. M.; Chabal, Y. J. *Langmuir* **2011**, *27*, 7337–7340.

[9] Ye, S.; Saito, T.; Nihonyanagi, S.; Uosaki, K.; Miranda, P. B.; Kim, D.; Shen, Y.-R. *Surface Science* **2001**, *476*, 121–128.

[10] Ishibashi, T.-a.; Ara, M.; Tada, H.; Onishi, H. *Chem. Phys. Lett.* **2003**, *367*, 376–381.

[11] Asanuma, H.; Noguchi, H.; Uosaki, K.; Yu, H.-Z. *J. Phys. Chem. B* **2006**, *110*, 4892–4899.

[12] Dreesen, L.; Sartenaer, Y.; Humbert, C.; Mani, A. A.; Lemaire, J. J.; Méthivier, C.; Pradier, C. M.; Thiry, P. A.; Peremans, A. *Thin Solid Films* **2004**, *464-465*, 373–378.

[13] Asanuma, H.; Noguchi, H.; Uosaki, K.; Yu, H.-Z. *J. Am. Chem. Soc.* **2008**, *130*, 8016–8022.

[14] Rogero, C.; Chaffey, B. T.; Mateo-Martí, E.; Sobrado, J. M.; Horrocks, B. R.; Houlton, A.; Lakey, J. H.; Briones, C.; Martín-Gago, J. A. *J. Phys. Chem. C* **2008**, *112*, 9308–9314.

[15] Armstrong, J. A.; Bloembergen, N.; Ducuing, J.; Pershan, P. S. *Phys. Rev.* **1962**, *127*, 1918–1939.

[16] Bloembergen, N.; Pershan, P. S. *Phys. Rev.* **1962**, *128*, 606–622.

[17] Nihonyanagi, S.; Miyamoto, D.; Idojiri, S.; Uosaki, K. *J. Am. Chem. Soc.* **2004**, *126*, 7034–7040.

[18] Lu, R.; Gan, W.; Wu, B.-h.; Zhang, Z.; Guo, Y.; Wang, H.-f. *J. Phys. Chem. B* **2005**, *109*, 14118–14129.

[19] Romero, C.; Baldelli, S. *J. Phys. Chem. B* **2006**, *110*, 6213–6223.

[20] Ishiyama, T.; Sokolov, V. V.; Morita, A. *J. Chem. Phys.* **2011**, *134*, 024510.

[21] Cecchet, F.; Lis, D.; Caudano, Y.; Mani, A. A.; Peremans, A.; Champagne, B.; Guthmuller, J. *J. Phys.: Condens. Matter* **2012**, *24*, 124110.

[22] Tetsassi Feugmo, C. G.; Champagne, B.; Caudano, Y.; Cecchet, F.; Chabal, Y. J.; Liégeois, V. *J. Phys.: Condens. Matter.* **2012**, *24*, 124111.

[23] Kett, P.; Casford, M.; Davies, P. B. *J. Phys. Chem. Lett.* **2012**, *3*, 3276–3280.

[24] Jacob, J. D. C.; Rittikulsittichai, S.; Lee, T. R.; Baldelli, S. *J. Phys. Chem. C* **2013**, *117*, 9355–9365.

[25] Tetsassi Feugmo, C. G.; Liégeois, V. *ChemPhysChem* **2013**, *14*, 1633–1645.

[26] Roeters, S. J.; van Dijk, C. N.; Torres-Knoop, A.; Backus, E. H. G.; Campen, R. K.; Bonn, M.; Woutersen, S. *J. Phys. Chem. A* **2013**, *117*, 6311–6322.

[27] Jang, J. H.; Lydiatt, F.; Lindsay, R.; Baldelli, S. *J. Phys. Chem. A* **2013**, *117*, 6288–6302.

[28] Lu, X.; Myers, J. N.; Chen, Z. *Langmuir* **2014**, *30*, 9418–9422.

[29] Hall, S. A.; Jena, K. C.; Covert, P. A.; Roy, S.; Trudeau, T. G.; Hore, D. K. *J. Phys. Chem. B* **2014**, *118*, 5617–5636.

[30] Roy, S.; Covert, P. A.; FitzGerald, W. R.; Hore, D. K. *Chem. Rev.* **2014**, *114*, 8388–8415.

[31] Liu, S.; Fourkas, J. T. *J. Phys. Chem. B* **2014**, *118*, 8406–8419.

[32] Schleeger, M.; Nagata, Y.; Bonn, M. *J. Phys. Chem. Lett.* **2014**, *5*, 3737–3741.

[33] Hirose, C.; Akamatsu, N.; Domen, K. *J. Phys. Chem.* **1992**, *96*, 997–1004.

[34] Morita, A.; Hynes, J. T. *J. Phys. Chem. B* **2002**, *106*, 673–685.

[35] Brown, M. G.; Walker, D. S.; Raymond, E. A.; Richmond, G. L. *J. Phys. Chem. B* **2003**, *107*, 237–244.

[36] Lambert, A. G.; Davies, P. B.; Neivandt, D. J. *App. Spectro. Rev.* **2005**, *40*, 103–145.

[37] Backus, E. H. G.; Bonn, M. *Chem. Phys. Lett.* **2005**, *412*, 152–157.

[38] Morita, A.; Ishiyama, T. *Phys. Chem. Chem. Phys.* **2008**, *10*, 5801–5816.

[39] Guthmuller, J.; Cecchet, F.; Lis, D.; Caudano, Y.; Mani, A. A.; Thiry, P. A.; Peremans, A.; Champagne, B. *ChemPhysChem* **2009**, *10*, 2132–2142.

[40] Busson, B.; Tadjeddine, A. *J. Phys. Chem. C* **2009**, *113*, 21895–21902.

[41] Humbert, C.; Pluchery, O.; Lacaze, E.; Tadjeddine, A.; Busson, B. *Phys. Chem. Chem. Phys.* **2012**, *14*, 280–289.

[42] Cecchet, F.; Lis, D.; Guthmuller, J.; Champagne, B.; Fonder, G.; Mekhalif, Z.; Caudano, Y.; Mani, A. A.; Thiry, P. A.; Peremans, A. *J. Phys. Chem. C* **2010**, *114*, 4106–4113.

[43] Nagata, Y.; Mukamel, S. *J. Am. Chem. Soc.* **2010**, *132*, 6434–6442.

[44] Jena, K. C.; Hung, K.-K.; Schwantje, T. R.; Hore, D. K. *J. Chem. Phys.* **2011**, *135*, 044704.

[45] Liégeois, V.; Champagne, B. *Theor. Chem. Acc.* **2012**, *131*, 1284.

[46] O'Brien, D. B.; Massari, A. M. *J. Chem. Phys.* **2013**, *138*, 154708.

[47] Velarde, L.; Wang, H.-f. *Phys. Chem. Chem. Phys.* **2013**, *15*, 19970.

[48] Sulpizi, M.; Salanne, M.; Sprik, M.; Gaigeot, M.-P. *J. Phys. Chem. Lett.* **2013**, *4*, 83–87.

[49] Zheng, R.-H.; Wei, W.-M.; Liu, H.; Jing, Y.-Y.; Wang, B.-Y.; Shi, Q. *J. Chem. Phys.* **2014**, *140*, 104702.

[50] Asanuma, H.; Noguchi, H.; Huang, Y.; Uosaki, K.; Yu, H.-Z. *J. Phys. Chem. C* **2009**, *113*, 21139–21146.

[51] Frisch, M. J. et al. Gaussian 09 Revision B.01. Gaussian Inc. Wallingford CT 2009.

[52] Chai, J.-D.; Head-Gordon, M. *Phys. Chem. Chem. Phys.* **2008**, *10*, 6615–6620.

[53] Scott, A. P.; Radom, L. *J. Phy. Chem.* **1996**, *100*, 16502–16513.

[54] Zhang, L.; Wesley, K.; Jiang, S. *Langmuir* **2001**, *17*, 6275–6281.

[55] Yoder, C. Common Bond Energies (D) and Bond Length (r). 2014; http://www.wiredchemist.com/chemistry/data/bond_energies_lengths.html.

[56] Rosenbaum, E. J. *J. Phys. Chem.* **1941**, *9*, 295–297.

[57] Fedorovsky, M. PyVib2, a program for analyzing vibrational motion and vibrational spectra. http://pyvib2.sourceforge.net, 2007.

[58] Lis, D.; Peremans, A.; Sartenaer, Y.; Caudano, Y.; Mani, A. A.; Dreesen, L.; Thiry, P. A.; Guthmuller, J.; Champagne, B.; Cecchet, F. *J. Phys. Chem. C* **2009**, *113*, 9857–9864.

[59] Schubert, E. F. Refractive index and extinction coefficient of materials. https://www.ecse.rpi.edu/~schubert/Educational-resources/Materials-Refractive-index-and-extinction-coefficient.pdf.

Tetsassi Feugmo, C. G.; Liégeois, V.; Caudano, Y.; Cecchet, F.; Champagne, B. **2018**, submitted

**Personal contribution:** I selected the systems with my co-authors, then I ran all calculations, and simulated the SFG signatures with the new Python program. Finally, I proposed analyses, discussed these with my co-authors, and I wrote the first draft of the paper.

# Chapter 8

# Probing Alkylsilane Molecular Structure on Amorphous Silica Surfaces by Vibrational Sum-Frequency Generation Spectroscopy: First Principles Calculations

In this chapter, the SFG signatures of octadecyl-trichlorosilane (OTS) and dodecyl-dimethyl-chlorosilane (DDCS) monolayers on silica were simulated in the C−H stretching region for three polarization combinations (ppp, sps, and ssp), showing the impact of the additional Si-linked methyl groups of DDCS on its SFG signatures. These simulations are based on a two-step procedure where i) the molecular properties (vibrational frequencies, IR and Raman intensities) are evaluated using first principles methods and ii) the three-layer model is employed to calculate the macroscopic responses from these molecular responses, the geometry of the experimental set-up, and the optical properties of the layers. These first principles calculations adopt the ONIOM approach, which describes the successive layers of the system at different levels of approximation. Here, the same $\omega$B97X-D exchange-correlation functional is used but the lower layer is described with a smaller atomic basis set (STO-3G, 3-21G, or 6-31G) than the higher one (6-311G*). Calculations show that for describing the low layer the minimal STO-3G basis set already provides reliable spectral profiles. For OTS, the results are compared to experiment, demonstrating a good agreement for ppp and sps configurations, provided the refractive index of the layer $n_l$ is set to 1.1. To highlight the origin of the SFG signatures, two chemical models were used, one includes explicitly the $SiO_2$ surface in the first principles calculations (*adsorbed-model*) and the other only considers the silane chain (*isolated-model*). Simulations show that OTS and DDCS display similar spectral patterns where, for ppp and sps configurations, the $r^-$ $CH_3$ stretching vibrations are dominant in comparison to the $r^+$ stretching ones. Still, in

the case of DDCS, the $r^-$ peak presents a shoulder, which is assigned to the vibrations of the Si-linked methyl groups. This shoulder vanishes when these $CH_3$ groups are frozen. Then, using the *isolated-model*, the rotation angle ($\xi$) was gradually changed, showing that in the ppp SFG spectrum the $r^-/r^+$ intensity ratio decreases from 73.4 at 0° to 1.7 at 180°.

## 8.1 Motivations

Since many decades a great interest has been dedicated to the study of silane monolayers on silica due to their particular tribological properties, [1–4] their adhesion [5–7] and adsorption [8–10] characteristics, as well as their thermal and mechanical stabilities [11–15]. These properties have led to versatile applications, including in coatings,[16, 17] in optoelectronics, [18–21] and in biosensors. [5, 10, 22] For instance, among silane derivatives, alkylsilanes are especially interesting because they can be used as $SiO_2$-based micro- and nano-electromechanical systems (MEMS and NEMS) [23–25]. Depending on the nature of the end group, hydrophobic or hydrophilic surfaces can be achieved [5, 9, 10, 15], while the orientation and the conformation of the silanes plays a crucial role in their function. Therefore, knowing and controlling the relative location and orientation of the silanes layer is required to obtain the targeted properties. In order to understand the relationships between the chemical composition and the layer properties, many investigations have been carried out where the size of the silane and its chemical functionalization have been varied and where the characterizations are performed using Atomic Force Microscopy (AFM) [12, 22, 26], X-ray Photoelectron Spectroscopy (XPS) [1, 27] Infrared Spectroscopy, (FTIR, ATR) [22, 26, 28, 29], and, from time to time, infrared-visible Sum Frequency Generation (SFG) vibrational spectroscopy [10, 30–32].

SFG [33] is a powerful and versatile method for *in situ* investigations of surfaces and interfaces. In SFG experiment a tunable infrared laser beam of angular frequency $\omega_{IR}$ is mixed with a visible beam of angular frequency $\omega_{Vis}$ to produce an output beam at the sum frequency, $\omega_{SFG} = \omega_{IR}+\omega_{Vis}$. SFG is a second-order nonlinear optical process, which is dipole-allowed only in media lacking inversion symmetry. At surfaces and interfaces, the inversion symmetry is intrinsically broken, making SFG highly surface specific. When scanning the IR frequency, active vibrational modes of the molecules at the interface give resonant contributions to the SFG signal, which are signatures of their nature and spatial organization.

To our knowledge, the first SFG experiment on silanes monolayers adsorbed onto a silica surface was carried out by Guyot-Sionnest et al. [30] They reported that n-octadecyl-trichlorosilane (OTS) monolayers on silica are oriented almost normal to the surfaces ($\theta < 15°$), while the tilt angle ($\alpha$) of the terminal methyl groups was estimated to range between 40° and 50°. Few years later, Löbau et al. [31] performed *in situ* SFG monitoring of surface contaminations under normal atmospheric conditions to assess the effectiveness of cleaning and activation of alkyl-trichlorosilanes [propyl-trichlorosilane (PTS) and OTS] on glass and silicon, and they reported

tilt angle values for the terminal methyl groups of $23 \pm 2°$ and $25 \pm 2°$ for PTS and OTS, respectively. In 2001, the conformational changes occuring during the adsorption process of OTS self-assembled monolayers on fused silica surfaces were monitored by SFG.[34] Later on, Yang et al. [32] used SFG to study self-assembled triethoxysilane thin films adsorbed onto hydrophilic SiOx/Si substrates. They showed that SAMs made of silanes with short (propyl) or branched (2-(diphenylphosphino)ethyl) alkyl chains exhibit poor ordering, whereas longer alkyl chains (octadecyl and decyl) lead to more ordered monolayers.

Due to their complementarity, numerical simulations based on classical or quantum mechanics were performed to assist experimental studies on the characterization of the structure of alkylsilane monolayers. Most of these calculations relied on molecular dynamics (MD), [1, 24, 35–37] because the lower computational costs allowed studying systems containing several adsorbed molecules. These studies highlighted the dependence of the average tilt angle on the monolayer density and on the chain length. For OTS on silica, the calculated tilt angle value was reported to range from 16° to 23° [37–39] at high coverage ($4.3 - 5.0$ molecule/nm$^2$). On the other hand, to access detailed information on the structure of the surface anchoring point as well as on the vibrational signatures, first principles calculations are more accurate. So far, first principles calculations were used to study silane-functionalized surfaces, but they reported on surface reaction mechanisms, [26, 40–42] not on the vibrational signatures.

Herein, we carry out first principles calculations to simulate and interpret the SFG signatures of alkylsilanes adsorbed onto amorphous silica surfaces. Considering the availability of experimental data, we first study the OTS system. Then, we predict the SFG signatures of dodecyl-dimethyl-chlorosilane (DDCS) molecule on silica surfaces, to highlight the impact of the additional Si-linked methyl groups closed to the silica surface. By adopting the procedure presented in Ref. [43], SFG spectra are simulated by a two-step procedure that combines i) the calculation of the molecular properties (vibrational frequencies, IR and Raman intensities) using first principles methods and ii) the three-layer model to calculate the macroscopic responses from the above molecular responses, the geometry of the experimental set-up, and the optical properties of the layers. In particular, the first principles calculations adopt the ONIOM approach, which describes each part (successive layers) of the system at different levels of approximation (different basis sets). These calculations provide direct information on the anchoring point as well as on the structure of the $CH_2$ and $CH_3$ groups of the silanes alkyl chain, whose stretching modes are the main signatures of the SFG spectra in the probed region (between 2800 and 3000 cm$^{-1}$). The work is organized as follows: i) the simulation method is described in the next Section, then ii) the results are presented and discussed in Section III before iii) conclusions are drawn in Section IV.

## 8.2 Main SFG equations and computational approach

For a surface with X-Z and Y-Z mirror planes there are four optically active polarization combinations, denoted as ppp, ssp, sps, and pss (by convention, given in the SFG, Vis, IR order). Still, note that the sps and pss combinations differ only by the Fresnel and trigonometric factors (since $\chi^{(2)}_{YZY} = \chi^{(2)}_{ZYY}$). The corresponding intensities read:

$$\underbrace{\frac{I_{ssp}}{I_{IR}I_{Vis}}}_{\mathrm{m^2w^{-1}}} = \underbrace{\frac{\omega^2_{SFG}}{2c^3\varepsilon_0 n_1(\omega_{SFG})n_1(\omega_{IR})n_1(\omega_{Vis})\cos^2\theta_{SFG}}}_{\mathrm{m^{-2}C^{-1}Vs}} \times \underbrace{\left|\sin\theta_{IR}\chi^{(2)}_{YYZ}F^{SFG}_Y F^{Vis}_Y F^{IR}_Z\right|^2}_{\mathrm{m^4V^{-2}}}, \tag{8.1}$$

$$\frac{I_{sps}}{I_{IR}I_{Vis}} = \frac{\omega^2_{SFG}}{2c^3\varepsilon_0 n_1(\omega_{SFG})n_1(\omega_{IR})n_1(\omega_{Vis})\cos^2\theta_{SFG}} \times \left|\sin\theta_{Vis}\chi^{(2)}_{YZY}F^{SFG}_Y F^{Vis}_Z F^{IR}_Y\right|^2, \tag{8.2}$$

$$\begin{aligned}\frac{I_{ppp}}{I_{IR}I_{Vis}} =& \frac{\omega^2_{SFG}}{2c^3\varepsilon_0 n_1(\omega_{SFG})n_1(\omega_{IR})n_1(\omega_{Vis})\cos^2\theta_{SFG}} \times \\ &\Big| -\cos\theta_{SFG}\cos\theta_{Vis}\sin\theta_{IR}\,\chi^{(2)}_{XXZ}\,F^{SFG}_X F^{Vis}_X F^{IR}_Z \\ &-\cos\theta_{SFG}\sin\theta_{Vis}\cos\theta_{IR}\,\chi^{(2)}_{XZX}\,F^{SFG}_X F^{Vis}_Z F^{IR}_X \\ &+\sin\theta_{SFG}\cos\theta_{Vis}\cos\theta_{IR}\,\chi^{(2)}_{ZXX}\,F^{SFG}_Z F^{Vis}_X F^{IR}_X \\ &+\sin\theta_{SFG}\sin\theta_{Vis}\sin\theta_{IR}\,\chi^{(2)}_{ZZZ}\,F^{SFG}_Z F^{Vis}_Z F^{IR}_Z\Big|^2,\end{aligned} \tag{8.3}$$

where $\theta_{Vis}$ and $\theta_{IR}$ are the angles of incidence of the IR ($\omega_{IR}$) and visible ($\omega_{Vis}$) beams (with respect to the normal to the surface), while $\theta_{SFG}$ is the angle between the light reflected at $\omega_{SFG}$ and the normal to the surface. $n_1(\omega)$ is the refractive index of the incident medium at frequency $\omega$, $\varepsilon_0$ is the vacuum permittivity, and $c$ is the speed of light in vacuum. The $F_I$ quantities are the Fresnel factors (*vide supra* Eq. (8.6)) and the $\chi^{(2)}_{IJK}$ are the components of the surface second-order nonlinear susceptibility tensor, containing a resonant (vibrational) and a non-resonant (electronic) term.

$$\chi^{(2)}_{IJK} = \overbrace{\left|\chi^{(2),NR}_{IJK}\right| e^{i\varphi_{SFG}}}^{non-resonant} + \overbrace{\underbrace{\frac{N_s}{\varepsilon_0}}_{\mathrm{VC^{-1}m^{-1}}} \sum_{\alpha,\beta,\gamma} \langle T_{I\alpha J\beta K\gamma}(\phi,\theta,\xi)\beta_{\alpha\beta\gamma}(-\omega_{SFG};\omega_{Vis},\omega_{IR})\rangle}^{resonant}, \tag{8.4}$$

$$\chi^{(2),R}_{IJK} \equiv [\mathrm{m^2V^{-1}}]$$

where the $\alpha\beta\gamma$ element of the molecular vibrational first hyperpolarizability tensor reads

$$\beta_{\alpha\beta\gamma}(-\omega_{SFG};\omega_{Vis},\omega_{IR}) = \sum_p \underbrace{\frac{1}{4\omega_p}\frac{\left(\frac{\partial\alpha_{\alpha\beta}(\omega_{Vis})}{\partial Q_p}\right)_e\left(\frac{\partial\mu_\gamma}{\partial Q_p}\right)_e}{\left(\omega_p-\omega_{IR}-i\Gamma_p\right)}}_{\mathrm{C^3m^3J^{-2}}} \tag{8.5}$$

In Eq. (8.4), $\varphi_{SFG}$ is the phase shift angle between the resonant and non-resonant terms, $N_S$ is the molecular surface density, $T$ is the transformation matrix between the laboratory and molecular coordinates systems (related through the Euler angles $\phi, \theta$, and $\xi$). In Eq. (8.5), $\Gamma_p$ is the damping coefficient, $\omega_p$ is the frequency of the $p^{th}$ vibrational normal mode, $\omega_{IR}$ is the frequency of the incident IR light, and $\left(\frac{\partial \mu_\gamma}{\partial Q_p}\right)_e$ and $\left(\frac{\partial \alpha_{\alpha\beta}(\omega_{Vis})}{\partial Q_p}\right)_e$ are the derivatives of the $\gamma$ and the $\alpha\beta$ components of the dipole moment and dynamic polarizability (at $\omega_{Vis}$) with respect to the normal coordinate $Q_p$ evaluated at the equilibrium geometry, respectively. Within the three layers approach, the Fresnel factors for non-magnetic media read

$$F_I = \begin{cases} \mathrm{F_X}(\varepsilon_1, \varepsilon_2, \theta) & = & \dfrac{2\varepsilon_1\sqrt{\varepsilon_2 - \varepsilon_1 \sin^2\theta}}{\varepsilon_2\sqrt{\varepsilon_1}\cos\theta + \varepsilon_1\sqrt{\varepsilon_2 - \varepsilon_1\sin^2\theta}}, \\ \mathrm{F_Y}(\varepsilon_1, \varepsilon_2, \theta) & = & \dfrac{2\sqrt{\varepsilon_1}\cos\theta}{\sqrt{\varepsilon_1}\cos\theta + \sqrt{\varepsilon_2 - \varepsilon_1\sin^2\theta}}, \\ \mathrm{F_Z}(\varepsilon_1, \varepsilon_l, \varepsilon_2, \theta) & = & \dfrac{\varepsilon_1}{\varepsilon_l}\dfrac{2\varepsilon_2\sqrt{\varepsilon_1}\cos\theta}{\varepsilon_2\sqrt{\varepsilon_1}\cos\theta + \varepsilon_1\sqrt{\varepsilon_2 - \varepsilon_1\sin^2\theta}}. \end{cases} \tag{8.6}$$

where $\varepsilon_1$, $\varepsilon_l$, $\varepsilon_2$, are the relative electric permittivity of the incident medium, of the thin layer, and of the substrate, respectively, which depend on the refractive index $n$ and extinction coefficient $k$ of that medium [$\varepsilon = (n + ik)^2$ is real for a transparent medium]. $\theta$ is either the IR or visible incident angle, or the SFG reflected angle. The refractive indices and extinction coefficients of $SiO_2$ were interpolated from the values in Ref [44] for visible, SFG, and IR wavelengths. In the previous equations, all the molecular properties [$(\partial\mu/\partial Q)$ and $(\partial\alpha/\partial Q)$] are evaluated at *ab initio* quantum chemistry levels.

Calculations of the molecular property were performed at the density functional theory (DFT) level of approximation and using the "Own N-layered Integrated Orbital Molecular Mechanics" (ONIOM) method. [45] It is a hybrid computational approach that enables different levels of approximation [e.g. Quantum Mechanics (QM) , Semi-Empirical (SE), Molecular Mechanics (MM), Coarse-Grained (CG), and Continuum Model (CM) methods] to be applied to different parts of a molecule/system, and to be combined to produce reliable results at reduced computational costs. In this work, we use the two-layered ONIOM scheme implemented in the Gaussian package. [46] We described both layers at the QM level using DFT and the $\omega$B97X-D exchange-correlation functional, [47] but different atomic basis sets. We found the 6-311G* basis set adequate to describe the high-layer, whereas we used three different basis sets for the low-layer: STO-3G, 3-21G, and 6-31G.

To model the silane monolayer on silica and its SFG signatures, two approaches used: the *isolated-model* and the *adsorbed-model*. The former applies the QM calculation to the silane

molecule. To mimic adsorption, the chlorine atoms of OTS and DDCS were replaced by hydroxyl groups (−OH). This model has been used in several previous works to deduce the molecular orientation of adsorbed species from experimental data. [48–51] The latter model carries out first principles calculations on both the silane molecule and the fragment of $SiO_2$ to which it is attached. Here, the $SiO_2$ cluster was made from a (111) $\beta$-cristobalite surface. Indeed, previous theoretical calculations showed that the $SiO_2$/Si surface (SAMs on oxidized Si wafer surfaces) was well represented by a (111) surface of $\beta$-cristobalite. [1, 24, 52–54] Then, the oxygen atoms were saturated by hydrogens, and finally one hydrogen atom was replaced by the hydroxyl form of an alkylsilane (OTS or DDCS) molecule. In both cases, the (remaining) surrounding effects were taken into account via the three-layer model and the electric permitivity of the surface, introduced in the Fresnel factors. Then, using the molecular properties as well as the geometry of the experimental set-up and the optical properties of the layers, the surface second-order nonlinear optical susceptibility, the Fresnel factors, and the SFG intensities were calculated within the three-layer model. Finally, the SFG spectra were simulated. More details can be found in Ref [43]. These simulations are carried out using a homemade Python program.

## 8.3 Results and discussions

### 8.3.1 Geometrical parameters

The geometries were optimized under the constraint that the residual forces must be smaller than $10^{-5}$au. Fig. 8.1 presents the optimized geometries of the OTS and DDCS models. In the *adsorbed-model*, the high-layer consists of the alkylsilane molecule and the top $SiO_2$ layer, while the low-layer consists of the remaining $SiO_2$ layers (bulk-like). The molecular system coordinates are defined with the red ($x$), green ($y$) and blue ($z$) arrows, whereas the laboratory $Z$-axis is represented by the cyan arrow. This latter is calculated using the least-squares approach as the normal to the best plane through the Si atoms highlighted with blue dots in Fig. 8.1, while the molecular $z$-axis is fitted using the least-squares approach as the best vector through the Si atom and the C atoms of the silane molecule. The tilt angle of the alkyl chain $\theta$ is therefore defined as the angle between that $z$-axis and the laboratory $Z$-axis, while $\alpha$ is the tilt angle of the terminal ($CH_2$−$CH_3$) bond with respect to the $Z$-axis. $\xi$ defines the rotation of the plane of the alkyl chain (the plane containing the zig-zag carbon backbone) around the molecular $z$-axis, with respect to the situation where the backbone plane coincides with the plane defined by the $z-$ and $Z$-axes.

Using the *adsorbed-model*, the angles describing the orientation of the alkyl chain as determined from ONIOM geometry optimizations are reported in Table 8.1 as a function of the basis sets employed to describe the low-layer. In the case of OTS, upon enlarging this basis set, the $\theta$ and $\xi$ angles remain constant at 12° and 80°, respectively, whereas $\alpha$ decreases by 5°. These calculated values for $\theta$ are close to the $\theta < 15°$ result, deduced analytically [55] from the ratio of

the symmetric $CH_3$ stretching intensities measured in the ssp and sps polarization combinations, [30] while they are smaller than those calculated with MD simulations ($16° \leq \theta \leq 23°$). [37–39] Moreover, the $\alpha$ values ($33° \leq \alpha \leq 38°$) are in close agreement with those reported by Guyot-Sionnest et al. [30] ($40° < \alpha < 50°$). For DDCS, when extending the low-layer basis set, $\theta$ and $\alpha$ values slightly vary: $12° \leq \theta \leq 22°$ and $18° \leq \alpha \leq 25°$, whereas $\xi$ remains almost constant ($\xi \sim 59°$). However, in comparison to OTS it appears that the $\theta$ angle increases by 7° while the $\alpha$ and $\xi$ values decrease by 13 to 19°. This behavior may be explained by the presence of two additional $CH_3$ groups in the DDCS, which leads to an increased tilting of the chain.

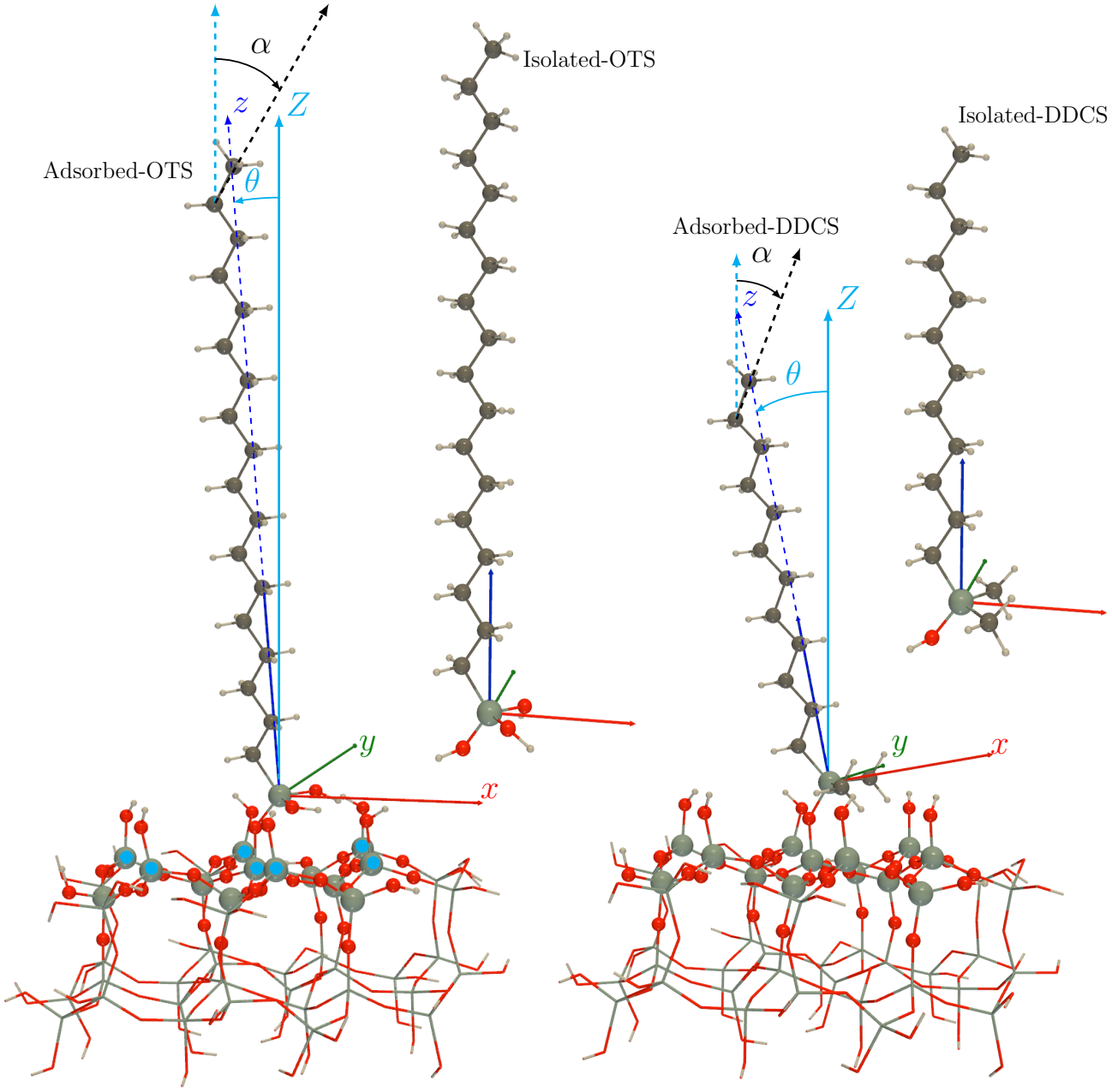


FIGURE 8.1: Optimized geometries determined at the ONIOM($\omega$B97X-D/6-311G*:$\omega$B97X-D/STO-3G) (*adsorbed-model*) or $\omega$B97X-D/6-311G* (*isolated-model*) levels of approximation. Left) OTS, Right) DDCS. The atoms of the ONIOM low-layer are represented with sticks and those of the high-layer with balls and sticks. See the text for more details on the coordinates axes. Models are illustrated using DrawMol [56].

TABLE 8.1: Orientation angles of the alkyl chain of OTS and DDCS on the $SiO_2$ cluster as determined at the ONIOM($\omega$B97X-D/6-311G*:$\omega$B97X-D/*basis*) level of approximation (*basis* $\equiv$ STO-3G, 3-21G, and 6-31G).

| | OTS | | | DDCS | | |
|---|---|---|---|---|---|---|
| | $\theta$ [°] | $\xi$ [°] | $\alpha$ [°] | $\theta$ [°] | $\xi$ [°] | $\alpha$ [°] |
| STO-3G | 12 | 80 | 38 | 12 | 58 | 25 |
| 3-21G | 12 | 80 | 33 | 22 | 59 | 18 |
| 6-31G | 12 | 79 | 33 | 19 | 60 | 20 |

### 8.3.2 Vibrational frequencies, IR and Raman activities

For the optimized geometries, the vibrational frequencies, IR and Raman activities were calculated for both OTS and DDCS systems, at the same level of approximation. During that step, all the atoms of the low-layer (Fig. 8.1) were kept fixed. Harmonic vibrational frequencies and normal modes were calculated analytically at the same level of approximation, by setting atomic masses of 1000 amu for the atoms of the low-layer (freezing procedure [43, 57]), as well as for the H atoms saturating the oxygen dangling bonds (i.e. those that do not belong to the top area), to mimic larger and thicker $SiO_2$ layers. To account for missing anharmonic effects as well as for the limitations of the XC functional, the harmonic vibrational frequencies were scaled by a factor of 0.95. [58, 59] Frequencies of selected C−H stretching normal modes as well as their IR and Raman intensities are summarized in Table 8.2 for OTS and Table 8.3 for DDCS, while they are represented in Fig. 8.2 for OTS and Fig. 8.3 for DDCS. For OTS, upon adsorption, the vibrational frequencies remain almost constant. It is also the case when enlarging the basis set of the low-layer. The same behavior is observed for the IR and Raman intensities. Nevertheless, contrary to what might be expected for the $CH_2$ groups in a all-trans conformation, the $d^+$ [$(CH_2)_{sym}$] mode (localized on the $CH_2$ adjacent to the $CH_3$, Fig. 8.2) is both IR and Raman active, and therefore expected to be SFG active (However, it is worth noting that in addition to the symmetry selection rules, SFG activity of the $CH_2$ groups is also killed by the rotational average at the surface).

For the DDCS system, knowing that the molecule possesses two additional $CH_3$ groups, the vibrations of those $CH_3$ groups (bottom groups) were *controlled*, i.e. in some cases they were frozen (their vibrations were hampered by setting large masses on atoms) on purpose during the calculations in order to highlight vibrational signatures of the top $CH_3$ group. These cases are distinguished by the use of the "two frozen methyl or 2FM" suffix. Only the results obtained with the STO-3G low-layer basis set are presented here. Indeed, in spite of the change in the geometric parameters ($\theta$ and $\xi$, Table 8.1) observed with the different basis sets of the low-layer, the SFG spectral profiles are almost similar (Fig. E.2 in Appendix E). Like for OTS, the vibrational frequencies remain almost constant upon adsorption (Table 8.3, from Isolated to Adsorbed). Then by freezing the two $CH_3$ groups (Isolated to Isolated-2FM or Adsorbed to

Adsorbed-2FM), vibrational frequencies also remain similar, besides the obvious consequence that the corresponding vibrations disappeared. Again, the same behavior is observed for the IR and Raman intensities. Moreover, for each $CH_3$ group there are three C−H stretching modes [$r^+ \equiv (CH_3)_{\text{sym}}$, $r_a^- \equiv (CH_3)_{\text{asym}}$, and $r_b^- \equiv (CH_3)_{\text{asym}}$] and each of them appear at separate frequencies leading to several spectral SFG signatures.

TABLE 8.2: Vibrational frequencies ($cm^{-1}$), IR [L $mol^{-1}cm^{-1}$] and Raman [$Å^2sr^{-1}\times10^{16}$] intensities of the OTS system determined at the ωB97X-D/6-311G* and the ONIOM[ωB97X-D/6-311g*:ωB97X-D/*basis*] levels of approximation (*basis* ≡ STO-3G, 3-21G, and 6-31G), for the *isolated-* and *adsorbed-models*, respectively

| | Isolated | | | Adsorbed/STO-3G | | | Adsorbed/3-21G | | | Adsorbed/6-31G | | |
|---|---|---|---|---|---|---|---|---|---|---|---|---|
| Label | Freq | IR | Raman | Freq | IR | Raman | Freq | IR | Raman | Freq | IR | Raman |
| $d^+$ | 2884 | 257 | 69 | 2884 | 271 | 51 | 2886 | 266 | 53 | 2886 | 286 | 49 |
| $r^+$ | 2888 | 44 | 266 | 2888 | 45 | 287 | 2888 | 44 | 277 | 2889 | 45 | 297 |
| $r_a^-$ | 2955 | 87 | 48 | 2955 | 87 | 52 | 2956 | 88 | 47 | 2956 | 87 | 51 |
| $r_b^-$ | 2961 | 50 | 162 | 2961 | 50 | 180 | 2961 | 50 | 165 | 2961 | 50 | 179 |

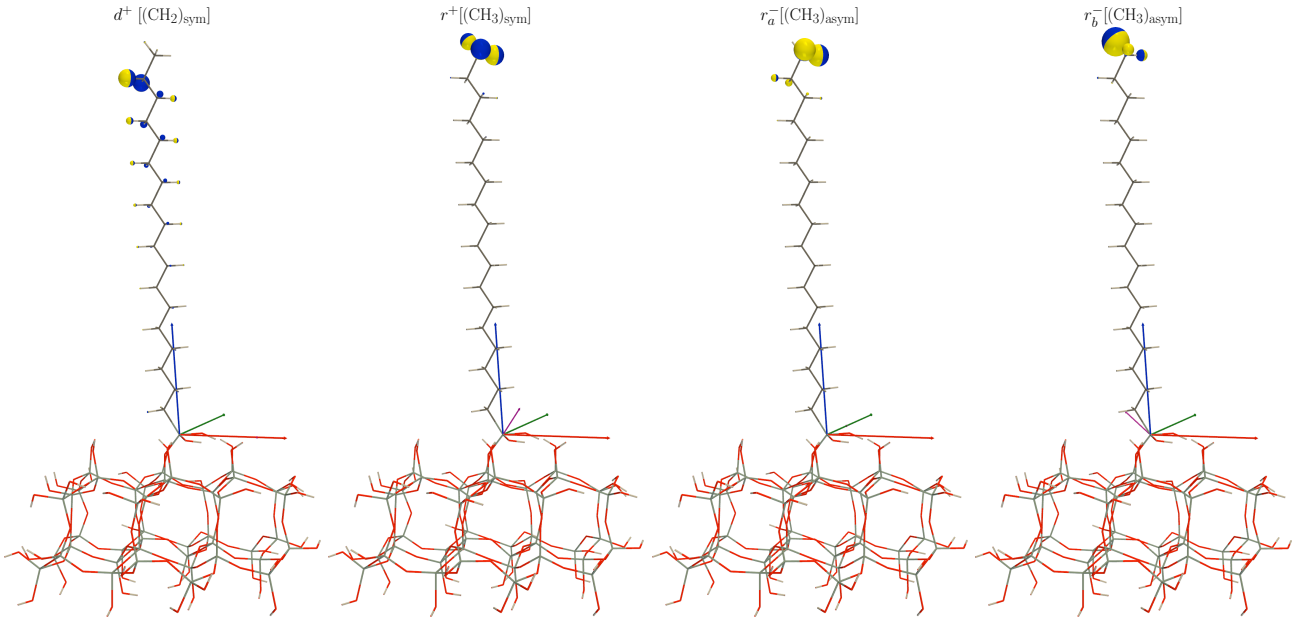


FIGURE 8.2: Sketches of selected vibrational stretching modes of OTS *adsorbed-model* (both IR and Raman active) determined at the ONIOM(ωB97X-D/6-311g*:ωB97X-D/STO-3G) level of approximation. The direction of the atomic displacements is perpendicular to the junction plane between the two hemispheres of distinct color, whereas their amplitudes are proportional to the sphere radius. Mode labels are given on top. Normal modes are illustrated using DrawMol [56].

TABLE 8.3: Vibrational frequencies ($cm^{-1}$), IR [$Lmol^{-1}cm^{-1}$] and Raman [$Å^2sr^{-1}\times10^{16}$] intensities of the DDCS system, determined at the $\omega$B97X-D/6-311G* and the ONIOM[$\omega$B97X-D/6-311G*:$\omega$B97X-D/STO-3G] levels of approximation, for *isolated-* and *adsorbed-model*, respectively. $1r$ refers to the top $CH_3$ group, while $2r$ and $3r$ refer to the bottom groups (Fig. 8.3).

| | | Isolated | | | Isolated-2FM | | | Adsorbed | | | Adsorbed-2FM | | |
|---|---|---|---|---|---|---|---|---|---|---|---|---|---|
| | Label | Freq | IR | Raman | Freq | IR | Raman | Freq | IR | Raman | Freq | IR | Raman |
| | $d^+$ | 2886 | 184 | 6 | 2886 | 182 | 8 | 2885 | 208 | 2 | 2885 | 223 | 7 |
| top | $1r^+$ | 2889 | 43 | 27 | 2889 | 43 | 27 | 2888 | 45 | 26 | 2888 | 45 | 26 |
| top | $1r_a^-$ | 2956 | 79 | 5 | 2956 | 89 | 5 | 2956 | 85 | 5 | 2956 | 85 | 5 |
| top | $1r_b^-$ | 2961 | 50 | 16 | 2961 | 50 | 16 | 2961 | 49 | 17 | 2961 | 49 | 17 |
| bottom | $2r^+$ | 2886 | 5 | 19 | - | - | - | 2885 | 21 | 22 | - | - | - |
| bottom | $2r_a^-$ | 2956 | 27 | 9 | - | - | - | 2961 | 12 | 7 | - | - | - |
| bottom | $2r_b^-$ | 2964 | 8 | 8 | - | - | - | 2978 | 3 | 9 | - | - | - |
| bottom | $3r^+$ | 2893 | 5 | 22 | - | - | - | 2895 | 7 | 17 | - | - | - |
| bottom | $3r_a^-$ | 2973 | 15 | 16 | - | - | - | 2985 | 7 | 13 | - | - | - |
| bottom | $3r_b^-$ | 2968 | 28 | 16 | - | - | - | 2969 | 13 | 11 | - | - | - |

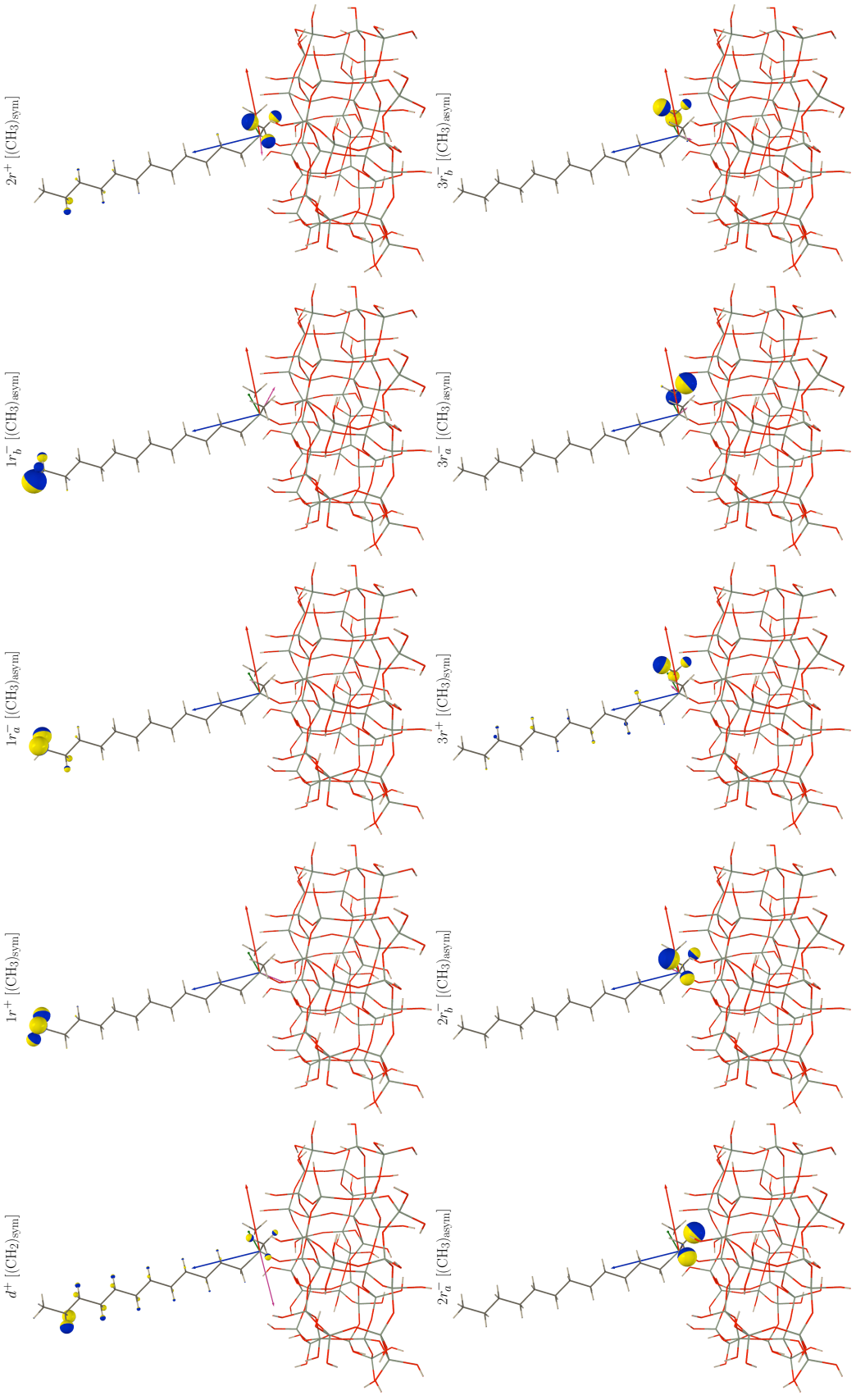


FIGURE 8.3: Sketches of selected vibrational stretching modes of the DDCS *adsorbed-model* (both IR and Raman active, see Table 8.3) determined at ONIOM($\omega$B97X-D/6-311G*: $\omega$B97X-D/STO-3G) level of approximation. The direction of the atomic displacements is perpendicular to the junction plane between the two hemispheres of distinct color, whereas their amplitudes are proportional to the sphere radius. Mode labels are given on top. Normal modes are illustrated using DrawMol [56].

### 8.3.3 SFG signatures of the silica-OTS-air interface

#### 8.3.3.1 General considerations

The SFG spectra were simulated for three polarization combinations (ppp, sps and ssp) and compared to experiments (Fig. 8.4). The main features of the SFG spectra are the stretching modes of the $CH_3$ group ($r^+$ and $r^-$). Indeed, within an all-trans conformation of the alkyl chain, only the terminal $CH_3$ group lacks inversion symmetry, while the $CH_2$ groups are arranged in zig-zag conformation, which owns an inversion point in each C-C bond. Therefore, the absence of $CH_2$ stretching signatures indicates that the molecules are straight, whereas their presence indicates the formation of defects in the chains [50, 51, 60]. In general, the simulation of SFG spectra of molecular films at interfaces takes into account different key parameters: the Euler angles [$\phi$, $\theta$, and $\xi$, Eq. (8.4)], the relative electric permitivity of the thin film $\varepsilon_l$ [Eq. (8.6)], the damping coefficient $\Gamma_p$ [Eq. (8.5)] of each normal mode, the non resonant term of the susceptibility ($\chi^{(2),NR}_{IJK}$), and the phase shift angle [ $\varphi$, Eq. (8.4)]. The following assumptions and properties simplify the variable parameters to $\theta$, $\xi$, $\varepsilon_l$, and $\Gamma_p$: $\phi$ vanishes with the average rotation at the surface and $\chi^{(2),NR}_{IJK}$ is set to 0. We also assume the same value of $\Gamma_p$ for all normal modes, so that its impact is expected to be similar for all peaks. In addition, when adopting the *adsorbed-model*, the $\theta$ and $\xi$ angles are determined by the geometry optimization. Therefore, the only remaining parameter to investigate is $\varepsilon_l$.

#### 8.3.3.2 Effect of $\varepsilon_l$, the electric permitivity of the thin film

So, by using the STO-3G basis set (see Fig. E.1 in Appendix E for the other basis sets and the *isolated-model*) for the low-layer ($\theta = 12°$ and $\xi = 80°$), simulations were performed for four values of $n_l$ (1.0, 1.1, 1.2, and 1.3) and $\Gamma_p = 6$ cm$^{-1}$ (according to the work of Guyot-Sionnest et al. [30]) and the spectra are displayed in Fig. 8.4 (first column). We observe that by increasing $n_l$ ($n_l = \sqrt{\varepsilon_l}$), the intensities of both peaks ($r^+$ and $r^-$) decrease, while the relative intensities change, since the $r^-$ intensity decreases much more. These variations originate from the $F_Z$ [Eq. (8.6)] quantity that modifies the SFG intensities depending on the polarization combination and the normal mode. Indeed, when increasing $n_l$ (so $\varepsilon_l$), $F_Z$ decreases, and the SFG intensity is affected proportionally to the amplitude of this latter. Moreover, for the ppp configuration, which depends on four susceptibility components ($\chi^{(2)}_{XXZ}, \chi^{(2)}_{XZX}, \chi^{(2)}_{ZXX}$, and $\chi^{(2)}_{ZZZ}$) the impact on a normal mode will also vary with the weight of each component ($\chi^{(2)}_{IJK} F_I F_J F_K$). In the ppp configuration, the calculated $r^-/r^+$ ratio amounts to 3.7, 7.2, 20.0, and 60.6 for $\varepsilon_l$ equal to 1.0, 1.1, 1.2, and 1.3, respectively, whereas in the ssp combination it remains constant and equal to 8.7. By comparison with the experimental values [30], that is 10.7 for ppp and 5.0 for sps, it turns out that an appropriate value for $n_l$ is 1.1. Then, by taking $n_l = 1.1$, the simulations were performed with the two models.

#### 8.3.3.3 The *isolated-model*

We calculated SFG spectra of the *isolated-model* (third column of Fig. 8.4) using the angles obtained from the *adsorbed-model* (Table 8.1): $\theta = 12°$ and $\xi = 80°$. As in the experiment, the ppp spectrum was dominated by two peaks associated to $r^-$ (2960 $cm^{-1}$) and $r^+$ (2890 $cm^{-1}$). However, the intensity of the latter was overestimated; in addition, it presented a shoulder that did not exist in the experiment (second column). On the contrary in the sps spectrum the intensity of the $r^+$ was underestimated. Finally, for the ssp configuration discrepancy with experiment is more important. Indeed, in the experiment the intensities of both peaks are quite similar, whereas in our simulation that of the peak around 2960 $cm^{-1}$ ($r^-$) is almost zero. This observation can be related to the lack of anharmonicity in our simulations.

#### 8.3.3.4 The *adsorbed-model*

For the *adsorbed-model* the impact of the low-layer basis set was first addressed (third column of Fig. 8.4), evidencing that the $r^-$ intensity is overestimated (ppp) or underestimated (sps) with respect to the calculations performed with the split-valence basis sets. Still, the global pattern of the spectrum remained similar and, like in the experimental spectrum, two peaks are present. For the ppp and sps combinations, the agreement with experiment was rather good. Indeed, for both polarization combinations the spectrum was dominated by the $r^-$, with a much smaller $r^+$ peak. However, for the ssp combination, the relative intensity of the peak around 2950 $cm^{-1}$ ($r^-$) was not reproduced: in the experiment both peaks have similar intensities whereas in the simulations that of $r^-$ was much smaller. This discrepancy originates from the lack of anharmonicity contributions, necessary to describe the Fermi resonance between $r^+$ and the overtone of the C−H bending mode which corresponds to the peak at around 2945 $cm^{-1}$ in the experimental spectrum.

### 8.3.4 SFG signatures of the silica-DDCS-air interface

#### 8.3.4.1 Impact of the $\xi$ angle

Using the DDCS *isolated-model*, the impact of the $\xi$ angle was scrutinized by simulating the ppp spectrum for $-180° < \xi < 180°$ (Fig. 8.5, top). First, one noticed a quasi symmetric distribution with respect to $\xi = 0°$, which allowed focusing only on positive $\xi$ values. When $\xi$ increases, the intensity of the $r^-$ peak ($2950 - 2975\,cm^{-1}$) decreases (red to green), whereas that of $r^+$ peak ($2875 - 2900\,cm^{-1}$) increases (blue to green). Indeed, the maximum intensity for $r^-$ is around $\xi = 0°$, whereas that of $r^+$ is near to $\xi = 180°$. In order to illustrate these observations, spectra for specific values of $\xi$ (0°, 60°, 120°, and 180°) were simulated (Fig. 8.5, bottom). These showed that the spectral profile strongly depends on the value of $\xi$. In particular, the relative intensities

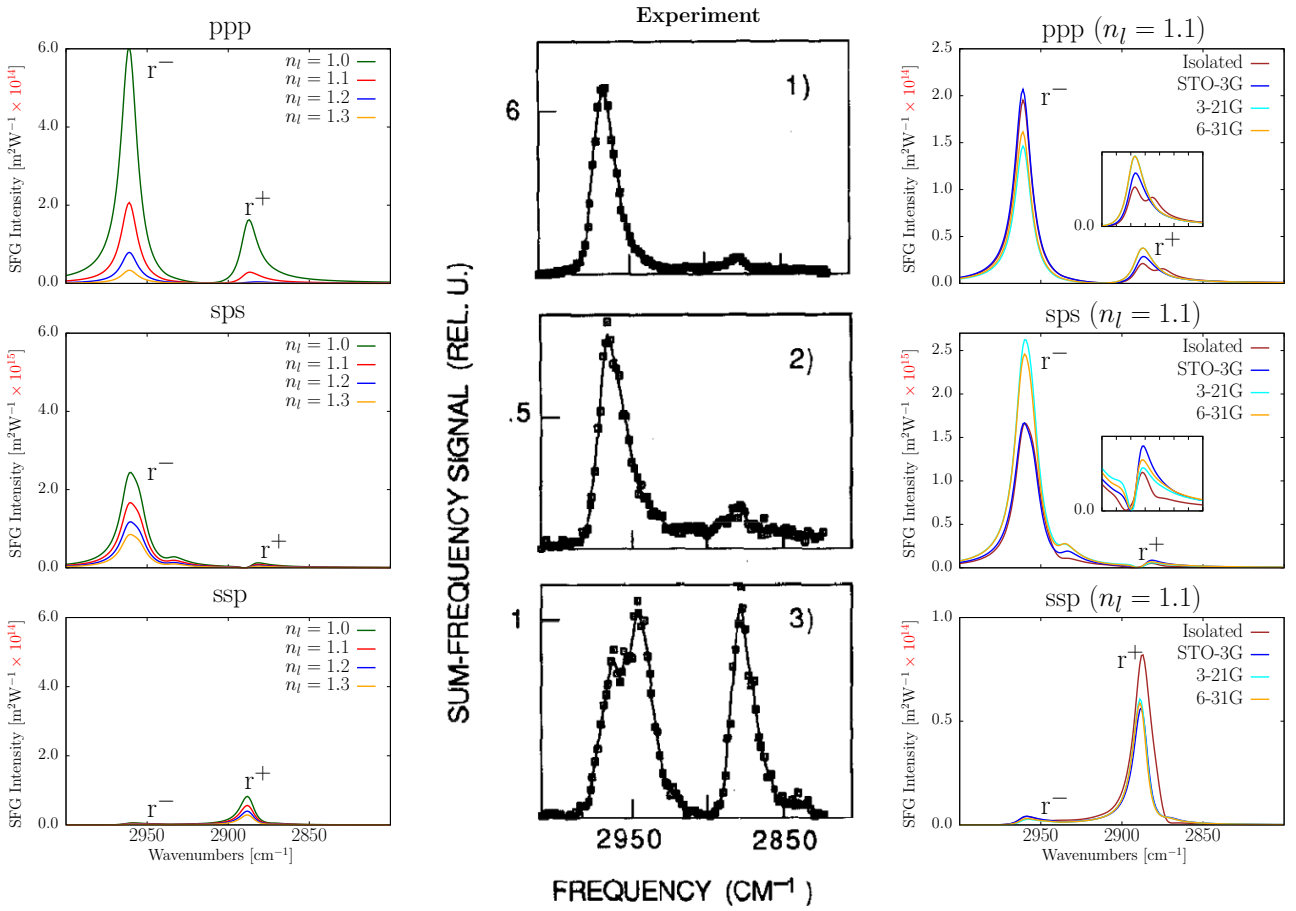


FIGURE 8.4: Comparison between experimental and simulated SFG spectra of OTS. Left) SFG spectra of OTS *adsorbed-model* determined at the ONIOM[$\omega$B97X-D/6-311G*: $\omega$B97X-D/STO-3G] level of approximation for different values of the relative electric permittivity of the OTS thin film. Middle) Experimental SFG spectra at the silica-OTS-air interface for various polarization combinations: (1) ppp; (2) sps; (3) ssp (adapted with permission from Guyot-Sionnest et al. [30]). The solid lines are guides for the eye. Right) SFG spectra of OTS *adsorbed-model* determined for different basis sets of the low-layer (STO-3G, 3-21G, and 6-31G).

of the $r^+$ and $r^-$peaks changes considerably: when $\xi$ increases, the intensity of the peak $r^-$ decreases while that of the peak $r^+$ increases till becoming slightly higher at $\xi = 180°$.

#### 8.3.4.2 SFG spectra of DDCS models

The SFG spectra at the silica-DDCS-air interface were simulated for the three polarization combinations (ppp, sps, and ssp), with $n_l = 1.1$ and $\Gamma_p = 4\,\mathrm{cm}^{-1}$ (Fig. 8.6). The values of the $\theta$ and $\xi$ angles are taken from the optimized *adsorbed-model* of DDCS (Table 8.1). Using the ONIOM($\omega$B97X-D/6-311G*:$\omega$B97X-D/STO-3G level of approximation, like for OTS, the SFG spectra were dominated by two peaks. The stronger at 2960 $\mathrm{cm}^{-1}$ assigned to $r^-$ and the weaker at 2890 $\mathrm{cm}^{-1}$ being assigned to $r^+$. The former presents a shoulder, which disappears when freezing the methyl groups bonded to the Si atom (bottom groups) as well as when considering the *isolated-model*. This shoulder at 2970 $\mathrm{cm}^{-1}$ is assigned to $2r^-_{a,b}$ and $3r^-_{a,b}$ (the asymmetric

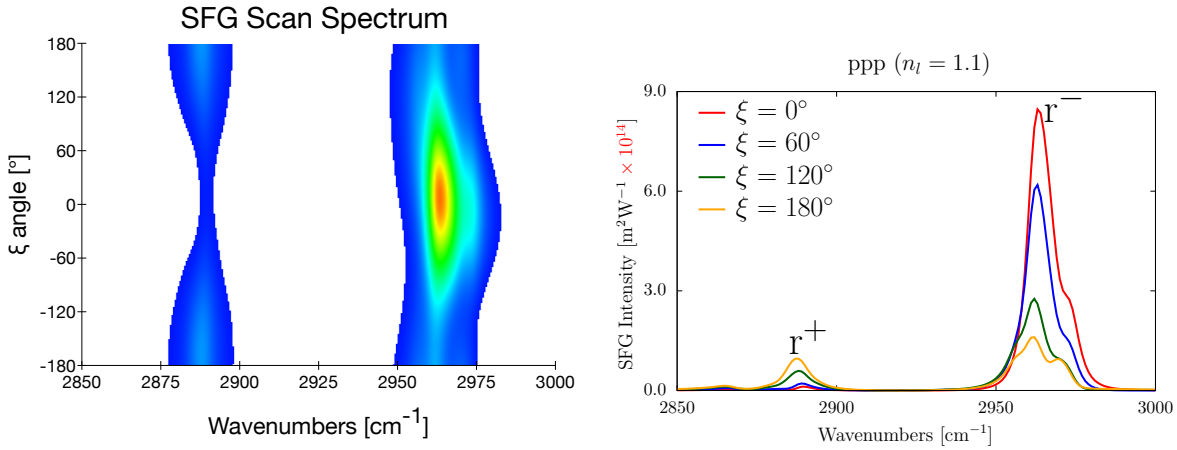


FIGURE 8.5: Map of the ppp intensity of DDCS as a function of the $\xi$ angle ($\theta = 12°$) and corresponding spectra for specific values of $\xi$. For the map, the intensity values are expressed by color variations from blue to red (from 0.0 to $1.6 \times 10^{-14}$ m$^2$w$^{-1}$). White regions correspond to the lack of signal.

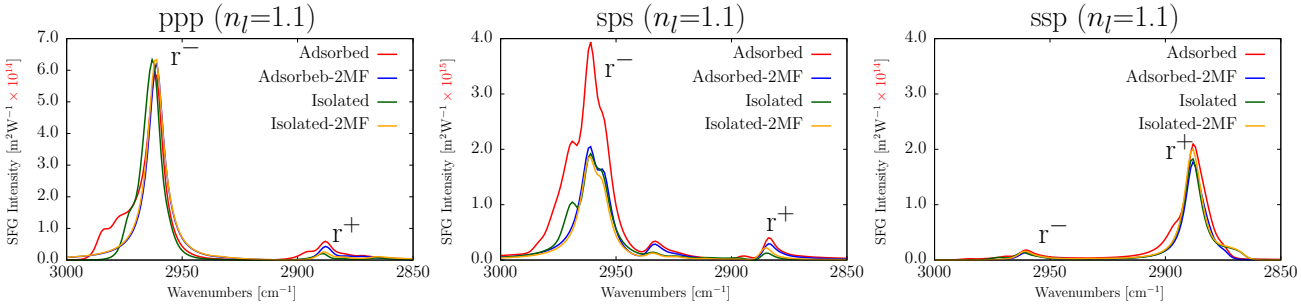


FIGURE 8.6: SFG spectra of DDCS models determined at the ONIOM($\omega$B97X-D/6-311G*:$\omega$B97X-D/STO-3G) level of approximation.

stretching vibrations of these methyl groups). In the sps spectrum, the shoulder also disappears when freezing these bottom methyl groups and the overall intensity decreases. Finally for the ssp spectrum, the intensity of the $r^-$ peak becomes negligible with respect to that of $r^+$ as observed for OTS. Indeed, for both models and for both molecules, the $r^-/r^+$ ratio is equal to 0.1.

## 8.4 Conclusions

In this work, the SFG signatures of octadecyl-trichlorosilane (OTS) and dodecyl-dimethyl-chlorosilane (DDCS) monolayers on silica were simulated in the C−H stretching region for three polarization combinations (ppp, sps, and ssp), showing the impact of the additional Si-linked methyl groups of DDCS on the SFG signatures. For OTS, the results were compared to the experiment, demonstrating a good agreement for ppp and sps polarization configurations when the refractive index of the layer $n_l$ was set to 1.1. These simulations are based on a two-step procedure: i) the molecular properties were evaluated using first principles methods, *i.e.* DFT with the $\omega$B97X-D exchange-correlation functional, and ii) the three-layer model was employed

to calculate the macroscopic responses from the molecular ones, and considering the geometry of the experimental set-up and the optical properties of the layers. In this investigation, for the first time, the first principles calculations adopted the ONIOM approach, which describes the successive layers of the system at different levels of approximation. Here, we used the same exchange-correlation functional, while the lower layer was described with a smaller atomic basis set (STO-3G, 3-21G, or 6-31G) than the higher layer (6-311G*). Calculations showed that describing the low layer with the minimal STO-3G basis set provides the same spectral profiles as with the split-valence basis sets. To highlight the origin of the SFG signatures, we used two chemical models, one including explicitly the $SiO_2$ surface in the first principles calculations (*adsorbed-model*) and the other only considering the silane chain (*isolated-model*). Simulations showed that OTS and DDCS have similar spectral patterns where, for ppp and sps configurations, the $r^-$ $CH_3$ stretching vibrations were dominant in comparison to the $r^+$ stretching ones. Still, in the case of DDCS, the $r^-$ peak presented a shoulder, which was assigned to the vibrations of the Si-linked methyl groups. This shoulder vanished when the bottom $CH_3$ groups were frozen. With the *isolated-model*, the effect of the rotation angle ($\xi$) on the SFG profiles was assessed. This work illustrated the strength of the two-step procedure to simulate the SFG spectra of functionalized surfaces, to assign the origin of the SFG resonances, as well as to investigate the effects of the beams polarization, of the interface refractive index, and of the orientation of the adsorbed chain.

# References

[1] Booth, B. D.; Vilt, S. G.; Lewis, J. B.; Rivera, J. L.; Buehler, E. A.; McCabe, C.; Jennings, G. K. *Langmuir* **2011**, *27*, 5909–5917.

[2] Zhenhua, L. *J. Thermoplast. Compos.* **2014**, *27*, 297–305.

[3] Wang, P.; Teng, S.-H. *Thin Solid Films* **2015**, *592*, 105–109.

[4] Nishitani, Y.; Kajiyama, T.; Yamanaka, T. *Materials* **2017**, *10*.

[5] Faucheux, N.; Schweiss, R.; Lützow, K.; Werner, C.; Groth, T. *Biomaterials* **2004**, *25*, 2721–2730.

[6] Prime, K.; Whitesides, G. *Science* **1991**, *252*, 1164–1167.

[7] Matinlinna, J. P.; Lung, C. Y. K.; Tsoi, J. K. H. *Dent. Mater. J.* **2018**, *34*, 13–28.

[8] Nishiyama, N.; Shick, R.; Ishida, H. *J. Colloid Interface Sci* **1991**, *143*, 146–156.

[9] Maidenberg, Y.; Zhang, S.; Luo, K.; Akhavein, N.; Koberstein, J. T. *Langmuir* **2013**, *29*, 11959–11965.

[10] Mauri, S.; Volk, M.; Byard, S.; Berchtold, H.; Arnolds, H. *Langmuir* **2015**, *31*, 8892–8900.

[11] Geerken, M. J.; Van Zanten, T. S.; Lammertink, R. G. H.; Borneman, Z.; Nijdam, W.; van Rijn, C. J. M.; Wessling, M. *Adv. Eng. Mater.* **2004**, *6*, 749–754.

[12] Park, J. Y.; Qi, Y.; Ashby, P. D.; Hendriksen, B. L. M.; Salmeron, M. *J. Chem. Phys.* **2009**, *130*, 114705.

[13] Rivera, J. L.; Jennings, G. K.; McCabe, C. *J. Chem. Phys.* **2012**, *136*, 244701.

[14] Bush, B. G.; Del Rio, F. W.; Jaye, C.; Fischer, D. A.; Cook, R. F. *J. Microelectromech. S.* **2013**, *22*, 34–43.

[15] Wang, H.; Zhou, H.; Liu, S.; Shao, H.; Fu, S.; Rutledge, G. C.; Lin, T. *RSC Advances* **2017**, *7*, 33986–33993.

[16] Amirsadeghi, A.; Brumfield, L.; Choi, J.; Brown, E.; Lee, J. J.; Park, S. *J. Appl. Phys.* **2017**, *121*, 044909.

[17] Graeve, I. D.; Vereecken, J.; Franquet, A.; Schaftinghen, T. V.; Terryn, H. *Prog. Org. Coat.* **2007**, *59*, 224 – 229.

[18] Herzer, N.; Hoeppener, S.; Schubert, U. S. *Chem. Comm.* **2010**, *46*, 5634–5652.

[19] Haensch, C.; Hoeppener, S.; Schubert, U. S. *Chem. Soc. Rev.* **2010**, *39*, 2323–2334.

[20] Halik, M.; Hirsch, A. *Adv. Mater.* **2011**, *23*, 2689–2695.

[21] Lessel, M.; Bäumchen, O.; Klos, M.; Hähl, H.; Fetzer, R.; Paulus, M.; Seemann, R.; Jacobs, K. *Surf. Interface Anal.* **2015**, *47*, 557–564.

[22] Aissaoui, N.; Bergaoui, L.; Landoulsi, J.; Lambert, J.-F.; Boujday, S. *Langmuir* **2011**, *28*, 656–665.

[23] Bhushan, B.; Kasai, T.; Kulik, G.; Barbieri, L.; Hoffmann, P. *Ultramicroscopy* **2005**, *105*, 176 – 188.

[24] Black, J. E.; Iacovella, C. R.; Cummings, P. T.; McCabe, C. *Langmuir* **2015**, *31*, 3086–3093.

[25] Summers, A. Z.; Iacovella, C. R.; Cummings, P. T.; MCabe, C. *Langmuir* **2017**, *33*, 11270–11280.

[26] Escorihuela, J.; Pujari, S. P.; Zuilhof, H. *Langmuir* **2017**, *33*, 2185–2193.

[27] Rye, R. R.; Nelson, G. C.; Dugger, M. T. *Langmuir* **1997**, *13*, 2965–2972.

[28] Tian, R.; Seitz, O.; Li, M.; Hu, W.; Chabal, Y. J.; Gao, J. *Langmuir* **2010**, *26*, 4563–4566.

[29] Ide, M.; El-Roz, M.; De Canck, E.; Vicente, A.; Planckaert, T.; Bogaerts, T.; Van Driessche, I.; Lynen, F.; Van Speybroeck, V.; Thybault-Starzyk, F.; Van Der Voort, P. *Phys. Chem. Chem. Phys.* **2013**, *15*, 642–650.

[30] Guyot-Sionnest, P.; Superfine, R.; Hunt, J. H.; Shen, Y. R. *Chem. Phys. Lett.* **1988**, *144*, 1–5.

[31] Löbau, J.; Rumphorst, A.; Galla, K.; Seeger, S.; Wolfrum, K. *Thin Solid Films* **1996**, *289*, 272–281.

[32] Yang, Y.; Bittner, A. M.; Baldelli, S.; Kern, K. *Thin Solid Films* **2008**, *516*, 3948–3956.

[33] (a) Shen, Y. R. *Nature* **1989**, *337*, 519–525; (b) Shen, Y. R. *J. Phys. Chem. C* **2012**, *116*, 15505–15509.

[34] Liu, Y.; Wolf, L. K.; Messmer, M. C. *Langmuir* **2001**, *17*, 4329–4335.

[35] Stevens, M. J. *Langmuir* **1999**, *15*, 2773–2778.

[36] Kapila, V.; Deymier, P. A.; Raghavan, S. *Modelling Simul. Mater. Sci. Eng.* **2006**, *14*, 283–297.

[37] Roscioni, O. M.; Muccioli, L.; Mityashin, A.; Cornil, J.; Zannoni, C. *J. Phys. Chem. C* **2016**, *120*, 14652–14662.

[38] Tidswell, I. M.; Rabedeau, T. A.; Pershan, P. S.; Kosowsky, S. D.; Folkers, J. P.; Whitesides, G. M. *J. Chem. Phys.* **1991**, *95*, 2854–2861.

[39] Wang, M.; Liechti, K. M.; Wang, Q.; White, J. M. *Langmuir* **2005**, *21*, 1848–1857.

[40] Iarlori, S.; Ceresoli, D.; Bernasconi, M.; Donadio, D.; Parrinello, M. *J. Phys. Chem. B* **2001**, *105*, 8007–8013.

[41] Dkhissi, A.; Estève, A.; Jeloaica, L.; Estève, D.; Rouhani, M. D. *J. Am. Chem. Soc.* **2005**, *127*, 9776–9780.

[42] Deng, X.; Song, Y.; Li, J.; Pu, Y. *Appl. Surf. Sci.* **2014**, *305*, 247–251.

[43] Tetsassi Feugmo, C. G.; Liégeois, V.; Champagne, B. *J. Phys. Chem. C* **2015**, *119*, 3180–3191.

[44] Gao, L.; Lemarchand, F.; Lequime, M. *Opt. Express* **2012**, *20*, 15734–15751.

[45] (a) Svensson, M.; Humbel, S.; Froese, R. D. J.; Matsubara, T.; Sieber, S.; Morokuma, K. *J. Phys. Chem.* **1996**, *100*, 19357–19363; (b) Dapprich, S.; Komáromi, I.; Byun, K. S.; Morokuma, K.; Frisch, M. J. *J. Mol. Struct. Theochem* **1999**, *461-462*, 1–21; (c) Chung, L. W.; Sameera, W. M. C.; Ramozzi, R.; Page, A. J.; Hatanaka, M.; Petrova, G. P.; Harris, T. V.; Li, X.; Ke, Z.; Liu, F.; Li, H.-B.; Ding, L.; Morokuma, K. *Chem. rev.* **2015**, *115*, 5678–5796.

[46] Frisch, M. J. et al. Gaussian 09 Revision D.01. Gaussian Inc. Wallingford CT 2009.

[47] Chai, J.-D.; Head-Gordon, M. *Phys. Chem. Chem. Phys.* **2008**, *10*, 6615.

[48] Mani, A. A.; Schultz, Z. D.; Caudano, Y.; Champagne, B.; Humbert, C.; Dreesen, L.; Gewirth, A. A.; White, J. O.; Thiry, P. A.; Peremans, A. *J. Phys. Chem. B* **2004**, *108*, 16135–16138.

[49] Mani, A. A.; Schultz, Z. D.; Champagne, B.; Humbert, C.; Dreesen, L.; Gewirth, A. A.; White, J. O.; Thiry, P. A.; Peremans, A.; Caudano, Y. *App. Sur. Sci.* **2004**, *237*, 445–450.

[50] Lis, D.; Peremans, A.; Sartenaer, Y.; Caudano, Y.; Mani, A. A.; Dreesen, L.; Thiry, P. A.; Guthmuller, J.; Champagne, B.; Cecchet, F. *J. Phys. Chem. C* **2009**, *113*, 9857–9864.

[51] Cecchet, F.; Lis, D.; Guthmuller, J.; Champagne, B.; Caudano, Y.; Silien, C.; Mani, A. A.; Thiry, P. A.; Peremans, A. *ChemPhysChem* **2010**, *11*, 607–615.

[52] Jiang, D. E.; Carter, E. A. *Physical Review B - Condensed Matter and Materials Physics* **2005**, *72*.

[53] Arasa, C.; Gamallo, P.; Sayós, R. *J. Phys. Chem. B* **2005**, *109*, 14954–14964.

[54] Shen, J.; Muthukumar, K.; Jeschke, H. O.; Valentí, R. *New J. Phys.* **2012**, *14*.

[55] Hirose, C.; Yamamoto, H.; Akamatsu, N.; Domen, K. *J. Phys. Chem.* **1993**, *97*, 10064–10069.

[56] Liégeois, V. DrawMol, UNamur. http://www.unamur.be/sciences/chimie/drawmol.

[57] Cecchet, F.; Lis, D.; Caudano, Y.; Mani, A. A.; Peremans, A.; Champagne, B.; Guthmuller, J. *J. Phys. Condens. Matter* **2012**, *24*.

[58] Merrick, J. P.; Moran, D.; Radom, L. *J. Phys. Chem.* **2007**, *111*, 11683–11700.

[59] Scott, A. P.; Radom, L. *J. Phys. Chem.* **1996**, *100*, 16502–16513.

[60] Weeraman, C.; Yatawara, A. K.; Bordenyuk, A. N.; Benderskii, A. V. *J. Am. Chem. Soc.* **2006**, *128*, 14244–14245.

Tetsassi Feugmo, C. G.; Liégeois, V.; Champagne, B. *Phys. Chem. Chem. Phys.* **2017**, 19, 29822–29832

**Personal contribution:** I selected the system and the strategy with my co-authors, then I ran all calculations, and simulated the SFG signatures with our custom Python program. Finally, I proposed analyses, discussed these with my co-authors, and I wrote the first draft of the paper.

# Chapter 9

# Coupled-cluster SFG Signatures of Methyl $CH_3$ and Methylene $CH_2$ Groups

In this chapter, the first vibrational Sum Frequency Generation (SFG) spectra based on molecular properties calculated at the coupled cluster singles and doubles (CCSD) level of approximation have been simulated for interfacial model alkyl chains, providing benchmarks data for comparisons with approximate methods, including density functional theory (DFT). The approach proceeds in three steps. In the two first steps, the molecular spectral properties are determined: the vibrational normal modes and frequencies and then the derivatives of the dipole moment $\left(\frac{\partial \mu}{\partial Q}\right)$ and of the polarizability $\left(\frac{\partial \alpha}{\partial Q}\right)$ with respect to the normal coordinates. These derivatives are evaluated with a numerical differentiation approach, of which the accuracy was monitored using Romberg's procedure. Then, in the last step, the three-layer model is employed to evaluate the macroscopic second-order nonlinear optical responses and thereof the simulated SFG spectra of the alkyl interface. Results emphasize that i) the dipole and polarizability derivatives calculated at the DFT level with the B3LYP exchange-correlation functional can differ, with respect to CCSD, by as much as ±10-20% and ±20-50% for the $CH_3$ and $CH_2$ vibrations, respectively, that ii) these differences are enhanced when considering the SFG intensities as well as their variations as a function of the experimental configuration (*ppp* versus *ssp*) and as a function of the tilt and rotation angles, defining the orientation of the alkyl chain at the interface, that iii) these differences originate from both the vibrational normal coordinates and from the Cartesian derivatives of the dipole moment and polarizability, that iv) freezing successive fragments of the alkyl chain modifies strongly the SFG spectrum and enables to highlight the delocalization effects between the terminal $CH_3$ group and its neighboring $CH_2$ units, and finally that v) going from the free chain to the free methyl model, and further to $C_3v$ constraints on $\left(\frac{\partial \alpha}{\partial Q}\right)$ leads to large variations of two ratios that are frequently used to probe the molecular orientation at the

interface, the $(r_a^- + r_b^-)/r^+$ ratio for both antisymmetric and symmetric $CH_3$ vibrations and the $I_{ppp}/I_{ssp}$ ratio.

## 9.1 Motivations

Since its first demonstration in 1989 by Shen [1], vibrational Sum-Frequency Generation (SFG) has been developed to become a powerful spectroscopic technique, currently employed in a broad range of multidisciplinary research fields, including surface science, materials chemistry, biophysics, and electrochemistry. Indeed, its intrinsic surface specificity and extreme sensitivity makes SFG a technique of choice to probe systems at their molecular scale. So, SFG has been used to analyze interfacial structures, providing qualitative and quantitative insights into surface coverage [2–4], composition and environment [5, 6], as well as molecular order and orientation [4, 7–9].

In SFG [10] two input beams at frequencies $\omega_1$ and $\omega_2$ interact in a medium and generate an output beam at the sum frequency $\omega_3 = \omega_1 + \omega_2$. Being a second-order nonlinear optical process, within the electric-dipole approximation, SFG is only allowed in media without inversion symmetry. In traditional SFG set-up, one of the frequencies is fixed in the visible ($\omega_{vis}$) and the other is scanned in the infrared region ($\omega_{IR}$), which generates a vibrational spectrum. Indeed, when $\omega_{IR}$ is equal to one of the SFG-allowed vibrational transitions of the material, the vibrational first hyperpolarizabilty ($\beta$) of the constitutive molecular components is enhanced and so are the macroscopic second-order nonlinear susceptibility ($\chi^{(2)}$) of the material and the SFG signal. This non-zero vibrational $\beta$ results, in the harmonic approximation, from a vibrational normal mode that is both IR $\left(\frac{\partial \mu}{\partial Q} \neq 0\right)$ and Raman $\left(\frac{\partial \alpha}{\partial Q} \neq 0\right)$ active ($\mu$, $\alpha$, and $Q$ are the dipole moment, the polarizability, and the vibrational normal mode coordinate, respectively).

Revealing molecular and material properties from experimental spectra is a challenge and often the extracted information remains very cursory in comparison to the complexity and richness of the signal. Thorough interpretation is therefore a challenge to which theoretical simulations and more particularly those derived from quantum chemistry and physics can contribute. Still, as is the case of any property, the quality of the simulated spectra and its ability to unravel molecular and material signatures is determined by the level of the computational method. Up to now, most of the SFG simulations are based on molecular properties evaluated using Density Functional Theory (DFT) [11–13], with few analyses of the performance of various exchange-correlation (XC) functionals. Among these assessments of XC functionals, Cecchet et al. [12] have shown little differences in the SFG signatures of a terminal methyl group when using the B3LYP, B97-1, M06, M06-2X, and CAM-B3LYP XC functionals. On the other hand, to our knowledge, highly-correlated methods such as Coupled-Cluster Singles and Doubles (CCSD) have not yet been employed whereas they have already been used to simulate many molecular properties [14–16] (dipole moment, polarizability and hyperpolarizability), and other types of vibrational spectra,

including IR and Raman signatures [17]. In this paper, the vibrational SFG signatures of the methyl ($CH_3$) and methylene ($CH_2$) groups of alkyl chains are investigated at this CCSD level in order to provide, within the harmonic approximation, very accurate results. Numerical aspects related to calculating $\left(\frac{\partial\mu}{\partial Q}\right)$ and $\left(\frac{\partial\alpha}{\partial Q}\right)$ quantities are also addressed as well as the impact of the chemical model on the SFG responses. The choice of the C−H vibrational signatures comes from their fingerprint and from their omnipresence in many fields where the interface structure is of interest, e.g. electronics, catalysis, and biosensors [6, 7, 18]. Moreover, several works have already been carried out on their SFG signatures but at the DFT level [6, 19, 20], which will allow for comparisons. Hence, another purpose of this study is the analysis of the accuracy of density functional IR vectors and Raman tensors in comparison to those evaluated from highly correlated *ab initio* methods in order to assess the validity of density functional theory for the calculation of SFG spectra for large molecules.

## 9.2 Theory and computational procedure

### 9.2.1 SFG expressions

The generated SFG signal at the frequency $\omega_{SFG}$ is reflected from the substrate, according to the phase-matching condition,

$$\omega_{SFG}\sin\theta_{SFG} = \omega_{vis}\sin\theta_{vis} + \omega_{IR}\sin\theta_{IR} \quad . \tag{9.1}$$

where $\theta_{vis}$ and $\theta_{IR}$ are the angles of incidence of the IR ($\omega_{IR}$) and visible ($\omega_{vis}$) lights (with respect to the normal to the surface), while $\theta_{SFG}$ is the angle between the light reflected at $\omega_{SFG}$ and the normal to the surface. Different polarizations can be used for the visible and the IR electric fields and therefore for the recorded SFG electric field. For an achiral surface with mirror plane there are four allowed polarization combinations denoted as *ppp*, *ssp*, *sps*, *pss* (given, by convention, in the SFG, vis, and IR order). The intensities of the *ssp* and *ppp* sets of polarizations are given by

$$\underbrace{\frac{I_{ssp}}{I_{IR}I_{vis}}}_{\mathrm{J^{-1}sm^2}} = \underbrace{\frac{\omega_{SFG}^2}{2c^3\varepsilon_0 n_1(\omega_{SFG})n_1(\omega_{IR})n_1(\omega_{vis})\cos^2\theta_{SFG}}}_{\mathrm{m^{-2}C^{-1}Vs}} \underbrace{\left|\sin\theta_{IR}\chi^{(2)}_{YYZ}F_Y^{SFG}F_Y^{vis}F_Z^{IR}\right|^2}_{|\chi^{(2),\,eff}_{YYZ}|^2 \equiv \mathrm{m^4V^{-2}}} \tag{9.2}$$

$$\begin{aligned}\frac{I_{ppp}}{I_{IR}I_{vis}} =& \frac{\omega_{SFG}^2}{2c^3\varepsilon_0 n_1(\omega_{SFG})n_1(\omega_{IR})n_1(\omega_{vis})\cos^2\theta_{SFG}} \times \\ & \Big| -\cos\theta_{SFG}\cos\theta_{vis}\sin\theta_{IR}\,\chi^{(2)}_{XXZ}\,F_X^{SFG}F_X^{vis}F_Z^{IR} - \cos\theta_{SFG}\sin\theta_{vis}\cos\theta_{IR}\,\chi^{(2)}_{XZX}\,F_X^{SFG}F_Z^{vis}F_X^{IR} \\ & + \sin\theta_{SFG}\cos\theta_{vis}\cos\theta_{IR}\,\chi^{(2)}_{ZXX}\,F_Z^{SFG}F_X^{vis}F_X^{IR} + \sin\theta_{SFG}\sin\theta_{vis}\sin\theta_{IR}\,\chi^{(2)}_{ZZZ}\,F_Z^{SFG}F_Z^{vis}F_Z^{IR}\Big|^2\end{aligned} \tag{9.3}$$

In Eqs. (9.2) and (9.3), each component of the effective surface second-order nonlinear susceptibility tensor, containing a resonant (vibrational) and a non-resonant (electronic) term, reads

$$\chi^{(2),eff}_{IJK} \propto F^{SFG}_I F^{vis}_J F^{IR}_K \Bigg[ \overbrace{\left|\chi^{(2),NR}_{IJK}\right| e^{i\Phi_{SFG}}}^{non-resonant} + \overbrace{\underbrace{\frac{N_s}{\varepsilon_0}}_{\mathrm{VC^{-1}m^{-1}}} \sum_{\alpha,\beta,\gamma} \langle T_{I\alpha J\beta K\gamma}(\phi,\theta,\xi)\rangle \beta_{\alpha\beta\gamma}(-\omega_{SFG};\omega_{vis},\omega_{IR})}^{resonant} \Bigg],$$
$$\chi^{(2),R}_{IJK} \equiv [\mathrm{m^2V^{-1}}] \tag{9.4}$$

with

$$\beta_{\alpha\beta\gamma}(-\omega_{SFG};\omega_{vis},\omega_{IR}) = \sum_p \underbrace{\frac{1}{4\omega_p} \frac{\left(\frac{\partial\alpha_{\alpha\beta}(\omega_{vis})}{\partial Q_p}\right)_e \left(\frac{\partial\mu_\gamma}{\partial Q_p}\right)_e}{\left(\omega_p - \omega_{IR} - i\Gamma_p\right)}}_{\mathrm{C^3m^3J^{-2}}} \tag{9.5}$$

$\Phi_{SFG}$ is the phase angle between the resonant and non-resonant terms, $N_S$ is the surface density, the $F_I$ terms are the Fresnel factors, which depend on the refractive index and extinction coefficient of the substrate, $T$ is the transformation matrix between the laboratory and molecular coordinate systems (connected by the Euler angles $\phi, \theta$, and $\xi$), and $\beta_{\alpha\beta\gamma}$ is the $\alpha\beta\gamma$ element of the molecular vibrational first hyperpolarizability tensor. In Eq. (9.5), $\Gamma_p$ is the damping coefficient, $\omega_p$ is the vibrational frequency of the $p^{th}$ vibrational mode, and $\omega_{IR}$ is the frequency of the incident IR light. $\left(\frac{\partial\mu_\gamma}{\partial Q_p}\right)_e$ and $\left(\frac{\partial\alpha_{\alpha\beta}(\omega_{vis})}{\partial Q_p}\right)_e$ are the derivatives of the $\gamma$ and the $\alpha\beta$ components of the dipole moment and dynamic polarizability (at $\omega_{vis}$) with respect to the normal coordinate $Q_p$ evaluated at the equilibrium geometry, respectively. As discussed below, these property derivatives and the vibrational frequencies can be obtained from quantum chemical calculations.

### 9.2.2 Quantum chemical calculations

The calculations were performed at two levels of approximation, at the CCSD level as well as within DFT with the B3LYP XC functional, both with the aug-cc-pVDZ basis set [21]. First, the ground state equilibrium structures were optimized with a threshold on the forces of $10^{-5}$ a.u.. Then, the force constants (Hessian) matrix was evaluated and used to determine the vibrational normal modes and frequencies. This Hessian matrix, which is a second-order derivative of the energy with respect to the atomic Cartesian coordinates, was evaluated analytically at the DFT level, using the coupled-perturbed Kohn-Sham method. On the other hand, at the CCSD level, it was calculated numerically from the gradients. Finally, the derivatives of the dipole moment

and the polarizability with respect to the atomic Cartesian coordinates were determined and projected on the normal modes to obtain the derivatives of the dipole moment and of the polarizability with respect to the vibrational normal coordinates, needed in Eq. (9.5). Again, at the DFT level, these (atomic Cartesian coordinates) derivatives were evaluated analytically whereas a numerical procedure was employed at the CCSD level. Note that selected DFT derivatives were also carried out using the numerical approach in order to test its numerical accuracy. The polarizability derivatives were evaluated at a wavelength of 532 nm, corresponding to the visible light wavelength. In the case of the $\alpha$ component of the dipole moment (the generalization to any component of the polarizability tensor is straightforward), the finite difference expression reads:

$$\left(\frac{\partial \mu_\alpha}{\partial r_{i\beta}}\right)_e = \frac{\mu_\alpha\left((r_{i\beta})_e + \Delta r_{i\beta}\right) - \mu_\alpha\left((r_{i\beta})_e - \Delta r_{i\beta}\right)}{2\Delta r_{i\beta}} \tag{9.6}$$

where $(r_{i\beta})_e$ is the $\beta$-Cartesian coordinate of atom $i$ at equilibrium geometry and $\Delta r_{i\beta}$ the amplitude of its variation. So, a first estimate of these atomic Cartesian coordinates derivatives is obtained from combining dipole moment values evaluated at a pair of distorted geometries. Then, to remove the higher-order contaminations to these numerical derivatives as well as to control its accuracy, the automatic Romberg's method described in de Wergifosse et al. [22] has been employed. The numerical accuracy of this approach is assessed in Section 9.3.1

Gaussian-09 [23] was used to optimize the geometries and to calculate the Hessian at both the B3LYP and CCSD levels as well as to evaluate the property derivatives at the DFT level. DFT calculations were carried out using the `UltraFine` and `SuperFine` integration grids. The first grid consists of 99 radial shells and 590 angular points per shell whereas the second is more dense, 175 (first-row atoms) or 250 (second-row atoms and further) shells of 974 angular points. DALTON [24] was employed to calculate the CCSD dipole moments and frequency-dependent polarizabilities. The latter were evaluated using the coupled-cluster linear response theory (CC-LRT) [25] method. The numerical differentiations were carried out using using a homemade program.

First, this approach was employed in a consistent way, *i.e.* the molecular properties are evaluated at the same level as the corresponding equilibrium geometry and Hessian. Then, in order to disentangle both effects and to assess the influence of the method to determine the Hessian on the SFG signatures, hybrid calculations were also carried out. In these calculations, a first method was used to optimize the geometry as well as to calculate the vibrational normal modes and frequencies. Subsequently, a second method was used to evaluate the Cartesian derivatives of the dipole moment and polarizability, using the geometry and vibrational coordinates obtained with the first method. The influence of two parameters were investigated, i) the impact of the CCSD force field was evaluated by projecting the B3LYP/aug-cc-pVDZ Cartesian derivatives onto the CCSD/aug-cc-pVDZ normal modes and by comparing those results with the SFG signatures obtained with the full B3LYP/aug-cc-pVDZ and CCSD/aug-cc-pVDZ calculations,

and ii) the impact of the basis set on the normal modes was assessed by projecting the aug-cc-pVDZ Cartesian derivatives onto the normal modes obtained with the cc-pVTZ basis set [21], using both CCSD and B3LYP methods and by comparing these with the results obtained in a consistent way with the aug-cc-pVDZ basis set.

### 9.2.3 Butane as model compound to describe the $CH_2$ and $CH_3$ SFG signatures

The butane molecule has been chosen to describe the $CH_2$ and $CH_3$ SFG signatures. To model the experimental conditions where, for instance, a functionalized alkane molecule is anchored on a substrate, the atomic displacements of a fragment of the butane molecule were frozen. Three cases have been considered (Fig. 9.1), where the $CH_3{-}CH_2{-}CH_2$, $CH_3{-}CH_2$, and $CH_3$ fragments are successively frozen by setting the masses of their atoms to 1000 amu when evaluating the vibrational normal modes. The substrate is considered to be platinum and its optical characteristics (electric permittivity) are taken into account to evaluate the Fresnel factors in Eq. (9.4). The refractive indices and extinction coefficients of Pt were interpolated from the values in ref [26] for visible, SFG, and IR wavelengths. Moreover it is worth noting that Pt does not possess any electronic transition close to the visible and/or SFG wavelengths, [27] so that the non-resonant contribution to the second-order nonlinear susceptibility can be assumed negligible.

Then, owing to the local $C_{3v}$ point group symmetry of the $CH_3$ group [28], the $z$ axis of the molecular frame has been aligned on the terminal C−C bond to coincide with the $C_3$ axis (Fig. 9.2). Assuming the $C_{3v}$ symmetry, the $CH_3$ group possesses three stretching modes, which are all IR and Raman-active (Table 9.1), i) one symmetric mode ($A_1$), denoted herein as $r^+$, and a pair of doubly-degenerate asymmetric modes ($E$), denoted herein as $r_a^-$ and $r_b^-$ (Fig. 9.3). Similarly, a $C_{2v}$ point group symmetry is usually attributed to the $CH_2$ groups [28]. They are characterized by symmetric ($d^+(d_1^+,\ d_2^+)$) and asymmetric ($d^-(d_1^-,\ d_2^-)$) stretching modes (Fig. 9.3).

In several works [3, 20, 29–31], the empirical bond additivity model (BAM) derived by Hirose et al. [28] and reviewed by Wu et al. [32] has been used for calculating the first hyperpolarizability tensor elements of the $CH_3$ and $CH_2$ groups. In general, for the $C_{3v}$ point group, combining the non-zero components of the derivatives of the dipole moment and of the polarizability leads to 11 non-zero components of the third-rank first hyperpolarizability tensor (Table 9.1), of which only four are independent. Within BAM, to simplify the expressions, the following hyperpolarizability ratio, $R = \beta_{xxz}/\beta_{zzz} = (\frac{\partial \alpha_{xx}}{\partial Q})/(\frac{\partial \alpha_{zz}}{\partial Q})$ has been defined. It can be determined experimentally from the Raman depolarization ratio [3, 28, 32]. It was found that $1 < R \leq 4$ [29] and that it is non transferable from one molecule to another [3]. On the other hand, in our simulations, all components of the dipole and polarizability derivatives are taken into account, which allows highlighting the symmetry effects as well as the deviations with respect to BAM.

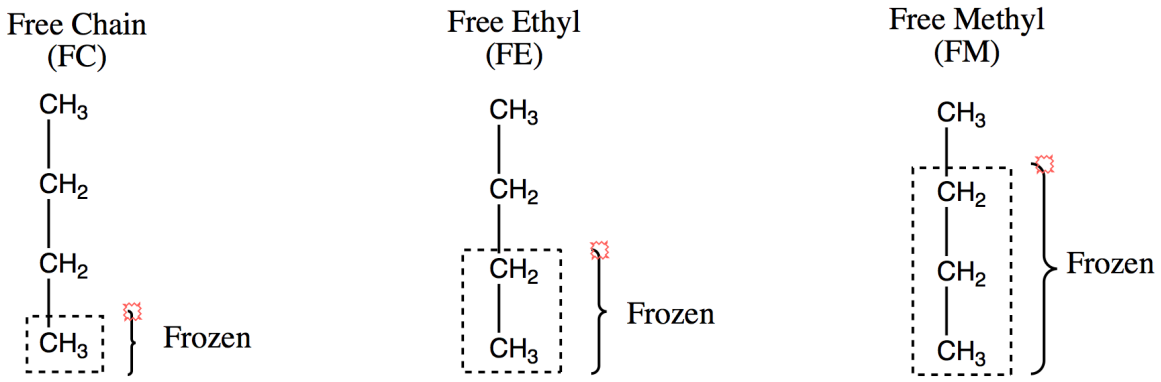


FIGURE 9.1: Schematic representation of the molecular models.

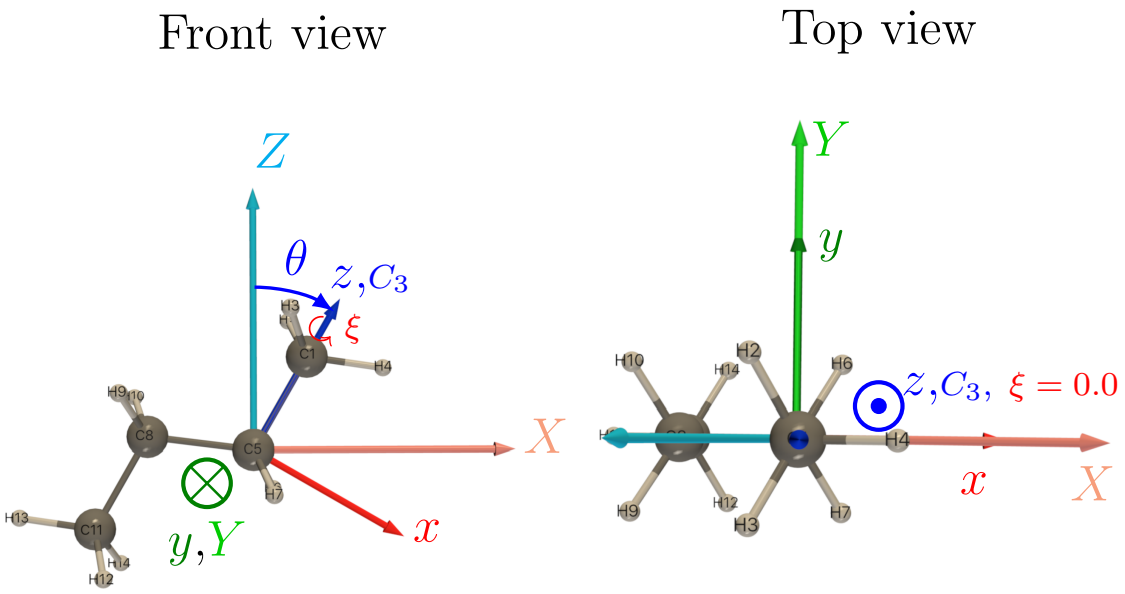


FIGURE 9.2: Definition of the laboratory $(X, Y, Z)$ and molecular $(x, y, z)$ frames. $\theta$ and $\xi$ are the Euler tilt and azimuthal angles, respectively.

TABLE 9.1: Dipole and polarizability components for $C_{3v}$ point group. (The " $'$ " indicates the derivative with respect to the normal coordinate, R=$\alpha'_{xx}/\alpha'_{zz}$).

| | $A_1$ | $E^{\dagger}$ |
|---|---|---|
| $\partial\mu/\partial Q$ | $\mu'_z$ | $(\mu'_x)_1 = (\mu'_y)_2$ |
| $\partial\alpha/\partial Q$ | $\alpha'_{xx} = \alpha'_{yy} = R\alpha'_{zz}$ | $(\alpha'_{xx})_1 = -(\alpha'_{yy})_1 = \pm(\alpha'_{xy})_2$<br>$(\alpha'_{xx})_2 = -(\alpha'_{yy})_2 = \pm(\alpha'_{xy})_1$<br>$(\alpha'_{xz})_1 = \pm(\alpha'_{yz})_2$; $(\alpha'_{yz})_1 = \pm(\alpha'_{xz})_2$ |
| $\beta$ | $\beta_{xxz} = \beta_{yyz} = R\beta_{zzz}$ | $\beta_{xzx} = \beta_{yzy} = \beta_{zxx} = \beta_{zyy}$<br>$\beta_{xxx} = -\beta_{yyx} = -\beta_{xyy} = \beta_{yxy}$ |

$^{\dagger}$ The subscripts 1 and 2 correspond to the doubly-degenerate modes.

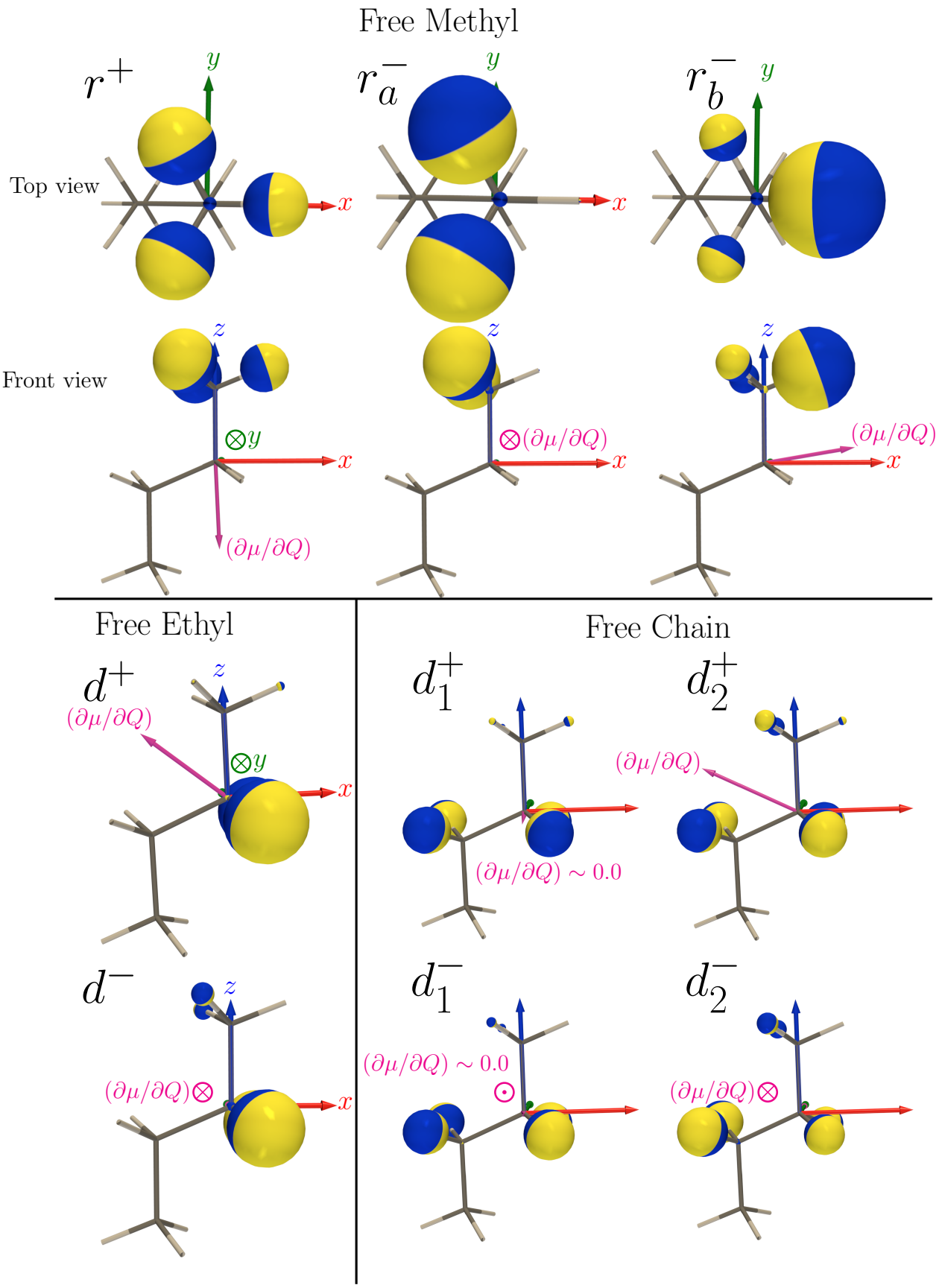


FIGURE 9.3: Sketch of selected C−H stretching modes. Modes were visualized with DrawMol [33]. The direction of the atomic displacements is perpendicular to the junction plane between the two hemispheres with distinct colors, and their amplitudes are proportional to the sphere radius. The IR vectors $(\partial\mu/\partial Q)$ along the molecular frame axes ($x$, $y$, $z$) are shown as purple arrows

## 9.3 Results and discussion

### 9.3.1 Accuracy of the numerical differentiation procedure

Selected derivatives of the dipole moment and dynamic polarizability were evaluated (at the DFT level) using Eq. (9.6) together with seven amplitudes for the geometrical distortions ($\Delta r$ = 0.005, 0.01, 0.02, 0.04, 0.08, 0.16, 0.32 Å). These are listed in the columns $n = 0$ of Table 9.2 (for both integration grids) as well as in Table F.1 for additional derivatives. The derivative values obtained with the smallest distortion amplitude are in good agreement with the reference analytical results but when the distortion amplitude increases, the deviation grows and becomes non negligible (from a few percents to a factor of 5). Then, successive Romberg's iterations were performed to remove higher-order contaminations. Most of these contaminations are eliminated after the first iteration ($n = 1$). Analysis of these tables allows to conclude that the numerical differentiation procedure is accurate within about $10^{-4}$ and $10^{-3}$ a.u. for the dipole moment and the polarizability derivatives, respectively. In addition, this accuracy can be achieved by using only two distortion amplitudes, $\Delta r = 0.01$ and 0.02 Å, together with a single Romberg's iteration. Moreover, as expected, the derivatives obtained with the numerical `SuperFine` grid are more accurate than those obtained with the `UltraFine` grid. The difference amounts roughly to one order of magnitude for both properties. On this basis this "two distortion amplitudes" procedure was adopted for evaluating the derivatives of the CCSD properties.

### 9.3.2 IR vector and Raman tensors

The CCSD results for the characteristics C−H stretching modes (vibrational frequencies, dipole and polarizability derivatives) are summarized in Table 9.3 for the three model systems (B3LYP results in table SI-2). Knowing that the normal modes are defined up to a phase, the absolute values of the derivatives are given. In the case of the $CH_3$ stretching modes ($r^+$, $r_a^-$, and $r_b^-$) one observes that freezing a part of the chain has little impact on the vibrational frequencies (differences of 1 to 4 $cm^{-1}$) but that it has larger effects on the dipole moment and polarizability derivatives. This is particularly visible for situations where the $CH_2$ next to the $CH_3$ head is frozen. Indeed, the larger the frozen moiety, the smaller the derivative (with very few exceptions), especially for the dipole moment as well as for the polarizability of the $r^+$ mode. These are expected to modify accordingly the SFG spectra.

TABLE 9.2: Romberg's triangles for the dipole moment and the polarizability derivatives with respect to the $x$-atomic Cartesian coordinate of $C_1$ (in a.u.). Calculations were performed at the B3LYP/aug-cc-pVDZ level, for seven amplitudes of geometrical distortion ($\Delta r = 0.005$, 0.01, 0.02, 0.04, 0.08, 0.16, and 0.32 Å). The selected "best" values are highlighted in boxes, and the analytic derivatives (at the same level of calculation) are also reported. $n$ is the Romberg's iteration number. The $\partial\mu_y/\partial x_{C_1}$ values were not reported because they are zero by symmetry.

| | SuperFine grid | | | | | | | UltraFine grid | | | | | | |
|---|---|---|---|---|---|---|---|---|---|---|---|---|---|---|
| $\Delta r/n$ | 0 | 1 | 2 | 3 | 4 | 5 | 6 | 0 | 1 | 2 | 3 | 4 | 5 | 6 |
| | | | | | | $\partial\mu_x/\partial x_{C_1}$ | | | | | | | | |
| **0.005** | 0.09890 | 0.09890 | 0.09890 | 0.09890 | 0.09890 | 0.09890 | 0.09890 | 0.09892 | 0.09892 | 0.09892 | 0.09892 | 0.09892 | 0.09892 | 0.09892 |
| **0.010** | 0.09889 | 0.09890 | 0.09890 | 0.09890 | 0.09890 | 0.09890 | | 0.09890 | 0.09892 | 0.09892 | 0.09892 | 0.09892 | 0.09892 | |
| **0.020** | 0.09883 | 0.09890 | 0.09890 | 0.09890 | 0.09890 | | | 0.09885 | 0.09892 | 0.09892 | 0.09892 | 0.09892 | | |
| **0.040** | 0.09861 | 0.09891 | 0.09891 | 0.09891 | | | | 0.09862 | 0.09893 | 0.09893 | 0.09893 | | | |
| **0.080** | 0.09768 | 0.09895 | 0.09891 | | | | | 0.09769 | 0.09897 | 0.09893 | | | | |
| **0.160** | 0.09387 | 0.09953 | | | | | | 0.09387 | 0.09954 | | | | | |
| **0.320** | 0.07688 | | | | | | | 0.07687 | | | | | | |
| ***Analytic*** | | | | **0.09892** | | | | | | | **0.09896** | | | |
| | | | | | | $\partial\mu_z/\partial x_{C_1}$ | | | | | | | | |
| **0.005** | −0.04573 | -0.04573 | −0.04573 | −0.04573 | −0.04573 | −0.04573 | −0.04573 | −0.04571 | −0.04570 | −0.04570 | −0.04570 | −0.04570 | −0.04570 | −0.04570 |
| **0.010** | −0.04575 | −0.04573 | −0.04573 | −0.04573 | −0.04573 | −0.04573 | | -0.04572 | −0.04570 | −0.04570 | −0.04570 | −0.04570 | −0.04570 | |
| **0.020** | −0.04579 | −0.04573 | −0.04573 | −0.04573 | −0.04573 | | | −0.04576 | −0.04570 | −0.04570 | −0.04570 | −0.04570 | | |
| **0.040** | −0.04597 | −0.04573 | −0.04574 | −0.04574 | | | | −0.04595 | −0.04571 | −0.04571 | −0.04571 | | | |
| **0.080** | −0.04670 | −0.04569 | −0.04573 | | | | | −0.04668 | −0.04566 | −0.04571 | | | | |
| **0.160** | −0.04973 | −0.04502 | | | | | | −0.04972 | −0.04501 | | | | | |
| **0.320** | −0.06386 | | | | | | | −0.06386 | | | | | | |
| ***Analytic*** | | | | **−0.04574** | | | | | | | **−0.04568** | | | |
| | | | | | | $\partial\alpha_{xx}/\partial x_{C_1}$ | | | | | | | | |
| **0.005** | −5.06319 | −5.06302 | −5.06302 | −5.06302 | −5.06302 | −5.06302 | −5.06302 | −5.06237 | −5.06220 | −5.06220 | −5.06220 | −5.06220 | −5.06220 | −5.06220 |
| **0.010** | −5.06370 | -5.06302 | −5.06302 | −5.06302 | −5.06302 | −5.06302 | | −5.06288 | -5.06220 | −5.06220 | −5.06220 | −5.06220 | −5.06220 | |
| **0.020** | −5.06573 | −5.06301 | −5.06303 | −5.06304 | −5.06304 | | | −5.06491 | −5.06220 | −5.06219 | −5.06219 | −5.06219 | | |
| **0.040** | −5.07389 | −5.06272 | −5.06245 | −5.06241 | | | | −5.07304 | −5.06231 | −5.06220 | −5.06220 | | | |
| **0.080** | −5.10740 | −5.06679 | −5.06509 | | | | | −5.10522 | −5.06405 | −5.06221 | | | | |
| **0.160** | −5.22925 | −5.09222 | | | | | | −5.22873 | −5.09159 | | | | | |
| **0.320** | −5.64035 | | | | | | | −5.64013 | | | | | | |
| ***Analytic*** | | | | **−5.06234** | | | | | | | **−5.06140** | | | |
| | | | | | | $\partial\alpha_{yy}/\partial x_{C_1}$ | | | | | | | | |
| **0.005** | 4.70193 | 4.70196 | 4.70195 | 4.70195 | 4.70195 | 4.70195 | 4.70195 | 4.70199 | 4.70202 | 4.70202 | 4.70202 | 4.70202 | 4.70202 | 4.70202 |
| **0.010** | 4.70184 | 4.70196 | 4.70196 | 4.70196 | 4.70196 | 4.70196 | | 4.70190 | 4.70202 | 4.70202 | 4.70202 | 4.70202 | 4.70202 | |
| **0.020** | 4.70147 | 4.70196 | 4.70196 | 4.70195 | 4.70195 | | | 4.70153 | 4.70202 | 4.70202 | 4.70202 | 4.70202 | | |
| **0.040** | 4.70000 | 4.70198 | 4.70207 | 4.70208 | | | | 4.70008 | 4.70195 | 4.70199 | 4.70199 | | | |
| **0.080** | 4.69407 | 4.70067 | 4.70112 | | | | | 4.69447 | 4.70135 | 4.70189 | | | | |
| **0.160** | 4.67428 | 4.69390 | | | | | | 4.67383 | 4.69320 | | | | | |
| **0.320** | 4.61542 | | | | | | | 4.61573 | | | | | | |
| ***Analytic*** | | | | **4.70169** | | | | | | | **4.70240** | | | |
| | | | | | | $\partial\alpha_{zz}/\partial x_{C_1}$ | | | | | | | | |
| **0.005** | −0.15980 | −0.15962 | −0.15962 | −0.15962 | −0.15962 | −0.15962 | −0.15962 | −0.16110 | −0.16092 | −0.16092 | −0.16092 | −0.16092 | −0.16092 | −0.16092 |
| **0.010** | −0.16034 | -0.15962 | −0.15962 | −0.15962 | −0.15962 | −0.15962 | | −0.16163 | -0.16092 | −0.16092 | −0.16092 | −0.16092 | −0.16092 | |
| **0.020** | −0.16249 | −0.15962 | −0.15962 | −0.15962 | −0.15962 | | | −0.16378 | −0.16092 | −0.16091 | −0.16091 | −0.16091 | | |
| **0.040** | −0.17111 | −0.15956 | −0.15947 | −0.15945 | | | | −0.17239 | −0.16097 | −0.16091 | −0.16091 | | | |
| **0.080** | −0.20573 | −0.16102 | −0.16036 | | | | | −0.20663 | −0.16187 | −0.16116 | | | | |
| **0.160** | −0.33987 | −0.17089 | | | | | | −0.34092 | −0.17253 | | | | | |
| **0.320** | −0.84680 | | | | | | | −0.84610 | | | | | | |
| ***Analytic*** | | | | **−0.15946** | | | | | | | **−0.15952** | | | |

As shown in Table 9.1, for perfect $C_{3v}$ symmetry, the IR vectors of the three $CH_3$ vibrations should be oriented along the three directions of the molecular coordinates system ($z$ for $r^+$, $y$ for $r_a^-$, and $x$ for $r_b^-$). However, owing to their chemical bonding with the neighboring units and their apparent symmetry, one observes that there are slight deviations (especially for the $x$-component of $r^+$ and the $z$-component of $r_b^-$, which should tend to zero). Of course, these deviations are strongly reduced when freezing the neighboring $CH_2$ groups. Then, these deviations grow in the case of the polarizability derivatives, especially the $xz$-component of $r^+$ and the $zz$-component of $r_b^-$, which should also tend to zero. Furthermore, the $\alpha'_{zz}$ of $r^+$ is close to $\alpha'_{xx}$ and $\alpha'_{yy}$ (the latter two are supposed to be equal for the perfect $C_{3v}$ symmetry). So the R parameter evaluated herein as $R = [(\alpha'_{xx} + \alpha'_{yy})/2]/\alpha'_{zz}$ amounts to 1.2, 1.2, and 1.1 for the Free Chain, Free Ethyl , and Free Methyl model, respectively. On the basis of the amplitude of the deviations with respect to the ideal symmetry, one confirms that the local $C_{3v}$ symmetry is best reproduced with the Free Methyl model, which is mechanically and structurally obvious since the rest of the chain is frozen while the electronic effects remain non negligible. Finally, as expected, one observes that the three modes are both IR and Raman active, therefore SFG active also.

Second, when analyzing the IR vectors and the normal modes displacements of the $CH_2$ units (Fig. 9.3) it appears that $d_2^{+,-}$ (Free Chain) intensities match mostly the $d^{+,-}$(Free Ethyl) intensities, though with larger amplitudes. This originates from the fact that the $d_{1,2}^+$ and $d_{1,2}^-$ modes consist in the in-phase and out-of-phase combinations of $d^+$ and $d^-$ vibrations on neighboring methylene units, respectively and that of the out-of-phase combination is odd, i.e. IR-active. Conversely, the Raman tensors of the $d^+$ and $d^-$ vibrations determine the amplitude of the $d_1^+$ and $d_1^-$ modes whereas the other phase combination gives negligible amplitudes. In summary, $d^{+,-}$ are both IR and Raman active, the $d_2^{+,-}$ modes are mostly IR active, and the $d_1^{+,-}$ ones Raman active. Finally, in general, all these values related to the $CH_2$ groups are smaller than those of the $CH_3$ group, and are therefore expected to contribute to a lesser extent to the SFG signatures. This is consistent with the fact that in the Free Chain model the two $CH_2$ groups display locally an inversion center, detrimental to the SFG signal.

Finally the CCSD results were compared to the B3LYP values (Table F.2 in Appendix F). Besides the fact that the wavenumbers are smaller with B3LYP than CCSD, the dipole and/or polarizability derivatives calculated at the B3LYP level can differ, with respect to CCSD, by as much as ±10-20% and ±20-50% for the $CH_3$ and $CH_2$ vibrations, respectively. This is particularly the case of the diagonal components of the $\alpha'$ tensor of the $d_2^+$ mode. These differences will therefore impact the profiles of the SFG spectra.

TABLE 9.3: Vibrational frequencies* ($cm^{-1}$) and (absolute values of the) derivatives of the dipole moment ($\partial\mu_\alpha/\partial Q$) and polarizability ($\partial\alpha_{\alpha\beta}/\partial Q$),‡ computed at the CCSD/aug-cc-pVDZ level.† The vibrational normal modes are sketched in Fig. 9.3. The " ′ " indicates the derivative with respect to the corresponding normal coordinate.

| | $r^+$ | $r_a^-$ | $r_b^-$ | $d^+(d_1^+/d_2^+)$§ | $d^-(d_1^-/d_2^-)$§ |
|---|---|---|---|---|---|
| | 2909 | 2978 | 2984 | 2898/2904 | 2926/2948 |
| Freq | 2908 | 2977 | 2984 | 2901 | 2936 |
| | 2908 | 2974 | 2984 | | |
| | 0.031 | 0.000 | 0.205 | 0.003/0.003 | 0.000/0.000 |
| $\mu'_x$ | 0.019 | 0.000 | 0.202 | 0.144 | 0.000 |
| | 0.006 | 0.000 | 0.190 | | |
| | 0.000 | 0.258 | 0.000 | 0.000/0.000 | 0.012/0.205 |
| $\mu'_y$ | 0.000 | 0.230 | 0.000 | 0.000 | 0.136 |
| | 0.000 | 0.185 | 0.000 | | |
| | 0.190 | 0.000 | 0.021 | 0.043/0.143 | 0.000/0.000 |
| $\mu'_z$ | 0.155 | 0.000 | 0.023 | 0.146 | 0.000 |
| | 0.178 | 0.000 | 0.032 | | |
| | 8.703 | 0.000 | 5.953 | 6.175/0.451 | 0.000/0.000 |
| $\alpha'_{xx}$ | 7.971 | 0.000 | 6.062 | 3.992 | 0.000 |
| | 7.161 | 0.000 | 5.615 | | |
| | 9.605 | 0.000 | 2.807 | 9.099/1.110 | 0.000/0.000 |
| $\alpha'_{yy}$ | 8.739 | 0.000 | 2.672 | 6.478 | 0.000 |
| | 7.480 | 0.000 | 3.298 | | |
| | 7.555 | 0.000 | 1.336 | 3.373/0.687 | 0.000/0.000 |
| $\alpha'_{zz}$ | 7.170 | 0.000 | 1.401 | 2.202 | 0.000 |
| | 6.698 | 0.000 | 1.123 | | |
| | 0.000 | 2.448 | 0.000 | 0.000/0.000 | 7.977/0.360 |
| $\alpha'_{xy}$ | 0.000 | 1.974 | 0.000 | 0.000 | 6.111 |
| | 0.000 | 3.553 | 0.000 | | |
| | 0.118 | 0.000 | 5.021 | 3.170/0.304 | 0.000/0.000 |
| $\alpha'_{xz}$ | 0.100 | 0.000 | 4.989 | 2.504 | 0.000 |
| | 0.000 | 0.000 | 5.171 | | |
| | 0.000 | 3.728 | 0.000 | 0.000/0.000 | 5.145/0.910 |
| $\alpha'_{yz}$ | 0.000 | 3.488 | 0.000 | 0.000 | 4.318 |
| | 0.000 | 4.530 | 0.000 | | |

*The harmonic vibrational frequencies have been scaled by a factor of 0.96.
†For each property the first, second, and third rows correspond to the Free Chain, Free Ethyl, and Free Methyl models, respectively.
‡ $\alpha'_{xy} = \alpha'_{yx}$; $\alpha'_{xz} = \alpha'_{zx}$; $\alpha'_{yz} = \alpha'_{zy}$.
§ $d_1^+$, $d_2^+$, $d_1^-$, $d_2^-$ ≡ Free Chain; $d^+$, $d^-$ ≡ Free Ethyl.

### 9.3.3 SFG spectra

#### 9.3.3.1 CCSD results and comparison with B3LYP

After the analysis of the IR vectors and Raman tensors, SFG spectra were simulated (with the Free Chain model) at the CCSD level and then compared to B3LYP (Fig. 9.4). This is illustrated using $\theta = 60°$ and $\xi = 150°$. In the *ppp* configuration, using the CCSD level the $(r_a^- + r_b^-)/r^+$ ratio amounts to 2.3 whereas it is larger (3.6) at the B3LYP level. This is also observed for the *ssp* configuration [$(r_a^- + r_b^-)/r^+ = 0.11$ at the CCSD level versus 0.14 using DFT and B3LYP], though in this case the intensity of the asymmetric modes is much larger. Moreover, with both levels of calculations there are additional weak-intensity peaks near the $r^+$ peak, which are more intense at the B3LYP level, consistent with the discussion at the end of the previous paragraph. These peaks appear in the region of the $d^+_{1,2}$ vibrational frequencies and are associated to the methylene vibrations.

In order to highlight the influence of the method for determining the Hessian in the SFG signatures, the B3LYP/aug-cc-pVDZ Cartesian derivatives were projected onto the CCSD/aug-cc-pVDZ normal modes (Fig. F.1 and Table F.3) and the resulting simulated SFG spectra were compared to the results obtained with the full B3LYP/aug-cc-pVDZ and CCSD/aug-cc-pVDZ (Fig. F.1 and Tables 9.3 and F.2). The mixed approach shows an increase of the intensities of $r^+$ , $r_a^-$ and $r_b^-$ modes compared to CCSD but the $(r_a^- + r_b^-)/r^+$ ratios (Table F.7) remain the same and amount to 2.3 and 0.12 for the *ppp* and *ssp* configurations, respectively. Therefore, the change of signatures between the CCSD and B3LYP spectra not only comes from the description of the normal modes (ratios) but also from electronic responses (absolute intensities).

Second, the impact of the basis set on the normal modes was assessed by projecting the aug-cc-pVDZ Cartesian derivatives onto the normal modes obtained with the cc-pVTZ basis set using both CCSD (Table F.4) and B3LYP (Table F.5) methods. The spectra are shown in Fig. F.2. The vibrational frequencies obtained by using B3LYP/cc-pVTZ are almost identical to those obtained by B3LYP/aug-cc-pVDZ while they increase by about 15–18 $cm^{-1}$ when going from CCSD/aug-cc-pVDZ to CCSD/cc-pVTZ[1]. Concomitantly, the SFG intensities changes: the $r_a^- + r_b^-$ intensity increases with B3LYP for the *ppp* polarization while the $r^+$ intensity decreases with CCSD, which leads to an increase of the $(r_a^- + r_b^-)/r^+$ ratio in both cases. At last, Cartesian derivatives of the properties calculated at B3LYP/aug-cc-pVDZ level have been projected on the normal modes calculated at the CCSD/cc-pVTZ level (Table F.6). Once again, when B3LYP properties are projected onto CCSD normal modes, there is an increase in the intensities of $r^+$, $r_a^- + r_b^-$ modes compared to CCSD. However, the $(r_a^- + r_b^-)/r^+$ ratio is similar to the one obtained with CCSD (3.6), which is lower than the B3LYP ratio (4.0).

[1]Note that here the focus is not set on comparison with experiment but rather on the difference between B3LYP and CCSD response properties. As a matter of fact, the same scaling factor of 0.96 has been employed.

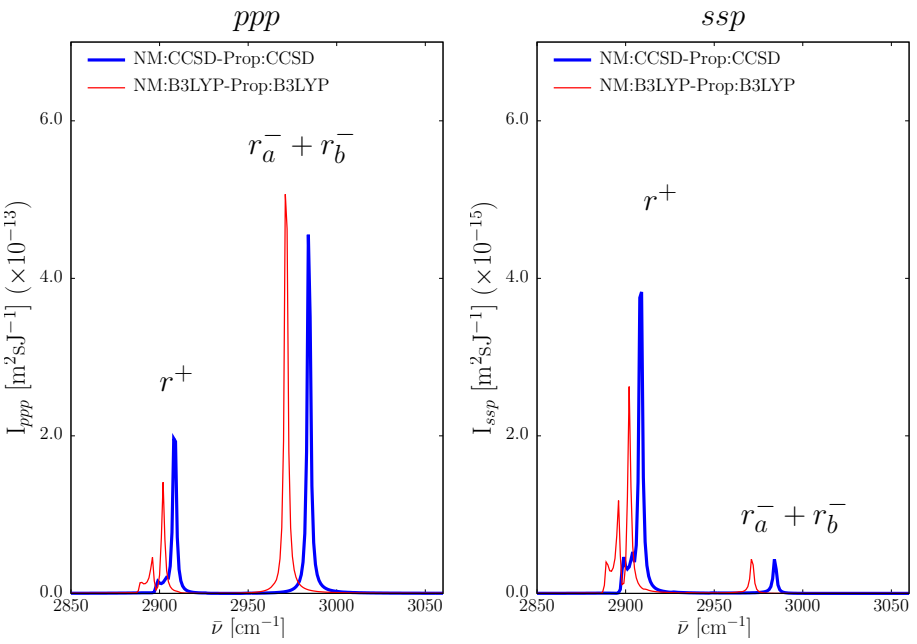


FIGURE 9.4: Comparison of the SFG spectra calculated at the CCSD/aug-cc-pVDZ and B3LYP/aug-cc-pVDZ (with the `SuperFine` integration grids) levels. NM ≡ Normal Modes, Prop ≡ Cartesian derivatives of the properties ($\partial\mu_\alpha/\partial r_{i\gamma}$ and $\partial\alpha_{\alpha\beta}/\partial r_{i\gamma}$). The spectra have been simulated for the Free Chain model, at $\theta = 60°$ and $\xi = 150°$, and for *ppp* and *ssp* sets of polarizations. $\Gamma = 1$ cm$^{-1}$.

#### 9.3.3.2 Approximate CCSD schemes

For both sets of polarizations the SFG spectra were plotted by starting from the Free Chain Model and freezing gradually one and two methylene groups (Fig. 9.5). Then, within the Free Methyl Model additional approximations were made to get closer and closer to the BAM approach *i*) $\alpha'_{xz}(r^+) = 0.0$ and *ii*) for $r^+$, $\alpha'_{xx} = \alpha'_{yy} = (\alpha'_{xx} + \alpha'_{yy})/2$ and $\alpha'_{xz} = 0.0$ together with $R = 2$ and 4 ($\alpha'_{zz} = \alpha'_{xx}/R = \alpha'_{yy}/R$). The vibrational normal modes and response properties were all evaluated at the CCSD/aug-cc-pVDZ level of approximation. First, comparison between the three molecular models shows that for both sets of polarizations, the Free Ethyl displays the largest intensities, especially for $r^+$ with *ssp* configuration. This results from the molecular structure, which does not display local inversion symmetry for the $CH_2$ groups (since only one is present) leading to simultaneous IR and Raman activities of these modes whereas centrosymmetry leads to mutually-excluding intensities. In the *ppp* configuration the $(r_a^- + r_b^-)/r^+$ ratio attains 2.3, 1.4, and 1.6 for the FC, FE, and FM molecular models, highlighting the expected slightly improved similarity between FC and FM. Then, within FM, setting $\alpha'_{xz} = 0$, the ratio increases little (=1.8) whereas further simplifications with $R = 2$ and 4 give values of 2.0 and 2.4, respectively. For *ssp* configuration the $(r_a^- + r_b^-)/r^+$ ratio is much smaller but, on a relative basis, it changes substantially from one model to another. From 0.11 for FC, it decreases by a factor of 2 (0.06) for FE, and then increases by a factor of 3 (0.17). Setting $\alpha'_{xz} = 0$ slightly reduces this ratio (0.16). Eventually, with $R = 2$ and $R = 4$, the ratio amounts to 0.21 and 0.27, which is about 100% and 150% larger than with the most complete model. This contrasts

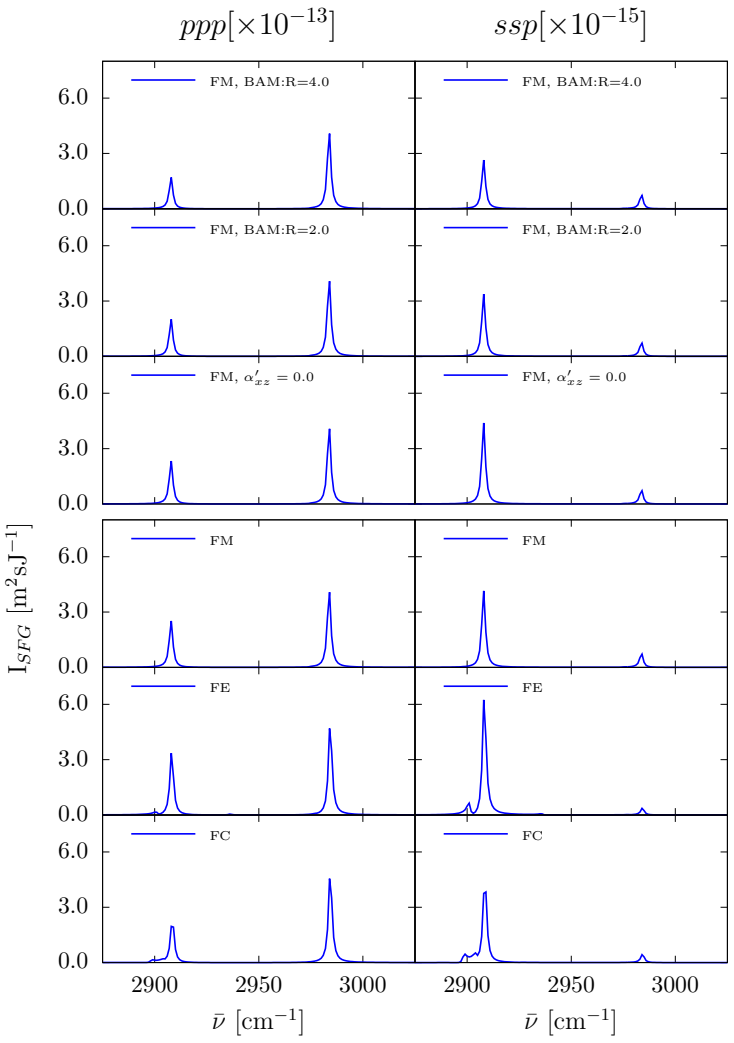


FIGURE 9.5: Comparison of different molecular models and approximation schemes. All spectra were simulated starting from CCSD response properties. $\theta = 60°$, $\xi = 150°$, and $\Gamma = 1$ cm$^{-1}$

with the BAM results obtained for the *ppp* $(r_a^- + r_b^-)/r^+$ ratio. Note that within FC and FE models there is again a small peak near $r^+$, which is absent in the FM case, confirming that it is associated to the $CH_2$ group(s).

#### 9.3.3.3 Impact of the tilt ($\theta$) and rotation ($\xi$) angles

In order to determine the tilt angle of the chain ($\theta$) it is customary to plot the dependence of the *ppp*/*ssp* intensity ratio of the $r^+$ peak as a function of $\theta$ [7, 20]. The SFG spectra were plotted for two values of the rotation angle (0 and 60°), two values of the damping factor [Eq. (9.4)], and for the three molecular models (Fig. 9.6). The two values of the damping factor [Eq. (9.4)], $\Gamma = 1$ cm$^{-1}$ and $\Gamma = 10$ cm$^{-1}$, are justified by the interval between the $r_a^-$ and $r_b^-$ wavenumbers. Since for a perfect $C_{3v}$ symmetry the $\xi = 0$ and 60° intensities should be identical, the observed difference demonstrates a clear deviation, but to a lower extent for the FM case. Then, the

comparisons between the different spectra show that both the level of approximation and the molecular model have drastic impacts on this intensity ratio and that increasing the damping factor enhances these differences.

Finally, as shown in Fig. 9.7 for the FM model, the variations of the $I_{ppp}/I_{ssp}$ ratios versus $\theta$ are also strongly impacted by the approximate scheme to describe the $\alpha'$ tensor. These results also highlight that the differences between the $I_{ppp}/I_{ssp}$ ratios obtained with the 0 and 60° rotation angles decrease when imposing symmetry constraints to the $\alpha'$ tensor, at least as far as the tilt angle does not approach 90°.

For the $CH_3$ stretching modes, further comparisons between the different models were carried out for $\theta = 60°$ as a function of the rotation angle (Fig. 9.8). For $\xi = 0$, the different models give similar and small $((r_a^- + r_b^-)/r^+)$ values but large differences appear when increasing $\xi$. These differences are exalted when going from $\Gamma = 1$ cm$^{-1}$ to $\Gamma = 10$ cm$^{-1}$.

## 9.4 Conclusions

Vibrational SFG spectra of interfacial alkyl chains have been simulated using molecular properties calculated at the CCSD level of approximation, providing therefore benchmark data for comparisons with lower levels of approximation, including the broadly used density functional theory methods. Our approach combines three steps, of which the first two concern the spectral molecular properties: i) first the calculation of the vibrational normal modes and frequencies, ii) then the evaluation of the derivatives of the dipole moment $\left(\frac{\partial \mu}{\partial Q}\right)$ and of the polarizability $\left(\frac{\partial \alpha}{\partial Q}\right)$ with respect to the normal coordinates, performed with a numerical differentiation approach, of which the accuracy was improved and monitored using Romberg's procedure, and iii) the three-layer model to evaluate the macroscopic nonlinear optical responses of the interface and simulate the SFG spectra

The work has concentrated on a model system, a terminal alkyl chain, represented by a butane molecule, of which successive segments are frozen to highlight the effects of the model and to show "delocalization" effects between the terminal $CH_3$ group and the neighboring $CH_2$ units. Comparisons are also made with the Bond Additivity Model, frequently used to describe the SFG signal of the $CH_3$ group. Results emphasize that the dipole and polarizability derivatives calculated at the B3LYP level can differ, with respect to CCSD, by as much as ±10-20% and ±20-50% for the $CH_3$ and $CH_2$ vibrations, respectively. Furthermore, these differences are enhanced when considering the SFG intensities as well as the variation of the latter as a function of the experimental configuration (*ppp* versus *ssp*) and as a function of the tilt and rotation angles. Our results also demonstrate that going from the free chain to the free methyl model, and further to $C_3v$ constraints on $\left(\frac{\partial \alpha}{\partial Q}\right)$ leads to large variations of two ratios that are frequently used to probe the molecular orientation (tilt and rotation angles) at the interface, the $(r_a^- + r_b^-)/r^+$ ratio for both antisymmetric and symmetric methyl vibrations and the $I_{ppp}/I_{ssp}$ ratio.

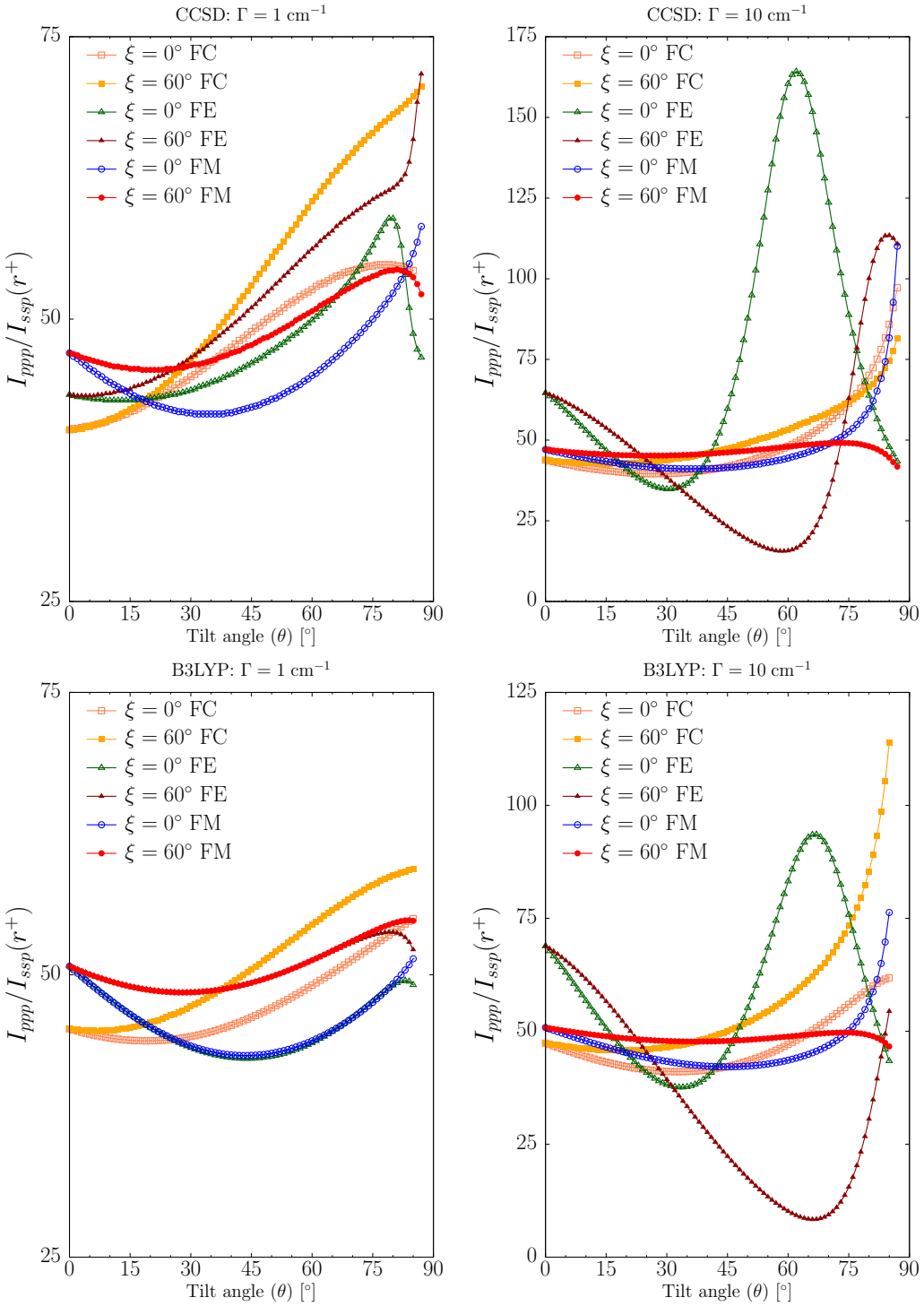


FIGURE 9.6: Dependence of the *ppp*/*ssp* intensity ratios of $r^+$ mode as a function of the tilt angle $\theta$. CCSD (top) compared to B3LYP (bottom) for two values of the damping factor, 1 $cm^{-1}$ (left) and 10 $cm^{-1}$ (right).

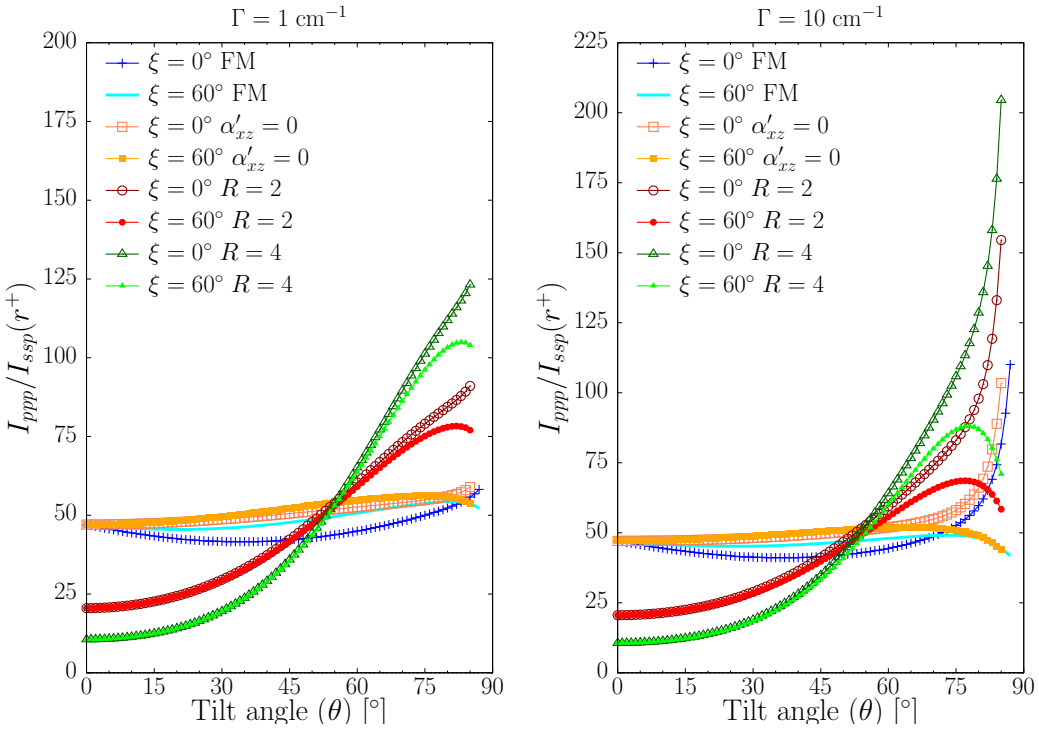


FIGURE 9.7: Dependence of the *ppp*/*ssp* intensity ratios of the $r^+$ mode (Free methyl model) as a function of the tilt angle $\theta$ for different approximate schemes. Two values of the rotation angle ($\xi = 0$ and 60°) and two values of the damping factor ($\Gamma = 1$ and 10 cm$^{-1}$) were considered.

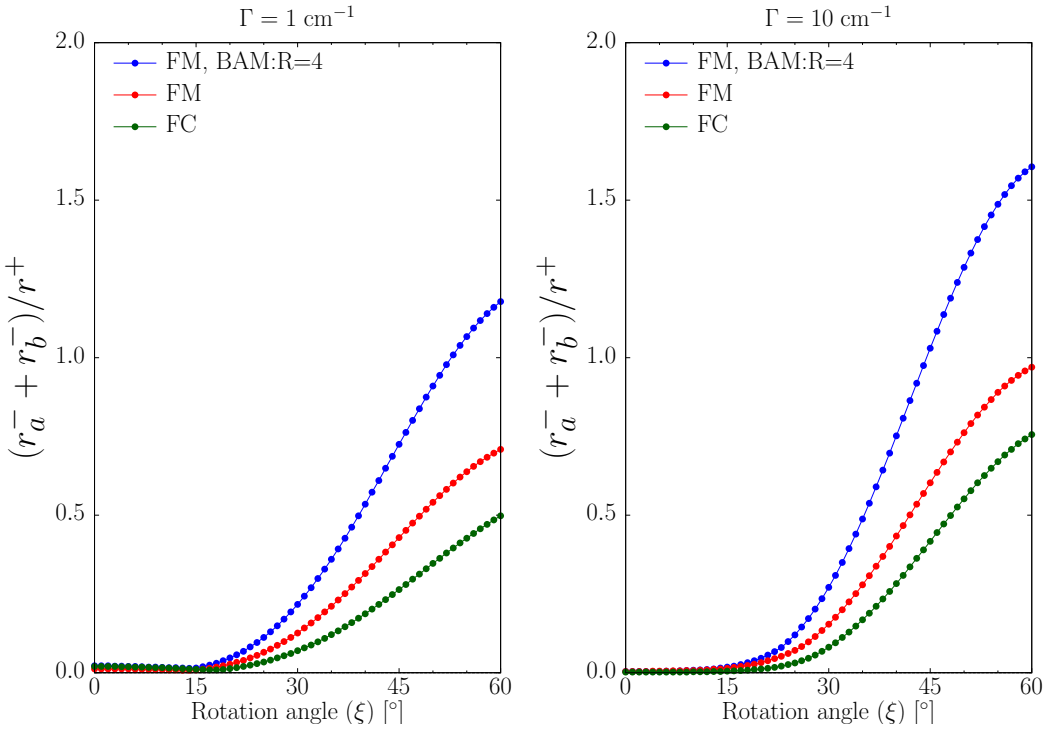


FIGURE 9.8: Ratio of the intensities of peaks $r_a^- + r_b^-$ and $r^+$ for the *ppp* configuration calculated at $\theta = 60°$ as a function of the rotation angle $\xi$.Two values of the damping factor ($\Gamma = 1$ and 10 cm$^{-1}$) were considered.

# References

[1] Shen, Y. R. *Nature* **1989**, *337*, 519–525.

[2] (a) Jacob, J. D. C.; Rittikulsittichai, S.; Lee, T. R.; Baldelli, S. *J. Phys. Chem. C* **2013**, *117*, 9355–9365; (b) Zhang, C.; Myers, J. N.; Chen, Z. *Langmuir* **2014**, *30*, 12541–12550, PMID: 25263030.

[3] Wang, H.-f.; Gan, W.; Lu, R.; Rao, Y.; Wu, B.-h. *Int. Rev. Phys. Chem.* **2005**, *24*, 191–256.

[4] Roeters, S. J.; Van Dijk, C. N.; Torres-Knoop, A.; Backus, E. H. G.; Campen, R. K.; Bonn, M.; Woutersen, S. *J. Phys. Chem. A* **2013**, *117*, 6311–6322.

[5] (a) Tang, C. Y.; Allen, H. C. *J. Phys. Chem. A* **2009**, *113*, 7383–7393; (b) Park, Y. B.; Lee, C. M.; Kafle, K.; Park, S.; Cosgrove, D. J.; Kim, S. H. *Biomacromolecules* **2014**, *15*, 2718–2724; (c) Ennist, J. H.; Gobrogge, E. A.; Schlick, K. H.; Walker, R. A.; Cloninger, M. J. *ACS Appl. Mater. Interfaces* **2014**, *6*, 18087–18097.

[6] (a) Meltzer, C.; Paul, J.; Dietrich, H.; Jäger, C. M.; Clark, T.; Zahn, D.; Braunschweig, B.; Peukert, W. *J. Am. Chem. Soc.* **2014**, *136*, 10718–10727; (b) Sorenson, S. A.; Patrow, J. G.; Dawlaty, J. M. *J. Am. Chem. Soc.* **2017**, *139*, 2369–2378.

[7] (a) Lis, D.; Peremans, A.; Sartenaer, Y.; Caudano, Y.; Mani, A. A.; Dreesen, L.; Thiry, P. A.; Guthmuller, J.; Champagne, B.; Cecchet, F. *J. Phys. Chem. C* **2009**, *113*, 9857–9864; (b) Cecchet, F.; Lis, D.; Guthmuller, J.; Champagne, B.; Fonder, G.; Mekhalif, Z.; Caudano, Y.; Mani, A. A.; Thiry, P. A.; Peremans, A. *J. Phys. Chem. C* **2010**, *114*, 4106–4113; (c) Lis, D.; Cecchet, F. *ChemPhysChem* **2016**, *17*, 2645–2649.

[8] (a) Verreault, D.; Hua, W.; Allen, H. C. *J. Phys. Chem. Lett.* **2012**, *3*, 3012–3028; (b) Rich, C. C.; Mattson, M. A.; Krummel, A. T. *J. Phys. Chem. C* **2016**, *120*, 6601–6611; (c) Takeshita, N.; Okuno, M.; Ishibashi, T.-a. *Phys. Chem. Chem. Phys.* **2017**, *19*, 2060–2066.

[9] (a) Jang, J. H.; Lydiatt, F.; Lindsay, R.; Baldelli, S. *J. Phys. Chem. A* **2013**, *117*, 6288–6302; (b) Lu, X.; Myers, J. N.; Chen, Z. *Langmuir* **2014**, *30*, 9418–9422; (c) Wang, Z.; Han, X.; He, N.; Chen, Z.; Brooks, C. L. *J. Phys. Chem. B* **2014**, *118*, 12176–12185, PMID: 25265065; (d) Liu, S.; Fourkas, J. T. *J. Phys. Chem. B* **2014**, *118*, 8406–8419.

[10] (a) Shen, Y. R. *J. Phys. Chem. C* **2012**, *116*, 15505–15509; (b) Shen, Y. R. *Fundamentals of Sum-Frequency Spectroscopy*; Cambridge University Pres: Cambridge, 2016.

[11] (a) Tadjeddine, A.; Peremans, A.; Le Rille, A.; Zheng, W. Q.; Tadjeddine, M.; Flament, J.-P. *J. Chem. Soc., Faraday Trans.* **1996**, *92*, 3823–3828; (b) Rupprechter, G.; Morkel, M.; Freund, H. J.; Hirschl, R. *Surf. Sci.* **2004**, *554*, 43–59; (c) Mani, A. A.; Schultz, Z. D.; Champagne, B.; Humbert, C.; Dreesen, L.; Gewirth, A. A.; White, J. O.; Thiry, P. A.; Peremans, A.; Caudano, Y. *App. Surf. Sci.* **2004**, *237*, 445–450; (d) Morita, A.; Ishiyama, T. *Phys. Chem. Chem. Phys.* **2008**, *10*, 5801–5816; (e) Sulpizi, M.; Salanne, M.; Sprik, M.;

Gaigeot, M.-P. *J. Phys. Chem. Lett.* **2013**, *4*, 83–87; (f) Lee, C. M.; Mohamed, N. M. A.; Watts, H. D.; Kubicki, J. D.; Kim, S. H. *J. Phys. Chem. B* **2013**, *117*, 6681–6692; (g) Ishiyama, T.; Imamura, T.; Morita, A. *Chem. Rev.* **2014**, *114*, 8447–8470; (h) Mifflin, A. L.; Velarde, L.; Ho, J.; Psciuk, B. T.; Negre, C. F. A.; Ebben, C. J.; Upshur, M. A.; Lu, Z.; Strick, B. L.; Thomson, R. J.; Batista, V. S.; Wang, H.-F.; Geiger, F. M. *J. Phys. Chem. A* **2015**, *119*, 1292–1302; (i) Zheng, R.-H.; Wei, W.-M.; Shi, Q. *Phys. Chem. Chem. Phys.* **2015**, *17*, 9068–9073; (j) Meister, K.; Roeters, S. J.; Paananen, A.; Woutersen, S.; Versluis, J.; Szilvay, G. R.; Bakker, H. J. *J. Phys. Chem. Lett.* **2017**, *8*, 1772–1776; (k) Hosseinpour, S.; Tang, F.; Wang, F.; Livingstone, R. A.; Schlegel, S. J.; Ohto, T.; Bonn, M.; Nagata, Y.; Backus, E. H. G. *J. Phys. Chem. Lett.* **2017**, *8*, 2195–2199.

[12] Cecchet, F.; Lis, D.; Caudano, Y.; Mani, A. A.; Peremans, A.; Champagne, B.; Guthmuller, J. *J. Phys.: Condens. Matt.* **2012**, *24*, 124110.

[13] Tetsassi Feugmo, C. G.; Liégeois, V.; Champagne, B. *J. Phys. Chem. C* **2015**, *119*, 3180–3191.

[14] (a) Sekino, H.; Bartlett, R. J. *J. Phys. Chem.* **1993**, *98*, 3022–3027; (b) Datta, B.; Sen, P.; Mukherjee, D. *J. Phys. Chem.* **1995**, *99*, 6441–6451; (c) Yang, J.; Hättig, C. *J. Phys. Chem. A* **2009**, *131*, 074102–12; (d) Hickey, A. L.; Rowley, C. N. *J. Phys. Chem. A* **2014**, *118*, 3678–3687.

[15] (a) Hättig, C.; Christiansen, O.; Jørgensen, P. *J. Phys. Chem. Lett.* **1998**, *282*, 139–146; (b) Hammond, J. R.; Kowalski, K. *J. Chem. Phys.* **2009**, *130*, 194108–12; (c) Verma, P.; Perera, A.; Morales, J. A. *Mol. Phys.* **2016**, *114*, 547–561.

[16] (a) de Wergifosse, M.; Castet, F.; Champagne, B. *J. Chem. Phys.* **2015**, *142*, 194102–8; (b) Beaujean, P.; Champagne, B. *J. Chem. Phys.* **2016**, *145*, 044311–10.

[17] (a) Florian, J.; Leszczynski, J.; Johnson, B. G.; Goodman, L. *Mol. Phys.* **1997**, *91*, 439–447; (b) Perera, A.; Bartlett, R. J. *Chem. Phys. Lett.* **1999**, *314*, 381–387–448; (c) Galabov, B.; Yamaguchi, Y.; Remington, R. B.; Schaefer, H. F. *J. Phys. Chem. A* **2002**, *106*, 819–832; (d) Neugebauer, J.; Reiher, M.; Hess, B. A. *J. Chem. Phys.* **2002**, *117*, 8623–8633; (e) O'Neill, D. P.; Kállay, M.; Gauss, J. *Mol. Phys.* **2007**, *105*, 2447–2453; (f) Crawford, T. D.; Ruud, K. *ChemPhysChem* **2011**, *12*, 3442–3448; (g) Villa, M.; Senent, M. L.; Dominguez-Gomez, R.; Alvarez-Bajo, O.; Carvajal, M. *J. Phys. Chem. A* **2011**, *115*, 13573–13580; (h) Hoobler, P. R.; Turney, J. M.; Schaefer, H. F. *J. Chem. Phys.* **2016**, *145*, 174301.

[18] (a) Himmelhaus, M.; Eisert, F.; Buck, M.; Grunze, M. *J. Phys. Chem. B* **2000**, *104*, 576–584; (b) Asanuma, H.; Noguchi, H.; Uosaki, K.; Yu, H.-Z. *J. Phys. Chem. B* **2006**, *110*, 4892–4899; (c) Santos, C. S.; Baldelli, S. *J. Phys. Chem. B* **2007**, *111*, 4715–4723; (d) Schleeger, M.; Nagata, Y.; Bonn, M. *J. Phys. Chem. Lett.* **2014**, *5*, 3737–3741; (e) Myers, J. N.; Zhang, X.; Bielefeld, J.; Lin, Q.; Chen, Z. *J. Phys. Chem. B* **2015**, *119*, 1736–1746.

[19] Guthmuller, J.; Cecchet, F.; Lis, D.; Caudano, Y.; Mani, A. A.; Thiry, P. A.; Peremans, A.; Champagne, B. *ChemPhysChem* **2009**, *10*, 2132–2142.

[20] Cecchet, F.; Lis, D.; Guthmuller, J.; Champagne, B.; Caudano, Y.; Silien, C.; Mani, A. A.; Thiry, P. A.; Peremans, A. *ChemPhysChem* **2010**, *11*, 607–615.

[21] Dunning, T. H. *J. Phys. Chem.* **1989**, *90*, 1007–1023.

[22] de Wergifosse, M.; Liégeois, V.; Champagne, B. *Int. J. Quantum Chem.* **2014**, *114*, 900–910.

[23] Frisch, M. J. et al. Gaussian-09 Revision D.01. Gaussian Inc. Wallingford CT 2009.

[24] Aidas, K. et al. *WIREs Comput. Mol. Sci.* **2014**, *4*, 269–284.

[25] Christiansen, O.; Halkier, A.; Koch, H.; Jørgensen, P.; Helgaker, T. *J. Phys. Chem.* **1998**, *108*, 2801–17.

[26] (a) Windt, D. L.; Cash, W. C.; Scott, M.; Arendt, P.; Newnam, B.; Fisher, R. F.; Swartzlander, A. B. *Appl. Opt.* **1988**, *27*, 246–278; (b) Refractive index database. https://refractiveindex.info/?shelf=main&book=Pt&page=Windt.

[27] Dreesen, L.; Humbert, C.; Celebi, M.; Lemaire, J. J.; Mani, A. A.; Thiry, P. A.; Peremans, A. *Appl. Phys. B* **2002**, *74*, 621–625.

[28] (a) Hirose, C.; Akamatsu, N.; Domen, K. *J. Chem. Phys.* **1992**, *96*, 997–1004; (b) Hirose, C.; Yamamoto, H.; Akamatsu, N.; Domen, K. *J. Phys. Chem.* **1993**, *97*, 10064–10069.

[29] Zhuang, X.; Miranda, P.; Kim, D.; Shen, Y. *Phys. Rev. B* **1999**, *59*, 12632–12640.

[30] Lu, R.; Gan, W.; Wu, B.-h.; Zhang, Z.; Guo, Y.; Wang, H.-f. *J. Phys. Chem. B* **2005**, *109*, 14118–14129.

[31] Jena, K. C.; Hung, K.-K.; Schwantje, T. R.; Hore, D. K. *J. Chem. Phys.* **2011**, *135*, 044704.

[32] Wu, H.; Zhang, W.-k.; Gan, W.; Cui, Z.-f.; Wang, H.-f. *J. Chem. Phys.* **2006**, *125*, 133203–13.

[33] Liégeois, V. DrawMol. UNamur, www.unamur.be/drawmol.

# Part IV

# Summary, General Conclusion, and Outlooks

# Summary, General Conclusion, and Outlooks

My work aimed at developing new tools for the simulations and the interpretation of sum-frequency generation (SFG) signatures of functionalized surfaces. Indeed, SFG is a powerful and versatile method for *in situ* investigation of surfaces and interfaces. In SFG experiments a pulsed tunable infrared ($\omega_{IR}$) laser beam is mixed with a visible ($\omega_{VIS}$) beam to produce an output at the sum frequency ($\omega_{SFG} = \omega_{IR} + \omega_{VIS}$). SFG is a second-order nonlinear optical process, which is allowed only in media lacking inversion symmetry. At surfaces or interfaces, the inversion symmetry is necessarily broken: it makes SFG highly surface specific. As the IR wavelength is scanned, active vibrational modes of molecules at the interface give a resonant contribution to the SFG signal. In fact, a vibrational mode is active in SFG if it is simultaneously active in IR and Raman. The resonant enhancement provides therefore spectral information on surface characteristic vibrational transitions.

So, I developed an approach for simulating and interpreting SFG signatures of molecules adsorbed on different substrates. This approach encompasses two steps. First, the molecular properties (vibrational frequencies, IR and Raman quantities) are evaluated using first principles approaches implemented in standard quantum chemistry programs. Second, the macroscopic optical responses (the second-order nonlinear optical susceptibility tensor) of the adsorbate on its substrate are determined within the three-layer model of the interface. For this latter step, I have designed and worked out a Python program (software package) named "`SFG-from-QM`", that can be installed on different operating systems (Mac OS X, Unix, Linux, Windows) so that the script called "`SFG-from-QM.py`" can take the input and output data files as command-line arguments. The program reads the molecular properties (vibrational frequencies, IR and Raman quantities) evaluated using first-principles approaches implemented in standard quantum chemistry programs, calculates the Fresnel factor and accounts for the molecular orientation in the lab frame, and then generates the SFG spectra for different combinations of molecular orientations and experimental set-ups. The particularities of the approach are i) the substrate is included in the system during the calculations; ii) all the simulations are based on first-principles calculations. Combining these two aspects is a sophisticated task, and it greatly improves the analysis of experimental spectra, and the determination of molecular orientation. In addition to `SFG-from-QM.py`, our approach is now a part of **DrawVib** (www.unamur.be/drawvib) and

**DrawSpectrum** (www.unamur.be/drawspectrum) programs available on the Apple App Store for the Mac OS operating systems. **DrawVib** has similar interface to **DrawSpectrum**, and allows visualizing simultaneously the spectrum and the molecule or its normal modes in 3-D leading to an easier assignment of peaks and analysis of spectra.

In practice, my approach consists of two models, one with the surface (*adsorbed-model*: where a fragment of the surface is included in the quantum chemistry calculations and the rest is characterized by its electric permittivity) and the other (*isolated-model*) with only implicit surface (electric permittivity). The first has the advantage of defining directly the orientation of the molecule with respect to the surface, while the second allows to study the impact of that orientation on the SFG intensities. Indeed, with the *adsorbed-model*, the parameters such as the tilt and rotation angles between the molecular and laboratory framework are defined by the optimized geometry. On the other hand, in the *isolated-model* these parameters can be tuned, highlighting the IR wavelength region where the SFG intensities are strong. Moreover, for each model, I also used *sub-models* in which vibrations of parts of the system can be frozen independently in order to highlight selectively SFG signatures or different groups of chemical functions.

My approach has been applied to a variety of systems including organic monolayers covalently bonded to inorganic surfaces. These results are important for the scientific community using nonlinear vibrational SFG spectroscopy because they address questions related to the quantification of the SFG signal, a tricky task in this domain, and because functionalized semiconductor surfaces are extensively used in the manufacturing of biosensors and in optoelectronics. Given that the SFG intensity is directly related to the IR and Raman activity, I started our investigations with the simulation of the IR and Raman signatures of aromatics thiols adsorbed on small gold clusters mimicking the different types of adsorption site. Using analysis tools such as normal mode overlaps (Section 5.2.1), the group coupling matrices, and the atomic contribution patterns (decomposition of IR and Raman intensities into atomic or group of atoms contributions, Section 5.2.2), I bring out the effects of the adsorption and of the coordination site on the IR and Raman signatures, and therefore I show the reliability of small clusters for mimicking surfaces. Moreover, formula for evaluating enhancement factors in SERS spectroscopy have been derived and applied.

Then, I carried out SFG simulations on alkyl chains covalently bonded to hydrogen-terminated Si(111) substrates and alkylsilanes adsorbed onto amorphous silica surfaces for three polarization combinations (ppp, sps and ssp). Different models have been considered so that again normal modes overlaps have been used to analyze their vibrational signatures. In addition to reproducing the spectral profiles, I also provided a detailed analysis of the experiment showing that our approach is reliable. Indeed, including surface in the simulation improves its quality, while tuning the rotation angle of the alkyl chain in the *isolated-model* shows its strong impact of the spectral profile. Considering these observations, I predicted SFG signatures for other systems of interest whose experimental data are not yet available. Finally, since all the previous calculations were carried out at DFT level of approximation, I reported for the first time simulation of SFG spectra

for interfacial model alkyl chains based on molecular properties calculated with high-level wave function methods, at the coupled cluster singles and doubles (CCSD) level of approximation. I provided a detailed analysis of the signature of terminal alkyl chains and I assessed several, electronic and mechanical, approximate schemes, providing benchmark data for comparisons with approximate methods, including density functional theory (DFT)

However, my work can be viewed as a first but necessary step towards improved simulations and interpretations. Indeed, all the calculations were performed under the double harmonic approximation [Eqs. (3.87) and (3.88)] and the non-resonant contribution of the susceptibility [Eq. (3.104)] was always set to zero. On the one hand, going beyond the harmonic approximation will allow us to describe effects such as Fermi resonances. Indeed, in the double harmonic approximation, in addition to the Hamiltonian truncated at the quadratic term (blue terms, i.e. the vibrational wavefunctions are limited to the harmonic contribution), the Taylor expansions of the molecular properties (dipole moment and polarizability) are also limited, at the first-order derivatives with respect to the normal modes (green terms).

$$\hat{H} = -\frac{\hbar^2}{2}\sum_k \frac{\partial^2}{\partial Q_k^2} + \frac{1}{2}\sum_k \omega_k^2 Q_k^2 + \frac{1}{6}\sum_k\sum_l\sum_m F_{klm} Q_k Q_l Q_m + \dots$$

$$P(Q) = P^0 + \sum_k \left(\frac{\partial P}{\partial Q_k}\right)_e Q_k + \frac{1}{2}\sum_k\sum_l \left(\frac{\partial^2 P}{\partial Q_k \partial Q_l}\right)_e Q_k Q_l + \dots$$

So, anharmonicity can be introduced by considering higher-order terms, either on the nuclear Hamiltonian or on the molecular properties (that will change the expression of the first hyperpolarizability, see equation below), or on both. Note that, some groups have already employed approaches that include the Fermi resonances and combination bands in SFG spectra [1–3]. On the other hand, including the non-resonant part of the susceptibility will allow working with substrates with electronic transitions close to the visible (incident) and/or SFG wavelengths such as gold and silver.

$$\beta_{\alpha\beta\gamma}(-\omega_{SFG};\omega_{vis},\omega_{IR}) = \sum_p \frac{1}{4\omega_p} \frac{\left(\frac{\partial \alpha_{\alpha\beta}(\omega_{vis})}{\partial Q_p}\right)_e \left(\frac{\partial \mu_\gamma}{\partial Q_p}\right)_e}{(\omega_p - \omega_{IR} - i\Gamma_p)}$$

Different schemes to include the electric field gradients effects and quadrupole contributions to SFG spectra have been proposed and would constitute an interesting extension of this work [4–7]. Other extensions encompass the used of quantum mechanical/molecular mechanical (QM/MM) approaches to investigate several molecules at the surface (figure below) and thus to better reflect real systems. Indeed, due to the very demanding computational cost, the application of QM is still limited to relatively small systems consisting of up to few hundreds of atoms, or even smaller systems when the highest levels of theory are employed (CCSD for example). Algorithms

that combine quantum mechanics and molecular mechanics provide a solution to this problem. These algorithms in principle combine the accuracy of a quantum mechanical description with the low computational cost of molecular mechanics. The incorporation of quantum mechanics into molecular mechanics can be accomplished in various ways, and one of them, the so-called "ONIOM" method, was briefly presented in Section 4.6 and applied in Chapter 8. This approach makes possible the study of the interactions between molecules adsorbed at the surface and their dynamics. Moreover, periodic first principles calculations constitute another way to consider many molecules and taking into account the interactions between them. However, to our knowledge these approaches still present practical limitations to calculate the IR and Raman quantities of systems with large unit cells.

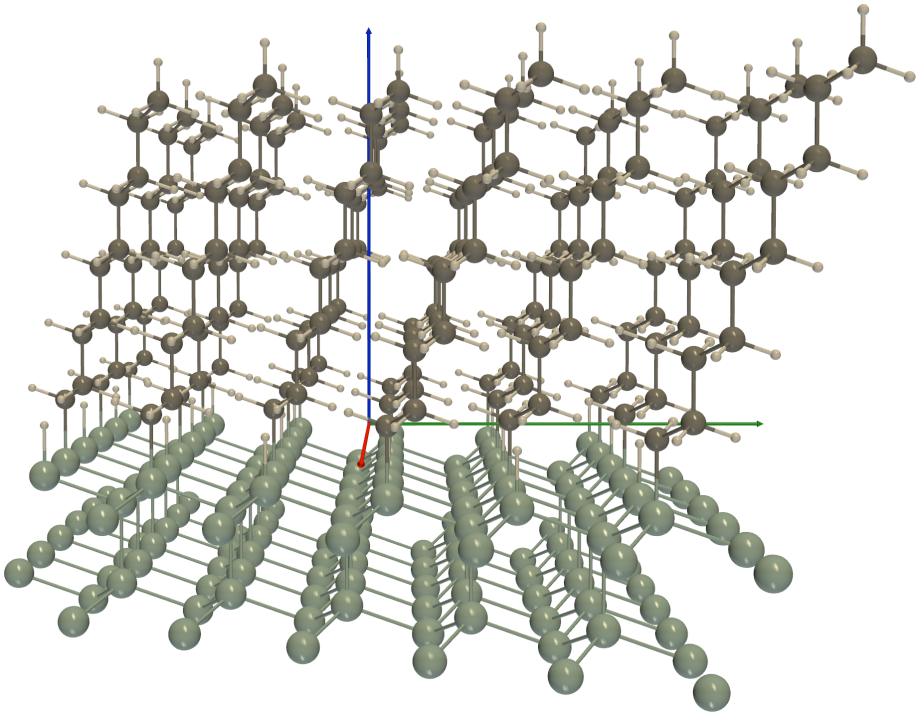

Model of functionalized H−Si(111) surfaces. Eighteen decyl molecules are grafted on the surface

# References

[1] Ho, J.; Psciuk, B. T.; Chase, H. M.; Rudshteyn, B.; Upshur, M. A.; Fu, L.; Thomson, R. J.; Wang, H.-f.; Geiger, F. M.; Batista, V. S. *J. Phys. Chem. C* **2016**, *120*, 12578–12589.

[2] Ohto, T.; Backus, E. H. G.; Mizukami, W.; Hunger, J.; Bonn, M.; Nagata, Y. *J. Phys. Chem. C* **2016**, *120*, 17435–17443.

[3] Yagi, K.; Hirata, S.; Hirao, K. *Phys. Chem. Chem. Phys.* **2008**, *10*, 1781–1788.

[4] Morita, A. *Theory of Sum Frequency Generation Spectroscopy*; Springer, 2018.

[5] (a) Busson, B.; Dalstein, L. *J. Chem. Phys.* **2018**, *149*, 154701; (b) Busson, B.; Dalstein, L. *J. Chem. Phys.* **2018**, *149*, 034701.

[6] Wan, Q.; Galli, G. *Phys. Rev. Lett.* **2015**, *115*, 246404.

[7] Yamaguchi, S.; Shiratori, K.; Morita, A.; Tahara, T. *J. Chem. Phys.* **2011**, *134*, 184705.

# Part V

# Appendices

# Appendix A

# Vibrational First Hyperpolarizability

In this section, we rely on the Symmetry relations to develop the full expression of the first hyperpolarizability given in Eq. (2.61). Then, we derive an expression for the molecular vibrational contribution to the simply IR resonant IR-visible Sum-Frequency Generation (SFG) process (Fig. A.1). Finally, from that vibrational first hyperpolarizability we also extract the expression of the transition polarizability and present the case of the Raman spectroscopy.

## A.1 Symmetry relations for the first hyperpolarizability

According to Eq. (2.61) the first hyperpolarizability reads

$$\beta^{\alpha\beta\gamma}(-\omega_q-\omega_r;\omega_q,\omega_r)=\frac{1}{\hbar^2}\sum_{l,m,n}\Bigg[\left(\rho^{(0)}_{mm}-\rho^{(0)}_{ll}\right)\frac{\mu^{\alpha}_{mn}\mu^{\gamma}_{lm}\mu^{\beta}_{nl}}{\left(\omega_{lm}-\omega_q-i\gamma_{lm}\right)\left(\omega_{nm}-\omega_q-\omega_r-i\gamma_{nm}\right)} \tag{A.1a}$$

$$-\left(\rho^{(0)}_{ll}-\rho^{(0)}_{nn}\right)\frac{\mu^{\alpha}_{mn}\mu^{\gamma}_{nl}\mu^{\beta}_{lm}}{\left(\omega_{nl}-\omega_q-i\gamma_{nl}\right)\left(\omega_{nm}-\omega_q-\omega_r-i\gamma_{nm}\right)}\Bigg] \tag{A.1b}$$

We have labeled the two terms that appear in this expression (A.1a) and (A.1b) so that we can keep track of how these terms contribute to our final expression. Eq. (A.1) does not possess intrinsic permutation symmetry, which we require the susceptibility to possess.

$$\beta^{\alpha\beta\gamma}(-\omega_q-\omega_r;\omega_q,\omega_r)\neq\beta^{\alpha\beta\gamma}(-\omega_q-\omega_r;\omega_r,\omega_q) \tag{A.2}$$

We therefore define the first hyperpolarizability to be one-half the sum of the right-hand side of Eq. (A.1) with an analogous expression obtained by simultaneously interchanging $\omega_q$ with $\omega_r$

$$\beta^{\alpha\beta\gamma}(-\omega_q-\omega_r;\omega_q,\omega_r)=\frac{1}{2}\left[\beta^{\alpha\beta\gamma}(-\omega_q-\omega_r;\omega_q,\omega_r)+\beta^{\alpha\beta\gamma}(-\omega_q-\omega_r;\omega_r,\omega_q)\right] \tag{A.3}$$

We thereby obtain the result

$$\beta^{\alpha\beta\gamma}(-\omega_q-\omega_r;\omega_q,\omega_r)=\frac{1}{2\hbar^2}\sum_{l,m,n}\Bigg\{\left(\rho^{(0)}_{mm}-\rho^{(0)}_{ll}\right)\Bigg[\frac{\mu^{\alpha}_{mn}\mu^{\gamma}_{lm}\mu^{\beta}_{nl}}{\left(\omega_{lm}-\omega_q-i\gamma_{lm}\right)\left(\omega_{nm}-\omega_q-\omega_r-i\gamma_{nm}\right)} \tag{A.4a}$$

$$+\frac{\mu^{\alpha}_{mn}\mu^{\beta}_{lm}\mu^{\gamma}_{nl}}{\left(\omega_{lm}-\omega_r-i\gamma_{lm}\right)\left(\omega_{nm}-\omega_q-\omega_r-i\gamma_{nm}\right)}\Bigg] \tag{A.4b}$$

$$-\left(\rho^{(0)}_{ll}-\rho^{(0)}_{nn}\right)\Bigg[\frac{\mu^{\alpha}_{mn}\mu^{\gamma}_{nl}\mu^{\beta}_{lm}}{\left(\omega_{nl}-\omega_q-i\gamma_{nl}\right)\left(\omega_{nm}-\omega_q-\omega_r-i\gamma_{nm}\right)} \tag{A.4c}$$

$$+\frac{\mu^{\alpha}_{mn}\mu^{\beta}_{nl}\mu^{\gamma}_{lm}}{\left(\omega_{nl}-\omega_r-i\gamma_{nl}\right)\left(\omega_{nm}-\omega_q-\omega_r-i\gamma_{nm}\right)}\Bigg]\Bigg\} \tag{A.4d}$$

This expression displays intrinsic permutation symmetry Since the indices $m$, $n$, and $l$ are summed over, they constitute dummy indices. We can therefore replace the indices $l$, $n$, and $m$ in the last two terms (A.15) and (A.16) by $m$, $l$, and $n$, respectively, so that the population difference term is the same as that of the first two terms. We thereby recast first hyperpolarizability into the form

$$\beta^{\alpha\beta\gamma}(-\omega_q-\omega_r;\omega_q,\omega_r)=\frac{1}{2\hbar^2}\sum_{l,m,n}\Bigg\{\left(\rho^{(0)}_{mm}-\rho^{(0)}_{ll}\right)\Bigg[\frac{\mu^{\alpha}_{mn}\mu^{\gamma}_{lm}\mu^{\beta}_{nl}}{\left(\omega_{lm}-\omega_q-i\gamma_{lm}\right)\left(\omega_{nm}-\omega_q-\omega_r-i\gamma_{nm}\right)} \tag{A.5a}$$

$$+\frac{\mu^{\alpha}_{mn}\mu^{\beta}_{lm}\mu^{\gamma}_{nl}}{\left(\omega_{lm}-\omega_r-i\gamma_{lm}\right)\left(\omega_{nm}-\omega_q-\omega_r-i\gamma_{nm}\right)}\Bigg] \tag{A.5b}$$

$$-\left(\rho_{ll}{}^{(0)}-\rho_{nn}{}^{(0)}\right)\Bigg[\frac{\mu^{\alpha}_{mn}\mu^{\gamma}_{nl}\mu^{\beta}_{lm}}{\left(\omega_{nl}-\omega_q-i\gamma_{nl}\right)\left(\omega_{nm}-\omega_q-\omega_r-i\gamma_{nm}\right)} \tag{A.5c}$$

$$+\frac{\bar{\mu}^{\alpha}_{mn}\mu^{\beta}_{nl}\mu^{\gamma}_{lm}}{\left(\omega_{nl}-\omega_r-i\gamma_{nl}\right)\left(\omega_{nm}-\omega_q-\omega_r-i\gamma_{nm}\right)}\Bigg]\Bigg\} \tag{A.5d}$$

The dummy indexes of the terms (A.5c) and (A.5d) are permuted

$$l\rightarrow m\rightarrow n\rightarrow l$$

$$\begin{aligned}\beta^{\alpha\beta\gamma}(-\omega_q-\omega_r;\omega_q,\omega_r) =& \frac{1}{2\hbar^2}\sum_{l,m,n}\Bigg\{\left(\rho^{(0)}_{mm}-\rho^{(0)}_{ll}\right)\Bigg[\frac{\mu^{\alpha}_{mn}\mu^{\gamma}_{lm}\mu^{\beta}_{nl}}{\left(\omega_{lm}-\omega_q-i\gamma_{lm}\right)\left(\omega_{nm}-\omega_q-\omega_r-i\gamma_{nm}\right)}\\ &+\frac{\mu^{\alpha}_{mn}\mu^{\beta}_{lm}\mu^{\gamma}_{nl}}{\left(\omega_{lm}-\omega_r-i\gamma_{lm}\right)\left(\omega_{nm}-\omega_q-\omega_r-i\gamma_{nm}\right)}\Bigg]\\ &-\left({\rho_{mm}}^{(0)}-{\rho_{ll}}^{(0)}\right)\Bigg[\frac{\mu^{\alpha}_{nl}\mu^{\gamma}_{lm}\mu^{\beta}_{mn}}{\left(\omega_{lm}-\omega_q-i\gamma_{lm}\right)\left(\omega_{ln}-\omega_q-\omega_r-i\gamma_{ln}\right)}\\ &+\frac{\mu^{\alpha}_{nl}\mu^{\beta}_{lm}\mu^{\gamma}_{mn}}{\left(\omega_{lm}-\omega_r-i\gamma_{lm}\right)\left(\omega_{ln}-\omega_q-\omega_r-i\gamma_{ln}\right)}\Bigg]\Bigg\}\\ =& \frac{1}{2\hbar^2}\sum_{l,m,n}\left({\rho_{mm}}^{(0)}-{\rho_{ll}}^{(0)}\right)\\ &\Bigg\{\frac{\mu^{\alpha}_{mn}\mu^{\gamma}_{lm}\mu^{\beta}_{nl}}{\left(\omega_{lm}-\omega_q-i\gamma_{lm}\right)\left(\omega_{nm}-\omega_q-\omega_r-i\gamma_{nm}\right)} &\text{(A.6a)}\\ &+\frac{\mu^{\alpha}_{mn}\mu^{\beta}_{lm}\mu^{\gamma}_{nl}}{\left(\omega_{lm}-\omega_r-i\gamma_{lm}\right)\left(\omega_{nm}-\omega_q-\omega_r-i\gamma_{nm}\right)} &\text{(A.6b)}\\ &-\frac{\mu^{\alpha}_{nl}\mu^{\gamma}_{lm}\mu^{\beta}_{mn}}{\left(\omega_{lm}-\omega_q-i\gamma_{lm}\right)\left(\omega_{ln}-\omega_q-\omega_r-i\gamma_{ln}\right)} &\text{(A.6c)}\\ &+\frac{\mu^{\alpha}_{nl}\mu^{\beta}_{lm}\mu^{\gamma}_{mn}}{\left(\omega_{lm}-\omega_r-i\gamma_{lm}\right)\left(\omega_{ln}-\omega_q-\omega_r-i\gamma_{ln}\right)}\Bigg\} &\text{(A.6d)}\end{aligned}$$

The dummy indexes $l$ and $m$ are switched

$$l \leftrightarrow m$$

$$\begin{aligned}\beta^{\alpha\beta\gamma}(-\omega_q-\omega_r;\omega_q,\omega_r) =& \frac{1}{2\hbar^2}\sum_{l,m,n}\left({\rho_{ll}}^{(0)}-{\rho_{mm}}^{(0)}\right)\\ &\Bigg\{\frac{\mu^{\alpha}_{ln}\mu^{\gamma}_{ml}\mu^{\beta}_{nm}}{\left(\omega_{ml}-\omega_q-i\gamma_{ml}\right)\left(\omega_{nl}-\omega_q-\omega_r-i\gamma_{nl}\right)} &\text{(A.7a)}\\ &+\frac{\mu^{\alpha}_{ln}\mu^{\beta}_{ml}\mu^{\gamma}_{nm}}{\left(\omega_{ml}-\omega_r-i\gamma_{ml}\right)\left(\omega_{nl}-\omega_q-\omega_r-i\gamma_{nl}\right)} &\text{(A.7b)}\\ &-\frac{\mu^{\alpha}_{nm}\mu^{\gamma}_{ml}\mu^{\beta}_{ln}}{\left(\omega_{ml}-\omega_q-i\gamma_{ml}\right)\left(\omega_{mn}-\omega_q-\omega_r-i\gamma_{mn}\right)} &\text{(A.7c)}\\ &-\frac{\mu^{\alpha}_{nm}\mu^{\beta}_{ml}\mu^{\gamma}_{ln}}{\left(\omega_{ml}-\omega_r-i\gamma_{ml}\right)\left(\omega_{mn}-\omega_q-\omega_r-i\gamma_{mn}\right)}\Bigg\} &\text{(A.7d)}\end{aligned}$$

We reorder the product of matrix elements in the numerator so that the subscripts $n$, $m$, and $l$ are "chained" in the sense shown and thereby obtain the result

$$\beta^{\alpha\beta\gamma}(-\omega_q-\omega_r;\omega_q,\omega_r)=\frac{1}{2\hbar^2}\sum_{l,m,n}\left(\rho^{(0)}_{ll}-\rho^{(0)}_{mm}\right)$$

$$\left\{\frac{\mu^{\alpha}_{ln}\mu^{\gamma}_{ml}\mu^{\beta}_{nm}}{\left(\omega_{ml}-\omega_q-i\gamma_{ml}\right)\left(\omega_{nl}-\omega_q-\omega_r-i\gamma_{nl}\right)}\right. \tag{A.8a}$$

$$+\frac{\mu^{\alpha}_{ln}\mu^{\beta}_{ml}\mu^{\gamma}_{nm}}{\left(\omega_{ml}-\omega_r-i\gamma_{ml}\right)\left(\omega_{nl}-\omega_q-\omega_r-i\gamma_{nl}\right)} \tag{A.8b}$$

$$-\frac{\mu^{\alpha}_{nm}\mu^{\gamma}_{ml}\mu^{\beta}_{ln}}{\left(\omega_{ml}-\omega_q-i\gamma_{ml}\right)\left(\omega_{mn}-\omega_q-\omega_r-i\gamma_{mn}\right)} \tag{A.8c}$$

$$\left.-\frac{\mu^{\alpha}_{nm}\mu^{\beta}_{ml}\mu^{\gamma}_{ln}}{\left(\omega_{ml}-\omega_r-i\gamma_{ml}\right)\left(\omega_{mn}-\omega_q-\omega_r-i\gamma_{mn}\right)}\right\} \tag{A.8d}$$

$$\beta^{\alpha\beta\gamma}(-\omega_q-\omega_r;\omega_q,\omega_r)=\frac{1}{2\hbar^2}\sum_{l,m,n}\left(\rho^{(0)}_{ll}-\rho^{(0)}_{mm}\right)$$

$$\left\{\frac{\mu^{\alpha}_{ln}\mu^{\beta}_{nm}\mu^{\gamma}_{ml}}{\left(\omega_{ml}-\omega_q-i\gamma_{ml}\right)\left(\omega_{nl}-\omega_q-\omega_r-i\gamma_{nl}\right)}\right. \tag{A.9a}$$

$$+\frac{\mu^{\alpha}_{ln}\mu^{\gamma}_{nm}\mu^{\beta}_{ml}}{\left(\omega_{ml}-\omega_r-i\gamma_{ml}\right)\left(\omega_{nl}-\omega_q-\omega_r-i\gamma_{nl}\right)} \tag{A.9b}$$

$$-\frac{\mu^{\beta}_{ln}\mu^{\alpha}_{nm}\mu^{\gamma}_{ml}}{\left(\omega_{ml}-\omega_q-i\gamma_{ml}\right)\left(\omega_{mn}-\omega_q-\omega_r-i\gamma_{mn}\right)} \tag{A.9c}$$

$$\left.-\frac{\mu^{\gamma}_{ln}\mu^{\alpha}_{nm}\mu^{\beta}_{ml}}{\left(\omega_{ml}-\omega_r-i\gamma_{ml}\right)\left(\omega_{mn}-\omega_q-\omega_r-i\gamma_{mn}\right)}\right\} \tag{A.9d}$$

$$\beta^{\alpha\beta\gamma}(-\omega_q-\omega_r;\omega_q,\omega_r)=\frac{1}{2\hbar^2}\sum_{l,m,n}\left(\rho^{(0)}_{ll}-\rho^{(0)}_{mm}\right)$$

$$\left\{\frac{\mu^{\alpha}_{ln}\mu^{\beta}_{nm}\mu^{\gamma}_{ml}}{\left(\omega_{ml}-\omega_q-i\gamma_{ml}\right)\left(\omega_{nl}-\omega_q-\omega_r-i\gamma_{nl}\right)}\right. \tag{A.10a}$$

$$+\frac{\mu^{\alpha}_{ln}\mu^{\gamma}_{nm}\mu^{\beta}_{ml}}{\left(\omega_{ml}-\omega_r-i\gamma_{ml}\right)\left(\omega_{nl}-\omega_q-\omega_r-i\gamma_{nl}\right)} \tag{A.10b}$$

$$+\frac{\mu^{\beta}_{ln}\mu^{\alpha}_{nm}\mu^{\gamma}_{ml}}{\left(\omega_{ml}-\omega_q-i\gamma_{ml}\right)\left(\omega_{nm}+\omega_q+\omega_r+i\gamma_{nm}\right)} \tag{A.10c}$$

$$\left.+\frac{\mu^{\gamma}_{ln}\mu^{\alpha}_{nm}\mu^{\beta}_{ml}}{\left(\omega_{ml}-\omega_r-i\gamma_{ml}\right)\left(\omega_{nm}+\omega_q+\omega_r+i\gamma_{nm}\right)}\right\} \tag{A.10d}$$

The first hyperpolarizability can be expressed in terms of a single level population

$$\beta^{\alpha\beta\gamma}(-\omega_q-\omega_r;\omega_q,\omega_r) = \frac{1}{2\hbar^2}\sum_{l,m,n}\rho^{(0)}_{ll}\left\{\frac{\mu^{\alpha}_{ln}\mu^{\beta}_{nm}\mu^{\gamma}_{ml}}{\left(\omega_{ml}-\omega_q-i\gamma_{ml}\right)\left(\omega_{nl}-\omega_q-\omega_r-i\gamma_{nl}\right)}\right. \tag{A.11a}$$

$$+\frac{\mu^{\alpha}_{ln}\mu^{\gamma}_{nm}\mu^{\beta}_{ml}}{\left(\omega_{ml}-\omega_r-i\gamma_{ml}\right)\left(\omega_{nl}-\omega_q-\omega_r-i\gamma_{nl}\right)} \tag{A.11b}$$

$$+\frac{\mu^{\beta}_{ln}\mu^{\alpha}_{nm}}{\left(\omega_{ml}-\omega_q-i\gamma_{ml}\right)\left(\omega_{nm}+\omega_q+\omega_r+i\gamma_{nm}\right)} \tag{A.11c}$$

$$\left.+\frac{\mu^{\gamma}_{ln}\mu^{\alpha}_{nm}\mu^{\beta}_{ml}}{\left(\omega_{ml}-\omega_r-i\gamma_{ml}\right)\left(\omega_{nm}+\omega_q+\omega_r+i\gamma_{nm}\right)}\right\} \tag{A.11d}$$

$$-\frac{1}{2\hbar^2}\sum_{l,m,n}\rho^{(0)}_{mm}\left\{\frac{\mu^{\alpha}_{ln}\mu^{\beta}_{nm}\mu^{\gamma}_{ml}}{\left(\omega_{ml}-\omega_q-i\gamma_{ml}\right)\left(\omega_{nl}-\omega_q-\omega_r-i\gamma_{nl}\right)}\right. \tag{A.11e}$$

$$-\frac{\mu^{\alpha}_{ln}\mu^{\gamma}_{nm}\mu^{\beta}_{ml}}{\left(\omega_{ml}-\omega_r-i\gamma_{ml}\right)\left(\omega_{nl}-\omega_q-\omega_r-i\gamma_{nl}\right)} \tag{A.11f}$$

$$-\frac{\mu^{\beta}_{ln}\mu^{\alpha}_{nm}\mu^{\gamma}_{ml}}{\left(\omega_{ml}-\omega_q-i\gamma_{ml}\right)\left(\omega_{nm}+\omega_q+\omega_r+i\gamma_{nm}\right)} \tag{A.11g}$$

$$\left.-\frac{\mu^{\gamma}_{ln}\mu^{\alpha}_{nm}\mu^{\beta}_{ml}}{\left(\omega_{ml}-\omega_r-i\gamma_{ml}\right)\left(\omega_{nm}+\omega_q+\omega_r+i\gamma_{nm}\right)}\right\} \tag{A.11h}$$

We reorder the product of matrix elements in the numerator so that the subscripts $n$, $m$, and $l$ are"chained" in the sense shown and thereby obtain the result

$$\beta^{\alpha\beta\gamma}(-\omega_q-\omega_r;\omega_q,\omega_r) = \frac{1}{2\hbar^2}\sum_{l,m,n}\rho^{(0)}_{ll}\left[\frac{\mu^{\alpha}_{ln}\mu^{\beta}_{nm}\mu^{\gamma}_{ml}}{\left(\omega_{ml}-\omega_q-i\gamma_{ml}\right)\left(\omega_{nl}-\omega_q-\omega_r-i\gamma_{nl}\right)}\right. \tag{A.12a}$$

$$+\frac{\mu^{\alpha}_{ln}\mu^{\gamma}_{nm}\mu^{\beta}_{ml}}{\left(\omega_{ml}-\omega_r-i\gamma_{ml}\right)\left(\omega_{nl}-\omega_q-\omega_r-i\gamma_{nl}\right)} \tag{A.12b}$$

$$+\frac{\mu^{\beta}_{ln}\mu^{\alpha}_{nm}\mu^{\gamma}_{ml}}{\left(\omega_{ml}-\omega_q-i\gamma_{ml}\right)\left(\omega_{nm}+\omega_q+\omega_r+i\gamma_{nm}\right)} \tag{A.12c}$$

$$\left.+\frac{\mu^{\gamma}_{ln}\mu^{\alpha}_{nm}\mu^{\beta}_{ml}}{\left(\omega_{ml}-\omega_r-i\gamma_{ml}\right)\left(\omega_{nm}+\omega_q+\omega_r+i\gamma_{nm}\right)}\right] \tag{A.12d}$$

$$-\frac{1}{2\hbar^2}\sum_{l,m,n}\rho^{(0)}_{mm}\left[\frac{\mu^{\alpha}_{ln}\mu^{\beta}_{nm}\mu^{\gamma}_{ml}}{\left(\omega_{ml}-\omega_q-i\gamma_{ml}\right)\left(\omega_{nl}-\omega_q-\omega_r-i\gamma_{nl}\right)}\right. \tag{A.12e}$$

$$-\frac{\mu^{\alpha}_{ln}\mu^{\gamma}_{nm}\mu^{\beta}_{ml}}{\left(\omega_{ml}-\omega_r-i\gamma_{ml}\right)\left(\omega_{nl}-\omega_q-\omega_r-i\gamma_{nl}\right)} \tag{A.12f}$$

$$-\frac{\mu^{\beta}_{ln}\mu^{\alpha}_{nm}\mu^{\gamma}_{ml}}{\left(\omega_{ml}-\omega_q-i\gamma_{ml}\right)\left(\omega_{nm}+\omega_q+\omega_r+i\gamma_{nm}\right)} \tag{A.12g}$$

$$\left.-\frac{\mu^{\gamma}_{ln}\mu^{\alpha}_{nm}\mu^{\beta}_{ml}}{\left(\omega_{ml}-\omega_r-i\gamma_{ml}\right)\left(\omega_{nm}+\omega_q+\omega_r+i\gamma_{nm}\right)}\right] \tag{A.12h}$$

$$l \to n \to m \to l$$

$$\beta^{\alpha\beta\gamma}(-\omega_q-\omega_r;\omega_q,\omega_r) = \frac{1}{2\hbar^2}\sum_{l,m,n}\rho_{ll}^{(0)}\Bigg[\frac{\mu_{ln}^{\alpha}\mu_{nm}^{\beta}\mu_{ml}^{\gamma}}{\left(\omega_{ml}-\omega_q-i\gamma_{ml}\right)\left(\omega_{nl}-\omega_q-\omega_r-i\gamma_{nl}\right)} \tag{A.13a}$$

$$+\frac{\mu_{ln}^{\alpha}\mu_{nm}^{\gamma}\mu_{ml}^{\beta}}{\left(\omega_{ml}-\omega_r-i\gamma_{ml}\right)\left(\omega_{nl}-\omega_q-\omega_r-i\gamma_{nl}\right)} \tag{A.13b}$$

$$+\frac{mu_{ln}^{\beta}\mu_{nm}^{\alpha}\mu_{ml}^{\gamma}}{\left(\omega_{ml}-\omega_q-i\gamma_{ml}\right)\left(\omega_{nm}+\omega_q+\omega_r+i\gamma_{nm}\right)} \tag{A.13c}$$

$$+\frac{\mu_{ln}^{\gamma}\mu_{nm}^{\alpha}\mu_{ml}^{\beta}}{\left(\omega_{ml}-\omega_r-i\gamma_{ml}\right)\left(\omega_{nm}+\omega_q+\omega_r+i\gamma_{nm}\right)}\Bigg] \tag{A.13d}$$

$$-\frac{1}{2\hbar^2}\sum_{l,m,n}\rho_{ll}{}^{(0)}\Bigg[\frac{\mu_{nm}^{\alpha}\mu_{ml}^{\beta}\mu_{ln}^{\gamma}}{\left(\omega_{ln}-\omega_q-i\gamma_{ln}\right)\left(\omega_{mn}-\omega_q-\omega_r-i\gamma_{mn}\right)} \tag{A.13e}$$

$$-\frac{\mu_{nm}^{\alpha}\mu_{ml}^{\gamma}\mu_{ln}^{\beta}}{\left(\omega_{ln}-\omega_r-i\gamma_{ln}\right)\left(\omega_{mn}-\omega_q-\omega_r-i\gamma_{mn}\right)} \tag{A.13f}$$

$$-\frac{\mu_{nm}^{\beta}\mu_{ml}^{\alpha}\mu_{ln}^{\gamma}}{\left(\omega_{ln}-\omega_q-i\gamma_{ln}\right)\left(\omega_{ml}+\omega_q+\omega_r+i\gamma_{ml}\right)} \tag{A.13g}$$

$$-\frac{\mu_{nm}^{\gamma}\mu_{ml}^{\alpha}\mu_{ln}^{\beta}}{\left(\omega_{ln}-\omega_r-i\gamma_{ln}\right)\left(\omega_{ml}+\omega_q+\omega_r+i\gamma_{ml}\right)}\Bigg] \tag{A.13h}$$

Dipoles moment are moved to present the same transition order.

$$\beta^{\alpha\beta\gamma}(-\omega_q-\omega_r;\omega_q,\omega_r) = \frac{1}{2\hbar^2}\sum_{l,m,n}\rho_{ll}^{(0)}\Bigg[\frac{\mu_{ln}^{\alpha}\mu_{nm}^{\beta}\mu_{ml}^{\gamma}}{\left(\omega_{ml}-\omega_q-i\gamma_{ml}\right)\left(\omega_{nl}-\omega_q-\omega_r-i\gamma_{nl}\right)} \tag{A.14a}$$

$$+\frac{\mu_{ln}^{\alpha}\mu_{nm}^{\gamma}\mu_{ml}^{\beta}}{\left(\omega_{ml}-\omega_r-i\gamma_{ml}\right)\left(\omega_{nl}-\omega_q-\omega_r-i\gamma_{nl}\right)} \tag{A.14b}$$

$$+\frac{\mu_{ln}^{\beta}\mu_{nm}^{\alpha}\mu_{ml}^{\gamma}}{\left(\omega_{ml}-\omega_q-i\gamma_{ml}\right)\left(\omega_{nm}+\omega_q+\omega_r+i\gamma_{nm}\right)} \tag{A.14c}$$

$$+\frac{\mu_{ln}^{\gamma}\mu_{nm}^{\alpha}\mu_{ml}^{\beta}}{\left(\omega_{ml}-\omega_r-i\gamma_{ml}\right)\left(\omega_{nm}+\omega_q+\omega_r+i\gamma_{nm}\right)}\Bigg] \tag{A.14d}$$

$$-\frac{1}{2\hbar^2}\sum_{l,m,n}\rho_{ll}{}^{(0)}\Bigg[\frac{\mu_{ln}^{\gamma}\mu_{nm}^{\alpha}\mu_{ml}^{\beta}}{\left(\omega_{ln}-\omega_q-i\gamma_{ln}\right)\left(\omega_{mn}-\omega_q-\omega_r-i\gamma_{mn}\right)} \tag{A.14e}$$

$$-\frac{\mu_{ln}^{\beta}\mu_{nm}^{\alpha}\mu_{ml}^{\gamma}}{\left(\omega_{ln}-\omega_r-i\gamma_{ln}\right)\left(\omega_{mn}-\omega_q-\omega_r-i\gamma_{mn}\right)} \tag{A.14f}$$

$$-\frac{\mu_{ln}^{\gamma}\mu_{nm}^{\beta}\mu_{ml}^{\alpha}}{\left(\omega_{ln}-\omega_q-i\gamma_{ln}\right)\left(\omega_{ml}+\omega_q+\omega_r+i\gamma_{ml}\right)} \tag{A.14g}$$

$$-\frac{\mu_{ln}^{\beta}\mu_{nm}^{\gamma}\mu_{ml}^{\alpha}}{\left(\omega_{ln}-\omega_r-i\gamma_{ln}\right)\left(\omega_{ml}+\omega_q+\omega_r+i\gamma_{ml}\right)}\Bigg] \tag{A.14h}$$

The frequencies and the damping are modified to give a positive expression.

$$\beta^{\alpha\beta\gamma}(-\omega_q-\omega_r;\omega_q,\omega_r) = \frac{1}{2\hbar^2}\sum_{l,m,n}\rho_{ll}^{(0)}\Bigg[\frac{\mu_{ln}^{\alpha}\mu_{nm}^{\beta}\mu_{ml}^{\gamma}}{\left(\omega_{ml}-\omega_q-i\gamma_{ml}\right)\left(\omega_{nl}-\omega_q-\omega_r-i\gamma_{nl}\right)} \tag{A.15a}$$

$$+\frac{\mu_{ln}^{\alpha}\mu_{nm}^{\gamma}\mu_{ml}^{\beta}}{\left(\omega_{ml}-\omega_r-i\gamma_{ml}\right)\left(\omega_{nl}-\omega_q-\omega_r-i\gamma_{nl}\right)} \tag{A.15b}$$

$$+\frac{\mu_{ln}^{\beta}\mu_{nm}^{\alpha}\mu_{ml}^{\gamma}}{\left(\omega_{ml}-\omega_q-i\gamma_{ml}\right)\left(\omega_{nm}+\omega_q+\omega_r+i\gamma_{nm}\right)} \tag{A.15c}$$

$$+\frac{\mu_{ln}^{\gamma}\mu_{nm}^{\alpha}\mu_{ml}^{\beta}}{\left(\omega_{ml}-\omega_r-i\gamma_{ml}\right)\left(\omega_{nm}+\omega_q+\omega_r+i\gamma_{nm}\right)}\Bigg] \tag{A.15d}$$

$$+\frac{1}{2\hbar^2}\sum_{l,m,n}\rho_{ll}^{(0)}\Bigg[\frac{\mu_{ln}^{\gamma}\mu_{nm}^{\alpha}\mu_{ml}^{\beta}}{\left(\omega_{nl}+\omega_q+i\gamma_{nl}\right)\left(\omega_{mn}-\omega_q-\omega_r-i\gamma_{mn}\right)} \tag{A.15e}$$

$$+\frac{\mu_{ln}^{\beta}\mu_{nm}^{\alpha}\mu_{ml}^{\gamma}}{\left(\omega_{nl}+\omega_r+i\gamma_{nl}\right)\left(\omega_{mn}-\omega_q-\omega_r-i\gamma_{mn}\right)} \tag{A.15f}$$

$$+\frac{\mu_{ln}^{\gamma}\mu_{nm}^{R}\mu_{ml}^{\alpha}}{\left(\omega_{nl}+\omega_q+i\gamma_{nl}\right)\left(\omega_{ml}+\omega_q+\omega_r+i\gamma_{ml}\right)} \tag{A.15g}$$

$$+\frac{\mu_{ln}^{\beta}\mu_{nm}^{\gamma}\mu_{ml}^{\alpha}}{\left(\omega_{nl}+\omega_r+i\gamma_{nl}\right)\left(\omega_{ml}+\omega_q+\omega_r+i\gamma_{ml}\right)}\Bigg] \tag{A.15h}$$

We obtain a sum of 8 resonant and non-resonant terms .

$$\beta^{\alpha\beta\gamma}(-\omega_q-\omega_r;\omega_q,\omega_r) = \frac{1}{2\hbar^2}\sum_{l,m,n}\rho_{ll}^{(0)}\Bigg[\frac{\mu_{ln}^{\alpha}\mu_{nm}^{\beta}\mu_{ml}^{\gamma}}{\left(\omega_{ml}-\omega_q-i\gamma_{ml}\right)\left(\omega_{nl}-\omega_q-\omega_r-i\gamma_{nl}\right)} \tag{A.16a}$$

$$+\frac{\mu_{ln}^{\alpha}\mu_{nm}^{\gamma}\mu_{ml}^{\beta}}{\left(\omega_{ml}-\omega_r-i\gamma_{ml}\right)\left(\omega_{nl}-\omega_q-\omega_r-i\gamma_{nl}\right)} \tag{A.16b}$$

$$+\frac{\mu_{ln}^{\beta}\mu_{nm}^{\alpha}\mu_{ml}^{\gamma}}{\left(\omega_{ml}-\omega_q-i\gamma_{ml}\right)\left(\omega_{nm}+\omega_q+\omega_r+i\gamma_{nm}\right)} \tag{A.16c}$$

$$+\frac{\mu_{ln}^{\gamma}\mu_{nm}^{\alpha}\mu_{ml}^{\beta}}{\left(\omega_{ml}-\omega_r-i\gamma_{ml}\right)\left(\omega_{nm}+\omega_q+\omega_r+i\gamma_{nm}\right)} \tag{A.16d}$$

$$+\frac{\mu_{ln}^{\gamma}\mu_{nm}^{\alpha}\mu_{ml}^{\beta}}{\left(\omega_{nl}+\omega_q+i\gamma_{nl}\right)\left(\omega_{mn}-\omega_q-\omega_r-i\gamma_{mn}\right)} \tag{A.16e}$$

$$+\frac{\mu_{ln}^{\beta}\mu_{nm}^{\alpha}\mu_{ml}^{\gamma}}{\left(\omega_{nl}+\omega_r+i\gamma_{nl}\right)\left(\omega_{mn}-\omega_q-\omega_r-i\gamma_{mn}\right)} \tag{A.16f}$$

$$+\frac{\mu_{ln}^{\gamma}\mu_{nm}^{\beta}\mu_{ml}^{\alpha}}{\left(\omega_{nl}+\omega_q+i\gamma_{nl}\right)\left(\omega_{ml}+\omega_q+\omega_r+i\gamma_{ml}\right)} \tag{A.16g}$$

$$+\frac{\mu_{ln}^{\beta}\mu_{nm}^{\gamma}\mu_{ml}^{\alpha}}{\left(\omega_{nl}+\omega_r+i\gamma_{nl}\right)\left(\omega_{ml}+\omega_q+\omega_r+i\gamma_{ml}\right)}\Bigg] \tag{A.16h}$$

## A.2 Vibrational first hyperpolarizability for SFG

In this section, we treat the molecular vibrational contribution to the simply IR resonant IR-visible Sum-Frequency Generation (SFG) process (Fig. A.1).

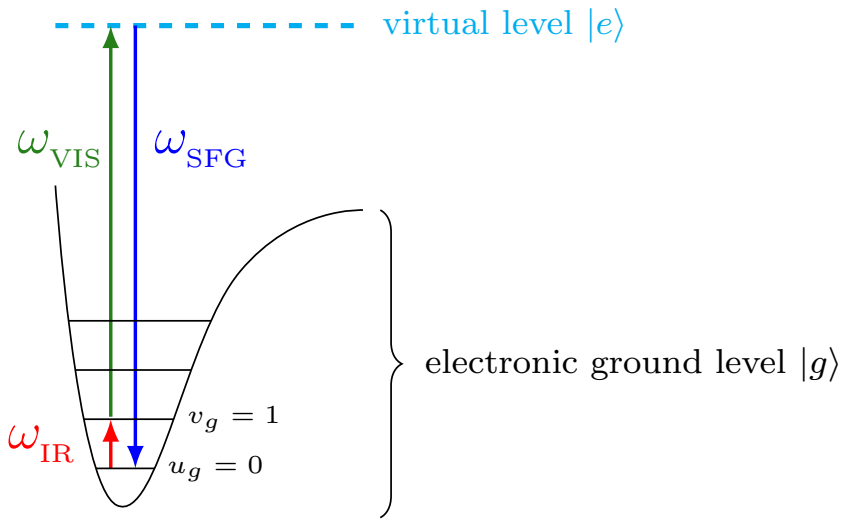


FIGURE A.1: Energy levels in SFG process

The first hyperpolarizability can be expressed in terms of a single level population as

$$\beta^{\alpha\beta\gamma}(-\omega_q-\omega_r;\omega_q,\omega_r) = \frac{1}{2\hbar^2}\sum_{l,m,n}\rho_{ll}^{(0)}\left[\frac{\mu_{ln}^{\alpha}\mu_{nm}^{\beta}\mu_{ml}^{\gamma}}{\left(\omega_{ml}-\omega_q-i\gamma_{ml}\right)\left(\omega_{nl}-\omega_q-\omega_r-i\gamma_{nl}\right)}\right. \tag{A.17a}$$

$$+\frac{\mu_{ln}^{\alpha}\mu_{nm}^{\gamma}\mu_{ml}^{\beta}}{\left(\omega_{ml}-\omega_r-i\gamma_{ml}\right)\left(\omega_{nl}-\omega_q-\omega_r-i\gamma_{nl}\right)} \tag{A.17b}$$

$$+\frac{\mu_{ln}^{\beta}\mu_{nm}^{\alpha}\mu_{ml}^{\gamma}}{\left(\omega_{ml}-\omega_q-i\gamma_{ml}\right)\left(\omega_{nm}+\omega_q+\omega_r+i\gamma_{nm}\right)} \tag{A.17c}$$

$$+\frac{\mu_{ln}^{\gamma}\mu_{nm}^{\alpha}\mu_{ml}^{\beta}}{\left(\omega_{ml}-\omega_r-i\gamma_{ml}\right)\left(\omega_{nm}+\omega_q+\omega_r+i\gamma_{nm}\right)} \tag{A.17d}$$

$$+\frac{\mu_{ln}^{\gamma}\mu_{nm}^{\alpha}\mu_{ml}^{\beta}}{\left(\omega_{nl}+\omega_q+i\gamma_{nl}\right)\left(\omega_{mn}-\omega_q-\omega_r-i\gamma_{mn}\right)} \tag{A.17e}$$

$$+\frac{\mu_{ln}^{\beta}\mu_{nm}^{\alpha}\mu_{ml}^{\gamma}}{\left(\omega_{nl}+\omega_r+i\gamma_{nl}\right)\left(\omega_{mn}-\omega_q-\omega_r-i\gamma_{mn}\right)} \tag{A.17f}$$

$$+\frac{\mu_{ln}^{\gamma}\mu_{nm}^{\beta}\mu_{ml}^{\alpha}}{\left(\omega_{nl}+\omega_q+i\gamma_{nl}\right)\left(\omega_{ml}+\omega_q+\omega_r+i\gamma_{ml}\right)} \tag{A.17g}$$

$$\left.+\frac{\mu_{ln}^{\beta}\mu_{nm}^{\gamma}\mu_{ml}^{\alpha}}{\left(\omega_{nl}+\omega_r+i\gamma_{nl}\right)\left(\omega_{ml}+\omega_q+\omega_r+i\gamma_{ml}\right)}\right] \tag{A.17h}$$

In the case of the SFG the first hyperpolarizability can be therefore rewritten as

$$\beta^{\alpha\beta\gamma}(-\omega_{SFG};\omega_{IR},\omega_{vis}) = \frac{1}{2\hbar^2}\sum_{l,m,n}\rho_{ll}^{(0)}\Bigg[\frac{\mu_{ln}^{\alpha}\mu_{nm}^{\beta}\mu_{ml}^{\gamma}}{\left(\omega_{ml}-\omega_{IR}-i\gamma_{ml}\right)\left(\omega_{nl}-\omega_{SFG}-i\gamma_{nl}\right)} + \frac{\mu_{ln}^{\alpha}\mu_{nm}^{\gamma}\mu_{ml}^{\beta}}{\left(\omega_{ml}-\omega_{vis}-i\gamma_{ml}\right)\left(\omega_{nl}-\omega_{SFG}-i\gamma_{nl}\right)} + \frac{\mu_{ln}^{\beta}\mu_{nm}^{\alpha}\mu_{ml}^{\gamma}}{\left(\omega_{ml}-\omega_{IR}-i\gamma_{ml}\right)\left(\omega_{nm}+\omega_{SFG}+i\gamma_{nm}\right)} + \frac{\mu_{ln}^{\gamma}\mu_{nm}^{\alpha}\mu_{ml}^{\beta}}{\left(\omega_{ml}-\omega_{vis}-i\gamma_{ml}\right)\left(\omega_{nm}+\omega_{SFG}+i\gamma_{nm}\right)} + \frac{\mu_{ln}^{\gamma}\mu_{nm}^{\alpha}\mu_{ml}^{\beta}}{\left(\omega_{nl}+\omega_{IR}+i\gamma_{nl}\right)\left(\omega_{mn}-\omega_{SFG}-i\gamma_{mn}\right)} + \frac{\mu_{ln}^{\beta}\mu_{nm}^{\alpha}\mu_{ml}^{\gamma}}{\left(\omega_{nl}+\omega_{vis}+i\gamma_{nl}\right)\left(\omega_{mn}-\omega_{SFG}-i\gamma_{mn}\right)} + \frac{\mu_{ln}^{\gamma}\mu_{nm}^{\beta}\mu_{ml}^{\alpha}}{\left(\omega_{nl}+\omega_{IR}+i\gamma_{nl}\right)\left(\omega_{ml}+\omega_{SFG}+i\gamma_{ml}\right)} + \frac{\mu_{ln}^{\beta}\mu_{nm}^{\gamma}\mu_{ml}^{\alpha}}{\left(\omega_{nl}+\omega_{vis}+i\gamma_{nl}\right)\left(\omega_{ml}+\omega_{SFG}+i\gamma_{ml}\right)}\Bigg] \tag{A.18}$$

The terms are reorganized according to resonant factor of the pump beams

$$\beta^{\alpha\beta\gamma}(-\omega_{SFG};\omega_{IR},\omega_{vis}) = \frac{1}{2\hbar^2}\sum_{l,m,n}\rho_{ll}^{(0)}\Bigg[\frac{\mu_{ml}^{\gamma}}{\left(\omega_{ml}-\omega_{IR}-i\gamma_{ml}\right)}\frac{\mu_{ln}^{\alpha}\mu_{nm}^{\beta}}{\left(\omega_{nl}-\omega_{SFG}-i\gamma_{nl}\right)} + \frac{\mu_{ml}^{\gamma}}{\left(\omega_{ml}-\omega_{IR}-i\gamma_{ml}\right)}\frac{\mu_{ln}^{\beta}\mu_{nm}^{\alpha}}{\left(\omega_{nm}+\omega_{SFG}+i\gamma_{nm}\right)} + \frac{\mu_{ln}^{\gamma}}{\left(\omega_{nl}+\omega_{IR}+i\gamma_{nl}\right)}\frac{\mu_{nm}^{\alpha}\mu_{ml}^{\beta}}{\left(\omega_{mn}-\omega_{SFG}-i\gamma_{mn}\right)} + \frac{\mu_{ln}^{\gamma}}{\left(\omega_{nl}+\omega_{IR}+i\gamma_{nl}\right)}\frac{\mu_{nm}^{\beta}\mu_{ml}^{\alpha}}{\left(\omega_{ml}+\omega_{SFG}+i\gamma_{ml}\right)} + \frac{\mu_{ml}^{\beta}}{\left(\omega_{ml}-\omega_{vis}-i\gamma_{ml}\right)}\frac{\mu_{ln}^{\alpha}\mu_{nm}^{\gamma}}{\left(\omega_{nl}-\omega_{SFG}-i\gamma_{nl}\right)} + \frac{\mu_{ml}^{\beta}}{\left(\omega_{ml}-\omega_{vis}-i\gamma_{ml}\right)}\frac{\mu_{ln}^{\gamma}\mu_{nm}^{\alpha}}{\left(\omega_{nm}+\omega_{SFG}+i\gamma_{nm}\right)} + \frac{\mu_{ln}^{\beta}}{\left(\omega_{nl}+\omega_{vis}+i\gamma_{nl}\right)}\frac{\mu_{nm}^{\alpha}\mu_{ml}^{\gamma}}{\left(\omega_{mn}-\omega_{SFG}-i\gamma_{mn}\right)} + \frac{\mu_{ln}^{\beta}}{\left(\omega_{nl}+\omega_{vis}+i\gamma_{nl}\right)}\frac{\mu_{nm}^{\gamma}\mu_{ml}^{\alpha}}{\left(\omega_{ml}+\omega_{SFG}+i\gamma_{ml}\right)}\Bigg] \tag{A.19}$$

The dummy indexes are switched in the third, fourth, seventh, and eighth terms.

$$n \Leftrightarrow m$$

$$\begin{aligned}\beta^{\alpha\beta\gamma}(-\omega_{SFG};\omega_{IR},\omega_{vis}) = \frac{1}{2\hbar^2}\sum_{l,m,n}\rho_{ll}^{(0)}\Bigg[&\frac{\mu_{ml}^{\gamma}}{(\omega_{ml}-\omega_{IR}-i\gamma_{ml})}\frac{\mu_{ln}^{\alpha}\mu_{nm}^{\beta}}{(\omega_{nl}-\omega_{SFG}-i\gamma_{nl})}\\ &+\frac{\mu_{ml}^{\gamma}}{(\omega_{ml}-\omega_{IR}-i\gamma_{ml})}\frac{\mu_{ln}^{\beta}\mu_{nm}^{\alpha}}{(\omega_{nm}+\omega_{SFG}+i\gamma_{nm})}\\ &+\frac{\mu_{lm}^{\gamma}}{(\omega_{ml}+\omega_{IR}+i\gamma_{ml})}\frac{\mu_{mn^{\alpha}}\mu_{nl}^{\beta}}{(\omega_{nm}-\omega_{SFG}-i\gamma_{nm})}\\ &+\frac{\mu_{lm}^{\gamma}}{(\omega_{ml}+\omega_{IR}+i\gamma_{ml})}\frac{\mu_{mn^{\beta}}\mu_{nl}^{\alpha}}{(\omega_{nl}+\omega_{SFG}+i\gamma_{nl})}\\ &+\frac{\mu_{ml}^{\beta}}{(\omega_{ml}-\omega_{vis}-i\gamma_{ml})}\frac{\mu_{ln}^{\alpha}\mu_{nm}^{\gamma}}{(\omega_{nl}-\omega_{SFG}-i\gamma_{nl})}\\ &+\frac{\mu_{ml}^{\beta}}{(\omega_{ml}-\omega_{vis}-i\gamma_{ml})}\frac{\mu_{ln}^{\gamma}\mu_{nm}^{\alpha}}{(\omega_{nm}+\omega_{SFG}+i\gamma_{nm})}\\ &+\frac{\mu_{lm}^{\beta}}{(\omega_{ml}+\omega_{vis}+i\gamma_{ml})}\frac{\mu_{mn}^{\alpha}\mu_{nl}^{\gamma}}{(\omega_{nm}-\omega_{SFG}-i\gamma_{nm})}\\ &+\frac{\mu_{lm}^{\beta}}{(\omega_{ml}+\omega_{vis}+i\gamma_{ml})}\frac{\mu_{mn}^{\gamma}\mu_{nl}^{\alpha}}{(\omega_{nl}+\omega_{SFG}+i\gamma_{nl})}\Bigg]\end{aligned} \tag{A.20}$$

At low temperature, only the vibrational states of the fundamental electronic state is occupied. We distinguish the electronic states $(g,e,f)$ from the vibrational states $(u,v,w)$. $\rho_{ll}^{(0)} = |gu\rangle$ and $\omega_{IR} = |\omega_{ml}|$ ($\rightarrow gu$, $m \rightarrow gv$, and $n \rightarrow ew$)

$$\begin{aligned}\beta^{\alpha\beta\gamma}(-\omega_{SFG};\omega_{IR},\omega_{vis}) = \frac{1}{2\hbar^2}\sum_{u,v}\Bigg[&\frac{\mu_{gv,gu}^{\gamma}}{(\omega_{gv,gu}-\omega_{IR}-i\gamma_{gv,gu})}\sum_{ew}\frac{\mu_{gu,ew}^{\alpha}\mu_{ew,gv}^{\beta}}{(\omega_{ew,gu}-\omega_{SFG}-i\gamma_{ew,gu})}\\ &+\frac{\mu_{gv,gu}^{\gamma}}{(\omega_{gv,gu}-\omega_{IR}-i\gamma_{gv,gu})}\sum_{ew}\frac{\mu_{gu,ew}^{\beta}\mu_{ew,gv}^{\alpha}}{(\omega_{ew,gv}+\omega_{SFG}+i\gamma_{ew,gv})}\\ &+\frac{\mu_{gu,gv}^{\gamma}}{(\omega_{gv,gu}+\omega_{IR}+i\gamma_{gv,gu})}\sum_{ew}\frac{\mu_{gv,ew}^{\alpha}\mu_{ew,gu}^{\beta}}{(\omega_{ew,gv}-\omega_{SFG}-i\gamma_{ew,gv})}\\ &+\frac{\mu_{gu,gv}^{\gamma}}{(\omega_{gv,gu}+\omega_{IR}+i\gamma_{gv,gu})}\sum_{ew}\frac{\mu_{gv,ew}^{\beta}\mu_{ew,gu}^{\alpha}}{(\omega_{ew,gu}+\omega_{SFG}+i\gamma_{ew,gu})}\\ &+\frac{\mu_{gv,gu}^{\beta}}{(\omega_{gv,gu}-\omega_{vis}-i\gamma_{gv,gu})}\sum_{ew}\frac{\mu_{gu,ew}^{\alpha}\mu_{ew,gv}^{\gamma}}{(\omega_{ew,gu}-\omega_{SFG}-i\gamma_{ew,gu})}\\ &+\frac{\mu_{gv,gu}^{\beta}}{(\omega_{gv,gu}-\omega_{vis}-i\gamma_{gv,gu})}\sum_{ew}\frac{\mu_{gu,ew}^{\gamma}\mu_{ew,gv}^{\alpha}}{(\omega_{ew,gv}+\omega_{SFG}+i\gamma_{ew,gv})}\\ &+\frac{\mu_{gu,gv}^{\beta}}{(\omega_{gv,gu}+\omega_{vis}+i\gamma_{gv,gu})}\sum_{ew}\frac{\mu_{gv,ew}^{\alpha}\mu_{ew,gu}^{\gamma}}{(\omega_{ew,gv}-\omega_{SFG}-i\gamma_{ew,gv})}\end{aligned}$$

$$+\frac{\mu^{\beta}_{gu,gv}}{\left(\omega_{gv,gu}+\omega_{vis}+i\gamma_{gv,gu}\right)}\sum_{ew}\frac{\mu^{\gamma}_{gv,ew}\mu^{\alpha}_{ew,gu}}{\left(\omega_{ew,gu}+\omega_{SFG}+i\gamma_{ew,gu}\right)}\Bigg] \tag{A.21}$$

Only the fundamental electronic state is thermally occupied.

$$\begin{aligned}\mu_{gv,gu}&=\langle v_g|\langle g|\mu|g\rangle|u_g\rangle\\&=\langle v_g|\mu_{gg}|u_g\rangle\end{aligned} \tag{A.22}$$

$$\omega_{gv,gu}=\omega_{vu} \tag{A.23}$$

Under the Placzek's polarizability approximation,

$$\omega_{ew,gu}\simeq\omega_{ew,gv}\simeq\omega_{eg} \tag{A.24}$$

$$\begin{aligned}\sum_{ew}\mu_{gu,ew}\mu_{ew,gv}&=\sum_{ew}\langle u_g|\langle g|\mu|e\rangle|w\rangle\langle w|\langle e|\mu|g\rangle|v_g\rangle\\&=\sum_{e}\langle u_g|\mu_{ge}\mu_{eg}|v_g\rangle\end{aligned} \tag{A.25}$$

$$\begin{aligned}\beta^{\alpha\beta\gamma}(-\omega_{SFG};\omega_{IR},\omega_{vis})=\frac{1}{2\hbar}\sum_{u,v}\Bigg[&\frac{\langle v_g|\mu^{\gamma}_{gg}|u_g\rangle}{\left(\omega_{vu}-\omega_{IR}-i\gamma_{vu}\right)}\left\langle u_g\right|\frac{1}{\hbar}\sum_{e}\frac{\mu^{\alpha}_{ge}\mu^{\beta}_{eg}}{\left(\omega_{eg}-\omega_{SFG}-i\gamma_{eg}\right)}\left|v_g\right\rangle\\&+\frac{\langle v_g|\mu^{\gamma}_{gg}|u_g\rangle}{\left(\omega_{vu}-\omega_{IR}-i\gamma_{vu}\right)}\left\langle u_g\right|\frac{1}{\hbar}\sum_{e}\frac{\mu^{\beta}_{ge}\mu^{\alpha}_{eg}}{\left(\omega_{eg}+\omega_{SFG}+i\gamma_{eg}\right)}\left|v_g\right\rangle\\&+\frac{\langle u_g|\mu^{\gamma}_{gg}|v_g\rangle}{\left(\omega_{vu}+\omega_{IR}+i\gamma_{vu}\right)}\left\langle v_g\right|\frac{1}{\hbar}\sum_{e}\frac{\mu^{\alpha}_{ge}\mu^{\beta}_{eg}}{\left(\omega_{eg}-\omega_{SFG}-i\gamma_{eg}\right)}\left|u_g\right\rangle\\&+\frac{\langle u_g|\mu^{\gamma}_{gg}|v_g\rangle}{\left(\omega_{vu}+\omega_{IR}+i\gamma_{vu}\right)}\left\langle v_g\right|\frac{1}{\hbar}\sum_{e}\frac{\mu^{\beta}_{ge}\mu^{\alpha}_{eg}}{\left(\omega_{eg}+\omega_{SFG}+i\gamma_{eg}\right)}\left|u_g\right\rangle\\&+\frac{\langle v_g|\mu^{\beta}_{gg}|u_g\rangle}{\left(\omega_{vu}-\omega_{vis}-i\gamma_{vu}\right)}\left\langle u_g\right|\frac{1}{\hbar}\sum_{e}\frac{\mu^{\alpha}_{ge}\mu^{\gamma}_{eg}}{\left(\omega_{eg}-\omega_{SFG}-i\gamma_{eg}\right)}\left|v_g\right\rangle\\&+\frac{\langle v_g|\mu^{\beta}_{gg}|u_g\rangle}{\left(\omega_{vu}-\omega_{vis}-i\gamma_{vu}\right)}\left\langle u_g\right|\frac{1}{\hbar}\sum_{e}\frac{\mu^{\gamma}_{ge}\mu^{\alpha}_{eg}}{\left(\omega_{eg}+\omega_{SFG}+i\gamma_{eg}\right)}\left|v_g\right\rangle\\&+\frac{\langle u_g|\mu^{\beta}_{gg}|v_g\rangle}{\left(\omega_{vu}+\omega_{vis}+i\gamma_{vu}\right)}\left\langle v_g\right|\frac{1}{\hbar}\sum_{e}\frac{\mu^{\alpha}_{ge}\mu^{\gamma}_{eg}}{\left(\omega_{eg}-\omega_{SFG}-i\gamma_{eg}\right)}\left|u_g\right\rangle\\&+\frac{\langle u_g|\mu^{\beta}_{gg}|v_g\rangle}{\left(\omega_{vu}+\omega_{vis}+i\gamma_{vu}\right)}\left\langle v_g\right|\frac{1}{\hbar}\sum_{e}\frac{\mu^{\gamma}_{ge}\mu^{\alpha}_{eg}}{\left(\omega_{eg}+\omega_{SFG}+i\gamma_{eg}\right)}\left|u_g\right\rangle\Bigg]\end{aligned} \tag{A.26}$$

Knowing that $\omega_{vis}\gg\omega_{IR}$, the last four terms can be neglected, one therefore obtain

$$\beta^{\alpha\beta\gamma}(-\omega_{SFG};\omega_{IR},\omega_{vis}) = \frac{1}{2\hbar}\sum_{u,v}\Bigg[\frac{\langle v_g|\mu^{\gamma}_{gg}|u_g\rangle}{(\omega_{vu}-\omega_{IR}-i\gamma_{vu})}\Big\langle u_g\Big|\frac{1}{\hbar}\sum_{e}\frac{\mu^{\alpha}_{ge}\mu^{\beta}_{eg}}{(\omega_{eg}-\omega_{SFG}-i\gamma_{eg})}\Big|v_g\Big\rangle + \frac{\langle v_g|\mu^{\gamma}_{gg}|u_g\rangle}{(\omega_{vu}-\omega_{IR}-i\gamma_{vu})}\Big\langle u_g\Big|\frac{1}{\hbar}\sum_{e}\frac{\mu^{\beta}_{ge}\mu^{\alpha}_{eg}}{(\omega_{eg}+\omega_{SFG}+i\gamma_{eg})}\Big|v_g\Big\rangle + \frac{\langle u_g|\mu^{\gamma}_{gg}|v_g\rangle}{(\omega_{vu}+\omega_{IR}+i\gamma_{vu})}\Big\langle v_g\Big|\frac{1}{\hbar}\sum_{e}\frac{\mu^{\alpha}_{ge}\mu^{\beta}_{eg}}{(\omega_{eg}-\omega_{SFG}-i\gamma_{eg})}\Big|u_g\Big\rangle + \frac{\langle u_g|\mu^{\gamma}_{gg}|v_g\rangle}{(\omega_{vu}+\omega_{IR}+i\gamma_{vu})}\Big\langle v_g\Big|\frac{1}{\hbar}\sum_{e}\frac{\mu^{\beta}_{ge}\mu^{\alpha}_{eg}}{(\omega_{eg}+\omega_{SFG}+i\gamma_{eg})}\Big|u_g\Big\rangle\Bigg] \tag{A.27}$$

$$\beta^{\alpha\beta\gamma}(-\omega_{SFG};\omega_{IR},\omega_{vis}) = \frac{1}{2\hbar}\sum_{u,v}\Bigg[\frac{\langle v_g|\mu^{\gamma}_{gg}|u_g\rangle}{(\omega_{vu}-\omega_{IR}-i\gamma_{vu})}\Big\langle u_g\Big|\frac{1}{\hbar}\sum_{e}\frac{\mu^{\alpha}_{ge}\mu^{\beta}_{eg}}{(\omega_{eg}-\omega_{SFG}-i\gamma_{eg})}+\frac{\mu^{\beta}_{ge}\mu^{\alpha}_{eg}}{(\omega_{eg}+\omega_{SFG}+i\gamma_{eg})}\Big|v_g\Big\rangle + \frac{\langle u_g|\mu^{\gamma}_{gg}|v_g\rangle}{(\omega_{vu}+\omega_{IR}+i\gamma_{vu})}\Big\langle u_g\Big|\frac{1}{\hbar}\sum_{e}\frac{\mu^{\alpha}_{ge}\mu^{\beta}_{eg}}{(\omega_{eg}-\omega_{SFG}-i\gamma_{eg})}+\frac{\mu^{\beta}_{ge}\mu^{\alpha}_{eg}}{(\omega_{eg}+\omega_{SFG}+i\gamma_{eg})}\Big|v_g\Big\rangle\Bigg] \tag{A.28}$$

For positive frequencies (i.e., for $\omega_{IR} > 0$), only the first term can become resonant. The second term is known as the antiresonant term. We can often drop the second term, especially when $\omega_{IR}$ is close to one of the vibrational resonance frequencies of the molecule.

$$\beta^{\alpha\beta\gamma}(-\omega_{SFG};\omega_{IR},\omega_{vis}) = \frac{1}{2\hbar}\sum_{u,v}\frac{\langle v_g|\mu^{\gamma}_{gg}|u_g\rangle}{(\omega_{vu}-\omega_{IR}-i\gamma_{vu})}\Big\langle u_g\Big|\frac{1}{\hbar}\sum_{e}\frac{\mu^{\alpha}_{ge}\mu^{\beta}_{eg}}{(\omega_{eg}-\omega_{SFG}-i\gamma_{eg})}+\frac{\mu^{\beta}_{ge}\mu^{\alpha}_{eg}}{(\omega_{eg}+\omega_{SFG}+i\gamma_{eg})}\Big|v_g\Big\rangle \tag{A.29}$$

## A.3 Transition polarizability for Raman spectroscopy

In Eq. (A.29) we recognize the $\alpha\beta$ component of the transition polarizability $(\alpha)_{uv}$

$$\left(\alpha^{\alpha\beta}\right)_{uv} = \left\langle u_g \middle| \frac{1}{\hbar} \sum_e \frac{\mu^{\alpha}_{ge}\mu^{\beta}_{eg}}{\left(\omega_{eg} - \omega_0 - i\gamma_{eg}\right)} + \frac{\mu^{\beta}_{ge}\mu^{\alpha}_{eg}}{\left(\omega_{eg} + \omega_0 + i\gamma_{eg}\right)} \middle| v_g \right\rangle \tag{A.30}$$

Since electronic wavefunction are real,

$$\langle u_g | \mu^{\alpha}_{ge}\mu^{\beta}_{eg} \, | v_g \rangle = \langle u_g | \mu^{\beta}_{ge}\mu^{\alpha}_{eg} | v_g \rangle \tag{A.31}$$

$$\alpha^{\alpha\beta} = \frac{1}{\hbar} \sum_e \mu^{\alpha}_{ge}\mu^{\beta}_{eg} \left[ \frac{1}{\left(\omega_{eg} - \omega_0 - i\gamma_{eg}\right)} + \frac{1}{\left(\omega_{eg} + \omega_0 + i\gamma_{eg}\right)} \right] \tag{A.32}$$

$$\begin{aligned} A &= \frac{1}{\left(\omega_{eg} - \omega_0 - i\gamma_{eg}\right)} + \frac{1}{\left(\omega_{eg} + +i\gamma_{eg}\right)} \\ &= \frac{2\omega_{eg}}{\omega^2_{eg} - \left(\omega_0 + i\gamma_{eg}\right)^2} \\ &= \frac{2\omega_{eg}}{\omega^2_{eg} - \omega^2_0 - i2\gamma_{eg}\omega_{eg} + \gamma^2_{eg}} \quad \text{where} \quad \gamma^2_{eg} \approx 0 \\ &\approx \frac{2\omega_{eg}}{(\omega^2_{eg} - \omega^2_0) - i2\gamma_{eg}\omega_{eg}} \\ &\approx 2\omega_{eg} \frac{(\omega^2_{eg} - \omega^2_0) + i2\gamma_{eg}\omega_{eg}}{(\omega^2_{eg} - \omega^2_0)^2 + 4\gamma^2_{eg}\omega^2_{eg}} \end{aligned} \tag{A.33}$$

It is convenient to introduce dispersion and absorption lineshape functions $f$ and $g$, where

$$f = \frac{\omega^2_{eg} - \omega^2_0}{(\omega^2_{eg} - \omega^2_0)^2 + 4\gamma^2_{eg}\omega^2_{eg}} \tag{A.34a}$$

$$g = \frac{2\gamma_{eg}\omega_{eg}}{(\omega^2_{eg} - \omega^2_0)^2 + 4\gamma^2_{eg}\omega^2_{eg}} \tag{A.34b}$$

It results that

$$A = 2\omega_{eg}(f + ig) \tag{A.35}$$

Far from resonance $\gamma_{eg} \approx 0$ then,

$$\begin{aligned} \alpha^{\alpha\beta}_{uv} &= \left\langle u_g \middle| \frac{1}{\hbar} \sum_e \mu^{\alpha}_{ge}\mu^{\beta}_{eg} \left[ \frac{1}{\left(\omega_{eg} - \omega_0\right)} + \frac{1}{\left(\omega_{eg} + \omega_0\right)} \right] \middle| v_g \right\rangle \\ &= \frac{1}{\hbar} \sum_e \frac{2\omega_{eg}}{\left(\omega^2_{eg} - \omega^2_0\right)} \left\langle u_g \left| \mu^{\alpha}_{ge}\mu^{\beta}_{eg} \right| v_g \right\rangle \end{aligned} \tag{A.36}$$

# Appendix B

# Polarization and Orientation Factors

In this section, we address the relationships between the directions of the electric fields of the incoming beams, $\vec{E}_{1i}$ and $\vec{E}_{2i}$ and the intensity reflected by the interface at sum-frequency. The incoming electric fields are related to the polarization $\vec{P}^{(2)}$by

$$\begin{aligned}\vec{P}^{(2)} &\simeq \tilde{\tilde{\chi}}^{(2)} \vdots\, F_1 \vec{E}_{1i} F_2 \vec{E}_{2i} \\ &\simeq \tilde{\tilde{\chi}}^{(2)} \vdots\, F_{vis} \vec{E}(\omega_{vis}) F_{IR} \vec{E}(\omega_{IR})\end{aligned} \tag{B.1}$$

where the tilde notation indicates the dimensionality of the tensors. $\vec{E}$ is a first rank tensor (vector: $3 \times 1$), whereas $\tilde{\tilde{\chi}}^{(2)}$ is a third rank tensor ($3 \times 3 \times 3$ array)

Heinz [1] expressed this relationships as

$$I_{SFG} \propto \left| (F_{SFG} \cdot \vec{\hat{e}}^{\perp}) \cdot \tilde{\tilde{\chi}}^{(2)} \vdots\, F_{vis} \vec{E}(\omega_{vis}) F_{IR} \vec{E}(\omega_{IR}) \right|^2 . \tag{B.2}$$

The $F_I$ are the Fresnel factors and $\vec{\hat{e}}^{\perp}$ is a vector perpendicular to the SFG wave vector ($\vec{k}_{3r}$).

In this thesis, Caudano [2] has derived the field reflected by the interface at sum-frequency for each polarization in the form (see Eq. (1.124) for details)

$$E_{3r,s} = i\frac{\omega_3}{c}\frac{1}{2\sqrt{\varepsilon_{3r}}\cos\theta_{3r}}\left[\frac{2k_{3r,Z}}{k_{3r,Z}+k_{3t,Z}}\right]\hat{p}_Y \frac{P^{(2)}(Z_0)}{\varepsilon_0} e^{ik_{3r,Z}\,Z_0}, \tag{B.3a}$$

$$\begin{aligned}E_{3r,p} = {} & i\frac{\omega_3}{c}\frac{1}{2\sqrt{\varepsilon_{3r}}\cos\theta_{3r}}\left[\frac{2\varepsilon_{3r}k_{3t,Z}}{\varepsilon_{3t}k_{3r,Z}+\varepsilon_{3r}k_{3t,Z}}\right]\hat{p}_X(-\cos\theta_{3r})\frac{P^{(2)}(Z_0)}{\varepsilon_0} e^{ik_{3r,Z}\,Z_0} \\ & + i\frac{\omega_3}{c}\frac{1}{2\sqrt{\varepsilon_{3r}}\cos\theta_{3r}}\left[\frac{2\varepsilon_{3t}k_{3r}}{\varepsilon_{3t}k_{3r,Z}+\varepsilon_{3r}k_{3t,Z}}\frac{\varepsilon_{3r}}{\varepsilon_{NL}}\right]\hat{p}_Z\sin\theta_{3r}\frac{P^{(2)}(Z_0)}{\varepsilon_0} e^{ik_{3r,Z}\,Z_0},\end{aligned} \tag{B.3b}$$

The developments found below are similar to that proposed by Lin et al. [3].

## B.1 Tensor product

The electric field direction is commonly referenced to the input-output plane; this plane is defined by the beam propagation direction and the surface normal (Fig. 1.3).

Multiplication of a tensor $\vec{\vec{\chi}}^{(2)}$ by a vector $\vec{\boldsymbol{E}}(\omega_{IR})$ results in a matrix, multiplication of the resulting matrix by a vector $\vec{\boldsymbol{E}}(\omega_{vis})$ results in a vector. The final multiplication by the output vector, $\vec{e}^{\perp}$ gives a scalar; the absolute value squared of which gives the intensity.

$\vec{\vec{\chi}}^{(2)}$ is a $3 \times 3 \times 3$ array with elements $(i = X, Y, Z)$

$$\begin{pmatrix} \chi^{(2)}_{iXX} & \chi^{(2)}_{iXY} & \chi^{(2)}_{iXZ} \\ \chi^{(2)}_{iYX} & \chi^{(2)}_{iYY} & \chi^{(2)}_{iYZ} \\ \chi^{(2)}_{iZX} & \chi^{(2)}_{iZY} & \chi^{(2)}_{iZZ} \end{pmatrix} \begin{pmatrix} E^{IR}_X \\ E^{IR}_Y \\ E^{IR}_Z \end{pmatrix} \equiv \begin{pmatrix} \chi^{(2)}_{iXX} E^{IR}_X + \chi^{(2)}_{iXY} E^{IR}_Y + \chi^{(2)}_{iXZ} E^{IR}_Z \\ \chi^{(2)}_{iYX} E^{IR}_X + \chi^{(2)}_{iYY} E^{IR}_Y + \chi^{(2)}_{iYZ} E^{IR}_Z \\ \chi^{(2)}_{iZX} E^{IR}_X + \chi^{(2)}_{iZY} E^{IR}_Y + \chi^{(2)}_{iZZ} E^{IR}_Z \end{pmatrix} \tag{B.4}$$

$$\vec{\vec{\chi}}^{(2)} \cdot \vec{E}(\omega_{IR}) = \begin{pmatrix} \chi^{(2)}_{XXX} E^{IR}_X + \chi^{(2)}_{XXY} E^{IR}_Y + \chi^{(2)}_{XXZ} E^{IR}_Z & \chi^{(2)}_{XYX} E^{IR}_X + \chi^{(2)}_{XYY} E^{IR}_Y + \chi^{(2)}_{XYZ} E^{IR}_Z & \chi^{(2)}_{XZX} E^{IR}_X + \chi^{(2)}_{XZY} E^{IR}_Y + \chi^{(2)}_{XZZ} E^{IR}_Z \\ \chi^{(2)}_{YYX} E^{IR}_X + \chi^{(2)}_{YYY} E^{IR}_Y + \chi^{(2)}_{YYZ} E^{IR}_Z & \chi^{(2)}_{YYX} E^{IR}_X + \chi^{(2)}_{YYY} E^{IR}_Y + \chi^{(2)}_{YYZ} E^{IR}_Z & \chi^{(2)}_{YZX} E^{IR}_X + \chi^{(2)}_{YZY} E^{IR}_Y + \chi^{(2)}_{YZZ} E^{IR}_Z \\ \chi^{(2)}_{ZXX} E^{IR}_X + \chi^{(2)}_{ZXY} E^{IR}_Y + \chi^{(2)}_{ZXZ} E^{IR}_Z & \chi^{(2)}_{ZYX} E^{IR}_X + \chi^{(2)}_{ZYY} E^{IR}_Y + \chi^{(2)}_{ZYZ} E^{IR}_Z & \chi^{(2)}_{ZZX} E^{IR}_X + \chi^{(2)}_{ZZY} E^{IR}_Y + \chi^{(2)}_{ZZZ} E^{IR}_Z \end{pmatrix} \tag{B.5}$$

Dotting this matrix into the $\vec{\boldsymbol{E}}(\omega_{vis})$ gives the vector:

$$\begin{pmatrix} \chi^{(2)}_{XXX} E^{IR}_X + \chi^{(2)}_{XXY} E^{IR}_Y + \chi^{(2)}_{XXZ} E^{IR}_Z & \chi^{(2)}_{XYX} E^{IR}_X + \chi^{(2)}_{XYY} E^{IR}_Y + \chi^{(2)}_{XYZ} E^{IR}_Z & \chi^{(2)}_{XZX} E^{IR}_X + \chi^{(2)}_{XZY} E^{IR}_Y + \chi^{(2)}_{XZZ} E^{IR}_Z \\ \chi^{(2)}_{YXX} E^{IR}_X + \chi^{(2)}_{YXY} E^{IR}_Y + \chi^{(2)}_{YXZ} E^{IR}_Z & \chi^{(2)}_{YYX} E^{IR}_X + \chi^{(2)}_{YYY} E^{IR}_Y + \chi^{(2)}_{YYZ} E^{IR}_Z & \chi^{(2)}_{YZX} E^{IR}_X + \chi^{(2)}_{YZY} E^{IR}_Y + \chi^{(2)}_{YZZ} E^{IR}_Z \\ \chi^{(2)}_{ZXX} E^{IR}_X + \chi^{(2)}_{ZXY} E^{IR}_Y + \chi^{(2)}_{ZXZ} E^{IR}_Z & \chi^{(2)}_{ZYX} E^{IR}_X + \chi^{(2)}_{ZYY} E^{IR}_Y + \chi^{(2)}_{ZYZ} E^{IR}_Z & \chi^{(2)}_{ZZX} E^{IR}_X + \chi^{(2)}_{ZZY} E^{IR}_Y + \chi^{(2)}_{ZZZ} E^{IR}_Z \end{pmatrix} \cdot \begin{pmatrix} E^{vis}_X \\ E^{vis}_Y \\ E^{vis}_Z \end{pmatrix} \tag{B.6}$$

$$\vec{P^{(2)}} \equiv \begin{pmatrix} [\chi^{(2)}_{XXX}E^{IR}_X + \chi^{(2)}_{XXY}E^{IR}_Y + \chi^{(2)}_{XXZ}E^{IR}_Z]E^{vis}_X \\ +[\chi^{(2)}_{XYX}E^{IR}_X + \chi^{(2)}_{XYY}E^{IR}_Y + \chi^{(2)}_{XYZ}E^{IR}_Z]E^{vis}_Y \\ +[\chi^{(2)}_{XZX}E^{IR}_X + \chi^{(2)}_{XZY}E^{IR}_Y + \chi^{(2)}_{XZZ}E^{IR}_Z]E^{vis}_Z \\ \\ [\chi^{(2)}_{YXX}E^{IR}_X + \chi^{(2)}_{YXY}E^{IR}_Y + \chi^{(2)}_{YXZ}E^{IR}_Z]E^{vis}_X \\ +[\chi^{(2)}_{YYX}E^{IR}_X + \chi^{(2)}_{YYY}E^{IR}_Y + \chi^{(2)}_{YYZ}E^{IR}_Z]E^{vis}_Y \\ +[\chi^{(2)}_{YZX}E^{IR}_X + \chi^{(2)}_{YZY}E^{IR}_Y + \chi^{(2)}_{YZZ}E^{IR}_Z]E^{vis}_Z \\ \\ [\chi^{(2)}_{ZXX}E^{IR}_X + \chi^{(2)}_{ZXY}E^{IR}_Y + \chi^{(2)}_{ZXZ}E^{IR}_Z]E^{vis}_X \\ +[\chi^{(2)}_{ZYX}E^{IR}_X + \chi^{(2)}_{ZYY}E^{IR}_Y + \chi^{(2)}_{ZYZ}E^{IR}_Z]E^{vis}_Y \\ +[\chi^{(2)}_{ZZX}E^{IR}_X + \chi^{(2)}_{ZZY}E^{IR}_Y + \chi^{(2)}_{ZZZ}E^{IR}_Z]E^{vis}_Z \end{pmatrix}, \tag{B.7}$$

The vector in Eq. (B.7) is the generated polarization, and each component reads (cf Eq. (2.66)).

$$P^{(2)}_I(\omega_{vis},\omega_{IR}) = \varepsilon_0 \sum_{J,K} \chi^{(2)}_{IJK}(-\omega_{vis}-\omega_{IR};\omega_{vis},\omega_{IR}) E^{vis}_J E^{IR}_K. \tag{B.8}$$

The generated polarization can be projected onto the output field direction (Fig. 1.10). This direction can be defined for both polarizations of the field by

$$\begin{aligned} \vec{\hat{e}}^{\perp} &= \cos\Theta\vec{\hat{e}}_p + e^{i\varphi}\sin\Theta\vec{\hat{e}}_s, \\ &= \cos\Theta[\underbrace{-\cos\theta_i}_{\hat{e}^{\perp}_X}\vec{e_X}] + \sin\Theta\vec{e_Y}\ e^{i\varphi} + \cos\Theta[\underbrace{\sin\theta_i}_{\hat{e}^{\perp}_Z}\vec{e_Z}], \end{aligned} \tag{B.9}$$

where $\theta_i$ is the incidence angle, $\Theta$ is the angle between generated light electric field, $\vec{E}^{SFG}$, and the output plane, and $e^{i\varphi}$ defines the phase between the two polarizations. We can therefore write

$$E^{SFG} \propto \vec{P}^{(2)}(F^{SFG}\vec{\hat{e}}^{\perp}) \propto \begin{pmatrix} P^{(2)}_X\ (F^{SFG}_X\hat{e}^{\perp}_X)\ \cos\Theta \\ P^{(2)}_Y\ (F^{SFG}_Y\hat{e}^{\perp}_Y)\sin\Theta\ e^{i\varphi} \\ P^{(2)}_Z\ (F^{SFG}_Z\hat{e}^{\perp}_Z)\ \cos\Theta \end{pmatrix}, \tag{B.10}$$

where

$$\vec{\hat{e}}^{\perp} = \begin{pmatrix} \hat{e}^{\perp}_X\ \cos\Theta \\ e^{i\varphi}\sin\Theta \\ \hat{e}^{\perp}_Z\ \cos\Theta \end{pmatrix}, \tag{B.11}$$

and

$$\begin{aligned} \vec{P}^{(2)} &= P^{(2)}(\hat{p}_X\vec{e}_X + \hat{p}_Y\vec{e}_Y + \hat{p}_Z\vec{e}_Z) \\ &= P^{(2)}_X\vec{e}_X + P^{(2)}_Y\vec{e}_Y + P^{(2)}_Z\vec{e}_Z. \end{aligned} \tag{B.12}$$

The output intensity is proportional to the square of

$$
I^{SFG} \propto \left|
\begin{array}{c}
\Big\{[\chi^{(2)}_{XXX}E^{IR}_X + \chi^{(2)}_{XXY}E^{IR}_Y + \chi^{(2)}_{XXZ}E^{IR}_Z]E^{vis}_X \\
+[\chi^{(2)}_{XYX}E^{IR}_X + \chi^{(2)}_{XYY}E^{IR}_Y + \chi^{(2)}_{XYZ}E^{IR}_Z]E^{vis}_Y \\
+[\chi^{(2)}_{XZX}E^{IR}_X + \chi^{(2)}_{XZY}E^{IR}_Y + \chi^{(2)}_{XZZ}E^{IR}_Z]E^{vis}_Z\Big\} \cdot \left(F^{SFG}_X \hat{e}^{\perp}_X\right) \cos\Theta \\
+ \\
F^{SFG}_Y\Big\{[\chi^{(2)}_{YXX}E^{IR}_X + \chi^{(2)}_{YXY}E^{IR}_Y + \chi^{(2)}_{YXZ}E^{IR}_Z]E^{vis}_X \\
+[\chi^{(2)}_{YYX}E^{IR}_X + \chi^{(2)}_{YYY}E^{IR}_Y + \chi^{(2)}_{YYZ}E^{IR}_Z]E^{vis}_Y \\
+[\chi^{(2)}_{YZX}E^{IR}_X + \chi^{(2)}_{YZY}E^{IR}_Y + \chi^{(2)}_{YZZ}E^{IR}_Z]E^{vis}_Z\Big\} \cdot \left(F^{SFG}_Y \hat{e}^{\perp}_Y\right) \sin\Theta\, e^{i\varphi} \\
+ \\
\sin\theta_{SFG} F^{SFG}_Z\Big\{[\chi^{(2)}_{ZXX}E^{IR}_X + \chi^{(2)}_{ZXY}E^{IR}_Y + \chi^{(2)}_{ZXZ}E^{IR}_Z]E^{vis}_X \\
+[\chi^{(2)}_{ZYX}E^{IR}_X + \chi^{(2)}_{ZYY}E^{IR}_Y + \chi^{(2)}_{ZYZ}e_3(\omega_{IR}]E^{vis}_Y \\
+[\chi^{(2)}_{ZZX}E^{IR}_X + \chi^{(2)}_{ZZY}E^{IR}_Y + \chi^{(2)}_{ZZZ}E^{IR}_Z]E^{vis}_Z\Big\} \cdot \left(F^{SFG}_Z \hat{e}^{\perp}_Z\right) \cos\Theta
\end{array}
\right|^2 \tag{B.13}
$$

For a surface with both $X-Z$ and $Y-Z$ mirror planes and non-chiral the non-zero component of the second order non-linear susceptibility are those in blue:

$$
I^{SFG} \propto \left|
\begin{array}{c}
\Big\{[\chi^{(2)}_{XXX}E^{IR}_X + \chi^{(2)}_{XXY}E^{IR}_Y + \chi^{(2)}_{XXZ}E^{IR}_Z]E^{vis}_X \\
+[\chi^{(2)}_{XYX}E^{IR}_X + \chi^{(2)}_{XYY}E^{IR}_Y + \chi^{(2)}_{XYZ}E^{IR}_Z]E^{vis}_Y \\
+[\chi^{(2)}_{XZX}E^{IR}_X + \chi^{(2)}_{XZY}E^{IR}_Y + \chi^{(2)}_{XZZ}E^{IR}_Z]E^{vis}_Z\Big\} \cdot \left(F^{SFG}_X \hat{e}^{\perp}_X\right) \cos\Theta \\
+ \\
\Big\{[\chi^{(2)}_{YXX}E^{IR}_X + \chi^{(2)}_{YXY}E^{IR}_Y + \chi^{(2)}_{YXZ}E^{IR}_Z]E^{vis}_X \\
+[\chi^{(2)}_{YYX}E^{IR}_X + \chi^{(2)}_{YYY}E^{IR}_Y + \chi^{(2)}_{YYZ}E^{IR}_Z]E^{vis}_Y \\
+[\chi^{(2)}_{YZX}E^{IR}_X + \chi^{(2)}_{YZY}E^{IR}_Y + \chi^{(2)}_{YZZ}E^{IR}_Z]E^{vis}_Z\Big\} \cdot \left(F^{SFG}_Y \hat{e}^{\perp}_Y\right) \sin\Theta\, e^{i\varphi} \\
+ \\
\Big\{[\chi^{(2)}_{ZXX}E^{IR}_X + \chi^{(2)}_{ZXY}E^{IR}_Y + \chi^{(2)}_{ZXZ}E^{IR}_Z]E^{vis}_X \\
+[\chi^{(2)}_{ZYX}E^{IR}_X + \chi^{(2)}_{ZYY}E^{IR}_Y + \chi^{(2)}_{ZYZ}E^{IR}_Z]E^{vis}_Y \\
+[\chi^{(2)}_{ZZX}E^{IR}_X + \chi^{(2)}_{ZZY}E^{IR}_Y + \chi^{(2)}_{ZZZ}E^{IR}_Z]E^{vis}_Z\Big\} \cdot \left(F^{SFG}_Z \hat{e}^{\perp}_Z\right) \hat{e}^{\perp}_Z \cos\Theta
\end{array}
\right|^2 \tag{B.14}
$$

The output electric field is simplified by eliminating all elements of the second order non-linear susceptibility that are zero:

$$I^{SFG} \propto \left| \begin{array}{c} \left\{\chi^{(2)}_{XXZ} E^{IR}_Z E^{vis}_X + \chi^{(2)}_{XZX} E^{IR}_X E^{vis}_Z\right\} \cdot \left(F^{SFG}_X \hat{e}^{\perp}_X\right) \cos\Theta \\ + \\ \left\{\chi^{(2)}_{YYZ} E^{IR}_Z E^{vis}_Y + \chi^{(2)}_{YZY} E^{IR}_Y E^{vis}_Z\right\} \cdot \left(F^{SFG}_Y \hat{e}^{\perp}_Y\right) \sin\Theta\, e^{i\varphi} \\ + \\ \left\{\chi^{(2)}_{ZXX} E^{IR}_X E^{vis}_X + \chi^{(2)}_{ZYY} E^{IR}_Y E^{vis}_Y + \chi^{(2)}_{ZZZ} E^{IR}_Z E^{vis}_Z\right\} \cdot \left(F^{SFG}_Z \hat{e}^{\perp}_Z\right) \cos\Theta \end{array} \right|^2 \tag{B.15}$$

**Case I:** $\Theta = 0$ $(\sin\Theta = 0$ **and** $\cos\Theta = 1)$**.** The output becomes

$$I^{SFG} \propto \left| \begin{array}{c} \left\{\chi^{(2)}_{XXZ} E^{IR}_Z E^{vis}_X + \chi^{(2)}_{XZX} E^{IR}_X E^{vis}_Z\right\} \cdot \left(F^{SFG}_X \hat{e}^{\perp}_X\right) \cos\Theta \\ + \\ 0 \\ + \\ \left\{\chi^{(2)}_{ZXX} E^{IR}_X E^{vis}_X + \chi^{(2)}_{ZYY} E^{IR}_Y E^{vis}_Y + \chi^{(2)}_{ZZZ} E^{IR}_Z E^{vis}_Z\right\} \cdot \left(F^{SFG}_Z \hat{e}^{\perp}_Z\right) \cos\Theta \end{array} \right|^2 \tag{B.16}$$

Only the $p$-polarized sum frequency survives.

- If the visible and infrared are both $p$-polarized : $ppp$

$$I^{SFG} \propto \left| \begin{array}{c} \left\{\chi^{(2)}_{XXZ} E^{IR}_Z E^{vis}_X + \chi^{(2)}_{XZX} E^{IR}_X E^{vis}_Z\right\} \cdot \left(F^{SFG}_X \hat{e}^{\perp}_X\right) \\ + \\ \left\{\chi^{(2)}_{ZXX} E^{IR}_X E^{vis}_X + \chi^{(2)}_{ZZZ} E^{IR}_Z E^{vis}_Z\right\} \cdot \left(F^{SFG}_Z \hat{e}^{\perp}_Z\right) \end{array} \right|^2 \tag{B.17}$$

- If the visible and infrared are both $s$-polarized :$pss$

$$\left| \left\{\chi^{(2)}_{ZYY} E^{IR}_Y E^{vis}_Y\right\} \cdot \left(F^{SFG}_Z \hat{e}^{\perp}_Z\right) \right| \tag{B.18}$$

**Case II:** $\Theta = \frac{\pi}{2}$ $(\sin\Theta = 1$ **and** $\cos\Theta = 0)$ The output becomes

$$I^{SFG} \propto \left| \begin{array}{c} 0 \\ + \\ \left\{ \chi^{(2)}_{YYZ} E^{IR}_Z E^{vis}_Y + \chi^{(2)}_{YZY} E^{IR}_Y E^{vis}_Z \right\} \cdot \left( F^{SFG}_Y \hat{e}^{\perp}_Y \right) \\ + \\ 0 \end{array} \right|^2 \tag{B.19}$$

Only the $s$ term survives for sum frequency , this is *ssp* or *sps*.

- if the visible is $s$-polarized and IR is $p$-polarized: *ssp*

$$I^{SFG} \propto \left| \chi^{(2)}_{YYZ} E^{IR}_Z E^{vis}_Y \cdot \left( F^{SFG}_Y \hat{e}^{\perp}_Y \right) \right|^2 \tag{B.20}$$

- if the visible is $p$-polarized and IR is $s$-polarized: *sps*

$$I^{SFG} \propto \left| \chi^{(2)}_{YZY} E^{IR}_Y E^{vis}_Z \cdot \left( F^{SFG}_Y \hat{e}^{\perp}_Y \right) \right|^2 \tag{B.21}$$

## B.2 Expression of SFG intensities

Let us first introduce the Fresnel and field orientation factors

$$E_I = F E^{(0)} \hat{e}_I \tag{B.22}$$

$$IR, Vis \begin{cases} \hat{e}_X & \rightarrow \cos\theta \\ \hat{e}_Y & \rightarrow 1 \\ \hat{e}_Z & \rightarrow \sin\theta \end{cases} \qquad SFG = \hat{e}^{\perp} \begin{cases} \hat{e}_X & \rightarrow -\cos\theta \\ \hat{e}_Y & \rightarrow 1 \\ \hat{e}_Z & \rightarrow \sin\theta \end{cases} \tag{B.23}$$

### B.2.1 *ppp* Configuration

According to Eq. (B.17)

$$I_{ppp} \propto \left| \begin{array}{ll} - & \cos\theta_{SFG}\cos\theta_{vis}\sin\theta_{IR}\ F_X^{SFG}F_X^{vis}F_Z^{IR}\ \chi^{(2)}_{XXZ}\ E_p^{(0),vis}E_p^{(0),IR} \\ - & \cos\theta_{SFG}\sin\theta_{vis}\cos\theta_{IR}\ F_X^{SFG}F_Z^{vis}F_X^{IR}\ \chi^{(2)}_{XZX}\ E_p^{(0),vis}E_p^{(0),IR} \\ + & \sin\theta_{SFG}\cos\theta_{vis}\cos\theta_{IR}\ F_Z^{SFG}F_X^{vis}F_X^{IR}\ \chi^{(2)}_{ZXX}\ E_p^{(0),vis}E_p^{(0),IR} \\ + & \sin\theta_{SFG}\sin\theta_{vis}\sin\theta_{IR}\ F_Z^{SFG}F_Z^{vis}F_Z^{IR}\ \chi^{(2)}_{ZZZ}\ E_p^{(0),vis}E_p^{(0),IR} \end{array} \right|^2 \tag{B.24}$$

$$\begin{aligned} |E_{3r,p}|^2 = \Bigg| & i\underbrace{\frac{\omega_3}{c}\frac{1}{2\sqrt{\varepsilon_{3r}}\cos\theta_{3r}}}_{L^{SFG}}\underbrace{\left[\frac{2\varepsilon_{3r}k_{3t,Z}}{\varepsilon_{3t}k_{3r,Z}+\varepsilon_{3r}k_{3t,Z}}\right]}_{F_X^{SFG}}\hat{p}_X(-\cos\theta_{3r})\frac{P^{(2)}(Z_0)}{\varepsilon_0}e^{ik_{3r,Z}Z_0} \\ & + i\underbrace{\frac{\omega_3}{c}\frac{1}{2\sqrt{\varepsilon_{3r}}\cos\theta_{3r}}}_{L^{SFG}}\underbrace{\left[\frac{2\varepsilon_{3t}k_{3r}}{\varepsilon_{3t}k_{3r,Z}+\varepsilon_{3r}k_{3t,Z}}\frac{\varepsilon_{3r}}{\varepsilon_{NL}}\right]}_{F_Z^{SFG}}\hat{p}_Z\sin\theta_{3r}\frac{P^{(2)}(Z_0)}{\varepsilon_0}e^{ik_{3r,Z}Z_0}\Bigg|^2 \end{aligned} \tag{B.25}$$

considering that $Z_0 = 0 \Longleftrightarrow e^{ik_{3r,Z}Z_0} = 1$

$$\begin{aligned} -\cos\theta_{3r}\ \hat{p}_X\frac{P^{(2)}(Z_0)}{\varepsilon_0} = & -\cos\theta_{SFG}\cos\theta_{vis}\sin\theta_{IR}\,\chi^{(2)}_{XXZ}\ F_X^{SFG}F_X^{vis}F_Z^{IR}\ E_p^{(0),vis}E_p^{(0),IR} \\ & -\cos\theta_{SFG}\sin\theta_{vis}\cos\theta_{IR}\,\chi^{(2)}_{XZX}\ F_X^{SFG}F_Z^{vis}F_X^{IR}\ E_p^{(0),vis}E_p^{(0),IR} \end{aligned} \tag{B.26}$$

$$\begin{aligned} \sin\theta_{3r}\ \hat{p}_Z\frac{P^{(2)}(Z_0)}{\varepsilon_0} = & \sin\theta_{SFG}\cos\theta_{vis}\cos\theta_{IR}\,\chi^{(2)}_{ZXX}\ F_Z^{SFG}F_X^{vis}F_X^{IR}\ E_p^{(0),vis}E_p^{(0),IR} \\ & +\sin\theta_{SFG}\sin\theta_{vis}\sin\theta_{IR}\,\chi^{(2)}_{ZZZ}F_Z^{SFG}F_Z^{vis}F_Z^{IR}\ E_p^{(0),vis}E_p^{(0),IR} \end{aligned} \tag{B.27}$$

$$\begin{aligned} |E_{3r,p}|^2 = \Bigg| & -\cos\theta_{SFG}\cos\theta_{vis}\sin\theta_{IR}\ \chi^{(2)}_{XXZ}\ L^{SFG}F_X^{SFG}F_X^{vis}F_Z^{IR}\ E_p^{(0),vis}E_p^{(0),IR} \\ & -\cos\theta_{SFG}\sin\theta_{vis}\cos\theta_{IR}\ \chi^{(2)}_{XZX}\ L^{SFG}F_X^{SFG}F_Z^{vis}F_X^{IR}\ E_p^{(0),vis}E_p^{(0),IR} \\ & +\sin\theta_{SFG}\cos\theta_{vis}\cos\theta_{IR}\ \chi^{(2)}_{ZXX}\ L^{SFG}F_Z^{SFG}F_X^{vis}F_X^{IR}\ E_p^{(0),vis}E_p^{(0),IR} \\ & +\sin\theta_{SFG}\sin\theta_{vis}\sin\theta_{IR}\ \chi^{(2)}_{ZZZ}\ L^{SFG}F_Z^{SFG}F_Z^{vis}F_Z^{IR}\ E_p^{(0),vis}E_p^{(0),IR}\Bigg|^2 \end{aligned} \tag{B.28}$$

$$
\begin{aligned}
|E_{3r,p}|^2 = \Big| & -\cos\theta_{SFG}\cos\theta_{vis}\sin\theta_{IR}\,\chi^{(2)}_{XXZ}\,L^{SFG}F^{SFG}_{X}F^{vis}_{X}F^{IR}_{Z} \\
& -\cos\theta_{SFG}\sin\theta_{vis}\cos\theta_{IR}\,\chi^{(2)}_{XZX}\,L^{SFG}F^{SFG}_{X}F^{vis}_{Z}F^{IR}_{X} \\
& +\sin\theta_{SFG}\cos\theta_{vis}\cos\theta_{IR}\,\chi^{(2)}_{ZXX}\,L^{SFG}F^{SFG}_{Z}F^{vis}_{X}F^{IR}_{X} \\
& +\sin\theta_{SFG}\sin\theta_{vis}\sin\theta_{IR}\,\chi^{(2)}_{ZZZ}\,L^{SFG}F^{SFG}_{Z}F^{vis}_{Z}F^{IR}_{Z}\Big|^2 \left|E^{(0),vis}_{p}\right|^2 \left|E^{(0),IR}_{p}\right|^2
\end{aligned}
\tag{B.29}
$$

For a non-magnetic material

$$
I = \frac{1}{2}cn\varepsilon_0\left|E^{(0)}\right|^2, \tag{B.30}
$$

$$
\begin{aligned}
\frac{2I_{ppp}}{cn_1(\omega_{SFG})\varepsilon_0} = \Big| & -\cos\theta_{SFG}\cos\theta_{vis}\sin\theta_{IR}\,\chi^{(2)}_{XXZ}\,L^{SFG}F^{SFG}_{X}F^{vis}_{X}F^{IR}_{Z} \\
& -\cos\theta_{SFG}\sin\theta_{vis}\cos\theta_{IR}\,\chi^{(2)}_{XZX}\,L^{SFG}F^{SFG}_{X}F^{vis}_{Z}F^{IR}_{X} \\
& +\sin\theta_{SFG}\cos\theta_{vis}\cos\theta_{IR}\,\chi^{(2)}_{ZXX}\,L^{SFG}F^{SFG}_{Z}F^{vis}_{X}F^{IR}_{X} \\
& +\sin\theta_{SFG}\sin\theta_{vis}\sin\theta_{IR}\,\chi^{(2)}_{ZZZ}\,L^{SFG}F^{SFG}_{Z}F^{vis}_{Z}F^{IR}_{Z}\Big|^2 \frac{2I_{IR}}{cn_1(\omega_{IR})\varepsilon_0}\frac{2I_{vis}}{cn_1(\omega_{vis})\varepsilon_0}
\end{aligned}
\tag{B.31}
$$

$$
\begin{aligned}
I_{ppp} = \frac{2n_1(\omega_{SFG})}{c\varepsilon_0 n_1(\omega_{IR})n_1(\omega_{vis})}\Big| & -\cos\theta_{SFG}\cos\theta_{vis}\sin\theta_{IR}\,\chi^{(2)}_{XXZ}\,L^{SFG}F^{SFG}_{X}F^{vis}_{X}F^{IR}_{Z} \\
& -\cos\theta_{SFG}\sin\theta_{vis}\cos\theta_{IR}\,\chi^{(2)}_{XZX}\,L^{SFG}F^{SFG}_{X}F^{vis}_{Z}F^{IR}_{X} \\
& +\sin\theta_{SFG}\cos\theta_{vis}\cos\theta_{IR}\,\chi^{(2)}_{ZXX}\,L^{SFG}F^{SFG}_{Z}F^{vis}_{X}F^{IR}_{X} \\
& +\sin\theta_{SFG}\sin\theta_{vis}\sin\theta_{IR}\,\chi^{(2)}_{ZZZ}\,L^{SFG}F^{SFG}_{Z}F^{vis}_{Z}F^{IR}_{Z}\Big|^2 I_{IR}I_{vis}
\end{aligned}
\tag{B.32}
$$

$$
L_{SFG} = \frac{\omega_{SFG}}{c}\frac{1}{2\sqrt{\varepsilon_{3r}}\cos\theta_{SFG}}
$$

$$
(L_{SFG})^2 = \frac{\omega^2_{SFG}}{c^2}\frac{1}{4n_1^2(\omega_{SFG})\cos^2\theta_{SFG}}
$$

$$\begin{aligned}\frac{I_{ppp}}{I_{IR}I_{vis}} =& \frac{\omega_{SFG}^2}{2c^3\varepsilon_0 n_1(\omega_{SFG})n_1(\omega_{IR})n_1(\omega_{vis})\cos^2\theta_{SFG}} \times \\ & \Big| -\cos\psi_{SFG}\cos\theta_{vis}\sin\theta_{IR}\,\chi^{(2)}_{XXZ}\,F_X^{SFG}F_X^{vis}F_Z^{IR} \\ & -\cos\psi_{SFG}\sin\theta_{vis}\cos\theta_{IR}\,\chi^{(2)}_{XZX}\,F_X^{SFG}F_Z^{vis}F_X^{IR} \\ & +\sin\psi_{SFG}\cos\theta_{vis}\cos\theta_{IR}\,\chi^{(2)}_{ZXX}\,F_Z^{SFG}F_X^{vis}F_X^{IR} \\ & +\sin\psi_{SFG}\sin\theta_{vis}\sin\theta_{IR}\,\chi^{(2)}_{ZZZ}\,F_Z^{SFG}F_Z^{vis}F_Z^{IR}\Big|^2 \end{aligned} \tag{B.33}$$

### B.2.2 *pss* Configuration

According to Eq. (B.18)

$$I_{pss} \propto \left|\sin\theta_{SFG}\,F_Z^{SFG}\chi^{(2)}_{ZYY}\,F_Y^{vis}F_Y^{IR}\,E_s^{(0),vis}E_s^{(0),IR}\right|^2 \tag{B.34}$$

then, equating to Eq. (B.3b):

$$\begin{aligned} -\cos\theta_{3r}\,\hat{p}_X\frac{P^{(2)}(z_0)}{\varepsilon_0} &= 0 \\ \sin\theta_{3r}\,\hat{p}_Z\frac{P^{(2)}(z_0)}{\varepsilon_0} &= \sin\theta_{SFG}\,\chi^{(2)}_{ZYY}\,F_Z^{SFG}F_Y^{vis}F_Y^{IR}\,E_s^{(0),vis}E_s^{(0),IR} \end{aligned} \tag{B.35}$$

Therefore, using the same transformations from Eq. (B.28) to Eq. (B.33) one obtains:

$$\frac{I_{pss}}{I_{IR}I_{vis}} = \frac{\omega_{SFG}^2}{2c^3\varepsilon_0 n_1(\omega_{SFG})n_1(\omega_{IR})n_1(\omega_{vis})\cos^2\theta_{SFG}}\left|\sin\theta_{SFG}\chi^{(2)}_{ZYY}F_Z^{SFG}F_Y^{vis}F_Y^{IR}\right|^2 \tag{B.36}$$

### B.2.3 *ssp* Configuration

According to Eq. (B.20)

$$I_{ssp} \propto \left|\sin\theta_{IR}\,\chi^{(2)}_{YYZ}\,F_Y^{SFG}F_Y^{vis}F_Z^{IR}\,E_s^{(0),vis}E_p^{(0),IR}\right|^2 \tag{B.37}$$

When considering that $Z_0 = 0 \;\leftrightarrow\; e^{ik_{SFG,R,Z}\,Z_0} = 1$, Eq. (B.3a) reads

$$|E_{3r,s}|^2 = \left| i \underbrace{\frac{\omega_3}{c} \frac{1}{2\sqrt{\varepsilon_{3r}} \cos\theta_{3r}}}_{L^{SFG}} \underbrace{\left[\frac{2k_{3r,Z}}{k_{3r,Z} + k_{3t,Z}}\right]}_{F_Y^{SFG}} \hat{p}_Y \frac{P^{(2)}(Z_0)}{\varepsilon_0} \right|^2 \tag{B.38}$$

$$\hat{p}_Y \frac{P^{(2)}(Z_0)}{\varepsilon_0} = \sin\theta_{IR} \chi^{(2)}_{YYZ} \; F_Y^{SFG} F_Y^{vis} F_Z^{IR} \; E_s^{(0),vis} E_p^{(0),IR} \tag{B.39}$$

$$\begin{aligned} |E_{3r,s}|^2 &= \left| \sin\theta_{IR} L^{SFG} \chi^{(2)}_{YYZ} \; F_Y^{SFG} F_Y^{vis} F_Z^{IR} \; E_s^{(0),vis} E_p^{(0),IR} \right|^2 \\ &= \left| \sin\theta_{IR} \chi^{(2)}_{YYZ} L^{SFG} F_Y^{SFG} F_Y^{vis} F_Z^{IR} \right|^2 \left| E_s^{(0),vis} \right|^2 \left| E_p^{(0),IR} \right|^2 \end{aligned} \tag{B.40}$$

The intensity is related to the field by Eq. (B.30)

$$\frac{2I_{ssp}}{cn_1(\omega_{SFG})\varepsilon_0} = \left| \sin\theta_{IR} \chi^{(2)}_{YYZ} L^{SFG} F_Y^{SFG} F_Y^{vis} F_Z^{IR} \right|^2 \frac{2I_{IR}}{cn_1(\omega_{IR})\varepsilon_0} \frac{2I_{vis}}{cn_1(\omega_{vis})\varepsilon_0} \tag{B.41}$$

$$I_{ssp} = \frac{2n_1(\omega_{SFG})}{c\varepsilon_0 n_1(\omega_{IR}) n_1(\omega_{vis})} \left| \sin\theta_{IR} \chi^{(2)}_{YYZ} L^{SFG} F_Y^{SFG} F_Y^{vis} F_Z^{IR} \right|^2 I_{IR} I_{vis} \tag{B.42}$$

$$I_{ssp} = \frac{2n_1(\omega_{SFG})}{c\varepsilon_0 n_1(\omega_{IR}) n_1(\omega_{vis})} \left| \sin\theta_{IR} \chi^{(2)}_{YYZ} L^{SFG} F_Y^{SFG} F_Y^{vis} F_Z^{IR} \right|^2 I_{IR} I_{vis} \tag{B.43}$$

$$\underbrace{\frac{I_{ssp}}{I_{IR} I_{vis}}}_{\mathrm{J}^{-1}\mathrm{sm}^2} = \underbrace{\frac{\omega_{SFG}^2}{2c^3 \varepsilon_0 n_1(\omega_{SFG}) n_1(\omega_{IR}) n_1(\omega_{vis}) \cos^2\theta_{SFG}}}_{\mathrm{m}^{-2}\mathrm{C}^{-1}\mathrm{Vs}} \underbrace{\left| \sin\theta_{IR} \chi^{(2)}_{YYZ} F_Y^{SFG} F_Y^{vis} F_Z^{IR} \right|^2}_{|\chi^{(2),\,eff}_{YYZ}|^2 \equiv \mathrm{m}^4\mathrm{V}^{-2}} \tag{B.44}$$

### B.2.4 *sps* Configuration

According to Eq. (B.21)

$$I_{sps} \propto \left| \sin\theta_{vis}\ \chi^{(2)}_{YZY}\ F_Y^{SFG} F_Z^{vis} F_Y^{IR}\ E_p^{(0),vis} E_s^{(0),IR} \right|^2 \tag{B.45}$$

then, equating to Eq. (B.3a):

$$\hat{p}_Y \frac{P^{(2)}(Z_0)}{\varepsilon_0} = \sin\theta_{vis}\ \chi^{(2)}_{YZY}\ F_Y^{SFG} F_Z^{vis} F_Y^{IR}\ E_p^{(0),vis} E_s^{(0),IR} \tag{B.46}$$

Therefore, using the same transformations from Eq. (B.39) to Eq. (B.44) one obtains:

$$\frac{I_{sps}}{I_{IR} I_{vis}} = \frac{\omega_{SFG}^2}{2c^3 \varepsilon_0 n_1(\omega_{SFG}) n_1(\omega_{IR}) n_1(\omega_{vis}) \cos^2\theta_{SFG}} \left| \sin\theta_{vis} \chi^{(2)}_{YZY} F_Y^{SFG} F_Z^{vis} F_Y^{IR} \right|^2 \tag{B.47}$$

# References

[1] Heinz, T. F. In *Nonlinear Surface Electromagnetic Phenomena*; Ponath, H.-E., Stegeman, G., Eds.; Elsevier: Amsterdam, 1991; Chapter 5, pp 353–416.

[2] Caudano, Y. Contribution à l'étude d'interfaces par spectroscopies vibrationnelles linéaires et non linéaires. Ph.D. thesis, Facultés Universitaires Notre-Dame de la Paix, Namur, Belgium, 2000.

[3] Lin, S. H.; Lin, S. H.; Villaeys, A. A.; Fujimura, Y. *Advances In Multi-Photon Processes And Spectroscopy*; World Scientific Publishing Co, 2008; Vol. 18.

# Appendix C

# Relationships Between the Second-Order Susceptibility and First Hyperpolarizability Tensors in the Case of SFG

The macroscopic surface second-order surface susceptibility elements, $\chi^{(2)}_{IJK}$, result from the first hyperpolarizability elements $\beta_{\alpha\beta\gamma}$ and are related via the average of the projection of the $\alpha\beta\gamma$ onto the $IJK$ (Eq. (3.76)):

$$\begin{aligned}\chi^{(2)}_{IJK} &\simeq N_s \sum_{\alpha,\beta,\gamma} \langle IJK|\alpha\beta\gamma\rangle \beta_{\alpha\beta\gamma}, \\ &\simeq N_s \sum_{\alpha,\beta,\gamma} \langle T_{I\alpha,J\beta,K\gamma}(\phi,\theta,\xi)\rangle \beta_{\alpha\beta\gamma},\end{aligned} \tag{C.1}$$

In this equation both $\chi^{(2)}_{IJK}$ is defined in the laboratory system coordinates $(X, Y, Z)$, whereas $\beta_{\alpha\beta\gamma}$ is a molecular quantity i.e. calculated in the molecular system coordinates $(x, y, z)$. One therefore needs to transform it into the laboratory system coordinates. In the following paragraphs, a derivation of the relationships between second-order surface susceptibility and first hyperpolarizability tensors is presented for the case of SFG.

## C.1 The rotation matrix

We consider transforming between two coordinate systems labeled $X, Y, Z$ and $x, y, z$. Typically we are concerned with the molecular $(x, y, z)$ and the laboratory $(X, Y, Z)$ systems coordinates. The three Euler angles $\phi$, $\theta$, and $\xi$ shown in Fig. C.1 are used to make the transformation between the two coordinate systems.

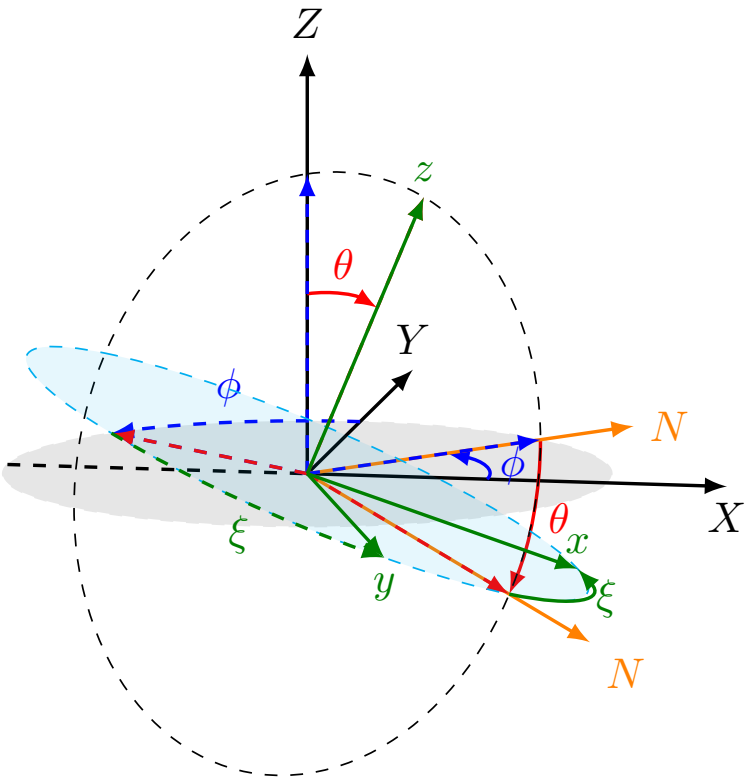


FIGURE C.1: Euler angles $(\phi, \theta, \xi)$ relating the molecular $(x, y, z)$ and the laboratory $(X, Y, Z)$ system coordinates.

The angles $\phi$ and $\theta$ are spherical polar coordinates where $\theta$ measures the angle from the Z axis to the z axis and $\phi$ measures the angle from the X axis to the line of nodes (projection of the Z axis on the XY plane). The angle $\theta$ measures the angle from the line of nodes N and the $x$ axis. Thus $\xi$ is an azimuthal angles about the $z$ axis just as $\phi$ is an azimuthal angle about the Z axis. Note that the line of nodes ON is perpendicular to both the z and Z axes. The Euler angles $\phi$, $\theta$, and $\xi$ should be regarded as defining a prescription whereby the XYZ frame (the space-fixed frame) may be made to coincide with the xyz frame (the body-fixed frame) by three successive rotations:

At last, the angles are defined in such a way that they are positive when they rotate counter-clockwise along the positive axis of rotation. $\phi$ and $\xi$ range are defined modulo $2\pi$. A valid range could be $[-\pi, \pi]$ or $[0, 2\pi]$. $\theta$ covers $\pi$ radians and its range is $[0, \pi]$.

The matrix representation of the rotation is the product of the three relative rotation matrices. The three matrices are multiplied in the order of the operation when we think about intrinsic rotation and in the opposite order when we think about extrinsic rotation.

The unitary transformation R is conveniently expressed as three Euler angle rotations:

$$R\,(\phi, \theta, \xi) = R_z(\phi) R_y(\theta) R_z(\xi) \tag{C.2}$$

where $\phi$ is a rotation about the original Z axis, $\theta$ is a rotation about the new y axis that coincides with the line of nodes N, and $\xi$ is a rotation about the final z axis. These rotations of the coordinate system axes are shown below.

First, we consider the rotation of $\phi$ about the laboratory Z axis (Fig. C.2).

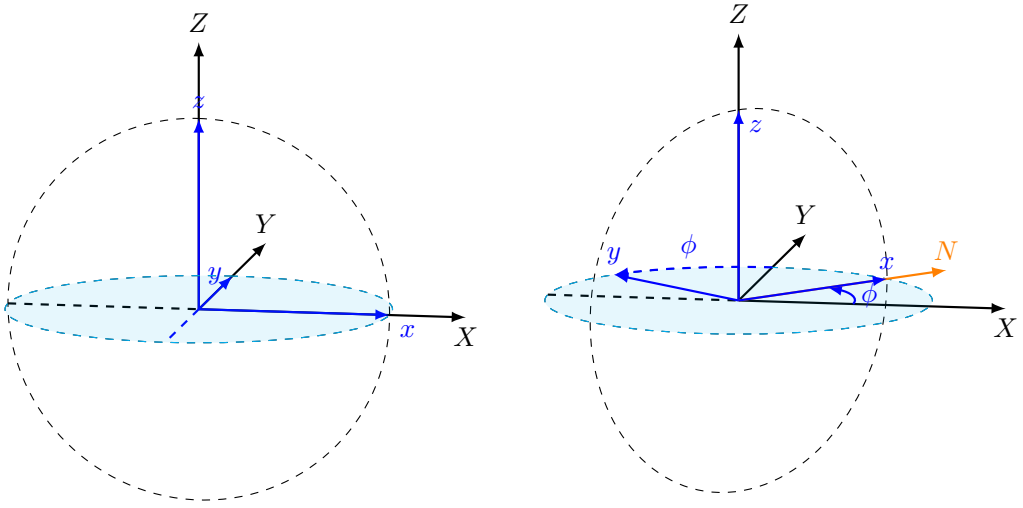


FIGURE C.2: Rotation of $\phi$ about the Z axis

This is followed by a rotation of $\theta$ about the new y axis which coincides with the line of nodes (Fig. C.3).

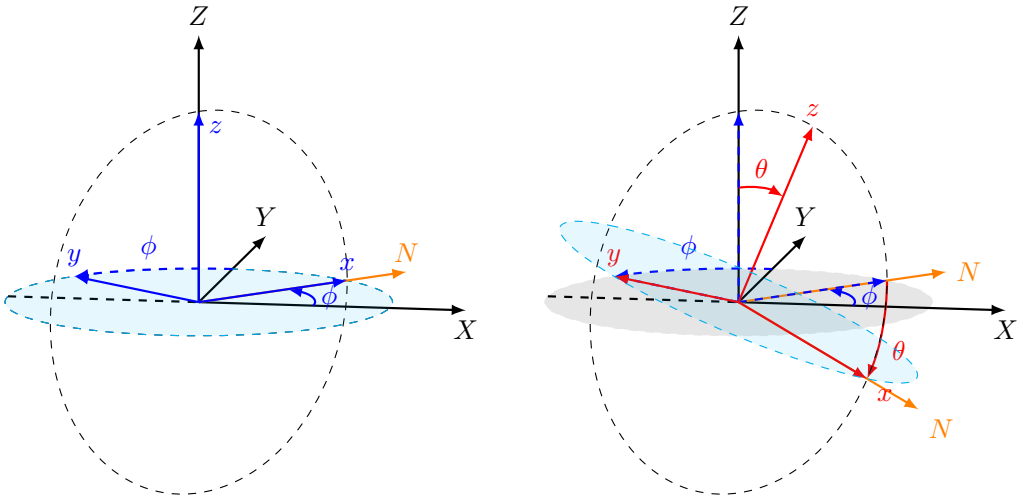


FIGURE C.3: Rotation of $\theta$ about the $y$ axis

Finally, a rotation of $\xi$ about the new $z$ axis completes the transformation (Fig. C.4).

The direction cosine matrix is obtained from the product of these transformations. That is

$$R = R_z(\phi)R_N(\theta)R_z(\xi) \tag{C.3}$$

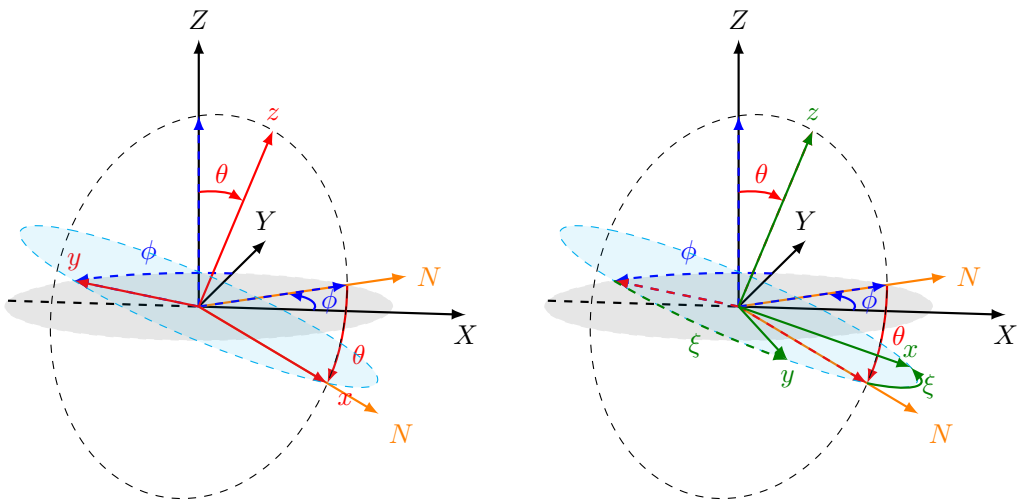


FIGURE C.4: Rotation of $\xi$ about the $z$ axis

This can be written explicitly as

$$R = \begin{pmatrix} \cos(\phi) & -\sin(\phi) & 0 \\ \sin(\phi) & \cos(\phi) & 0 \\ 0 & 0 & 1 \end{pmatrix} \begin{pmatrix} \cos(\theta) & 0 & \sin(\theta) \\ 0 & 1 & 0 \\ -\sin(\theta) & 0 & \cos(\theta) \end{pmatrix} \begin{pmatrix} \cos(\xi) & -\sin(\xi) & 0 \\ \sin(\xi) & \cos(\xi) & 0 \\ 0 & 0 & 1 \end{pmatrix} \tag{C.4}$$

$$= \begin{pmatrix} c(\phi)\,c(\theta)\,c(\xi) - s(\phi)\,s(\xi) & -c(\phi)\,c(\theta)\,s(\xi) - c(\xi)\,s(\phi) & c(\phi)\,s(\theta) \\ c(\phi)\,s(\xi) + c(\theta)\,c(\xi)\,s(\phi) & c(\phi)\,c(\xi) - c(\theta)\,s(\phi)\,s(\xi) & s(\phi)\,s(\theta) \\ -c(\xi)\,s(\theta) & s(\theta)\,s(\xi) & c(\theta) \end{pmatrix} \tag{C.5}$$

$$= \begin{pmatrix} R_{X,x} & R_{X,y} & R_{X,z} \\ R_{Y,x} & R_{Y,y} & R_{Y,z} \\ R_{Z,x} & R_{Z,y} & R_{Z,z} \end{pmatrix} = R_{\text{lab,mol}} \tag{C.6}$$

where $c$ and $s$ represent cosine and sine, respectively. Because R is a unitary transformation and the elements are real we have that $R^{-1}_{ab} = R_{ba}$. Thus,

$$R_{\text{mol,lab}} = \begin{pmatrix} c(\phi)\,c(\theta)\,c(\xi) - s(\phi)\,s(\xi) & c(\phi)\,s(\xi) + c(\theta)\,c(\xi)\,s(\phi) & -c(\xi)\,s(\theta) \\ -c(\phi)\,c(\theta)\,s(\xi) - c(\xi)\,s(\phi) & c(\phi)\,c(\xi) - c(\theta)\,s(\phi)\,s(\xi) & s(\theta)\,s(\xi) \\ c(\phi)\,s(\theta) & s(\phi)\,s(\theta) & c(\theta) \end{pmatrix} \tag{C.7}$$

$$= \begin{pmatrix} R_{x,X} & R_{x,Y} & R_{x,Z} \\ R_{y,X} & R_{y,Y} & R_{y,Z} \\ R_{z,X} & R_{z,Y} & R_{z,Z} \end{pmatrix} \tag{C.8}$$

## C.2 Applying rotation matrices on the second-order susceptibility

$$A'_{ijk} = \sum_l \sum_m \sum_n R_{i,l} R_{j,m} R_{k,n} A'_{lmn} \tag{C.9}$$

where, $i, j, k = \{X, Y, Z\}$ and $l, m, n = \{x, y, z\}$.

Thus

$$\begin{aligned} A'_{Xjk} =& \sum_l \sum_m \sum_n R_{X,l} R_{j,m} R_{k,n} A'_{lmn} \\ =& \sum_m \sum_n R_{X,x} R_{j,m} R_{k,n} A'_{xmn} \\ &+ \sum_m \sum_n R_{X,y} R_{j,m} R_{k,n} A'_{ymn} \\ &+ \sum_m \sum_n R_{X,z} R_{j,m} R_{k,n} A'_{zmn} \end{aligned} \tag{C.10}$$

$$\begin{aligned} A'_{Xjk} =& R_{X,x} \sum_m \sum_n R_{j,m} R_{k,n} A'_{xmn} \\ &+ R_{X,y} \sum_m \sum_n R_{j,m} R_{k,n} A'_{ymn} \\ &+ R_{X,z} \sum_m \sum_n R_{j,m} R_{k,n} A'_{zmn} \end{aligned} \tag{C.11}$$

$$\begin{aligned} A'_{Xjk} =& R_{X,x} \underbrace{\sum_m \sum_n R_{j,m} R_{k,n} A'_{xmn}}_{(RA'_x R^T)} \\ &+ R_{X,y} \underbrace{\sum_m \sum_n R_{j,m} R_{k,n} A'_{ymn}}_{(RA'_y R^T)} \\ &+ R_{X,z} \underbrace{\sum_m \sum_n R_{j,m} R_{k,n} A'_{zmn}}_{(RA'_z R^T)} \end{aligned} \tag{C.12}$$

$$A'_{Xjk} = R_{X,x}[RA'_x R^T] + R_{X,y}[RA'_y R^T] + R_{X,z}[RA'_z R^T] \tag{C.13}$$

One therefore obtains

$$\begin{cases} A'_{Xjk} = R_{X,x}[RA'_xR^T] + R_{X,y}[RA'_yR^T] + R_{X,z}[RA'_zR^T] \\ A'_{Yjk} = R_{Y,x}[RA'_xR^T] + R_{Y,y}[RA'_yR^T] + R_{Y,z}[RA'_zR]^T \\ A'_{Zjk} = R_{Z,x}[RA'_xR^T] + R_{Z,y}[RA'_yR^T] + R_{Z,z}[RA'_zR^T] \end{cases} \tag{C.14}$$

## C.3 Average over $\phi$ angle for the second-order susceptibility

Considering that the interface is invariant for arbitrary rotations around the surface plane (i.e., for a uniaxial film).

If we want to integrate over $\phi$, any function $f(\phi,\theta,\xi)$ becomes an expected value $\langle f(\phi,\theta,\xi)\rangle$:

$$\langle f(\phi,\theta,\xi)\rangle = \frac{1}{2\pi}\int_{-\pi}^{\pi} f(\phi,\theta,\xi)\,\mathrm{d}\phi \tag{C.15}$$

The values of the following integrals are therefore needed:

$$\begin{array}{lll} \int_{-\pi}^{\pi}\sin(x)\,\mathrm{d}x = 0 & \int_{-\pi}^{\pi}\cos(x)\,\mathrm{d}x = 0 & \int_{-\pi}^{\pi}\sin(x)\cos(x)\,\mathrm{d}x = 0 \\ \int_{-\pi}^{\pi}\sin^2(x)\,\mathrm{d}x = \pi & \int_{-\pi}^{\pi}\cos^2(x)\,\mathrm{d}x = \pi & \int_{-\pi}^{\pi}\sin^2(x)\cos(x)\,\mathrm{d}x = 0 \\ \int_{-\pi}^{\pi}\sin^3(x)\,\mathrm{d}x = 0 & \int_{-\pi}^{\pi}\cos^3(x)\,\mathrm{d}x = 0 & \int_{-\pi}^{\pi}\sin(x)\cos^2(x)\,\mathrm{d}x = 0 \end{array}$$

$$\begin{aligned} \langle\chi^{(2)}_{XXX}\rangle_\phi/N &= \sum_{\alpha\beta\gamma}^{\{x,y,z\}} \langle T_{X\alpha}T_{X\beta}T_{X\gamma}\rangle_\phi\beta_{\alpha\beta\gamma} \\ &= 0 \end{aligned} \tag{C.16}$$

$$\begin{aligned} \langle\chi^{(2)}_{YYY}\rangle_\phi/N &= \sum_{\alpha\beta\gamma}^{\{x,y,z\}} \langle T_{Y\alpha}T_{Y\beta}T_{Y\gamma}\rangle_\phi\beta_{\alpha\beta\gamma} \\ &= 0 \end{aligned} \tag{C.17}$$

$$\begin{aligned} \langle\chi^{(2)}_{ZZZ}\rangle_\phi/N &= \sum_{\alpha\beta\gamma}^{\{x,y,z\}} \langle T_{Z\alpha}T_{Z\beta}T_{Z\gamma}\rangle_\phi\beta_{\alpha\beta\gamma} \\ &= -\sin^3(\theta)\cos^3(\xi)\beta_{xxx} + \sin^3(\theta)\sin^3(\xi)\beta_{yyy} + \cos^3(\theta)\beta_{zzz} \\ &+ \sin^3(\theta)\cos^2(\xi)\sin(\xi)\Big[\beta_{xxy} + \beta_{xyx} + \beta_{yxx}\Big] \\ &+ \sin^3(\theta)\cos(\xi)\sin^2(\xi)\Big[-\beta_{xyy} - \beta_{yxy} - \beta_{yyx}\Big] \\ &+ \cos(\theta)\sin^2(\theta)\cos^2(\xi)\Big[\beta_{xxz} + \beta_{xzx} + \beta_{zxx}\Big] \\ &+ \cos(\theta)\sin^2(\theta)\sin^2(\xi)\Big[\beta_{yyz} + \beta_{yzy} + \beta_{zyy}\Big] \end{aligned}$$

$$
\begin{aligned}
&+ \cos^2(\theta)\sin(\theta)\cos(\xi)\Big[ -\beta_{xzz} - \beta_{zxz} - \beta_{zzx}\Big] \\
&+ \cos^2(\theta)\sin(\theta)\sin(\xi)\Big[\beta_{yzz} + \beta_{zyz} + \beta_{zzy}\Big] \\
&+ \cos(\theta)\sin^2(\theta)\cos(\xi)\sin(\xi)\Big[ -\beta_{xyz} - \beta_{yxz} - \beta_{xzy} - \beta_{zxy} - \beta_{yzx} - \beta_{zyx}\Big] \qquad \text{(C.18)}
\end{aligned}
$$

$$
\begin{aligned}
\langle\chi^{(2)}_{XXY}\rangle_\phi/N &= \sum_{\alpha\beta\gamma}^{\{x,y,z\}} \langle T_{X\alpha}T_{X\beta}T_{Y\gamma}\rangle_\phi \beta_{\alpha\beta\gamma} \\
&= 0 \qquad \text{(C.19)} \\
\langle\chi^{(2)}_{XYX}\rangle_\phi/N &= \sum_{\alpha\beta\gamma}^{\{x,y,z\}} \langle T_{X\alpha}T_{X\beta}T_{Y\gamma}\rangle_\phi \beta_{\alpha\gamma\beta} \\
&= 0 \qquad \text{(C.20)} \\
\langle\chi^{(2)}_{YXX}\rangle_\phi/N &= \sum_{\alpha\beta\gamma}^{\{x,y,z\}} \langle T_{X\alpha}T_{X\beta}T_{Y\gamma}\rangle_\phi \beta_{\gamma\beta\alpha} \\
&= 0 \qquad \text{(C.21)} \\
\langle\chi^{(2)}_{XYY}\rangle_\phi/N &= \sum_{\alpha\beta\gamma}^{\{x,y,z\}} \langle T_{X\alpha}T_{Y\beta}T_{Y\gamma}\rangle_\phi \beta_{\alpha\beta\gamma} \\
&= 0 \qquad \text{(C.22)} \\
\langle\chi^{(2)}_{YXY}\rangle_\phi/N &= \sum_{\alpha\beta\gamma}^{\{x,y,z\}} \langle T_{X\alpha}T_{Y\beta}T_{Y\gamma}\rangle_\phi \beta_{\beta\alpha\gamma} \\
&= 0 \qquad \text{(C.23)} \\
\langle\chi^{(2)}_{YYX}\rangle_\phi/N &= \sum_{\alpha\beta\gamma}^{\{x,y,z\}} \langle T_{X\alpha}T_{Y\beta}T_{Y\gamma}\rangle_\phi \beta_{\gamma\beta\alpha} \\
&= 0 \qquad \text{(C.24)} \\
\langle\chi^{(2)}_{XXZ}\rangle_\phi/N &= \frac{1}{2}\cos(\theta)\sin^2(\theta)\beta_{zzz} + \frac{1}{2}\cos(\theta)\Big[\beta_{xxz} + \beta_{yyz}\Big] \\
&+ \frac{1}{2}\sin^3(\theta)\cos^3(\xi)\Big[\beta_{xxx} - \beta_{xyy} - \beta_{yxy} - \beta_{yyx}\Big] \\
&+ \frac{1}{2}\sin^3(\theta)\sin^3(\xi)\Big[ -\beta_{yyy} + \beta_{xxy} + \beta_{xyx} + \beta_{yxx}\Big] \\
&+ \frac{1}{2}\sin(\theta)\cos(\xi)\Big[ -\beta_{xxx} - \beta_{yyx} + \beta_{xzz} + \beta_{zxz}\Big] \\
&+ \frac{1}{2}\sin(\theta)\sin(\xi)\Big[\beta_{yyy} + \beta_{xxy} - \beta_{yzz} - \beta_{zyz}\Big] \\
&+ \frac{1}{2}\sin^3(\theta)\sin(\xi)\Big[ -\beta_{xxy} - \beta_{xyx} - \beta_{yxx} + \beta_{yzz} + \beta_{zyz} + \beta_{zzy}\Big] \\
&+ \frac{1}{2}\sin^3(\theta)\cos(\xi)\Big[\beta_{xyy} + \beta_{yxy} + \beta_{yyx} - \beta_{xzz} - \beta_{zxz} - \beta_{zzx}\Big] \\
&- \frac{1}{2}\cos(\theta)\sin^2(\theta)\cos^2(\xi)\Big[\beta_{xxz} + \beta_{xzx} + \beta_{zxx}\Big]
\end{aligned}
$$

$$
\begin{aligned}
&- \frac{1}{2}\cos(\theta)\sin^2(\theta)\sin^2(\xi)\Big[\beta_{yyz}+\beta_{yzy}+\beta_{zyy}\Big] \\
&+ \frac{1}{2}\cos(\theta)\sin^2(\theta)\cos(\xi)\sin(\xi)\Big[\beta_{xyz}+\beta_{yxz}+\beta_{xzy}+\beta_{zxy}+\beta_{yzx}+\beta_{zyx}\Big] \qquad \text{(C.25)}
\end{aligned}
$$

$$
\begin{aligned}
\langle\chi^{(2)}_{XZX}\rangle_\phi/N &= \sum_{\alpha\beta\gamma}^{\{x,y,z\}} \langle T_{X\alpha}T_{X\beta}T_{Z\gamma}\rangle_\phi \beta_{\alpha\gamma\beta} \\
&= \frac{1}{2}\cos(\theta)\sin^2(\theta)\beta_{zzz} + \frac{1}{2}\cos(\theta)\Big[\beta_{xzx}+\beta_{yzy}\Big] \\
&+ \frac{1}{2}\sin^3(\theta)\cos^3(\xi)\Big[\beta_{xxx}-\beta_{xyy}-\beta_{yxy}-\beta_{yyx}\Big] \\
&+ \frac{1}{2}\sin^3(\theta)\sin^3(\xi)\Big[-\beta_{yyy}+\beta_{xxy}+\beta_{xyx}+\beta_{yxx}\Big] \\
&+ \frac{1}{2}\sin(\theta)\cos(\xi)\Big[-\beta_{xxx}-\beta_{yxy}+\beta_{xzz}+\beta_{zzx}\Big] \\
&+ \frac{1}{2}\sin(\theta)\sin(\xi)\Big[\beta_{yyy}+\beta_{xyx}-\beta_{yzz}-\beta_{zzy}\Big] \\
&+ \frac{1}{2}\sin^3(\theta)\sin(\xi)\Big[-\beta_{xxy}-\beta_{xyx}-\beta_{yxx}+\beta_{yzz}+\beta_{zyz}+\beta_{zzy}\Big] \\
&+ \frac{1}{2}\sin^3(\theta)\cos(\xi)\Big[\beta_{xyy}+\beta_{yxy}+\beta_{yyx}-\beta_{xzz}-\beta_{zxz}-\beta_{zzx}\Big] \\
&- \frac{1}{2}\cos(\theta)\sin^2(\theta)\cos^2(\xi)\Big[\beta_{xxz}+\beta_{xzx}+\beta_{zxx}\Big] \\
&- \frac{1}{2}\cos(\theta)\sin^2(\theta)\sin^2(\xi)\Big[\beta_{yyz}+\beta_{yzy}+\beta_{zyy}\Big] \\
&+ \frac{1}{2}\cos(\theta)\sin^2(\theta)\cos(\xi)\sin(\xi)\Big[\beta_{xyz}+\beta_{yxz}+\beta_{xzy}+\beta_{zxy}+\beta_{yzx}+\beta_{zyx}\Big] \qquad \text{(C.26)}
\end{aligned}
$$

$$
\begin{aligned}
\langle\chi^{(2)}_{ZXX}\rangle_\phi/N &= \sum_{\alpha\beta\gamma}^{\{x,y,z\}} \langle T_{X\alpha}T_{X\beta}T_{Z\gamma}\rangle_\phi \beta_{\gamma\beta\alpha} \\
&= \frac{1}{2}\cos(\theta)\sin^2(\theta)\beta_{zzz} + \frac{1}{2}\cos(\theta)\Big[\beta_{zxx}+\beta_{zyy}\Big] \\
&+ \frac{1}{2}\sin^3(\theta)\cos^3(\xi)\Big[\beta_{xxx}-\beta_{xyy}-\beta_{yxy}-\beta_{yyx}\Big] \\
&+ \frac{1}{2}\sin^3(\theta)\sin^3(\xi)\Big[-\beta_{yyy}+\beta_{xxy}+\beta_{xyx}+\beta_{yxx}\Big] \\
&+ \frac{1}{2}\sin(\theta)\cos(\xi)\Big[-\beta_{xxx}-\beta_{xyy}+\beta_{zxz}+\beta_{zzx}\Big] \\
&+ \frac{1}{2}\sin(\theta)\sin(\xi)\Big[\beta_{yyy}+\beta_{yxx}-\beta_{zyz}-\beta_{zzy}\Big] \\
&+ \frac{1}{2}\sin^3(\theta)\sin(\xi)\Big[-\beta_{xxy}-\beta_{xyx}-\beta_{yxx}+\beta_{yzz}+\beta_{zyz}+\beta_{zzy}\Big] \\
&+ \frac{1}{2}\sin^3(\theta)\cos(\xi)\Big[\beta_{xyy}+\beta_{yxy}+\beta_{yyx}-\beta_{xzz}-\beta_{zxz}-\beta_{zzx}\Big] \\
&- \frac{1}{2}\cos(\theta)\sin^2(\theta)\cos^2(\xi)\Big[\beta_{xxz}+\beta_{xzx}+\beta_{zxx}\Big] \\
&- \frac{1}{2}\cos(\theta)\sin^2(\theta)\sin^2(\xi)\Big[\beta_{yyz}+\beta_{yzy}+\beta_{zyy}\Big]
\end{aligned}
$$

$$+\frac{1}{2}\cos(\theta)\sin^2(\theta)\cos(\xi)\sin(\xi)\Big[\beta_{xyz}+\beta_{yxz}+\beta_{xzy}+\beta_{zxy}+\beta_{yzx}+\beta_{zyx}\Big] \tag{C.27}$$

$$\langle\chi^{(2)}_{XZZ}\rangle_\phi/N = \sum_{\alpha\beta\gamma}^{\{x,y,z\}}\langle T_{X\alpha}T_{Z\beta}T_{Z\gamma}\rangle_\phi\beta_{\alpha\beta\gamma}$$

$$=0 \tag{C.28}$$

$$\langle\chi^{(2)}_{ZXZ}\rangle_\phi/N = \sum_{\alpha\beta\gamma}^{\{x,y,z\}}\langle T_{X\alpha}T_{Z\beta}T_{Z\gamma}\rangle_\phi\beta_{\beta\alpha\gamma}$$

$$=0 \tag{C.29}$$

$$\langle\chi^{(2)}_{ZZX}\rangle_\phi/N = \sum_{\alpha\beta\gamma}^{\{x,y,z\}}\langle T_{X\alpha}T_{Z\beta}T_{Z\gamma}\rangle_\phi\beta_{\gamma\beta\alpha}$$

$$=0 \tag{C.30}$$

$$\begin{aligned}\langle\chi^{(2)}_{YYZ}\rangle_\phi/N &= \sin^2(\theta)\cos(\theta)[\beta_{zzz}]+\cos(\theta)[\beta_{xxz}+\beta_{yyz}]\\
&-\sin^2(\theta)\cos(\theta)\sin^2(\xi)[\beta_{yyz}+\beta_{yzy}+\beta_{zyy}]\\
&-\sin^2(\theta)\cos(\theta)\cos^2(\xi)[\beta_{xxz}+\beta_{xzx}+\beta_{zxx}]\\
&+\sin^2(\theta)\cos(\theta)\sin(\xi)\cos(\xi)[\beta_{zyx}+\beta_{yzx}+\beta_{zxy}+\beta_{xzy}+\beta_{yxz}+\beta_{xyz}]\\
&+\sin(\theta)\sin(\xi)[\beta_{yyy}+\beta_{xxy}-\beta_{yzz}-\beta_{zyz}]\\
&+\sin(\theta)\cos(\xi)[-\beta_{xxx}-\beta_{yyx}+\beta_{xzz}+\beta_{zxz}]\\
&+\sin^3(\theta)\sin(\xi)[-\beta_{xxy}-\beta_{xyx}-\beta_{yxx}+\beta_{yzz}+\beta_{zyz}+\beta_{zzy}]\\
&+\sin^3(\theta)\cos(\xi)[\beta_{xyy}+\beta_{yxy}+\beta_{yyx}-\beta_{xzz}-\beta_{zxz}-\beta_{zzx}]\\
&+\sin^3(\theta)\sin^3(\xi)[-\beta_{yyy}+\beta_{xxy}+\beta_{xyx}+\beta_{yxx}]\\
&+\sin^3(\theta)\cos^3(\xi)[\beta_{xxx}-\beta_{xyy}-\beta_{yxy}-\beta_{yyx}]\\
&=\langle\chi^{(2)}_{XXZ}\rangle_\phi/N\end{aligned} \tag{C.31}$$

$$\langle\chi^{(2)}_{YZY}\rangle_\phi/N = \sum_{\alpha\beta\gamma}^{\{x,y,z\}}\langle T_{Y\alpha}T_{Y\beta}T_{Z\gamma}\rangle_\phi\beta_{\alpha\gamma\beta}$$

$$=\langle\chi^{(2)}_{XZX}\rangle_\phi/N \tag{C.32}$$

$$\langle\chi^{(2)}_{ZYY}\rangle_\phi/N = \sum_{\alpha\beta\gamma}^{\{x,y,z\}}\langle T_{Y\alpha}T_{Y\beta}T_{Z\gamma}\rangle_\phi\beta_{\gamma\beta\alpha}$$

$$=\langle\chi^{(2)}_{ZXX}\rangle_\phi/N \tag{C.33}$$

$$\langle\chi^{(2)}_{YZZ}\rangle_\phi/N = \sum_{\alpha\beta\gamma}^{\{x,y,z\}}\langle T_{Y\alpha}T_{Z\beta}T_{Z\gamma}\rangle_\phi\beta_{\alpha\beta\gamma}$$

$$=0 \tag{C.34}$$

$$\langle\chi^{(2)}_{ZYZ}\rangle_\phi/N = \sum_{\alpha\beta\gamma}^{\{x,y,z\}}\langle T_{Y\alpha}T_{Z\beta}T_{Z\gamma}\rangle_\phi\beta_{\gamma\alpha\beta}$$

$$=0 \tag{C.35}$$

$$\begin{aligned}\langle\chi^{(2)}_{ZZY}\rangle_\phi/N &= \sum_{\alpha\beta\gamma}^{\{x,y,z\}} \langle T_{Y\alpha}T_{Z\beta}T_{Z\gamma}\rangle_\phi \beta_{\gamma\beta\alpha} \\ &= 0 \end{aligned} \tag{C.36}$$

$$\begin{aligned}\langle\chi^{(2)}_{XYZ}\rangle_\phi/N &= \frac{1}{2}\cos(\theta)\sin(\theta)\cos(\xi)\Big[\beta_{yxx}-\beta_{xyx}-\beta_{yzz}+\beta_{zyz}\Big] \\ &+ \frac{1}{2}\cos(\theta)\sin(\theta)\sin(\xi)\Big[\beta_{xyy}-\beta_{yxy}-\beta_{xzz}+\beta_{zxz}\Big] \\ &+ \frac{1}{2}\sin^2(\theta)\cos(\xi)\sin(\xi)\Big[\beta_{xzx}-\beta_{zxx}-\beta_{yzy}+\beta_{zyy}\Big] \\ &+ \frac{1}{2}\sin^2(\theta)\sin^2(\xi)\Big[\beta_{zxy}-\beta_{xzy}\Big] + \frac{1}{2}\sin^2(\theta)\cos^2(\xi)\Big[\beta_{yzx}-\beta_{zyx}\Big] \\ &+ \frac{1}{2}\cos^2(\theta)\Big[\beta_{xyz}-\beta_{yxz}\Big] \end{aligned} \tag{C.37}$$

$$\begin{aligned}\langle\chi^{(2)}_{XZY}\rangle_\phi/N &= \sum_{\alpha\beta\gamma}^{\{x,y,z\}} \langle T_{X\alpha}T_{Y\beta}T_{Z\gamma}\rangle_\phi \beta_{\alpha\gamma\beta} \\ &= \frac{1}{2}\cos(\theta)\sin(\theta)\cos(\xi)\Big[\beta_{yxx}-\beta_{xxy}-\beta_{yzz}+\beta_{zzy}\Big] \\ &+ \frac{1}{2}\cos(\theta)\sin(\theta)\sin(\xi)\Big[\beta_{xyy}-\beta_{yyx}-\beta_{xzz}+\beta_{zzx}\Big] \\ &+ \frac{1}{2}\sin^2(\theta)\cos(\xi)\sin(\xi)\Big[\beta_{xxz}-\beta_{zxx}-\beta_{yyz}+\beta_{zyy}\Big] \\ &+ \frac{1}{2}\sin^2(\theta)\sin^2(\xi)\Big[\beta_{zyx}-\beta_{xyz}\Big] + \frac{1}{2}\sin^2(\theta)\cos^2(\xi)\Big[\beta_{yxz}-\beta_{zxy}\Big] \\ &+ \frac{1}{2}\cos^2(\theta)\Big[\beta_{xzy}-\beta_{yzx}\Big] \end{aligned} \tag{C.38}$$

$$\begin{aligned}\langle\chi^{(2)}_{YXZ}\rangle_\phi/N &= \sum_{\alpha\beta\gamma}^{\{x,y,z\}} \langle T_{X\alpha}T_{Y\beta}T_{Z\gamma}\rangle_\phi \beta_{\beta\alpha\gamma} \\ &= -\langle\chi^{(2)}_{XYZ}\rangle_\phi/N \end{aligned} \tag{C.39}$$

$$\begin{aligned}\langle\chi^{(2)}_{YZX}\rangle_\phi/N &= \sum_{\alpha\beta\gamma}^{\{x,y,z\}} \langle T_{X\alpha}T_{Y\beta}T_{Z\gamma}\rangle_\phi \beta_{\beta\gamma\alpha} \\ &= -\langle\chi^{(2)}_{XZY}\rangle_\phi/N \end{aligned} \tag{C.40}$$

$$\begin{aligned}\langle\chi^{(2)}_{ZXY}\rangle_\phi/N &= \sum_{\alpha\beta\gamma}^{\{x,y,z\}} \langle T_{X\alpha}T_{Y\beta}T_{Z\gamma}\rangle_\phi \beta_{\gamma\alpha\beta} \\ &= \frac{1}{2}\cos(\theta)\sin(\theta)\cos(\xi)\Big[\beta_{xyx}-\beta_{xxy}-\beta_{zyz}+\beta_{zzy}\Big] \\ &+ \frac{1}{2}\cos(\theta)\sin(\theta)\sin(\xi)\Big[\beta_{yxy}-\beta_{yyx}-\beta_{zxz}+\beta_{zzx}\Big] \\ &+ \frac{1}{2}\sin^2(\theta)\cos(\xi)\sin(\xi)\Big[\beta_{xxz}-\beta_{xzx}-\beta_{yyz}+\beta_{yzy}\Big] \\ &+ \frac{1}{2}\sin^2(\theta)\sin^2(\xi)\Big[\beta_{yzx}-\beta_{yxz}\Big] + \frac{1}{2}\sin^2(\theta)\cos^2(\xi)\Big[\beta_{xyz}-\beta_{xzy}\Big] \end{aligned}$$

$$+\frac{1}{2}\cos^2(\theta)\Big[\beta_{zxy}-\beta_{zyx}\Big] \tag{C.41}$$

$$\langle\chi^{(2)}_{ZYX}\rangle_\phi/N=\sum_{\alpha\beta\gamma}^{\{x,y,z\}}\langle T_{X\alpha}T_{Y\beta}T_{Z\gamma}\rangle_\phi\beta_{\gamma\beta\alpha}$$

$$=-\langle\chi^{(2)}_{ZXY}\rangle_\phi/N \tag{C.42}$$

# Appendix D

# Supporting Information for Chapter 6

TABLE D.1: Best matching between the normal modes of the TP molecule and of its complexes with Au clusters calculated at the B3LYP/6-311G*(C, S, H)/cc-pVDZ (Au). Each line gives the normal mode number for the different clusters that gives the largest overlap with a given mode in the TP molecule, and is associated to a label for simplifications.

| Label | TP | C1 | C2 | C3 | C4 | C5 | C6 |
|---|---|---|---|---|---|---|---|
| | | Onefold | Onefold | Twofold | Twofold | Threefold | Twofold |
| $b$ | 3 | 22 | 28 | 29 | 41 | 41 | 47 |
| $c$ | 4 | 25 | 31 | 31 | 43 | 43 | 49 |
| $d$ | 5 | 24 | 30 | 30 | 42 | 42 | 48 |
| $e$ | 6 | 26 | 32 | 32 | 44 | 44 | 50 |
| $f$ | 7 | 27 | 33 | 33 | 45 | 45 | 51 |
| $g$ | 8 | 28 | 34 | 34 | 46 | 46 | 52 |
| $h$ | 9 | 29 | 35 | 35 | 47 | 47 | 53 |
| $i$ | 10 | 30 | 36 | 36 | 48 | 48 | 54 |
| $j$ | 11 | 31 | 37 | 37 | 49 | 49 | 55 |
| $k$ | 12 | 32 | 38 | 38 | 50 | 50 | 56 |
| $l$ | 14 | 33 | 39 | 39 | 51 | 51 | 57 |
| $m$ | 15 | 34 | 40 | 40 | 52 | 52 | 58 |
| $n$ | 16 | 35 | 41 | 41 | 53 | 53 | 59 |
| $o$ | 17 | 36 | 42 | 42 | 54 | 54 | 60 |
| $p$ | 18 | 38 | 43 | 44 | 56 | 56 | 62 |
| $q$ | 19 | 37 | 44 | 43 | 55 | 55 | 61 |
| $r$ | 20 | 39 | 45 | 45 | 57 | 57 | 63 |
| $s$ | 21 | 40 | 46 | 46 | 58 | 58 | 64 |
| $t$ | 22 | 41 | 47 | 47 | 59 | 59 | 65 |
| $u$ | 23 | 42 | 48 | 48 | 60 | 60 | 66 |
| $v$ | 24 | 43 | 49 | 49 | 61 | 61 | 67 |
| $w$ | 25 | 44 | 50 | 50 | 62 | 62 | 68 |
| $x$ | 26 | 45 | 51 | 51 | 63 | 63 | 69 |
| $y$ | 27 | 46 | 52 | 52 | 64 | 64 | 70 |
| $\alpha$ | 29 | 47 | 53 | 53 | 65 | 65 | 71 |
| $\beta$ | 30 | 48 | 54 | 54 | 66 | 66 | 72 |
| $\varepsilon$ | 31 | 49 | 55 | 55 | 67 | 67 | 73 |
| $\eta$ | 32 | 50 | 56 | 56 | 68 | 68 | 74 |
| $\sigma$ | 33 | 51 | 57 | 57 | 69 | 69 | 75 |

TABLE D.2: Wavenumbers ($cm^{-1}$) of the normal modes of the isolated TP and its complexes with Au clusters calculated at the B3LYP/6-311G*(C, S, H)/cc-pVDZ (Au) level (scaled by a factor of 0.96).

| Label | TP | C1 | C2 | C3 | C4 | C5 | C6 |
|---|---|---|---|---|---|---|---|
| | | Onefold | Onefold | Twofold | Twofold | Threefold | Twofold |
| $a$ | 176 | 177 | 177 | 175 | 162 | | 171 |
| | | | | | 168 | | |
| | | 331 | 313 | 282 | 261 | 238 | 275 |
| $b$ | 267 | 259 | 275 | 343 | 329 | 321 | 335 |
| $c$ | 393 | 401 | 399 | 397 | 400 | 414 | 397 |
| $d$ | 394 | 397 | 398 | 395 | 395 | 394 | 394 |
| $e$ | 457 | 472 | 473 | 468 | 465 | 459 | 466 |
| $f$ | 608 | 607 | 607 | 606 | 606 | 605 | 606 |
| $g$ | 672 | 674 | 674 | 668 | 670 | 670 | 669 |
| $h$ | 678 | 679 | 679 | 674 | 674 | 671 | 674 |
| $i$ | 710 | 723 | 722 | 721 | 719 | 719 | 720 |
| $j$ | 799 | 811 | 810 | 807 | 807 | 807 | 807 |
| $k$ | 853 | 877 | 874 | 877 | 875 | 879 | 878 |
| $\Omega_1$ | 901 | | | | | | |
| $l$ | 913 | 924 | 922 | 926 | 925 | 926 | 927 |
| $m$ | 942 | 945 | 942 | 950 | 950 | 952 | 952 |
| $n$ | 976 | 976 | 976 | 975 | 975 | 974 | 975 |
| $o$ | 1006 | 1003 | 1003 | 1002 | 1002 | 1000 | 1002 |
| $p$ | 1064 | 1054 | 1052 | 1059 | 1059 | 1058 | 1060 |
| $q$ | 1070 | 1051 | 1053 | 1049 | 1050 | 1042 | 1048 |
| $r$ | 1140 | 1137 | 1136 | 1140 | 1140 | 1140 | 1140 |
| $s$ | 1165 | 1157 | 1155 | 1161 | 1160 | 1159 | 1162 |
| $t$ | 1267 | 1255 | 1254 | 1261 | 1260 | 1262 | 1261 |
| $u$ | 1307 | 1296 | 1295 | 1300 | 1298 | 1298 | 1300 |
| $v$ | 1424 | 1415 | 1416 | 1418 | 1418 | 1418 | 1418 |
| $w$ | 1459 | 1450 | 1450 | 1453 | 1452 | 1450 | 1452 |
| $x$ | 1559 | 1550 | 1551 | 1556 | 1555 | 1555 | 1555 |
| $y$ | 1570 | 1560 | 1561 | 1562 | 1562 | 1559 | 1561 |
| $\Omega_2$ | 2486 | | | | | | |
| $\alpha$ | 3035 | 3032 | 3030 | 3040 | 3039 | 3041 | 3042 |
| $\beta$ | 3039 | 3041 | 3038 | 3047 | 3046 | 3048 | 3049 |
| $\varepsilon$ | 3049 | 3055 | 3053 | 3058 | 3055 | 3057 | 3059 |
| $\eta$ | 3054 | 3063 | 3061 | 3063 | 3061 | 3063 | 3064 |
| $\sigma$ | 3066 | 3067 | 3065 | 3069 | 3068 | 3069 | 3070 |

TABLE D.3: IR intensities (km/mol) of the vibrational normal modes of the isolated TP and its complexes with Au clusters calculated at the B3LYP/6-311G*(C, S, H)/cc-pVDZ (Au) level .

| Label | TP | C1 | C2 | C3 | C4 | C5 | C6 |
|---|---|---|---|---|---|---|---|
| | | Onefold | Onefold | Twofold | Twofold | Threefold | Twofold |
| $a$ | 20 | 2 | 3 | 3 | 2 | | 6 |
| | | | | 7 | | | |
| | 18 | 52 | 2 | 10 | 0 | 6 | |
| $b$ | 1 | 4 | 0 | 1 | 1 | 0 | 0 |
| $c$ | 1 | 1 | 0 | 1 | 0 | 0 | 1 |
| $d$ | 0 | 0 | 0 | 0 | 0 | 0 | 0 |
| $e$ | 11 | 5 | 5 | 10 | 8 | 6 | 9 |
| $f$ | 0 | 0 | 0 | 0 | 0 | 0 | 0 |
| $g$ | 24 | 16 | 13 | 7 | 10 | 19 | 9 |
| $h$ | 15 | 26 | 40 | 36 | 37 | 23 | 38 |
| $i$ | 59 | 41 | 35 | 41 | 39 | 44 | 42 |
| $j$ | 0 | 1 | 0 | 1 | 0 | 0 | 1 |
| $k$ | 1 | 2 | 1 | 2 | 1 | 0 | 2 |
| $\Omega_1$ | 12 | | | | | | |
| $l$ | 0 | 0 | 0 | 0 | 0 | 0 | 0 |
| $m$ | 0 | 0 | 0 | 0 | 0 | 0 | 0 |
| $n$ | 1 | 4 | 6 | 7 | 8 | 14 | 11 |
| $o$ | 12 | 8 | 21 | 11 | 19 | 22 | 15 |
| $p$ | 8 | 2 | 4 | 5 | 5 | 7 | 6 |
| $q$ | 27 | 4 | 11 | 1 | 7 | 5 | 1 |
| $r$ | 1 | 0 | 0 | 0 | 0 | 0 | 0 |
| $s$ | 3 | 4 | 7 | 5 | 5 | 6 | 8 |
| $t$ | 3 | 0 | 0 | 0 | 0 | 0 | 0 |
| $u$ | 1 | 2 | 1 | 4 | 4 | 4 | 4 |
| $v$ | 9 | 8 | 6 | 9 | 10 | 9 | 8 |
| $w$ | 37 | 17 | 33 | 26 | 40 | 40 | 35 |
| $x$ | 2 | 2 | 2 | 3 | 4 | 3 | 4 |
| $y$ | 35 | 7 | 30 | 14 | 28 | 31 | 18 |
| $\Omega_2$ | 7 | | | | | | |
| $\alpha$ | 5 | 2 | 5 | 2 | 4 | 3 | 3 |
| $\beta$ | 0 | 14 | 17 | 8 | 5 | 5 | 7 |
| $\varepsilon$ | 10 | 32 | 44 | 20 | 17 | 12 | 24 |
| $\eta$ | 40 | 18 | 22 | 12 | 17 | 15 | 12 |
| $\sigma$ | 19 | 16 | 25 | 22 | 32 | 36 | 27 |

TABLE D.4: Raman intensities (at 633 nm, in $Å^4$/amu) of the vibrational normal modes of the isolated TP and its complexes with Au clusters calculated at B3LYP/6-311G*(C, S, H)/cc-pVDZ (Au) level.

| Label | TP | C1 | C2 | C3 | C4 | C5 | C6 |
|---|---|---|---|---|---|---|---|
| | | Onefold | Onefold | Twofold | Twofold | Threefold | Twofold |
| $a$ | 2 | 4770 | 302 | 313 | 53500 | | 405 |
| | | | | | 1340 | | |
| | | 46000 | 33400 | 93 | 20700 | 2 | 8910 |
| $b$ | 1 | 197000 | 281 | 18 | 303 2 | 168 | |
| $c$ | 5 | 76500 | 23700 | 637 | 98000 | 226 9770 | |
| $d$ | 0 | 460000 | 1220 | 12 | 2960 | 1 | 8 |
| $e$ | 0 | 5130 | 73 | 131 | 142 | 1 | 80 |
| $f$ | 5 | 793 | 31 | 3 | 455 | 7 | 3 |
| $g$ | 0 | 339 | 11 | 106 | 2000 | 3 | 125 |
| $h$ | 5 | 6260 | 703 | 97 | 8830 | 100 | 2960 |
| $i$ | 0 | 1180 | 6 | 97 | 424 | 5 | 54 |
| $j$ | 1 | 6280 | 33 | 12 | 2440 | 1 | 3 |
| $k$ | 0 | 26 | 8 | 20 | 2240 | 3 | 121 |
| $\Omega_1$ | 939 | | | | | | |
| $l$ | 0 | 937 | 3 | 3 | 2350 | 0 | 11 |
| $m$ | 0 | 806 | 8 | 2 | 2680 | 2 | 268 |
| $n$ | 48 | 103000 | 8330 | 252 | 13400 | 303 | 1400 |
| $o$ | 25 | 9120 | 3830 | 944 | 54300 | 642 | 9830 |
| $p$ | 9 | 40100 | 21 | 2 | 34 | 0 | 23 |
| $q$ | 21 | 144000 | 730 | 2830 | 234000 | 1550 | 29900 |
| $r$ | 6 | 756 | 32 | 5 | 1410 | 14 | 14 |
| $s$ | 6 | 212000 | 7130 | 434 | 44600 | 262 | 3590 |
| $t$ | 3 | 23300 | 132 | 16 | 1400 | 4 | 21 |
| $u$ | 2 | 3170 | 4 | 2 | 2360 | 12 | 21 |
| $v$ | 2 | 16700 | 7 | 12 | 519 | 22 | 96 |
| $w$ | 1 | 23400 | 1660 | 854 | 92600 | 403 | 10800 |
| $x$ | 3 | 4640 | 3 | 5 | 2000 | 2 | 53 |
| $y$ | 64 | 129000 | 10900 | 4130 | 266000 | 2490 | 39800 |
| $\Omega_2$ | 122 | | | | | | |
| $\alpha$ | 15 | 4530 | 126 | 38 | 981 | 38 | 29 |
| $\beta$ | 114 | 372 | 343 | 134 | 197 | 193 | 170 |
| $\varepsilon$ | 134 | 17600 | 624 | 251 | 3310 | 264 | 546 |
| $\eta$ | 25 | 89 | 82 | 43 | 182 | 95 | 139 |
| $\sigma$ | 319 | 51700 | 349 | 126 | 25900 | 503 | 353 |

# Appendix E

# Supporting Information for Chapter 8

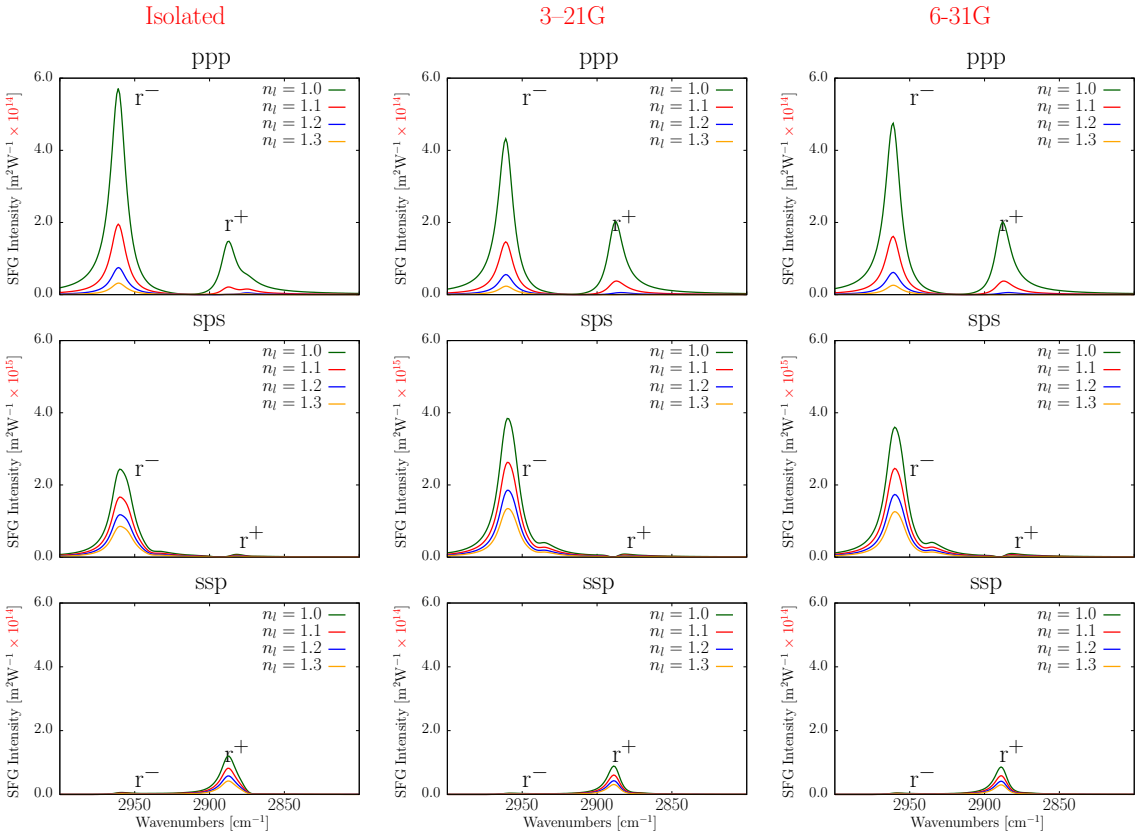


FIGURE E.1: Effect of $\varepsilon_l$ the electric permitivity of the OTS thin film ($\varepsilon_l = n_l^2$) on the SFG spectra. Spectra are calculated for three polarization combinations (ppp, sps, and ppp) and using the *Isolated-model* (left column) and the *Adsorbed-model* (central and right columns). For this latter two basis sets of the low-layer are presented (3-21G and 6-31G).

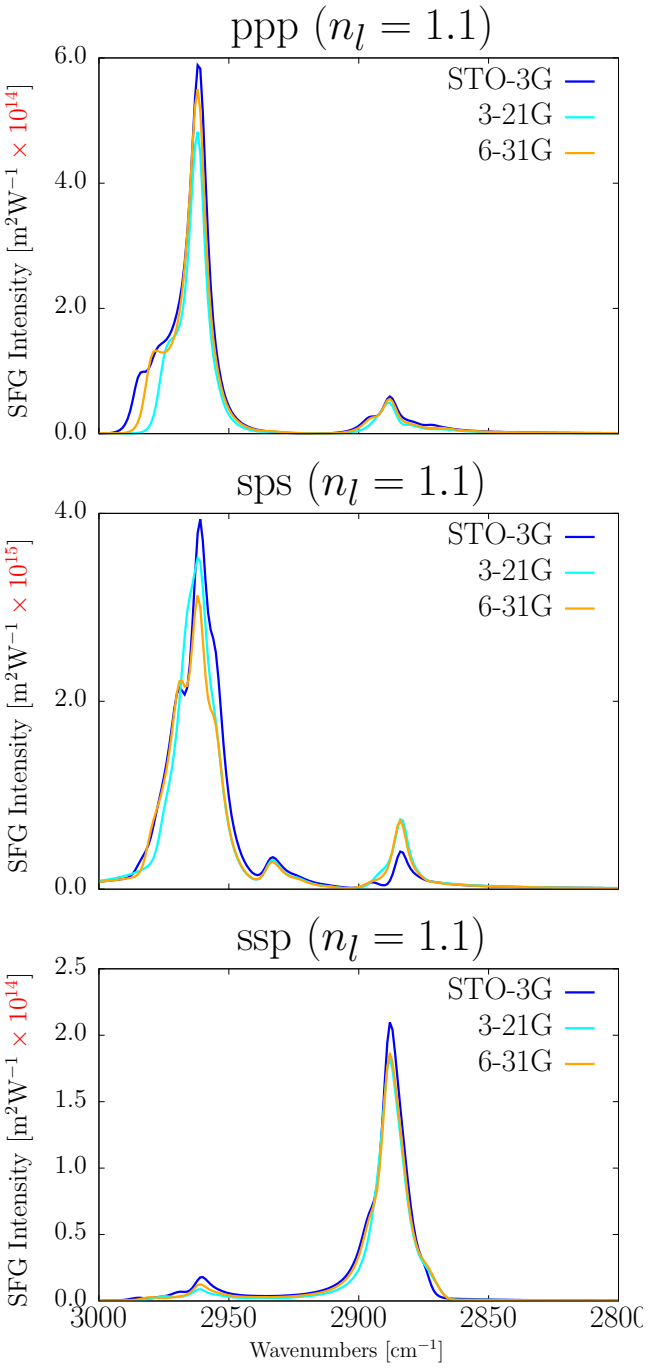


FIGURE E.2: Effect of the low-layer basis set on the DDCS SFG spectra. Spectra are calculated for three polarization combinations (ppp, sps, and ppp), and the refractive index is set to 1.1

# Appendix F

# Supporting Information for Chapter 9

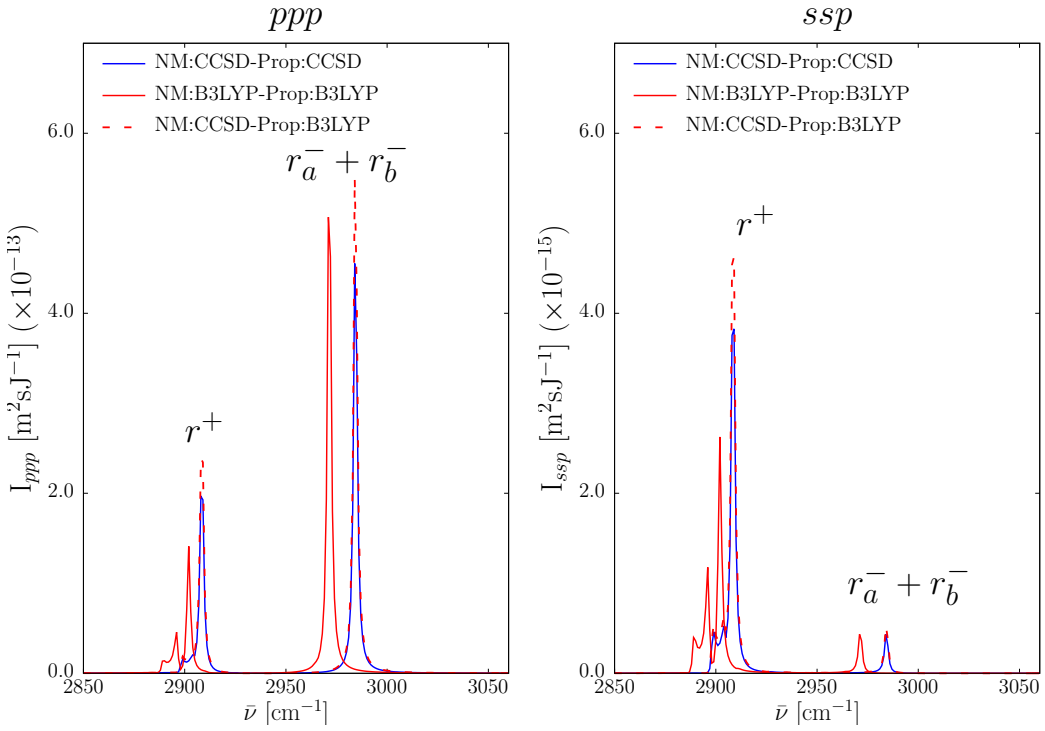


FIGURE F.1: Comparison of the SFG spectra calculated at the CCSD and B3LYP (with the `SuperFine` integration grids) levels. NM ≡ Normal Modes (aug-cc-pVDZ), Prop ≡ Cartesian derivatives of the properties : $\partial\mu_\alpha/\partial r_{i\gamma}$ and $\partial\alpha_{\alpha\beta}/\partial r_{i\gamma}$ (aug-cc-pVDZ). In the hybrid results (dashed-red curves), the Cartesian derivatives of the properties calculated using the B3LYP/aug-cc-pVDZ method were projected onto the CCSD/aug-cc-pVDZ normal modes. The spectra are reported for the Free Chain model, at $\theta = 60°$ and $\xi = 150°$, and for *ppp* and *ssp* sets of polarizations. $\Gamma = 1$ cm$^{-1}$.

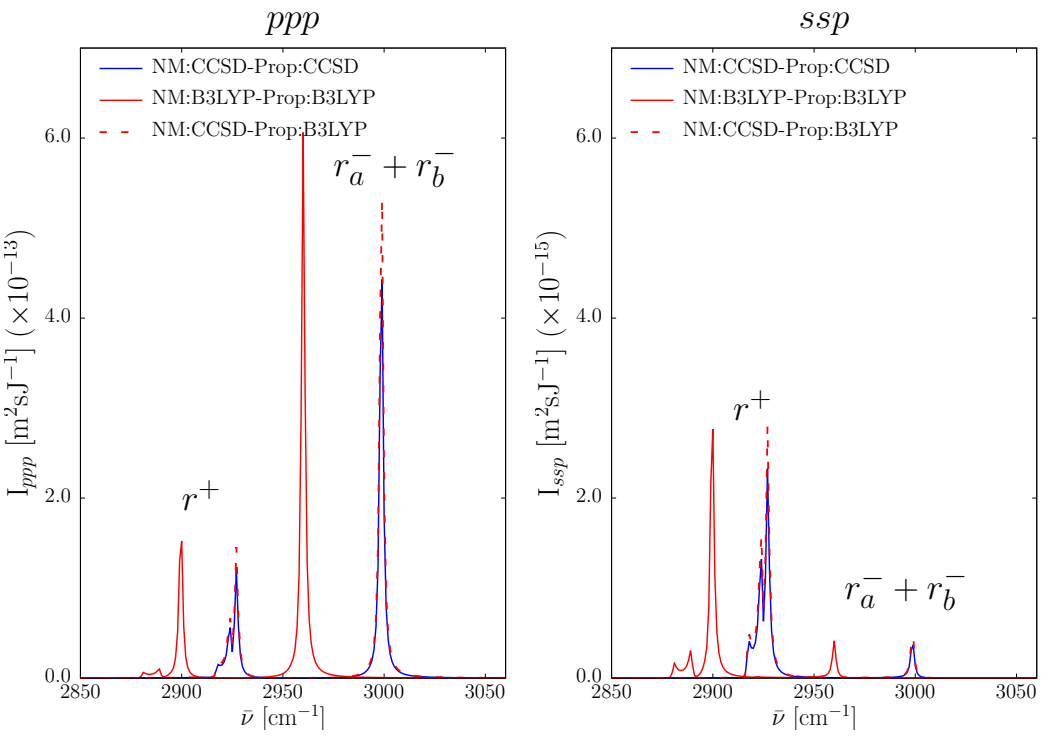


FIGURE F.2: Comparison of the SFG spectra calculated at the CCSD and B3LYP (with the `SuperFine` integration grids) levels. NM ≡ Normal Modes (cc-pVTZ), Prop ≡ Cartesian derivatives of the properties : $\partial\mu_\alpha/\partial r_{i\gamma}$ and $\partial\alpha_{\alpha\beta}/\partial r_{i\gamma}$ (aug-cc-pVDZ). The six spectra combine Cartesian derivatives calculated using the aug-cc-pVDZ basis set with cc-pVTZ normal modes. Thes spectra are reported for the Free Chain model, at $\theta = 60°$ and $\xi = 150°$, and for *ppp* and *ssp* sets of polarizations. $\Gamma = 1$ cm$^{-1}$.

TABLE F.1: Romberg's triangles for the dipole moment and the polarizability derivatives with respect to the $x$-atomic Cartesian coordinate of $H_2$ (in a.u.). Calculations were performed at the B3LYP/aug-cc-pVDZ level, for seven amplitudes of geometrical distortion ($\Delta r = 0.005$, 0.01, 0.02, 0.04, 0.08, 0.16, and 0.32 Å). The selected "best" values are highlighted in boxes, and the analytic derivatives (at the same level of calculation) are also reported. $n$ is the Romberg's iteration number. The $\partial\mu_y/\partial x_{H_2}$ values were not reported because they are zero by symmetry.

| | SuperFine grid | | | | | | | UltraFine grid | | | | | | |
|---|---|---|---|---|---|---|---|---|---|---|---|---|---|---|
| $\Delta r/n$ | 0 | 1 | 2 | 3 | 4 | 5 | 6 | 0 | 1 | 2 | 3 | 4 | 5 | 6 |
| | | | | | | $\partial\mu_x/\partial x_{H_2}$ | | | | | | | | |
| **0.005** | 0.00857 | 0.00857 | 0.00857 | 0.00857 | 0.00857 | 0.00857 | 0.00857 | 0.00857 | 0.00857 | 0.00857 | 0.00857 | 0.00857 | 0.00857 | 0.00857 |
| **0.010** | 0.00857 | 0.00857 | 0.00857 | 0.00857 | 0.00857 | 0.00857 | | 0.00857 | 0.00857 | 0.00857 | 0.00857 | 0.00857 | 0.00857 | |
| **0.020** | 0.00857 | 0.00857 | 0.00857 | 0.00857 | 0.00857 | | | 0.00857 | 0.00857 | 0.00857 | 0.00857 | 0.00857 | | |
| **0.040** | 0.00857 | 0.00857 | 0.00857 | 0.00857 | | | | 0.00857 | 0.00857 | 0.00857 | 0.00857 | | | |
| **0.080** | 0.00857 | 0.00857 | 0.00857 | | | | | 0.00857 | 0.00857 | 0.00857 | | | | |
| **0.160** | 0.00859 | 0.00850 | | | | | | 0.00859 | 0.00850 | | | | | |
| **0.320** | 0.00885 | | | | | | | 0.00885 | | | | | | |
| ***Analytic*** | | | **0.00857** | | | | | | | **0.00855** | | | | |
| | | | | | | $\partial\mu_y/\partial x_{H_2}$ | | | | | | | | |
| **0.005** | 0.09219 | 0.09219 | 0.09219 | 0.09219 | 0.09219 | 0.09219 | 0.09219 | 0.09219 | 0.09219 | 0.09219 | 0.09219 | 0.09219 | 0.09219 | 0.09219 |
| **0.010** | 0.09219 | 0.09219 | 0.09219 | 0.09219 | 0.09219 | 0.09219 | | 0.09219 | 0.09219 | 0.09219 | 0.09219 | 0.09219 | 0.09219 | |
| **0.020** | 0.09218 | 0.09219 | 0.09219 | 0.09219 | 0.09219 | | | 0.09218 | 0.09219 | 0.09219 | 0.09219 | 0.09219 | | |
| **0.040** | 0.09218 | 0.09219 | 0.09219 | 0.09219 | | | | 0.09218 | 0.09219 | 0.09219 | 0.09219 | | | |
| **0.080** | 0.09215 | 0.09219 | 0.09218 | | | | | 0.09215 | 0.09219 | 0.09218 | | | | |
| **0.160** | 0.09203 | 0.09222 | | | | | | 0.09203 | 0.09222 | | | | | |
| **0.320** | 0.09147 | | | | | | | 0.09147 | | | | | | |
| ***Analytic*** | | | **0.09218** | | | | | | | **0.09218** | | | | |
| | | | | | | $\partial\mu_z/\partial x_{H_2}$ | | | | | | | | |
| **0.005** | 0.06294 | 0.06294 | 0.06294 | 0.06294 | 0.06294 | 0.06294 | 0.06294 | 0.06294 | 0.06294 | 0.06294 | 0.06294 | 0.06294 | 0.06294 | 0.06294 |
| **0.010** | 0.06295 | 0.06295 | 0.06295 | 0.06295 | 0.06295 | 0.06295 | | 0.06295 | 0.06294 | 0.06294 | 0.06294 | 0.06294 | 0.06294 | |
| **0.020** | 0.06296 | 0.06295 | 0.06295 | 0.06295 | 0.06295 | | | 0.06296 | 0.06294 | 0.06294 | 0.06294 | 0.06294 | | |
| **0.040** | 0.06301 | 0.06295 | 0.06295 | 0.06295 | | | | 0.06300 | 0.06294 | 0.06294 | 0.06294 | | | |
| **0.080** | 0.06319 | 0.06295 | 0.06295 | | | | | 0.06318 | 0.06295 | 0.06294 | | | | |
| **0.160** | 0.06389 | 0.06299 | | | | | | 0.06389 | 0.06299 | | | | | |
| **0.320** | 0.06658 | | | | | | | 0.06658 | | | | | | |
| ***Analytic*** | | | **0.06295** | | | | | | | **0.06292** | | | | |
| | | | | | | $\partial\alpha_{xx}/\partial x_{H_2}$ | | | | | | | | |
| **0.005** | −1.19380 | −1.19377 | −1.19377 | −1.19377 | −1.19377 | −1.19377 | −1.19377 | −1.19490 | −1.19487 | −1.19487 | −1.19487 | −1.19487 | −1.19487 | −1.19487 |
| **0.010** | −1.19390 | −1.19377 | −1.19377 | −1.19377 | −1.19377 | −1.19377 | | −1.19500 | −1.19487 | −1.19487 | −1.19487 | −1.19487 | −1.19487 | |
| **0.020** | −1.19428 | −1.19377 | −1.19377 | −1.19377 | −1.19377 | | | −1.19538 | −1.19487 | −1.19487 | −1.19487 | −1.19487 | | |
| **0.040** | −1.19582 | −1.19377 | −1.19377 | −1.19377 | | | | −1.19690 | −1.19487 | −1.19487 | −1.19487 | | | |
| **0.080** | −1.20199 | −1.19376 | −1.19377 | | | | | −1.20299 | −1.19483 | −1.19486 | | | | |
| **0.160** | −1.22670 | −1.19359 | | | | | | −1.22745 | −1.19445 | | | | | |
| **0.320** | −1.32605 | | | | | | | −1.32647 | | | | | | |
| ***Analytic*** | | | **−1.19384** | | | | | | | **−1.19411** | | | | |
| | | | | | | $\partial\alpha_{yy}/\partial x_{H_2}$ | | | | | | | | |
| **0.005** | −2.30948 | −2.30952 | −2.30952 | −2.30952 | −2.30952 | −2.30952 | −2.30952 | −2.30956 | −2.30959 | −2.30959 | −2.30959 | −2.30959 | −2.30959 | −2.30959 |
| **0.010** | −2.30938 | −2.30952 | −2.30952 | −2.30952 | −2.30952 | −2.30952 | | −2.30945 | −2.30959 | −2.30959 | −2.30959 | −2.30959 | −2.30959 | |
| **0.020** | −2.30897 | −2.30952 | −2.30952 | −2.30952 | −2.30952 | | | −2.30904 | −2.30959 | −2.30959 | −2.30959 | −2.30959 | | |
| **0.040** | −2.30734 | −2.30951 | −2.30952 | −2.30952 | | | | −2.30741 | −2.30958 | −2.30959 | −2.30959 | | | |
| **0.080** | −2.30081 | −2.30949 | −2.30950 | | | | | −2.30087 | −2.30955 | −2.30957 | | | | |
| **0.160** | −2.27479 | −2.30926 | | | | | | −2.27484 | −2.30928 | | | | | |
| **0.320** | −2.17140 | | | | | | | −2.17150 | | | | | | |
| ***Analytic*** | | | **−2.30943** | | | | | | | **−2.30957** | | | | |
| | | | | | | $\partial\alpha_{zz}/\partial x_{H_2}$ | | | | | | | | |
| **0.005** | −1.81362 | −1.81363 | −1.81363 | −1.81363 | −1.81363 | −1.81363 | −1.81363 | −1.81537 | −1.81538 | −1.81538 | −1.81538 | −1.81538 | −1.81538 | −1.81538 |
| **0.010** | −1.81361 | −1.81363 | −1.81363 | −1.81363 | −1.81363 | −1.81363 | | −1.81535 | −1.81537 | −1.81537 | −1.81537 | −1.81537 | −1.81537 | |
| **0.020** | −1.81354 | −1.81363 | −1.81363 | −1.81363 | −1.81363 | | | −1.81528 | −1.81537 | −1.81537 | −1.81537 | −1.81537 | | |
| **0.040** | −1.81328 | −1.81363 | −1.81363 | −1.81363 | | | | −1.81499 | −1.81538 | −1.81538 | −1.81538 | | | |
| **0.080** | −1.81220 | −1.81366 | −1.81365 | | | | | −1.81383 | −1.81539 | −1.81539 | | | | |
| **0.160** | −1.80784 | −1.81386 | | | | | | −1.80916 | −1.81539 | | | | | |
| **0.320** | −1.78978 | | | | | | | −1.79045 | | | | | | |
| ***Analytic*** | | | **−1.81383** | | | | | | | **−1.81381** | | | | |

TABLE F.7: Ratio between the intensity (maximum) of the peaks $r_a^- + r_b^-$ and $r^+$ calculated within the Free Chain model ( see Figs. F.1 and F.2 )

| | | *ppp* | *ssp* |
|---|---|---|---|
| | | NM: aug-cc-pVDZ | Properties: aug-cc-pVDZ |
| NM:CCSD | Properties:CCSD | 2.3 | 0.1 |
| NM:B3LYP | Properties:B3LYP | 3.6 | 0.2 |
| NM:CCSD | Properties:B3LYP | 2.3 | 0.2 |
| | | NM: cc-pVTZ | Properties: aug-cc-pVDZ |
| NM:CCSD | Properties:CCSD | 3.6 | 0.2 |
| NM:B3LYP | Properties:B3LYP | 4.0 | 0.1 |
| NM:CCSD | Properties:B3LYP | 3.6 | 0.2 |

TABLE F.2: Vibrational frequencies* ($cm^{-1}$) and derivatives of the dipole moment ($\partial\mu_\alpha/\partial Q$) and of the polarizability ($\partial\alpha_{\alpha\beta}/\partial Q$),‡ computed at the B3LYP/aug-cc-pVDZ (with the `SuperFine` grid) level.†.The " ′ " indicates the derivative with respect to the corresponding normal coordinate.

| | $r^+$ | $r_a^-$ | $r_b^-$ | $d^+(d_1^+/d_2^+)$§ | $d^-(d_1^-/d_2^-)$§ |
|---|---|---|---|---|---|
| | 2902 | 2965 | 2971 | 2889/2896 | 2911/2934 |
| Freq | 2902 | 2965 | 2972 | 2893 | 2922 |
| | 2901 | 2961 | 2971 | | |
| | 0.075 | 0.000 | 0.205 | 0.006/0.208 | 0.000/0.000 |
| $\mu'_x$ | 0.006 | 0.000 | 0.202 | 0.150 | 0.000 |
| | 0.008 | 0.000 | 0.188 | | |
| | 0.000 | 0.263 | 0.000 | 0.000/0.000 | 0.013/0.203 |
| $\mu'_y$ | 0.000 | 0.233 | 0.000 | 0.000 | 0.135 |
| | 0.000 | 0.186 | 0.000 | | |
| | 0.225 | 0.000 | 0.019 | 0.029/0.104 | 0.000/0.000 |
| $\mu'_z$ | 0.183 | 0.000 | 0.021 | 0.122 | 0.000 |
| | 0.185 | 0.000 | 0.031 | | |
| | 8.203 | 0.000 | 6.486 | 7.402/2.022 | 0.000/0.000 |
| $\alpha'_{xx}$ | 7.379 | 0.000 | 6.618 | 5.581 | 0.000 |
| | 7.303 | 0.000 | 6.091 | | |
| | 8.799 | 0.000 | 2.926 | 10.248/2.943 | 0.000/0.000 |
| $\alpha'_{yy}$ | 7.865 | 0.000 | 2.770 | 8.153 | 0.000 |
| | 7.753 | 0.000 | 3.486 | | |
| | 7.562 | 0.000 | 1.489 | 4.172/2.243 | 0.000/0.000 |
| $\alpha'_{zz}$ | 7.273 | 0.000 | 1.568 | 3.523 | 0.000 |
| | 7.233 | 0.000 | 1.246 | | |
| | 0.000 | 2.505 | 0.000 | 0.000/0.000 | 8.771/0.346 |
| $\alpha'_{xy}$ | 0.000 | 1.961 | 0.000 | 0.000 | 6.708 |
| | 0.000 | 3.775 | 0.000 | | |
| | 0.198 | 0.000 | 5.475 | 3.374/0.346 | 0.000/0.000 |
| $\alpha'_{xz}$ | 0.515 | 0.000 | 5.439 | 2.653 | 0.000 |
| | 0.556 | 0.000 | 5.655 | | |
| | 0.000 | 4.053 | 0.000 | 0.000/0.000 | 5.607/1.040 |
| $\alpha'_{yz}$ | 0.000 | 3.791 | 0.000 | 0.000 | 4.738 |
| | 0.000 | 4.978 | 0.000 | | |

*The harmonic vibrational frequencies have been scaled by a factor of 0.96.
†For each property the first, second, and third rows correspond to the Free Chain, Free Ethyl, and Free Methyl models, respectively.
‡ $\alpha'_{xy} = \alpha'_{yx}$; $\alpha'_{xz} = \alpha'_{zx}$; $\alpha'_{yz} = \alpha'_{zy}$.
§ $d_1^+$, $d_2^+$, $d_1^-$, $d_2^-$ ≡ Free Chain; $d^+$, $d^-$ ≡ Free Ethyl.

TABLE F.3: Vibrational frequencies* ($cm^{-1}$), and derivatives of the dipole moment ($\partial\mu_\alpha/\partial Q$) and of the polarizability ($\partial\alpha_{\alpha\beta}/\partial Q$),‡. Cartesian dipole moment and polarizability derivatives have been calculated at B3LYP/aug-cc-pVDZ (with the `SuperFine` grid) level and projected onto the CCSD/aug-cc-pVDZ normal modes.†.The " ′ " indicates the derivative with respect to the corresponding normal coordinate.

| | $r^+$ | $r_a^-$ | $r_b^-$ | $d^+(d_1^+/d_2^+)$§ | $d^-(d_1^-/d_2^-)$§ |
|---|---|---|---|---|---|
| | 2909 | 2978 | 2984 | 2898/2904 | 2926/2948 |
| Freq | 2908 | 2977 | 2984 | 2901 | 2936 |
| | 2908 | 2974 | 2984 | | |
| | 0.032 | 0.000 | 0.205 | 0.003/0.219 | 0.000/0.000 |
| $\mu'_x$ | 0.021 | 0.000 | 0.202 | 0.149 | 0.000 |
| | 0.005 | 0.000 | 0.190 | | |
| | 0.000 | 0.260 | 0.000 | 0.000/0.000 | 0.013/0.207 |
| $\mu'_y$ | 0.000 | 0.232 | 0.000 | 0.000 | 0.137 |
| | 0.000 | 0.186 | 0.000 | | |
| | 0.197 | 0.000 | 0.021 | 0.045/0.147 | 0.000/0.000 |
| $\mu'_z$ | 0.161 | 0.000 | 0.023 | 0.151 | 0.000 |
| | 0.185 | 0.000 | 0.032 | | |
| | 9.089 | 0.000 | 6.466 | 6.712/0.449 | 0.000/0.000 |
| $\alpha'_{xx}$ | 8.296 | 0.000 | 6.583 | 4.346 | 0.000 |
| | 7.420 | 0.000 | 6.102 | | |
| | 10.013 | 0.000 | 3.060 | 9.576/1.165 | 0.000/0.000 |
| $\alpha'_{yy}$ | 9.104 | 0.000 | 2.919 | 6.825 | 0.000 |
| | 7.779 | 0.000 | 3.577 | | |
| | 8.151 | 0.000 | 1.490 | 3.569/0.740 | 0.000/0.000 |
| $\alpha'_{zz}$ | 7.741 | 0.000 | 1.559 | 2.324 | 0.000 |
| | 7.240 | 0.000 | 1.264 | | |
| | 0.000 | 2.594 | 0.000 | 0.000/0.000 | 8.776/0.364 |
| $\alpha'_{xy}$ | 0.000 | 2.070 | 0.000 | 0.000 | 6.705 |
| | 0.000 | 3.806 | 0.000 | | |
| | 0.070 | 0.000 | 5.556 | 3.419/0.331 | 0.000/0.000 |
| $\alpha'_{xz}$ | 0.162 | 0.000 | 5.522 | 2.709 | 0.000 |
| | 0.643 | 0.000 | 5.718 | | |
| | 0.000 | 4.096 | 0.000 | 0.000/0.000 | 5.639/1.002 |
| $\alpha'_{yz}$ | 0.000 | 3.834 | 0.000 | 0.000 | 4.736 |
| | 0.000 | 4.976 | 0.000 | | |

*The harmonic vibrational frequencies have been scaled by a factor of 0.96.
†For each property the first, second, and third rows correspond to the Free Chain, Free Ethyl, and Free Methyl models, respectively.
‡ $\alpha'_{xy} = \alpha'_{yx}$; $\alpha'_{xz} = \alpha'_{zx}$; $\alpha'_{yz} = \alpha'_{zy}$.
§ $d_1^+$, $d_2^+$, $d_1^-$, $d_2^-$ ≡ Free Chain; $d^+$, $d^-$ ≡ Free Ethyl.

TABLE F.4: Vibrational frequencies* ($cm^{-1}$), and derivatives of the dipole moment ($\partial\mu_\alpha/\partial Q$) and of the polarizability ($\partial\alpha_{\alpha\beta}/\partial Q$),‡. Cartesian dipole moment and polarizability derivatives have been calculated at the CCSD/aug-cc-pVDZ level and projected onto CCSD/cc-pVTZ normal modes.†.The " ′ " indicates the derivative with respect to the corresponding normal coordinate.

| | $r^+$ | $r_a^-$ | $r_b^-$ | $d^+(d_1^+/d_2^+)$§ | $d^-(d_1^-/d_2^-)$§ |
|---|---|---|---|---|---|
| | 2927 | 2993 | 2999 | 2917/2924 | 2941/2963 |
| Freq | 2926 | 2992 | 2999 | 2921 | 2951 |
| | 2926 | 2989 | 2998 | | |
| | 0.074 | 0.003 | 0.202 | 0.004/0.198 | 0.000/0.003 |
| $\mu'_x$ | 0.007 | 0.003 | 0.200 | 0.142 | 0.002 |
| | 0.006 | 0.002 | 0.186 | | |
| | 0.001 | 0.258 | 0.003 | 0.000/0.003 | 0.012/0.197 |
| $\mu'_y$ | 0.000 | 0.229 | 0.003 | 0.002 | 0.131 |
| | 0.000 | 0.182 | 0.003 | | |
| | 0.216 | 0.000 | 0.020 | 0.035/0.100 | 0.000/0.000 |
| $\mu'_z$ | 0.165 | 0.000 | 0.022 | 0.133 | 0.000 |
| | 0.176 | 0.000 | 0.032 | | |
| | 7.978 | 0.069 | 5.828 | 6.440/2.044 | 0.208/0.015 |
| $\alpha'_{xx}$ | 7.459 | 0.056 | 5.926 | 4.509 | 0.168 |
| | 7.015 | 0.100 | 5.439 | | |
| | 8.551 | 0.066 | 2.646 | 9.364/2.843 | 0.227/0.003 |
| $\alpha'_{yy}$ | 7.994 | 0.052 | 2.526 | 7.039 | 0.165 |
| | 7.315 | 0.097 | 3.208 | | |
| | 6.983 | 0.001 | 1.352 | 3.707/2.123 | 0.005/0.004 |
| $\alpha'_{zz}$ | 6.853 | 0.002 | 1.410 | 2.758 | 0.001 |
| | 6.585 | 0.001 | 1.105 | | |
| | 0.013 | 2.331 | 0.119 | 0.048/0.001 | 7.806/0.348 |
| $\alpha'_{xy}$ | 0.006 | 1.831 | 0.119 | 0.035 | 5.997 |
| | 0.004 | 3.467 | 0.122 | | |
| | 0.100 | 0.046 | 4.872 | 3.145/0.280 | 0.068/0.014 |
| $\alpha'_{xz}$ | 0.306 | 0.043 | 4.844 | 2.481 | 0.059 |
| | 0.538 | 0.059 | 5.046 | | |
| | 0.004 | 3.574 | 0.065 | $0.039 - 0.010$ | 5.069/0.928 |
| $\alpha'_{yz}$ | 0.003 | 3.325 | 0.065 | 0.035 | 4.278 |
| | 0.007 | 4.413 | 0.068 | | |

*The harmonic vibrational frequencies have been scaled by a factor of 0.96.
†For each property the first, second, and third rows correspond to the Free Chain, Free Ethyl, and Free Methyl models, respectively.
‡ $\alpha'_{xy} = \alpha'_{yx}$; $\alpha'_{xz} = \alpha'_{zx}$; $\alpha'_{yz} = \alpha'_{zy}$.
§ $d_1^+,\ d_2^+,\ d_1^-,\ d_2^- \equiv$ Free Chain; $d^+,\ d^- \equiv$ Free Ethyl.

TABLE F.5: Vibrational frequencies* ($cm^{-1}$), and derivatives of the dipole moment ($\partial\mu_\alpha/\partial Q$) and of the polarizability ($\partial\alpha_{\alpha\beta}/\partial Q$),‡. Cartesian dipole moment and polarizability derivatives have been calculated at the B3LYP/aug-cc-pVDZ (with the `SuperFine` grid) level and projected onto B3LYP/cc-pVTZ (with the `SuperFine` grid) normal modes.†.The " ′ " indicates the derivative with respect to the corresponding normal coordinate.

| | $r^+$ | $r_a^-$ | $r_b^-$ | $d^+(d_1^+/d_2^+)$§ | $d^-(d_1^-/d_2^-)$§ |
|---|---|---|---|---|---|
| | 2900 | 2955 | 2960 | 2881/2889 | 2897/2921 |
| Freq | 2899 | 2954 | 2960 | 2885 | 2907 |
| | 2899 | 2951 | 2959 | | |
| | 0.052 | 0.002 | 0.204 | 0.004/0.212 | 0.000/0.001 |
| $\mu'_x$ | 0.016 | 0.001 | 0.201 | 0.146 | 0.001 |
| | 0.008 | 0.001 | 0.185 | | |
| | 0.000 | 0.257 | 0.001 | 0.000/0.001 | 0.012/0.205 |
| $\mu'_y$ | 0.000 | 0.229 | 0.001 | 0.001 | 0.135 |
| | 0.000 | 0.184 | 0.001 | | |
| | 0.212 | 0.000 | 0.017 | 0.016/0.126 | 0.000/0.000 |
| $\mu'_z$ | 0.189 | 0.000 | 0.020 | 0.110 | 0.000 |
| | 0.183 | 0.000 | 0.032 | | |
| | 7.601 | 0.020 | 6.463 | 7.975/0.778 | 0.096/0.002 |
| $\alpha'_{xx}$ | 6.902 | 0.015 | 6.584 | 5.891 | 0.069 |
| | 7.178 | 0.035 | 6.006 | | |
| | 8.051 | 0.026 | 2.744 | 10.910/1.594 | 0.088/0.004 |
| $\alpha'_{yy}$ | 7.236 | 0.020 | 2.598 | 8.541 | 0.071 |
| | 7.659 | 0.039 | 3.393 | | |
| | 7.301 | 0.002 | 1.548 | 4.811/1.231 | 0.003/0.001 |
| $\alpha'_{zz}$ | 6.961 | 0.002 | 1.620 | 3.923 | 0.002 |
| | 7.151 | 0.002 | 1.268 | | |
| | 0.000 | 2.499 | 0.047 | 0.014/0.005 | 8.627/0.324 |
| $\alpha'_{xy}$ | 0.004 | 1.981 | 0.047 | 0.013 | 6.591 |
| | 0.003 | 3.714 | 0.048 | | |
| | 0.435 | 0.026 | 5.360 | 3.355/0.283 | 0.030/0.006 |
| $\alpha'_{xz}$ | 0.666 | 0.024 | 5.325 | 2.639 | 0.025 |
| | 0.559 | 0.029 | 5.572 | | |
| | 0.001 | 4.020 | 0.032 | 0.019/0.001 | 5.504/0.981 |
| $\alpha'_{yz}$ | 0.005 | 3.766 | 0.031 | 0.014 | 4.633 |
| | 0.004 | 4.899 | 0.032 | | |

*The harmonic vibrational frequencies have been scaled by a factor of 0.96.
†For each property the first, second, and third rows correspond to the Free Chain, Free Ethyl, and Free Methyl models, respectively.
‡ $\alpha'_{xy} = \alpha'_{yx}$; $\alpha'_{xz} = \alpha'_{zx}$; $\alpha'_{yz} = \alpha'_{zy}$.
§ $d_1^+$, $d_2^+$, $d_1^-$, $d_2^-$ ≡ Free Chain; $d^+$, $d^-$ ≡ Free Ethyl.

TABLE F.6: Vibrational frequencies* ($cm^{-1}$), and derivatives of the dipole moment ($\partial\mu_\alpha/\partial Q$) and of the polarizability ($\partial\alpha_{\alpha\beta}/\partial Q$),‡. Cartesian dipole moment and polarizability derivatives have been calculated at the B3LYP/aug-cc-pVDZ (with the `SuperFine` grid) level and projected onto CCSD/cc-pVTZ normal modes.†.The " ′ " indicates the derivative with respect to the corresponding normal coordinate.

| | $r^+$ | $r_a^-$ | $r_b^-$ | $d^+(d_1^+/d_2^+)$§ | $d^-(d_1^-/d_2^-)$§ |
|---|---|---|---|---|---|
| | 2927 | 2993 | 2999 | 2917/2924 | 2941/2963 |
| Freq | 2926 | 2992 | 2999 | 2921 | 2951 |
| | 2926 | 2989 | 2998 | | |
| | 0.076 | 0.003 | 0.202 | 0.004/0.204 | 0.000/0.003 |
| $\mu'_x$ | 0.008 | 0.003 | 0.200 | 0.147 | 0.002 |
| | 0.006 | 0.002 | 0.186 | | |
| | 0.001 | 0.260 | 0.003 | 0.000/0.003 | 0.012/0.199 |
| $\mu'_y$ | 0.000 | 0.230 | 0.003 | 0.002 | 0.132 |
| | 0.000 | 0.183 | 0.002 | | |
| | 0.223 | 0.000 | 0.019 | 0.036/0.103 | 0.000/0.000 |
| $\mu'_z$ | 0.171 | 0.000 | 0.021 | 0.137 | 0.000 |
| | 0.183 | 0.000 | 0.032 | | |
| | 8.314 | 0.073 | 6.323 | 6.975/2.105 | 0.229/0.016 |
| $\alpha'_{xx}$ | 7.737 | 0.058 | 6.427 | 4.873 | 0.184 |
| | 7.259 | 0.107 | 5.903 | | |
| | 8.897 | 0.070 | 2.885 | 9.838/2.966 | 0.249/0.003 |
| $\alpha'_{yy}$ | 8.311 | 0.054 | 2.760 | 7.399 | 0.181 |
| | 7.598 | 0.104 | 3.476 | | |
| | 7.522 | 0.002 | 1.502 | 3.927/2.285 | 0.006/0.004 |
| $\alpha'_{zz}$ | 7.387 | 0.002 | 1.564 | 2.923 | 0.001 |
| | 7.102 | 0.002 | 1.239 | | |
| | 0.014 | 2.466 | 0.130 | 0.048/0.001 | 8.581/0.349 |
| $\alpha'_{xy}$ | 0.007 | 1.913 | 0.129 | 0.035 | 6.574 |
| | 0.004 | 3.711 | 0.132 | | |
| | 0.162 | 0.050 | 5.384 | 3.387/0.295 | 0.074/0.015 |
| $\alpha'_{xz}$ | 0.381 | 0.047 | 5.354 | 2.677 | 0.065 |
| | 0.633 | 0.065 | 5.571 | | |
| | 0.005 | 3.922 | 0.072 | 0.042/0.011 | 5.552/1.020 |
| $\alpha'_{yz}$ | 0.004 | 3.650 | 0.072 | 0.037 | 4.688 |
| | 0.008 | 4.841 | 0.075 | | |

*The harmonic vibrational frequencies have been scaled by a factor of 0.96.

†For each property the first, second, and third rows correspond to the Free Chain, Free Ethyl, and Free Methyl models, respectively.

‡ $\alpha'_{xy} = \alpha'_{yx}$; $\alpha'_{xz} = \alpha'_{zx}$; $\alpha'_{yz} = \alpha'_{zy}$.

§ $d_1^+$, $d_2^+$, $d_1^-$, $d_2^-$ ≡ Free Chain; $d^+$, $d^-$ ≡ Free Ethyl.